UNIVERSITY OF BELGRADE

FACULTY OF MECHANICAL ENGINEERING

Mustafa Mohamed Ali Aldarwish

STRESS INTENSITY FACTORS EVALUATION AT TIPS OF MULTIPLE SITE CRACKS IN 2024-T3 ALUMINUM PANELS

DOCTORAL THESIS

BELGRADE, 2018

UNIVERZITET U BEOGRADU
MAŠINSKI FAKULTET

Mustafa Mohamed Ali Aldarwish

Faktori intenziteta napona višestrukih prslina na duraluminijumskim panelima

doktorska disertacija

Beograd, 2018

SUPERVISOR:
Dr. Aleksandar Grbović, associate professor
Faculty of Mechanical Engineering, Belgrade

BOARD OF COMMISSION:

Dr Aleksandar Sedmak, full professor,

University of Belgrade, Faculty of Mechanical Engineering

Dr Danilo Petrašinović, associate professor

University of Belgrade, Faculty of Mechanical Engineering

Dr Dragan Milković, associate professor

University of Belgrade, Faculty of Mechanical Engineering

Dr Gordana Kastratović, associate professor

University of Belgrade, Faculty of Transportation

Date of defense:

DEDICATION

To my parents, my wife, my kids, my teachers, and to the heroes of my country and my city;
To my brothers and sisters for their boundless support,
I dedicate this thesis.

Acknowledgements

First of all, I would like to express my sincere gratitude to my supervisor Professor Aleksandar Grbovic. He offers continuous support to my paper writing, thesis revision and other academic activities such as international conferences, offering numerous suggestions and guides to my research. I also thank Dr. Gordana Kastratović for her encouragement, guidance and support...

A special thank is given to the staffs of Mechanical Engineering Faculty. I appreciate their help and their kindness.

My sincere appreciation, thanks and gratitude to the Libyan academic attaché in Serbia, which has supported me to my further education.

Finally, my sincere appreciation, thanks and gratitude to my wife and kids for their patience during the period of my study.

STRESS INTENSITY FACTORS EVALUTION AT TIPS OF MULTIPLE SITE CRACKS IN 2024-T3 ALUMINUM PANELS

Abstract:

The aim of this thesis was to establish and demonstrate significant capacity and performances of extended finite element method (XFEM) to calculate stress intensity factors (SIFs) histories versus crack length for problems involving multiple, interacting cracks resulting from multiple site damage (MSD). The thesis includes two deferent types of a typical aero structural configuration were analyzed: the first was unstiffened flat panel made of aluminum Al 2024-T3, containing 11 holes, each of which is a site for crack growth. Analyzed model makes a unique 3D configuration with 22 cracks, propagating at the same time; the applied stresses were equal to 50,100 and 200 MPa. The computations were carried out in Morfeo/Crack for Abaqus software which relies on the implementation of XFEM. The accuracy of these computations was verified through FRANC2D/L software and superposition based approximate method. The conducted analysis showed that XFEM is efficient tool for the simulation of crack propagation even in the case of 3D configurations with MSD, and that the obtained solutions can be used for the prediction of SIFs in analyzed MSD configuration with acceptable accuracy.

The second type of aero structural configuration which analyzed in this research using XFEM as following:-

- The first model was unstiffened curved panel with 3 rivet holes containing 6 cracks propagating at the same time; the applied average pressure was (0.054 MPa).
- The second model was unstiffened curved panel with 5 rivet holes containing 10 cracks propagating at the same time; the applied pressure was (0.054 MPa).
- The third model was unstiffened curved panel with 7 rivet holes containing 14 cracks propagating at the same time; the applied average pressure was (0.054 MPa).
- The forth model was unstiffened curved panel with 11 rivet holes containing 22 cracks propagating at the same time; the applied average pressure was (0.054 MPa).

- All curved panels simulations study includes the relationship between crack length and its corresponding SIFs values for every crack propagation step, Also, the study includes the effect of change fuselage diameters from 1.6m, 2.4 m, 3.2 m to 4 m on every crack of the whole models and its SIF values.
- Also, the computations were carried out in Morfeo/Crack for Abaqus software which relies on the implementation of XFEM. The conducted analysis showed that XFEM is efficient tool for the simulation of crack propagation even in the case of 3D configurations with MSD, and that the obtained solutions can be used for the prediction of SIFs in analyzed MSD configuration with acceptable accuracy.
- Additionally, the research includes study and comparisons of SIF values for two flat and curved panels which had the same dimensions and number of the cracks (22 cracks); and study the effect of truss by adding frames on the curved model with 22 cracks, the results showed a high decreasing in SIF values.
- Finally, the research includes some SIFs calculations using standard model. The calculations are done using the empirical equations and NASGROW software. The comparisons showed excellent and accurate results using both methods.

Keywords: fatigue crack growth, multi site damage (MSD), extended Finite Element Method (*XFEM*), NASGRO, FRANC2D/L, *LEFM* - linear-elastic fracture mechanics, stress intensity factor- K_I, curved and flat panels.

Scientific discipline:
Mechanical engineering

Scientific sudiscipline:
Aircraft fatigue design

UDC number:
629.7.023 : 669.71.018] : [539.219.2 : 629.7.018.4(043.3)

FAKTORI INTENZITETA NAPONA VIŠESTRUKIH PRSLINA NA DURALUMINIJUMSKIM PANELIMA

Apstrakt:

Osnovni cilj ove teze jeste demonstracija mogućnosti i značaja proširene metode konačnih elemenata (PMKE) u izračunavanju vrednosti faktora intenziteta napona (FIN) u slučajevima višestrukih međusobno uticajnih prslina nastalih kao posledica pojave višestrukih oštećenja na strukturi (VOS). Teza obuhvata analizu dve tipične aero-strukturne konfiguracije.

Prva od njih je neojačana ravna ploča od duraluminijuma 2024-T3 sa 11 otvora za zakivke, od kojih svaki predstavlja mesto gde je rast prsline vrlo verovatan. Analizirani model čini jedinstvena 3D konfiguracija sa 22 prsline koje rastu istovremeno. Primenjeni naponi na krajevima ploče iznosili su 50, 100 i 200 MPa. Proračuni su sprovedeni u programu Morfeo/Crack for Abaqus koji se oslanja na implementaciju PMKE-a. Tačnost dobijenih rezultata verifikovana je pomoću softvera FRANC2D/L i približne metode zasnovane na principu superpozicije. Izvedena analiza pokazala je da je PMKE efikasan alat za simulaciju širenja prslina u slučaju ravnih 3D konfiguracija sa VOS i da se dobijena rešenja mogu koristiti za predviđanje FIN-a u analiziranoj VOS konfiguraciji sa prihvatljivom tačnošću.

Druga aero-strukturna konfiguracija koja je analizirana korišćenjem PMKE u okviru ovog istraživanja sastojala se iz nekoliko modela VOS-a:

- Prvi model bio je neojačani zakrivljeni panel sa 3 otvora za zakivke i ukupno 6 prslina koje se istovremeno šire iz otvora; primenjeni diferencijalni pritisak iznosio je 0,054 MPa.

- Drugi model bio je neojačani zakrivljeni panel sa 5 otvora za zakivke i ukupno 10 prslina koje se istovremeno šire iz otvora; primenjeni diferencijalni pritisak iznosio je 0,054 Mpa.

- Treći model bio je neojačani zakrivljeni panel sa 7 otvora za zakivke i ukupno 14 prslina koje se istovremeno šire iz otvora; primenjeni diferencijalni pritisak iznosio je 0,054 MPa.

- Četvrti model bio je neojačani zakrivljeni panel sa 11 otvora za zakivke i ukupno 22 prsline koje se istovremeno šire iz otvora; primenjeni diferencijalni pritisak iznosio je 0,054 Mpa.

Sve simulacija širenja višestrukih prslina na zakrivljenim pločama uključuju vezu između dužine prslina i odgovarajućih vrednosti FIN-a za svaki korak širenja prsline. Takođe, u istraživanju je u obzir uzet i efekat promene prečnika krivine panela, pa su vrednosti FIN-a računate za sva četiri modela u slučajevima zakrivljenosti od 1,6 m, 2,4 m, 3,2 m i 4 m. I u ovim slučajevima proračuni su vršeni u programu Morfeo/Crack for Abaqus zasnovan na PMKE.

Analiza dobijenih rezultata pokazala je da je PMKE efikasan alat za simulaciju širenja prslina u slučaju 3D konfiguracija sa VOS i da se dobijena rešenja mogu koristiti za predviđanje zamornog veka sa prihvatljivom tačnošću.

Pored toga, istraživanje predstavljeno u ovoj tezi uključilo je i proučavanje i upoređivanje vrednosti FIN-a u slučaju ravnog i zakrivljenog panela istih dimenzija i broja prslina (dvadeset i dve), kao i proučavanje efekta ojačanja panela dodavanjem okvira na zakrivljenom modelu sa 22 prsline. Rezultati su pokazali značajno smanjenje vrednosti FIN-a na ojačanom panelu.

Najzad, istraživanje je obuhvatilo i određivanje FIN-a korišćenjem standardnih modela u svrhu evaluacije rezultata dobijenih pomoću PMKE. Proračuni su vršeni korišćenjem empirijskih jednačina i NASGRO softvera. Poređenje rezultata je pokazalo vrlo dobro poklapanje vrednosti dobijenih korišćenjem različitih metoda.

Ključne reči: rast zamornih prslina, višestruko oštećene strukture (VOS), proširena metoda konačnih elemenata (PMKE), NASGRO, FRANC2D/L, linearna elastična mehanika loma, faktor intenziteta napona (FIN), zakrivljeni i ravni duraluminijumski paneli.

Nomenclature

FAA	Federal Aviation Administration
WFD	Wide Spread Fatigue Damage
E	Young's modulus
G	Shear stress
ν	Poisson's ratio
K_t	Stress concentration factor
σ_{peak}	Peak stress
σ_{normal}	Normal stress
K	Stress intensity factor
ρ	Tip radius of elliptical hole
K_{1c}	Fracture toughness
K_I, K_{II} K_{III}	Stress intensity factor on tension, sliding and tearing modes
r	The distance between crack tip and the stress element
σ_x, σ_y	Tensile stress in directions X and Y
τ_{xy}	Shear stress normal to x and in y direction
$\frac{da}{dN}$	Fatigue crack growth rate
σ_y	Yield stress
COD	Crack opening displacement
ΔS_{eff}	Effective stress range
S_{op}	Crack opening stress
R	Stress ratio
CL	Crack length
β	Geometry factor
ΔK_{th}	The threshold value

Table of contents

Figures Content

List of tables

Chapter 1 Multiple Crack Problems

1.1 DAMAGE CLASSIFICATION

According to relevant literature [1, 2, and 3], it can be concluded that aircraft structure that contains multiple cracks can be classified into two different categories:

1. Multiple-site damage (MSD): simultaneous development of fatigue cracks on multiple sites in the same structural element, such that the fatigue cracks can be merged into one big crack.
2. Multiple element damage (MED): simultaneous development of fatigue cracks in similar adjacent structural elements, which leads to multiple interactions of these cracks.

1.2 SITES AND CAUSES OF MULTIPLE DAMAGE OCCURENCE

The whole aircraft structure is composed from of large number of parts, which are connected by means of permanent connection elements such as so-called full rivets. During the flight the joint is loaded by membrane stress due to putting the passenger carbine under pressure. As the result of this load stress concentration appears around connection holes. It is concentration of stress that leads to the occurrence of initial cracks that lead to the occurrence of the above-mentioned multiple damage.

Therefore, it can be concluded that multiple cracks appear in zones where there is a concentration of stress, and those are joints in the first place. Of course, some joints are more vulnerable to phenomena of multiple damage.

1.2.1 Aircraft parts those are more vulnerable to the occurrence of fatigue damage

- Longitudinal skin and frame lap joints (MSD/MED);
    - At outer skin the upper row of holes;

- At inner skin lower row of holes;

- Circumvential joints and stringers (MSD/MED);
- Fuselage frames (MED);
- Connections of stringers and frames (MED);
- Fasteners on fuselage frames loaded in shear (MSD/MED);
- Sudden changes in the structure or the thickness of the skin (MSD/MED);
- Structure parts around windows (MSD/MED);
- Connections of skin and wing rib (MSD/MED).
- Typical wing and tail surfaces constructions (MSD/MED);

The zones where these kinds of damage appear are critical zones in terms of structural integrity of the aircraft; therefore the accumulated damage in these zones can result in the loss of it, which in the worst scenario it can lead to catastrophic failure.

As stated before, rivet holes in aircraft structures are common sources of stress concentration. On those sites local stresses may be increased three or more times [4]. Besides being directly dependent on putting pressure on the fuselage, membrane stress depends on aerodynamic pressure. Aerodynamic pressure appears from point to point due to the aircraft fuselage shape, and its values are around 3.3 kPa. This will locally increase the difference between pressure and therefore, the stresses. This can be explained why the production of MSD prevails on the joints of fuselage at rear right after the pilot cabin.

More one area where this effect is evident is near the connection of the aircraft wing-fuselage [5].

Under ideal conditions, longitudinal fracture cracks (that are more dangerous than edge cracks due to major peripheral stresses) will be stopped whether on frame or reinforcement or they will be bended in peripheral direction. The aircraft accident of Aloha Airline shows that the design caracteristics under the principle "fail-safety", when it comes to the joints on the fuselage lap, can be cancelled, and therefore it can be allowed the expansion of longitudinal fracture through the distance between several frames. In aging of transport aircrafts with huge fuselage, the MSD problem is composed of combined effects of fatigue and corrosion. This phenomenon is characterized by the existence of small, longitudinal cracks that begin to spread from adjacent rivet holes. The probability of its detection,

associated with conventional non-destructive inspection methods (NDI) is relatively low: but still, these small cracks can be merged in domino effect and cause unstable longitudinal fracture which can cancel the installed "fail-safety" design principle [6]. MSD is particularly tricky because it is often difficult to be detected. The MSD problem can be further aggravated by the existence of cracks in structural elements associated with varying degrees of debonding and corrosion of joints on the lap.

When it is untouched, the connection by bonding that connects the joint on the lap is very effective way of transferring the load, and really, it reduces the load transfer via the rivets. In order MSD to become a problem, this connection firstly has to be degraded. As the consequence, it is unlikely that the MSD occurs at the beginning of usage, because it takes time to debond. Because of that, and because the probability for discover is actually zero in earlier phases of MSD, it is uneconomical adhere the prescribed intervals between inspections from the initial moment of exploitation. Because of that is established the inspection threshold as the condition that the MSD inspections are not necessary to be performed before certain number of flights [7].

MSD is a major importance because the small cracks, those do not represent the safety threat themselves, can be merged, which leads to catastrophically structure failure. The same, critical magnitude (longitude) of the crack for MSD, based on the size of the external crack can be much smaller than that in the case of individual cracks, which make the critical crack harder to be detected and makes the performance of standard inspection procedure unsuccessful [8].

Figure 1.1 shows the comparison of crack growth curves for individual isolated damage and for multiple damage. From this figure it can be seen that the time for MSD discovery is significantly shorter due to occurrence of merging, than it is the case of individual damage.

To predict the crack growth and fracture strength of connections with rivets that have been subjected to widespread fatigue damage, it is requires accurate stress and fracture analysis of edge and surface cracks in the rivet holes. The examination of aged aircraft , that is performed throughout the world, is focused on development and introduction of advanced ideas of fracture mechanics and fatigue analysis methodology of tolerated (allowed) damage for the old, current and next-generation aircraft fleet. This operation includes the

development and introduction of new methodologies for widespread fatigue damage (WFD) [9].

From reports made according the experience from the exploatation, connections with rivet joints on lap are identified as one of the critical locations on aircrafts that are susceptible to WFD. WFD is usually occurred at those connections in the form of multiple cracks that

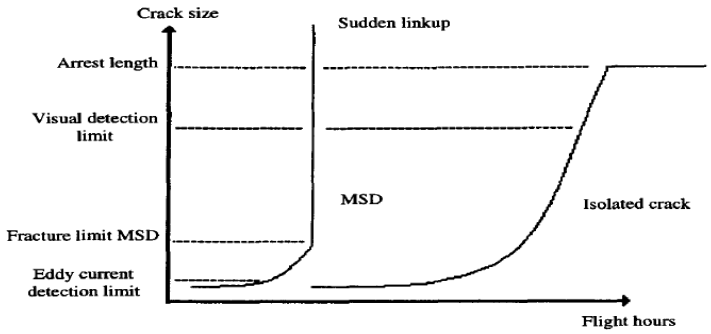

Figure 1-1 Crack growth with and without MSD

begin with the expansion of sources of stress concentration at the rivet holes. Therefore, one of the goals of research programme of aircraft aging with widespread fatigue damage of Federal aviation administration the technology development that will enable the prediction of crack occurrence, crack growth rate, as well as the residual strength of aircraft structures that are exposed to WFD. In order to predict with certainly the speed of crack growth and the fracture strength of connections with rivets that are under WFD, it is necessary the precise analysis of stresses and fractures of angular and surface cracks on rivet holes.

1.2.2 Parameters that influence to the emergence and development of multiple damage and cracks

- Age;
- Construction:
    - Errors in the production – surface preparation processes;
- Production:
    - Surface preparation;
    - Countersunk connection holes, fitting of the connection elements;

- Load:
    - High stresses- pulling and pressure combined;
    - Large load transfers – large local stresses;
- Material:
    - Material characteristics;
    - Inhomogeneities in the material;
- Surrounding:
    - Corrosion;
    - Separation (ungluing);

Regarding the causes of multiple cracks, first of all stated is fatigue that is a result of aircraft aging and many years of their exploitation. Beside it, the occurrence of multiple cracks is affected by design and manufacture of aircraft parts, during which it may occur defects and microscopic damage that are the nucleus from which begins the development of initial cracks. Also, during the assembly of the aircraft subassemblies it may also appear the damage during the preparation of surfaces and elements fits.

Load is also one of the major causes of multiple cracks in many ways. In addition to the basic cyclic loading that occurs during each year as a result of putting the aircraft under pressure, there is a load transfer from one to another structural component, whereby, due to the sudden changes in geometry, the load concentrations occur, e.g. high local stresses.

Material of which the aircraft parts is made also an important factor, and the material properties, and inhomogeneities in its structure, which resulted in the technological process, and which is, at present, impossible to avoid.

Finally, the various environments in which the aircraft is exploited affects the structure weakening and the emergence of multiple damage, that caused the inevitable corrosion of metal parts as well as damage to the materials used for bonding.

It is possible to define only empirically the impact of most of these parameters. Which of them will have the greatest impact on the emergence and development of multiple cracks depends exclusively on the operating conditions that differ from aircraft to aircraft. This suggests that differences in terms of production and exploitation, no matter how small they

are, represent themselves one of the parameters of occurrence and development of multiple cracks.

1.3 TOLERATED (ALLOWED) DAMAGE

Based on the above, we can conclude that the processes of aircraft design and construction are closely linked with the problems of multiple fatigue damage, ie. that with adequate rules for the production and, in particular, the exploitation of the aircraft, the occurrence of these defects can be prevented and controlled in order to increase the safety and reliability of aircraft in use, which will ultimately lead to an increase in the projected lifetime of use.
There are three different approaches to the production and design of aircraft.
The first approach is the approach of "safe lifetime". With this design principle for the given component it is assumed to be safe under the conditions of prescribed workload for a given number of operating cycles. After this limit is exceeded, the component is automatically replaced. Reliable period of selected lifetime largely relies on experimental data. The disadvantage of this method is that some components are often replaced unnecessarily, and there is a tendency creating many oversized components in order to provide an acceptable lifetime. This tendency towards design with excessive safety coefficient (oversizing), and the rejection of the components that are still potentially useful, inevitably leads to reduced efficiency. This is why most of the aviation industry moved to the design principle "failure-safe". When applying the design principle "fail-safe" it is understood that the whole structure must be able to withstand a certain amount of damage without catastrophic failure of the entire structure. This design principle generally leads to the inclusion of additional elements of load paths and elements for preventing the occurrence of cracks in the structure. The key of this principle is that the designer must know the areas that are critical to fracture and must be able to review them, so that maintenance can be carried out. But determining exactly where the critical areas are is not easy.

In December 1978, FAA conducted updates of its demands for the assessment of fatigue for airplanes from transport category in order to take into account the principle of designing "tolerated (allowed) damage" [10].

In the approach of tolerated (allowed) damage to aircraft safety, for each structure it is assumed to contain the initial cracks or defects that will be larger during the usage. Therefore the suitable inspection techniques must be defined and the intervals between them so the critical cracks could be detected and the repairs or modifications / replacements performed. This design principle is based on a thorough knowledge of lifetimes of structures that are exposed to fatigue, and they must be complemented with the rigorous analytical and experimental studies.

In the analysis of tolerated damage, the zones in aircraft structures which are critical for fracture should be identified and analyzed in order to deterministically anticipate the development and growth of (assumed) initial fatigue cracks. These analyzes require:

(a) a representative stress range from which it can be performed stress distribution during the flights;

(b) Coefficients of stress intensity factors in order to take into account differences in the geometry of the elements; and

(c) Crack growth rate as a function of the stress intensity factor.

That information can be used to predict crack growth ratio in time, in the working environment. These ratios, together with probability of detection curves (POD) for measuring the ability of the inspection, give curves from which it can be expressed the approach of tolerated damage to establishing the interval between inspections [11].

The big advantage of this approach is that with constant monitoring of the growth of cracks during the usage it is provided the feedback loop mechanism due to which inspection techniques and the intervals between them can be modified in order to achieve a continuous flight capacity.

The application of the design principle of tolerated damage requires the knowledge of the required number of load cycles for the crack growth from a minimum length that can be detected up to a critical crack length. On that basis it should be evaluated the intervals between inspections, as well as based on the data obtained from laboratory tests and

experience in usage. On the other hand, it should be shown that the fatigue crack growth to a critical length requires so much time that, even taking into account the excellent dissipation factor, it covers a designed time of structure usage. For the real structures, forecasting the growth rate of fatigue cracks and time of growth crack require the use of representative results of tests conducted under realistic load, work environment and load during the flight [12]. Big mistakes often occur in the analysis of the growth and development of cracks because of the introduction of assumptions and idealization, such as, for example, the assumption that circular cracks in relation to the cyclical ones can influence the increase of the factors for assessing the lifetime to 2 or 3 times [13].

Aircraft structures are designed so that at any stage of their usage life should not appear that the residual strength is below the limit load. It is assumed the structure is fractured and it is also assumed that there is a growth and development of cracks. In the early stages of usage the crack growth is proportionally slow. If the control is not performed, the length of the crack will eventually reach a critical size. Therefore, cracks must be detected and repaired before they reach the maximum allowed length, which is by definition less than the critical size. Requirements of tolerated damage determine the minimum of permitted residual strength.

According to the diagram of residual strength, an aircraft manufacturer can calculate the permitted length (the size) of the crack. Requirements of tolerated damage also define (the smallest) size of the crack which can be detected, and which is herein defined as "apparent size (length)". The interval between inspections is so defined that two intervals pass before it reaches the permitted size of the crack [13].

The requirements of tolerated damage and for the US Air Force and Civil Aviation suggest that the crack should be checked at least twice before it reaches the permitted size, regardless of when it occurred. This means that the aircraft can be used indefinitely until every crack that appears is detected, controlled and if the appropriate maintenance actions are taken. For civil aircraft the best interest for the manufacturer to ensure that the inspections are not too often because it directly affects the maintenance costs, which, in turn, affect the sales. If the interval between inspections is too short, there are various options that producers can use to extend the interval:

(i) The use of complex techniques of inspection, for example, testing with the eddy currents rather than visual inspection, which can detect cracks of smaller size;

(ii) Reduce the stress or stress concentration in structural elements in order to obtain a slower development of crack;

(iii) The use of different materials with better properties in terms of growth of the crack (ie slower growth); or

(iv) Creating additional "fail-safe" features.

Briefly, the main objective of tolerated damage is to ensure that the structure bears the greater part of its designed load, even when the damage occurs.

The basic philosophy of tolerance structural damage is based on:

Acceptance of the fact that the damage is to occur in any event, in spite of all taken precautions. Adequately prescribed control system, such that the damage can be seen and to perform the repair in time. Adequate residual strength (fracture toughness) of damaged material, so that during the period between controls in which the damage is still undiscovered, fatal failure is not possible.

The importance of adapting the approach of tolerated damage during the design of the structure must be emphasized for the following reasons:

Great difficulties of predicting the place and moment of damage due to fatigue due to the large difference in workloads; after several years of using, the structure itself will not be the same as the one tested in the design phase, due to the harmonization of corrections and modifications realized during usage.

Chapter 2 Background and Literature Review

2.1 FRACTURE MECHANICS FUNDAMENTALS

Fracture Mechanics is that technology concerned with the modeling of cracking phenomena. Bulk (smooth specimen) properties are not normally useful in design for determining a material's tolerance to cracks or crack-like defects, because material tolerance to flaws resides in a material's ability to deform locally. Since the source of fractures can be identified with the lack of material tolerance to cracks, it seems only natural that attention should be focused on the crack tip region where the material must resist crack extension. This section will introduce the principal features of a mechanical model that characterizes a crack movement in structural components fabricated from materials having low tolerance to flaws, [14].

2.1.1 Stress Concentration at Notches

Calculations on the strength of structures are primarily based on the theory of elasticity. If the yield stress is exceeded plastic deformation occurs and the more complex theory of plasticity has to be used. Fatigue, however, and also stress corrosion, is phenomena which usually occur at relatively low stress levels, and elastic behavior may well be assumed to be applicable. The macroscopic elastic behavior of an isotropic material is characterized by three elastic constants, the elastic modulus or Young's modulus (*E),* shear Modulus (*G*) and Poisson's ratio (*ν*). The well-known relation between the constants is $E = 2G(1 + \nu)$.

In a structure, geometrical notches such as holes cannot be avoided. The notches are causing an inhomogeneous stress distribution, see Figure 2.1, with a stress concentration at the "root of the notch". The (theoretical) stress concentration factor, *Kt,* is defined as the ratio between the peak stress at the root of the notch and the nominal stress which would be present if a stress concentration did not occur.

The severity of the stress concentration is depending on the geometry of the notch configuration, generally referred to as the shape of the notch. Designers should always try

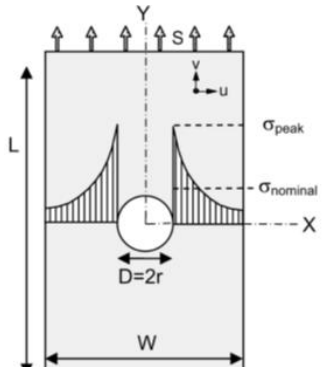

Figure 2-1 Strip with central hole as a prototype of a notched part

$$K_t = \frac{\sigma_{peak}}{\sigma_{normal}} \qquad 2.1$$

to reduce stress concentrations as much as possible in order to avoid fatigue problems.

2.1.2 Stress Intensity Factors of Cracks

Stress concentration factor Kt as an important parameter for characterizing the severity of the stress distribution around the notch. The crack initiation life is highly dependent on the Kt -value. The crack initiation period is followed by the fatigue crack growth period, see Figure 2.2. For a crack, the K_t-value is no longer a meaningful concept to indicate the severity of the stress distribution around the crack tip. Because a crack is a notch with a zero tip radius, K_t would become infinite, and this would be true for any crack length. A new concept to describe the severity of the stress distribution around the crack tip is the so-called stress intensity factor K. This concept was originally developed through the work of Irwin [15]. The application of the stress intensity factor to present fatigue crack growth data and to predict fatigue crack growth is referred to as "linear elastic fracture mechanics".

The difference between a notch and a crack can be illustrated by considering an elliptical hole (semi-axes a and b, tip radius ρ). In an infinite sheet loaded in tension, the stress concentration factor Kt is given by:

$$K_t = S\left(1 + 2\frac{a}{b}\right) = S(1 + 2\sqrt{\frac{a}{\rho}}) \qquad (2.2)$$

with the tip radius $\rho = b^2/a$. The elliptical hole becomes a crack by decreasing the minor axis b to zero. If $b = 0$ the hole is a crack with a tip radius $\rho = 0$, and according to

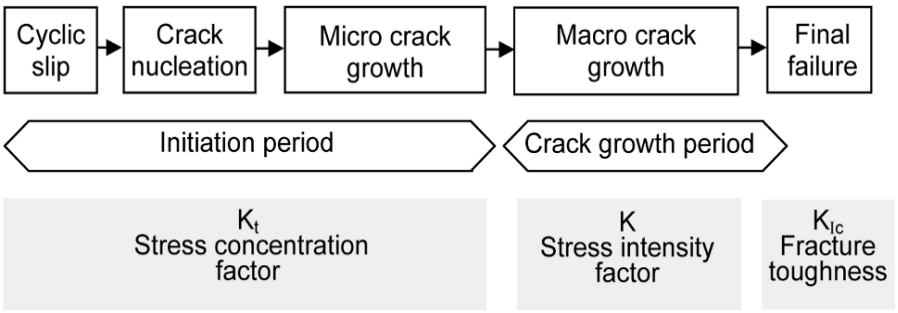

Figure 2-2 Different phases of the fatigue life and relevant factors.

Equation (2.2) $K_t = \infty$, regardless of the semi-crack length. This result is not useful. However, the stress distribution around the tip of a crack shows a characteristic picture. This is illustrated in Figure 2.3 by photo-elastic results of a specimen with three cracks loaded in tension. Apparently, similar isochromatic pictures occur at the tips of the three cracks, which suggests similar stress distributions at the crack tips. The "intensity" of the crack tip stress distribution is depending on the stress intensity factor K which can be written as:

$$K = \beta S \sqrt{\pi a} \tag{2.3}$$

In this equation, S is the remote loading stress, a is the crack length, and β is a dimensionless factor depending on the geometry of the specimen or structural component. The important feature is that stress distribution around the crack tip can be fully described as a linear function of the stress intensity factor K. The concept of the stress intensity factor is presented in this section. First, different types of cracks are listed, followed by more details about stress intensity factors for several geometries. Some basic aspects of the stress analysis of cracked configurations are addressed including differences between plane stress and plane strain situations, crack tip plasticity and determination of K factors. The basic principle of the application of K factors to fatigue crack growth is considered.

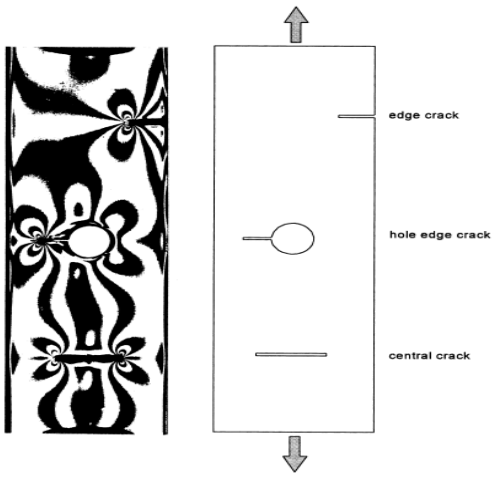

Figure 2-3 Photo-elastic pictures of a specimen with three different types of cracks. Note the similar butterfly pattern at each crack tip.

2.1.2.1 Different types of cracks

Fatigue cracks in service usually grow in a direction which is macroscopically perpendicular to the main principle stress. In many cases that is perpendicular to the tensile stress that tries to open the crack. This kind of crack opening is called "mode I", see Figure 2.4. In principle, other modes of crack opening are possible, see modes II and III in the same figure. It could be supposed that these modes will occur under cyclic shear stress.

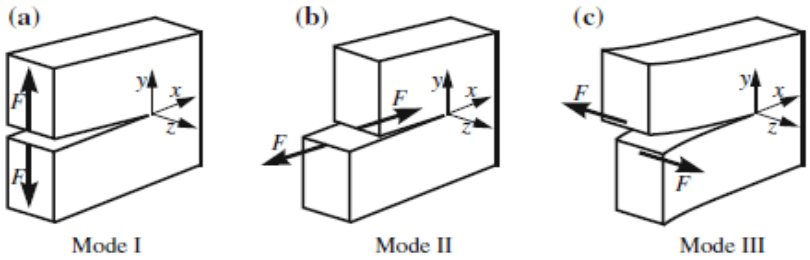

Figure 2-4 Three different crack opening modes.

However, experience has shown that small cracks, nucleated under pure shear loading, quickly exhibit a transition to fatigue crack growth in the tensile mode, i.e. mode I. This appears to be reasonable from a physical point of view, because the tensile stress component, which opens the crack, will certainly promote the conversion of cyclic plastic

deformation into crack extension. Fatigue cracks growing through the entire thickness are referred to as through the thickness cracks, or simply *through cracks*, see Figure 2.5. If the fatigue load is cyclic tension only,

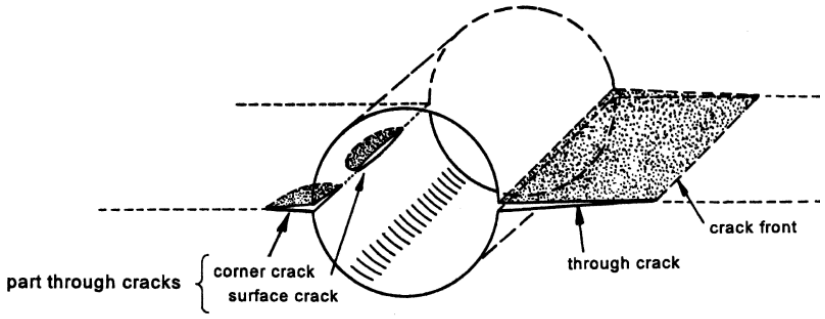

Figure 2-5 Different types of cracks starting from a hole.

without bending, the crack front is perpendicular to the material surface. However, in thick material, and in general for smaller cracks, the crack front does not pass through the full thickness. The crack front then is generally curved. Figure 2.5 shows two such cracks, a *corner crack* and a *surface crack*. Corner cracks and surface cracks are also labeled as *part through cracks*. A through crack with the crack front perpendicular to the material surface is usually treated as a two-dimensional (2D) problem. For part through cracks this is no longer allowed. The stress analysis then is a 3D problem, and thus more complicated.

2.1.2.2 Definition of the stress intensity factor

Because a crack can be considered to be an elliptical hole with zero height, an exact solution is also available for an infinite sheet with a crack. Unfortunately, the stress components cannot be written as simple functions of the (x,y) coordinates. However, if the attention is restricted to the area around the crack tip, explicit functions are obtained by considering analytic limits for a short distance of a point (x,y) to the crack tip, i.e. relatively short as compared to the crack length. In Figure 2.6 it implies that

$$r \ll a \tag{2.4}$$

With polar coordinates the following equations are then obtained for a crack in an infinite sheet loaded in tension, see Figure 2.6:

$$\sigma_x = \frac{S\sqrt{\pi a}}{\sqrt{2\pi r}} cos\frac{\theta}{2}\left(1 - sin\frac{\theta}{2} sin\frac{3\theta}{2}\right) - S \tag{2.5a}$$

$$\sigma_y = \frac{S\sqrt{\pi a}}{\sqrt{2\pi r}} cos\frac{\theta}{2}\left(1 + sin\frac{\theta}{2} sin\frac{3\theta}{2}\right) \tag{2.5b}$$

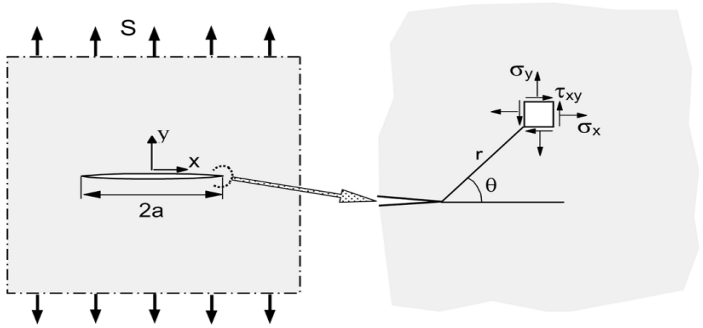

Figure 2-6 Infinite sheet with a mode I crack. Definition of coordinates.

$$\tau_{xy} = \frac{S\sqrt{\pi a}}{\sqrt{2\pi r}}\ cos\frac{\theta}{2}\ sin\frac{\theta}{2}\ cos\frac{3\theta}{2} \tag{2.5c}$$

The equations are asymptotically correct for small values of r. It implies that they are a good approximation in the crack tip region. The equations are characterized by some noteworthy features:

(i)The stress distribution at the crack tip shows a singularity, because all stress components go to infinity for $r \rightarrow 0$ for each value of θ. They increase with $1/\sqrt{r}$. Of course an infinite stress cannot be present at the crack tip. Some crack tip plasticity must occur.

(ii) A non-singular finite term (S) occurs in Equation (2.5a) for σ_x. In general, this term is negligible as compared to the first singular term of the equation. For this reason, the term -S is usually omitted. But an interesting result applies to the upper and lower edge of the crack, i.e. for $\theta = \pm 180^\circ$. For these θ-values the singular term is zero, and thus $\sigma_x = S$, a compressive stress equal to the remote tensile stress.

Although Equations (2.5) apply to the crack tip area only, the exact solution for the full sheet indicates that $\sigma_x = S$ along the entire upper and lower edges of the crack.

(iii) It is noteworthy that π occurs in the square root terms of both numerator and denominator in Equations (2.5). Consequently, π could have been omitted, and that would change the definition of the K factor by a factor, $\sqrt{\pi}$. Although this was done in some older publications, it was not done later on, and historically the π survived.

After neglecting the non-singular term $(-S)$ in Equation (2.5a), the three equations can be written as

$$\sigma_{i,j} = \frac{K}{\sqrt{2\pi r}} f_{i,j}(\theta) \tag{2.6}$$

With

$$K = S\sqrt{\pi a} \tag{2.7}$$

The above equations apply to a mode I crack in an infinite sheet loaded in tension. However, it can be shown that the equations are also applicable to elements with finite dimensions provided that the geometry is symmetric with respect of the X-axis in order to have still mode I cracks. The finite dimensions are accounted for by a geometry correction factor β in the equation for the stress intensity factor:

$$K = \beta\, S\sqrt{\pi a} \tag{2.8}$$

for an infinite sheet β = 1.

The function $f_{i,j}(\theta)$ in Equation (2.6) determines the picture of the stress distribution around the crack tip, while K represents the severity of the stress intensity with (β) as the dimensionless geometry factor. The term $1/\sqrt{\pi . r}$ indicates how fast stresses decrease away from the crack tip. In summary, Equation (2.8) defines K as the characteristic parameter for the stress intensity around the crack tip. According to Equation (2.8), the unit of the stress intensity factor is $(\frac{N}{m^2})\sqrt{m}$ = Pa$\sqrt{m}$ (N= Newton, Pa = Pascal = $\frac{\mathrm{N}}{\mathrm{m}^2}$).

Because $Pa\sqrt{m}$ is a rather small unit, the 106 times larger unit,$MPa\sqrt{m}$, is usually adopted. Another unit is $ksi\sqrt{in}$ with 1 $ksi\sqrt{in}$ = 1.10 $MPa\sqrt{m}$ which implies a 10% difference.

It is not correct to think that the stress concentration factor Kt and the stress intensity factor K are somewhat similar concepts for a notch and a crack respectively. Both concepts are

based on the theory of elasticity. However, K_t is a dimensionless shape factor which accounts for the geometry only, and not for the load applied. The stress intensity factor K accounts for both, and thus can no longer be dimensionless. It may be said that K_t and β both serve a similar purpose by accounting for the shape only.

2.1.3 Description of fatigue crack growth properties

2.1.3.1 Fatigue crack growth regions

Fatigue crack growth results as shown in Figure 2.7 cover a range of ΔK-values and crack growth rates. It does not give indications about crack growth rates outside this range. More extensive experiments have shown that two vertical asymptotes occur in a da/dN-ΔK graph, see Figure 2.7. The left asymptote at $\Delta K = \Delta K_{th}$ indicates that ΔK-values below this threshold level are too low to cause crack growth.

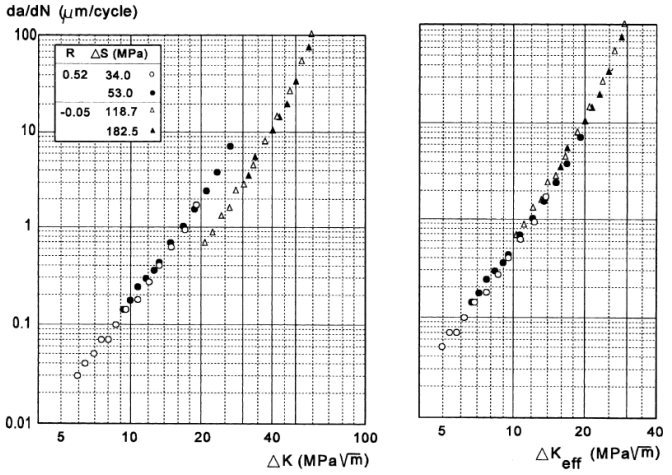

(a) da/dN as a function of ΔK (b) The results of (a) plotted as a function of ΔK_{eff}

Figure 2-7 The crack growth rate in sheet specimens of an Al-alloy (2024-T3) for two R-values and two S_a-values for each R-value [14].

The other asymptote at the right-hand side occurs for a ΔK cycle with $K_{max} = Kc$. It means that (K_{max}) reaches a critical value which leads to complete failure of the specimen. If da/dN is plotted as a function of ΔK on a double log scale, the function da/d$N = f_R(\Delta K)$ is supposed to cover three different parts, indicated by I, II and III in Figure 2.8. The corresponding ΔK-regions are referred to as:

(i) The threshold ΔK-region, (ii) the Paris-ΔK-region, and (iii) the stable tearing crack growth region.

The threshold region

The threshold region is not associated with the non-propagating microcracks. These

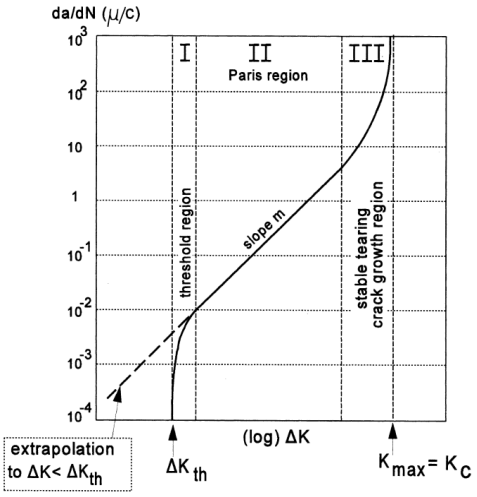

Figure 2-8 Three regions of the crack growth rate as a function of ΔK.

microcracks were nucleated at the material surface, but due to microstructural barriers, they could not penetrate into the material. The cracks remained microcracks. The threshold value ΔK_{th} in this section is associated with macro fatigue crack growth. It implies that ΔK_{th} is concerned with fatigue cracks which have grown to a macroscopic size at a ΔK level above ΔK_{th}. If ΔK is then decreased, crack growth slows down and it is assumed that no further growth occurs if ΔK is below ΔK_{th}.

The Paris region

According to Paris [16], the relation between $\frac{da}{dN}$ and K can be described by a power function:

$$\frac{da}{dN} = C\,\Delta K^{m} \tag{2.9}$$

with C and the exponent m as material constants. The equation in a double log plot gives a linear relation: $\log\left(\frac{da}{dN}\right) = \log(C) + m\,log(K)$ with m as the slope of the linear function,

see Figure 2.8. Equation (2.9) has some limitations. It does not account for the *R*-effect on crack growth, neither for the asymptotic behavior in regions I and III. Several alternative functions have been proposed in the literature to overcome this problem. Some are mentioned below. Forman [17] proposed the following:

$$\frac{da}{dN} = \frac{C\,\Delta K^m}{(1-R)(Kc-Kmax)} \tag{2.10}$$

Because of the term $(Kc - K_{max})$ in the denominator, d*a*/d*N* will become very large if K_{max} is approaching K_c. The right asymptote in Figure 2.8 is thus taken care of by Equation (2.9). The effect of the stress ratio R is also accounted for by the term (1−R) in the denominator. But the ΔK_{th} asymptote is not yet included. This is obviously done in the numerator of an equation proposed by Priddle [18]:

$$\frac{da}{dN} = C\left[\frac{\Delta K-\Delta K_{th}}{K_C-K_{max}}\right]^m \tag{2.11}$$

More similar equations satisfying the two asymptotic conditions are possible, e.g. a similar function as Equation (2.11), but with different exponents m_1 and m_2 for the numerator and the denominator respectively. The value of ΔK_{th} in such equations is supposed to be a function of *R*, for which again functions were proposed in the literature, e.g. by Klesnil and Lukáš [19]:

$$\Delta K_{th} = A(1-R)^{\gamma} \tag{2.12}$$

Constants in the above equations depend on the type of the material. It should be understood that none of the formulas can claim a physical background. They are proposed to agree with trends observed in test results. It then requires some regression analysis to arrive at the values of the constants. It sometimes requires a K_c-value different from the measured fracture toughness. It is suggested in the literature that such equations are useful in view of prediction algorithms but this argument is not really appropriate. However, a useful indication can be drawn from the Paris relation (Equation 2.9) if the exponent m is known from experiments. Substitution of the K formula in the Paris relation gives:

$$\frac{da}{dN} = C\left(\beta\,\Delta S\,\sqrt{\pi.a}\right)^m = C\left(\beta\sqrt{\pi a}\right)^m \Delta S^m \tag{2.13}$$

If the design stress level on a structure is changed, the value $C\left(\beta\sqrt{\pi a}\right)^m$ remains the same because it depends on the crack length only. A different design stress level affects ΔS but it leaves the R ratio unaffected. As a consequence, the crack growth rate is changed proportionally to ΔS^m. Because that is true for any crack length, the crack growth life is inversely proportional to ΔS^m. As an example, consider an increase in the stress level of 25%. For m = 3, which is the order of magnitude for several materials, the crack growth rate is increased with a factor $1.25^3 = 1.95 \approx 2$. It implies that the crack growth life in the Paris region is approximately halved.

Stable-tearing crack growth region

The crack growth rate in the stable-tearing crack growth region is high, in the order of 0.01 mm/cycle and above. Observations on the fatigue fracture surface in the electron microscope still reveal patches of fatigue striations caused by a number of successive cycles. However, the striation spacing is generally smaller than da/dN derived from the crack growth curve a(N). Local areas of ductile tearing are observed between the patches of striations. Ductile tearing does not yet occur along the entire crack front, and for that reason crack growth is still a stable process. Further crack growth requires additional cyclic loading, but the stable ductile tearing areas indicate that unstable final failure is imminent. The crack growth life spent in this region is very short, which implies that its engineering significance is limited. Predictions on the occurrence of the final unstable failure are apparently simple, because it should occur if $K_{max} = K_c$. By definition, K_c is the stress intensity factor causing final failure. However, usually Kc for structural materials is not a constant material property. Final failure for several materials with some ductility occurs when the remaining net section is plastically yielding over its entire width (net section yielding). In such cases, the value K_c as a stress intensity factor is meaningless. The stress intensity factor is based on elastic material behavior with small-scale yielding at the crack tip only. Moreover, in K_c experiments substantial stable crack extension can occur before the unstable situation is reached. It depends on the dimensions of the specimen.

2.1.4 Crack closure

2.1.4.1 Plasticity induced crack closure and ΔKeff

In the late sixties, Elber [20] discovered that a fatigue crack under a tension load was already closed during unloading before the tension stress became zero. It implies that the crack tip is closed at a positive tension stress, which was an unexpected result at that time. This observation has significant consequences for crack growth predictions. How it is possible that crack closure occurs at a positive stress, and how can it be shown to occur in experiments. Furthermore, what are the consequences for fatigue crack growth predictions based on the similarity principle? A sheet specimen with a central crack is considered for a discussion on these questions. During cyclic loading, plastic deformation occurs at the crack tip. Although this is "small-scale yielding", it implies that a plastic zone is created when the stress goes from S_{min} to S_{max} ("uploading"). The size of the plastic zone at S_{max} is proportional to $(K_{max}/\sigma_{yield})^2$. The plastic zone is plastically elongated in the loading direction. It becomes longer than it was before. As a consequence, the zone is loaded in compression during unloading, and reversed plasticity occurs. As pointed out by Rice [21], reversed plasticity requires a local stress increment in the reversed direction in the order of twice σ_{yield}. It implies that the reversed plastic zone size should be in the order of 1/4 of the plastic zone created during loading. Thus the reversed plastic zone is significantly smaller than the plastic zone obtained when S_{max} is reached as schematically indicated in Figure 2.9. Plastic deformation in the much larger area of the plastic zone outside the reversed plastic zone has occurred only during loading to S_{max}. This is called monotonic plasticity, and it is this monotonic plastic deformation which is causing a permanent elongation in the loading direction. Crack tip plasticity occurs in every cycle and the crack is thus growing through plastic zones of previous cycles. As a result, plastic deformation is left in the wake of the crack. In this plastic wake field, the larger part of the material has been subjected to monotonic plasticity during uploading (Figure 2.9). A much smaller rim of material along the crack edges has been subjected to cyclic plasticity. The material in the plastic wake field is plastically extended in the loading direction. This explains why the crack can be closed during unloading while the specimen is still under a positive tensile stress, i.e. before the specimen is unloaded. The phenomenon is known in the literature as *plasticity induced*

crack closure, sometimes labeled as the Elber mechanism.

Elber observed the occurrence of crack closure by measuring the crack opening displacement (COD) between points A and B at the centre of the specimen close to the crack edges, see Figure 2.10. He measured the COD as a function of the remote stress *S.*

The COD-S record started with a non-linear part until S = Sop. Above this stress level, a linear relation was found as expected for an elastic behavior. Unloading from Smax to S= 0

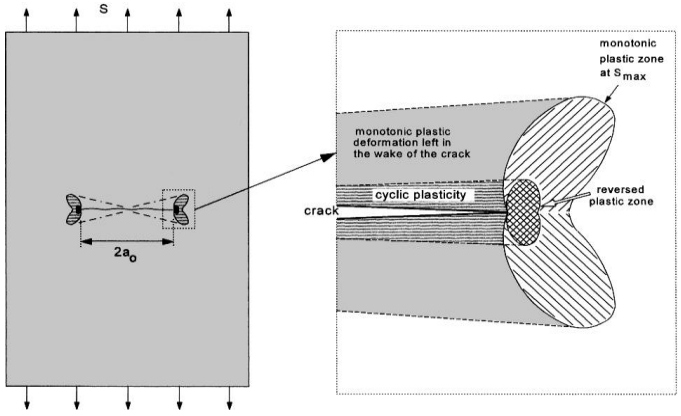

Figure 2-9 Plastic zones of a growing crack leave plastic deformation in the wake of the crack.

occurred practically along the same COD-S record in the reversed direction as indicated in Figure 2.10. A specimen with a saw cut instead of a fatigue crack does not have a plastic wake field, and the COD-S record shows a fully linear behavior. If the fatigue crack and saw cut have the same length, the linear parts of the two COD-S records are parallel, see Figure 2.10. The same slopes indicate the same stiffness. Moreover, the slope agreed with the calculated stiffness for the specimen with an open crack.

The fatigue crack thus must be fully open during the linear part of the COD-S record. For *S* lower than *S*op, the slope of the non-linear part of the COD-S record becomes larger, the stiffness is higher, and the specimen behaves as if the crack is shorter. This is a consequence of the crack being partly closed due to the excess of plastically elongated material in the wake of the crack. Upon unloading, crack closure starts at the tip of the crack, which continues away from the crack tip at a decreasing stress level.

During cyclic loading, crack closure occurs if S_{min} < Sop (Figure 2.11). The crack is partly (or fully) closed at S_{min}. The crack tip during loading is just fully open at S = S_{op}, and then remains open up to S_{max}.

Upon unloading, the crack is open until crack closure starts at the crack tip. The corresponding closure stress level, S_{cl}, is usually assumed to be approximately equal to S_{op}. Although small differences between S_{op} and S_{cl} might occur, accurate measurements of these stress levels are difficult also because they are a transition point between a linear and a non-linear part of the COD-S record in Figure 2.10. The important aspect to be

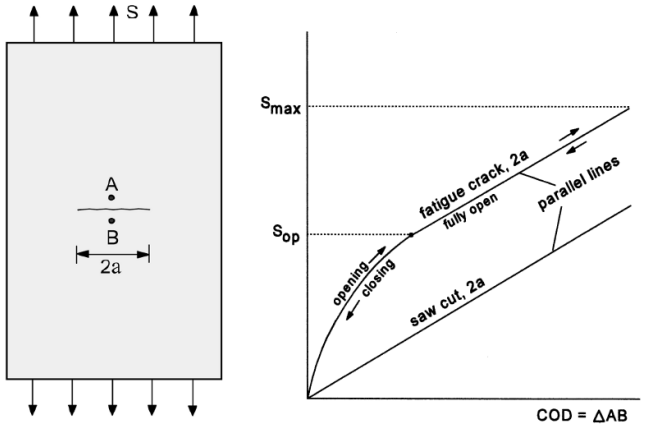

Figure 2-10 Measurements of the crack opening displacement (COD) are confirming crack closure at a positive tensile stress.

recognized is that the stress singularity at the tip of the crack, defined by the stress intensity factor K, is present as long as the crack tip is open. As soon as the tip is closed the stress singularity is no longer present at the tip of the crack. In other words, the large stress variations at the crack tip occurring if the crack is fully open do not occur any longer as soon as the crack tip is closed. Elber proposed that the stress variation will contribute to crack extension only if the stress singularity occurs at the crack tip.

He defined an effective stress range ΔS_{eff} as shown in Figure 2.11. It implies that:

$$\Delta S_{eff} = S_{max} - S_{op} \tag{2.14}$$

The corresponding effective stress intensity factor range is then:

$$\Delta K_{eff} = \beta\, \Delta S_{eff} \sqrt{\pi a} \tag{2.15}$$

According to the concept of Elber, the fatigue crack growth rate depends on ΔK_{eff} only:

$$\frac{da}{dN} = f(\Delta K_{eff}) \tag{2.16}$$

This relation includes the effect of the stress ratio R because the reversed crack tip plasticity depends on S_{min}, and as a consequence the plastic wake field of the crack depends on R. Elber carried out experiments on the Al-alloy 2024-T3 and found that S_{op} was approximately constant during a fatigue test. This empirical observation implies that S_{op} was independent of the crack length (a) and only dependent of the applied cyclic stress. Elber defined the ratio (U) as:

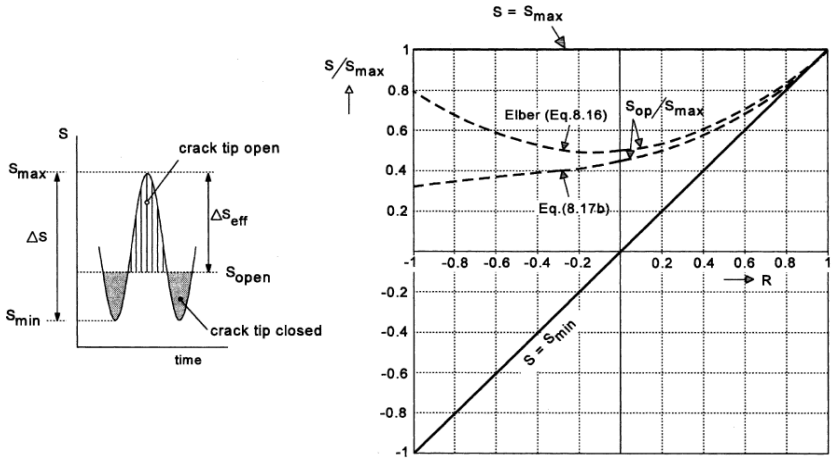

Figure 2-11 Crack closure: the crack tip is open during a part of the load cycle.

$$U = \frac{\Delta K_{eff}}{\Delta K} = \frac{\Delta S_{eff}}{\Delta S} \tag{2.17}$$

Which is the percentage of the K-range (or ΔS-range) during which the crack tip is open. Elber's crack closure measurements on an Al-alloy (2024-T3) specimens indicated that the ratio (U) depends on the stress ratio R. Elber has used R-values in the range of 0.1 to 0.7 and he could describe the test results by a simple equation:

$$U = 0.5 + 0.4R \tag{2.18}$$

and thus

$$\Delta K_{eff} = (0.5 + 0.4R)\,\Delta K \tag{2.19}$$

The equation was used for Figure 2.7a to plot the results of Figure 2.7b as a function of ΔK_{eff} in Figure 2.7b. The graph confirms a very good correlation of d*a*/d*N* with ΔK_{eff}. It still should be recognized that Equation (2.18) is a fit to empirical data obtained in tests

carried out with R-values between 0.1 and 0.7. Extrapolation outside this range is not necessarily justified. Actually, Equation (2.18) cannot be valid for more negative R-values down to R = −1 (S_m = 0). This can easily be shown by considering the ratio S_{op}/S_{max} as a function of (R). With Equations (2.14) and (2.17):

$$\frac{S_{op}}{S_{max}} = \frac{S_{max} - \Delta S_{eff}}{S_{max}} = 1 - \frac{U\,\Delta S}{S_{max}} = 1 - \frac{U(S_{max} - S_{\min})}{S_{max}} = 1 - U(1 - R) \quad (2.20)$$

Substitution of Equation (2.18) gives:

$$\frac{S_{op}}{S_{max}} = 0.5 + 0.1R + 0.4R^2 \quad (2.21)$$

This $\frac{S_{op}}{S_{max}}$ ratio is plotted in Figure 2.11 as a function of (R). It shows that the ratio is increasing again for larger negative R-value. This is physically unrealistic. An improved function with a more realistic *S*op behavior for negative *R*-values was proposed in [22]:

$$U = 0.55 + 0.33R + 0.12R^2 \quad (2.22a)$$

Substitution in Equation (2.20) gives:

$$\frac{S_{op}}{S_{max}} = 0.45 + .0.22R + 0.21R^2 + 0.12R^3 \quad (2.22b)$$

The equation is also plotted in Figure 2.11 which shows a continuously decreasing S_{op} for a decreasing R-value. This trend should be expected because a decreasing (R) for the same S_{max} corresponds to a decreasing S_{min} (and also a decreasing S_m). The equation was checked in another test program on 2024-T3 sheet specimens including results for *R*-values between −1 to 0.54 [23]. All results of d*a*/d*N* as a function of ΔK_{eff} calculated with Equation (2.22a) were concentrated in a single scatter band. This is a useful result because it implies that crack growth data obtained at a certain R-value can be used to calculate crack growth data for other R-values.

2.2 LITERATURE REVIEW

2.2.1 PREFACE

On April 28, 1988, at 1346, a Boeing 737-200, N73711, operated by Aloha Airlines Inc., as flight 243, experienced an explosive decompression and structural failure at 24,000 feet, while en route from Hilo, to Honolulu, Hawaii. Approximately 18 feet from the cabin skin and structure aft of the cabin entrance door and above the passenger floorline separated from the airplane during flight. The National Transportation Safety Board determines that the probable cause of this accident was the failure of the Aloha Airlines maintenance program to detect the presence of significant disbonding and fatigue damage which ultimately led to failure of the lap joint at S-10L and the separation of the fuselage upper lobe, [24]. At the time of the accident, the N73711 had accumulated 35,496 flight hours and 89,680 flight cycles (landings), the second highest number of cycles in the worldwide B-737 fleet. Due to the short distance between destinations on some Aloha Airlines routes, the maximum pressure differential of 7.5 psi was not reached on every flight. Therefore, the number of equivalent full pressurization cycles on the accident airplane is significantly less than the 89,680 cycles accumulated on the airplane. A post-failure investigation of the aircraft by the U.S. National Transportation Safety Board (Aircraft Accident Report 1989) revealed the cause of the mishap: "The failure mechanism was a result of multiple site fatigue cracking of the skin adjacent to rivet holes along the lap joint upper rivet row and tear strap disband which negated the fail-safe characteristics of the fuselage". This mechanism was promoted by corrosion due to the disbonding of epoxy adhesive used to bond the skin sheets, see Fig. 2.12a. Water was able to enter the crevices and started the corrosion process. The aircraft operated in a coastal environment with an exposure to salt and humidity. Examination of several pieces of the aircraft skin showed a moderate corrosion along most of the joints. In that early version of the B 737 joint, countersunk rivet heads created the "knife-edge effect" condition in the outer skin that increased the risk of fatigue crack initiation. The accident occurred after 89,681 flights (most Aloha flights were of short distance), whereas the design service goal (DSG) was 75,000 flights. The design

life of 20 years was, however, not exceeded because the aircraft had been in commercial operation for 19 years. After the Aloha accident the problem got its name: Multiple-Site Damage. This particular type of failure led to awareness of the so-called aging aircraft problem which has become the major focus of airframe fatigue related research. Also, many conferences have been devoted to this topic. Eastin and Mowery (2007) claimed that MSD was the reason for 7 out of 11 aircraft accidents that they analyzed in detail within the years 1968–2002, [25]. Previous and current research programs focused on the characteristics of MSD in transport aircraft fuselage lap joints through full-scale fuselage testing, sub-scale testing, and analytical simulations. Some of these studies are highlighted in the following sections.

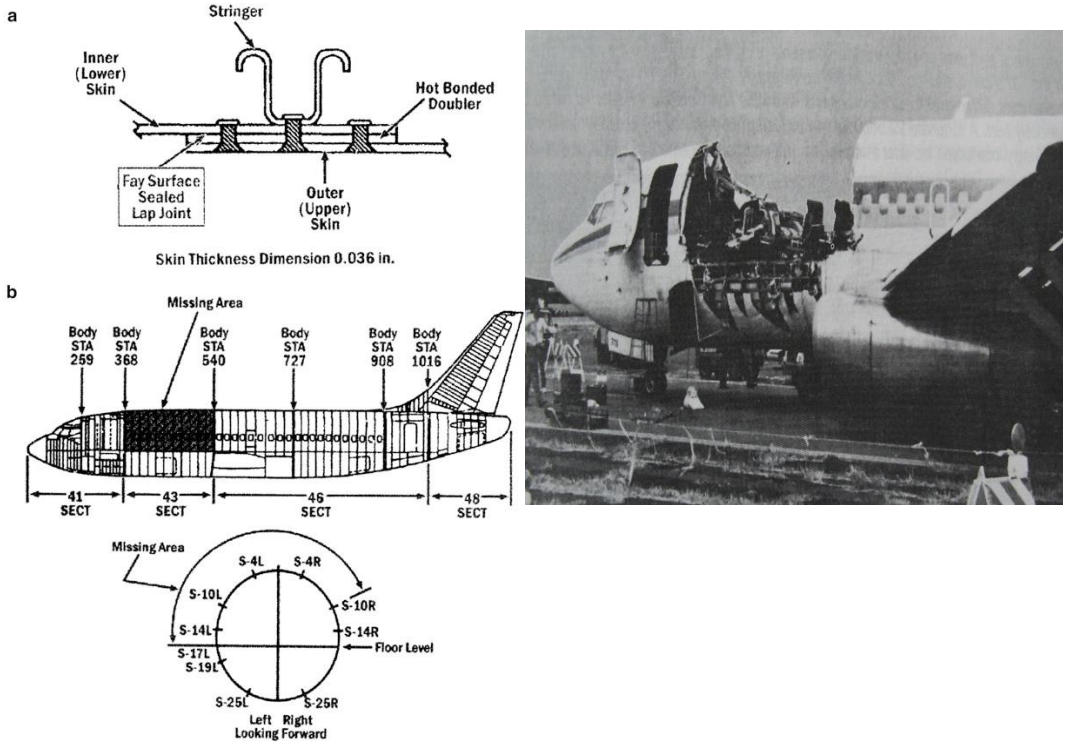

Figure 2-12 Aloha Boeing 737 accident: (a) longitudinal lap joint design; (b) fuselage damage area; (c) aircraft after landing (Aircraft Accident Report NTSB/AAR-89/03 1989)

2.2.2 Multi site damage in flat and curved un-stiffened panels

Using three softwares: FRANC2D/L, Approximation Method and CAELinux2010 ,***G. Kastratovic et al***, investigated the stress intensity factors in structures with multi site damage. The SIFs were determined for a 2024-T3 thin plate with three circular holes

subjected to uni-axial tensile stress, the middle hole has two radial cracks and other two holes have one radial crack. The results show excellent agreement between results obtained by finite element based computer program, approximate procedure which uses influential coefficient, and FRANC2D, especially for cracks 1 and 2.All differences are less than 5% except in two cases where difference was about 10%.Those cases are the ones where adjacent cracks were large, with plastic zones that suggest link up occurrence. For cracks 3 and 4, the agreements between results obtained by FEM based software and approximate procedure is excellent, but solution obtained in FRANC2D/L differs more from these results, as the cracks grow. [26]

Similar results were reported by ***E. Rakipovski et al***, in a study on MSD using MorfeoCrack software for Abaqus, based on extended finite element method for fatigue life predictions in aircraft structure. In that study similar model was used (dimensions of $L_1 \times L_2$ = 600×400 mm, Fig.2.13) with 3 holes (radii r = 2.4 mm at distances b = 25 mm) subjected to uni-axial tensile stress (value = 100 MPa) is created

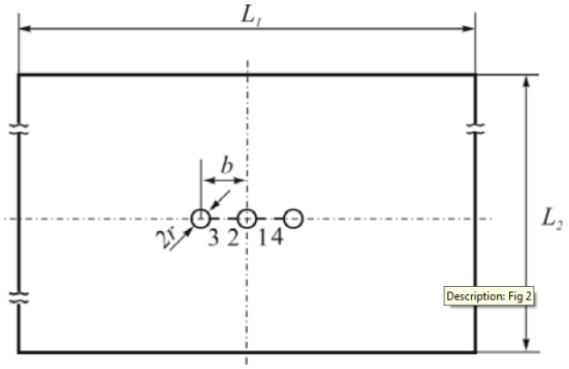

Figure 2-13 Analyzed configuration with MSD

The results are verified through super position based approximate procedure, The analysis of results has shown that the obtained solutions can be used for prediction of SIFs of analysed configuration with acceptable accuracy from engineering view of point. [27]

Comparable results obtained for the previous modal on research of ***G. Kastratovic et al***, on determination of SIFs in case of multiple site damage, the calculations was used for obtaining interaction effect coefficients which take into consideration the increase of stress intensity factor of analyzed crack tip due to interaction with existing adjacent crack, those coefficients were executed thru MathCAD computer program. The accuracy of the

procedure was verified by comparison with the solutions for the same model, obtained by finite element method, where analysis demanded solutions for 2D models with cracks, and extended finite element method where analysis allowed simulation of crack growth in 3D. The analysis of the results had shown that the solutions obtained by proposed approximate procedure are in very good agreement with the results calculated with *Ansys v14* and Morfeo/Crack for Abaqus software, and that these solutions can provide stress intensity factors of the analyzed configuration with acceptable accuracy. [28]

G. Kastratovic et al, published a research on the estimation of SIFs in case of two coplanar penny shaped cracks nested in three dimensional infinite elastic solid, subjected to remote un-axial tensile loading. The cracks are different in size and located in the same plane at different distances, and the applied stress is perpendicular to the cracks, (Fig.2.14)

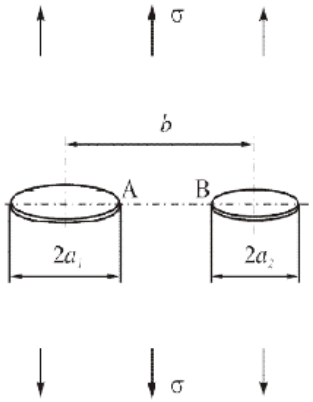

Figure 2-14 Two coplanar penny shaped cracks in three dimensional infinite elastic solid

The results obtained by approximate procedure and were compared against existed results for the same configuration, the differences between SIFs solutions in three different manners (b=10, 15 and 25 mm) are actually very good, since all differences are within 5%. Also the comparison between results showed the significance of accurate calculation of SIFs, in order to provide a better understanding and predictions of 3D multiple cracks propagation. [29]

G. Kastratovic, investigated the assessment of the interaction between multiple cracks tips effect on stress intensity factor for typical aero structural configuration, it's a thin plate

subjected to uniform stress with array of cracked circular holes, and thus, tension perpendicular to the line of cracks will prevail, Fig.2.15.

The stress intensity factors are calculated for 1000 different models with different crack sizes for all the cracks in the configuration, and different distances *b*. The results obtained with approximate procedure are compared with FEM based computer program solutions, the relative error in most cases is considerably below 10%. In merely 13 cases the relative

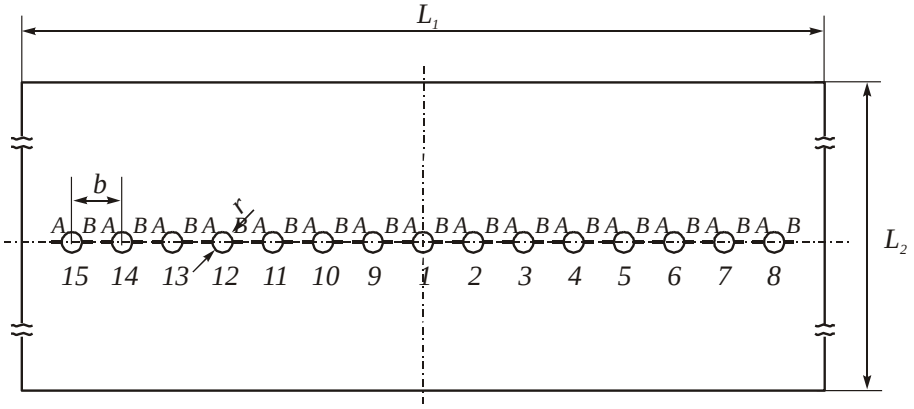

Figure 2-15 typical aero structure configurations with Multi-site damage

Error is between 10 and 11% and only in one cases its 13.9%. The analysis of the results had shown that the obtained solutions can be used for estimation the effect of interaction between multiple crack tips. [30]

H. Rajiyah et al, carried out investigation on evaluation of K- factors and weight function for 2-D mixed-mode multiple cracks by the boundary element alternating method in conjunction with the concept of the Schwartz-Neumann alternating method to solve the stresses in an un cracked body and an analytical solution for an embedded 2-D crack subjected to arbitrary crack face loading in an infinite domain. Edge cracks, as well as multiple cracks under mixed mode are considered. The concluded results show the evaluation of K- factors and weight functions for 2-D mixed mode cracks by boundary element alternating technique leads to accurate and efficient results. [31]

Bert L. Smith et al, performed experimental research work on the strength of 2024-T3 Aluminum panels with multiple site damage based on linkup model or the plastic-zone-touch mode. A schematic diagram of the model with MSD is shown in Fig.2.16. It has a central lead crack of length 2a and collinear MSD cracks emerging from the adjacent holes.

Three different modifications to the linkup model were developed, based on test data from different flat un-stiffened panels with MSD. Excellent results were obtained from the first of these modified models, the latter two which referred as Wichita State University (WSU) are easier to use and still give accurate results for a large range of parameters including panel thickness and width, lead crack length (from 1.5 to 10.75 in), MSD crack length (from 0.05 to 0.2 in), and ligament length (from 0.15 to 1.5 in). The modified models show significantly improved correlation with test data over a wide range of configuration for flat 2024-T3 aluminum panels with MSD at open holes. [36]

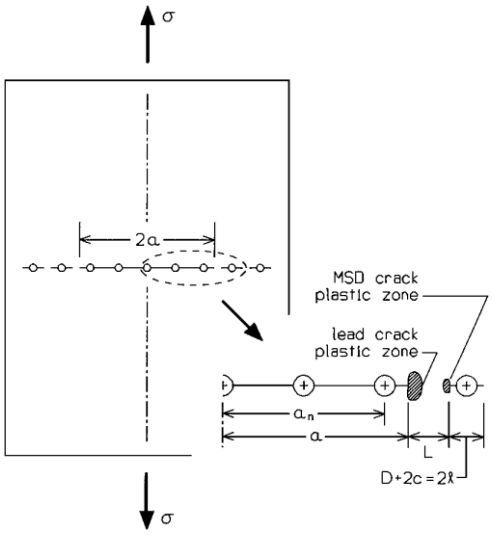

Figure 2-16 Panel configurations

J. H. Kuang et al, published a research on the use of strip yield approach for MSD failure scenarios, the research used an alternating iteration method for solving MSD cracking problem with the embodiment of Dugdale's plastic zone model (Dugdale, D. S., "Yielding of Steel Sheets Containing Slits," Journal of Mechanics and Physics of Solids, Vol. 8, No. 2, 1960, pp. 100–104) and Swift's link-up criterion (Swift, T., "Damage Tolerance Capability," Fatigue of Aircraft Materials, Delft Univ. Press, Delft, The Netherlands, 1992, pp. 351–387). The 2024-T3 eleven thin flat panels were monotonically loaded in the uni-axial direction, where each panel width is 508 mm, length is 1016 mm, and thickness is 1 mm. the research concluded the following:

1) With Dugdale's strip yield model and Swift's6 link up criterion, an alternating iteration method can be utilized to predict the link-up phenomenon in MSD failure. The absolute

averaged percentage difference between predictions and measured link-up stress is about 9%.

2) The value of CTOD at the link-up load can be used to examine whether stable crack absorption or a direct rupture may occur in MSD cracking problems. Results from multiple cracked 2024-T3 thin panels indicate that a good correlation is reached between the measured and the predicted MSD failure scenarios.

3) Consideration of the interaction between cracks appears to affect the accuracy of predictions for MSD link up. [33]

D. S. Dawicke et al, used an indirect technique of alternating boundary element (AIBE) to calculate stress intensity factors of mutually interactive cracks. These solutions were then used to estimate the lifetime (usage). With AIBE method are modelled two-dimensional cracked structures, presenting the external borders as a series of line segments or elements. As an alternative to approximate the influence of local details, whose explicit description would significantly increase the size of the MSD model, it was carrying out a precise ratio of modeled structural detail, describing its impact on the stress intensity factor. This ratio is then included in the calculation of the stress intensity factors for MSD. The stress intensity factors for the series (rows) of cracks that begin their expansion from the rows of holes were products of geometric factors for each hole and the stress intensity factor for each crack. Their analysis was then tested in the experiments that were conducted on a uniaxial loaded test panels with multiple cracks. This analysis revealed that the growth rates of fatigue cracks, for tests with uneven multiple cracks, were driven by the growth of the longest crack. What was difficult to determine with this paper is whether the positions of cracks in the structure have any influence. These authors have pointed out in their conclusion that the proposed development of a fatigue crack with AIBE method with geometric factors for holes within 20% of experimentally determined development in tests carried out on flat panels with a multiple cracks that started the expansion of the hole. This is obviously not a particularly satisfactory result if we take into account its use in determining the intervals between inspections. [34]

O. Partl et al, investigated Multi site damage in 2024-T3 alloy sheet. A simple computational procedure, using the principles of fracture mechanics and a compounding K-

solution, was developed for predicting fatigue crack growth if MSD is present. The prediction method was verified using a series of fatigue crack growth tests on 2024-T3 alloy thin and finite width sheet specimens with collinear row of open holes and artificially introduced flaws at three central holes. The three configurations are shown in figure (2.17). Crack starter notches (saw cuts) were introduced at three holes in the center of specimen. The three configurations include:

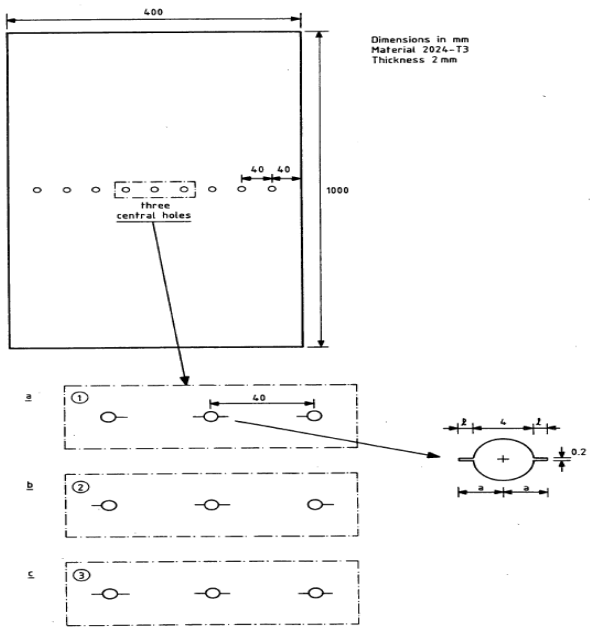

Figure 2-17 Sheet specimen with row of collinear cracks. Three configurations of crack starter notches at three central holes.

(1)A central hole with edge cracks at both sides, and both neighboring holes with one edge crack only, the latter cracks facing the central hole (see Fig. 2.17a).

(2)Similar to (1) but the single edge cracks at the holes, adjacent to the central hole, grow out of the sheet centre (see Fig. 2.17b).

(3)Three holes with edge cracks at both sides of the hole (see Fig. 2.17c).

The prediction is based on stress intensity factor (SIF) solutions and a ($\frac{\Delta a}{dN}$ vs. ΔK) relation obtained under constant amplitude (CA) loading. A good agreement was found between the test results and the predictions. An obvious crack interaction effect was found, but it mainly

occurred in the last part of the fatigue crack growth lives. The relative size of MSD cracks is significantly depending on scatter of the size of the initial crack nuclei. [35]

G. Labeas et al, carried out a research on crack link up for MSD using an energy density approach based on the magnitude of strain energy increase during the fracture of the ligament between two adjacent cracks. The energy of interest is calculated using elastic-plastic finite element analysis commercial code ANSYS. Numerical results obtained by proposed methodology are in correlation with experimental data. All MSD panels considered in the research are made of aluminum 2024-T3 material and have the basic geometry characteristics shown in Fig. 2.18.

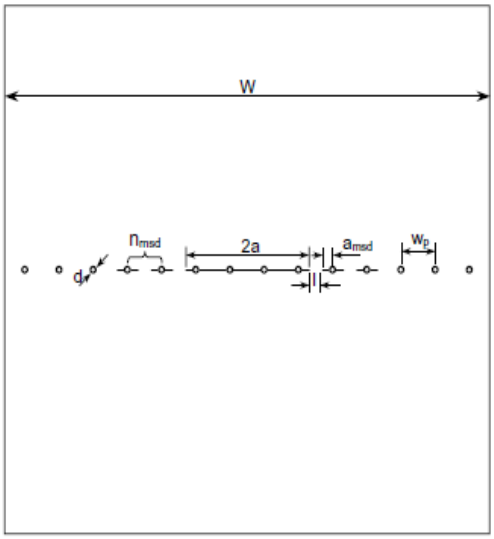

Figure 2-18 Typical MSD panel configuration.

The specific energy quantity has been shown to vary linearly with the degree of plastic deformation in the ligament area. The proposed quantity is of the same nature with the strain energy release rate concepts for crack increase. However, it has the advantage that the critical value of the specific energy quantity may be easily defined by a few experiments, while an application of J-integral for crack link-up prediction is quite complicated and demanding. Numerical results obtained by the proposed method are superior if compared to alternative link-up prediction methodologies, such as Swift and *Kc* criteria. A similar accuracy in the crack link-up predictions may be observed between the strain energy density criterion and the proposed criterion. As it has been shown that the

prior link-up history has no influence on subsequent crack link-up and final failure the present link-up criterion is extendable to the prediction the subsequent crack link-up stresses. [36]

C. Proppe, published a scientific paper on probabilistic analysis of multi-site damage in aircraft fuselage, considering the principle of structural element (PSE), where the uncertainties in crack initiation and crack growth as well as yield stress and fracture toughness are described by random variables. For crack growth calculations the finite element alternating method is used, which avoids a re-meshing of the finite element problem. After specifying link up and failure criteria, importance sampling is employed to obtain the probability of failure of the PSE due to MSD. The numerical model is a Al-2024-T3 plate with 14 holes with a diameter of 4.8 mm each, having a height of 900 mm, a width of 375 mm and a thickness of 1.6 mm, the distance between the centers of two neighboring holes is 25 mm, see Fig. 2.19. The two holes closet to the edge of the plate have been subjected to an expansion procedure, on the transverse direction, a constant amplitude load with a maximum stress level of 100 MPa and a relation of *R=0.1* has been applied.

The modeling of complex structures by means of finite elements as well as accounting for the most influential uncertainties during the analysis becomes possible. The approach has been tested against experimental results for a plate with holes available in the literature. Having determined the probability of failure as a function of the cycle number in a robust and efficient way, the expected total costs, including production, maintenance and repair costs can be calculated. [37]

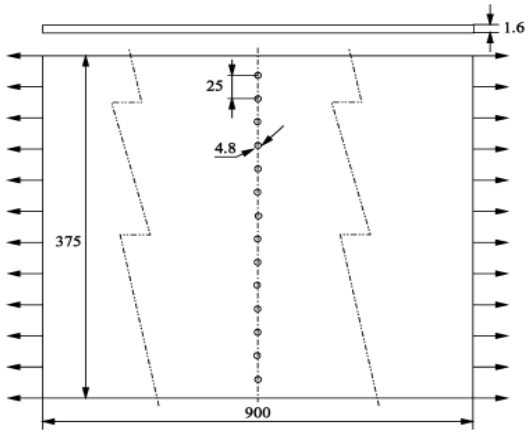

Figure 2-19 Sketch of the rectangular plate with 14 holes.

R. Elangovan et al, performed a research work on numerical estimation of stress intensity factors at a crack tip in an un-stiffened curved panel with a secondary crack in the vicinity of a primary cracks. Consider a curved plate of size of 2W× H with a central primary crack of size $2a_0$ and two secondary cracks of size $2a_{MSD}$ with a gap of lig1 between the two adjacent crack tips. The entire cracked region is well within the width of the panel as shown in Fig. 2.20. R is the radius of curvature of the curved panel. The analysis is confined to Linear Elastic Fracture Mechanics (LEFM). The rectangular coordinate system is used for analysis of all the problems in the panel. The O, O1, and O2 are the crack tips where stress intensity factors (SIF's) due to the applied loads are to be evaluated. The numerical results are obtained by using conventional finite element analysis. Four noded quadrilateral elements were used in the analysis, Fig.2.21. The finite element analysis is carried out using commercially available finite element analyses software package MSC/NASTRAN; whereas the computation of stress intensity factor is performed separately using locally developed software. The SIF in mode-I is evaluated through the estimation of Strain Energy Release Rate (SERR = G) in mode-I. The SERR is estimated using the well known Modified Virtual Crack Closure Integral (MVCCI) technique. The results are presented in the form of design charts.

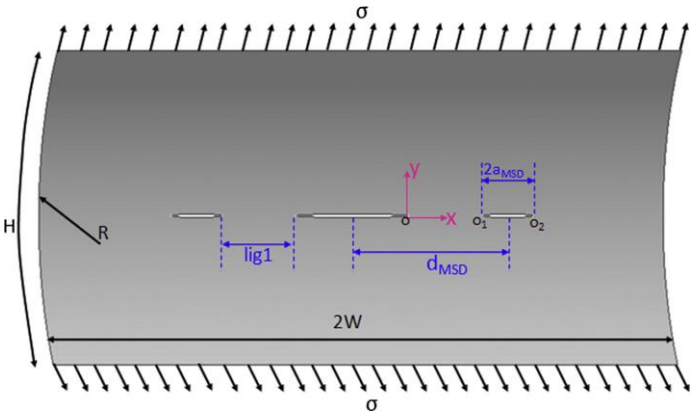

Figure 2-20 Geometric details of the configuration considered.

These results should be useful in evaluation in the damage tolerance evaluation of aircraft structures with multi-site damage. [38]

M. F. J. Koolloos et al, investigated and analysis the residual strength of flat and curved panels, with and without stiffeners, with multiple site damage. In his invetigation, a model

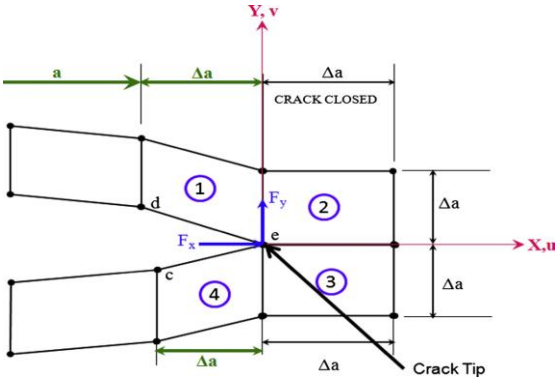

Figure 2-21 Typical FE mesh of crack tip region: 4-noded elements

to predict linkup and residual strength in flat and curved panels with a leading crack and MSD cracks and with or without stiffeners was developed. The model uses the strip yield model (as implemented in the NASGRO software), J-integral, and the compatibility methods. The strip yield method was used to calculate the stresses and deformations at the crack tips. These stresses and deformations were then used in the calculations of the J-integral values at the crack tips. The effect of the stiffeners on the deformation behavior of the panels was implemented by the displacement compatibility method, whereas the panel curvature was modelled using bulging factors. Finally, the model was verified with experimental data obtained from testing the flat and curved panels with or without stiffeners. The differences between these two tests on identical panels are rather large: 18% for first linkup, 44% for second linkup, and 32% for panel failure. Hence, the observed deviation of the predictions from the experimental results lie within the experimental variation. [39]

A. Ng et al, published investigation on the suitabilty of different crack growth models for analysing multi-site damage using two configuration; multiple embeded through carcks in a plate and multiple through cracks at holes, Fig.2.22 and 2.23. The investigation compared published geometry factors that were determined using the Finite Element Alternating Method (FEAM), Alternating Indirect Boundary Element (AIBE) method and hand-book solutions. The comparison found minimal discrepancies between the different sources and

methods of developing geometry factors. However, the scope of the comparison was limited by the limited range of the variables in published sources. [40]

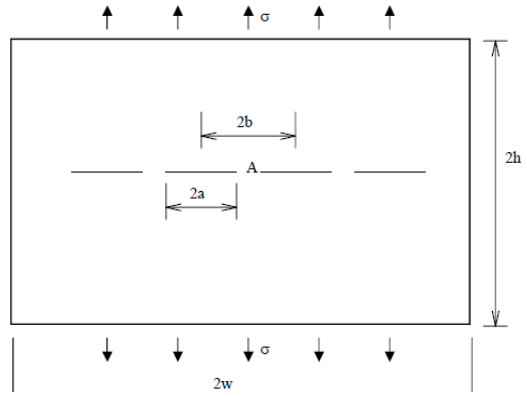

Figure 2-22 Typical multiple embedded through crack

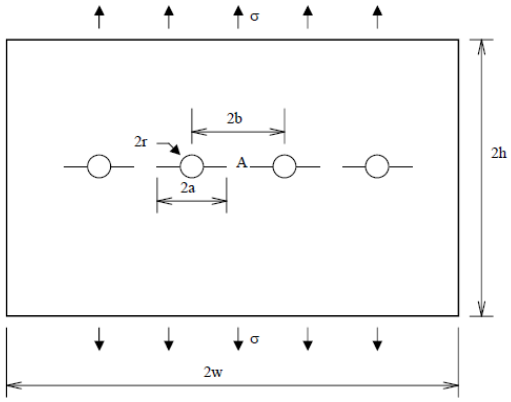

Figure 2-23 Typical multiple through cracks at holes.

A.R.Ingraffea et al, performed a research on crack interaction and multi site damage using FRANC2D/L to calculate stress intensity factors versus crack lentgh histories in a flat un-stiffened panels containing 11 holes, each of which is a site for crack growth, Fig. 2.24. 2024-T3 clad MSD panels were fabricated and tested to examine effects of MSD on fatigue crack growth rates. The stress intensity fator hisories are used to predict crack growth rates by using them as input data for AFROW of NASGROW software and in his reseach he

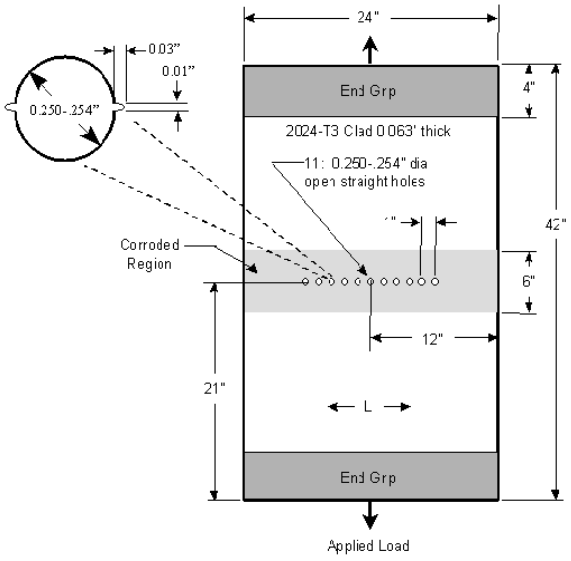

Figure 2-24 MSD Panel Geometry.

used another way of assessing the effect of crack interaction based on exited soltution[Newman 1971].This solution is for equal-length diametrically opposed cracks emanating from a single hole in an infinite plate. The results comparison show a very strong interaction effects present in this MSD problem with the stress intensity factor for crack 1 (and, therefore, the first 7 or 8 cracks) reaching a value more than 40% higher than that assuming no interaction. [41]

2.3 METHODS FOR DETERMINIG THE STRESS INTENSITY FACTORS

2.3.1 INTRODUCTION

In order to determine the characteristics of the residual strength of the aircraft structures, as well as the rate of growth cracks, which are needed to determine the set of intervals between inspections, and to meet the requirements of approach of tolerated damage to the safety of aircraft, it is required to determine accurately (reliably) the stress intensity factor . In the literature it can be found several techniques to calculate stress intensity factors for structures with individual cracks, and for a few selected structures with multiple cracks.
When it comes to structures with multiple cracks, numerical methods for determining stress intensity factors are generally spread, which are overwhelmingly based on finite and boundary elements. The use of these methods is directly linked to computers, so that they are presented in the form of computer codes (programs) that enable their use. Below some of the methods will be presented, as well as some of the few available solutions for stress intensity factors for configurations with multiple cracks.

In 1970 Isida presented [42] a general method for stress analysis in an infinite cracked panel subjected to plane stress at infinity. In his approach lsida used an analytical technique in which the stress function was assumed to be the sum of stress functions with singularities on the crack faces and at infinity. The unknown parameters were then determined from the boundary conditions using perturbation technique. In this study, the stress intensity factors

for various of two-dimensional configurations of multiple interactive cracks in an infinite body, subjected only to remote tension, were given as a power series formula.

This study also contains tables and charts that confirm some general directions of development later confirmed in [43].

In 1992 Isida and Igawa [44] continued this work by considering a double set of periodic and zigzag crack series in an infinite two-dimensional solid body that is subjected to tension. In this paper the technique of analysis was based on the eigenfunction expansions of the complex stress potentials for properly chosen unit rectangular regions. This theoretical analysis allowed them to perform approximately expression developed in the form of a polynomial expression for the stress intensity factor.

Rajiyah and Atluri [45] used the Schwartz-Neumann's alternating method, together with the boundary element method for solving problems of embedded two-dimensional cracks subjected to arbitrary load across the face of the crack. This numerical method is used to determine the stress intensity factor for the combined load modes and weight functions for cracks in finite bodies. In general, boundary problems of limit values for the body with cracks can be solved by several numerical methods such as finite element, the boundary integral equation techniques and Schwartz-Neumann alternating technique in conjunction with finite element or the boundary element method. Rajiyah and Atluri point out that it is generally recognized that alternating technique may be the simplest and the most cost effective technique of all of the previously mentioned methods.

For linear elastic-static boundary value problems, the boundary element method has a major considerable advantage over finite element method, because it reduces the dimensionality of the problem. Unlike the alternating finite element techniques, where the stresses at each point in the field are obtained through differential function of form associated with nodal displacements at an elementary level, the boundary element method allows the evaluation of the stress by finding derivatives of integral equation for the displacement field within the area. Accordingly, the boundary element method gives the possibility of more accurately estimates of the stress rather than the finite element method. The boundary element method only requires discretization of boundaries, as opposed to the

whole area discretization in finite element method. However, it must be noted that the industry often has access to existing (uncracked) networks of finite elements used in the original design of the structure. Rajiyah and Atluri used their analysis to compare the stress intensity factors which they have calculated for the cracks row and columns with those existing in published manuals. They, however, have not tried with the generalization of a series of cracks, as it was done in [43].

Binienda et al. [46] mentioned that, traditionally, the solution to a plane problem with multiple cracks was obtained by using one of these two techniques: complex potential method or singular integral equation technique. These authors have continued to use the singular integral equation technique, whereby the exhausting derivation of the system of singular integral equations was avoided by using a computer code that performed these equations symbolically and which can automatically generate the FORTRAN code by using collocation techniques needed. Once again, this paper analyzes the crack cases with infinite geometry.

Beuth and Hutchinson [47] carried out the two-dimensional, plane-stress elastic fracture mechanics analysis of cracked lap joint fastened by rigid pins. In this analysis, there were considered two types of MSD: MSD with the same length cracks and MSD with cracks of alternating lengths. The stress intensity factors for mode I load type are designated, as well as changes in compliance due to the existence of MSD. One of the goals of this study was to attempt to find the source phenomenon of "catching up" that explains the observed effect to when MSD occurs all the cracks are about the same length. It was emphasized that an additional objective of the study was accurate representation of K1 change with the length of the crack, which could be used to estimate the growth rate of fatigue cracks during usage after cracks have occurred. However, in this paper it was considered the two-dimensional analysis of the cracks growth under the rivet hole, and the plate was treated as being a plate of infinite thickness. To simulate the MSD it was used argument of symmetry, and hence the configuration of the infinite row of cracks. And the authors themselves point out that in their model of lap joint were neglected several important characteristics of the actual MSD ie bending outside the plane, and due to eccentric loads of the joint and due to the way in which real joints attached to the frame of the aircraft fuselage.

Rivets in the form of pins that were used in this model ignored the three-dimensional aspect of real geometry, as is the case with countersunk rivets. This model also ignores the three-dimensional eccentric load to which are subjected the actual rivets. To perform the analysis, the authors used a solution of two-dimensional finite element method using quadrilateral finite element for plane stress state. This level of fragmentation of the network was essential in order to get enough small finite elements around the tips of cracks. The formulated model like this one usually requires considerable time to prepare (create) networks, and also considerable time for computer resolving. As an example of this, it can be reviewed the work [43], in which among other things is discussed the body of finite size, with a row of 16 mutually interactive cracks. One of the main disadvantages of Beuth and Hutchinson is that the authors did not allow the tops of adjacent cracks to be close enough to achieve real effects of interaction. In their conclusion, it was stated that:

... Predicted stress intensity factor variation with the crack length is relatively weak suggestion that long and short cracks may grow at roughly the same rate. The ratio of separation cracks (where this ratio is defined as the ratio of double the value of the crack length and the distance between the centers of cracks) in their analysis ranges between 0.193 and 0.743. The second highest value of cracks separation was 0.61. As shown in [43] this relationship must be approximately 0.8 to detect any significant change in the stress intensity factor. In 1992 Dawicke and Newman [48] used an indirect technique of alternating boundary element (AIBE) to calculate stress intensity factors for multiple interacting cracks. These solutions were then used to estimate fatigue life. With AIBE method are modelled two-dimensional cracked structures, presenting the external boundaries as a series of line segments or elements. As an alternative to approximate the influence of local details, whose explicit description would significantly increase the size of the MSD model, it was carrying out a precise ratio of modeled structural detail, describing its impact on the stress intensity factor. This ratio is then included in the calculation of the stress intensity factors for MSD. The stress intensity factors for the series (rows) of cracks that begin their expansion from the rows of holes were products of geometric factors for each hole and the stress intensity factor for each crack.

Their analysis was then tested in the experiments that were conducted on a uniaxial loaded test panels with multiple cracks. This analysis revealed that the growth rates of fatigue cracks, for tests with uneven multiple cracks, were driven by the growth of the longest crack. What was difficult to determine with this paper is whether the positions of cracks in the structure have any influence. These authors have pointed out in their conclusion that the proposed development of a fatigue crack with AIBE method with geometric factors for holes within 20% of experimentally determined development in tests carried out on flat panels with a multiple cracks that started the expansion of the hole. This is obviously not a particularly satisfactory result if we take into account its use in determining the intervals between inspections. Tong and others [8] used hybrid finite element method, in conjunction with complex variable elasticity theory to calculate stress intensity factors at the cracks tips, stress concentration factor in the stiffeners, and the rivet loads for a stiffened structure with multiple cracks.

2.3.1.1 The stress intensity factor of two collinear cracks in a thin rectangular sheet subjected to a uniform uniaxial tensile stress

The rectangular thin sheet of width $2b$ and height $2h$ comprising two symmetrical edge cracks of length a (Fig. 2-25) is subjected to a uniform uniaxial tensile stress perpendicular to the crack. This case was analysed by Bowie [49] with the help of conform mapping technique, and Benthem and Koiter [50] with the interpolation

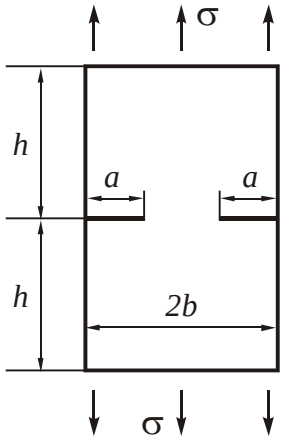

Figure 2-25 Stress intensity factor of two collinear cracks in a thin rectangular sheet subjected to a uniform uniaxial tensile stress

procedure. Bowie has calculated stress intensity factor for mode I of loading for ratios $\frac{h}{b} = 1$ and $\frac{h}{b} = 3$. Brown and Srawlay [51] have fitted the following polynomial of Bowie's result for $\frac{h}{b} = 3$ and $0 < \frac{a}{b} < 0.7$:

$$\frac{K_I}{K_O} = 1.12 - 0.20\left(\frac{a}{b}\right) - 1.20\left(\frac{a}{b}\right)^2 + 1.93\left(\frac{a}{b}\right)^3, \tag{2.23}$$

Where

$$K_O = \sigma\sqrt{\pi a}. \tag{2.24}$$

This equation can be used for all ratios $\frac{h}{b} \geq 3$. Benthem and Koiter got simple analytical expressions by interpolating between the two limiting cases of small and large lengths of cracks:

$$\lim_{\frac{a}{b}\to 0}\left\{\sqrt{1-\frac{a}{b}}\cdot\frac{K_I}{K_o}\right\} = 1.22\left(1-\frac{a}{2b}\right)$$

(2.25)

And

$$\lim_{\frac{a}{b}\to 1}\left\{\sqrt{1-\frac{a}{b}}\cdot\frac{K_I}{K_o}\right\} = \frac{2}{\pi}\left[1+\frac{1}{2}\left(1-\frac{a}{b}\right)\right]$$

(2.26)

Interpolation formula for calculating the stress intensity factor for this case, of the accuracy of up to 1% for all values of ratio $\frac{a}{b}$, is:

$$\frac{K_I}{K_o} = \frac{1.12\left[1-\frac{1}{2}\left(\frac{a}{b}\right)\right] - 0.15\left(\frac{a}{b}\right)^2 + 0.091\left(\frac{a}{b}\right)^3}{\sqrt{1-\frac{a}{b}}} \tag{2.27}$$

Discrepancies between the equations (2.23) and (2.27) sre for the ratios $\frac{a}{b} < 0.7$ smaller than 4%.

2.3.1.2 The two collinear cracks of equal length in a thin sheet subjected to uniform uniaxial tensile stress or uniaxial shear stress

Thin sheet containing two collinear cracks, the length of each $2a$ with the distance between their centers $2b$ is subject to one of the following stresses, furthered from cracks:

(i) uniform uniaxial tension stress perpendicular to the direction of cracks;

(ii) uniform shear stress that acts in the plane of the sheet and parallel to the direction of crack (Fig.2.26).

This configuration was analyzed Willmore [52], by using a complex functions of the stress, and Tranter [59] using the technique of integral equation. The stress intensity factor for

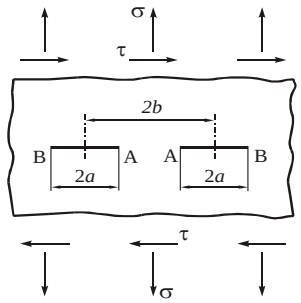

Figure 2-26 the two collinear cracks of equal length in a thin sheet subjected to uniform uniaxial tensile or shear stress

closer tips A is given by the following equation:

$$\frac{K_I}{K_o} = \frac{1}{k}\sqrt{\frac{1-\frac{a}{b}}{c\cdot\frac{a}{b}}}\cdot\left[\frac{E(k)}{K(k)} - c^2\right] \tag{2.28}$$

Where $c = \dfrac{1-\frac{a}{b}}{1+\frac{a}{b}}$, while $K(k)$ and $E(k)$ represent complete elliptic integrals of the first

and second types respectively, where $k = \sqrt{1-c^2}$.

The stress intensity factor for further tips B is given by the following equation:

$$\frac{K_I}{K_o} = \frac{1}{k}\sqrt{\frac{1-\frac{a}{b}}{\frac{a}{b}}\cdot\left[1-\frac{E(k)}{K(k)}\right]} \tag{2.29}$$

Whereas for the case (i)

$$K_O = \sigma\sqrt{\pi a}\,, \tag{2.30}$$

And for the case (ii)

$$K_O = \tau\sqrt{\pi a}\,. \tag{2.31}$$

The stress intensity factor for mode III of loading can also be calculated using the preceding equations, where:

$$K_O = \tau\sqrt{\pi a}\,, \tag{2.32}$$

Where τ stress out of plane is has effect away from the cracks in a plane that is parallel to the plane where the cracks are.

Limit values for $\frac{K_I}{K_O}$, as the internal peaks are approaching each other, for tip A are:

$$\lim_{a\to b}\left\{\frac{K_I}{K_o}\right\} = \infty, \tag{2.33}$$

And for tip B, these values are:

$$\lim_{a\to b}\left\{\frac{K_I}{K_o}\right\} = \sqrt{2} \tag{2.34}$$

From the previous equation (2.34) it can be seen that as the inner tips are approaching, the stress intensity factor becomes equal to that of a crack in a thin sheet of the length of $4a$

2.3.1.3 Two collinear cracks of different lengths in a thin sheet subjected to uniform uniaxail tensile stress or uniaxial shear stress

Thin sheet containing two cracks of different lengths ($2a_1$ and $2a_2$) was subjected to one of the following stresses, at distance from the cracks:

(i) Uniform uniaxial tensile stress perpendicular to the direction of cracks;

(ii) Uniform shear stress that is applied in the plane of the sheet and parallel to the direction of cracks (Fig.2.27).

The distance between the center of the first crack of the length of $2a_1$, to the nearest tip of the second crack, of the length of $2a_2$, is b (Fig.2.27). This configuration was analyzed using a complex function of the stresses and results given by Savin [54]. Isida [42] also reviewed this configuration for a limited number of variables, using perturbation techniques.

The results of the stress intensity factor for mode I of loading can be expressed in the form of coordinates of crack tips. If the cracks lay along the *X*-axis, where the tip B is point of origin, the coordinates of the tips A, C and D are given as bx_A, bx_C and bx_D; and dimensionless measures xA, xC and xD, and are defined as:

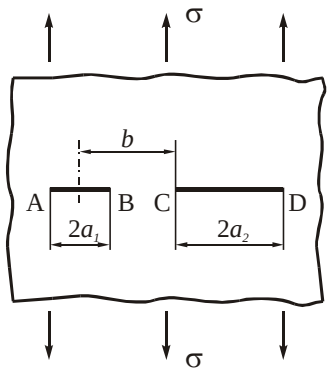

Figure 2-27 Two collinear cracks of different lengths in a thin sheet subjected to uniform uniaxail tensile or shear stress

$$x_A = \frac{2a_1}{b};\ x_c = 1 - \frac{a_1}{b};\qquad x_D = 1 - \frac{a_1}{b} + 2\frac{a_2}{b}, \tag{2.35}$$

The stress intensity factors for crack tips A, B, C and D are calculated by the following equations:

$$\beta_A = \frac{K_{IA}}{K_{01}} = \sqrt{\frac{2b}{a_1}} \cdot \frac{x_A{}^2 - C_1 x_A + C_2}{\sqrt{x_A\left(x_A + x_C\right)\left(x_A + x_D\right)}} \tag{2.36}$$

$$\beta_B = \frac{K_{IB}}{K_{01}} = \sqrt{\frac{2b}{a_1}} \cdot \frac{C_2}{\sqrt{x_A \cdot x_C \cdot x_D}} \tag{2.37}$$

$$\beta_C = \frac{K_{IC}}{K_{02}} = \sqrt{\frac{2b}{a_2}} \cdot \frac{{x_C}^2 + C_1 x_C + C_2}{\sqrt{x_C (x_A + x_C)(x_D - x_C)}} \tag{2.38}$$

$$\beta_D = \frac{K_{ID}}{K_{02}} = \sqrt{\frac{2b}{a_2}} \cdot \frac{{x_D}^2 + C_1 x_D + C_2}{\sqrt{x_D (x_A + x_D)(x_D - x_C)}} \tag{2.39}$$

Where:

$K_{01} = \sigma\sqrt{\pi a_1}$, for tips A and B and $K_{02} = \sigma\sqrt{\pi a_2}$ for tips C and D. Coefficients C_1 and C_2 are determined using the following:

$$C_1 = \frac{(x_A - x_D)\cdot K(k) - 2x_A \cdot \Pi(n,k) + 2x_D \cdot \Pi(m,k) + (x_A + x_D)\cdot [J(n,k) - J(m,k)]}{K(k) - \Pi(n,k) - \Pi(m,k)} \text{ , (2.40)}$$

$$C_2 = \frac{C_1}{K(k)} \cdot [x_A \cdot K(k) - (x_A + x_D)\cdot \Pi(n,k)] - \\ - \frac{1}{K(k)} \cdot \left[{x_A}^2 \cdot K(k) - 2x_A \cdot (x_A + x_D)\cdot \Pi(n,k) + (x_A + x_D)^2 \cdot J(n,k)\right], \tag{2.41}$$

Where $K(k)$ complete elliptical integral of the first type, while $\Pi(n,k)$ and $\Pi(m,k)$ are complete elliptical integrals of third type, which are given by the following equations:

$$K(k) = \int_0^{\frac{\pi}{2}} \frac{d\varphi}{\sqrt{1 - k^2 \sin^2 \varphi}} \tag{2.42}$$

$$\Pi(t,k) = \int_0^{\frac{\pi}{2}} \frac{d\varphi}{(1 + t \cdot \sin^2 \varphi)\cdot \sqrt{1 - k^2 \sin^2 \varphi}} \tag{2.43}$$

Where $t = n$ or $t = m$, and function J is defined as:

$$J(t,k)=\int_0^{\frac{\pi}{2}}\frac{d\varphi}{\left(1+t\cdot\sin^2\varphi\right)^2\cdot\sqrt{1-k^2\sin^2\varphi}} \tag{2.44}$$

Where as in the previous case $t=n$ or $t=m$. Parameters *n, m* and *k* are defined as:

$$n=\frac{x_D-x_C}{x_A+x_C};\quad m=\frac{x_A}{x_D};\quad k^2=m\cdot n \tag{2.45}$$

2.3.1.4 Three collinear cracks in a thin plate subjected to a uniform tensile or shear stress

Thin sheet containing three collinear cracks was subjected to uniform further uniaxial tensile stress σ or uniform shear stress τ (Fig.2.28). Central crack is of the length of $2a_1$, and other two cracks are of the length of $2a_2$. The distance between the center of central crack and closer tip of edge cracks B is labeled as b_1, and the distance of centers of edge cracks to the top A of the central crack is labeled as b_2. External tip of edge cracks is labeled as C. This configuration is analyzed by Sih [55] using the complex stress functions. That is how he obtained the expression for stress intensity factor for mode III loading (out of plane shear). This expression can be used and for other two modes of loading, and it has relatively simple form if it is presented in the function of parameters *a*, *b* and *c* which represent the distances of tips A, B and C respectively to the center of the central crack. The parameters *a*, *b* and *c* expressed in the function of the previously defined distances are:

$$\left.\begin{aligned} &a=a_1,\\ &b=b_1=b_2+a_1-a_2,\\ &c=b_1+2a_2=b_2+a_1+a_2, \end{aligned}\right\}\ \text{because}\ \ b_1-a_1=b_2-a_2. \tag{2.46}$$

Stress intensity factors for tip A, B and C are given sequentially:

$$\frac{K_{I-III}}{K_o}=\sqrt{\frac{c^2-a^2}{b^2-a^2}}\cdot\frac{E(k)}{K(k)} \tag{2.47}$$

$$\frac{K_{I-III}}{K_o} = \sqrt{\frac{2b\left(b^2-a^2\right)}{(c-b)\left(c^2-b^2\right)}} \cdot \left[1-\left(\frac{c^2-a^2}{c^2-b^2}\right)\cdot\frac{E(k)}{K(k)}\right]$$

(2.48)

$$\frac{K_{I-III}}{K_o} = \frac{1}{k}\sqrt{\frac{2c}{c-b}}\left[1-\frac{E(k)}{K(k)}\right] \tag{2.49}$$

Where $K(k)$ and $E(k)$ are complete elliptical integrals of first and second type, with the argument k, that is given as:

$$k = \sqrt{\frac{c^2-b^2}{c^2-a^2}} \tag{2.50}$$

For mode I loading K_O is calculated for the tip A as:

$$K_O = \sigma\sqrt{\pi a_1} \tag{2.51}$$

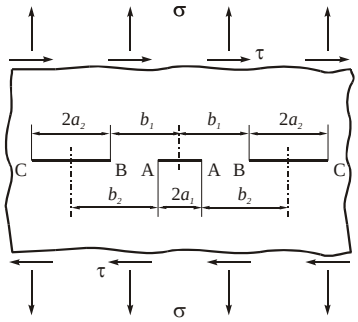

Figure 2-28 Three collinear cracks in a thin plate subjected to a uniform tensile or shear stress

And for tip B and:

$$K_O = \sigma\sqrt{\pi a_2} \tag{2.52}$$

For mode II loading , K_O is calculated using the previous two equations, where instead of tensile stress σ in them are placed further shear stress τ that is applied in the plane in a direction which is parallel to the direction of cracks. For mode III loading K_O is, also, calculated using the previous equations (2.27) and (2.28), but instead of tensile stress σ it is used shear stress out of the plane τ that is applied in the plane parallel to the plane with

cracks. In limit case, when a_1 tends to zero, the solutions for tips B and C become identical to those for two equal collinear cracks that are previously stated. As already stated, and what can be seen from the literature review, the methods used for determination of stress intensity factors are generally numerical and their use involves creating computer codes. In the following text it shall be presented in detail the indirect technique of alternating boundary elements (AIBE).

2.3.2 Alternating Indirect Boundary Element Technique (AIBE)

This technique on the principle of superposition of stresses associated with cracks and free (or loaded) boundaries. To illustrate the superposition of stresses it is considered a single crack in half-infinite thin plate, as shown in Figure 2.29 (MSD configuration is obtained by adding the additional cracks and free boundaries). Figure 2.29 Shows how the superposition is used to determine the function of the stress to crack in the thin half-infinite plate. Cracked infinite thin plate is subjected to uniform stress

on the face of the crack *S* is shown on Figure 2.30b. Uncracked thin plate is subjected to further uniform

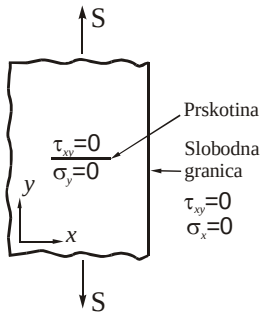

Figure 2-29 Half-infinite cracked thin plate

stress *S* is shown on Figure 2.33c. Figure 2.33d shows uncracked thin plate subjected to non-uniform stresses $\sigma_x^b(y)$ and $\tau_{xy}^b(x)$ that are applied on the line that is analogous to the free boundary and non-uniform stresses $\sigma_x^c(x)$ and $\tau_{xy}^c(x)$ that are applied along $y = 0, |x| < a$. The loading of the face of the crack is added to the loading of un cracked thin plate (Fig.2.30e) in order to get the face of the crack that is stress free (Figure 3.30a). The formulation requires the analytical expressions for stresses due to loadings expressed on Figure 3.30d and 3.30e. Analytical expressions derived by Goodier and Timoshenko [56],

Westergaard [57], and Tada and Irwin [58] are used for formulation of necessary expressions for stress distribution.

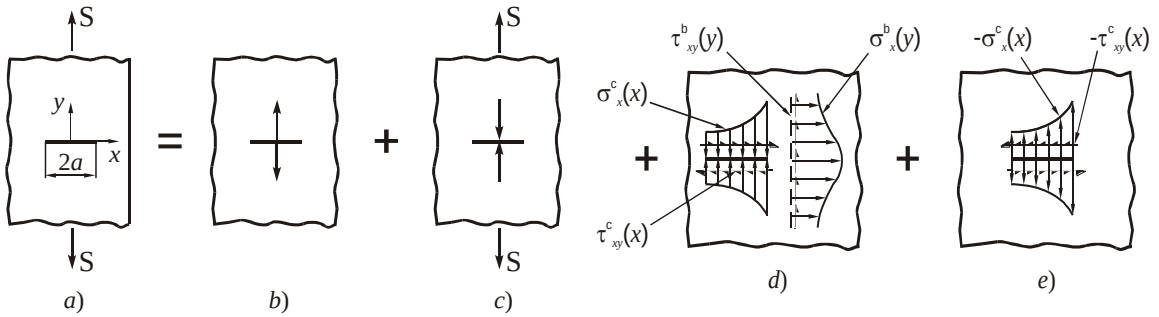

Figure 2-30 Principle of superposition is applied on crack in half-infinite plate

2.3.2.1 Uncracked thin plate with non-uniform line loading

Analytical expressions defined by Goodier and Timoshenko [62] for stresses in any point (*x, y*) due to effect of concentrated force on infinite body are used for obtaining the equations for stresses in un cracked infinite thin plate with non-uniform line loading (3.30d). In equations of previously mentioned authors, the concentrated force is applied in the beginning of the local coordinate system (*x, y*) as shown (Fig.2.31).

Stresses due to the action of the force *P* in the direction of *X*-axis are given as:

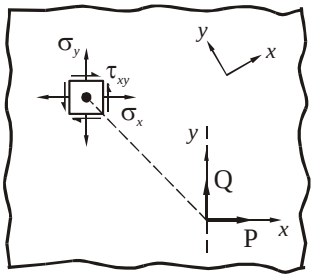

Figure 2-31 Concentrated forces P and Q on infinite body.

$$\sigma_x = \frac{P}{2\pi} \cdot \frac{x}{x^2 + y^2} \left[-(3+\nu) + 2(1+\nu) \frac{y^2}{x^2 + y^2} \right] \tag{2.53}$$

$$\sigma_y = \frac{P}{2\pi} \cdot \frac{x}{x^2 + y^2} \left[(1-\nu) - 2(1+\nu) \frac{y^2}{x^2 + y^2} \right] \tag{2.54}$$

$$\tau_{xy} = \frac{-P}{2\pi} \cdot \frac{y}{x^2 + y^2} \left[(1-\nu) + 2(1+\nu) \frac{x^2}{x^2 + y^2} \right] \tag{2.55}$$

Stresses due to the action of concentrated force Q in the direction of Y-axis are given as:

$$\sigma_x = \frac{Q}{2\pi} \cdot \frac{y}{x^2 + y^2} \left[(1-\nu) - 2(1+\nu) \frac{x^2}{x^2 + y^2} \right] \tag{2.56}$$

$$\sigma_y = \frac{Q}{2\pi} \cdot \frac{y}{x^2 + y^2} \left[-(3+\nu) + 2(1+\nu) \frac{x^2}{x^2 + y^2} \right] \tag{2.57}$$

$$\tau_{xy} = \frac{-Q}{2\pi} \cdot \frac{y}{x^2 + y^2} \left[(1-\nu) + 2(1+\nu) \frac{y^2}{x^2 + y^2} \right] \tag{2.58}$$

Where ν is Poisson ratio. Stresses due to normal and shear stress distributions are obtained by dividing the boundaries on the discrete elements and making the integrals of the previous six equations along each element (of the length of $2d_j$), as shown (Fig.2.32).

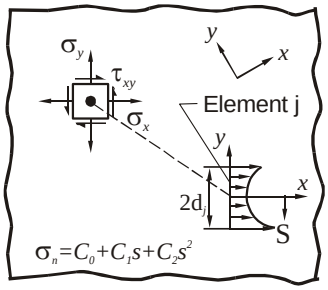

Figure 2-32 Line element with square normal distribution in infinite body (note: similar procedure is used for shear stresses)

Stresses due to normal stress distribution $\sigma_n(s)$ are given as:

$$\sigma_x = \frac{1}{2\pi} \int_{-d_j}^{d_j} \frac{x\sigma_n(s)}{x^2 + (y+s)^2} \left[-(3+\nu) + 2(1+\nu) \frac{(y+s)^2}{x^2 + (y+s)^2} \right] ds \tag{2.59}$$

$$\sigma_y = \frac{1}{2\pi} \int_{-d_j}^{d_j} \frac{x\sigma_n(s)}{x^2 + (y+s)^2} \left[(1-\nu) - 2(1+\nu) \frac{(y+s)^2}{x^2 + (y+s)^2} \right] ds \tag{2.60}$$

$$\tau_{xy} = \frac{-1}{2\pi}\int_{-d_j}^{d_j} \frac{(y+s)\cdot\sigma_n(s)}{x^2+(y+s)^2}\left[(1-\nu)+2(1+\nu)\frac{x^2}{x^2+(y+s)^2}\right]ds \tag{2.61}$$

Where it is assumed that $\boldsymbol{\sigma_n(s)}$ has square form

$$\sigma_n(s) = C_0 + C_1 s + C_2 s^2 \tag{2.62}$$

Stresses due to distribution of shear stresses $\boldsymbol{\tau(s)}$ are given as:

$$\sigma_x = \frac{1}{2\pi}\int_{-d_j}^{d_j} \frac{(y+s)\cdot\tau(s)}{x^2+(y+s)^2}\left[(1-\nu)-2(1+\nu)\frac{x^2}{x^2+(y+s)^2}\right]ds \tag{2.63}$$

$$\sigma_y = \frac{1}{2\pi}\int_{-d_j}^{d_j} \frac{(y+s)\cdot\tau(s)}{x^2+(y+s)^2}\left[-(3+\nu)+2(1+\nu)\frac{x^2}{x^2+(y+s)^2}\right]ds \tag{2.64}$$

$$\tau_{xy} = \frac{-1}{2\pi}\int_{-d_j}^{d_j} \frac{x\cdot\tau(s)}{x^2+(y+s)^2}\left[(1-\nu)+2(1+\nu)\frac{x^2}{x^2+(y+s)^2}\right]ds \tag{2.65}$$

Where it is assumed that $\tau(s)$ has square form

$$\tau(s) = D_0 + D_1 s + D_2 s^2 \tag{2.66}$$

Whereby C_i and D_i (i=0, 1, 2) are known for each element. It is performed the transformation of coordinate system in order to calculated stresses are suitable for global coordinate system (X, Y).

2.3.2.2 Cracked infinite thin plate with non-uniform loading of the face of the crack

Stresses in infinite thin plate with loading of the face of the crack, according to Westergaard [57], can be expressed in the form of two stress functions $\mathbf{Z_I}$ and $\mathbf{Z_{II}}$:

$$\sigma_x = \mathrm{Re}\, Z_I - y\,\mathrm{Im}\frac{dZ_I}{dz} + 2\,\mathrm{Im}\, Z_{II} + y\,\mathrm{Re}\frac{dZ_{II}}{dz} \tag{2.67}$$

$$\sigma_y = \mathrm{Re}\, Z_I + y\,\mathrm{Im}\frac{dZ_I}{dz} - y\,\mathrm{Re}\frac{dZ_{II}}{dz} \tag{2.68}$$

$$\tau_{xy} = -y\,\mathrm{Re}\frac{dZ_I}{dz} + \mathrm{Re}\,Z_{II} - y\,\mathrm{Im}\frac{dZ_{II}}{dz} \tag{2.69}$$

These Westergaard´s functions are defined for central forces P and Q that act on the crack of the length of **2a**, as demonstrated (figure 2.33), as function of stress for stress distribution along the face of the crack are obtained by dividing the crack on discrete elements and making the integrals of two previous equations along each crack element (of the length **2d$_j$**, as shown in figure 2.33.

$$Z_I(z) = \frac{P}{\pi}\cdot\frac{\sqrt{a^2-b^2}}{(z-b)\cdot\sqrt{z^2-a^2}} \tag{2.70}$$

$$Z_{II}(z) = \frac{Q}{\pi}\cdot\frac{\sqrt{a^2-b^2}}{(z-b)\cdot\sqrt{z^2-a^2}} \tag{2.71}$$

Where $z = x + i\cdot y$.

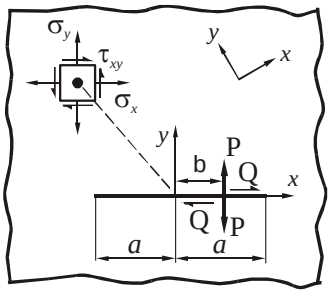

Figure 2-33 Concentrated forces P and Q that act on the crack in infinite body

Functions of the stress for stress distributions along the face of the crack are obtained by dividing the crack on discrete elements and making the integrals of two previous equations along each crack element (of the length of $\boldsymbol{2d_j}$), as shown (Fig. 2.34).The resulting stress functions for each element are given as:

$$Z_I(z) = \frac{1}{\pi}\int_{-d_j}^{d_j}\sigma_n(s)\cdot\frac{\sqrt{a^2-(b_j+s)^2}}{(z-b_j-s)\cdot\sqrt{z^2-a^2}}\cdot ds \tag{2.72}$$

$$Z_{II}(z)=\frac{1}{\pi}\int_{-d_j}^{d_j}\tau(s)\cdot\frac{\sqrt{a^2-(b_j+s)^2}}{(z-b_j-s)\cdot\sqrt{z^2-a^2}}\cdot ds \tag{2.73}$$

These equations can be analytically integrated but the numerical integration is more efficient in this case. It is performed the transformation of coordinate system so the calculated stresses are suitable for global coordinate system (X, Y).

2.3.2.3 Equations for stress intensity factor

Stress intensity factors for mode I and mode II loading due to concentrated loading P and Q that act on crack in infinite body ([59] and [58]) are given as:

$$K_I=\frac{P}{\sqrt{\pi a}}\sqrt{\frac{a+b}{a-b}} \tag{2.74}$$

$$K_{II}=\frac{Q}{\sqrt{\pi a}}\sqrt{\frac{a+b}{a-b}} \tag{2.75}$$

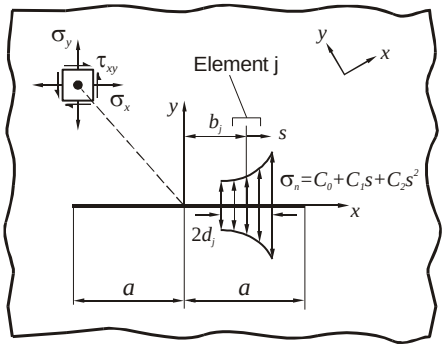

Figure 2-34 Crack element with square normal distribution for the crack in infinite body (note: similar procedure is used for shear stresses).

Stress intensity factors for stress distribution for face of the crack are designated by making integrals of two previous equations along each element of the crack (of the length of $\boldsymbol{2d_j}$) measured regarding the distance from the center of gravity of the element to the center of the crack $\boldsymbol{b_j}$ as :

$$K_I=\int_{b_j-d_j}^{b_j+d_j}\frac{1}{\sqrt{\pi a}}\cdot\sigma_n(s)\cdot\sqrt{\frac{a+s}{a-s}}\cdot ds \tag{2.76}$$

$$K_{II} = \int_{b_j - d_j}^{b_j + d_j} \frac{1}{\sqrt{\pi a}} \cdot \tau(s) \cdot \sqrt{\frac{a+s}{a-s}} \cdot ds \tag{2.77}$$

Total solutions for stress intensity factor are obtained by adding the contribution of each element of the crack.

2.3.3 Multiple site damage configurations

Two-dimensional cracked structure can be modeled using this technique of describing cracks and external boundaries with series of linear segments and elements. Boundaries have to be continuous and cracks have to be within the boundaries and cannot be mutually intersected. Elementary square stress distribution is used to reduce the number of elements (i.e. to reduce the number of degrees of freedom) necessary for describing the problem of the crack. Square stress distribution requires stresses to be defined in three nodal points in each element, $s = -0.6.\,d_j$ and $s = 0.6.\,d_j$. The solution is obtained by assuming the initial values of six stress coefficients $\mathrm{C_I}$ and D_i, $(i = 0, 1, 2)$ for each element. Initial value is not crucial, the unit value of each coefficient is sufficient for convergence but using the results from the previous solution (if that is possible) significantly reduces the number of iterations. Stresses for each element (three normal stresses and three shear stresses) are determined with current coefficient and are connected into vector of the length of $6n$, where n is the total number of elements, as:

$$\left\{\sigma^{old}\right\} = \begin{Bmatrix} \vdots \\ \tau(0.6d_{i-1}) \\ \sigma_n(-0.6d_i) \\ \tau(-0.6d_i) \\ \sigma_n(0) \\ \tau(0) \\ \sigma_n(0.6d_i) \\ \tau(0.6d_i) \\ \sigma_n(-0.6d_{i+1}) \\ \vdots \end{Bmatrix} = \begin{Bmatrix} \vdots \\ D_0^{i-1} + D_1^{i-1}(0.6d_{i-1}) + D_2^{i-1}(0.6d_{i-1})^2 \\ C_0^i + C_1^i(-0.6d_i) + C_2^i(-0.6d_i)^2 \\ D_0^i + D_1^i(-0.6d_i) + D_2^i(-0.6d_i)^2 \\ C_0^i \\ D_0^i \\ C_0^i + C_1^i(0.6d_i) + C_2^i(0.6d_i)^2 \\ D_0^i + D_1^i(0.6d_i) + D_2^i(0.6d_i)^2 \\ C_0^{i+1} + C_1^{i+1}(-0.6d_{i+1}) + C_2^{i+1}(-0.6d_{i+1})^2 \\ \vdots \end{Bmatrix} \tag{2.78}$$

Influential matrix [t] is created by using the equations (2.59)-(2.69) for determine the stress effect $\{\boldsymbol{\sigma^{old}}\}$ of the $\boldsymbol{i}$ element on stresses $\{\boldsymbol{\sigma^{new}}\}$ on element $\boldsymbol{j}$. It is the case of fully filled asymmetrical $\boldsymbol{6n \times 6n}$ matrix. New elementary stresses are defined so that the imposed stresses of connections $\{\boldsymbol{\sigma^{imposed}}\}$ are satisfied:

$$\{\sigma^{new}\} = \{\sigma^{imposed}\} - [t]\{\sigma^{old}\} \tag{2.79}$$

Imposed stresses of connections $\{\boldsymbol{\sigma^{imposed}}\}$ are either 0 for boundaries without stresses and cracks or are equal to acting stresses. When the stress distribution is calculated $\{\boldsymbol{\sigma^{new}}\}$, stress intensity factors are calculated using the equations (2.67) and (2.77).

The procedure is repeated until the solutions for stress intensity factors do not start to coverage, usually in limits smaller than 0.5%. Solutions can be obtained directly by inversion of influential matrix [t]:

$$\{\sigma^{new}\} = [t]^{-1}\{\sigma^{imposed}\} \tag{2.80}$$

2.3.4 Determination of stress intensity factor by using the finite element method

The finite element method can be used in two ways to obtain the stress intensity factor, i.e. directly and indirectly [7]. To resolve common problems of damage tolerance, the most reasonable is the indirect use of the finite element method. In that case the solution using the finite element method is obtained only for the structure without crack, and stress distribution in the future crack is being calculated. As a result it is used the rule of stress distribution that is without crack [7] for determine the stress intensity factor using of approximate methods, or by using Green´s of weight function, especially if there is a sofware that will perform any of these tasks. It is useful to note that stress distribution obtained by finite element method has limited accuracy. The assertion that the finite element stress analysis is the strictest available is exaggerated and naive; detailed analysis of many solutions obtained with this method points that out immediately. The only “strict” solution is obtained from differential equations in which the size element (dx dy dz) literally tends to zero. Unfortunately, these differential equations often cannot be solved.

The fact that the elements in finite element method are of finite size leads to the conclusion that the solution is approximate. Provided that the elements are sufficiently small, particularly in the areas of large stress gradients, it can be obtained very good solutions. However, in many practical solutions for the complex structure, model size limitations (degrees of freedom) and rough modeling in areas of large stress gradients are often the cause of limited accuracy. In areas with concentrations of stress and transfer loading to other parts of the structure, accuracy is rarely better than 10% of the calculated local stresses. It is not unusual error greater than 10%. At direct use of the finite element method for performance of stress intensity factor and geometric factors, the decision must be obtained for models with crack. Since there is a large stress gradient at the tip of the crack, the size of the elements around the tip of the crack must be very small, if not higher-order elements are used that can model the stress singularities. Finite element analysis can only provide stresses, displacement deformations and energy deformation. From these values can be obtained stress intensity factor and geometric factor using a number of methods. For example, a universal solution for the stress field on the tip of crack gives the stress on tip of the crack σy for θ=0 as:

$$\sigma_y = \frac{K}{\sqrt{2\pi x}} \ (\theta = 0). \tag{2.81}$$

The solution using the finite element method gives $\sigma\boldsymbol{y}$ on different places (x). By substituting the calculated $\sigma\boldsymbol{y}$ and the distance $\boldsymbol{r}$ on which it acts into the equation (2.81),

stress intensity is calculated as:

$$K = \sigma_{YFEM}\sqrt{2\pi x_{FEM}} \tag{2.82}$$

When equation (2.81) is valid only for very small x, stress intensity obtained from equation (2.82) is not correct if x is not extremely small. On the other hand, calculated value σy contains much significant error with smaller x (except in the case of singular elements). In order to circumvent this problem (2.58), the equation can be used infinite number of times using the calculated stresses$\boldsymbol{\sigma_y(r)}$ at distances $\boldsymbol{x_1}$,$\boldsymbol{x_2}$, $\boldsymbol{x_3}$, etc. For each combination ($\boldsymbol{\sigma_y}$;$\boldsymbol{x}$) is obtained an "apparent" value for K from the equation (2.82). Nothing of this is correct.

Those "apparent" values can be drawn as functions of distance $\boldsymbol{x}$, for which they are calculated. The line drawn through these points can be extrapolated up to x=0- for which the equation (2.81) is strict, as shown (Fig. 2.35). Extrapolated value for x=0 is required value K. In the end geometric factor also needs to be determined. By selecting the reference stress σref (it can be a stress that acts on the model or the stress which is calculated on a convenient place) geometric factor follows from the following equation:

$$\beta = \frac{K}{\sigma_{ref}\sqrt{\pi a}}, \tag{2.83}$$

Where $\boldsymbol{a}$ is the size of the crack on the model. Of course, damage tolerance analysis that follows should be based on the same reference stress. The previously stated gives β only for one size of crack and β is needed for the whole range of sizes of cracks. Therefore the procedure has to be repeated for several sizes of cracks (multiple solutions by finite elements). It should be noted that in any case reference stress should be used – in function of place and power – in order to get β from the equation (2.83); inconsistency in this regard may lead to serious errors.

There are plenty of other methods for obtaining geometric factors β from finite element models with cracks. Similar to the previous approach can be represented and displacement. For example, the displacement u at the distance r from the tip of the crack follows from the solution for stress field on the top of the crack as:

$$u = CK\sqrt{rf(\theta)} \tag{2.84}$$

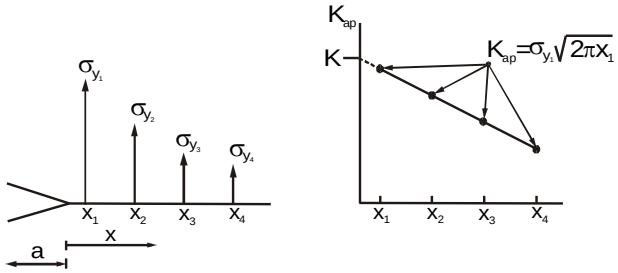

Figure 2-35 Determination of K on the basis of the model obtained by finite element method (a) Stresses on the model obtained by finite element method; (b) Stress intensity factor.

Which can be used in same way as equation (2.83) in order to get G from calculated displacements. On the other hand, β can be derived from energy of deformation *U*. The total energy of deformation U of the model is calculated for the crack of the size a. As a result the crack in the model will be extended for an elementary length (Δa) on $a + \Delta a$, and it will be again determined the energy of deformation that now corresponds to this crack length. The change of energy of deformation dU/da is approximated as:

$$\frac{dU}{da} = \frac{\Delta U}{\Delta A} = \frac{U_{a+\Delta a} - U_a}{\Delta a} \tag{2.85}$$

from which K is obtained as:

$$K = \sqrt{\frac{EdU}{da}} \tag{2.86}$$

and in the end β is obtained in the previously explained way.

Previous procedure allows larger elements and from that procedure it is pointed out that has a higher accuracy than the previous two. However, one should be careful because the equation (2.86) represents differentiation, which is quite inaccurate process. This includes the subtracting of two large numbers of the same order of magnitude. If both ones and $Ua + \Delta a$ with the precision of one percent, the accuracy of dU is not greater than 10%.

If only one loading acts on the model, the energy of deformation can be obtained as $Ua = 0.5P\delta a$, where δa is displacement of the point of loading action for the crack of size a. Similarly, for the crack whose size is a + Δa the energy of deformation shall be $Ua + \Delta a = 0.5P\delta a + \Delta a$. The calculation of K and β is performed as in the previous case from the equations (2.86) and (2.83).

Since $J = G = dU/da$ energy of deformation release rate can be obtained by determining the J-integral along a suitable path of integration into the finite element model [59]. K and β can be obtained in the previously stated way. Majority of finite element codes have post-processors that give K by using several or even all of the previously mentioned methods. It can not be stated a priori which method will give the best results; it will depend on the configuration of a particular modeling. As in the case of indirect use of the finite element method, accuracy depends mainly on the modeling of areas with concentrations of stresses

and loading transfer, and assumptions based on boundary conditions. Analysis of the damage tolerance always requires knowing the value of β (and not K) for certain crack size range. Therefore, a number of solutions have be obtained by a method of finite elements for greater of different sizes of crack, which requires a greater number of different models; It is really expensive when it comes to complex configuration. In literature, the accuracy of such analyzes is demonstrated on the basis of simple configuration such as centrally cracked panels. In the first place those solutions have always been known, but what is a problem is that the structures rarely resemble the centrally cracked models. Finite element models of real cracked structures are usually much heavier and more expensive; in addition they require many more assumptions in respect of borderline cases, loading transfer, etc., and also they demand small elements in the area of stress concentration, so that their overall accuracy is limited despite all endeavors. Simple procedures that are discussed here, with the possible use of finite element method for un cracked structure, are currently the most convenient method for engineering application. In relation to the inaccuracies introduced by the other assumptions they are also the most reasonable solution.

2.3.5 Combining Technique

The basic principle of combining method is to deliver solutions for stress intensity factors separating complex forms to more simple auxiliary forms that have known solutions. Every auxiliary form comprises, typically, a boundary which interacts with the crack. The influence of each auxiliary configuration is combined [60] according to the following formula:

$$K = \overline{K} + \sum_{sva\,n} \left(K_n - \overline{K} \right) + K_e \tag{2.87}$$

where K is the resulting stress intensity factor on all existing borders, Kn is stress intensity factor only for boundary n, $\overline{K}$ is the stress intensity factor in the absence of all boundaries, and Ke the effect of which may exist due to interactions between the boundaries. The previous formula is convenient to be expressed via normalized stress intensity factors $Q = K/\overline{K}$, since many of the known solutions (especially in [61]), are given in this form. Equation (2.87) then becomes:

$$Q = 1 + \sum_{sva\,n} (Q_n - 1) + Q_e \tag{2.88}$$

where $Qr = Kr/\overline{K}$, $Qn = Kn/\overline{K}$ and $Qe = Ke/\overline{K}$.

Combining method is applicable for three modes loading ($KI - KIII$).

A simple process of combining is performed by adding the effects of individual boundaries. Before taking into account the impact of other boundaries, the crack plus boundary through which it passes must be replaced by an equivalent crack [62, 63], which then interacts with other boundaries. Effects of other boundaries on the original crack with the boundary are now being considered as those same effects on the equivalent crack. In order to calculate these effects, it must be determined the distance of other boundaries from the equivalent crack. These distances are determined in the condition that each boundary must be at the same distance from the proximal tip of equivalent in each of the auxiliary configurations, as it was in the initial configuration. Combining formula (2.87) is now modified into:

$$K = \overline{K} + \sum_{n \neq 0} (K'_n - K_0) + K_e \tag{2.89}$$

where $K'n$ stress intensity factor for the equivalent crack in the presence of boundary n.

It should be noted that the assessment of Qe is often complicated; it can be formally expressed [65] based on the field of residual stresses at the boundaries using Schwarz's alternative techniques. Residual stresses were originally ignored in the equation derivation (2.89) which is based on the principle of superposition. For many of the problems of flat thin plates Qe is small (a few percentages) and can be ignored. The intensity of Qe depends on how it is defined, the number and type of boundary; it increases with the number of boundaries but also by approaching the crack to the boundary. The true boundaries have a greater impact than the curved boundaries, such as, for example, holes and other smaller cracks have less impact than the holes. For problems where this size matters, approximate methods are developed [63] for its assessment. The intensity of interaction boundary-boundary can be estimated by calculating the stress intensity factor of the equation (2.88) without Qe and for problems with cracks for which there are solutions [60].

Similarly, the rate of interaction can be obtained on the basis of differences stress concentration factor Kt on the edge of the hole in uncracked configuration, with and without boundaries [64, 65]. If the change Kt is significant, then the interaction boundary-boundary Ke in cracked configuration can also be significant, particularly in the case of short cracks, where the value of the stress intensity factor is proportional to Kt [63].This technique can also be used to calculate stress intensity factors and configurations with multiple cracks.

2.3.5.1 Calculation of the stress intensity factor using combining technique

The application of this method is demonstrated on the case for which there is a solution, which was previously mentioned in section **3.3.3**.

By applying equation (2.89) in the shown configuration in Figure 2.36, it is obtained the following equation for calculation of stress intensity factors of tips A and B [61]:

$$K_{IA} = K_{IB} = K_o + (K_{I1} - K_o) + (K_{I2} - K_o) = K_{I1} + K_{I2} - K_o \tag{2.90}$$

Whereby the effect of interaction between boundaries is omitted as insignificant, because it is a thin plate of infinite dimensions. Solutions for the stress intensity factor for the auxiliary configurations are also known and previously mentioned in section 3.3.1.3.

The stress intensity factor for the other tips in the configuration would require supporting different auxiliary configurations, but the same principle would be respected as for the tips A and B. It should be noted that in this case must take into account the proper distance b.

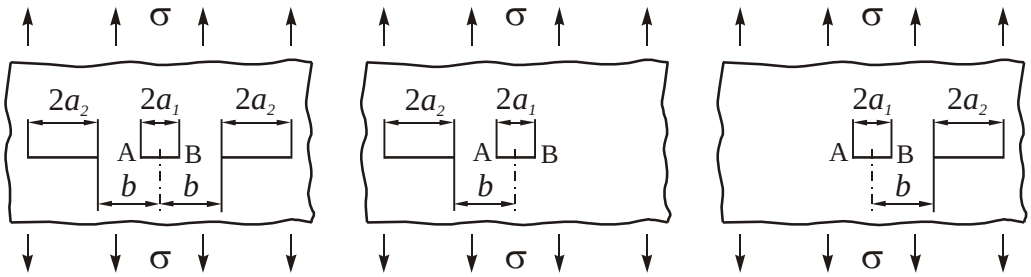

a) *b)* *c)*

Figure 2-36 Configuration with three collinear cracks: a) initial configuration; b) first auxiliary configuration; c) second auxiliary configuration.

Chapter 3 Numerical Methods for Cracks Analysis

3.1 EXTENDED FINITE ELEMENT METHOD

3.1.1 Introduction

The standard finite element method (FEM) provides substantial advantages in dealing with continuous field problems. However, for discontinuous field problems, it is computationally expensive to obtain accurate solutions with polynomial approximations. Alignment of mesh with discontinuity becomes a major difficulty when treating problems with evolving discontinuities where the mesh must be regenerated at each step, i.e re-meshing is needed continuously [66]. Modeling of cracks in structures and especially involving cracks requires the FEM mesh to conform the geometry of the crack and hence needs to be updated each time as the crack grows. This not only computationally costly and cumbersome but also results in loss of accuracy as the data is mapped from old mesh to the new mesh [67]**.** A re-meshing technique is traditionally used for modeling cracks within the frame work of finite element method where a re-meshing is done near the crack to align the element edges with the crack faces [68]. The Extended finite element method (XFEM), also known as generalized finite element method (GFEM) or Partition of unity method (PUM) is a numerical technique that extends the classical finite element method (FEM) approach by extending the solution space for solutions to different equations with discontinues functions. It was first introduced by Bolyteschko and Black [69]. The extended finite element method (XFEM) has proved to be a competent mathematical tool [70] since it is an extension of partition of unity; allows the presence of discontinuities in an element by enriching degrees of freedom with special displacement functions. [71]

In comparison to the classical finite element method, the XFEM provides significant benefits in the numerical modeling of crack propagation. The traditional formulation of the FEM, the existence of crack is modeled by requiring the crack to follow element edges. In contrast, the crack geometry in the XFEM need not to be aligned with the element edges, which provides flexibility and versatility in modeling. The Extended Finite Element method (XFEM) can dramatically simplify the solution of many problems in material modeling such as

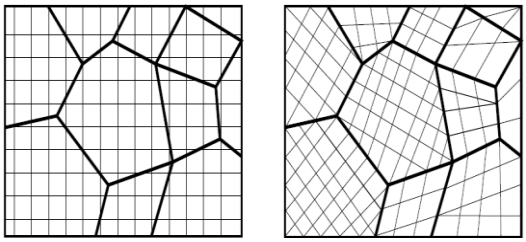

Figure 3-1 Mesh descretization in XFEM (left) and FEM (right) [78]

the propagation of cracks, the evolution of dislocations, the modeling of grain boundaries and the evolution of phase boundaries [72]. The method is based on enrollment of the FE model with additional degrees of freedom (DOF) that are tied to the nodes of the elements intersected by the crack [73], [74]. In this manner, the discontinuity is included in the numerical model without modifying the discretization, as the mesh is generated without taking into account the presence of the crack. Therefore, only a single mesh is needed for any crack length and orientation. In addition, nodes surrounding the crack tip are enriched with DOFs associated with functions that reproduce the asymptotic LEFM fields. This enables the modeling of the crack discontinuity within the crack tip and substantially increases the accuracy in the computation of the stress intensity factors (SIFs).

3.1.2 Partition of unity

Given a smooth manifold *M*, with an open cover U_i, a partition of unity subject this latter, is a collection of n nonnegative, smooth functions f_i such that, their support is included in $U_i$and the following relation holds

$$\sum_{i=1}^{n} f_i\,(\mathrm{x}) = 1 \qquad (3.1)$$

Often it is required that, the cover U_i have compact closure, which can be interpreted as finite, or bounded, open sets. If this condition is locally verified, any point x in $\boldsymbol{M}$ has only finitely many *i* with $f_i\,(x) \neq 0$. It can be easily demonstrated that, the sum in Eq. (3.1) does not have to be identically unity to work; indeed, for any arbitrary function $\Psi(x)$it is verified that

$$\sum_{\mathrm{i}=1}^{\mathrm{n}} \mathrm{f_i}\,(\mathrm{x})\Psi(\mathrm{x}) = \Psi(\mathrm{x}) \qquad (3.2)$$

Furthermore, it might be inferred that the partition of unity property is also satisfied by the set of isoparametric finite element shape functions $\mathrm{N_j}$. i.e.

$$\sum_{i=1}^{n} N_i(x) = 1 \qquad (3.3)$$

3.1.2.1 Partition of unity finite element method

To increase the order of completeness of a finite element approximation, the so-called enrichment procedure may be exploited. In other words, the accuracy of solution can be ameliorated, by simply including in the finite element discretization, the a priori analytical solution of the problem. For instance, in fracture mechanics problems, an improvement in predicting crack tip fields is achieved, if the analytical crack tip solution is included in the framework of the isoparametric finite element discretization. Computationally, this involves an increase in number of the nodal degrees of freedom.

The partition of unity finite element method (PUFEM) [75], using the concept of enrichment functions along with the partition of unity property in Eq. (3.3), allows to obtain the following approximation of the displacement within a finite element

$$u^h(x) = \sum_{i=1}^{n} N_i(x)\left(u_i + \sum_{i=1}^{n} p_i(x) a_{ji}\right) \qquad (3.4)$$

Where, $p_i(x)$are the enrichment functions and a_{ji} are the additional unknowns or degrees of freedom associated to the enriched solution. With *m* and *n* the total number of nodes of each finite element and the number of enrichment functions p_i, are indicated.

By virtue of Eqs. (3.2) and (3.3), for an enriched node x_k, Eq. (3.4) might be written as:

$$u^h(x_k) = \left(u_k + \sum_{i=1}^{n} p_i(x) a_{ji}\right) \qquad (3.5)$$

which is clearly not a plausible solution. To overcome this defect and satisfy interpolation at nodal point, i.e. $u^h(x) = u_i$, a slightly modified expression for the enriched displacement field is proposed below

$$u^h(x) = \sum_{j=1}^{m} N_j(x)\left[u_j + \sum_{i=1}^{n}(p_i(x) - p_i(x_j)) a_{ji}\right] \qquad (3.6)$$

3.1.2.2 Generalized finite element method

A breakthrough in increasing the order of completeness of a finite element discretization is provided by the so-called generalized finite element method (GFEM), in which two separate shape functions are employed for the ordinary and for the enriched part of the finite element approximation, i.e.

$$u^h(x) = \sum_{j=1}^{m} N_j(x) u_j + \sum_{j=1}^{m} \bar{N}_j(x)\left(\sum_{i=1}^{n}(p_i(x) a_{ji}\right) \qquad (3.7)$$

where $\bar{N}_j(x)$ are the shape functions associated with the enrichment basis functions $p_i(x)$.

For the reason explained in the previous section, Eq. (3.7) should be modified as follows

$$u^h(\mathrm{x}) = \sum_{\mathrm{j}=1}^{\mathrm{m}} \mathrm{N_i}\,(\mathrm{x})\mathrm{u_j} + \sum_{\mathrm{j}=1}^{\mathrm{m}} \overline{\mathrm{N}}_\mathrm{i}\,(\mathrm{x})\left(\sum_{\mathrm{i}=1}^{\mathrm{n}}(\mathrm{p_i}\,(\mathrm{x}) - p_i(\mathrm{x_j}))\mathrm{a_{ji}}\right) \quad (3.8)$$

3.1.3 Extended Finite Element Method

The extended Finite Element Method is a partition of unity based method in which, as for PUFEM and GFEM, the classical finite element approximation is enhanced by means of enrichment functions. However, in PUFEM and GFEM, the enrichment procedure involves the entire domain, whilst it is employed on a local level for the XFEM. Thus, only nodes close to the crack tip, as well as the ones required for the correct localization of the crack, are enriched. This evidently entails a tremendous computational advantage. The XFEM method was firstly introduced by Belytsckho and Black in 1999 [76]. Their work, in which a method for enriching finite element approximation in such a way that crack growth problems can be solved with minimal remeshing, represents a milestone in the XFEM history. Later on, much more elegant formulations, including the asymptotic near-tip field and the Heaviside function H(x) in the enrichment scheme, have been proposed [77]. The extended Finite Element method, furthermore, has been demonstrated to be well suited for three dimensional crack modeling. In this latter work, geometric issues associated with the representation of the crack and the enrichment of the finite element approximation have been addressed. A major step forward has been then achieved when a generalized methodology for representing discontinuities, located within the domain indipendetely from the mesh grid, has been proposed [77]. In such manner, the extended Finite Element Method allows to alleviate much of the burden related to the mesh generation, as the finite element mesh is not supposed to conform the crack geometry anymore. This represents certainly, one of the major advantages provided by the XFEM usage. The XFEM capabilities can be extended if employed in conjunction with the Level Set Method (LSM) [76]. Such method permits to represent the crack position, as well as the location of crack tips. Within this context, the XFEM has also been employed in concert with a particular type of level set method named Fast Marching Method.

3.1.3.1 Enrichment functions

In two-dimensional problems, crack modeling is obtained by means of two different types of enrichment functions:

-The Heaviside function

The Heaviside function *H*(x), is employed to enrich elements completely cut by the crack. The splitting of the domain by the crack causes a jump in the displacement field and the Heaviside function provides a tremendously simple mathematical tool to model such behavior.

Given a continuous curve Γ, representing a crack within the deformable body Ω, let us consider a point x (*x*; *y*) ϵ Ω. The whole aim is to determine the position of such point with respect to the crack location. In this context, if the closest point belonging to Γ is denoted with $\bar{x}$ ($\bar{x};\bar{y}$) and the outward normal vector to Γ in $\bar{x}$ with **n** (see Fig3.2), the Heaviside function might be defined as follows:

$$H(x,y) = \begin{cases} 1 \ for\ (x-\bar{x}).\mathbf{n} > 0 \\ -1 for\ (x-\bar{x}).\mathbf{n} < 0 \end{cases} \quad (3.9)$$

If no unique normal is defined, then the *H*(x) function will assume a positive value if (x-$\bar{x}$) belong to the con of normals in $\bar{x}$ (see Fig. (3.2)).

(a)Smoot crack (b) Kink crack

Figure 3-2 Evaluation of the Heaviside function

-Asymptotic near-tip field functions

In case of not completely cracked element, the Heaviside function cannot be used to approximate the displacement field over the entire element domain, since the element contains the crack tip. In [13] it has been proven that the displacement field from LEFM

theory, is included within the span of the following four functions, expressed in terms of the local crack tip coordinate system (r, θ)

$$\{F_i(r,\theta)\}_{i=1}^{4} = \{\sqrt{r}\cos(\frac{\theta}{2}), \sqrt{r}\sin\left(\frac{\theta}{2}\right), \sqrt{r}\sin\left(\frac{\theta}{2}\right)sin\theta\,, \sqrt{r}\ \cos(\frac{\theta}{2})\ \sin(\theta)\} \quad (3.10)$$

By using the enrichment functions in Eq. 3.100, four different additional degrees of freedom in each direction for each node are added to those related to the standard finite element discretization. It should be stressed that among the aforementioned enriching functions (see Fig. 3.3), only the second term $\sqrt{r}\sin(\frac{\theta}{2})$ is discontinuous along crack surfaces and hence, is responsible of the discontinuity in the approximation along the crack. The remaining three functions are used to enhance the solution approximation in the neighborhood of the crack tip.

Lastly, it should be highlighted that, referring to Eq. (3.10), the required singularity in the stress field, of order $\frac{1}{\sqrt{r}}$ is, therefore, readily introduced. By virtue of the above discussed enrichment functions, the following expression for the XFEM approximation might be formulated:

$$u^h(\mathrm{x}) = u_{FEM}(\mathrm{x}) + u_{ENR}(\mathrm{x}) =$$

$$\sum_{i\in I} N_i(\mathrm{x})u_i + \sum_{j\in J} N_j[H(\mathrm{x})]\,a_j + \sum_{k\in K_1} N_k(\mathrm{x})\left[\sum_{i=1}^{4} b_k^{i_1} F_i^1(\mathrm{x})\right] + \sum_{k\in K_2} N_k(\mathrm{x})\left[\sum_{i=1}^{4} b_k^{i_2} F_i^2(\mathrm{x})\right] \quad (3.11)$$

or, to eliminate the lack of interpolation property

$$u^h(\mathrm{x}) = \sum_{i\in I} N_i(\mathrm{x})\,u_i + \sum_{j=J} N_j\left[H(\mathrm{x}) - H(\mathrm{x}_j)\right] +$$

$$+\sum_{k\in K_1} N_k\left[\sum_{i=1}^{4} b_k^{i_1}\left[F_i^1(\mathrm{x}) - F_i^1(\mathrm{x}_k)\right]\right] + \sum_{k\in K_2} N_K(\mathrm{x})\left[\sum_{i=1}^{4} b_k^{i_2}\left[F_i^2(\mathrm{x}) - F_i^2(\mathrm{x}_k)\right]\right] \quad (3.12)$$

where, J indicates the set of nodes whose support domain is completely cut by the crack and thus enriched with the Heaviside function $H(\mathrm{x})$, K_1 and K_2 are the sets of nodes associated with the crack tips 1 and 2 in their inuence domain, respectively, and whose respective crack tip enrichment functions are $F_i^1(\mathrm{x})$ and $F_i^2(\mathrm{x})$. Moreover, u_i are the standard degrees of freedom, while a_j , $b_k^{i_1}$ and $b_k^{i_2}$ indicate the vectors of additional nodal degrees of freedom for modeling crack faces and the two crack tips, respectively.

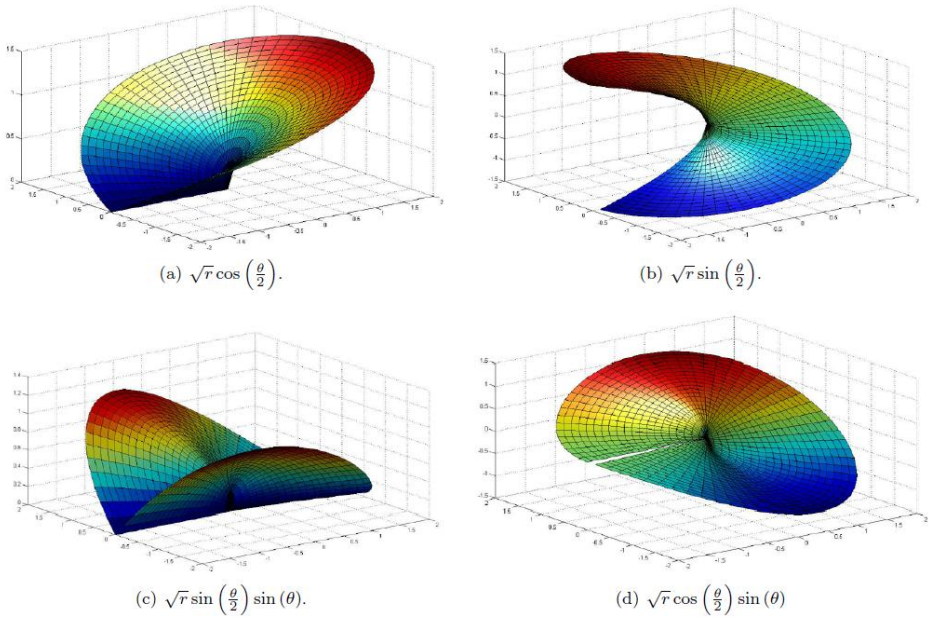

Figure 3-3 Near-tip enrichment function

3.1.3.2 Level set method for modeling discontinuities

In several cases, numerical simulations involve time-varying objects, like curves and surfaces on a fixed Cartesian grid, e.g. interfaces, discontinuities, etc. Their modeling and tracking is particularly cumbersome and is based on the complex mathematical procedure denominated parametrization. The Level Set Method [82] (often abbreviated as LSM) is an elegant numerical technique that allows to get over these difficulties. The key-point of such method is to represent discontinuities as a zero level set function. For this purpose, to fully characterize a crack, two different level set functions are defined:

1-A normal level set function, $\varphi(\mathrm{x})$.

2-A tangential level function, $\psi(\mathrm{x})$.

At this point, for the evaluation of the signed distance functions, let Γ_c be the crack surface (see Fig. 3.4) and x the point in which it is sought to evaluate the $\varphi(\mathrm{x})$ function. In an analogous manner of what done in the foregoing section, the normal level set function might be defined as:

$$\varphi = (\mathrm{x} - \bar{\mathrm{x}}).\,\mathbf{n} \qquad (3.13)$$

Where $\bar{\mathrm{x}}$ and **n** assume the previously stated meanings (see Fig. 3.2).

In Fig. 3.5 on the next page, the plot of the normal signed function φ(x). for an interior crack is provided. The tangential level set function ψ (x) is computed by finding the minimum signed distance to the normal at the crack tip; in case of an interior crack, two different functions can be individuated, (Fig. 3.6). However, a unique tangential level set function can be defined as:

$$\psi(\mathrm{x}) = \max\{\psi_1(\mathrm{x}), \psi_2(\mathrm{x})\} \qquad (3.14)$$

In conclusion, referring to Fig. 3, it may be written what follows:

$$\begin{cases} \text{for } \mathrm{x} \in \Gamma_{cr} & \varphi(x=0) \text{ and } \psi(x \le 0) \\ \text{for} \mathrm{x} \in \Gamma_{tip} & \varphi(x=0) \text{ and } \psi(x=0) \end{cases} \qquad (3.15)$$

Where Γ_{tip} indicates the crack tips location.

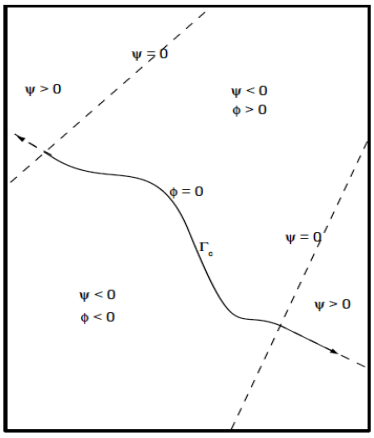

Figure 3-4 Construction of level set functions

3.1.3.3 Blending elements

Discussing different methods exploiting the partition of unity property, e.g. PUFEM and GFEM, the advantage in terms of computational cost related to the XFEM has been introduced. Indeed, unlike PUFEM and GFEM, in XFEM the enriching functions are introduced only in a local part of the domain, in order to capture the non-smooth solution characteristics. Elements, whose all nodes have been enriched are named reproducing elements since they allow to reproduce the enrichment functions exactly. Besides these, there are the so-called blending elements, whose role is to blend the enriched sub-domain with the rest of the domain, where, being the solution smooth, standard (not enriched) finite

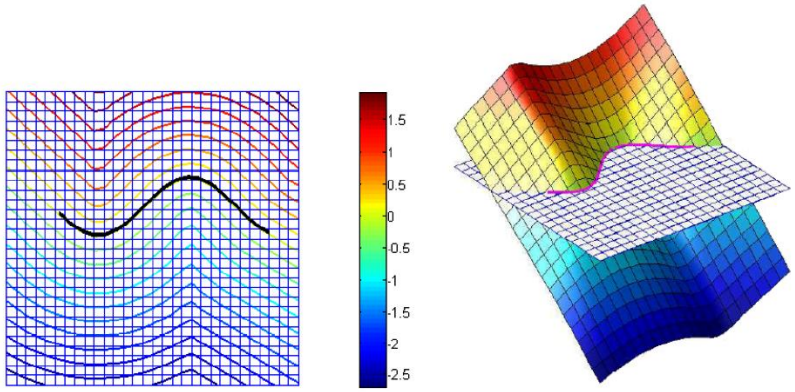

(a) 2D contour of $\varphi(\mathbf{x})$. (b) 3D contour of $\varphi(\mathbf{x})$.

Figure 3-5 Normal level set function φ(x) for an interior crack

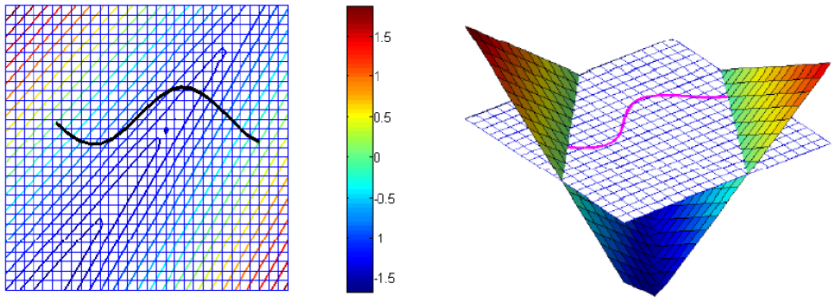

(a) 2D contour of $\psi(\mathbf{x})$. (b) 3D contour of $\psi(\mathbf{x})$.

Figure 3-6 Tangential level set function ψ (x) for an interior crack

elements are employed. Only some of nodes in blending elements are enriched. Enriched finite elements, blending elements and standard finite elements partition the whole domain in three different parts, an enriched domain, a blending domain and a standard domain, respectively, as shown in Fig. 3.7 on the next page. Two important drawbacks affect blending elements, i.e.

-Enrichment functions cannot be reproduced exactly in blending elements, since the partition of unity property is not satisfied within them;

-These elements produce unwanted terms in the approximation, which cannot be compensated by the FE part; for instance, if the enrichment introduces non-linear terms, a linear function can no longer be approximated within blending elements.

Unlike the first one, which does not represent a dramatic problem in the XFEM, the second drawback implies a significant reduction of the convergence rate for general enrichment functions; thus, suboptimal rate of convergence in XFEM may be caused by problems in blending elements [79]. A relatively straightforward method to circumvent this defect is to

exploit a blending ramp function R over the transition region connecting domains with and without enrichment, i.e.:

$$u^h(\mathrm{x}) = u^{FEM}(\mathrm{x}) + RU^{enr}(\mathrm{x}) \quad (3.16)$$

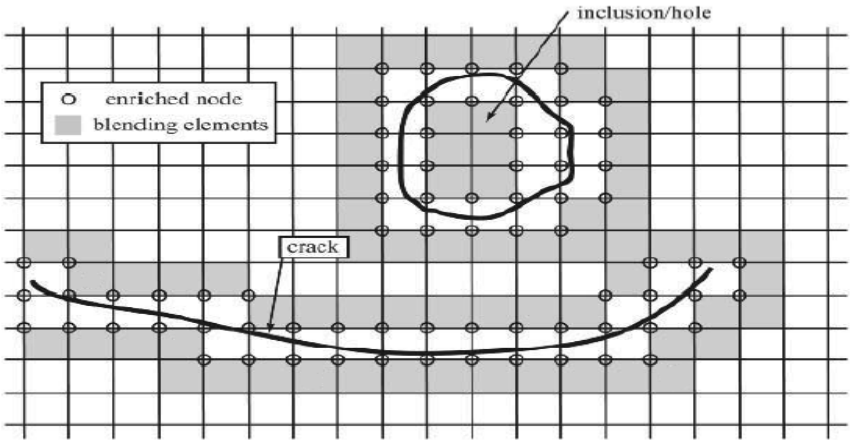

Figure 3-7 Standard, enriched and blending elements

Where R is set equal to 1 on the enrichment boundary, and equal to 0 on the standard finite element discretization boundary. This linear blending function R ensures the continuity in the displacement field but not in the strain field. To achieve this latter, higher order blending functions should be used. Other approaches prescribe to use enhanced strain techniques or p-refinement in blending elements, or to adjust the order of the FE shape functions depending on the enrichment. Recently, an interesting solution has been proposed in [80]; in particular, in this work the enrichment functions have been modified such that they vanish in standard elements, unchanged in elements with all their nodes being enriched and continuously varying within blending elements. In such approach all nodes of blending elements are enriched.

3.1.4 XFEM implementation in ABAQUS

The first formulation of the extended Finite Element Method goes back to the 1999 and, due to this; there is a shortage of commercial codes that have implemented such method. However, seeing the enormous capabilities provided by the XFEM implementation, among which the most important one is undoubtedly that the mesh has not to conform exactly the crack surfaces, several attempts have been done throughout the years to include them in both, stand-alone codes and Multi-purpose commercial FEM softwares. Among these latter,

the most famous ones are undoubtedly LS-DYNA and Abaqus [81], though other minor codes like ASTER and Morfeo include analogous facilities. The core implementation of XFEM is available in ANSYS; nevertheless it is still not available for the user. This can be justified by the still poor quality of such implementation. XFEM functionalities appear for the first time within the Abaqus/CAE framework, in 2009 with the Abaqus 6.9 release [81]. The XFEM implementation in Abaqus/Standard is based on the phantom nodes method [82]; in such method, these phantom nodes are superposed to the standard ones, to reproduce the presence of the discontinuity. Roughly speaking, phantom nodes are tied to their corresponding real nodes when the enriched element is intact. This situation holds until the element is not cut by a crack; as soon as the element is cracked, it is divided in two separate parts, each of them including both real and phantom nodes (see Fig. 3.8).

In particular, the separation procedure occurs when the equivalent strain energy release rate exceeds the critical strain energy release rate at the crack tip in an enriched element. Once this condition has been satisfied, every phantom node is no more restrained to its corresponding real one and thus, they can freely move apart.

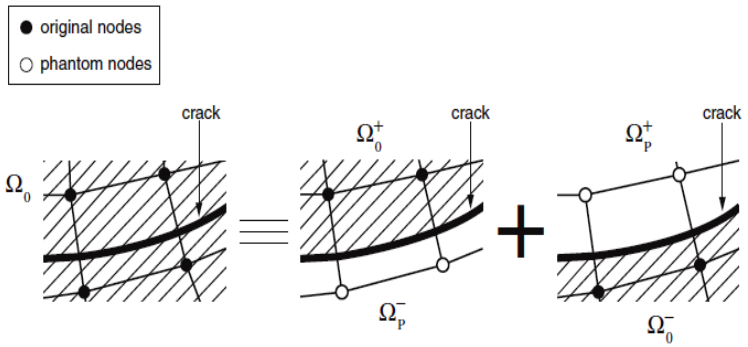

Figure 3-8 Phantom nodes method

3.2 FRANC2D\L

3.2.1 Introduction

The FRacture ANalysis Code (FRANC2D) was originally developed by Paul Wawrzynek at Cornell University. FRANC2D represented a significant step in the development of discrete fracture analysis programs because of its modular software design and topological

data structure. FRANC2D/L is a highly interactive program for the simulation of crack growth in layered structures. The program is an extension of FRANC2D to make possible there presentation of layered structures such as lap joints or bonded repairs. In addition, a linear bending option is available to account for the eccentricities of the layers when appropriate. Each layer is represented by a separate mesh that can overlap with other meshes and be connected with rivet or adhesive elements. Each layer is assumed to be flat, but either two-dimensional (in-plane) or three-dimensional (plate with bending) calculations can be performed.

3.2.2 Basics of Implementation

This section provides very brief descriptions of the implementation of the data base, data structure, and finite element concepts used in FRANC2D/L.

3.2.2.1 Data Structure

The core of the program is the data base (Fig.3.9). This is the repository of all the information used by the various parts of the program. The data base is only accessible through the data base access routines. All higher level routines are required to use the two types of access routines (modify and query routines) to store and retrieve information. The layer above the data base routines is the collection of routines which implement the computational functionality of the program. These are loosely grouped into six categories. Preprocessing routines perform modifications to the model description and boundary conditions. Re-mesh routines modify the element mesh for crack propagation. Fracture mechanics routines implement the various crack propagation theories and automatic load

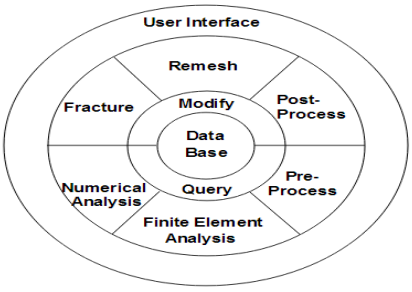

Figure 3-9 Conceptual organization of FRANC2D/L

factor modification. Post-processing routines display stress and displacement information. Finite element routines formulate element stiffness matrices, assemble global stiffness matrices, minimize problem bandwidths, solve for displacements, and recover element stresses. The numerical analysis routines perform functions necessary for the solution of systems of non-linear equations. Encircling the functional routines is the user interface, which is a collection of menu drivers and display routines to allow the analyst to interact with the program.The data structure used in FRANC2D/L is designed around a modified winged-edge data structure [84], [85] which was originally developed to store surface topology of polyhedra. The data structure consists of three topological entities: vertices, edges, and faces. Vertices correspond to finite element nodes, and faces represent finite elements (shown below).

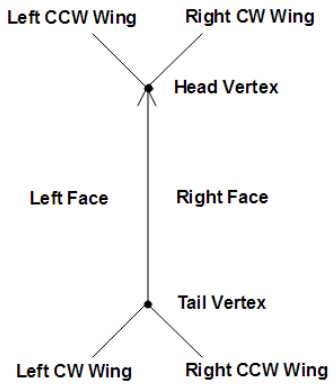

Figure 3-10 Winged-edge data structure

The main feature of this data structure is that each topological entity contains adjacency information which greatly reduces the time required to perform adjacency queries. The data structure is designed such that most adjacency queries are edge based, as the multiplicity of elements adjacent to an edge is known a priori, unlike that of a face or a vertex. An edge has two adjacent vertices, two adjacent faces, and four adjacent edges. The data base is accessed for modification or for queries. The local adjacency information embedded in the winged-edge data structure is very useful for performing tasks associated with finite element analysis. For example, it is a simple matter to identify the edges on the boundary of a structure being analyzed. This allows one to delete elements for crack propagation

without deleting the edges which define the structural boundary. The adjacency information also allows one to identify all the elements adjacent to a node so if the node is dragged to a different location element stiffness matrix can be recomputed.

3.2.2.2 Finite Elements

Continuum Elements

FRANC2D/L uses standard eight or six noded serendipity elements with quadratic shape functions. These elements perform well for elastic analysis and have the advantage that the stress singularity at the crack tip can be incorporated in the solution by moving the side nodes to the quarter-point locations [86].

Interface Elements

Interface elements are used to represent contact between surfaces. The user can specify a relationship between surface tractions and the relative displacements of the surfaces. The surface tractions are then integrated to give equivalent nodal loads. These loads are then included during the dynamic relaxation solution.

Rivet and Adhesive Elements

Rivets are treated as elastic shear springs, where the rivet stiffness is a material constant. Rivets can only be introduced at nodes. When a rivet connects two layers, it must be defined at a node in the upper layer. This eliminates the need to interpolate the displacements at a rivet point in order to calculate the rivet forces. At the same time it allows for efficient storage of information in the data base. An adhesive element is similar to a rivet element, except that the shear force is distributed over an entire element and is not confined to a node. It is assumed that the adhesive layer is homogenous, linear elastic and isotropic. The adhesive is assumed to deform only in shear and this deformation is uniform throughout the adhesive thickness. The surface shear transmitted through the adhesive is assumed to act as a surface traction on the adherents. The shear stresses in the adhesive are given by:

$$\tau = \frac{G}{h}(u_1 - u_2) \qquad (3.16)$$

Where:

t = Shear stress

G = Shear modulus

h = Thickness of adhesive

u = Displacements in layers 1 and 2

The adhesive forces are obtained by using the adhesive shear stresses as surface tractions on the layers and integrating. Since the surface tractions are proportional to the relative displacement of the two layers, the adhesive force can be expressed in terms of nodal displacements of the top and bottom layers. This gives a stiffness matrix for the adhesive elements.

3.2.3 Layers

A layered structure, such as a riveted lap-splice joint or a bonded lap joint, is actually a three dimensional structure. A three dimensional finite element or mathematical modeling of such a structure will involve several degrees of complexity. In FRANC2D/L simplifying assumptions are made which still allow us to capture the essential features of the response. The assumptions include:

-Each layer is considered as an individual two-dimensional structure under a state of plane-stress or plane-strain.

-Only linear out-of-plane displacements and bending effects are included.

-Individual layers can be connected with rivets or adhesive bonds.

-A rivet is treated as an elastic shear spring between two nodes of each layer. An adhesive is assumed to distribute shear forces across an entire element of each layer.

As noted, each layer is represented as a separate two dimensional finite element mesh. In the single layered version of FRANC2D/L the finite element information is stored in a central data base using a modified winged edge data structure. This data base is accessed by all the program subgroups. The strategy adopted to incorporate multiple layers in FRANC2D/L was to store the finite element mesh in a separate data-base for each layer. At any particular instant, only one layer is made available in the central data base. This is achieved by making use of two utility functions which load or unload a layer from the central data base. The analyst can choose to work on any particular layer by clicking on a menu button in the user interface. This strategy retains the modularity of the original

program. The data structure for the face has been modified to incorporate two additional pieces of information. These are face numbers corresponding to a face in the layers above and below it. This eases the navigation from one layer to another. To implement this all the layers must have exactly the same mesh in the regions in which they overlap where adhesives are used to attach the layers. This is required in the initial mesh and is automatically managed during remeshing. Although identical meshes simplify data management in the layers, identical meshes are also necessary to ensure correct integration of adhesive shear stresses on each side of a crack face. For regions where no adhesives will be used to attach layers the mesh is not required to be the same. The re-meshing routines will automatically detect whether the same mesh is required to preserve adhesive bonding and will automatically enforce the "same mesh" requirement when necessary.

3.2.4 Fracture

The fracture calculations incorporated in FRANC2D/L use two-dimensional linear elastic fracture mechanics (LEFM) concepts. The stress intensity factors which govern the fracture process in the LEFM context are calculated using the displacement correlation or modified crack closure techniques. FRANC2D/L can model quasi-static crack propagation and crack propagation due to fatigue loading. The crack will propagate in the direction predicted using any of the three propagation theories implemented in FRANC2D/L. They are the sigma theta max theory [88], the G theta max theory [89], and the S theta min theory [90]. Effectively, all approaches give the same crack trajectories and minimize the mode II stress intensity.

3.2.5 Re-meshing During Crack Growth

When performing a discrete crack analysis, not only the geometry of the crack is represented explicitly at each step, but the mesh must be modified at each step to reflect the current crack configuration. The automatic re-meshing strategy adopted in FRANC2D/L is to delete the elements in the vicinity of the crack tip, move the crack tip, and then insert a trial mesh to connect the new crack to the existing mesh, see figure 3.11 [83]. The modified Suhara-Fukuda algorithm [87] is used to generate this trial mesh of triangulated elements. The user is allowed to modify the mesh if it is not satisfactory. This technique exploits the

interactive nature of the software and ensures that the decision about the suitability of a mesh lies with the analyst.

3.2.6 Solution Procedures

Two solution methods are available to the user. The first is a direct linear equation solver for symmetric systems stored in skyline format. The linear solver is preferred and may be used for all cases except when nonlinear interface elements are being used. For this case it is necessary to use the dynamic relaxation solver. This solver is usually slower than the direct solver, but will always converge for nonlinear contact problems.

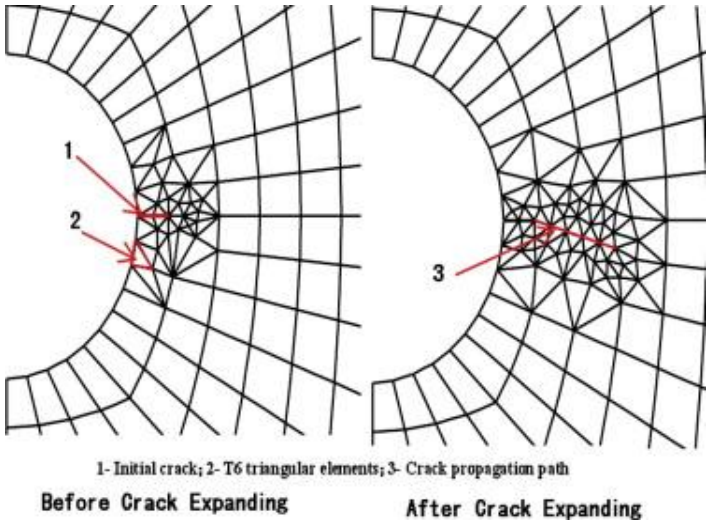

Figure 3-11 Sample of the singularized element growing along with the crack tip of 7050-T7451 aluminum alloy by Franc2D/L.

3.2.7 Computer Graphics

The FRANC2D/L program maximizes the graphical interaction between the user and the model by making graphical interaction an integral part of the algorithms. The ability to see a display of the model being analyzed and view the results in a graphical form is a very valuable functionality. The analyst interacts with the program through a menu driven user interface. This is a collection of routines which create and drive menus and call the appropriate action routines after an analyst chooses a menu option.

The low level graphics routines in the program have been encapsulated in one collection of routines called the application independent graphics subsystem (GRA). These routines are written in the C programming language to allow portability on UNIX platforms.

3.3 THE APPROXIMATE METHOD FOR DETERMINING STRESS INTENSITY FACTORS IN THE CASE OF MULTIPLE CRACKS BASED ON SUPERPOSITION

Linear-elastic fracture mechanics enables predicting crack growth based on a relationship between the stress intensity factor and the crack growth rate. The stress intensity factor can be calculated using various analytical and numerical methods. Closed form of solutions is usually there for a limited number of simple problems, such as infinite plane problems. Numerical methods such as the finite element method and boundary element methods, as noted above, are often used for the analysis of complex cracked structure. However, a large number of tips of cracks, which must be included in the analysis with the MSD problem, require major computing resources to be used for the finite element method. For this purpose it is necessary to introduce new and improve the existing approximate methods that will enable faster and simpler determination of the stress intensity factors of supporting aeronautical structures.

the case of the model, whose solutions for stress intensity factor are known and presented in section **2.3.1.3** (uniformly loaded infinite flat plate with two collinear cracks of different lengths), and which is shown in Figure 3-12 the stress intensity factor for the first crack (for its tip B which is closer to the next influential crack) shall be increased due to the presence of adjacent crack, and as such, can be represented as:

In:

$$K_{I1B} = K_{I1} + c_{2b} \cdot K_{I2} \tag{3-17}$$

Where:

K_{I1} - stress intensity factor of the first crack in the case it is the only crack in the structure;

K_{I2} - stress intensity factor of the second crack in the case it is the only crack in the structure;

K_{I1B} - stress intensity factor of the tip B of the first crack in the presence of adjacent crack;

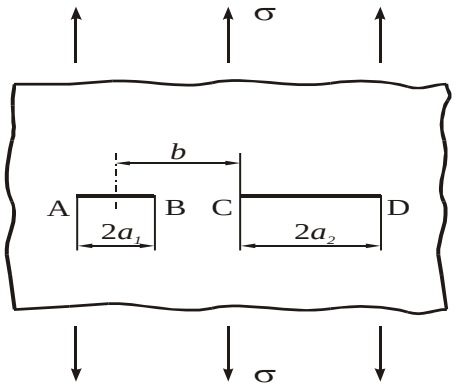

Figure 3-12 uniformly loaded infinite flat plate with two collinear cracks of different lengths

c_{2b} - coefficient which is used to take into account the increase of stress intensity factors of the tip B of the first crack due to the existence of adjacent one.

If the previous equation is written in function of geometric factors and cut with $\sigma\sqrt{a_1\pi}$, it is obtained:

$$\beta_{1B} = \beta_1 + c_{2b} \cdot \beta_2 \sqrt{\frac{a_2}{a_1}} \tag{3-18}$$

Where:

β_{1B} - Total geometric factor for the tip B of the first crack;

β_1 - Geometric factor for the first crack when it is the only crack in the structure;

β_2 - Geometric factor for the second crack when it is the only crack in the structure;

here after coefficient c_{2b} can be expressed as:

$$c_{2b} = \frac{\beta_{1B} - \beta_1}{\beta_2} \cdot \sqrt{\frac{a_1}{a_2}} \tag{3.19}$$

When for the shown configuration the geometric factors β1 and β2 are known and they have the value of one, for the coefficient c_{2b} is obtained:

$$c_{2b} = (\beta_{1B} - 1) \cdot \sqrt{\frac{a_1}{a_2}} \,. \tag{3.20}$$

Similarly is also obtained the coefficient which takes into account the increase of stress intensity factors of the left-further tip of the first crack due to the existence of adjacent one, as:

$$c_{2d} = (\beta_{1A} - 1) \cdot \sqrt{\frac{a_1}{a_2}} \,. \tag{3.21}$$

Where:

β_{1A} - Total geometric factor for the tip A of the first crack.

In the same way can be analyzed the tips C and D that belong to the second crack, where the corresponding coefficients are obtained:

$$c_{1b} = (\beta_{2C} - 1) \cdot \sqrt{\frac{a_2}{a_1}} \quad , \tag{3.22}$$

$$c_{1d} = (\beta_{2D} - 1) \cdot \sqrt{\frac{a_2}{a_1}} \quad , \tag{3.23}$$

Where:

- c_{1b} - coefficient which is used for taking into account the increase of stress intensity factor of the tip C of the second crack due to the existence of the adjacent one;
- c_{1d} - coefficient which is used for taking into account the increase of stress intensity factor of the tip D of the second crack due to the existence of the adjacent one;

In the case where the tips of cracks are furthered from the surrounding boundaries, these influence coefficients of first crack to the second one can be used in the case of other configurations. If we start from equation (3.23) of stress intensity factor of noticed crack in any of the analyzed configuration with n cracks it can be represented as:

$$K_{IjA,B} = c_{1b,d} \cdot K_{I1} + c_{2b,d} \cdot K_{I2} + \cdots + c_{jb,d} \cdot K_{Ij} + \cdots + c_{nb,d} \cdot K_{In} = \sum_{i=1}^{n} c_{ib,d} \cdot K_{Ii}\,, \tag{3.24}$$

Where:

$K_{IjA,B}$ - stress intensity factor of the tips A, B respectively of the observed crack in the presence of all the other cracks in the configuration;

K_{Ii} - Individual stress intensity factors of all the other cracks in the configuration, i.e. stress intensity factors of auxiliary configurations;

$c_{ib,d}$ - coefficient that takes into account the effect of the crack *i* on stress intensity factor of the observed crack (if the tip of analyzed crack is closer to the influential one, i.e. it is located on the same side, then it is taken c_{ib}, and if it is positioned futherly, then it is taken c_{id}), whereby it is assumed that the coefficient of influence of analyzed crack at itself is $c_{jb,d} = 1$.

For the determination of these coefficients can be used the equations (3.20) and (3.21), whereby one must take into account the distance between the cracks, as well as the influence on the position of the crack in relation to the analyzed crack. The stated equations for the general case can be expressed as:

$$c_{ib} = \left(\beta_{jB} - 1\right) \cdot \sqrt{\frac{a_j}{a_i}}\,, \tag{3.25}$$

$$c_{id} = \left(\beta_{jA} - 1\right) \cdot \sqrt{\frac{a_j}{a_i}}\,, \tag{3.26}$$

Where:

β_{jB}- Geometric factor of analyzed crack for tip B in the case that it and the influential crack are the only ones in configuration (it is determined using the equation (3.21));

β_{jA}- Geometric factor of analyzed crack for tip A in case that it and the influential crack the only ones in configuration (it is determined using the equation (3.22));

a_j - Length of analyzed crack;

a_i - length of influential crack;

Wherein for the calculation of the equation (3.21) and (3.22), due to their complexity, computer programs can be used. For that purpose here is used program package MatCad .

3.3.1 Verification of Proposed Method

Thus defined method was tested on a model whose solutions for stress intensity factor are known and presented in section 2.3.1.4, which is shown in the figure below (Figure 3-13).

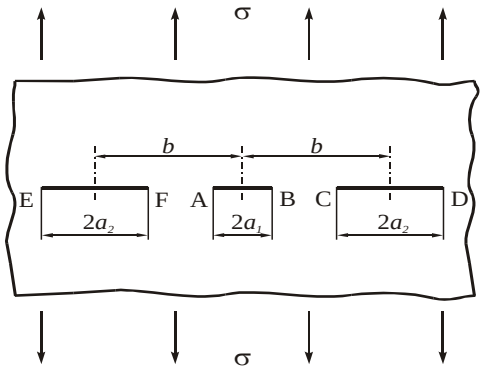

Figure 3-13 Uniformly loaded infinite flat plate with three collinear cracks

It is the case of uniformly loaded infinite flat plate with three collinear cracks. If it is added the designation 1 to the central crack, from its left side the designation 2, and from the right side designation 3 and if we apply the equation (3.24) for this model, for determination of stress intensity factor for tip B, the following equation is obtained:

$$K_{I1B} = c_{1b,d} \cdot K_{I1} + c_{2b,d} \cdot K_{I2} + c_{3b,d} \cdot K_{I3}, \tag{3.27}$$

Whereby

K_{I1} - stress intensity factor of the first crack;
K_{I2} - stress intensity factor of the second crack;
K_{I3} - stress intensity factor of the third crack;
$c_{ib,d}$ - Corresponding influential cracks, ($i = 1,\ldots 3$).

If we use the symmetry of the initial configuration ($K_{I2} = K_{I3}$ and $a_2 = a_3$), and if the previous equation is divided by $\sigma\sqrt{\pi \cdot a_1}$ then it is obtained:

$$\beta_{1B} = c_{1b}\beta_1 + \left(c_{2b} + c_{3d}\right)\cdot \beta_2 \sqrt{\frac{a_2}{a_1}}, \tag{3.28}$$

Where: $c_{1b,d} = 1$.

Since the geometrical factors of the individual cracks are equal to one in this case, the equation is finally obtained for the calculation of a geometric factor for the tip B:

$$\beta_{1B} = 1 + \left(c_{2b} + c_{3d}\right)\cdot \beta_2 \sqrt{\frac{a_2}{a_1}} \tag{3.29}$$

The same procedure is applied to determine the stress intensity factor of all other tips, whereby because of the symmetry $\beta_A = \beta_B,\ \beta_F = \beta_C$ i $\beta_E = \beta_D$:

$$\beta_F = c_{1b}\sqrt{\frac{a_1}{a_2}} + 1 + c_{3b}, \tag{3.30}$$

$$\beta_E = 1 + c_{2d} + c_{1d}\sqrt{\frac{a_1}{a_2}}. \tag{3.31}$$

Distances necessary for calculation of influential coefficients are shown on Figures 3-14, 3.15 and 3.16:

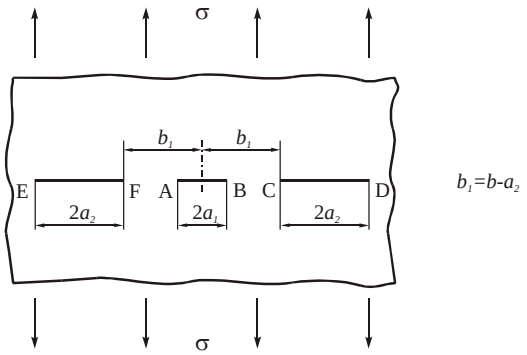

Figure 3-14 Calculation of influential coefficient at distance b_1

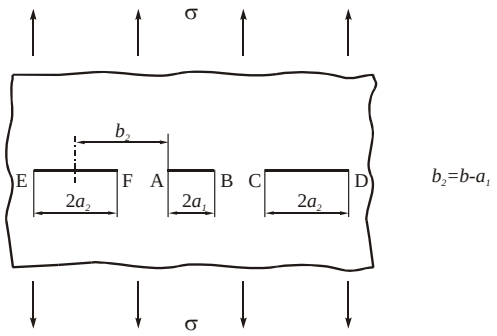

Figure 3-15 Calculation of influential coefficient at distance b_2

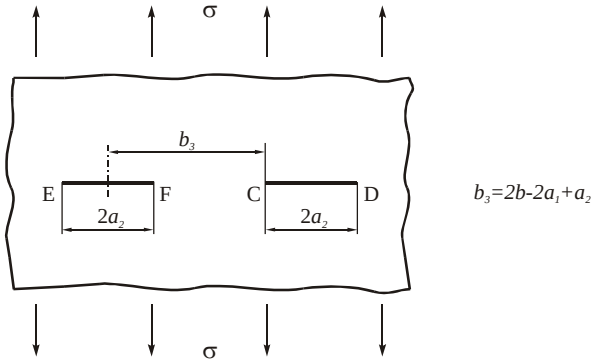

Figure 3-16 Calculation of influential coefficient at distance b_3

In determining the last distance it was out is the first crack because along that crack there is not load transfer. Influential coefficients are calculated using the equations (3.25) and (3.26), using the program package MatCad. All previously stated geometrical factors are calculated for different lengths of cracks, as well as for the various distances between the centers of the cracks.

Chapter 4 Stress Intensity Factor for Multiple Cracks on Flat Panel Made of 2024-T3 Aluminum alloy

4.1 THE ANALYSIS OF MSD CONFIGURATION USING XFEM

In this thesis a FE model of a flat, un-stiffened panel with 11 fasteners holes subjected to uniform uni-axial stress (values = 50, 100 and 200MPa) is created to examine effects of MSD on fatigue crack growth rates. The FE model was based on the configuration of panels tested by Luzar in 1997 [91]. 2024-T3 clad MSD panels were fabricated and tested to determine fatigue crack growth values of airframe structure materials with MSD. The panel thickness, fastener hole diameter and fastener pitch were selected as being representative of an actual aircraft lap joint configuration. The test panels were held by the grip end fixtures resulting in all of the test loads being transmitted through joint friction. The loading arrangement has been demonstrated to produce uniform stress and displacement conditions throughout the test section.

The model material and dimensions are described as following:

-Width $L_1 = 609.6$ mm

-Length $L_2 = 863.6$ mm

-Thickness $t = 1.6$ mm

-Distance between centers of holes $b = 25.4$ mm

-Holes radius $r = 3.23$ mm

-Young's elasticity modulus $E = 73000$ MPa

-Poisson's coefficient $\nu = 0.33$

A uniform tensile stresses were applied at the top and bottom edges of the model (Fig. 4.2). Each hole in the panel had two radial cracks, numbered from 1 to 22 in Fig. 4.1 and positioned as shown in Figure 4.3. Figure 4.3 also shows a portion of the mesh around the holes, and as it can be seen mesh was refined around the cracks at the edges of each hole

and a uniform template of elements around each crack front was used. Final mesh consisted of 163228 linear hexahedral elements of type C3D8R and 206800 nodes. This mesh was used to calculate SIFs at crack nodes as a function of crack length. The crack growth simulation capability of Morfeo/Crack for Abaqus was used for this purpose. Morfeo/Crack calls Abaqus at each propagation step and between the steps and reads the Abaqus solution, recovers a richer, improved XFEM solution in a small area surrounding the crack and computes the SIFs at crack front nodes [92]. After that, it determines the appropriate crack growth increment, extends each crack and then performs the next solution step. Results of this procedure can be seen in sections from (4.1.1) to (4.1.3). The initial crack length used was 0.5mm.

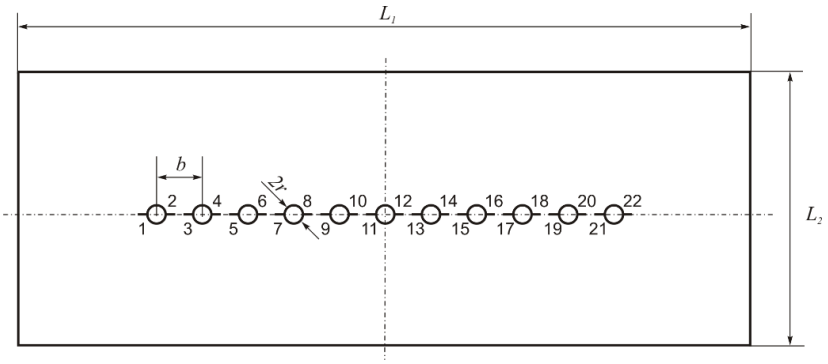

Figure 4-1 Analyzed configuration with multiple cracks (not drawn to scale)

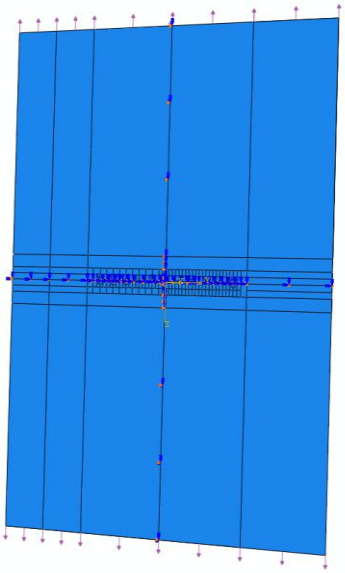

Figure 4-2 Panel with loads and boundary conditions (drawn to scale)

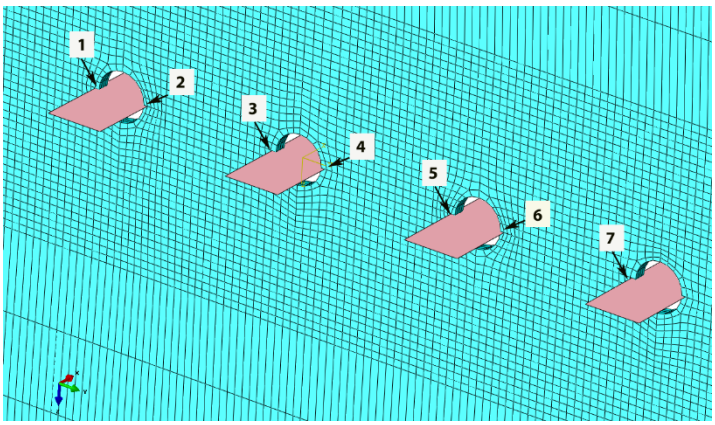

Figure 4-3 Crack's positions and numbering

4.1.1 Stress intensity factor results of 50MPa applied stress

As mentioned before, SIFs were calculated for each crack front and different crack sizes. Maximum values of SIFs calculated along the crack fronts were used as a reference. The SIF results shown in Figures from 4-4, to 4-8 8 represent the solutions for cracks from 1to crack 22.

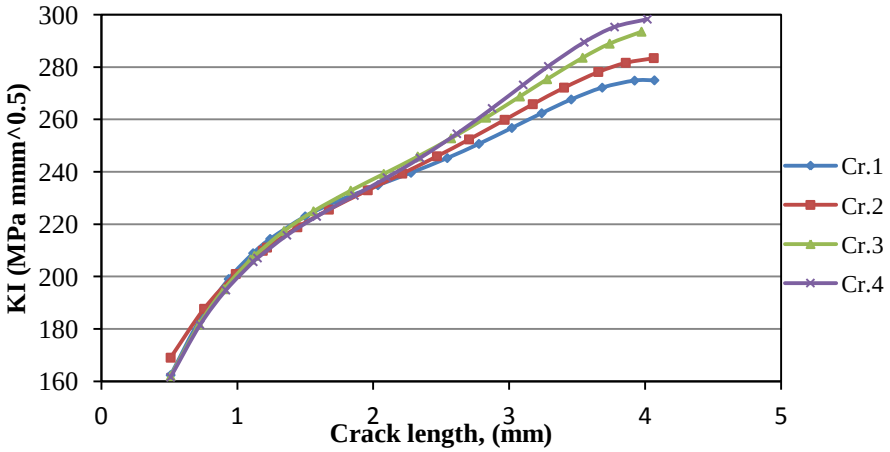

Figure 4-4 histories for selected cracks, applied stress 50 MPa

As shown in Figure 4-4, these histories were almost had identical trend for the first four crack tips (numbered left to right). There is an increase in values of stress intensity factors for the 4 cracks as the cracks grow. But the SIF greater value was recorded to crack number 4 because of interaction effect with surrounding cracks and holes. At the 17th growth step, the SIF for the rightmost crack tip (crack number 4, CL=4.0169mm and

SIF=298.2603 MPa$\sqrt{mm}$ and crack 1, CL=4.069mm, SIF=270.9276 MPa$\sqrt{mm}$)was about (9%) less than the average of the interacting crack tip, This means that this is the slowest growing crack, as seen in Figure 4-4.

As it can be seen in Fig. 4-5 the highest SIFs values are for crack 7 and 8, that is, for the cracks emanating after the rightmost two holes; the highest average difference stress intensity factor value between crack number 8 and 4 is (5%) and between crack number 3 and 7 is (8%) due to the increasing in stress concentration value closer the middle panel holes. The strongest effects of interactions with surrounding crack tips and stress concentration at this location are clear in Figure 4-6 (crack tips from 9 to 14), where

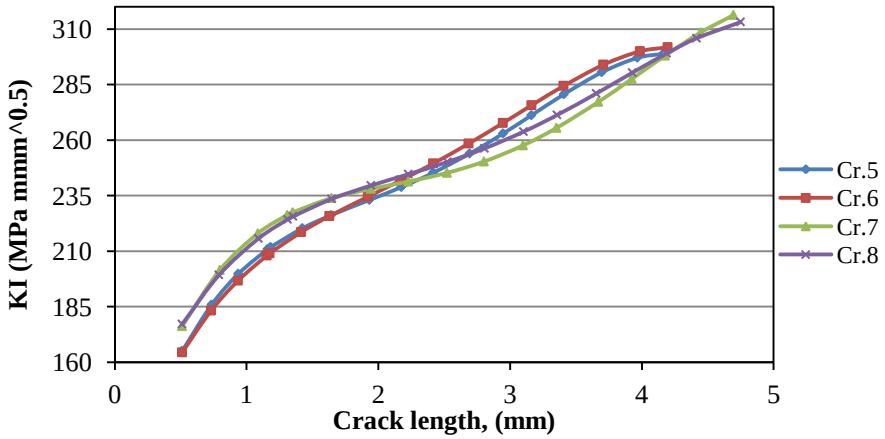

Figure 4-5 SIF histories of cracks from 5 to 8, applied stress 50MPa

intensification from interaction is expected to be more than that for all other cracks. The highest differential average SIF value was recorded between crack 9 (17%) (CL=4.4008mm, SIF=322.1087MPa$\sqrt{mm}$) and crack 1 (CL=4.069mm, SIF=274.9276MPa$\sqrt{mm}$).

Figures 4-7 shows SIF histories of the cracks from 15 to 18 (four cracks), the lowest value of SIF recorded to crack number 16 (CL=4.2173 mm, SIF=309.557 MPa$\sqrt{mm}$) and the highest was for crack 18 (CL=4.7857 mm, SIF= 319.7131 $MPa\sqrt{mm}$), the other cracks show the same trend. Due to the symmetry of the panel shape, crack 18 had the same position of crack 8 and the average differential in value of SIF was (2%), and almost equal

to (2.5%) between crack 6 (CL = 4.1954 mm, SIF= 301.8159 MPa$\sqrt{mm}$) and crack 16 (CL=4.2173 mm, SIF= 309.557MPa$\sqrt{mm}$) at the end of simulation procedure (step 17).

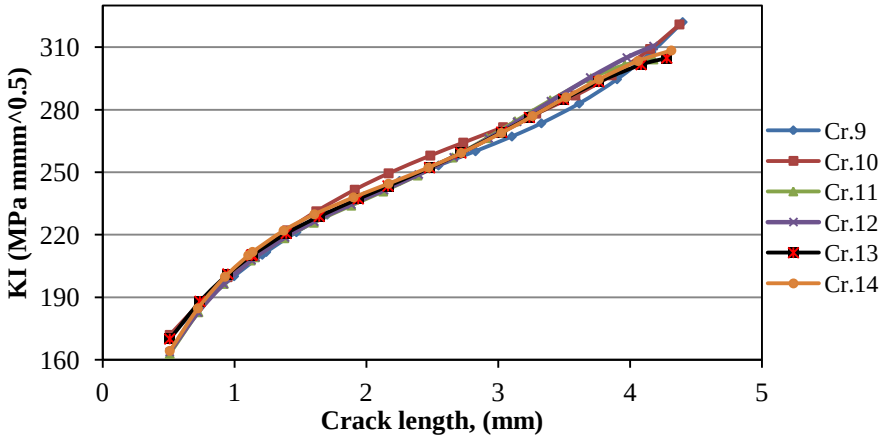

Figure 4-6 SIF histories of cracks from 9 to 14, applied stress 50MPa

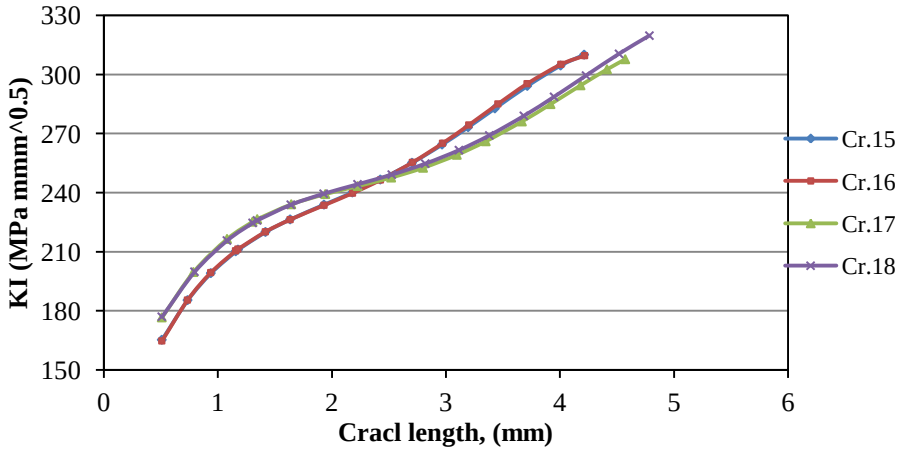

Figure 4-7 histories of cracks from 15 to 18, applied stress 50MPa

Figure 4-8 shows SIF histories for cracks 19, 20, 21, and 22, the highest SIF value was recorded to crack 20 (CL = 4.36 mm, SIF=301.0248 $\sqrt{mm}$) and the lowest for crack 22 (CL = 3.645 mm, SIF = 277.0445MPa $\sqrt{mm}$), those cracks had the same position coordinates of cracks 1 and 3 and the average difference between SIF were (0.77%) for the lowest and (6%) for the highest respectively.

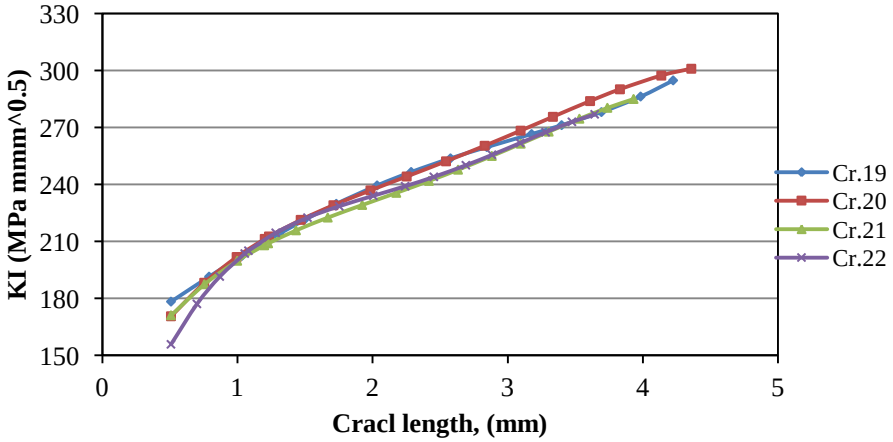

Figure 4-8 histories of cracks from 19 to 22, applied stress 50MPa

4.1.1.1 Comparison and Results Analysis

A constant-amplitude, cyclic loading condition was applied to the panel including tensile loading of 50 MPa with a stress ratio of R = 0.1. The fatigue cracks in this simulation usually grow in a direction perpendicular to the tensile stress that tries to open the crack. This kind of crack opening is called mode I, The simulation results show the K_I was the principle domain as shown in the following table:

Table 4-1Crack 1SIF's histories for first ten steps

Stp. No.	Crack length, (mm)	K_{eff}	K_I	K_{II}	K_{III}
1	0.51	163.981	162.3446	1.50226	-0.134752
2	0.727	187.64	183.723	0.846591	0.972004
3	0.937	200.376	199.0403	1.17381	-0.0851593
4	1.117	203.985	208.8989	178.714	119.123
5	1.242	217.907	214.3549	4.77696	2.70084
6	1.5	221.845	222.9718	2.04253	-3.14603
7	1.739	231.503	228.865	-1.56305	0.260962
8	2.035	233.741	234.8713	-2.8671	1.34936
9	2.278	240.097	239.6154	-4.70756	1.05455
10	2.545	244.911	245.2266	-2.96202	-1.03756

The crack propagation simulation carried out on un-stiffened panel with eleven holes and the cracks stared as shown in figure 4.1. Fig. 4.9 shows the stress distribution around the holes at first step, the plastic deformation occurs in every cycle and the crack is thus growing through plastic zones of previous cycles. Figures 4.10 and 4.11 show that the plastic zones of multi-site cracks started to contact each other at steps 5 and 10 as the cracks propagate.

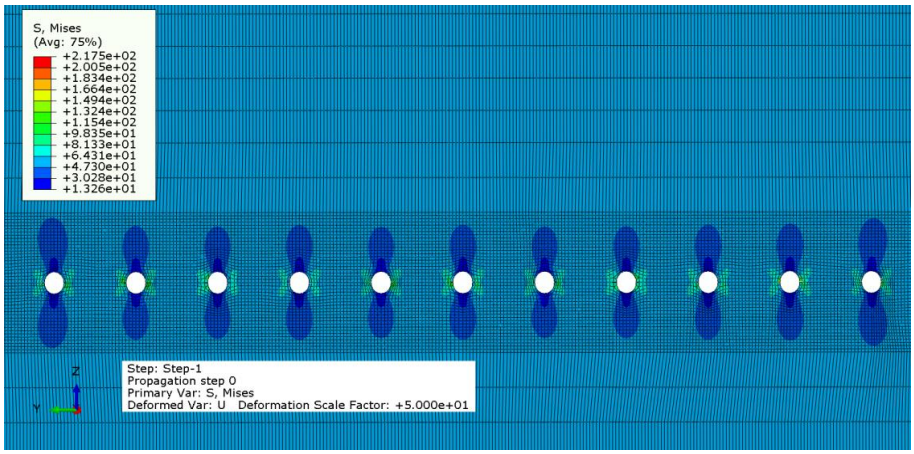

Figure 4-9 XFEM model of MSD panel after cracks' opening (the first step, σ=50MPa)

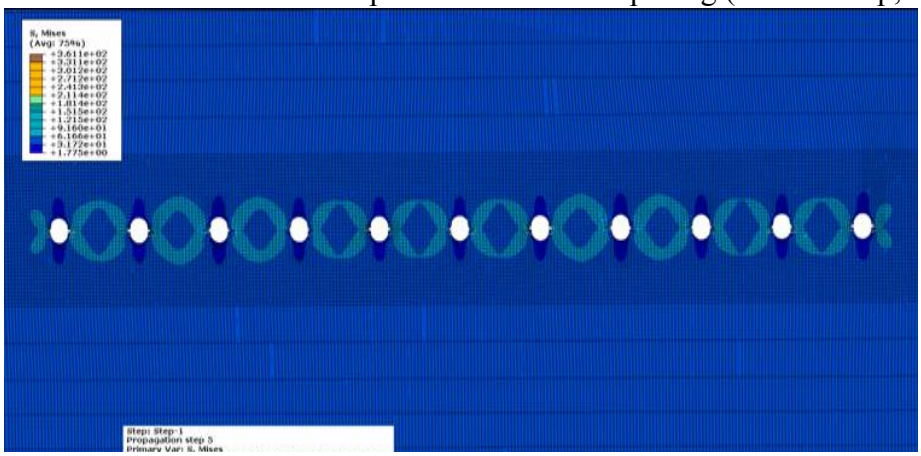

Figure 4-10 XFEM model of MSD panel after cracks' opening at fifth step

Figure 4.12 shows the variation in stress intensity factors with crack length for each crack increment of the XFEM. The highest values of SIFs are for the cracks11 and 12, that is, for the cracks emanating from the sixth hole. This becomes more obvious with cracks' growth. The values of SIFs for cracks at the first and eleventh hole are lesser and they are nearly the same, the maximum and minimum differential average value of SIF were between crack 1 and 12 (13%) and (0.77%) between cracks 1 and 22, respectively. This can be explained by the fact that the crack interaction effect is more dominant for the cracks at middle holes, than for the cracks at "edge" holes. And, as mentioned before, that is precisely why the cracks 1, 2, 11, 12, 21 and 22 are selected for results presentation. As the remote stress level increases, the plastic zone sizes of different cracks will increases and will eventually

touch each other. When the plastic zone of the lead crack meets the plastic zone from the nearest neighboring MSD crack, the ligament has effectively yielded, see figures 4.10 and 4.13. Once this occurs, the lead crack effectively extends to the far end of the MSD crack. Figure 4.13 shows a schematic of this linkup criterion. When the applied load reaches a level that causes the effective panel to yield, the panel will fail, [14].

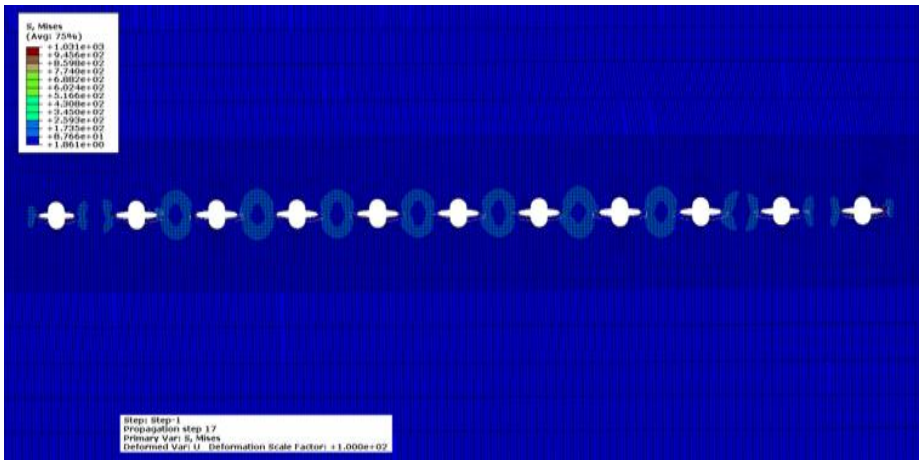

Figure 4-11 XFEM model of MSD panel after cracks' opening at seventeenth step

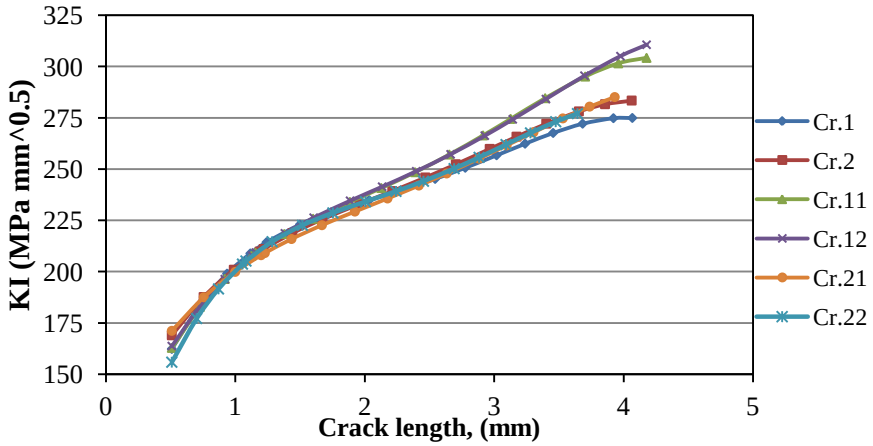

Figure 4-12 SIF histories for selected cracks in analyzed load case σ=50MPa

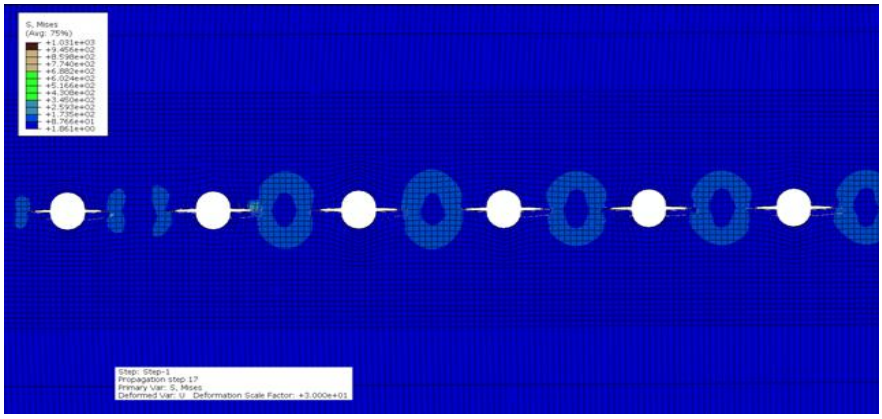

Figure 4-13 the interaction of cracks plastic zones

4.1.2 Stress intensity factor results of 100 MPa applied stress

In this section, the applied stress increased to 100 MPa and the results were plotted as a relation between crack length and stress intensity factor as following:

Figure 4.14 shows the growing trend of cracks 1, 2, 3 and 4, it is clear that as crack grows as the value of stress intensity factor increases. The recorded steps were 32 steps until the end of the simulation, it can be seen as the cracks approach each other and there is a rapid increase in SIF'S at crack tips especially the cracks 2(CL=5.884, K_I=755.0211MPa$\sqrt{mm}$) and crack 3 (CL=6.193mm, K_I=798.5618 MPa$\sqrt{mm}$). The highest SIF average difference value was recorded between cracks 1 and 4 (35%).

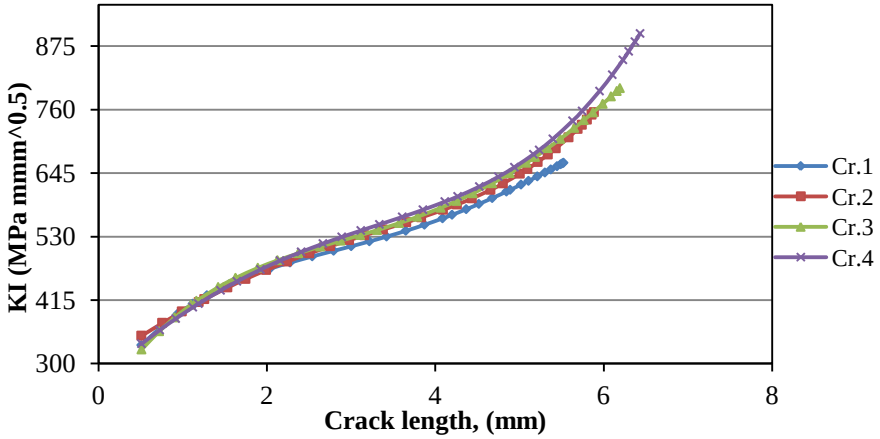

Figure 4-14 SIF histories of cracks from 1 to 4 in load case σ=100MPa

Figure 4.15 shows SIF histories of the cracks from 5 to 8, the highest SIF value was to crack 8 (CL=8.8219mm, SIF=1403.893MPa$\sqrt{mm}$) which was higher by (32%) than SIF of crack 5 (CL=7.2514mm, SIF=954.5087MPa$\sqrt{mm}$). Furthermore, it was higher more than (100%) comparing with SIF value of crack 1 due to crack 1 didn't interact with other cracks (interaction effect was present in this MSD problem).

Figure 4.16 shows that the cracks 11, 12, 13, and 14 had a little difference in crack lengths and SIF values (identical trend) in comparison with cracks 9 and 10 which had a lager crack lengths and SIF's. The maximum difference was between crack 9 (CL=8.431mm, SIF=1535.685MPa$\sqrt{mm}$) and 13 (CL=7.4263mm, SIF=1063.003MPa$\sqrt{mm}$) (44.5%).

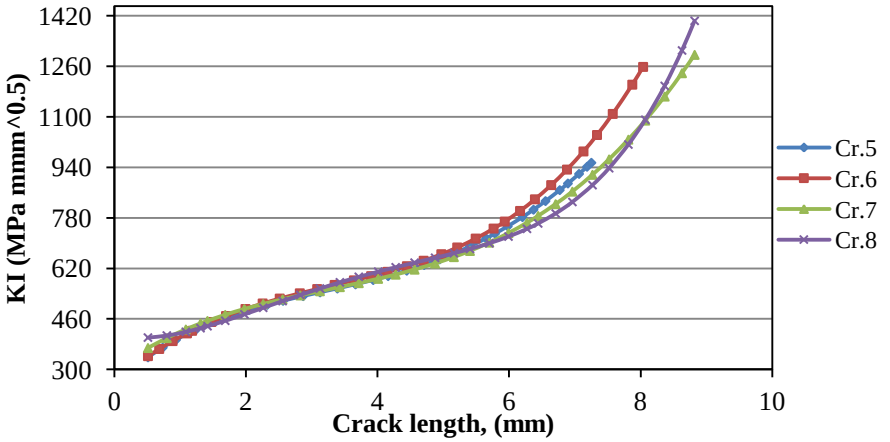

Figure 4-15 SIF histories of cracks from 5 to 8 in load case σ=100MPa

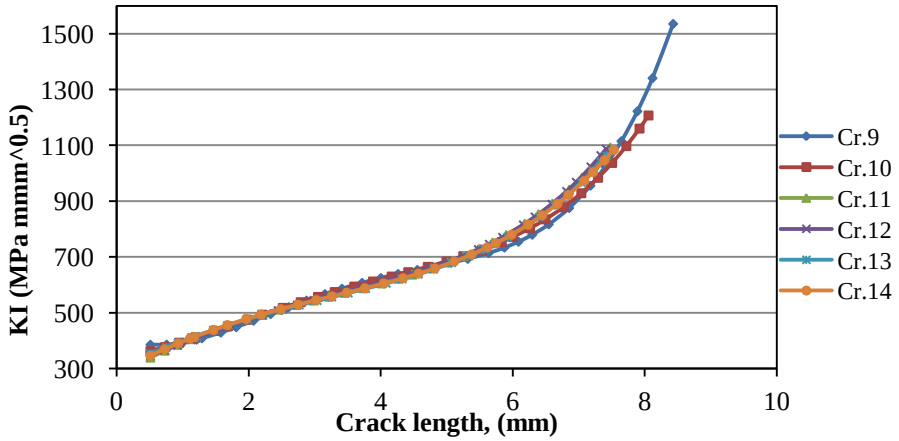

Figure 4-16 histories of cracks from 9 to 14 in load case σ=100MPa

Figure 4.17 shows the growing behavior of cracks 15, 16, 17 and 18, it is noted that as the cracks 16 and 17 grow as the value of SIF diverges and reaches its limit at the end of simulation (step 32) due to the effect increasing of stress concentration on their location. SIF value of crack 18 (CL = 8.38mm, SIF=1078.415 MPa$\sqrt{mm}$)was lower about (4.5%) from the highest SIF (crack16, CL = 7.9653 mm and SIF = 1126.949MPa$\sqrt{mm}$).

Figure 4.18 shows the fastest crack growing was recorded to crack 19 (CL = 7.5182 mm, SIF = 988.5834MPa$\sqrt{mm}$), and the lowest was to crack 22 (CL= 5.161mm, SIF= 689.2507MPa$\sqrt{mm}$) because of less interaction with surrounding cracks and holes.

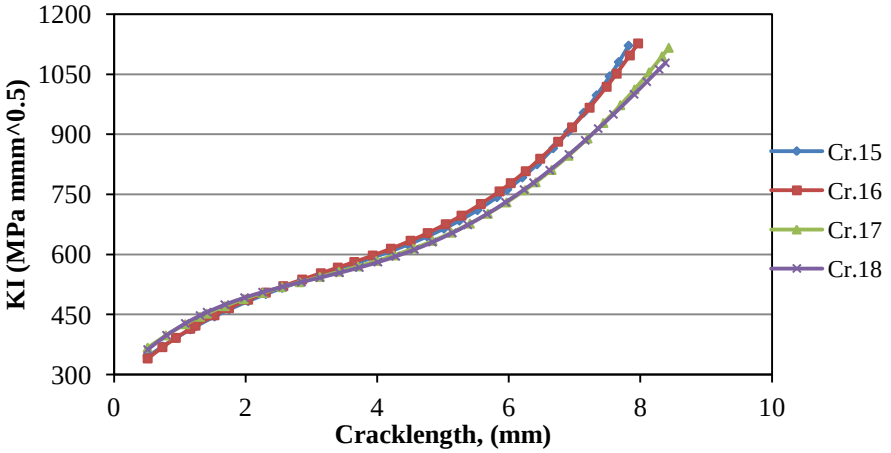

Figure 4-17 SIF histories of cracks from 15 to 18 in load case σ=100MPa

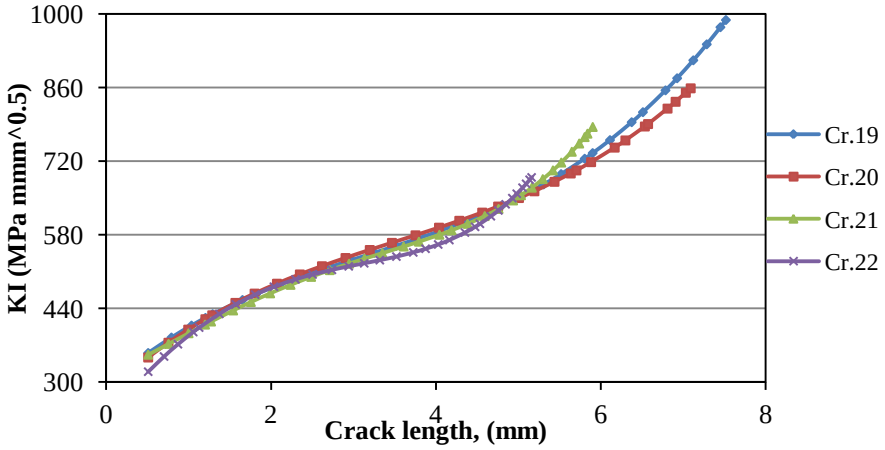

Figure 4-18 SIF histories of cracks from 19 to 22 in load case σ=100MPa

4.1.2.1 Comparison and Results Analysis

The second case of study is increasing the applied stress from 50 MPa to 100 MPa, the simulation results show an increase in SIF'S values and K_I was the principle fracture domain as shown in table 4-2 (crack1 as example). The holes are causing an inhomogeneous stress distribution as seen in figure 4.19; its clear from the figure the stress concentration was at the root of the holes. This phenomenon was confirmed by many authors, [14 and 93].

Figures from 4.20 to 4.23 show the cracks propagation of some selected steps, it can be seen as cracks from each two adjacent rivet holes grew toward each other as the plastic zones for each crack getting closer to each other and this causing increasing stress intensity value due to the yielding of the material. Once this occurs, the lead crack effectively extends to far end the MSD crack.

Table 4-2 Crack 1SIF's histories for first ten steps

Stp. No.	Crack length, (mm)	K_{eff}	K_I	K_{II}	K_{III}
1	0.5	329.119	333.1501	3.56977	-0.474797
2	0.727	375.28	364.223	1.693992	1.94449
3	0.937	400.752	389.4697	2.35129	-0.167836
4	1.117	407.969	408.0366	191.579	127.158
5	1.287	431.232	423.3144	2.17316	6.74677
6	1.555	436.014	443.6538	3.48205	-0.840761
7	1.766	457.455	457.0398	-1.427	-5.34901
8	2.035	469.935	471.5584	-3.70506	0.919928
9	2.274	482.198	482.7269	5.89359	-2.19525
10	2.538	489.629	493.8706	-4.24987	-8.30596

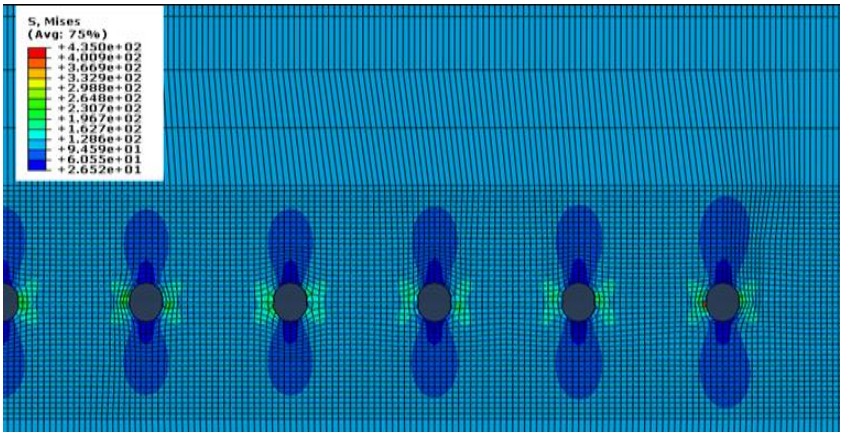

Figure 4-19 Stress distribution around the holes after first step load

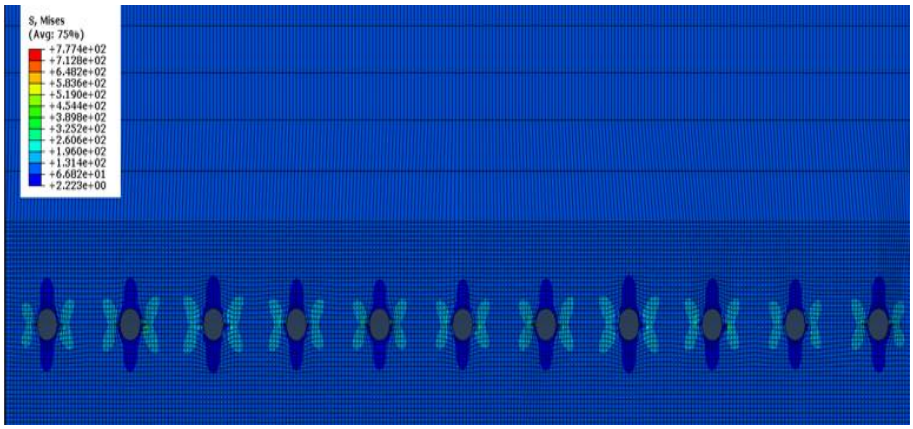

Figure 4-20 XFEM model of MSD panel after cracks' opening after 5 steps of crack propagation

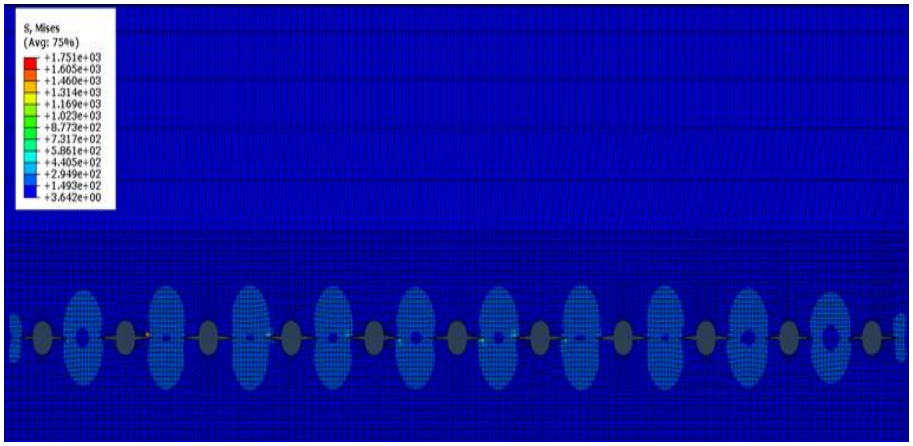

Figure 4-21 XFEM model of MSD panel after cracks' opening after 16 steps of crack propagation

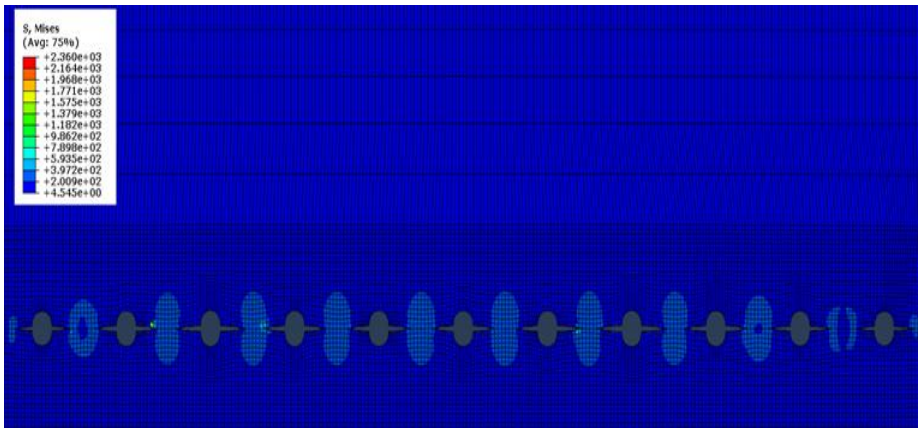

Figure 4-22 XFEM model of MSD panel after cracks' opening after 23 steps of crack propagation

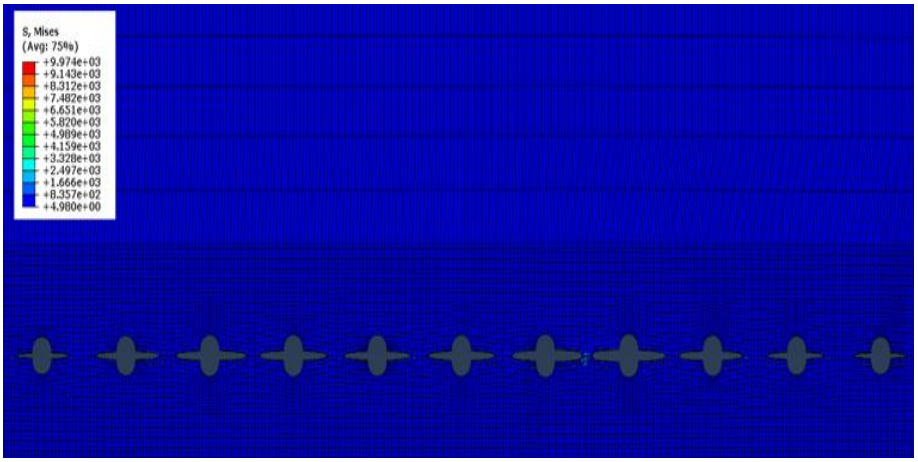

4-23 XFEM model of MSD panel after cracks' opening after 32 steps of crack propagation

Figure 4.24 shows the change in SIFs with crack length for each crack increment. The highest values of SIF's were for crack 11 and crack 12, i.e., for the cracks onset from the sixth hole. This explains the cracks interaction effect is dominant for the cracks in the middle hole, than the crack at the edge holes. The maximum differential average of SIF was (65%) between crack 11 and 1, (58%) between crack 11 and 22. And, as mentioned before, that is precisely why the cracks 1, 2, 11, 12, 21 and 22 are selected for the results presentation.

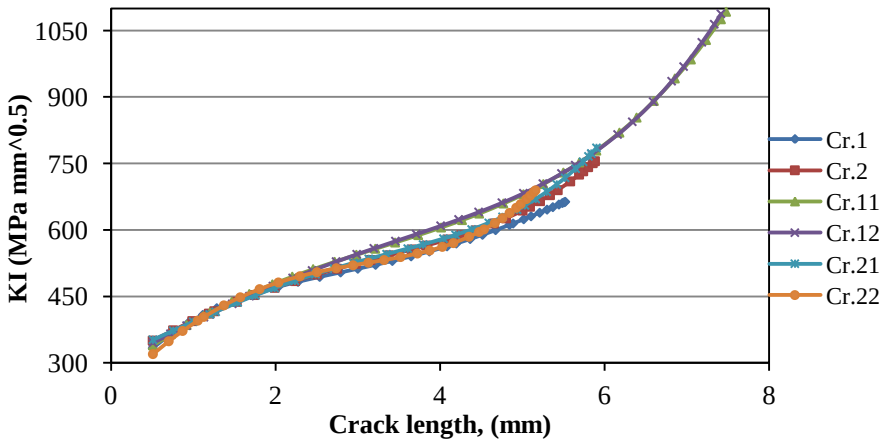

Figure 4-24 SIF histories for selected cracks in load case σ=100 MPa

4.1.3 Stress intensity factor results of 200 MPa applied stress

Application of a strictly increasing load to a flawed structure may not be critical at first since the load needs to be at some critical level in order for crack growth to occur. At this point stable or unstable crack growth occurs dependent on the characteristics of the material resistance to continuous growth and the driving force dependence vs. crack extension. However, at some point, assuming a strictly increasing load, the component or structure will fail due to loss of load bearing capacity or functionality, [94]. The third studying case was considering the effect of 200 MPa applied stress on the relation between crack length extension and stress intensity factor for each crack length increment. It is worth mentioning that, in this case 63 steps were recorded until the end of simulation using XFEM. The achieved results are described in charts as following:

Figure 4.25 shows the comparison between crack length and stress intensity factor for cracks 1, 2, 3, and 4; it can be seen from this figure the cracks behave and show a linear relation as crack extends until specific increment and then there is a rapid increase in SIF values comparing with crack length especially after specific simulation steps (from step 37 till 44). This behavior confirmed by many researchers [95] and [96].

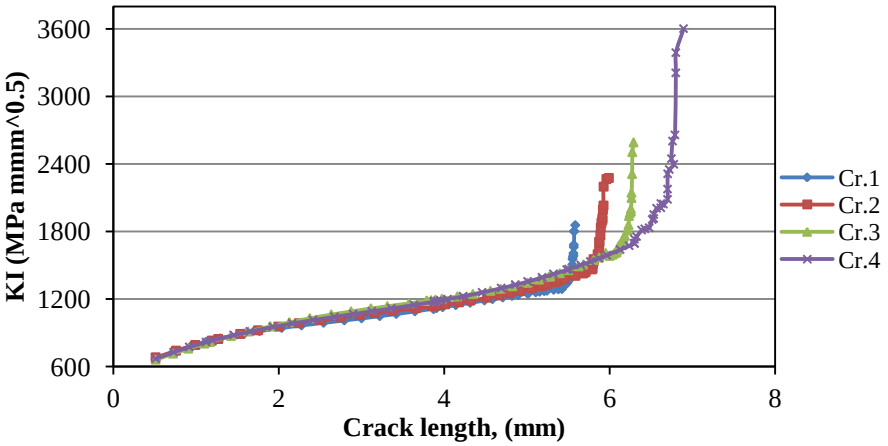

Figure 4-25 SIF histories of cracks from 1 to 4 in load case σ=200 MPa

Also the rapid increase in SIF values of crack 1 appeared at steps from step 36 till the end of simulation (step 63), SIF was equal to (1286.179MPa$\sqrt{mm}$) and reached (1855.59 $\sqrt{mm}$) for 0.204 mm (CL=5.379 mm to 5.583 mm) crack elongation. Also for crack 4 (the

longest crack length) the SIF value changed from (1588.916MPa$\sqrt{mm}$) at step 36 and reached (3601.88MPa$\sqrt{mm}$) for 0.9293 mm crack elongation (C.L = 5.9627 to 6.892 mm). This happened due to the high value of applied stress and the interaction between adjacent cracks especially the interaction influence between cracks 2 and 3 and between 4 and 5.

Figure 4.26 shows the same trend of the previous curve for the cracks 5, 6, 7, and 8, it can be observed that the values of SIF were higher due to the increase of stress concentration as we approaching to the middle of the panel. Additionally, SIF's rapid increase for the mentioned cracks were recorded; particularly this occurs starting from step 37 for crack 5 and at step 49 for crack 8 which had the longest crack length (9.4562 mm, SIF=5995.55 MPa$\sqrt{mm}$). Furthermore, the linkup between crack tips 4(see fig. 4.25) and 5 occurred at simulation step 50, at step 40 between crack tips 6 and 7 and at step 47 between 8 and 9.

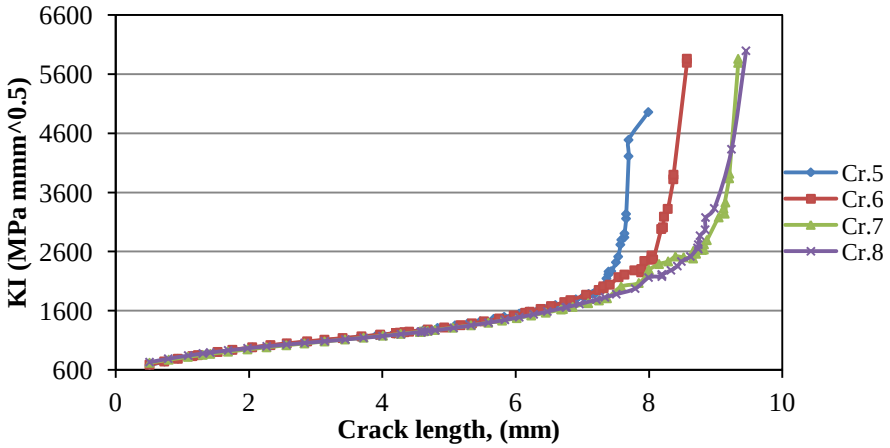

Figure 4-26 SIF histories for cracks from 5 to 8 in load case σ=200 MPa

Figure 4.27 represents the relationship between crack growth and SIF histories for cracks 9, 10, 11, 12, 13 and 14, it is noticeable that the rapid increase in SIF'S values occurs when the area between two adjacent cracks weakened by link up influence as observed in the previous graphs; 8 and 9 crack tips were linked up at step 47, crack tips 14 and 15 at step 54 and crack tips 12 and 13 at step 59, the longest crack length was recorded to crack 10 (CL=10.5543mm, SIF = 4113.89MPa$\sqrt{mm}$).

It is clear that from figure 4.28 that the longest crack is of that crack 16 which had the length of (9.439mm) and SIF (3515.9MPa$\sqrt{mm}$), also during the simulation, the linkup between cracks 16 and 17 occurred at step 61 and the rapid increase in SIF value take a

place at the last steps of simulation. Also the linking up between two crack tips 14 (9.4934mm, SIF=5134.8MPa$\sqrt{mm}$) and 15(9.3009 mm, SIF=4332.91MPa$\sqrt{mm}$) observed at step 54.

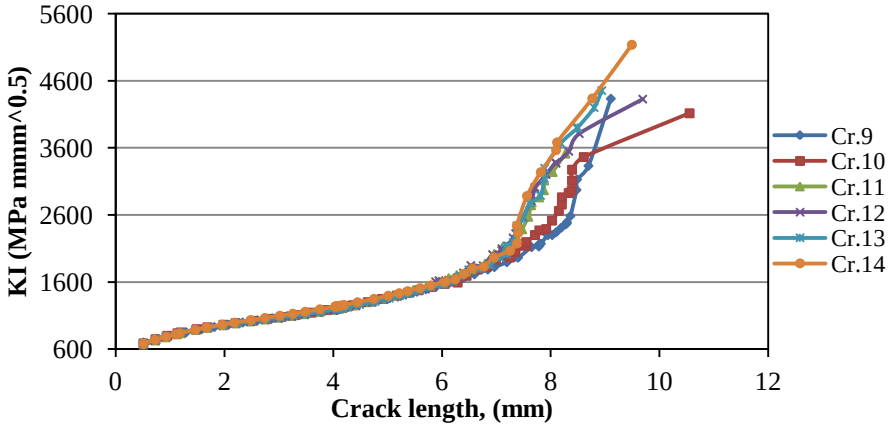

Figure 4-27 SIF histories for cracks from 9 to 14 in load case σ=200 MPa

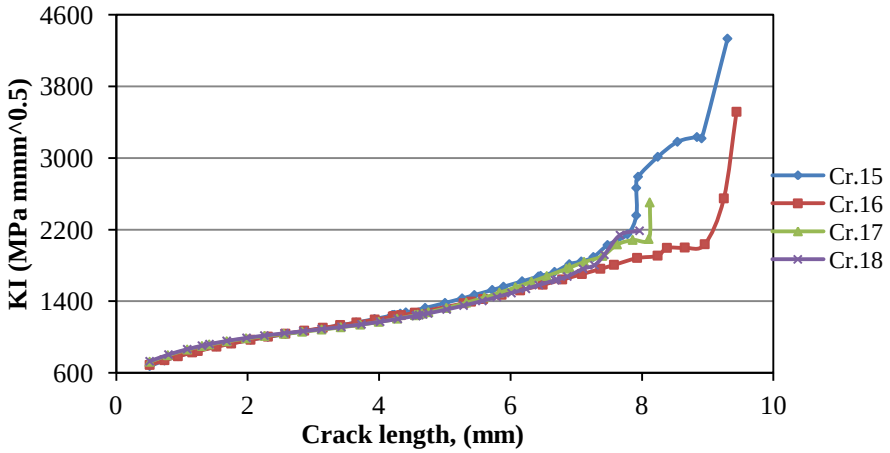

Figure 4-28 SIF histories for cracks from 15 to 18 in load case σ=200 MPa

Figure 4.29 shows the corresponding SIF value as the cracks grow; in this figure there is no interaction were recorded between crack tips and there were decrease in SIF values compared the previous curves due to decrease of stress concentration in this area. The highest SIF was to crack 19 (7.1429mm, SIF=1900.4 MPa$\sqrt{mm}$) and the lowest was to crack 22 (5.041 mm, SIF= 1330.14MPa$\sqrt{mm}$).

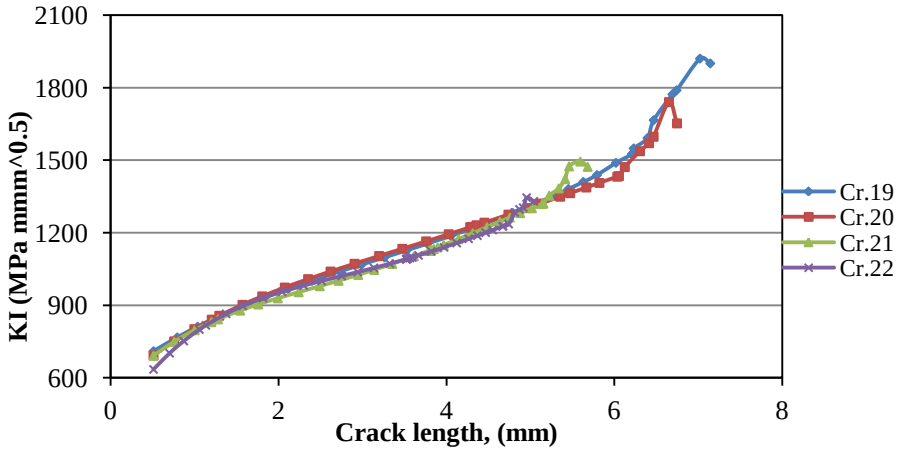

Figure 4-29 SIF histories for cracks from 19 to 22 in load case σ=200 MPa

4.1.3.1 Comparison and Results Analysis

Increasing applied stress to 200 MPa leads to an increase in crack growth and stress intensity factors comparing to previous applied stresses; also in this case the effect of interaction between every two adjacent cracks were very clear. The table 4-3 shows some results of simulation for crack 1, it is observed that mode I still the principle to the failure mode:

Table 4-3 Crack 1 SIF's histories for first ten steps

Stp. No.	Crack length, (mm)	K_{eff}	K_I	K_{II}	K_{III}
1	0.5	658.238	665.1107	7.13952	-0.949598
2	0.727	750.561	729.4707	3.38784	3.88898
3	0.937	801.504	781.1949	4.70247	-0.335719
4	1.117	815.96	818.5437	362.961	240.912
5	1.292	860.749	849.6518	3.43146	8.89996
6	1.583	871.231	892.2603	7.52887	1.86912
7	1.765	915.465	914.4177	-2.8944	-9.98003
8	2.034	940.076	942.7049	-6.55339	-3.17343
9	2.273	963.817	964.8844	-11.2649	-4.82481
10	2.54	979.201	987.9906	-8.30094	-17.5166

Figure 4.30 illustrates the stress distribution around the un-stiffened holes at first step of loading; the holes were creating an inhomogeneous stress distribution with a stress concentration at the root of the holes. Figures 4.31 shows the severity of stress distribution around the crack tips after the fifth step of loading, it can be seen that the cracks were

grown in the direction which perpendicular to the tension stress that tries to open the cracks ‘mode I’.

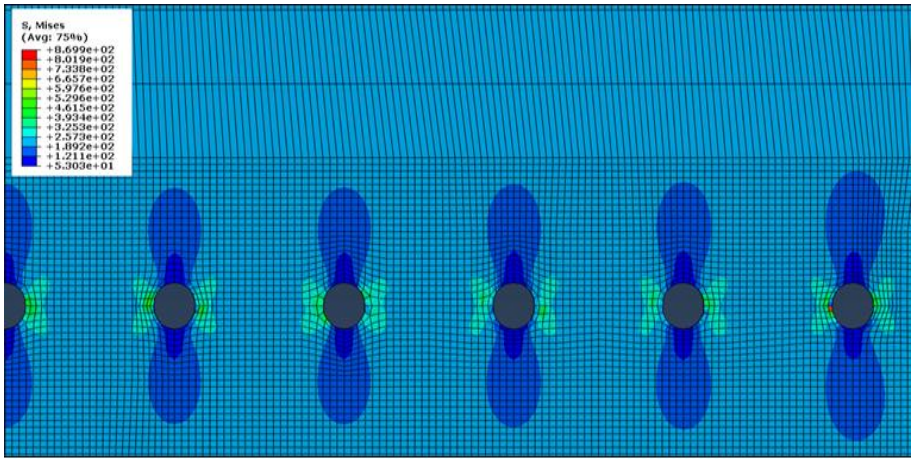

Figure 4-30 Von Mises stress distribution for first step loading

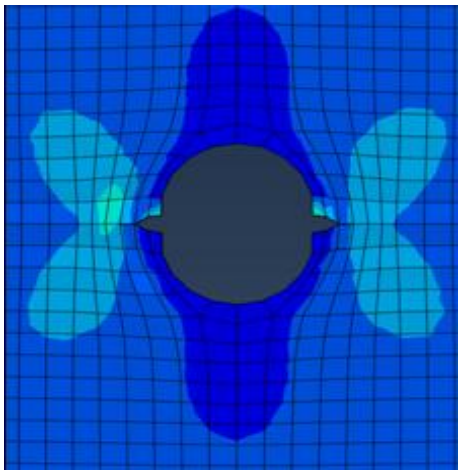

Figure 4-31 Von-Mises stress distribution around the sixth hole at fifth step loading

Figure 4.32 illustrates of plastic zone linkup criterion, it explains the failure criterions, meaning when the adjacent cracks will start to coalesce when their plastic zones come into contact with each other, conclusion can be made that the whole structure will destruct.

Figure 4.33 shows the influence of crack propagation of the adjacent cracks 6 and 7 at steps 39 and 40 which the cracks were completely linked up to form one new crack. This occurred due to the panel started to weaken by the rise of SIF values for both cracks. Also, figure 4.34 illustrates there is a linear rise in SIF values for both cracks until steep rise occurs at the last 10 steps of the simulation as the cracks approaching to each other

(Unstable crack growth). Crack 7 was longer (about 9%) than crack 6.

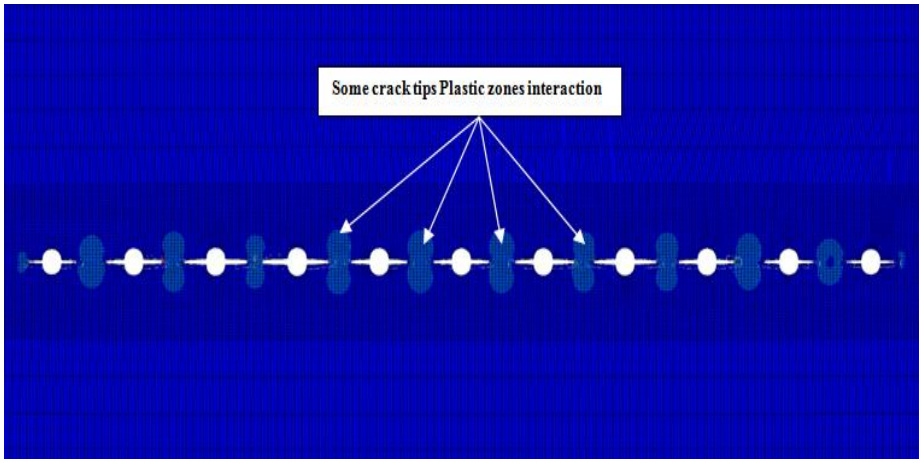

Figure 4-32 the interaction between crack tips plastic zones at thirty sixth steps loading

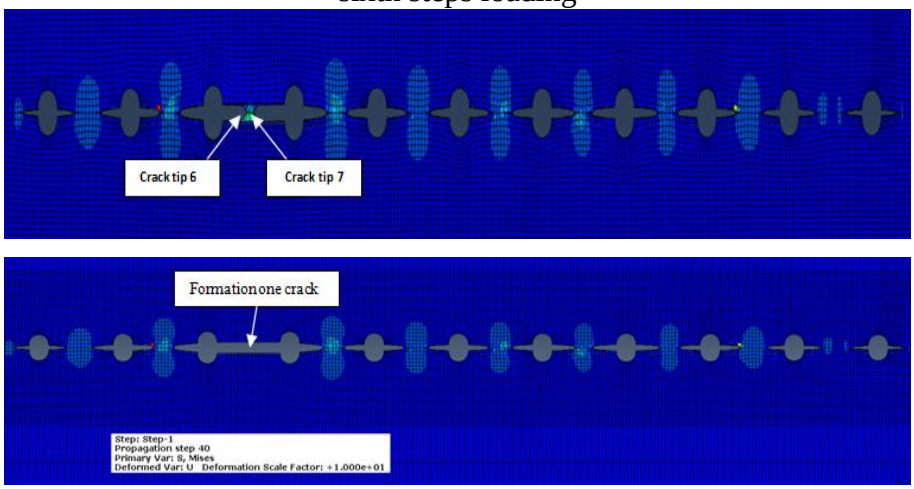

Figure 4-33 the linking up between crack 6 and 7 to form one crack at loading steps 39 and 40, σ = 200 MPa

As the cracks propagate at each increment, the second expected link up occurred between crack tips 8 and 9 due to the rose of SIF value as a result of first link up (crack tips 6 and 7), as shown in figures 4.35 and 4.36. In addition, figure 4.37 explains the relationship between crack extensions and SIF's values of cracks 8 and 9; crack 8 was longer at the end of simulation and its SIF value was higher about (38%). It is noticeable that the rapid increase in SIF values at the end of the simulation explains the effect of multi-site fatigue damage. After step 47, the leading crack which was formed from the linking up between crack 6, 7, 8, and 9 is extended to cause coalesce between its crack tip (crack tip 5) with crack tip 4

to form a new crack at step 50 (figures 4.38 and 4.39).

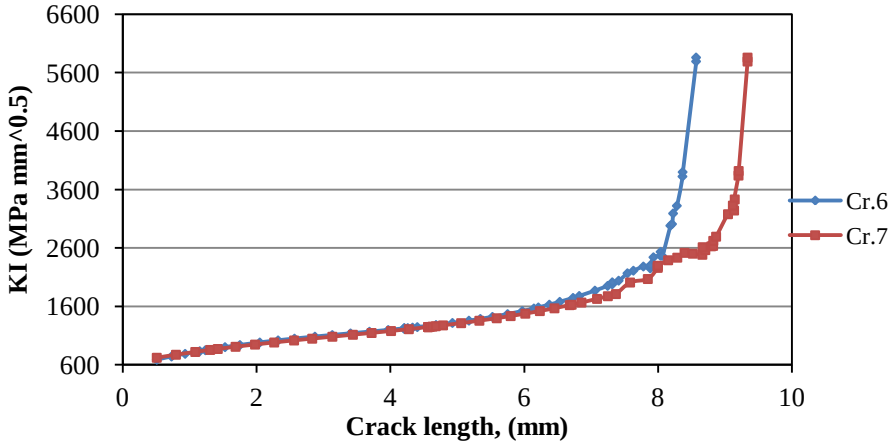

Figure 4-34 SIF histories of crack 6 and 7, step 40

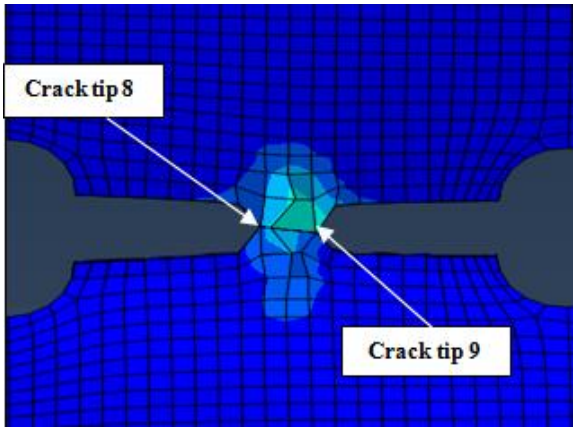

Figure 4-35 loading step 46 of crack tips 8 and 9 before linking up

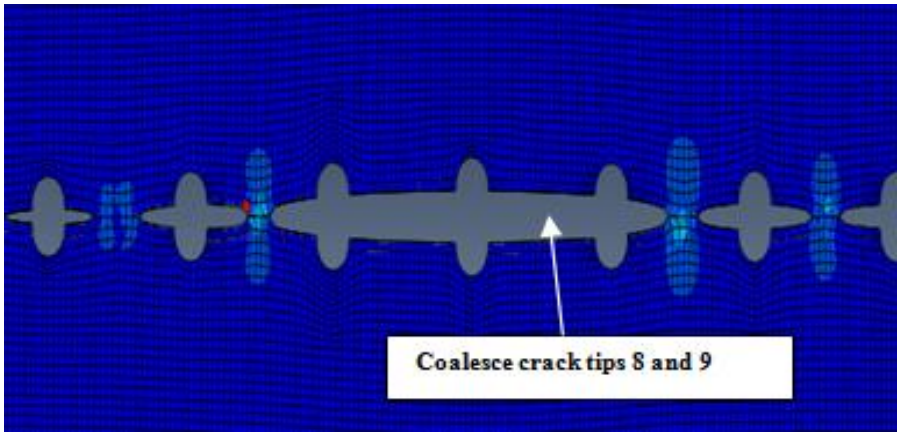

Figure 4-36 linking up between crack 8 and 9 to form one crack at step 47, σ = 200 MPa

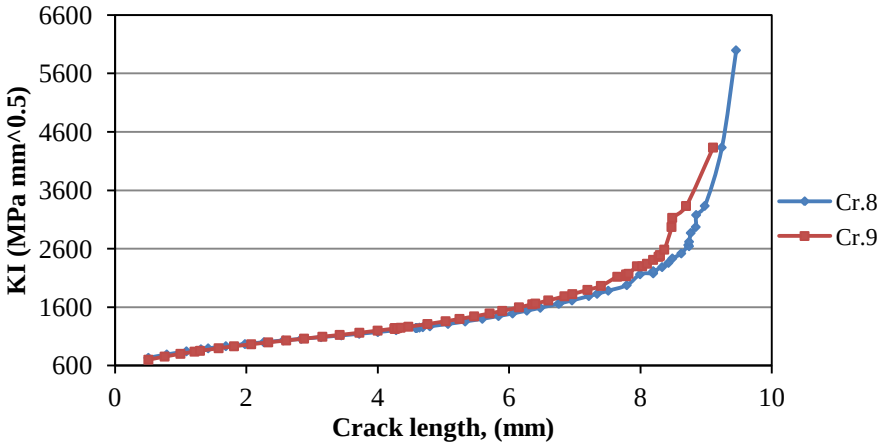

Figure 4-37 SIF histories of crack 8 and 9, σ = 200 MPa

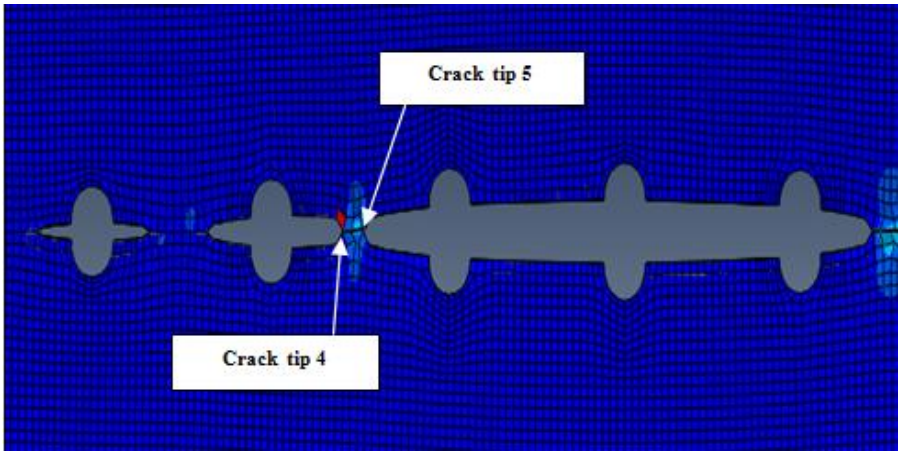

Figure 4-38 loading step 49 of crack tips 4 and 5 before linking up process

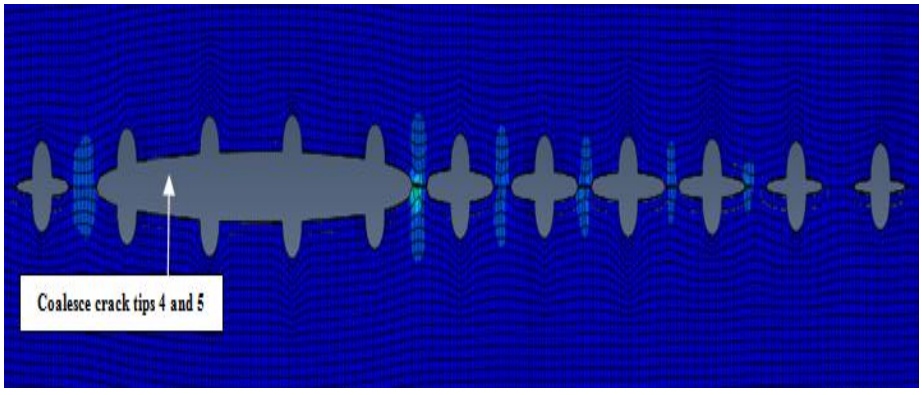

Figure 4-39 loading step 50 of crack tips 4 and 5 after linking up process

Furthermore, Figure 4.40 shows there is an increase rapid in SIF's values for crack tips 4 and 5 especially after step 50; SIF value of crack 5 was higher about (39%) from crack 4

and SIF value.

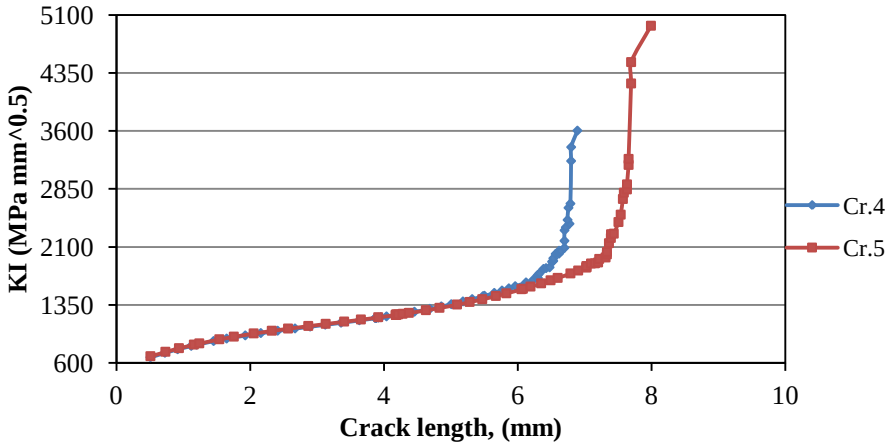

Figure 4-40 SIF histories of crack 4 and 5, σ = 200 MPa

When the simulation of MSD panel reaches step 53, the location of stress intensity location changed to which cracks 14 and 15 were located and the fourth link up occurred at step 54 between their tips to form one new crack as it can be seen in figures 4.41 and 4.42. SIF value of crack 14 and 15 were: (5134.8MPa$\sqrt{mm}$) and the recorded crack length (9.4934 mm), (4332.91 MPa$\sqrt{mm}$) and crack length equal to (9.3009 mm) at the end of simulation respectively.

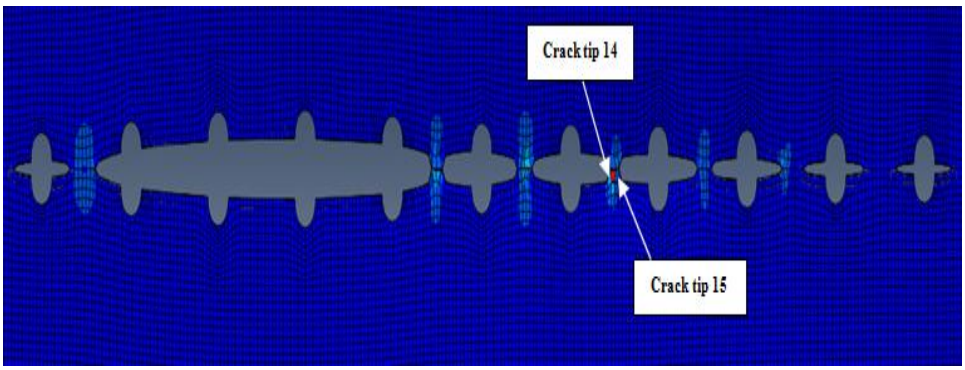

Figure 4-41 Simulation step 53 of crack tips 14 and 15 before linking up process

Also figure 4.43 describes represent the manner of crack growth as a function of SIF vales for crack tips 14 and 15, the first part shows there was a linear rise in SIF values as the cracks grow until a steep rise occurred after step simulation 54.

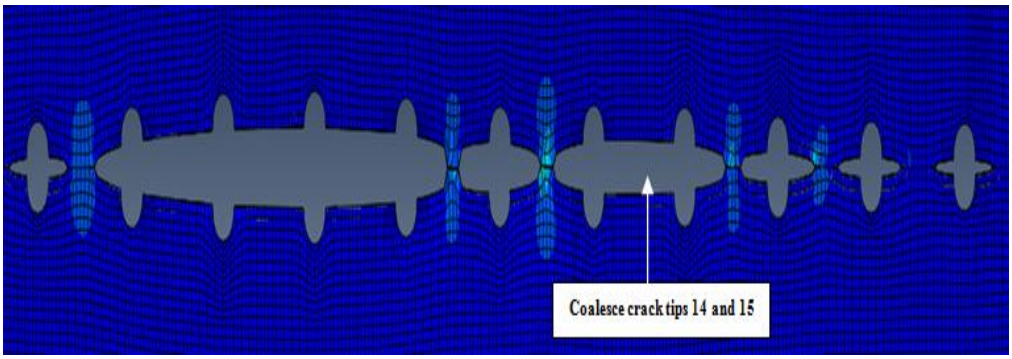

Figure 4-42 simulation step 54 of crack tips 14 and 15 after linking up

.

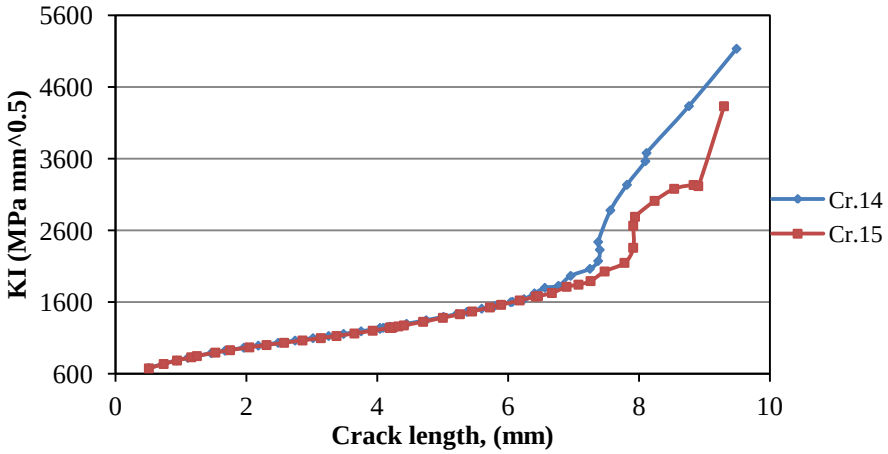

Figure 4-43 SIF histories of crack 14 and 15, σ = 200 MPa

The leading crack tip for the formed crack after the linking up between cracks 14 and 15 was crack tip 13 (CL=8.9412 mm, SIF=4511.68MPa$\sqrt{mm}$) at step 58 (figure 4.44), and at step 59 the linking up occurred between crack tip 12 and 13 to form a new crack consists from crack 12, 13,14 and 15 (figure 4.45). In addition, figure 4.46 shows SIF histories for cracks 12 and 13, the both cracks nearly had shown the same growing tendency.

Figures 4.45 and 4.47show the simulation step 60 before the linking up between cracks 16 and 17, the accumulative linking of cracks 12, 13, 14 and 15 to compose one new crack which had a new crack tip (crack tip 16) were linked with crack 17 at step 61. Also figure 4.45 shows there is a stress concentration at the location of crack tips 16 and 17 which cause a steep rise in SIF's values as shown in figure 4.43.

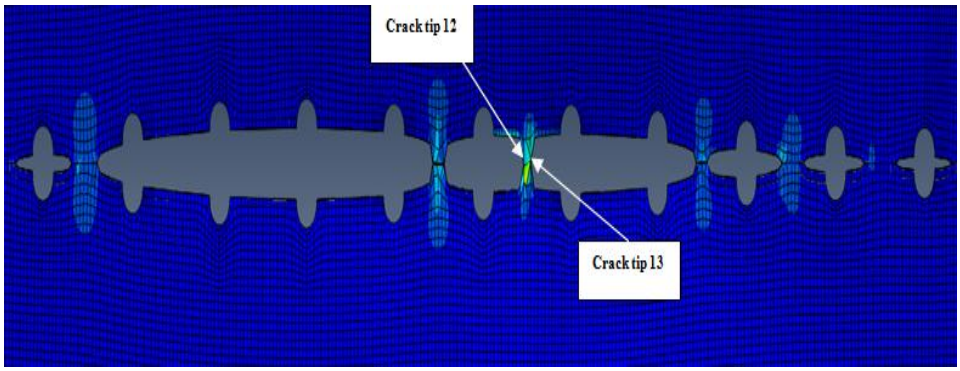

Figure 4-44 simulation step 58 of crack tips 12 and 13 before linking up process

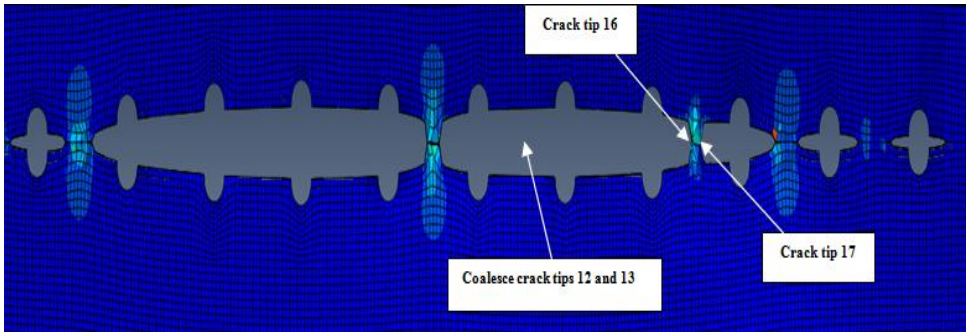

Figure 4-45 simulation steps 59 and 60 of crack tips 12 and 13 after linking up process

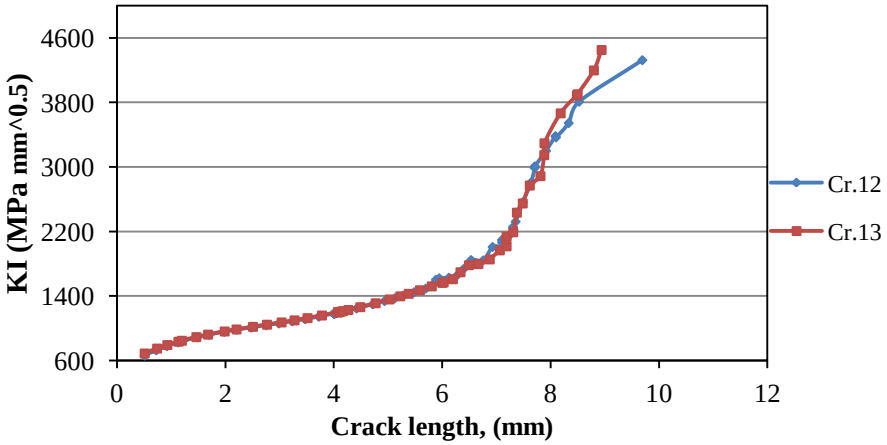

Figure 4-46 SIF histories of crack 14 and 15, σ = 200 MPa

Figure 4.48 shows SIF histories for cracks 16 and 17, it is a clear the leading formed crack at step 60 was crack tip 16 due to composing MSD fatigue cracks (linked cracks 12, 13 ,14and 15) it's on the left and the panel weakened at that location. At the end of simulation

the recorded length of crack 16 was equal to (9.439 mm) and SIF equal to (3515.9 MPa$\sqrt{mm}$), and (8.1185mm), (2503.11MPa$\sqrt{mm}$) for crack 17 respectively.

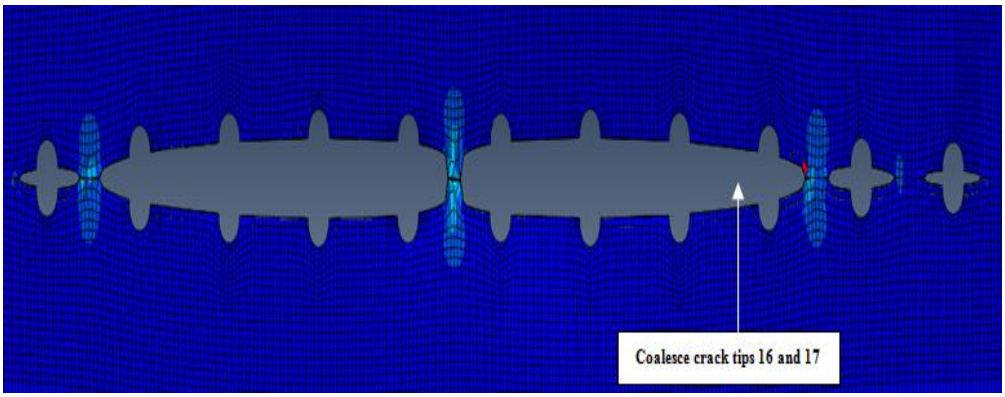

Figure 4-47 Simulation step 60 of crack tips 16 and 17 after linking up process

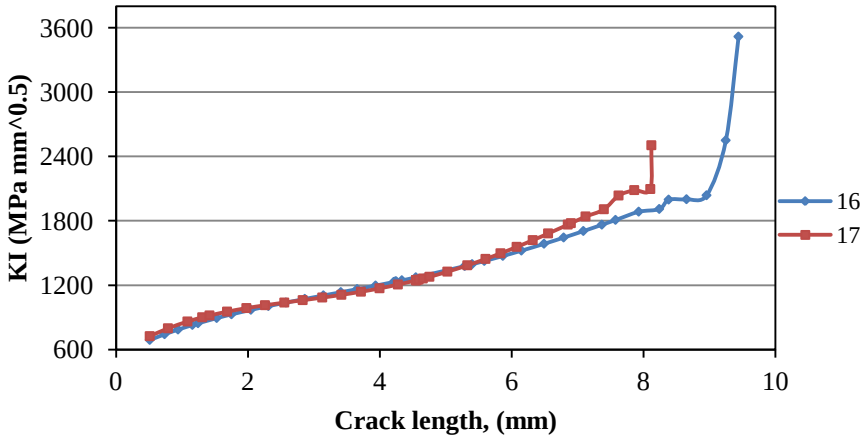

Figure 4-48 SIF histories of crack 16 and 17, σ = 200 MPa

Figure 4.49 shows the cracked panel at last step of simulation, two symmetry multi site fatigue cracks were formed, which can lead to catastrophic failure of the panel.

As it can be seen on Fig. 4.50 the highest values of SIFs are for the cracks11 and 12, that is, for the cracks emanating from the sixth hole. This becomes more obvious with cracks' growth. Also, this occurs for all three load cases. The values of SIFs for cracks at the first and eleventh hole are lesser and they are nearly the same. This can be explained by the fact that the crack interaction effect is more dominant for the cracks at middle holes, than for

the cracks at “edge” holes. And, as mentioned before, that is precisely why the cracks 1, 2, 11, 12, 21 and 22 are selected for results presentation.

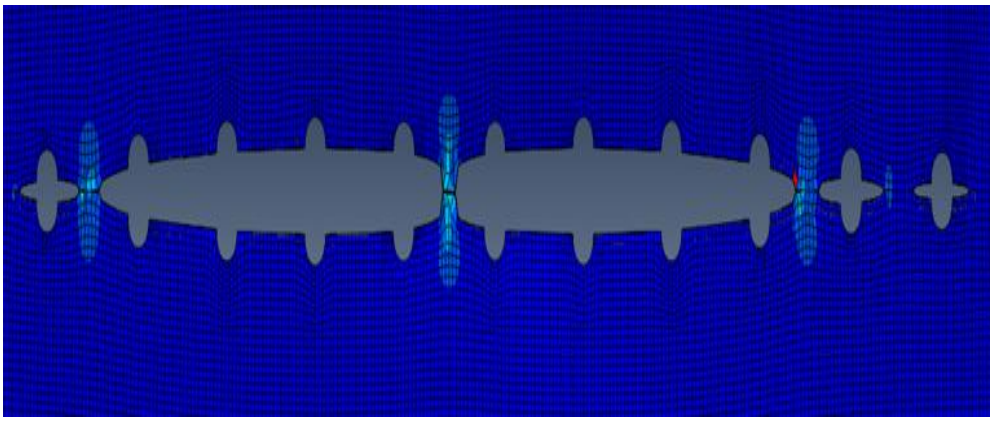

Figure 4-49 simulation step 63 of after linking up process

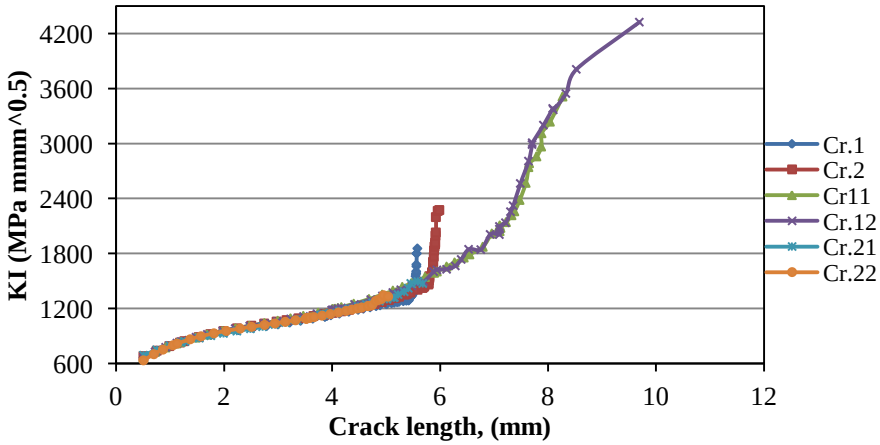

Figure 4-50 SIF histories for selected cracks in analyzed load case σ=200 MPa

4-2 THE ANALYSIS OF MSD CONFIGURATION USING FRANC2D/L

The same boundary conditions have been applied for the mentioned model in section 4.1. The following are the results if SIF histories using FRANC2D/L software:

4.2.1 Stress intensity factor results of 50 MPa applied stress

The SIF results shown in figures 4.51, 4.52 and 4.53 represent the solutions for cracks from 1 to 11; the growing behavior of crack from 12 till 22 are mentioned in appendix (A) section (1-A). Generally, as the crack extends as SIFs values increase; see figure 4.51. Crack 4 had the higher SIF value due to interaction with adjacent cracks and holes, while the lowest was recorded to crack 1 due to less interaction with the other cracks and it has more area to extend compared to the other cracks which their SIFs rise as approaching to the middle of the panel (effect of stress concentration). At the end simulation SIF value of crack 4 was higher about (16.6%) from the lowest SIF value which was recorded to crack 1.

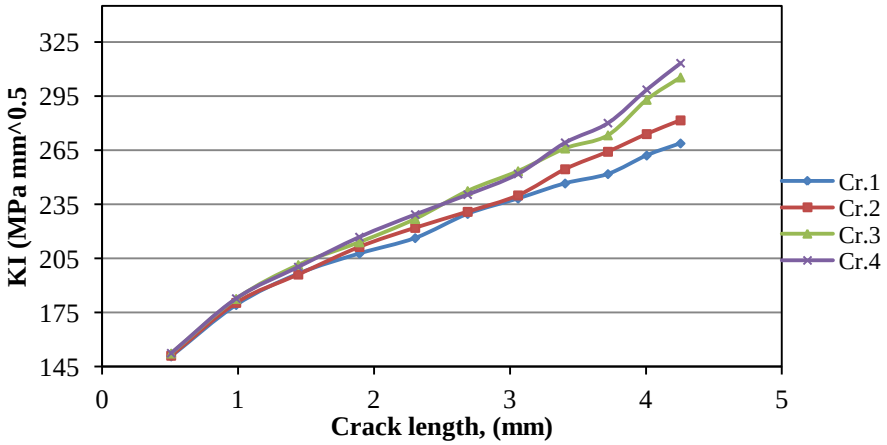

Figure 4-51 SIF histories of cracks from 1 to 4 in load case σ=50 MPa

It is notable from figure 4.52 the cracks were almost had identical values and trends and the maximum differential average in SIFs values were recorded between crack 5 and 8 (2.5%). Figure 4.53 shows the SIF histories for cracks from 9 to 11, those cracks expected to have the highest SIF values because they were located in the middle of the panel. In this figure

all cracks substantially had the same trend and the maximum differential average in SIF value were (1.8%) between cracks 9 and 11 at the end of the simulation.

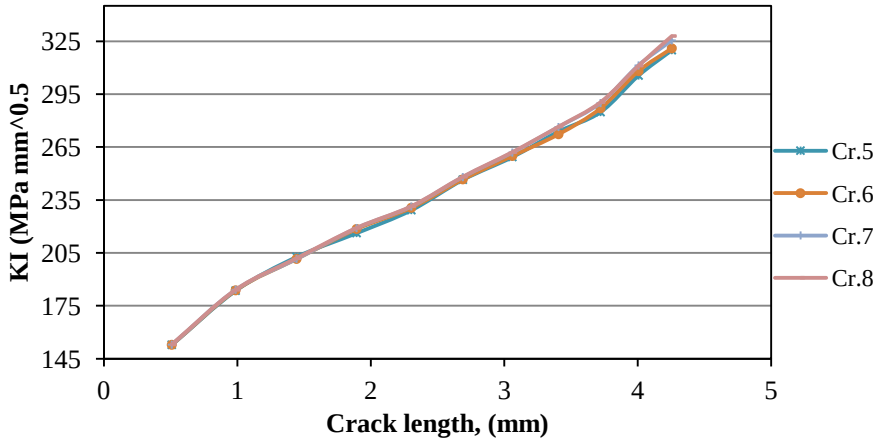

Figure 4-52 histories of cracks from 5 to 8 in load case σ=50 MPa

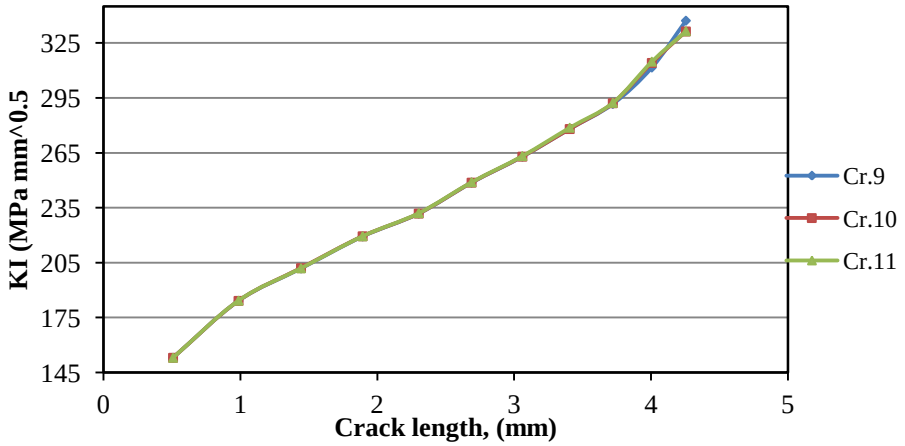

Figure 4-53 SIF histories of cracks from 9 to in load case σ=50 MPa

The above SIFs solutions chosen due to the symmetry of the solution which can be noticed in appendix (A), meaning crack 1 SIFs solution during the simulation were almost equal to the SIFs solution of crack 22.

Also, figure 4-54 describes the alteration of SIFs histories with crack length for each crack increment simulation. The highest values were recorded for crack 11 and 12 which emanating from the sixth hole. The maximum SIF average values was between cracks 1 and 12 (25.86%), and the minimum was (0.33%) between cracks 1 and 22. This can be

explained by the fact that the crack interaction effect is more dominant for the cracks at middle holes, than for the cracks at "edge" holes.

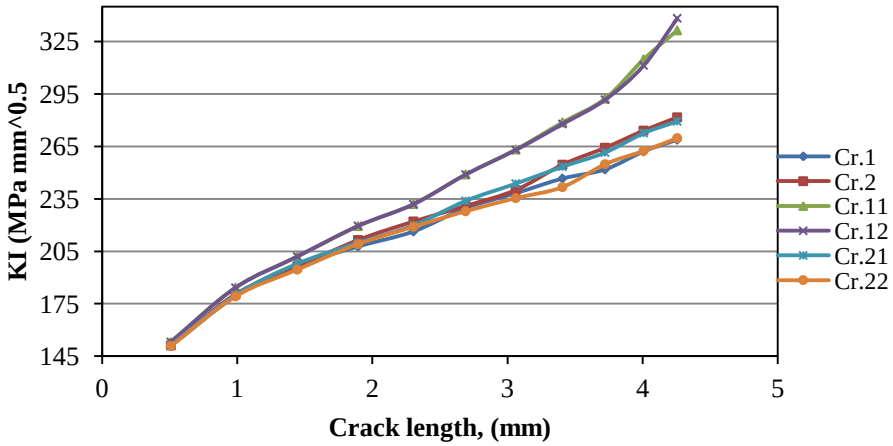

Figure 4-54 SIF histories comparison of some selected cracks, σ=50MPa

4.2.2 Stress intensity factor results of 100 MPa applied stress

Increasing the applied stress leads to increasing the stress intensity factor according to SIF formula $KI = \beta.\sigma\sqrt{\pi.a}$, furthermore the obtained results in this section were the same trend comparing to the previous results (applied stress 50 MPa), except the rose of SIF values. The following figures describe the behavior of crack growth versus of stress intensity factor for crack tips from 1 to 11:

Stress intensity factor histories in figure 4-55 have identical behavior of crack growth comparing with SIF histories which described in figure 4.51 even in the value of maximum deviation between crack tips 1 and 4, the only difference is that the value of SIFs increased as we increase the applied stress from 50 MPa to 100 MPa. The tables which are mentioned in appendix (A) section (1-A) explain the effect of changing the applied stress from 50 MPa to 100 MPa for some selected cracks.

Figure 4.56 describes the cracks extension trend of cracks 5 till 8, it is clear that the cracks had almost identical trend and the maximum differential average in SIFs values was recorded between cracks 5 and 8 (2.5%) and the lowest was (0.33%) between crack 5 and 6. Also, there is a crack growth trend similarity (see figures 4.51and 4.52).

It is notably that there is a trend parallelism in crack extension for crack tips which have the same position coordinates, in other words, regardless of the increase of SIFs all crack had

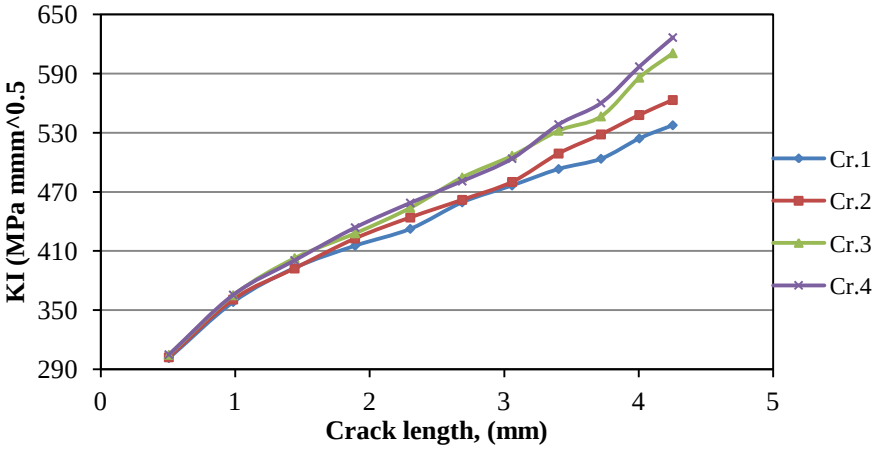

Figure 4-55 SIF histories of cracks from 1 to 4 in analyzed load case σ=100 MPa

the same growth trend, see Figures 4.53 and 4.57. Additionally, figure 4.57 shows the same value of the maximum differential average of SIFs (1.7%) between cracks 9 and 11, the lowest was (0.0%) between 10 and 11.

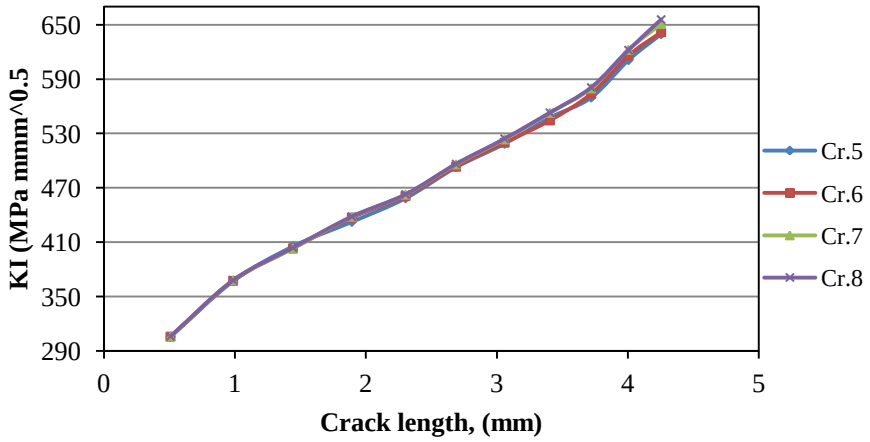

Figure 4-56 SIF histories of cracks from 5 to 8 in analyzed load case σ=100 MPa

The above SIFs solutions chosen due to the symmetry of the solution which can be noticed in appendix (A) section (2-A), meaning crack 1 SIFs solution during the simulation were almost equal to the SIFs solution of crack 22.

As mentioned before to the effect of stress concentration on SIF values of some selected cracks which located on the edge and the middle of the panel. Almost the same variation recorded between cracks 1 and 12 (25.87%) for the maximum differential SIF value and the minimum was between 1 and 22 (0.32%), see figure 4-58.

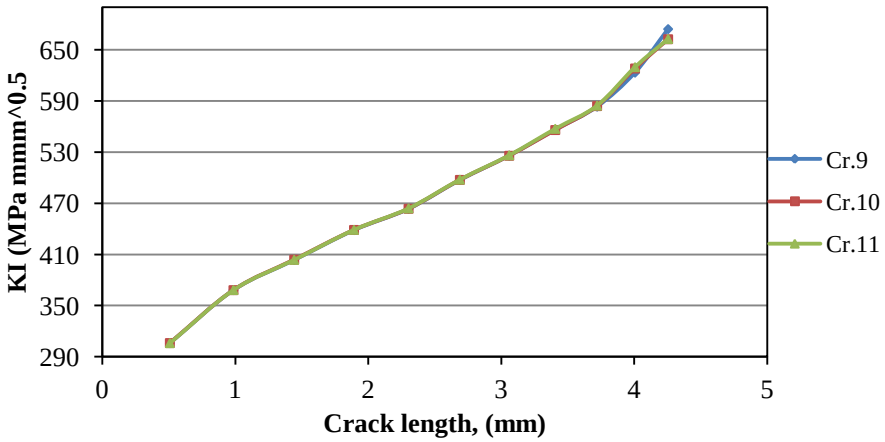

Figure 4-57 SIF histories of cracks from 9 to 11 in analyzed load case σ=100 MPa

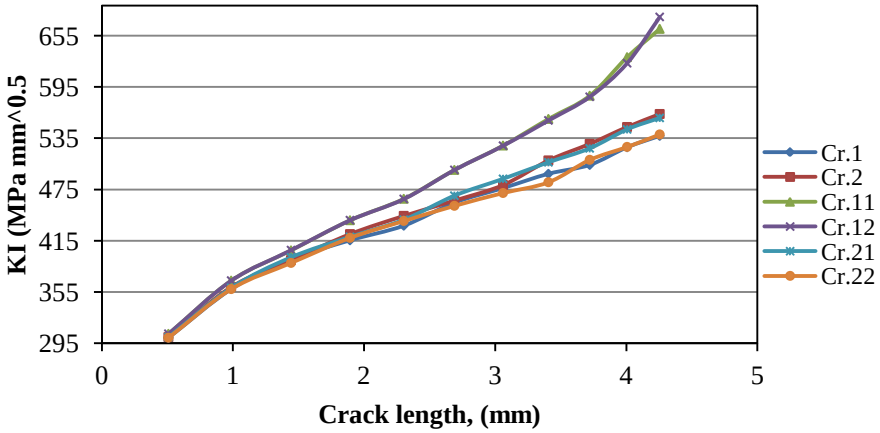

Figure 4-58 SIF histories comparison of some selected cracks, σ=100MPa

4.2.3 Stress intensity factor results of 200 MPa applied stress

The third case is increasing the applied stress to 200 MPa, the same growing trend has been obtained similar the two previous cases, with the exception of the rise in stress intensity factor values as the stress increased to 200 MPa. Table (3) which is mentioned in appendix (A) describes the above-mentioned information. The following figures show the results of crack extension versus stress intensity factor:

Figure 4-59 shows SIF histories of crack from 1 to 4, it's clear those cracks had the same trend for figures 4-51 and 4-55 and the highest stress intensity factor was recorded to crack tip 4 (CL=4.255mm, SIF=1253MPa$\sqrt{mm}$), it was higher about (16.6%) of the SIF value of

crack tip 1 (CL= 4.255, SIF =1075MPa$\sqrt{mm}$) at the end of simulation due to crack tip 1 has less interaction with the other cracks and holes.

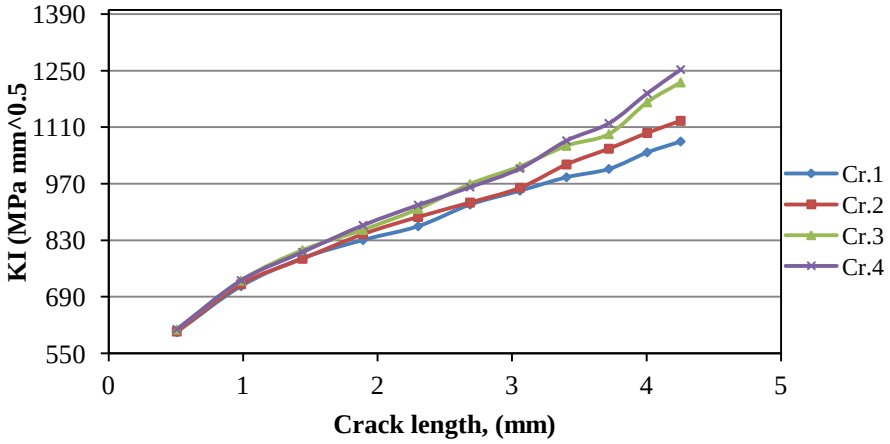

Figure 4-59 SIF histories of cracks from 1 to 4 in load case σ=200 MPa

Also, this explains why SIF rises as approaching the middle of the panel (stress concentration effect). In like manner, Figure 4-60 describes the relationship between stress intensity factors and crack lengths of cracks from 5 to 8; it is clear that SIFs value increase as cracks grow, the SIF values diverges especially at the end of simulation and SIF of crack tip 8 was higher about (2.6%) of SIF of crack tip 5 and about (22%) of SIF crack tip1.

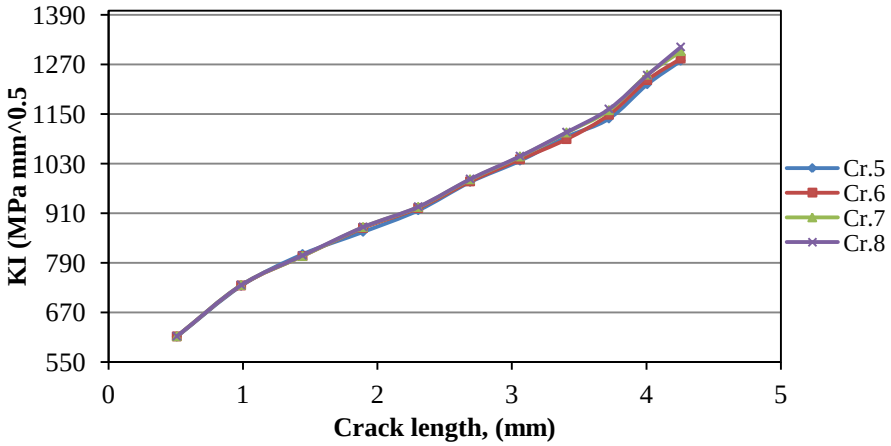

Figure 4-60 SIF histories of cracks from 5 to 8 in load case σ=200 MPa

Figure 4-61 shows the cracks growth behavior of crack from 9 to 11 which are located almost in the middle of the panel; all cracks had symmetric growth trend and the highest SIFs values were recorded for those cracks. The highest SIF value was for crack 9

(CL=4.255mm, SIF=1349MPa$\sqrt{mm}$) where it was higher about (25.49%) than SIF value of crack tip 1.

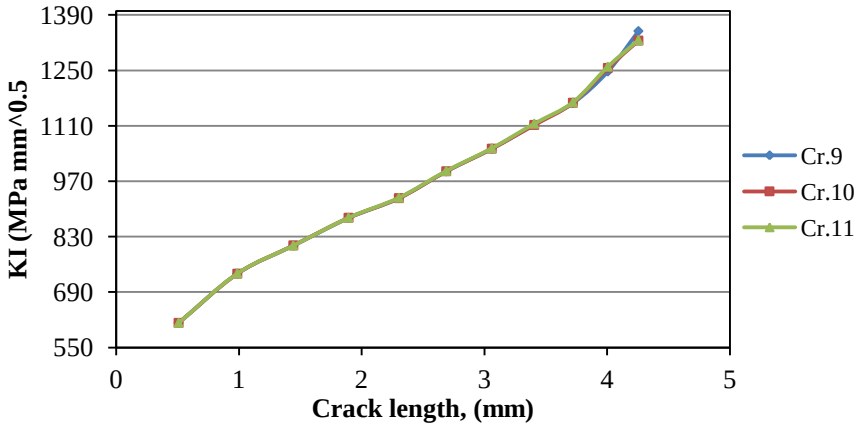

Figure 4-61 SIF histories of cracks from 9 to 11 in load case σ=200 MPa

Due to the symmetry of the panel, the SIF solutions of the rest cracks showed a symmetrical solution, i.e. crack 1 SIFs had the same SIF histories of cracks 22, also the solutions were the same for the other cracks which had the same coordinate position, see appendix (A) section 3-(A). Figure 4-62 describes the effect of crack position on the value of stress intensity factor values; it is clear from the figure the highest SIF values were recorded to cracks 11 and 12, in other words, the cracks which emanating from the middle hole (sixth hole). The maximum differential average was recorded between SIF of crack tip 12 and SIF of crack tip 1 (25.86%) and the lowest was between crack tips 1 and 22 (0.37%).

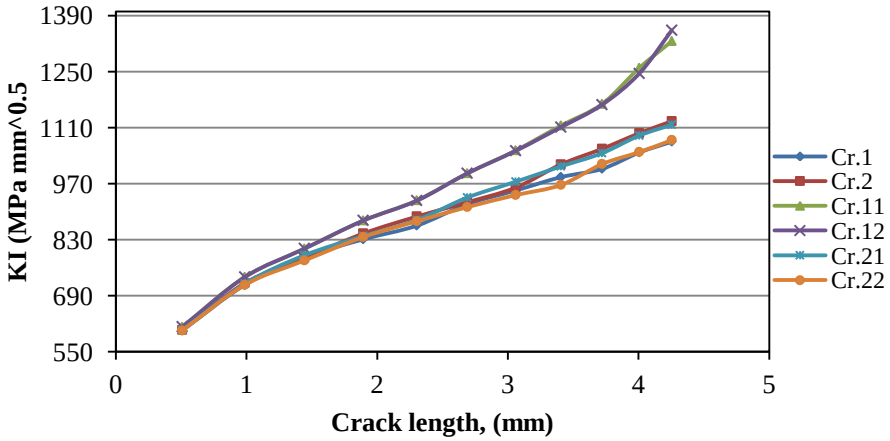

Figure 4-62 SIF histories comparison of some selected cracks, σ=200MPa

4.2.4 Comparison and Results Analysis

Figure 4.63 shows the meshed panel and the mesh around the rivet holes, also, the same crack numbering, loading and boundary conditions were used as prescribed in the solution using XFEM.

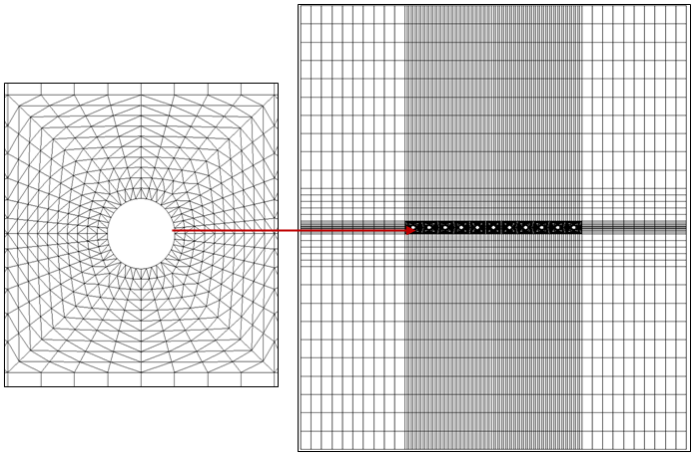

Figure 4-63 The meshed panel and the meshing around the hole

Figure 4.64 describes the principle tensile stress contours, it showed that the highest stresses at the location around the holes (Y=0 and X= 3.23). These are likely locations of cracks initiation. At those locations, we will start the cracks at the edges of the holes, normal to the holes. Additionally, Figure 4-65 shows the process of the re-meshing around the initial crack tip position after placing the position of the crack tip; this will cause finer initial meshes and more elements to be used, and thus give more accurate stress intensity factors.

Figure 4-66 shows the contours of stress intensity around the tip of the initial crack, it is a clear from this figure the maximum tensile stress was observed around the crack tip.

In this analysis, all graphs have identical crack growing trend even when we change the applied stress from 50, 100 and 200 MPa, this happened due to the re-mesh process around the crack tips until the end of simulation (step 11) , the following tables and describe the above mentioned aspect:

As shown in table 4-4 and figure 4-67, for the same crack length (or the same step) the increasing of applied stress from 50 MPa to 100 leads to increasing the value of stress

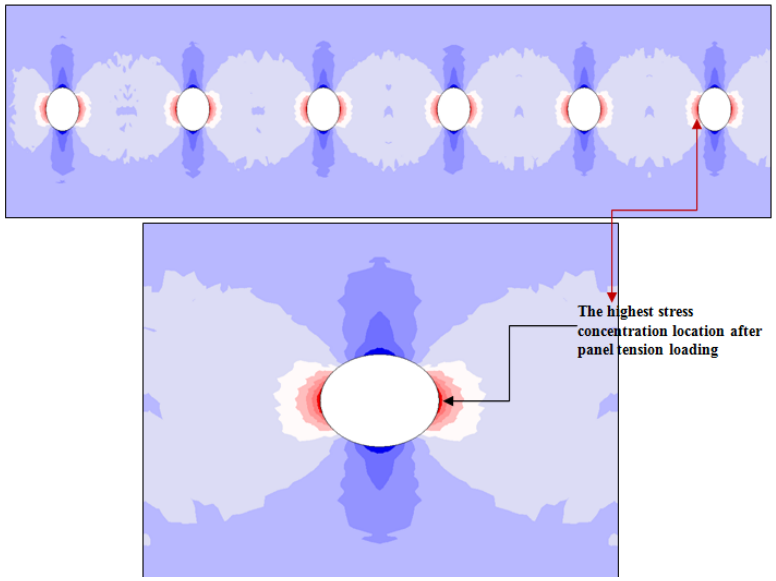

Figure 4-64 Stress distribution around the rivet holes

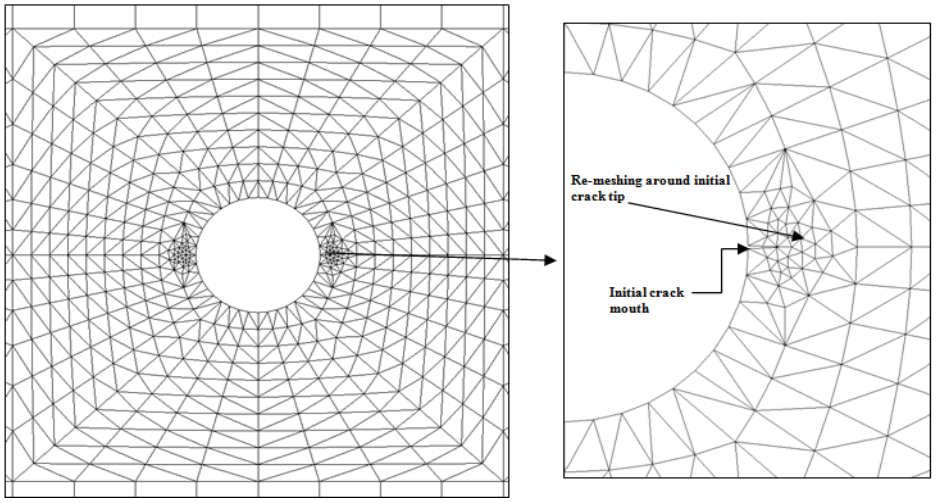

Figure 4-65 Re-meshing process after the initial crack

intensity factor (doubled). Additionally, increasing the applied stress from 100 MPa to 200 MPa also leads to increase the stress intensity factor for the same crack length (doubled value).

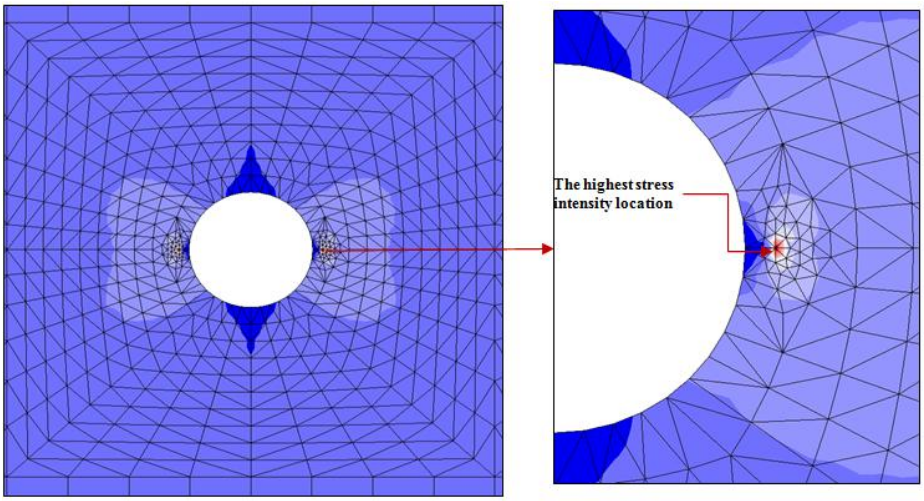

Figure 4-66 Stress distribution around the holes after first initial crack

Table 4-4 SIF histories for crack tip 1, σ=50,100 and 200 MPa

	C.L.(mm)	K_I(50MPa)	K_I(100MPa)	K_I(200MPa)
Crack tip1	0.508	150.7	301.4	602.9
	0.9864	179.2	358.3	716.6
	1.443	196.5	392.9	785.8
	1.893	207.7	415.4	830.8
	2.303	216.3	432.5	865.1
	2.689	229.7	459.4	918.7
	3.06	238.2	476.5	953
	3.406	246.6	493.2	986.4
	3.721	251.8	503.6	1007
	4.006	262.1	524.2	1048
	4.255	268.8	537.6	1075

Regarding the above-mentioned information, the same results obtained to crack tip 2, crack tip 11 and crack tip 12, as it shown in table 4-5, 4-6 and 4-7 and figures 4-68, 4-69 and 4-70, meaning SIFs values increased as the applied stress increased from 50 MPa to 100 MPa and from 100 MPa to 200 MPa for the same crack length.

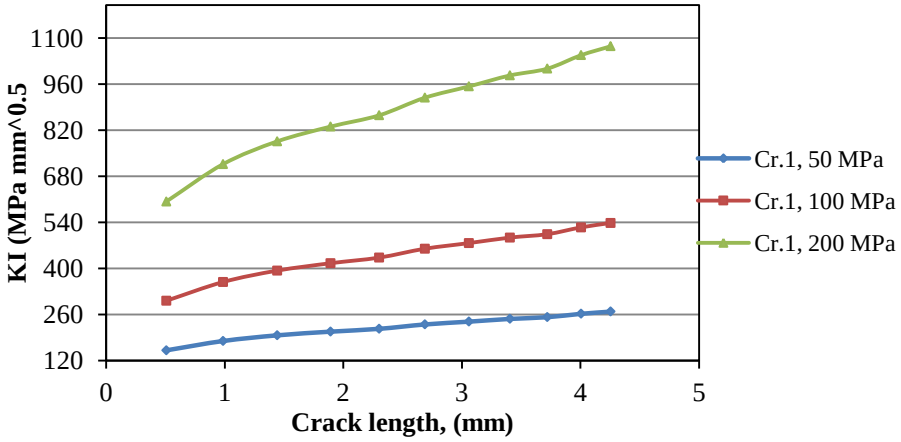

Figure 4-67 SIF histories of crack tip 1

Table 4-5 SIF histories for crack tip 2, σ=50,100 and 200 MPa

	C.L.(mm)	K_I(50MPa)	K_I(100MPa)	K_I(200MPa)
Crack tip2	0.508	151.1	302.2	604.3
	0.9864	180.4	360.8	721.6
	1.443	196.1	392.3	784.5
	1.893	211.4	422.7	845.5
	2.303	222	444	888
	2.689	230.9	461.9	923.7
	3.06	240	480.1	960.2
	3.406	254.5	508.9	1018
	3.721	264.2	528.3	1057
	4.006	274	548	1096
	4.255	281.6	563.2	1126

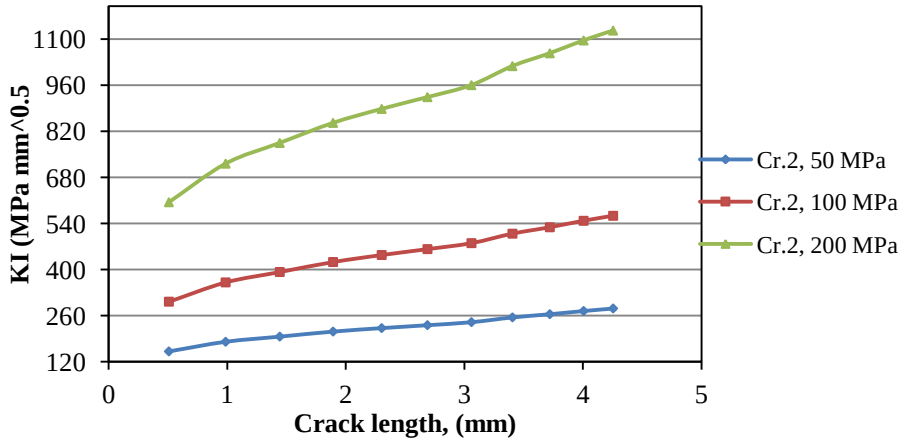

Figure 4-68 SIF histories of crack tip 2

Table 4-6 SIF histories for crack tip 11, σ=50,100 and 200 MPa

	C.L.(mm)	K_I(50MPa)	K_I(100MPa)	K_I(200MPa)
Crack tip11	0.508	153	306	612
	0.9864	184.2	368.3	736.7
	1.443	201.9	403.7	807.4
	1.893	219.4	438.9	877.7
	2.303	232	464	928.1
	2.689	248.9	497.8	995.7
	3.06	263.2	526.3	1053
	3.406	278.7	557.4	1115
	3.721	292.3	584.6	1169
	4.006	314.8	629.7	1259
	4.255	331.4	662.8	1326

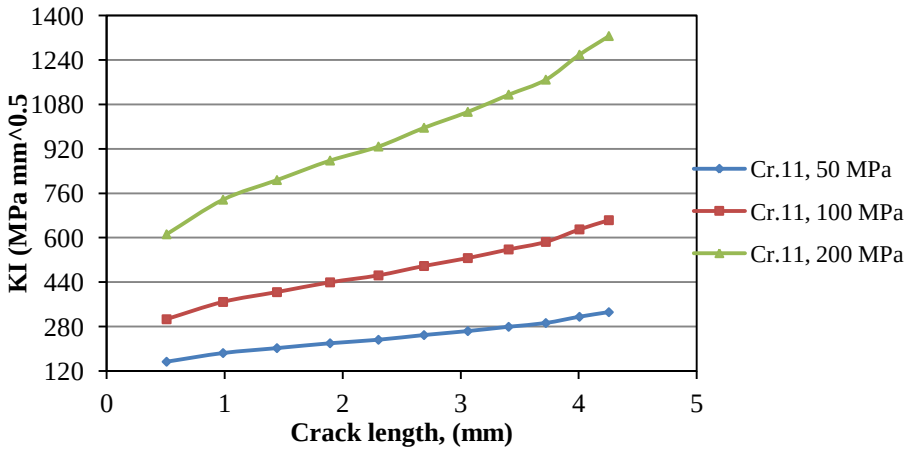

Figure 4-69 SIF histories of crack tip 11

Table 4-7 SIF histories for crack tip 12, σ=50,100 and 200 MPa

	C.L.(mm)	K_I(50MPa)	K_I(100MPa)	K_I(200MPa)
Crack tip12	0.508	153.1	306.1	612.3
	0.9864	184.1	368.3	736.6
	1.443	202	404	807.9
	1.893	219.5	439	877.9
	2.303	231.9	463.8	927.6
	2.689	248.9	497.8	995.7
	3.06	263	526.1	1052
	3.406	277.8	555.7	1111
	3.721	291.7	583.3	1167
	4.006	311.3	622.6	1245
	4.255	338.3	676.7	1353

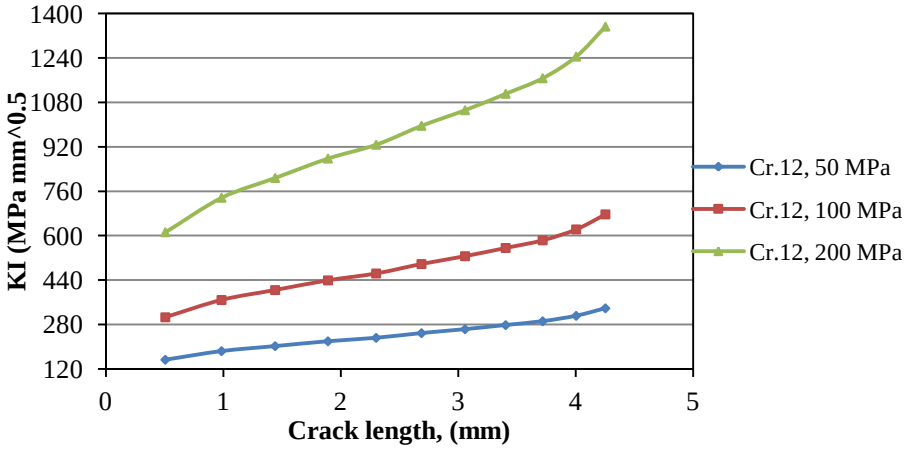

Figure 4-70 SIF histories of crack tip 12

Figure 4-71 describes the final deformed shape of the panel after at the end of the simulation using FRAN2D, each rivet hole have two cracks placed perpendicular to Y- axis and the direction of the cracks propagation was predicted by the program.

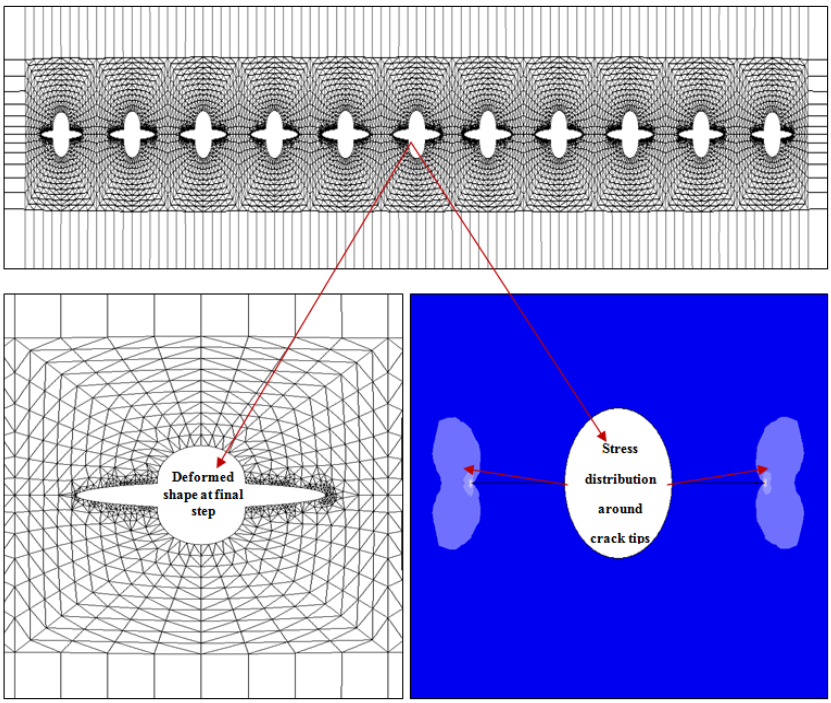

Figure 4-71Deformed panel and stresses distribution around crack tip at the end of simulation

As mentioned at figure 4-63, the primary panel mesh will be replaced after positioning the placing the initial crack coordinates, the finer mesh will be updated and fill the region for every crack increment around the crack tips, see figure 4-72. The finer mesh will cause more elements to be used, and thus give more precise stress intensity factors calculations. Also, the figure shows the principle tensile stress contours and the highest stresses were around the crack tips.

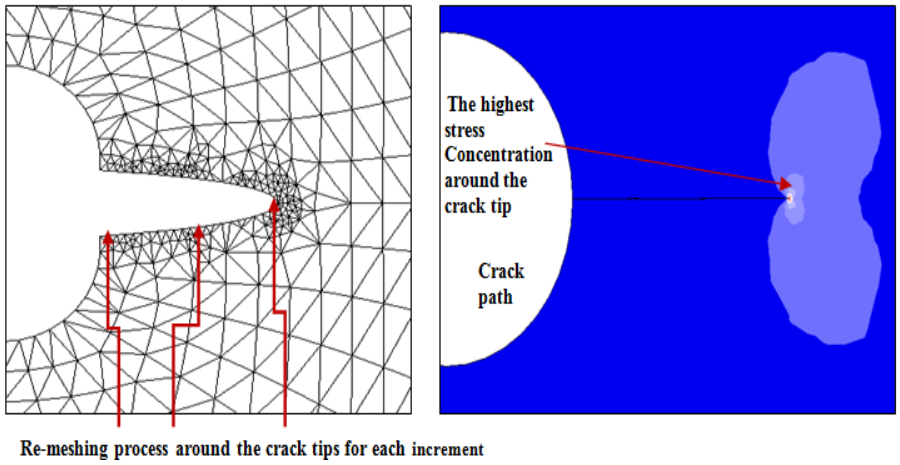

Figure 4-72 Re-meshing process around the crack tip of the sixth rivet hole

4.3 THE ANALYSIS OF MSD CONFIGURATION USING APPROXIMATION METHOD

The approximate procedure for calculating stress intensity factors is based on principle of superposition. According to this procedure, the SIF for opening mode of analyzed crack in any given configuration with n cracks (Fig.4-73) can be estimated as:

$$K_{IjA,B} = c_{1b,d} \cdot K_{I1} + \cdots + c_{jb,d} \cdot K_{Ij} + \cdots + c_{nb,d} \cdot K_{In} = \sum_{i=1}^{n} c_{ib,d} \cdot K_{Ii} \quad , \tag{4.1}$$

where:

$K_{IjA,B}$ - represents stress intensity factor for tip A, or B of analyzed crack in presence of all other cracks in configuration;

K_{Ii} - individual stress intensity factor of all cracks in configuration, i.e., stress intensity factors of auxiliary configurations;

$c_{ib,d}$ - the coefficient that takes into consideration influence of i-th crack on stress intensity factor of analyzed crack, (the influential coefficient of the analyzed crack on itself is $c_{jb,d} = 1$).

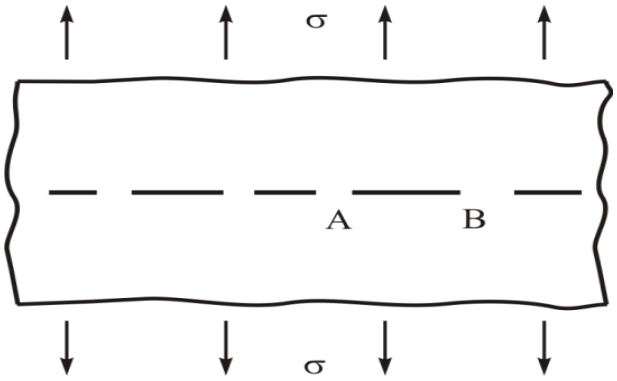

Figure 4-73 Configuration with multiple cracks

In this manner the analyzed complex 2D or 3D configuration can be represented as a combination of several simpler (auxiliary) configurations. The number of those configurations is equal to the number of cracks, such that every auxiliary configuration usually contains only one crack. Hence, the determination of SIF at analyzed crack tip is reduced to determination of influence that every crack in the initial configuration has on the

analyzed one. The influential coefficients were estimated for vast number of crack lengths and distances between them, i.e. for their combinations, in [97]. Here, eleven auxiliary configurations were used, which were all the same: thin plate with a central circular hole with two radial cracks subjected to uniform uniaxial tensile stress, with well-known Bowie's solution for stress intensity factor [58]. It should be noted that the SIFs were calculated for models with different crack sizes for all the cracks in the configuration, but with the same crack increment for all cracks, because the service data showed that in MSD all cracks are roughly the same length [98] (so called "catch-up" phenomenon).

4.3.1 Stress intensity factor results of 50 MPa applied stress

Figure 4-74 shows the relationship between crack 1, 2, 3 and 4 extensions and the corresponding SIF value for each crack increment, it showed that as the cracks propagate as SIF values rise; at the end calculation using approximation method SIF value of crack 4 was higher about (3.8%) from SIF value of crack 1 and about (0.04%) higher at the initial calculation step (crack length = 0.5 mm).

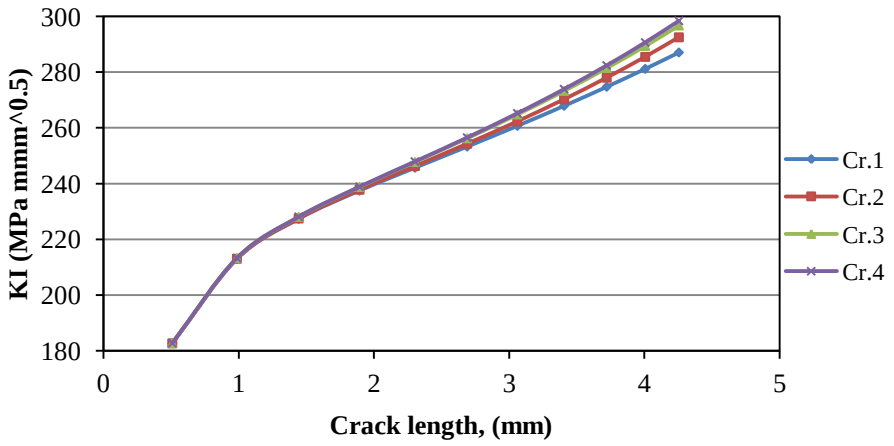

Figure 4-74 SIF histories of cracks 1, 2, 3 and 4

Figure 4-75 represent SIF histories of cracks from 5 to 8, it showed that SIF histories were almost identical, the maximum differential average was equal to (0.5%) between SIF values of cracks 5 and 8 at the end of the calculation, while the lowest was equal to (0.16%) at the initial step of calculation (crack length = 0.5 mm).

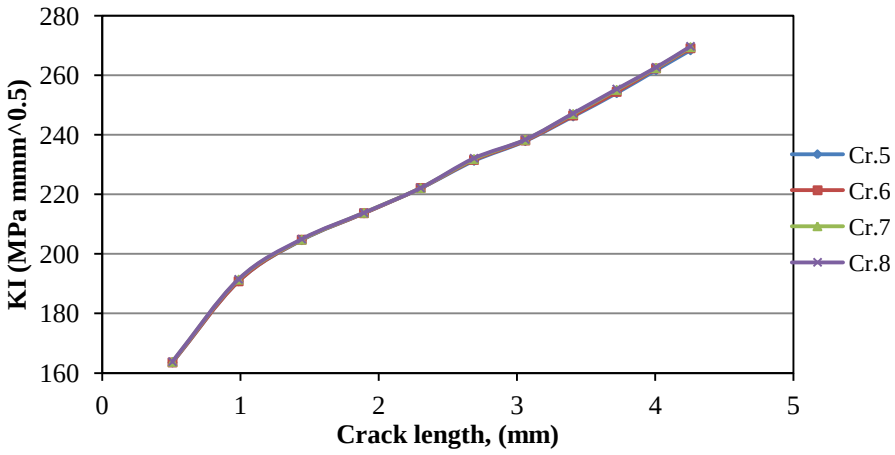

Figure 4-75 SIF histories of cracks 5, 6, 7 and 8

Figure 4-76 describes SIF histories of cracks from 9 to 11 (middle holes cracks); it showed that there was identification between cracks 11 and 12 and between cracks 9 and 10. SIF values between the two groups diverge after step 5 and the maximum differential average value was equal to (0.12%) between cracks 11 and 9.

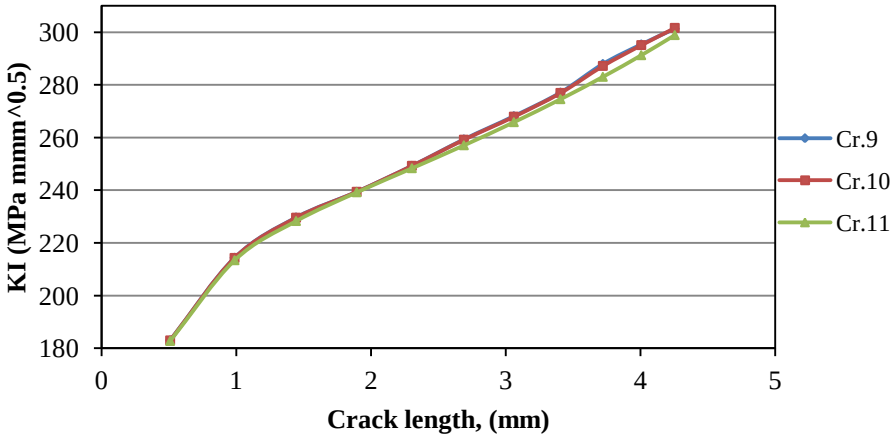

Figure 4-76 SIF histories of cracks 9, 10 and 11

Due to the symmetry of SIFs solution using this method, the rest solution of cracks from 12 to 22 recorded in appendix (B) section 1-B.

Figure 4-77 describes the effect of crack position on the value of stress intensity factor values; it is clear from the figure the highest SIF values were recorded to cracks 11 and 12, in other words, the cracks which emanating from the middle hole (sixth hole). The

maximum differential average was recorded between SIF of crack tip 12 and SIF of crack tip 1 (4.2%) and the lowest was between crack tips 1 and 22 (0%).

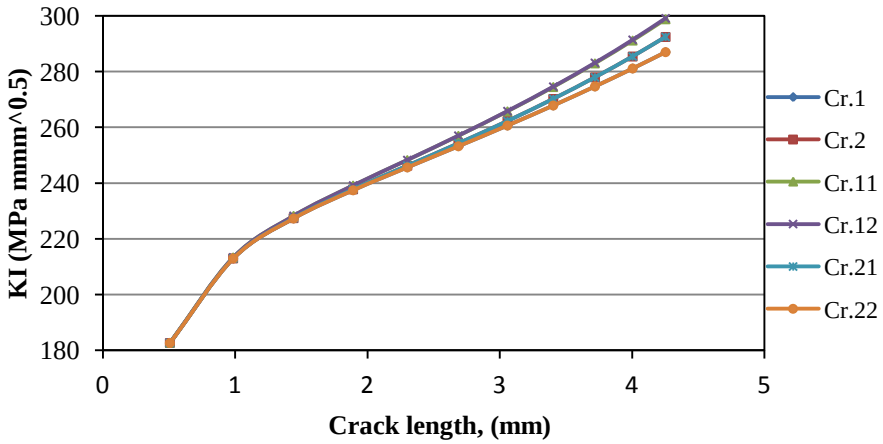

Figure 4-77 SIF histories comparison of some selected cracks, σ=50 MPa

4.3.2 Stress intensity factor results of 100 MPa applied stress

In this case, the applied stress is doubled compared to the previous case, and the results show all figures, in this case, had the same propagation trend and the same maximum and minimum differential average values of SIF. The major difference was SIF values were doubled. The following are some selected figures which explain the previous fact:

Figure 4-78 shows SIF histories of cracks 1, 2, 3 and 4, this figure matches the figure 4-74, but in this case, SIF values are doubled while the maximum and minimum differential average values between cracks 1 and 4 are (0.04% min. and 3.8% max.)

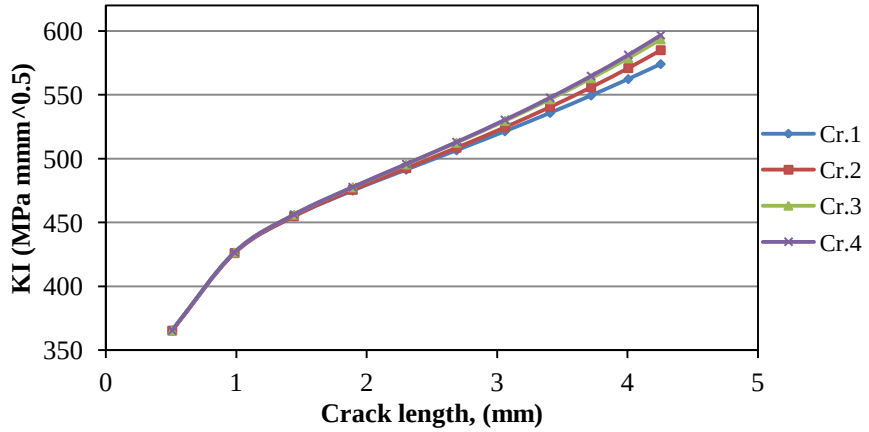

Figure 4-78 SIF histories of cracks 1, 2, 3 and 4

Figure 4-79 shows there is a similarity with figure 4-75 except the SIF values, in this case, are doubled; also, the same differential average values are recorded.

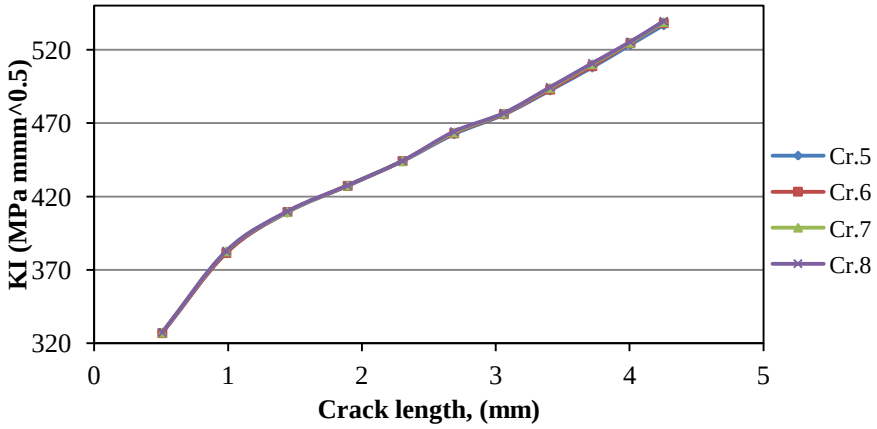

Figure 4-79 SIF histories of crack 5, 6, 7, and 8

Also, figure 4-80 shows there is a similarity in propagation trend which described in figure 4-76, but, in this case SIF values are doubled. Furthermore, the maximum and the minimum differential average values which mentioned in figure 4-76 also was the same in figure 4-76.

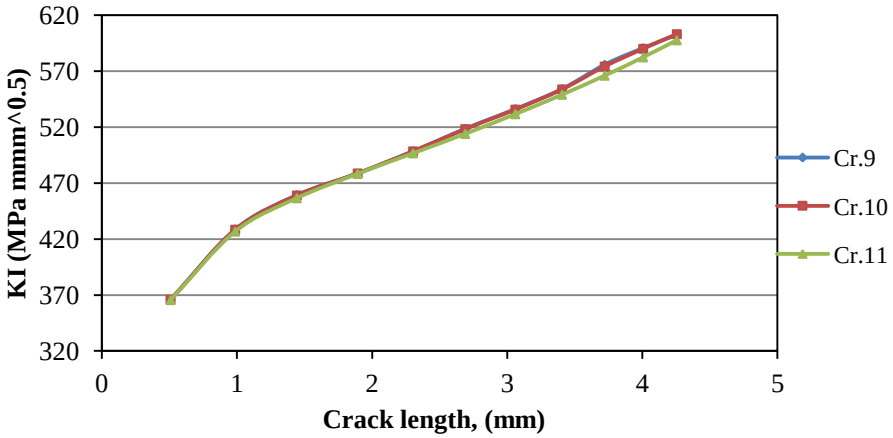

Figure 4-80 SIF histories of crack from 9, 10 and 11

Due to the symmetry of SIFs solution using this method, the rest solution of cracks from 12 to 22 recorded in appendix (B) section 2-B.

4.3.3 Stress intensity factor results of 200 MPa applied stress

Figures 4-81, 4-82 and 4-83 are some selected SIF solution using approximation method in the case of applied stress 200 MPa, the solution shows there is a similarity in cracks propagation trend between the above mentioned figures with the figures in the case of applied stress 100 MPa (figures 4-78, 4-79 and 4-80).Also, the solution showed the cracks had the same differential average values which recorded in the case of 50 MPA and 100 MPa.

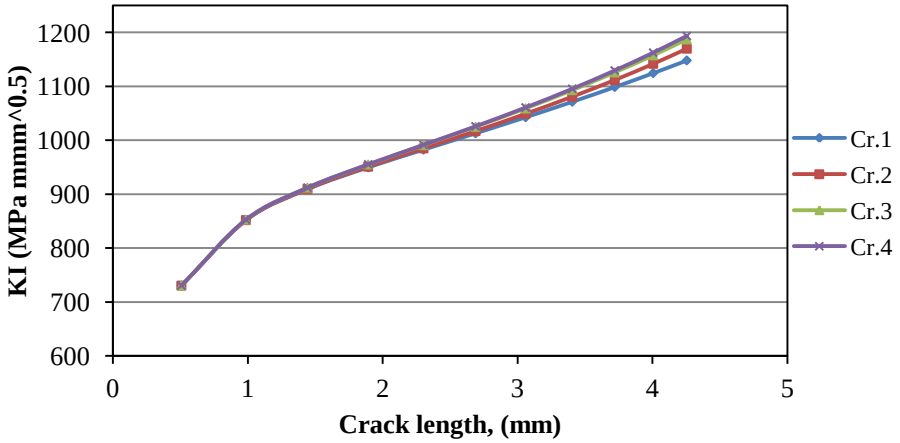

Figure 4-81 SIF histories of cracks 1, 2, 3 and 4

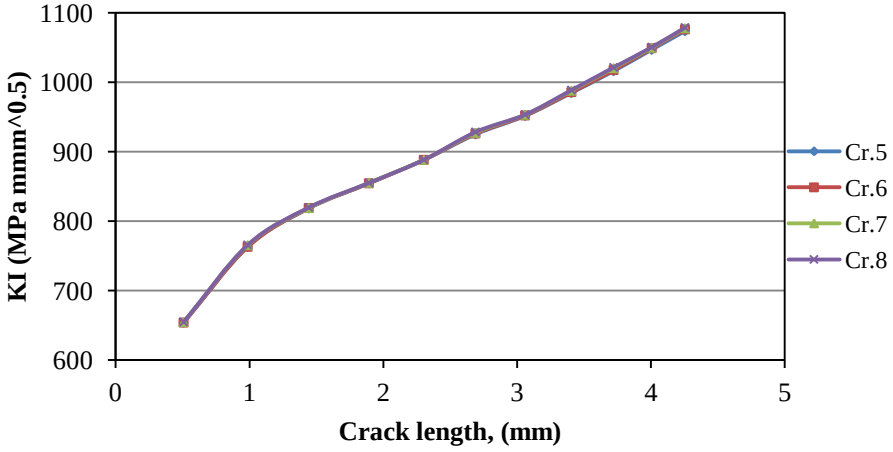

Figure 4-82 SIF histories of cracks from 5 to 8

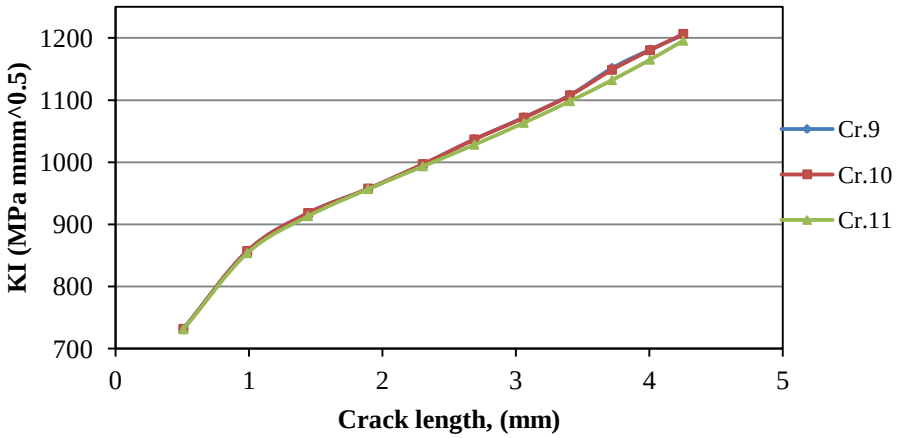

Figure 4-83 SIF histories of cracks 9, 10 and 11

Due to the symmetry of SIFs solution using this method, the rest solution of cracks from 12 to 22 recorded in appendix (B) section 3-B.

4-4 ANALYSIS OF RESULTS

In order to verify results obtained by means of XFEM, SIFs calculated in Morfeo/Crack for Abaqus are compared with results obtained using classical FEM (FRANC2D/L software) and previously described approximate method. The results are presented through normalized stress intensity factors (geometry factor $\beta = \frac{K_I}{\sigma\sqrt{\pi a}}$) for six selected cracks and are shown in the following section. Factor β is function of the stress intensity factor for mode I (K_I), stress σ and crack length a.

4-4-1 Results analysis in the case of applied stress 50 MPa

Comparing the results obtained by XFEM (Morfeo/crack for Abaqus) and FEM (FRANC2D/L) it can be seen that SIFs histories for selected cracks (1, 2, 11, 12, 21 and 22) differ up to 11.71% (in the case of crack 21). The minimum differences occur for the initial crack size, due to the proximity of the hole boundary. For the cracks on the first hole the difference between XFEM and FEM results decreases with cracks growth to 1.45% (crack

1), i.e. 0.44% (crack 2). For the sixth hole (which cracks 11 and 12 emanating from) this difference starts to increase with cracks growth up to 8.48% (crack 11) and 8.53%(crack 12), but with cracks further growth it decreases up to 1.1% (crack 11) and 1.55 (crack 12), then the differences starts to rise and reaches 8.91% (crack 11) and 8.35% (crack 12) at the end of the simulation, see figures 4-84, 4-85, 4-86 and 4-87.

The cracks 21 and 22 exhibit the same growth trend of cracks 1 and 2 due to their position, the highest recorded difference reaches 11.71% (crack 21) and 11.69% (crack 22), the difference decreased and reached the lowest percentage at the end of the simulation, 3.78% (crack 21) and 3.07% (crack 22), see figures 4-88 and 4-89.

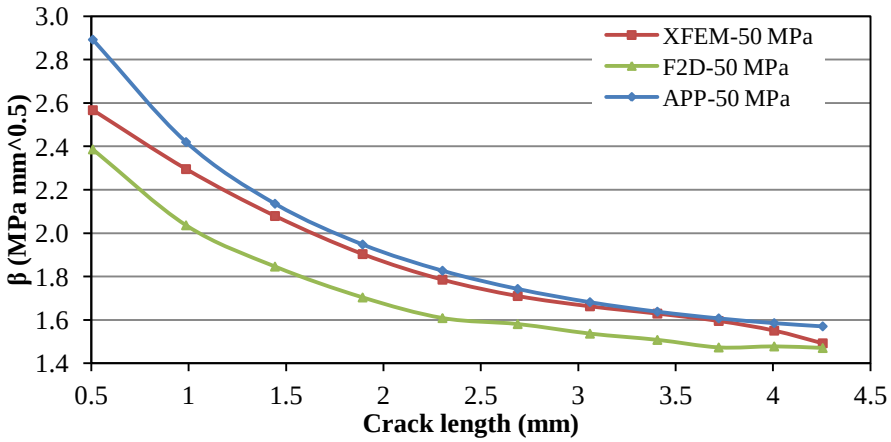

Figure 4-84 SIF comparison obtained by three different methods, crack 1

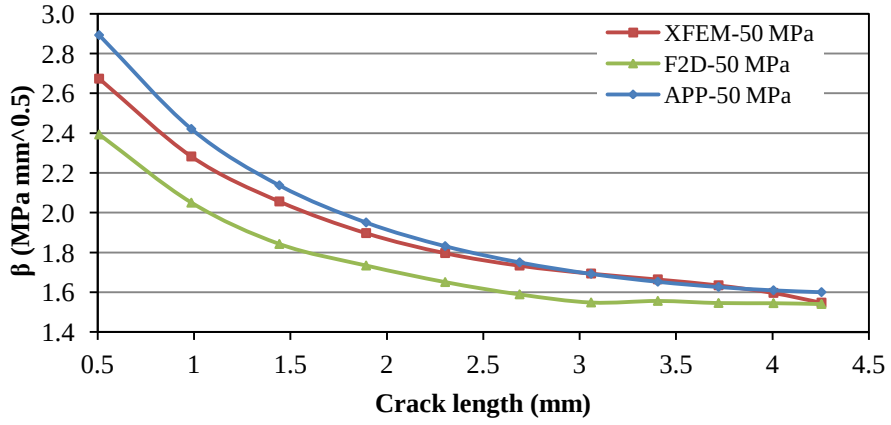

Figure 4-85 SIF comparison obtained by three different methods, crack 2

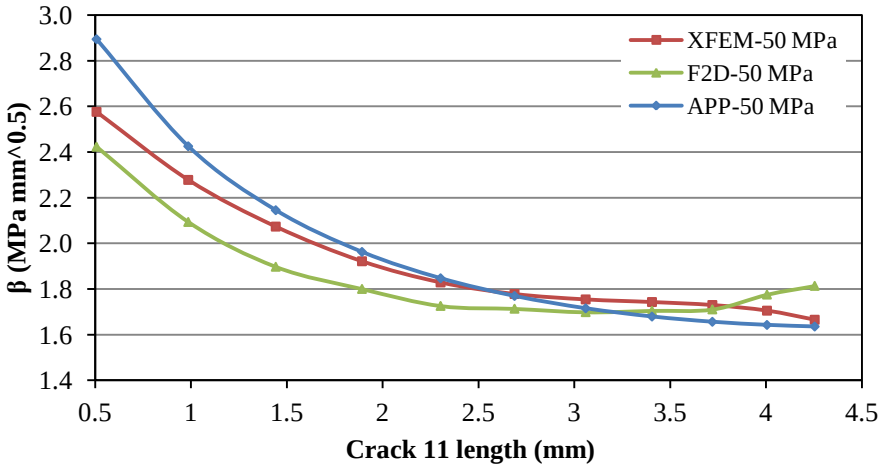

Figure 4-86 SIF comparison obtained by three different methods, crack 11

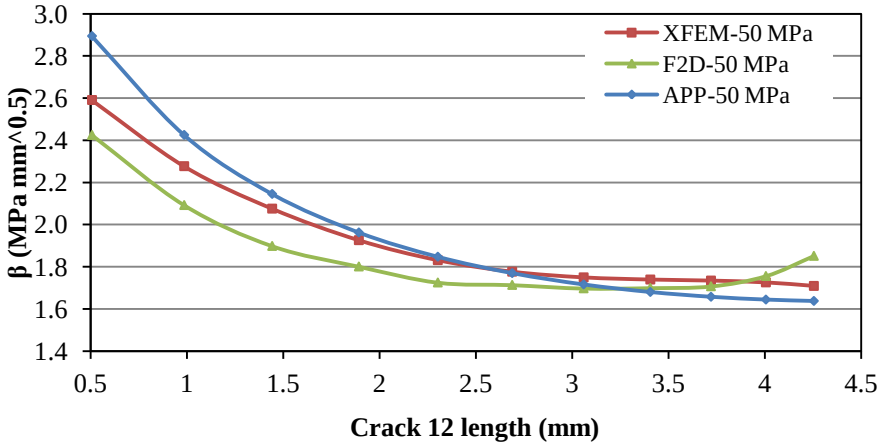

Figure 4-87 SIF comparison obtained by three different methods, crack 12

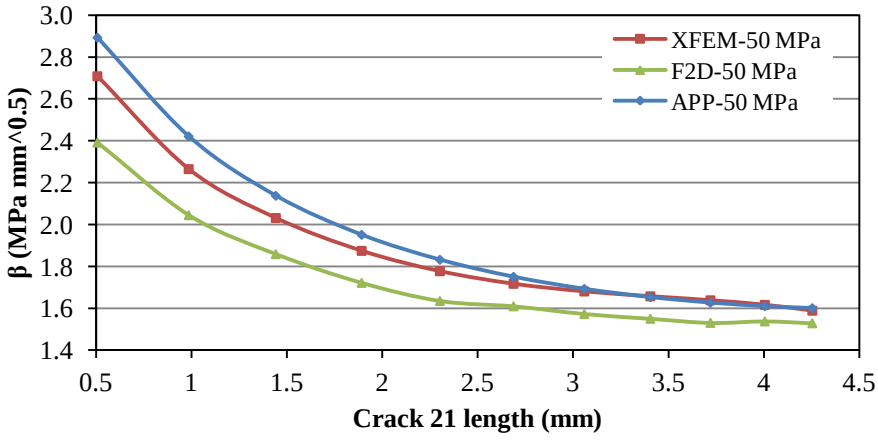

Figure 4-88 SIF comparison obtained by three different methods, crack 21

Comparing the XFEM results with results calculated by means of approximation method showed better agreement as it can be seen from the figures from 4-84 to 4-89. SIFs histories for the selected cracks differ up to 17.35% (crack 22), also, for the initial crack size. But, with the cracks growing, these differences decrease, and for the cracks length of 2 mm they are under 4.1%and the lowest recorded difference was 0.008% (crack 22). Since used approximation method defines the influential coefficients that take into consideration cracks interaction effect for every crack in the analyzed structure, this leads to conclusion that XFEM also takes cracks interaction effect into consideration in a very good manner.

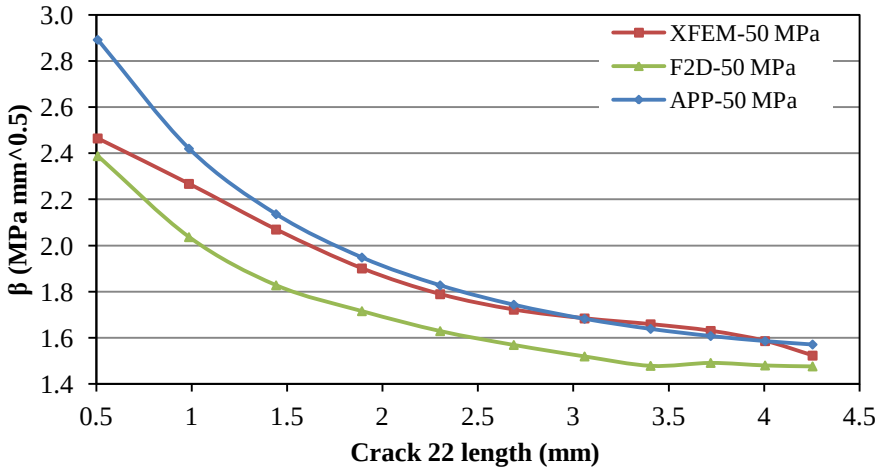

Figure 4-89 SIF comparison obtained by three different methods, crack 22

4-4-2 Results analysis in the case of applied stress 100 MPa

In this case and using the same procedure in the previous section, the comparison results between XFEM and FEM (F2D) are shown in figures from figure 4-90 till figure 4-95, that the relationship between β (geometry factor) difference and crack lengths was: as crack propagate as the difference percentage decreases. Also, SIF histories for the selected cracks (1, 2, 11, 12, 21 and 22) differ up to 14.14% (in the case of crack 21). For crack 1 the difference between XFEM and FEM increased and reached the maximum value at the fifth step of the simulation 10.64% and started to decrease after that step, the lowest recorded difference value was 6.09% at the last step of the simulation, see figure 4-90.

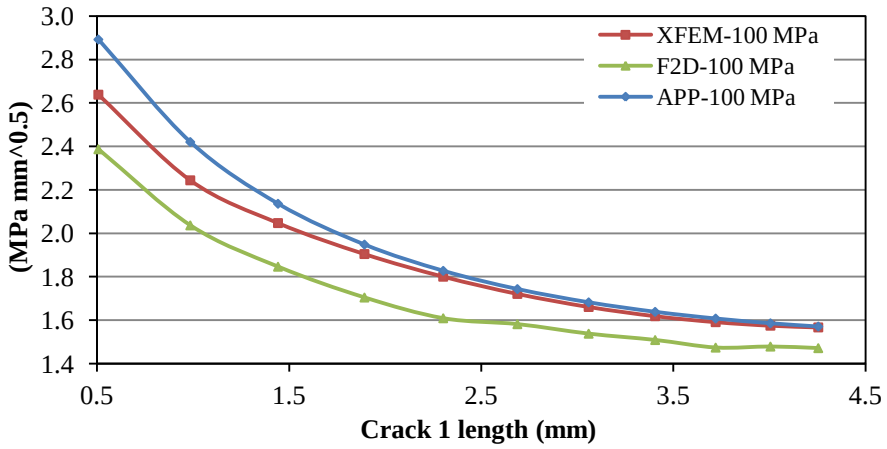

Figure 4-90 SIF comparison obtained by three different methods, crack 1

Crack 2 shows the maximum difference at the first step (initial crack) 13.7% while the lowest difference recorded was 4.18%, see figure 4-91.

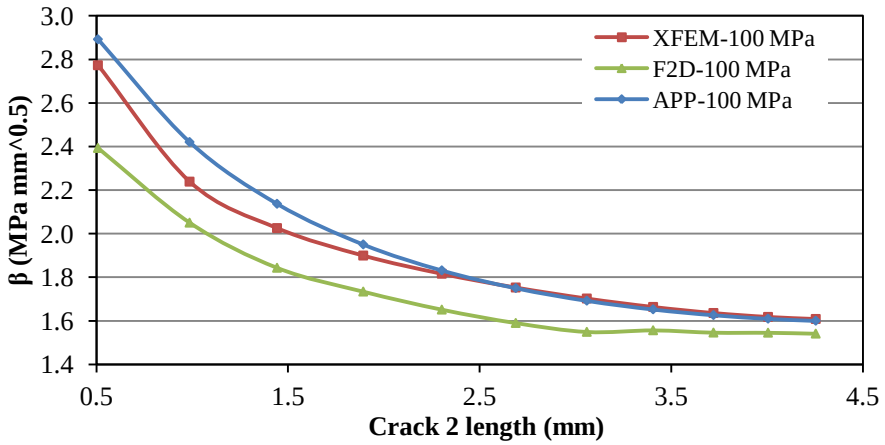

Figure 4-91 SIF comparison obtained by three different methods, crack 2

For the cracks 11 and 12 (emanating from the sixth hole) the difference start to decrease after the initial crack size and reaches 0.48% (crack11), 1.01% (crack 12) at the ninth point on the XFEM curve and the difference starts to decrease , the overlapping between the curves occurred after the crack reaches 4.006 mm length. The recorded difference at the last point on the curve was 6.27% (crack 11) and 8.11% (crack 12), see figure 4-92 and 4-93.

It is clear that cracks 21 and 22 exhibit the same trend of cracks 1 and 2 at it can be seen from figures 4-90, 4-91 and 4-94, 4-95. The difference value is increased and reached its

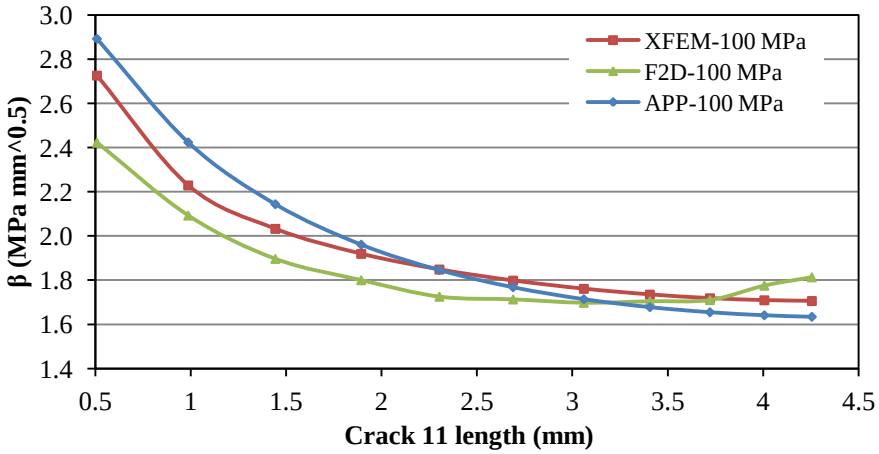

Figure 4-92 SIF comparison obtained by three different methods, crack 11

highest value at step 5 11.62% (crack 22), then the difference started to decrease and reached its lowest value at the last point on the curve 6.51%, see figure 4-95.

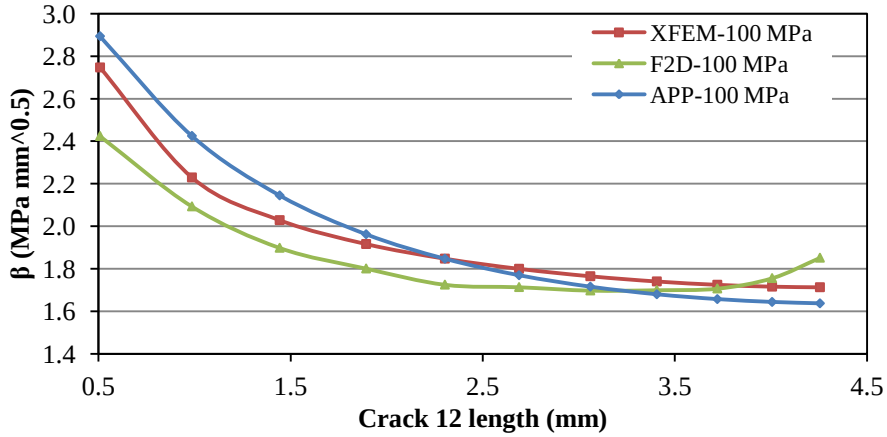

Figure 4-93 SIF comparison obtained by three different methods, crack 12

The highest recorded difference was equal to 14.14% (crack 21) at the initial crack step and the difference started to decrease till the third step (7.73%). The lowest recorded difference In the case of crack 21 was 5.69%, see figure 4.94.

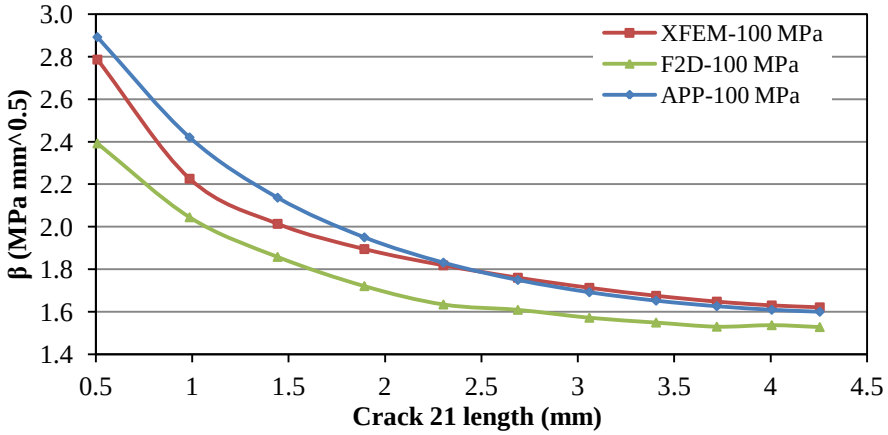

Figure 4-94 SIF comparison obtained by three different methods, crack 21

Comparing the XFEM results with results calculated by means of approximation method showed better agreement as it can be seen from the figures from 4-90 to 4-95. SIFs histories for the selected cracks differ up to 14.34% (crack 22), also, for the initial crack size. But, with the cracks growing, these differences decrease, and for the cracks length of 2 mm they are under 0.53% and the lowest recorded difference was 0.026% (crack 12). Since used approximation method defines the influential coefficients that take into consideration cracks interaction effect for every crack in the analyzed structure, this leads to conclusion that XFEM also takes cracks interaction effect into consideration in a very good manner.

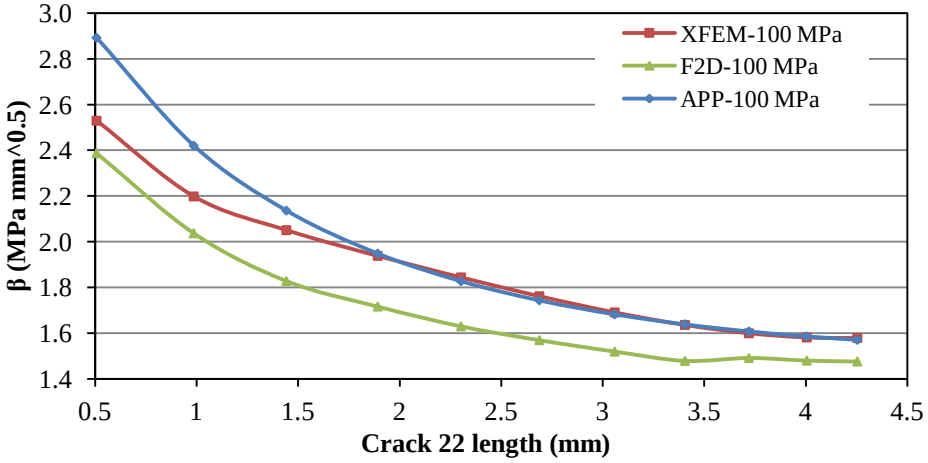

Figure 4-95 SIF comparison obtained by three different methods, crack 22

4-4-3 Results analysis in the case of applied stress 200 MPa

Comparing the results obtained by XFEM (Morfeo/Crack for Abaqus) and FEM (FRANC2D/L) it can be seen that SIFs histories for selected cracks differ up to 12.54% (in the case of crack 21). The maximum differences occur for initial crack size, due to the proximity of the hole boundary. For the cracks on the first hole the difference between XFEM and FEM results decreases with cracks growth up to 6.39% (crack 1), i.e. 4.1% (crack 2), see figures 4-96 and 4-97.

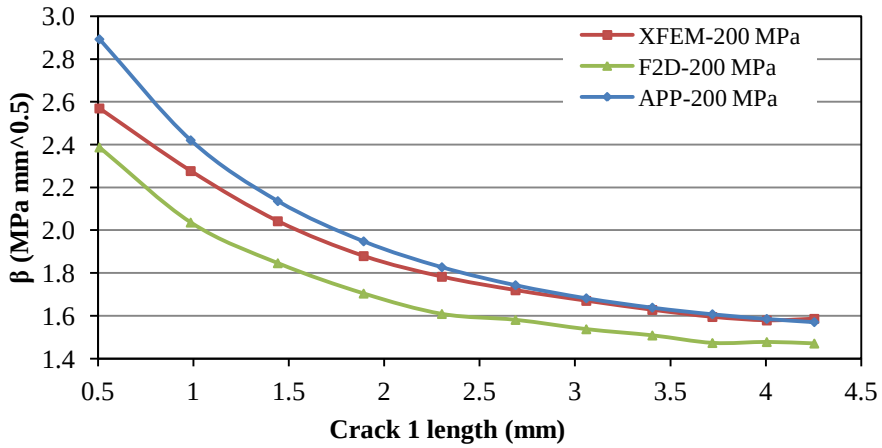

Figure 4-96 SIF comparison obtained by three different methods, crack 1

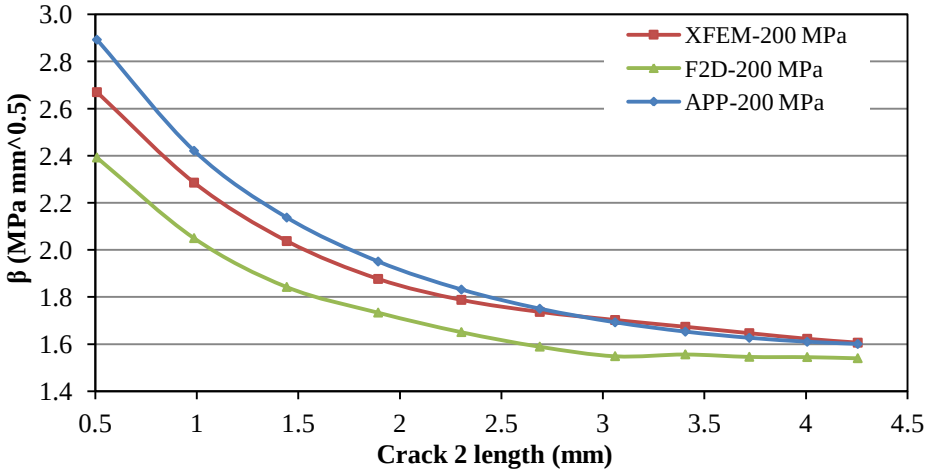

Figure 4-97 SIF comparison obtained by three different methods, crack 2

For cracks at sixth hole this difference starts to decrease with cracks growth to 0.03% (crack 11), i.e. 0.64% (crack 12), but with further cracks growth it increases up to 6.79% (crack 11), i.e. 8.26% (crack 12), see figures 4-98 and 4-99. The cracks 21 and 22 at eleventh hole exhibit the similar trend, see figures 4-100 and 4-101. In all of these cases XFEM gives slightly higher results than FEM. This can be explained by the fact that the initial crack size was less than the thickness of the plate in the case of FRANC2D/L; whilst in the case of Morfeo/Crack 3D solid model was used. The trend of increasing differences with cracks growth may be explained by the different manner in which these two methods implement mutual cracks interaction. Anyway, the difference can probably be reduced by increasing the number of nodes in the regions among the cracks on 3D model; nevertheless, the obtained solutions for SIFs are acceptable from an engineering point of view.

Comparing the XFEM results with the results calculated by means of approximate method better agreement can be seen (Fig. 4-98). SIFs histories for selected cracks differ up to 15.20% (crack 22), also for initial crack size. But, with cracks' growth, these differences decrease, and for the cracks' length of 2 mm they are well under 1.13%. Since used approximation method defines the influential coefficients that take into consideration cracks interaction effect for every crack in the analyzed structure, this leads to conclusion that XFEM also takes cracks interaction effect into consideration in a very good manner.

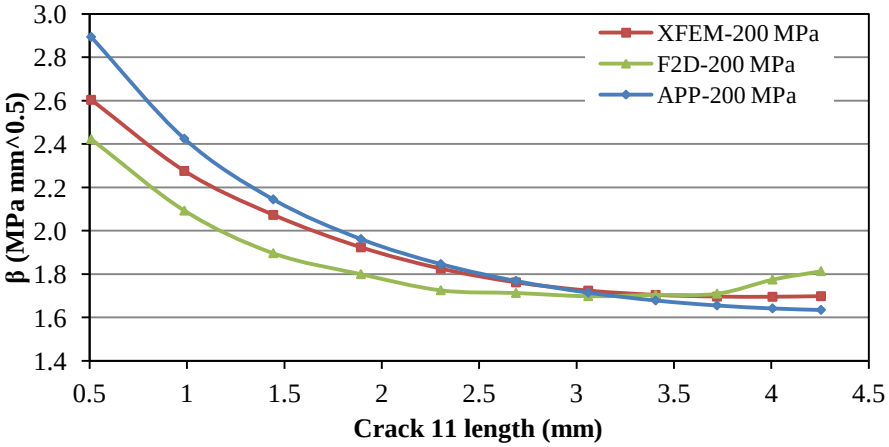

Figure 4-98 SIF comparison obtained by three different methods, crack 11

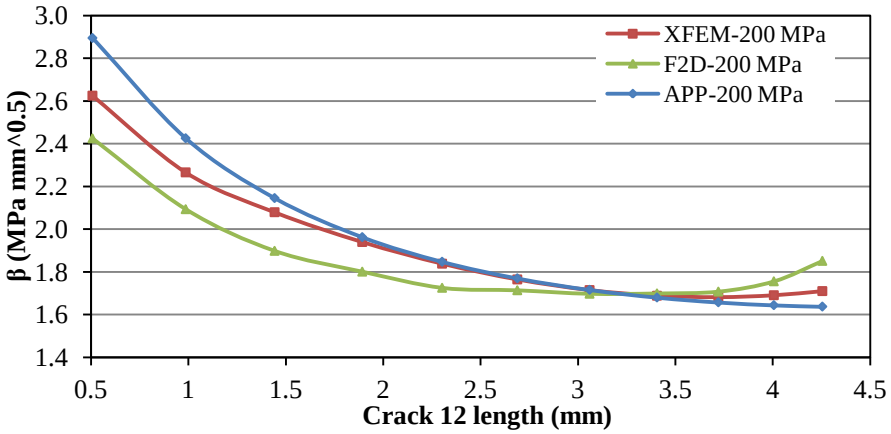

Figure 4-99 SIF comparison obtained by three different methods, crack 12

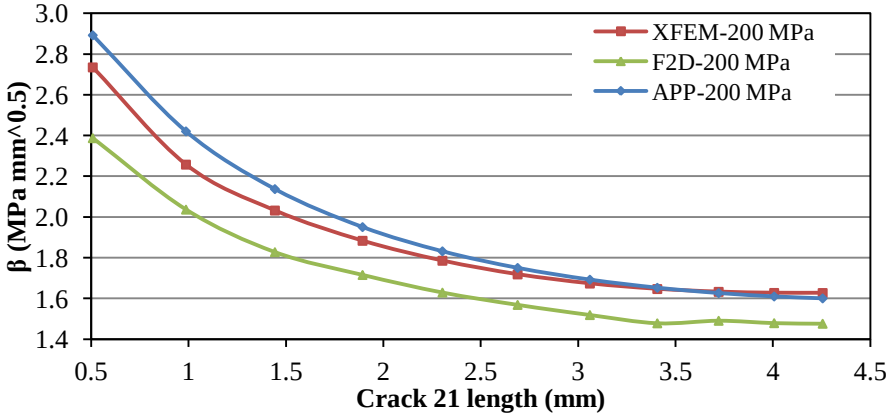

Figure 4-100 SIF comparison obtained by three different methods, crack 21

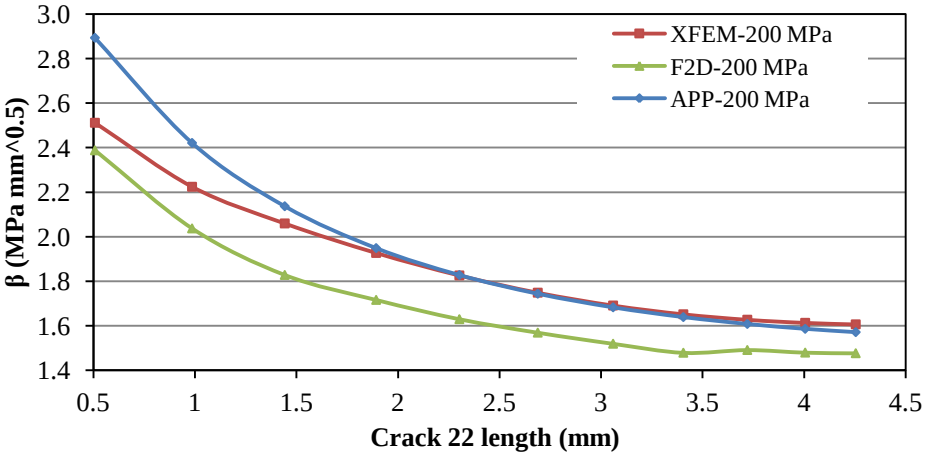

Figure 4-101 SIF comparison obtained by three different methods, crack 22

Chapter 5 Stress Intensity Factor for Multiple Cracks on Curved Panels Made of 2024-T3 aluminum alloy

5-1 FIRST NUMERICAL EXAMPLE

5.1.1 The analysis of MSD configuration using XFEM

In this section, a FE model of curved, unstiffened panel (dimensions $L_1 \times L_2$=600×400 mm, thickness=1.6 mm, D the diameter of the aircraft fuselage will equal to 1.6, 2.4, 3.2 and 4 m), with 3 fastener holes (radii=2.4 mm at distance b=25 mm), see figure 5.1. The panel subjected to uniform internal pressurization equal to 0.054 MPa to examine effects of multiple site damage on fatigue crack growth rates.

Typical material properties for 2024-T3 aluminum – Young's modulus of 73000 MPa, Poisson's ratio of 0.33 – were used in the analyses. A uniform pressure was applied at the internal face of the model Fig. (5.2). Each hole in the panel had two radial cracks, numbered from 1 to 6 in Fig.5-1 and positioned as shown in Fig.(5-3). Figure 5-3 also shows a portion of the mesh around the holes, and as it can be seen mesh was refined around the cracks at the edges of each hole and a uniform template of elements around each crack front was used.

The characteristics of final mesh are summarized in table 5.1. This mesh was used to calculate SIFs at crack nodes as a function of crack length. The crack growth simulation capability of Morfeo/Crack for Abaqus was used for this purpose. Morfeo/Crack calls Abaqus at each propagation step and between the steps and reads the Abaqus solution, recovers a richer, improved XFEM solution in a small area surrounding the crack and computes the SIFs at crack front nodes [22]. After that, it determines the appropriate crack growth increment, extends each crack and then performs the next solution step. Results of this procedure can be seen in the following section. The initial crack length used was 0.5mm.

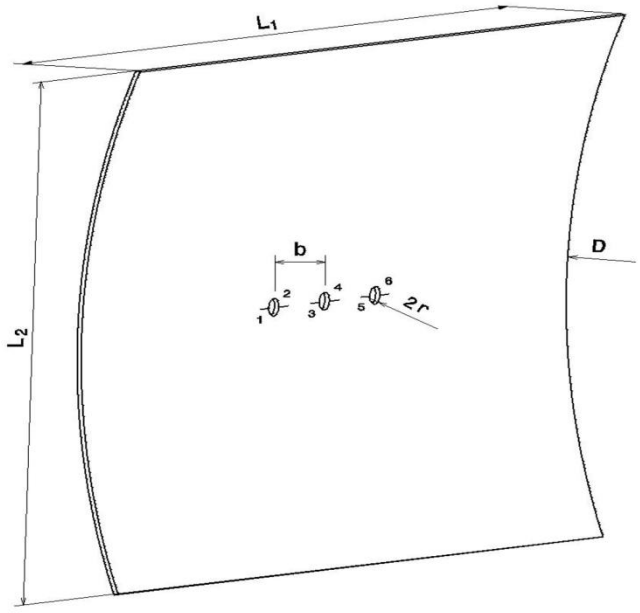

Figure 5-1 Analyzed configuration with multiple cracks (not to scale)

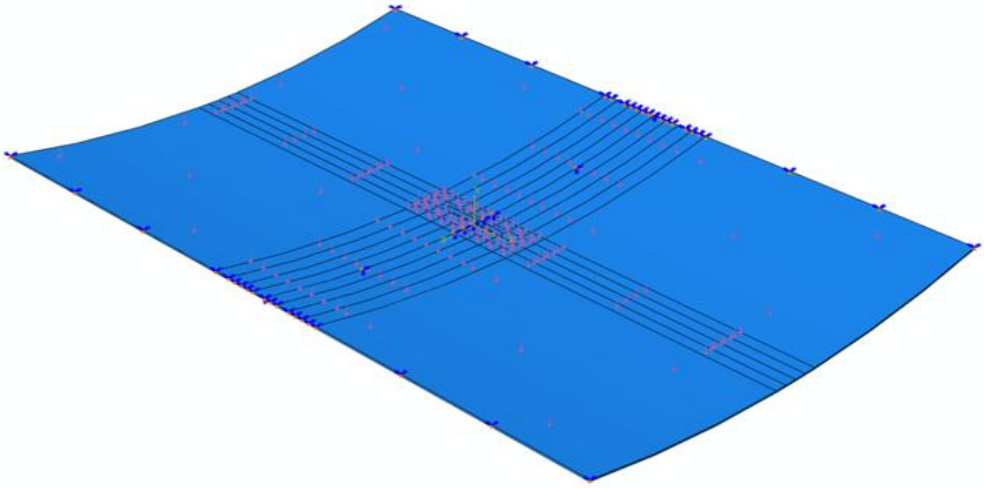

Figure 5-2 Panel with pressure load and boundary condition

Table 5-1 Characteristics of the panel final mesh

D (m)	No. of steps	No. of nodes	No. of elements	Type of element
1.6	34	93196	68880	C3D8R
2.4	41	80012	59040	C3D8R
3.2	37	80012	59040	C3D8R
4	52	79624	58752	C3D8R

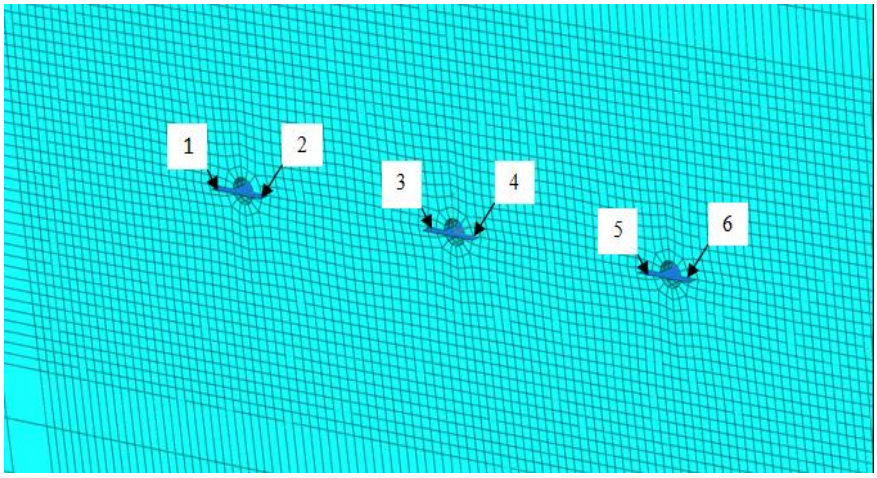

Figure 5-3 Cracks positioning and numbering

5.1.1.1 SIF evaluation of crack 1 at different fuselage diameters

SIFs were calculated for each crack front and different crack sizes and maximum values of SIFs calculated along the crack fronts were used as a reference. Also, in this section SIF of the cracks from 1 to 6 will be evaluated individually to investigate the effect of changing fuselage diameter from 1.6 m to 4 m. The SIF results were described in figures 5.4 to 5.8.

It can be seen from figure 5.4 that the longest crack 1 length was recorded when fuselage diameter equal to 2.4m (CL =17.1846 mm, KI = 2870.65 MPa$\sqrt{mm}$) followed by when D=4m (CL=13.0871 mm, KI = 4370.75 MPa $\sqrt{mm}$), D=3.2m (CL=11.1326mm, KI = 2915 MPa$\sqrt{mm}$) and D=1.6m (CL = 3.4541, KI = 3623.16 MPa$\sqrt{mm}$) respectively.

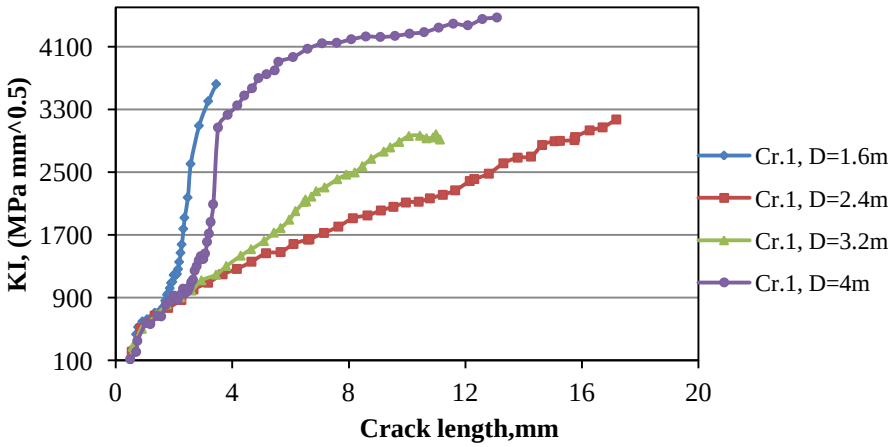

Figure 5-4 SIF histories of crack 1

Tables 5.2, 5.3, 5.4 and 5.5 which are mentioned in appendix (C) section (1-C) show some selected simulation steps for crack 1 as the fuselage diameter changed from 1.6 to 4 m, they describe the effect of K_{III} (stress intensity factor tearing mode) was existed in this simulation. It is worth to mention that the significant increase in the values of K_I occurred in this simulation due to the clear existence effects of K_{III} values (tearing mode). Figures from 5.5 to 5.8 show the simulation at steps 1, 15, 36, and the final step.

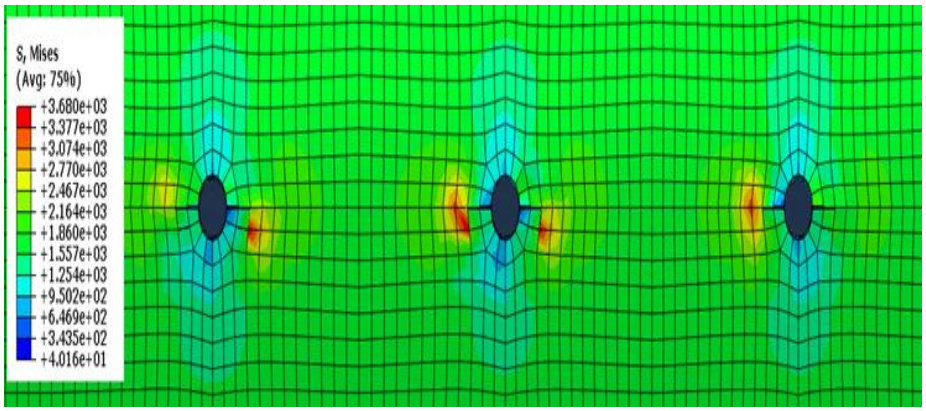

Figure 5-5 XFEM model of MSD after cracks opening (the first step), D=2.4m

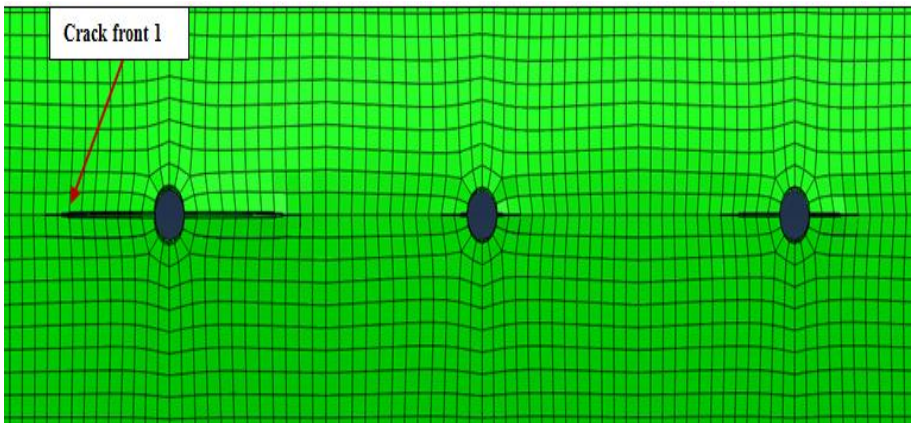

Figure 5-6 XFEM model of MSD after cracks opening (step 15), D=2.4m

Figure 5.8 shows the deformed panel at crack 1 position, it illustrates that this type of loading leads mode I is still dominant, but according to the mentioned tables, this type of fatigue crack growth is considered as mixed mode failure (mode I and mode III) especially

at the last steps of the simulation. Also, the linking up between cracks 2 and 3 occurred at step 41 to form a new crack.

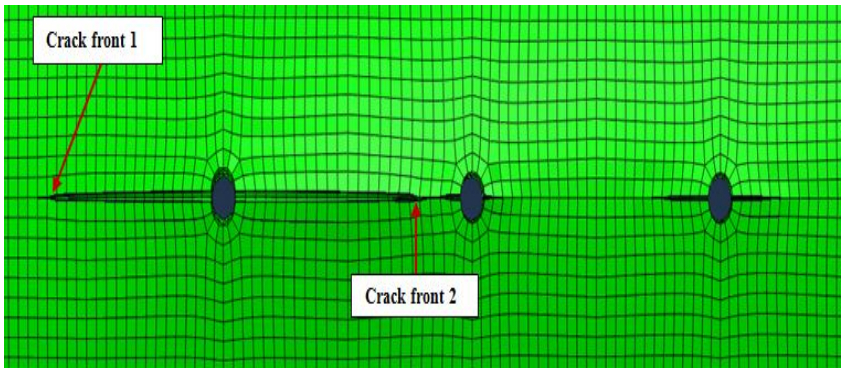

Figure 5-7 XFEM model of MSD after cracks opening (step 36), D=2.4m

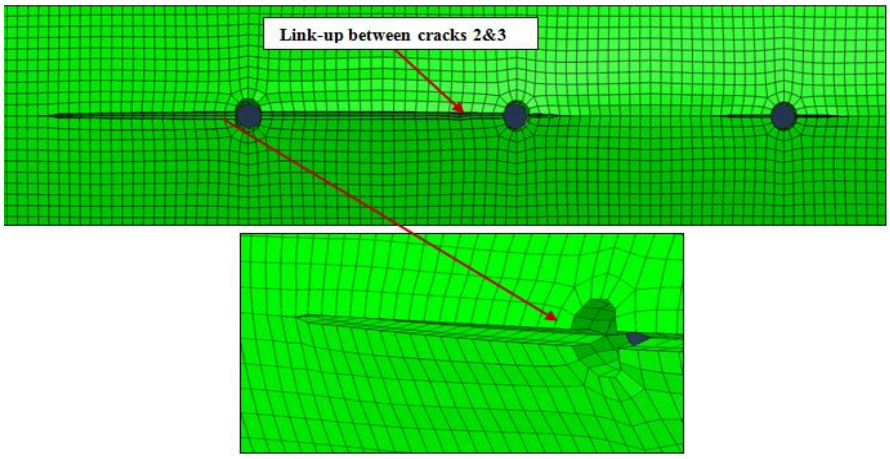

Figure 5-8 XFEM model of MSD after cracks opening (step 41), D=2.4m

Figure from 5.9 to 5.12 describes the simulation steps of the crack 1 when the fuselage diameter equal to 4 m (C.L. =13 mm, KI $= 4370.75$ MPa$\sqrt{\text{mm}}$).

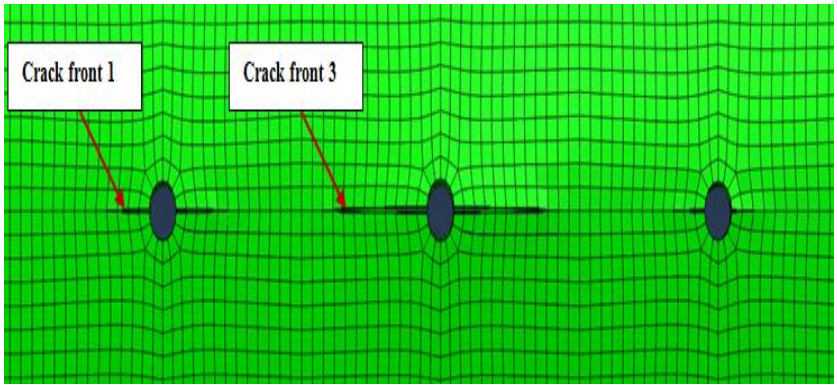

Figure 5-9 XFEM model of MSD at step 15, D=4m

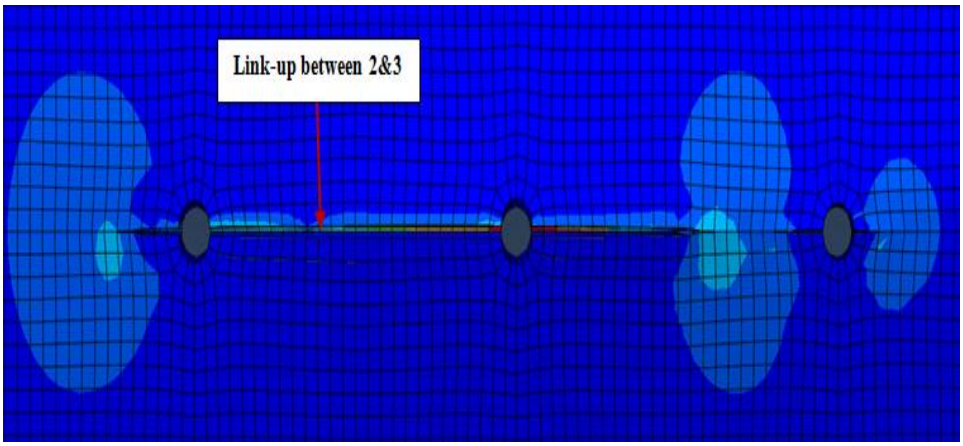

Figure 5-10 XFEM model of MSD at step 28, D=4m

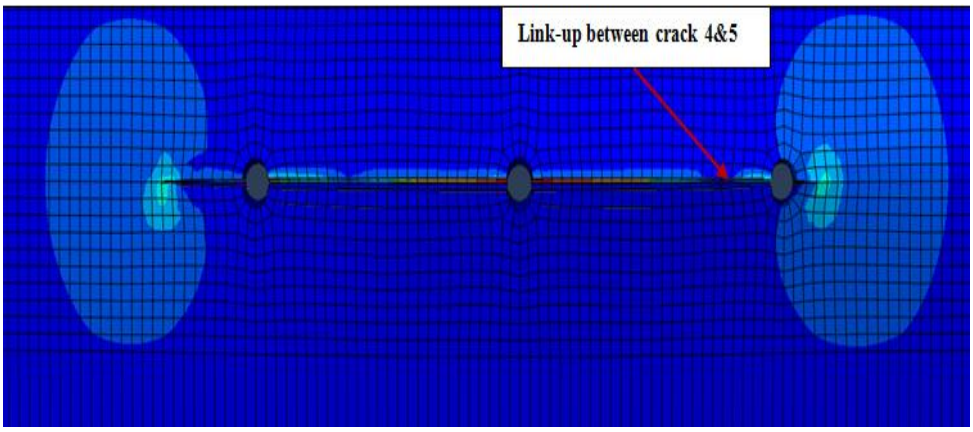

Figure 5-11 XFEM model of MSD at step 36, D=4m

5.1.1.2 SIF evaluation of crack 2 at different fuselage diameters

At the end of the simulation, It is observed in figure 5.12 that, the longest crack 2 length was recorded when D equal to 2.4 m (CL = 17.81802 mm, KI $= 3000\ \text{MPa}\sqrt{\text{mm}}$), then followed by when D equal to 3.2 m (CL = 10.108 mm, KI $= 3200.2\ \text{MPa}\sqrt{\text{mm}}$) at step 21 (it is notable from table 5.8 (see appendix (C) section (1-C-2)) K_I values had a minus sign which means it is no more effective while K_{III} had a positive value which means it had effect at the end of the simulation).

The tables 8, 9, 10 and 11 in appendix (C) section (1-C-2) show some selected SIF results of crack 2 due to three loading modes during the changing of fuselage diameter from 1.6 m to 4m; especially at the last steps of simulation.

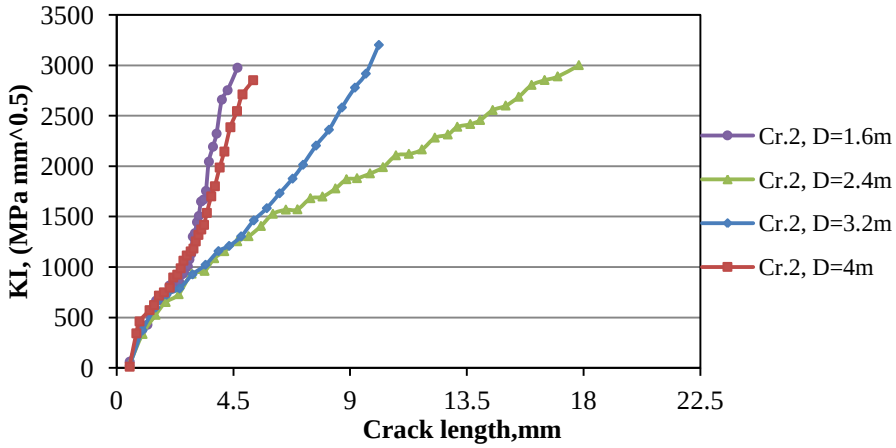

Figure 5-12 SIF histories of crack 2

As mention in section 5.1.1.1 above, figures 5.7 and 5.8 steps 36 and 41 describe that the longest cracks were 1 and 2 when D equal to 2.4 m due to the difference in the stress fields at their location, see figure 5.13. However, crack 2 was longer than crack 1 because of the effect of the interaction effect between crack front 2 and 3 as shown in figure 5.13. The link-up resulted in a lead crack of a total length 20.2 mm at step 37, see figure 5.8.

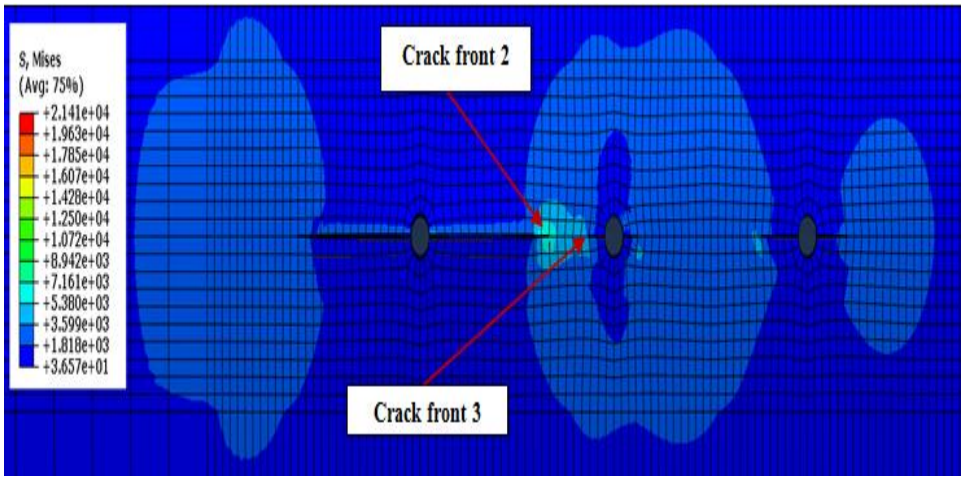

Figure 5-13 XFEM model of MSD at step 29, D=2.4m

The second longest length to crack 2 was recorded when D equal to 3.2 m (CL=10.7057 mm) at the end of simulation; Figures 5.14 and 5.15 show that the cracks 2 and 3 which were emanating from the holes rivets 1 and 2 grew towards each other almost simultaneously. Crack 2 length at D equal to 2.4 was longer about 66.4% than crack 2 when

D equal to 3.2 m and longer about 2.8 times compared with its length when D equal to 1.6 m, 2.4 times higher when D equal to 4 m.

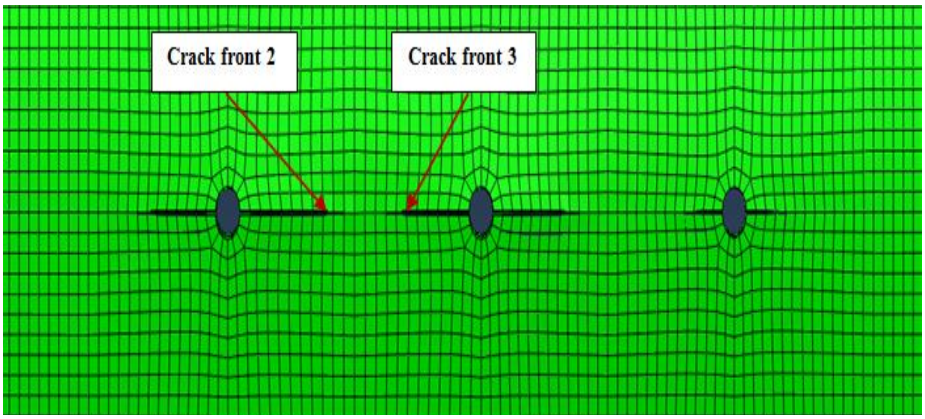

Figure 5-14 XFEM model of MSD at step 16, D=3.2m

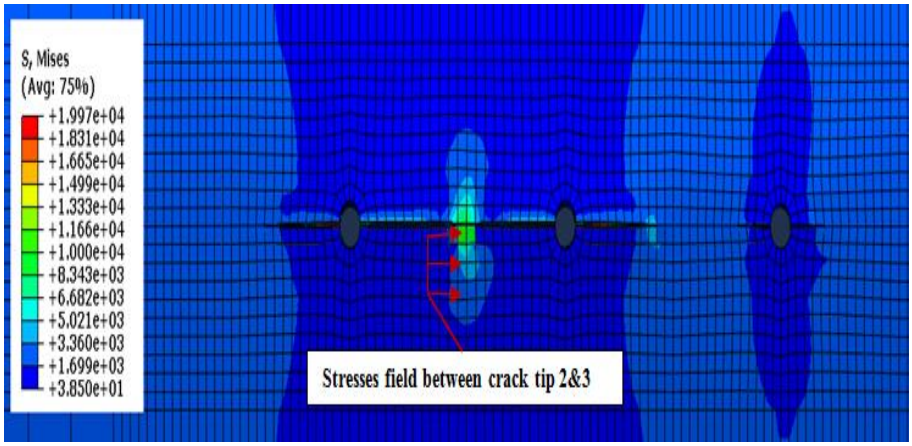

Figure 5-15 XFEM model of MSD at step 21, D=3.2m

5.1.1.3 SIF evaluation of crack 3 at different fuselage diameters

Figure 5.16 illustrates the relationship between crack lengths and crack 3 SIFs histories and the effect changing D from 1.6 m till 4 m, it showed that the longest crack length was observed when D equal to 1.6 m (C.L = 14.8103 mm, KI = 3176.95 MPa$\sqrt{\text{mm}}$) followed by when D equal to 4 m (CL = 13.8217 mm, KI = 3394.32 MPa$\sqrt{\text{mm}}$), and then when D equal to 3.2 m (C.L = 8.2243 mm, KI = 3100 MPa$\sqrt{\text{mm}}$ at step 21). The shortest crack 3

length was recorded when D equal to 2.4 m at the end of the simulation (CL =1.72394 mm,KI = 6273.94 MPa $\sqrt{mm}$).

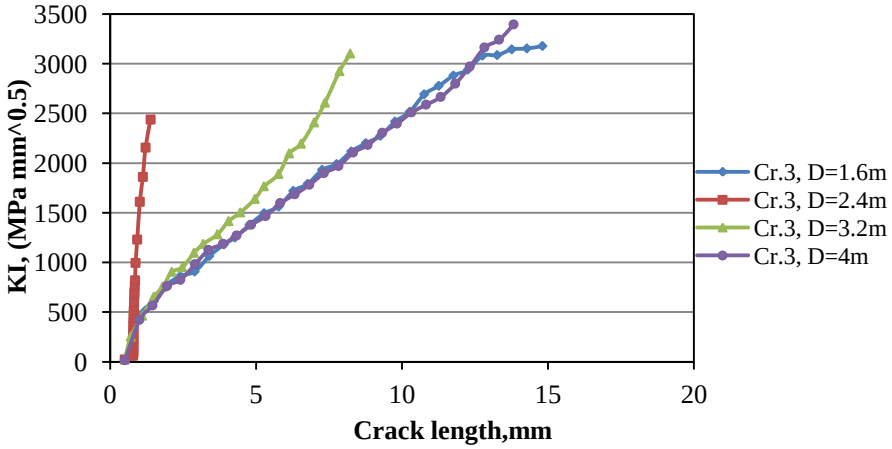

Figure 5-16 SIF histories of crack 3

It is noticeable in this section that crack 3 was longer about 7% and about 88% than when D were equal to 4 m and 2.4 m respectively. Tables 12, 13, 14 and 15 in appendix (C) section (1-C-3) show some selected simulation steps for crack 3, it is clear that K_{II} (shearing mode) and K_{III} (tearing mode) had noticed effect because they had positive values on some steps. This might be the reason for the rise in K_I values. Figure 5.17 shows the

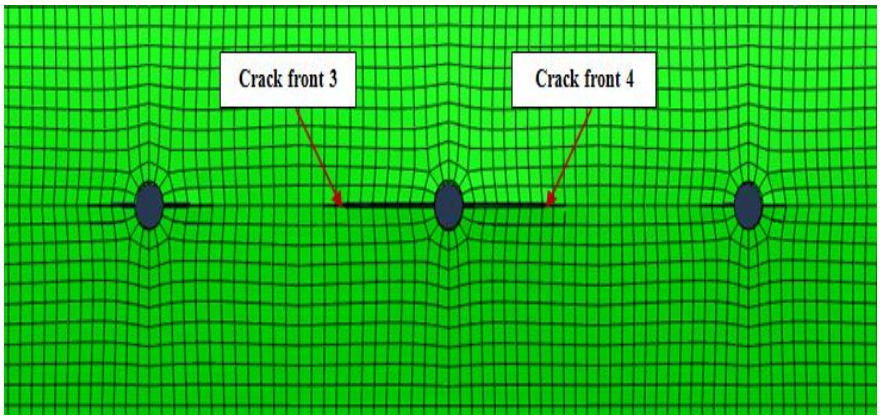

Figure 5-17 XFEM model of MSD at step 15, D=1.6m

simulation step 15 (D=1.6m), it explained that the cracks 3 and 4 had the longest crack lengths due to stress concentration at the location of rivet hole 3. Also, figure 5.18 shows the simulation step 29 before the linking up step between crack 2 and 3, the growing rate

of crack 3 increased and the length was longer than crack 2 and the linking up process occurred at step 30, as shown in figure 5.19.

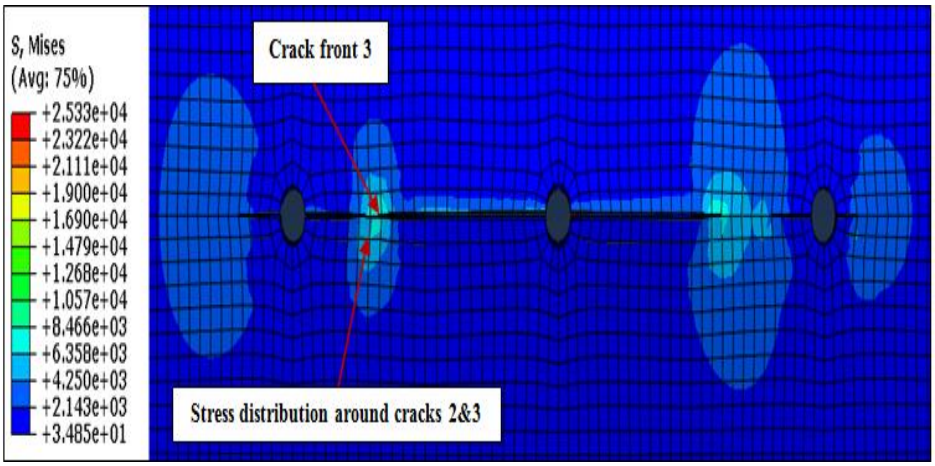

Figure 5-18 XFEM model of MSD at step 29, D=1.6m

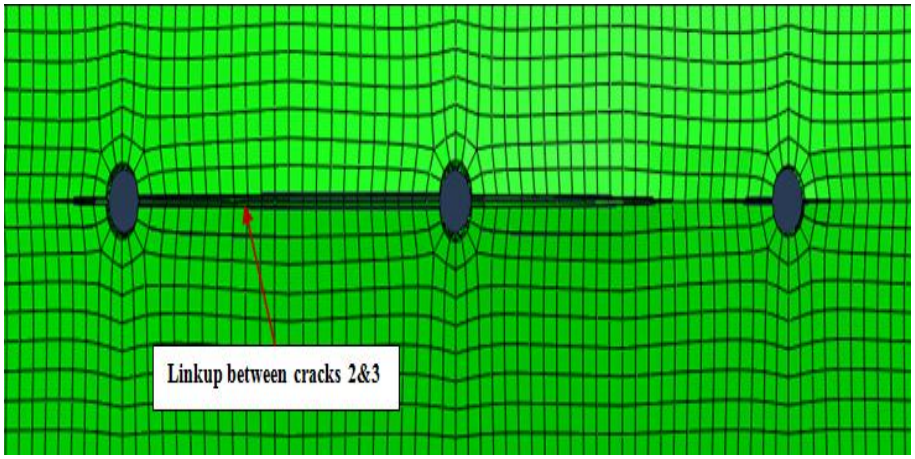

Figure 5-19 XFEM model of MSD at step 30, D=1.6m

Additionally, figure 5.20 illustrates the final step of the simulation (step 36) when D = 3.2 m, at this step crack 2 length was equal to (10.108 mm) and crack 3 length was equal to (8.2243 mm), meanwhile linking up didn't occur at this simulation. The linkup between cracks 2 and 3 occurred at step 37 when fuselage diameter equal to 4 m, and crack 3 was longer than crack 2 at the end of the simulation (13.8217 mm).

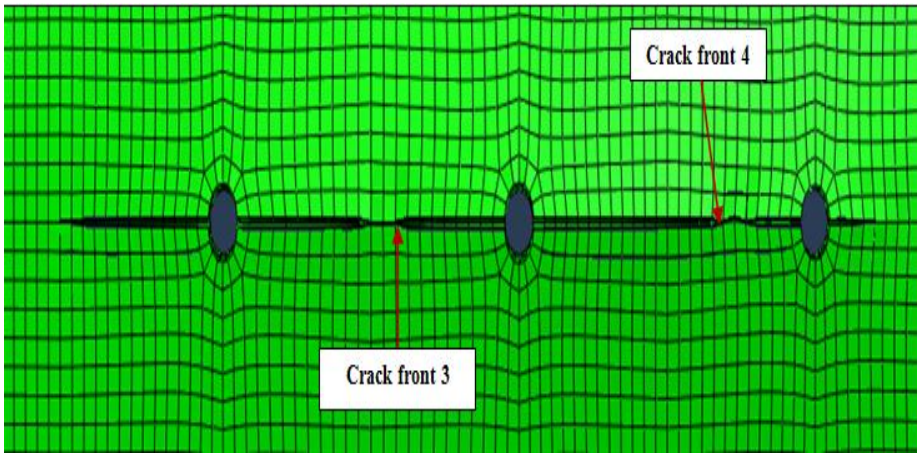

Figure 5-20 XFEM model of MSD at step 36, D=3.2m

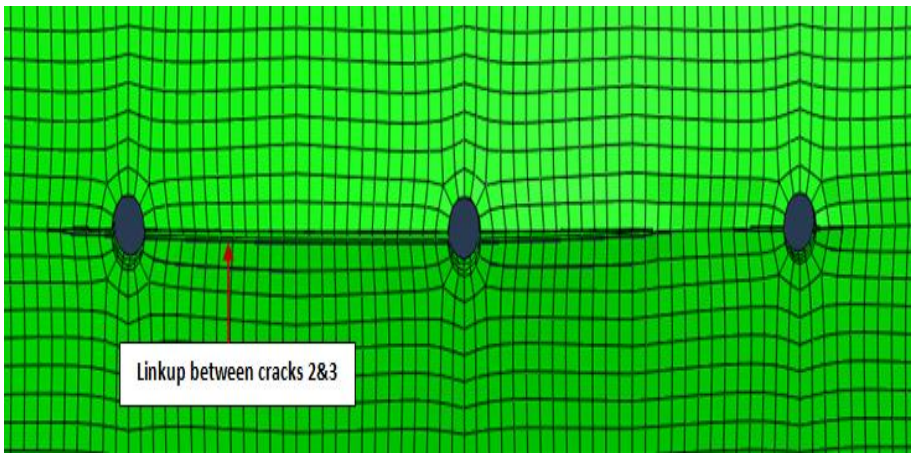

Figure 5-21 XFEM model of MSD at step 37, D=4m

5.1.1.4 SIF evaluation of crack 4 at different fuselage diameters

Crack 4 SIF histories and the effect of changing fuselage diameters (D) from 1.6 m till 4 m were represented in figure 5.23, it showed that the longest length for crack 4 was recorded when D equal to 4 m (CL = 16.4065 mm, KI $= 5465.33$ MPa $\sqrt{\text{mm}}$) followed by when D equal to 3.2 m (CL = 15.3173 mm, KI $= 4325.47$ MPa $\sqrt{\text{mm}}$), and then D equal to 1.6 m (CL = 14.6038 mm, KI $= 4451.25$ MPa $\sqrt{\text{mm}}$) and finally when D equal to 2.4 m (CL = 1.67265 mm, KI $= 3475.21$ MPa $\sqrt{\text{mm}}$).

Additionally, tables 16, 17, 18 and 19 in appendix (C) section (1-C-4) represent some selected simulation steps which were related to the results plotted in figure 5.22. The tables show that K_{II} and K_{III} had minus signs and small values which mean they did not have a

higher effect comparing to K_I values, so K_I, in this case, was the principle of the failure mode.

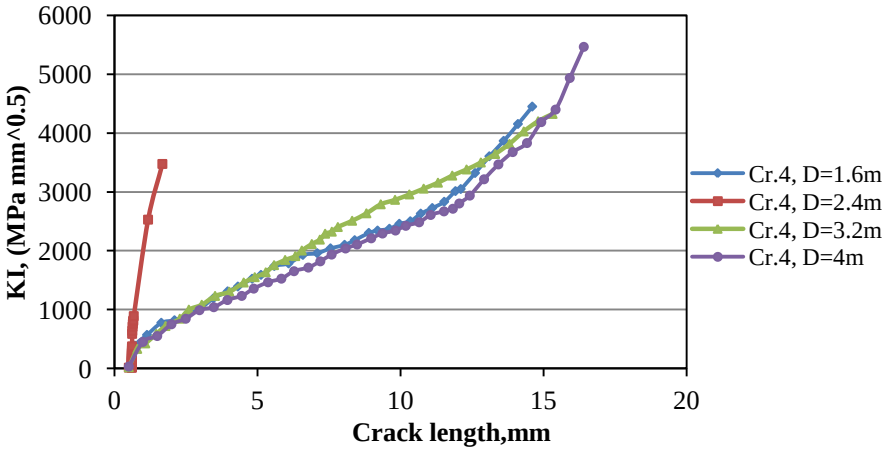

Figure 5-22 SIF histories of crack 4

As mentioned before in figure 5.21, the fastest crack growing rate were clearly to cracks 3 and 4 due to the stress concentration at the location of the middle hole (rivet hole 2), but crack 3 was faster than crack 4 and the linking up between cracks 2 and 3 occurred at step 28, afterwards, the second linkup occurred between crack 4 and 5 at step 36, as shown in figure 5.24. Also, figure 5.20 in section 5.1.1.3 shows the final crack length of crack 4 at the end of the simulation was (15.3173 mm), at this simulation there no linkup occurred.

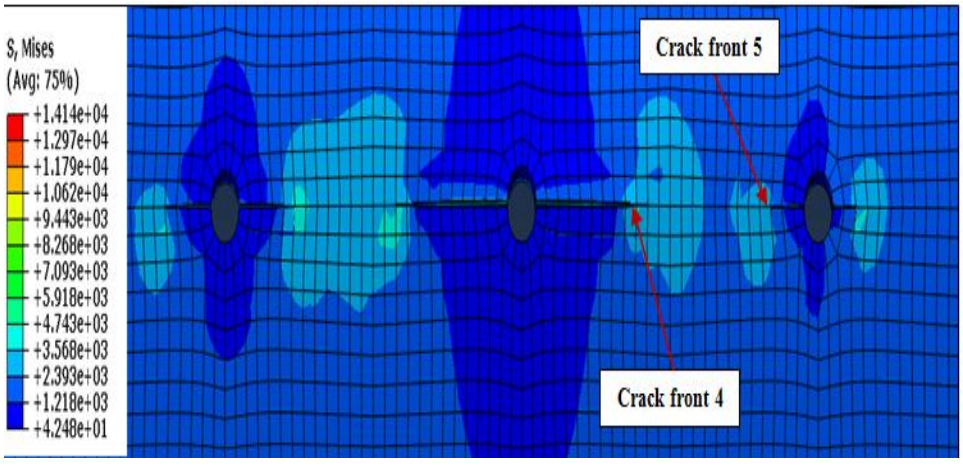

Figure 5-23 XFEM model of MSD at step 15, D=4m

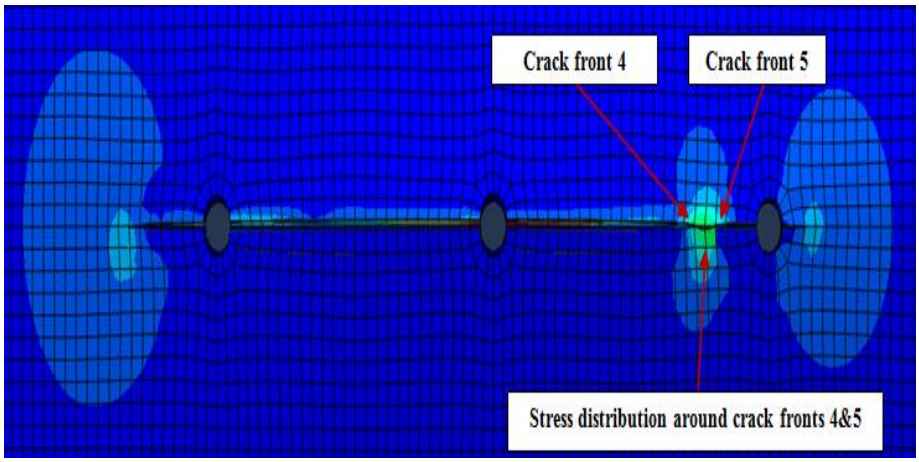

Figure 5-24 XFEM model of MSD at step 35, D=4m

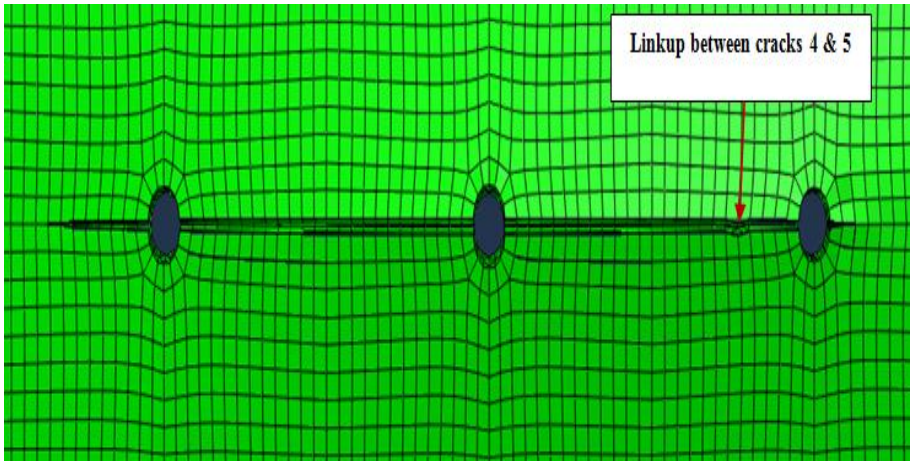

Figure 5-25 XFEM model of MSD at step 36, D=4m

5.1.1.5 SIF evaluation of crack 5 at different fuselage diameters

As shown in figure 5.26 the lengths of crack 5 were somewhat short for all fuselage diameters. Though the obtained results, crack 5 when D equal to 2.4 m (3.8838 mm, KI = 1640.88 MPa $\sqrt{\text{mm}}$) was longer about 1.6% compared to its length when D equal to 3.2 m (CL=3.8802 mm) , 31% longer compared to its length when D equal to 4 m (2.667 mm, KI = 3000.3 MPa $\sqrt{\text{mm}}$), and about 48% longer when D equal to 1.6 m (2.0124 mm, KI = 2242.56 MPa $\sqrt{\text{mm}}$). Furthermore, tables 20, 21, 22 and 23 in appendix (C) section (1-C-5) represent some selected simulation steps and they showed that K_I still the domain failure mode (mode I) with existence effect of K_{III}. K_{II} in this simulation had minus signs at the most steps which lead it did not affect to failure of the panel.

In addition to the above mentioned information, figure 5.27 shows the deformed panel at the rivet holes location and the final crack 5 length was (3.8838 mm), (D = 2.4 m) and it was 3.8202 mm when D equal to 3.2 m as shown in figure 5.28.

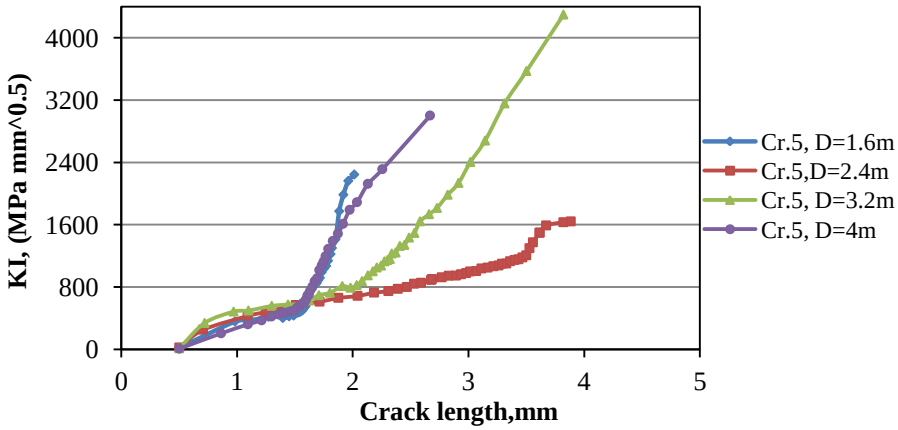

Figure 5-26 SIF histories of crack 5

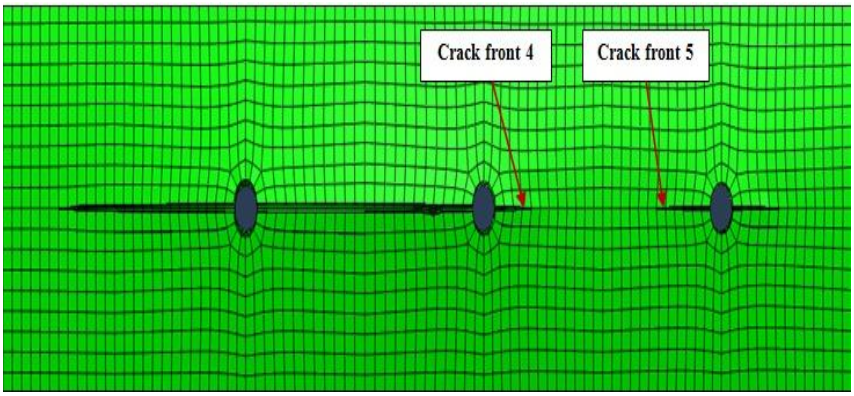

Figure 5-27 XFEM model of MSD at step 41, D=2.4 m

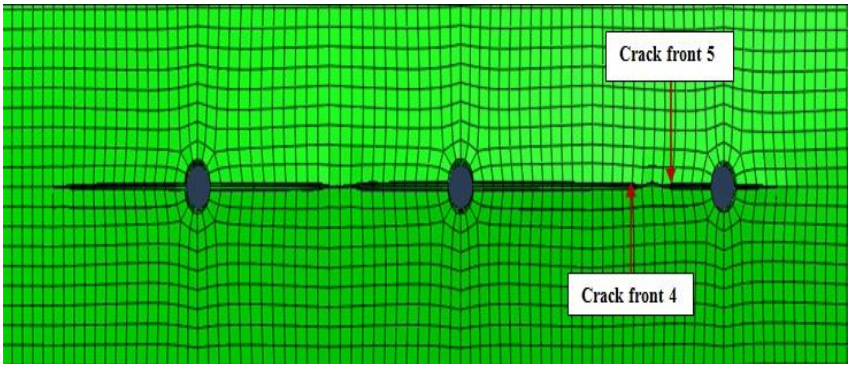

Figure 5-28 XFEM model of MSD at step 37, D=3.2 m

5.1.1.6 SIF evaluation of crack 6 at different fuselage diameters

Figure 5.29 shows that the longest crack 6 length was recorded when D equal to 2.4 m (2.9628 mm, KI = 1457.55 MPa $\sqrt{mm}$) followed by when D equal 3.2 m (CL=2.3378 mm , KI = 2542.81 MPa $\sqrt{mm}$), D equal to 4 m (CL = 0.7601 mm ,KI = 480.2524 MPa $\sqrt{mm}$) and when D equal to 1.6 m (C.L=0.7047 mm, KI = 200.2285 MPa $\sqrt{mm}$. Also, it is worth to mention that crack 6 at D equal to 1.6 m has stopped to propagate after the third step of the simulation as shown in table 24 in appendix (C) section (1-C-6), and at step 29 when D equal to 4 m.

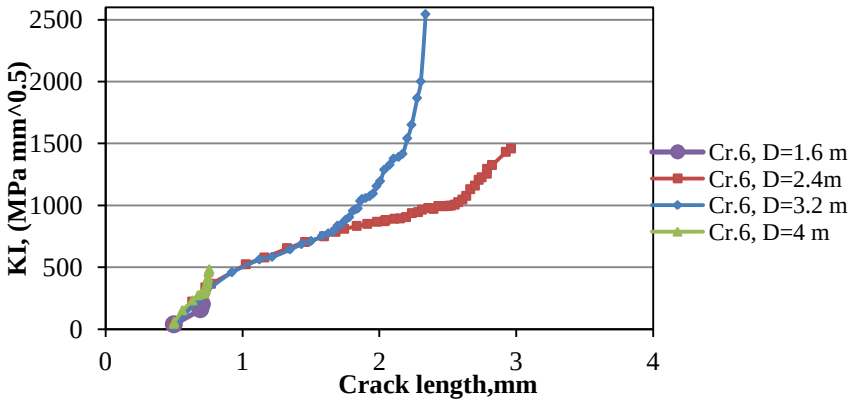

Figure 5-29 SIF histories of crack 6

Figures 5.8, 5.13, 5.27 and 5.30 explain the failure mechanism of crack 6 at different fuselage diameters, it showed that the fastest crack growing rate were recorded to crack 1 and 2 when D equal to 2.4 m due to the stress concentration was located in the position of rivet hole 1 (which crack 1 and were emanating from). Crack 1 reached its final length (17.1846 mm) at step 41 and cracks 2 and 3 were linked up at step 37 and they reached their final length 17.81802 mm and 1.72654 mm respectively, this mechanism caused the shortage lengths of the cracks 6 and 5.

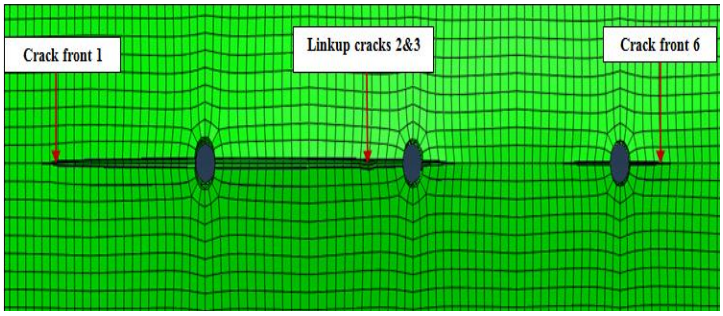

Figure 5-30 XFEM model of MSD at step 41, D=2.4 m

5-2 SECOND NUMERICAL EXAMPLE

In this simulation, the same panel material, dimentions and boundary conditions which mention in section 5.1 are used, except the number of the rivet holes in this case are increased to 5 holes. Figure 5.31 shows the cracks positioning and numbering. Also, a uniform pressure was applied at the internal face of the model Fig. 5.32.

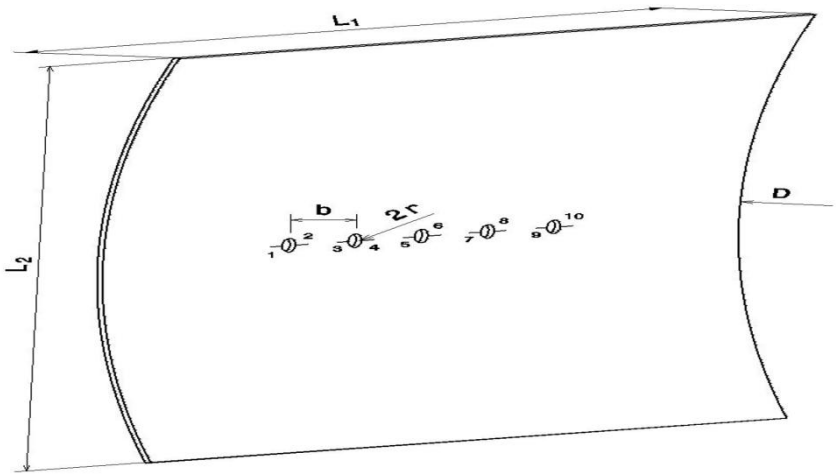

Figure 5-31 Analyzed configuration with multiple cracks (not to scale)

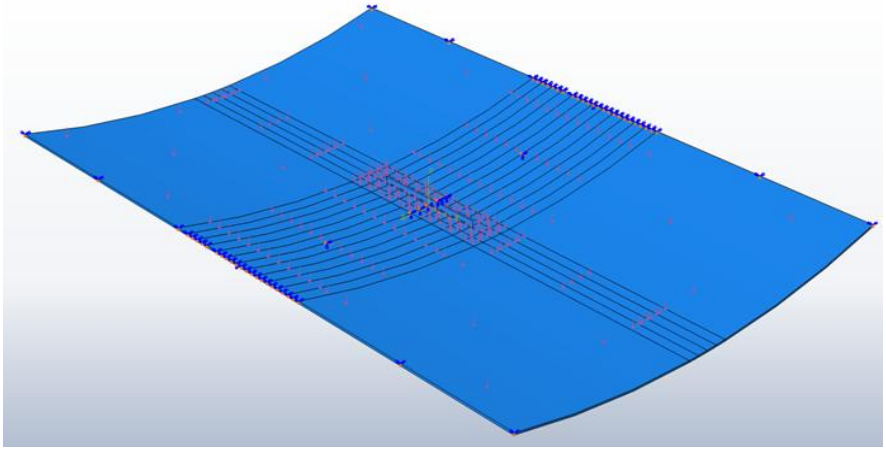

Figure 5-32 Panel with pressure load and boundary conditions

Each hole in the panel had two radial cracks, numbered from 1 to 10 in Fig.5.31 and positioned as shown in Fig. (5.33). Figure 5.33 also shows a portion of the mesh around the

holes, and as it can be seen mesh was refined around the cracks at the edges of each hole and a uniform template of elements around each crack front was used. The characteristics of the final mesh are summarized in table 5-2.

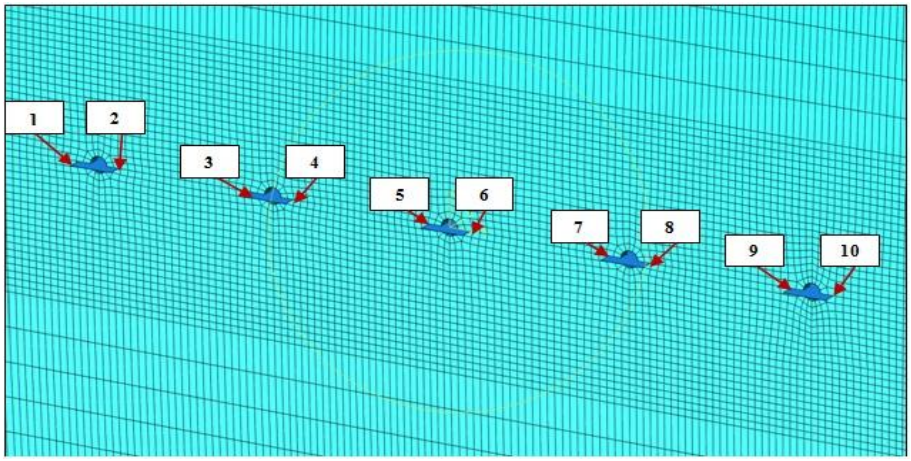

Figure 5-33 Cracks positions and numbering

Table 5-2 Characteristics of the panel final mesh

D (m)	No. of steps (max.)	No. of nodes	No. of elements	Type of element
1.6	54	136360	107536	C3D8R
2.4	147	135230	106640	C3D8R
3.2	20	136360	107536	C3D8R
4	59	136340	107520	C3D8R

5.2.1 SIF evaluation of crack 1 at different fuselage diameters

SIFs were calculated for each crack front and different crack sizes and maximum values of SIFs calculated along the crack fronts were used as a reference. Also, in this section SIF of the cracks from 1 to 10 will be evaluated individually to investigate the effect of changing fuselage diameter from 1.6 m to 4 m. The SIF results were described in figures 5.34 to 5.35. Figures 5.34 and 5.35 shows the relationship between crack lengths and stress intensity factor histories, it can be seen that the longest crack 1 length recorded when fuselage diameter (D) equal to 2.4 m (CL =42.6233 mm,KI = 14184.5 MPa$\sqrt{\text{mm}}$) followed by when D equal to 1.6 m (CL=6.7426 mm,KI = 5740.28 MPa$\sqrt{\text{mm}}$), then when D equal to 3.2 m (CL=5.6411 mm,KI = 4366.58 MPa$\sqrt{\text{mm}}$) and lastly when D equal to 4

m (CL=5.6118 mm,KI = 4873.37 MPa$\sqrt{mm}$). It is worth to mention that crack 1 when D equal to 2.4 separated due to its long length and the high values of SIFs. Also, the figures show the SIFs histories rises as the crack extends, in some cases unstable crack growth occurs at the end of the simulation (D=2.4 and 4 m).

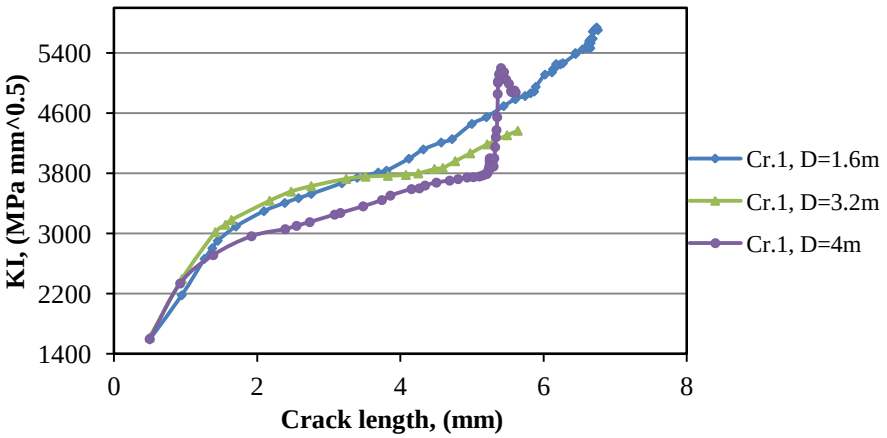

Figure 5-34 SIF histories of crack 1

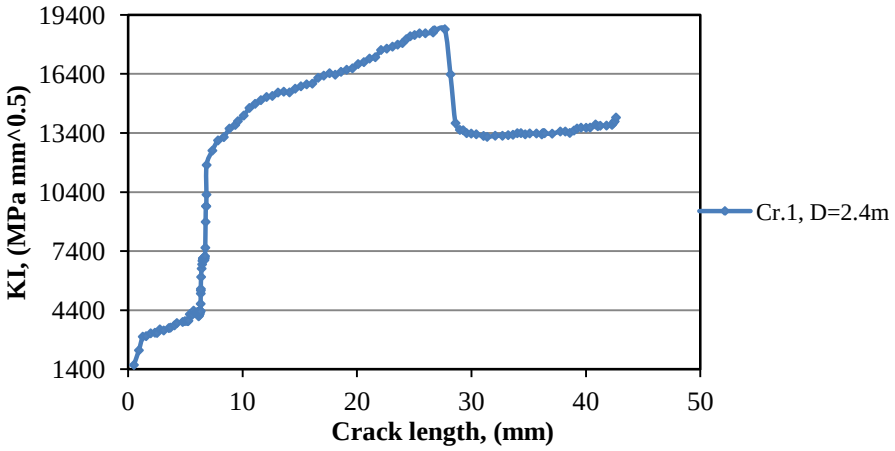

Figure 5-35 SIF histories of crack 1, D=2.4m

Tables 28, 29, 30 and 31 in appendix (C) section (2-C-1) represent some selected results:

Table 28 shows some selected simulation results of crack 1 when D equal to 1.6 m, its explains that the principle effect of the failure mode is still mode I (opening mode), but K_{II} (shearing mode) shared the effect of the failure of the panel because it had a values

especially at steps from 20 till 35, meanwhile K_{III} had a limited effect due to minus signs in the most simulation results.

Due to the lager amount of obtained simulation results when D equal to 2.4 m (147 steps), some selected results are shown in table 29 in appendix (C) section (2-C-1); the results showed mode I still the principle of the failure mode with the existence effect of K_{II} and K_{III}. Crack 1 results which described in tables 30 and 31 (D=3.2m and D=4m respectively) showed the same attitude of the previous results, meaning KI still the major parameter which effects to the failure of the panel with the effective presence of K_{II} and K_{III}.

For a more extensively description of the results, the following are some selection of simulation images when D equal to 2.4 m represented in figures from 5.36 to 5-43:

Figure 5-36 show the first step loading and the stress distribution around the rivet holes. The rose of the stress (Von Mises) was due to the effect of K_{II} and K_{III}.

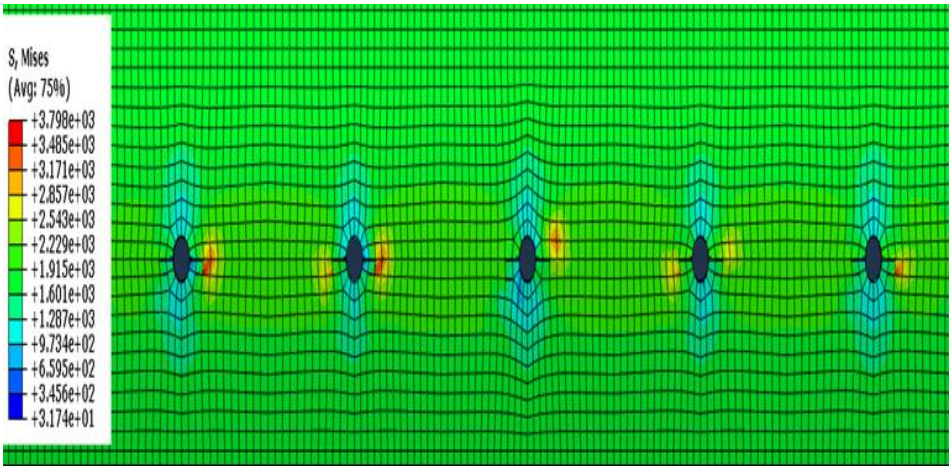

Figure 5-36 XFEM model of MSD after cracks opening (first step), D=2.4 m

Also, figure 5-37 show the step twenty, it illustrates that the middle hole (hole number 3) which cracks 5 and 6 were emanating had the longest crack lengths due to the stress were concentrated at this location. Furthermore, crack 1 reached 5.5973 mm at this step.

Crack 1 was growing in normal way till step 20 but, from step 20 till step 62 the crack 1 was growing at a very low rate and it reaches (6.8422 mm) after 42 steps of the simulation. This occurred due to the panel was weakened at the location of cracks 6 and 7 as it can be seen in figure 5-38 which describes the first linkup between cracks 6 and 7.

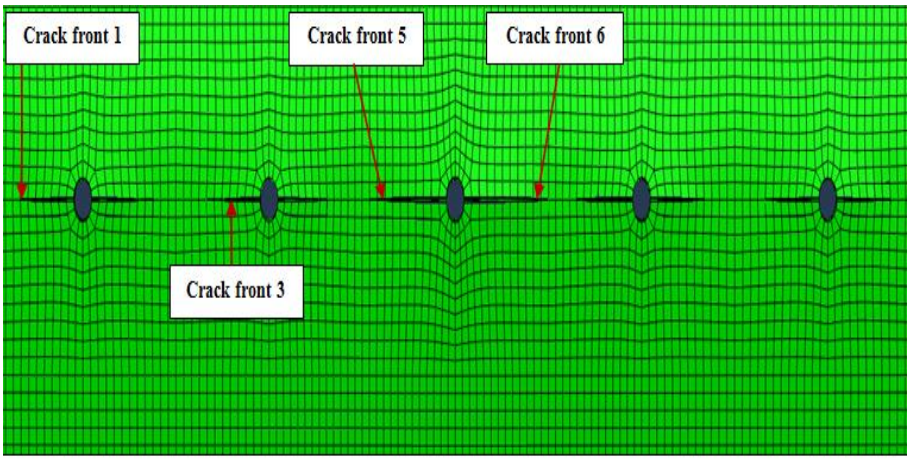

Figure 5-37 XFEM model of MSD after cracks opening (step 20), D=2.4 m

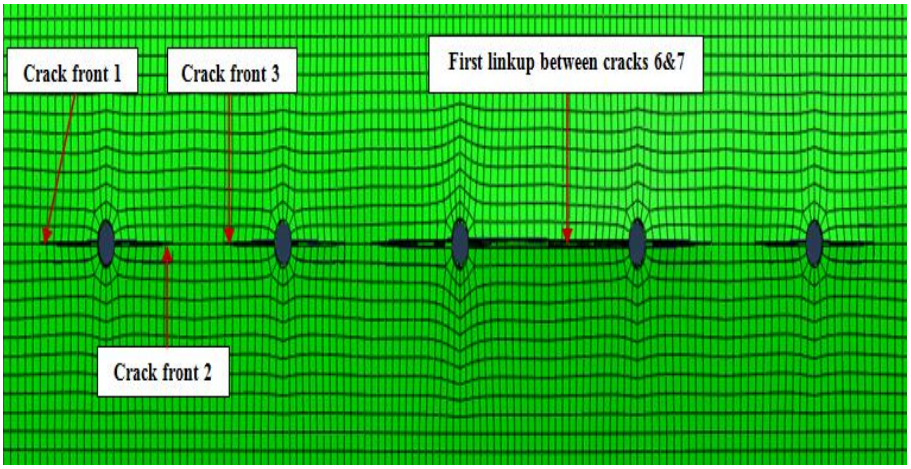

Figure 5-38 XFEM model of MSD after cracks opening (step 26), D=2.4 m

Figures 5-39, 5-40 and 4-41 show the second and the third linking up between cracks 4, 5, 8 and 9 which produce a one lead crack.

Figures 5-42 and 5-43 show the later crack extension stages after the final linkup between cracks from 2 till 9, crack 1 and 10 started to grow in a faster manner after that and it reaches 35.7693 mm just after 84 steps (after step 62). At the end of the simulation, crack 1 reached 42.6233 mm and crack 10 reached 29.0878 mm at step 146.

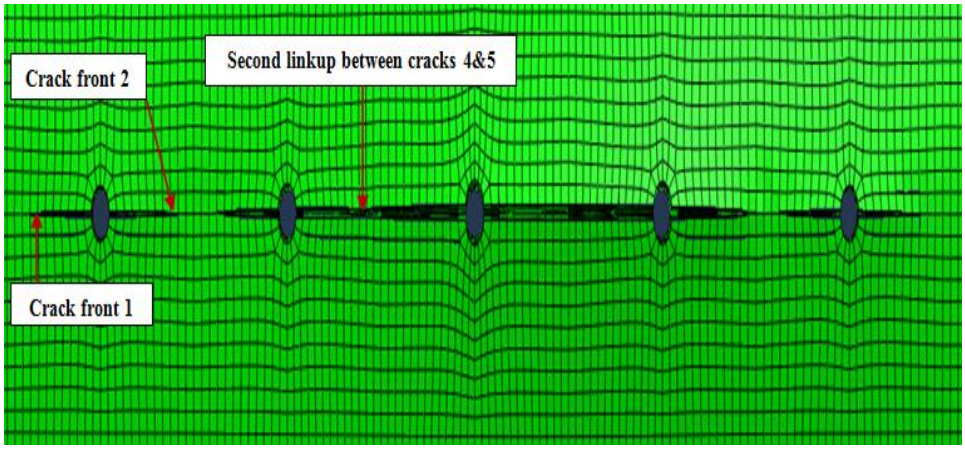

Figure 5-39 XFEM model of MSD after cracks opening (step 38), D=2.4 m

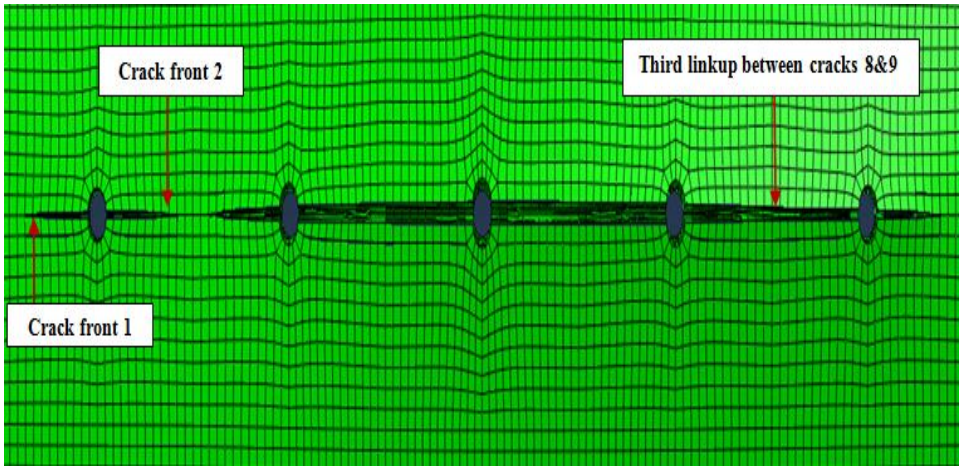

Figure 5-40 XFEM model of MSD after cracks opening (step 46), D=2.4 m

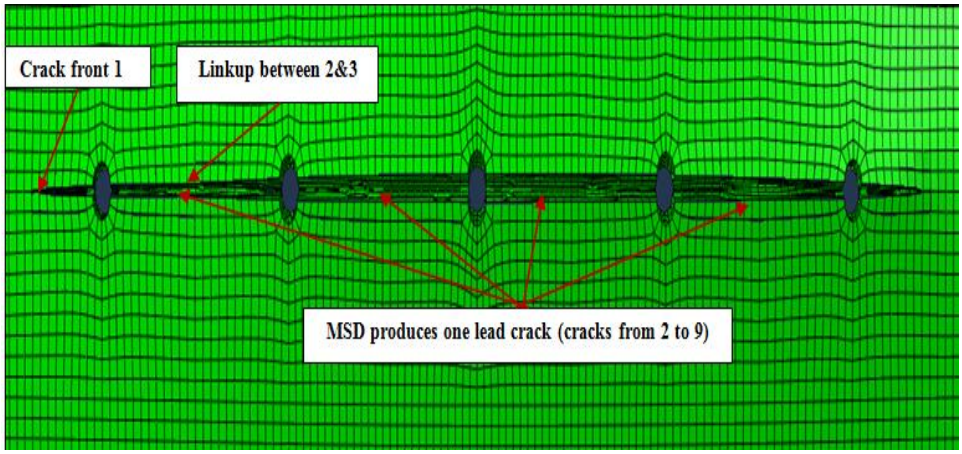

Figure 5-41 XFEM model of MSD after cracks opening (step 58), D=2.4 m

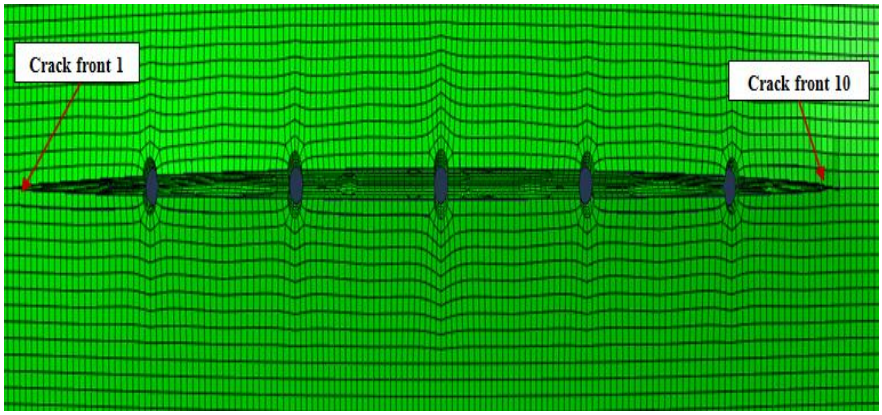

Figure 5-42 XFEM model of MSD after cracks opening (step 90), D=2.4 m

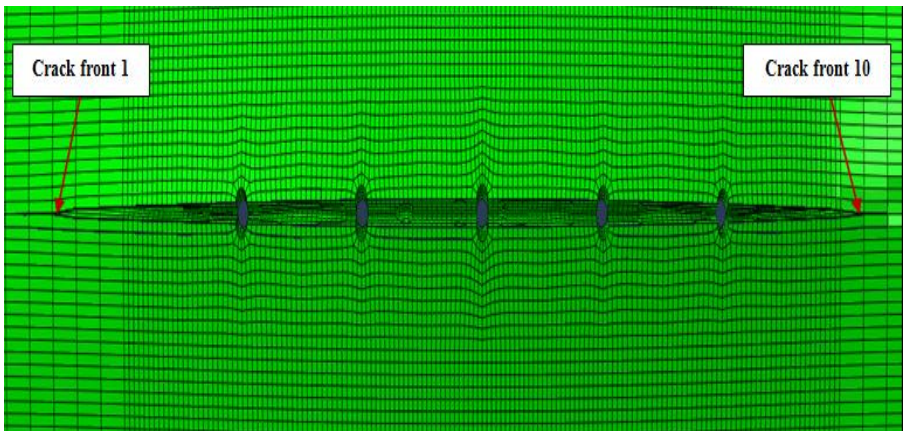

Figure 5-43 XFEM model of MSD after cracks opening (step 146), D=2.4 m

5.2.2 SIF evaluation of crack 2 at different fuselage diameters

Figures 5-44 and 5-45 explain the study of effect changing fuselage diameter D from 1.6 m to 4 m on crack 2 SIFs histories; they show that the longest crack 2 length was recorded when D equal to 2.4 m (CL =8.1199 mm,KI = 27667.8 MPa$\sqrt{\text{mm}}$), followed by when D equal to 1.6 m (CL= 7.2165 mm,KI = 10191.8 MPa$\sqrt{\text{mm}}$), then when D equal to 3.2 m (CL= 6.0305 mm,KI = 5157.15 MPa$\sqrt{\text{mm}}$) and lastly when D equal to 4 m (CL =2.3956 mm,KI = 8823.78 MPa$\sqrt{\text{mm}}$).

In addition, the figures showed there were unstable crack growth in three cases at the end of the simulation steps (D= 1.6, 2.4 and 4 m), SIF histories of crack 2 when D equal to 2.4 m was separated due to its higher values of SIFs. Also, tables 32, 33, 34 and 35 in appendix (C) section (2-C-2) show some selected simulation results, they showed that the K_I was the principle of the failure mode (mode I) with the existence effect of K_{II} and K_{III} with a limited effect on the failure mechanism. It is worth to mention that table 35 showed the results of

crack 2 when D equal to 4 m, crack 2 was not growing for twenty steps (from step 3 till step 23) due to K_I, K_{II} and K_{III} had minus signs and those steps were canceled from the figure 5-44.

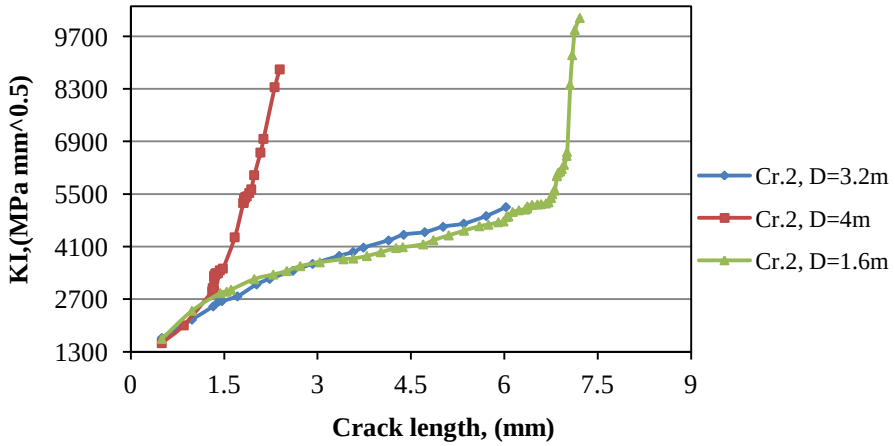

Figure 5-44 SIF histories of crack 2

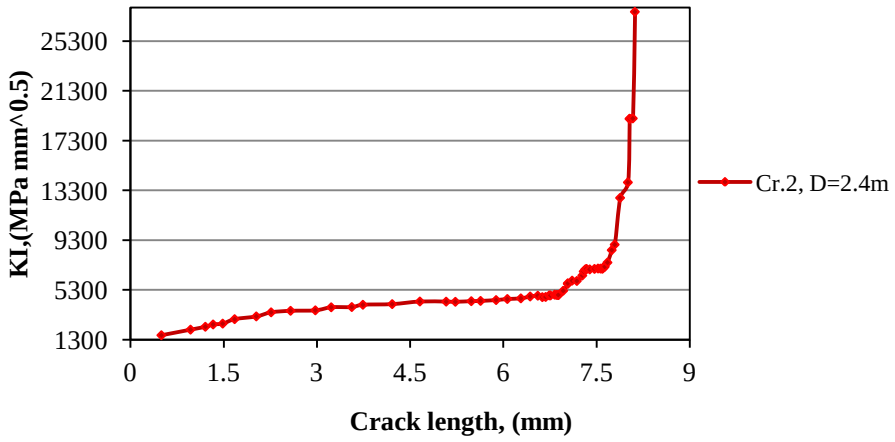

Figure 5-45 SIF histories of crack 2, D=2.4m

The above mentioned figures in section (5.2.1) also illustrates the growing steps of crack 2, where figure 5-39 (step 38) shows that crack 2 reached (7.1865 mm) and crack 3 which supposed to interact with crack 2 reached the length of (6.3759 mm), at step 46 as shown in figure 5-40 crack 2 reached (7.5271 mm) and crack 3 length was equal to (7.7021 mm) after the linking up process between cracks 4 and 5 and between cracks 8 and 9, meaning crack 3 had faster crack growing than crack 2 after linking up process. Also, figure 5-46 shows the step before linkup process between cracks 2 and 3, at this step crack 2 length was

equal to 8.0081 mm and crack 3 was equal to (10.8978 mm). Figure 5-41 shows the linking up process between crack 2 and 3.

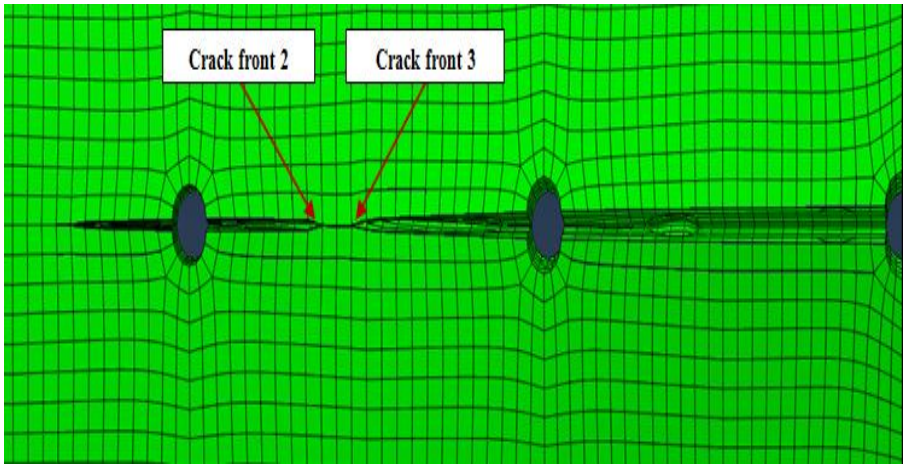

Figure 5-46 XFEM model of MSD after cracks opening (step 57), D=2.4 m

5.2.3 SIF evaluation of crack 3 at different fuselage diameters

At the end of the simulation, crack 3 obtained results showed the longest reached length was when D equal to 2.4m (CL =12.557 mm, KI= 21349 MPa$\sqrt{mm}$), followed by when D equal to 4 m (CL = 10.6367mm, K_I=12918.2 MPa$\sqrt{mm}$) then when D equal to 1.6 m (CL = 8.7315 mm, K_I=16156.7 MPa$\sqrt{mm}$) and lastly when D equal to 3.2 m (CL =5.2919 mm, K_I = 4897.17 MPa$\sqrt{mm}$). Figure 5-47 shows SIF histories of Crack 3 versus crack extension, it can be seen in this figure that the crack 3 had stable crack growth until specific simulation step and then unstable crack growth occurred (crack growth is low compared to K_I values) and stable growing occurred once again (D= 1.6, 2.4 and 4 m).

Additionally, tables 36, 37, 38 and 39 in appendix (C) section (2-C-3) show some selected simulation steps, it can be realized that K_I was still the main dominant of the failure mode (mode I, opening mode) with the existence influence of K_{II} and K_{III}. K_{II} and K_{III} shared the failure mechanism because they had effective values especially when D equal to 2.4 m.

Return back to the selected figures from 5-37 till 5-41, they show the cracks propagation stages also to crack 3. In figure 5-37 crack 3 reached (4.7219 mm) (step 20) and crack 2 reached lengths of 5.8821 mm until this step crack 2 had faster crack growing rate. Also, figure 5-38 shows the simulation step 26 of crack growing, at this step the recorded crack 3

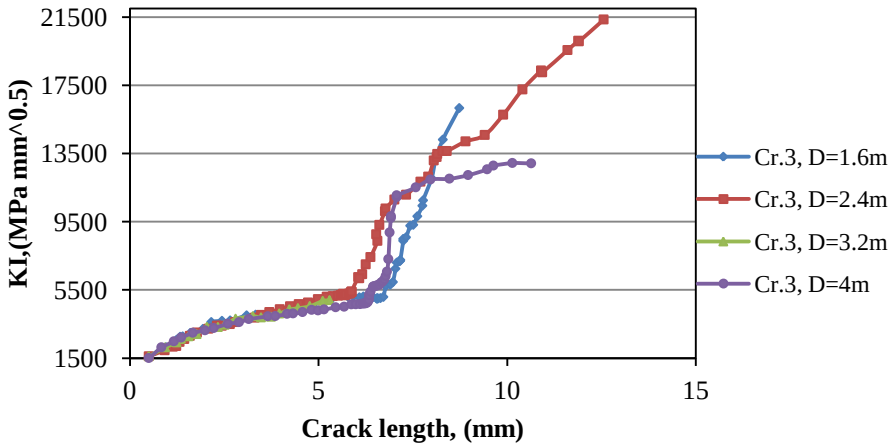

Figure 5-47 SIF histories of crack 3

length was equal to 5.6448 mm and crack 2 lengths was equal to(6.6846 mm). At this step, the first linking up occurred between cracks 6 and 7 which mean this position was the weakest point at this panel.

Figure 5-39 illustrates step 38, it showed that the second linking up had occurred between cracks 4 and 5, at this stage of cracks propagation, crack 3 reaches (6.3759 mm) and crack 2 (7.1865 mm). The third linkup occurred at step 46 between cracks 8 and 9, at this step crack 3 recorded length was equal to (7.7021 mm) and crack 2 was equal to (7.5271 mm); referring to obtained crack length of 2 and 3 till this stage, it is clear that crack 3 had a faster crack growing (the length difference 6.1759mm for crack 3 and equal to 2.126 mm for crack 2). Additionally, figure 5-41 shows cracks 2 and 3 before the linking up process (step 57), at this step, crack 3 recorded lengths was equal to (10.8978 mm) and crack 2 was equal to (8.0081 mm). The linking up process between cracks 2 and 3 occurred at step 58 as illustrated in figure 5-46.

5.2.4 SIF evaluation of crack 4 at different fuselage diameters

Figure 5-48 shows the SIF histories of crack 4 as a function of the fuselage diameter, it showed that crack 4 when D equal to 4 m had a steep rise in SIFs compared to its extension (CL =4.1988 mm,KI $= 16982.5$ MPa$\sqrt{\text{mm}}$), while crack 4 when D equal to 1.6 and 2.4 m had unstable crack growth at the last steps of the simulation (CL = 7.9364 mm,KI $=$ 13713.2 MPa$\sqrt{\text{mm}}$, and CL = 8.1057 mm, KI $= 16528.3$ MPa$\sqrt{\text{mm}}$ respectively). Crack 4

reached 4.9804 mm when D equal to 3.2 m at the end of the simulation. So, the longest crack 4 length was recorded when D equal to 2.4 m. In addition, tables 40, 41, 42 and 43 in appendix (C), section (2-C-4) show some selected simulation results, they appear that K_I still the dominant of the failure mechanism with existence effect of K_{II} and K_{III} at some steps. It is worth to mention that crack 4 when D equal to 4 m was not growing from step 2 till step 19 due to the values of K_I, K_{II} and K_{III} had a negative value which means the crack is not growing.

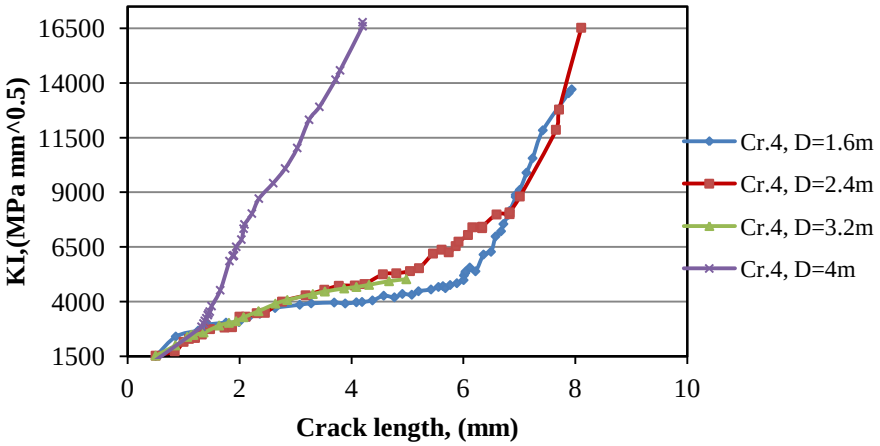

Figure 5-48 SIF histories of crack 4

The figures below illustrate some selected simulation steps of the tested panel when D equal to 2.4 m and 1.6 m, where the figure 5-49 shows the step 5 of the simulation, at this stage the recorded length of crack 4 was equal to 1.204 mm while crack 5 length was equal to 2.41939 mm. At step 25 as shown in figure 5-50, crack 4 lengths was equal to 5.6108 mm and crack 5 length was equal to 8.9253 mm. This figure also shows that the longest crack lengths were recorded to crack 5 (8.9253 mm) and crack 6 (11.5281 mm) which means at this location the stress was concentrated.

Furthermore, figure 5-51 shows the first linkup occurred between cracks 6 and 7 and the recorded length for crack 4 at this stage was equal to (7.0089 mm) and (11.3163 mm) for crack 5. The coalesced cracks 6 and 7 had a new crack tips, meaning crack tip 5 became a crack tip for coalesced cracks 5, 6, 7 and 8.

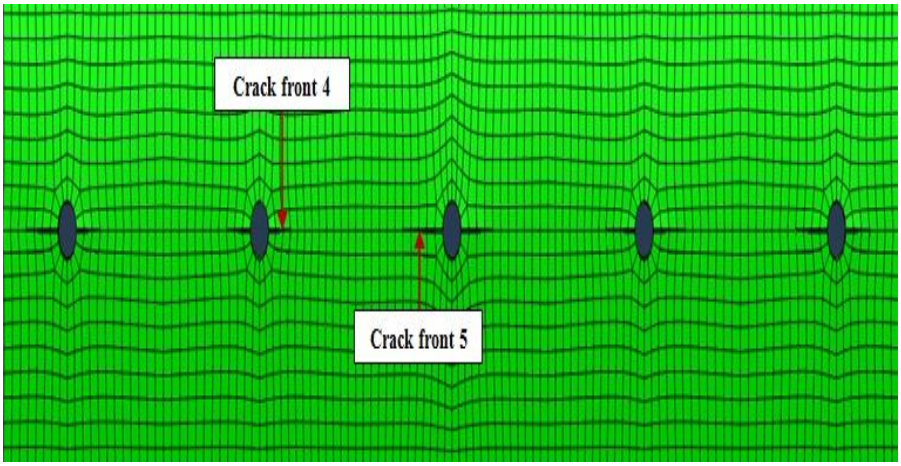

Figure 5-49 XFEM model of MSD after cracks opening (step 5), D=2.4 m

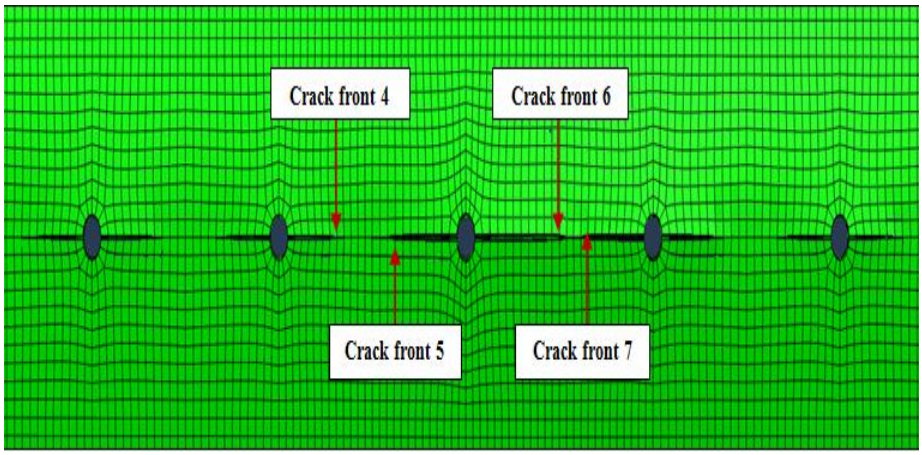

Figure 5-50 XFEM model of MSD after cracks opening (step 25), D=2.4 m

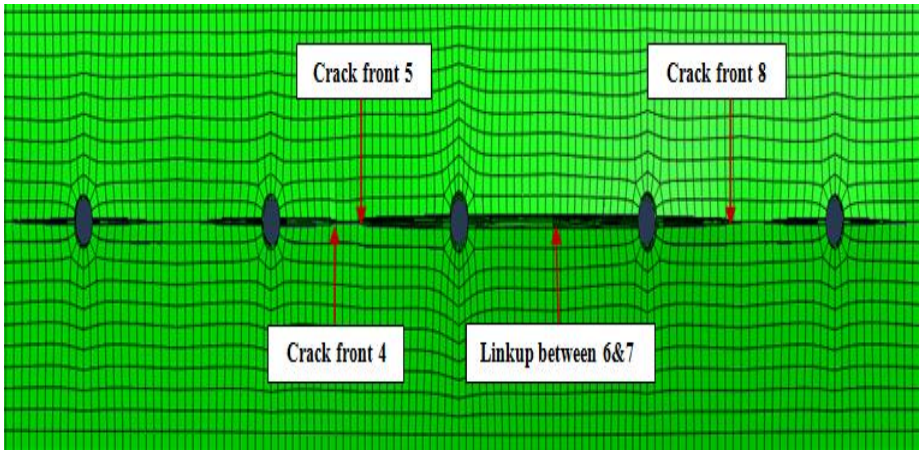

Figure 5-51 XFEM model of MSD after cracks opening (step 37), D=2.4 m

Also, figure 5-52 explains the second linkup which occurred between cracks 4 and 5. At this stage crack front 3 and crack front 8 became the crack fronts of coalesced lead crack.

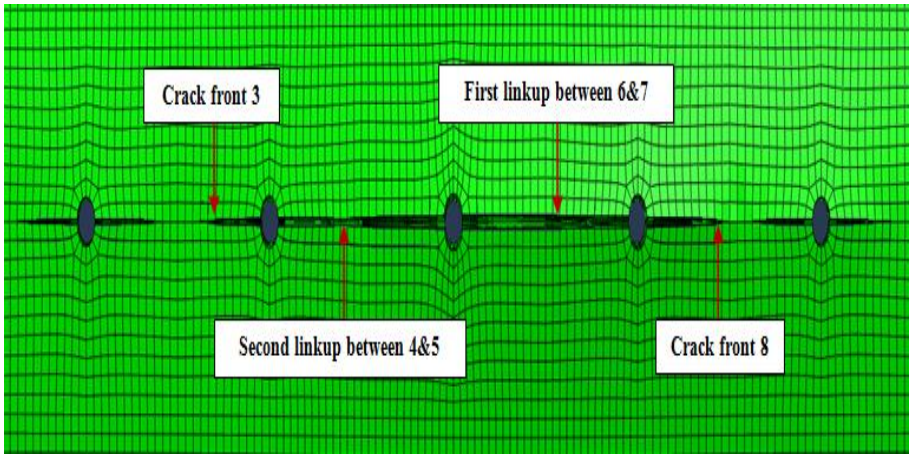

Figure 5-52 XFEM model of MSD after cracks opening (step 38), D=2.4 m

Figures from 5-53 till 5-56 illustrate the simulation steps for the tested panel when D equal to 1.6 m, where figure 5-53 shows the simulation step 24, at this stage crack 4 length was equal to (5.5548 mm) and crack 5 length was equal to (5.71159 mm). Also in this stage the first linkup occurred between cracks 8 and 9.

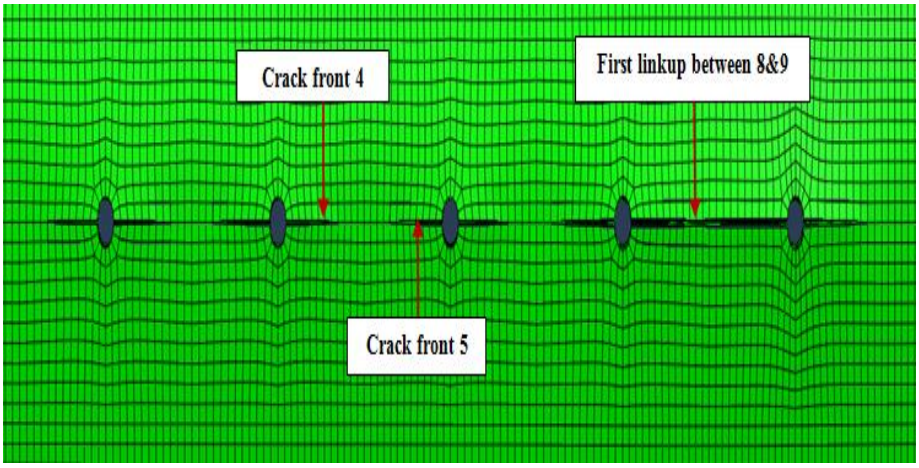

Figure 5-53 XFEM model of MSD after cracks opening (step 24), D=1.6 m

Figure 5-54 shows the step 37, at this step the second linkup occurred between cracks 6 and 7 and crack 4 lengths was equal to (6.5754 mm) and crack 5 length was equal to (7.945 mm). At step 49 of the simulation, (see figure 5-55), crack 4 length was equal to (7.8812 mm) and crack 5 was equal to (11.7391 mm); a further step (step 50) the third linkup

occurred between crack 4 and 5 as illustrates in figure 5-56. Also, the figure shows the formed lead crack which consisted from crack 3 till 10. In addition to the previous explanation, the crack fronts 3 and 10 became the crack fronts of the formed lead crack.

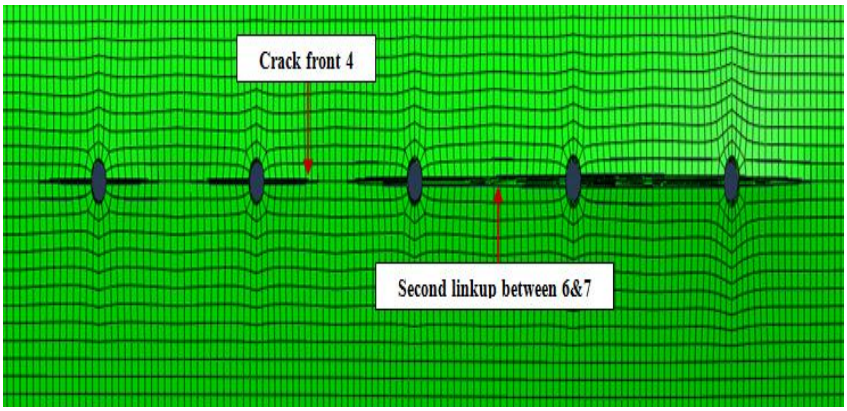

Figure 5-54 22XFEM model of MSD after cracks opening (step 37), D=1.6 m

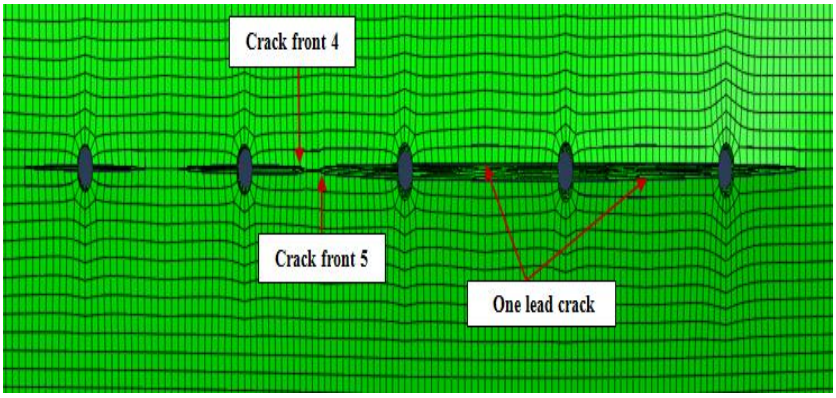

Figure 5-55 XFEM model of MSD after cracks opening (step 49), D=1.6 m

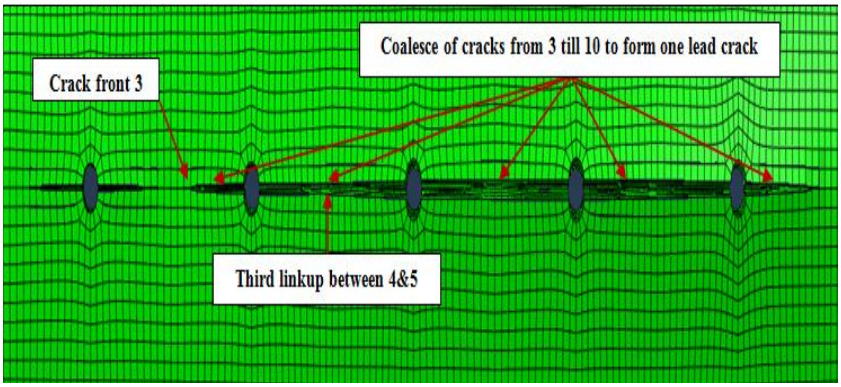

Figure 5-56 XFEM model of MSD after cracks opening (step 50), D=1.6 m

5.2.5 SIF evaluation of crack 5 at different fuselage diameters

Figure 5-57 illustrates the relationship between crack 5 lengths versus SIFs at different fuselage diameters; it showed that as the crack grows as SIF increases. In the most cases unstable crack growth occurred especially at the last steps of the simulation, for example, unstable growing occurred when D equal 4 after step 24 of the simulation. Also, it can be observed the longest crack 5 lengths recorded when D equal to 4 m (15.7302 mm, K_I = 16920.6 MPa $\sqrt{mm}$), followed by when D equal to 2.4 m (12.4537 mm, K_I = 17499.6 MPa$\sqrt{mm}$), and then when D equal to 1.6 m (11.781 mm, K_I = 13809.7 MPa $\sqrt{mm}$) and lastly when D equal to 3.2 m (5.82082 mm, K_I = 4337.31 MPa $\sqrt{mm}$).

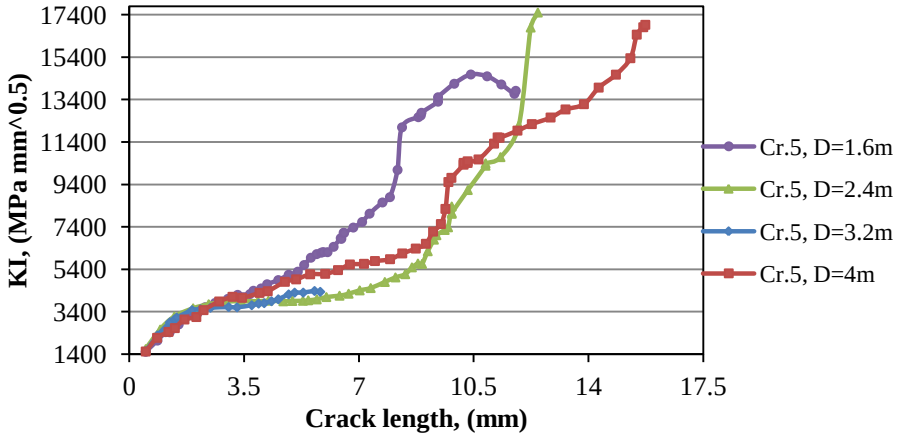

Figure 5-57 SIF histories of crack 5

Tables 44, 45, 46 and 47 in appendix (C) section (2-C-5) show some selected results at different diameters, it showed that K_I is the dominant to the failure mechanism with existence effect of K_{II} and K_{III} especially in the case of D equal to 1.6 m, the most values were a positive, but K_{II} and K_{III} were negative when D equal to 2.4 m.

The following figures describe the simulation of multiple cracks propagation:

Figure 5-58 shows the first step loading, it showed the stress distribution around the rivet holes; while figure 5-59 shows the tenth step of cracks propagation, at this step crack 5 recorded length was equal to (3.43663 mm) and crack 4 length was equal to (0.5 mm).

At step 20 of the simulation, crack 5 length reached (7.48748 mm) and crack 4 was not growing till this step. The other cracks such as 6 and 7 had fast crack growing rate, the

recorded lengths were (7.858 mm) and (6.7436 mm) respectively, see figure 5-60.

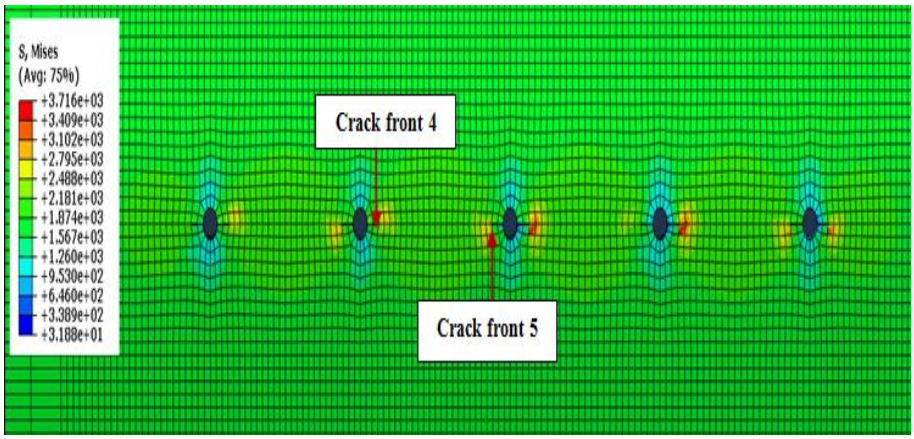

Figure 5-58 XFEM model of MSD after cracks opening (first step), D=4 m

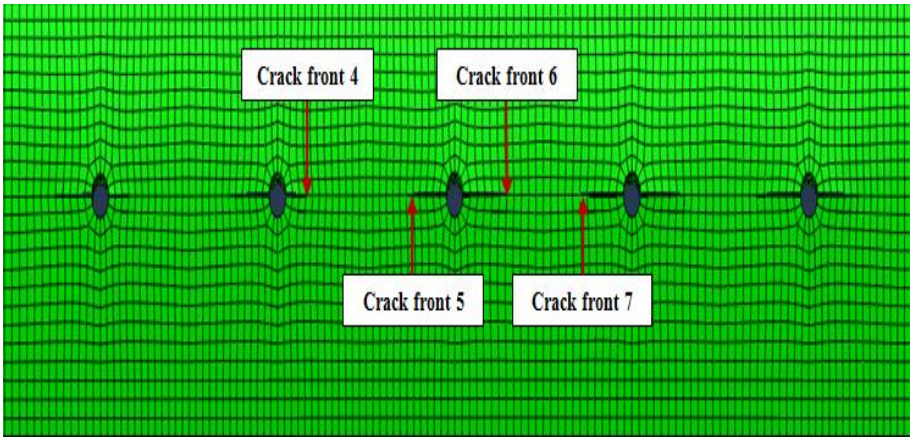

Figure 5-59 XFEM model of MSD after cracks opening (step 10), D=4 m

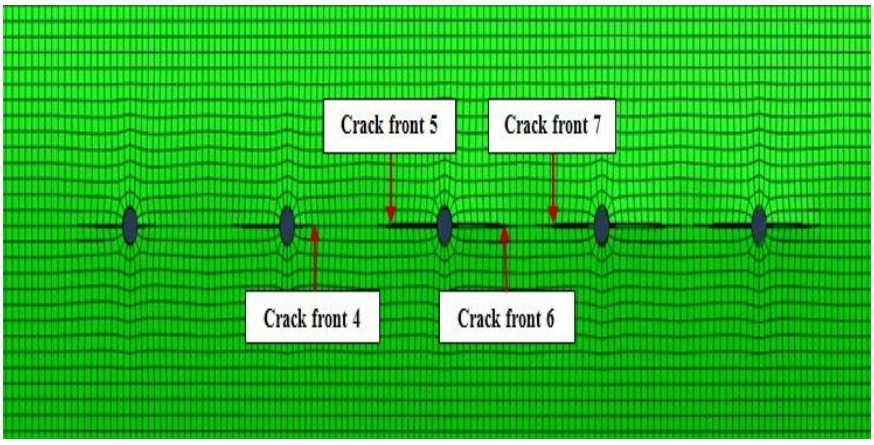

Figure 5-60 XFEM model of MSD after cracks opening (step 20), D=4 m

Figure 5-61 illustrates the simulation step 24, at this step crack 5 recorded lengths was equal to (9.0403 mm) and crack 4 length was equal to (1.4321 mm), crack 5 had a faster crack growing than 4 due to the tested panel weakened at the location of the holes 3, 4 and 5; the recorded lengths of crack 6, 7, and 8 were equal to (9.6504, 8.209 and 10.5682 mm) respectively.

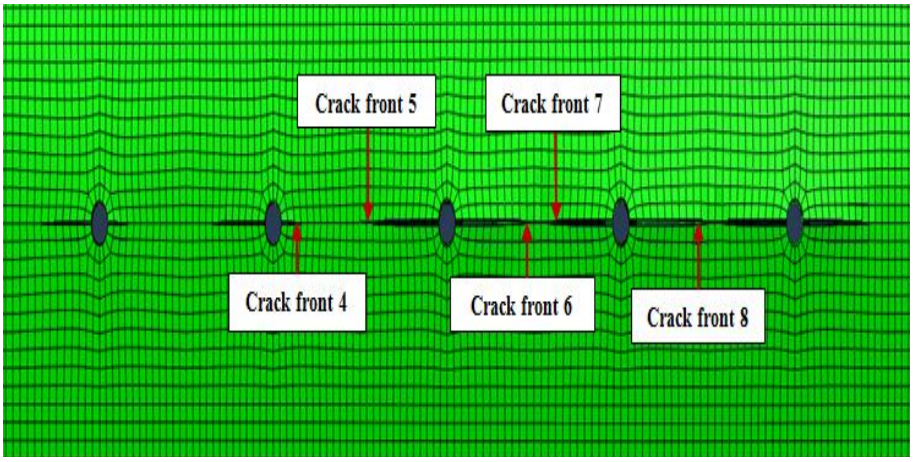

Figure 5-61 XFEM model of MSD after cracks opening (step 24), D=4 m

Figure 5-62 describes the first linkup which occurred between cracks 8 and 9 at step 25, the recorded crack lengths of cracks 4, 5, 6 and 7 at this step were equal to (1.4454 mm, 9.2607 mm, 9.8816 mm and 8.5039 mm) respectively.

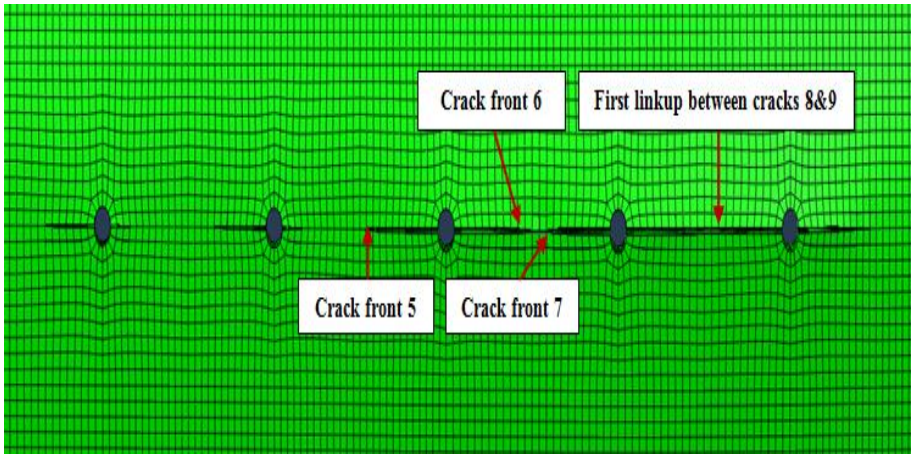

Figure 5-62 XFEM model of MSD after cracks opening (step 25), D=4 m

The second linkup in this simulation occurred at step 27 as illustrated in figure 5-63, at this step crack 5 reached (9.6368 mm) while crack 4 length was equal to (1.4994 mm). crack 5

had a faster crack growing due to the lead crack was created on the right-hand side which consists from cracks 6, 7, 8, and 9 with crack fronts of crack tip 10 and 5.

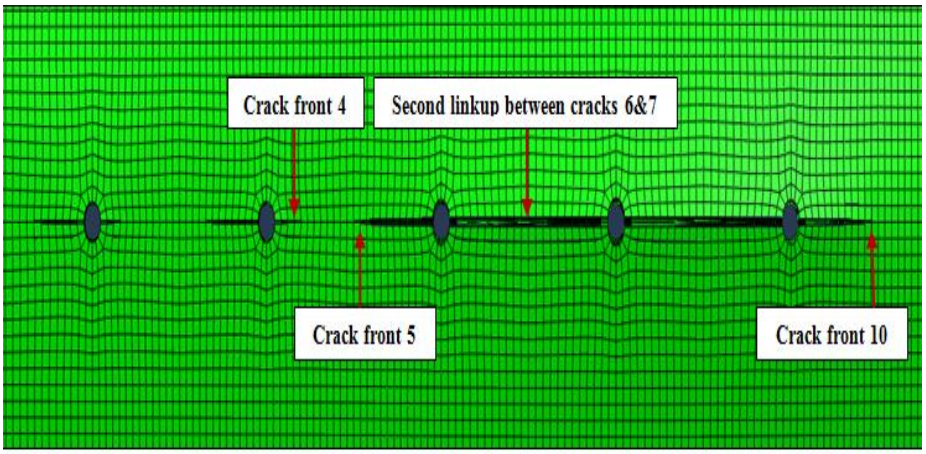

Figure 5-63 XFEM model of MSD after cracks opening (step 27), D=4 m

As mention before, the new lead crack had fronts of crack 10 and 5, as shown in figure 5-64 which describe the simulation step 45; at this step crack 5 recorded length was (15.274 mm) and crack 4 length was (3.716 mm).

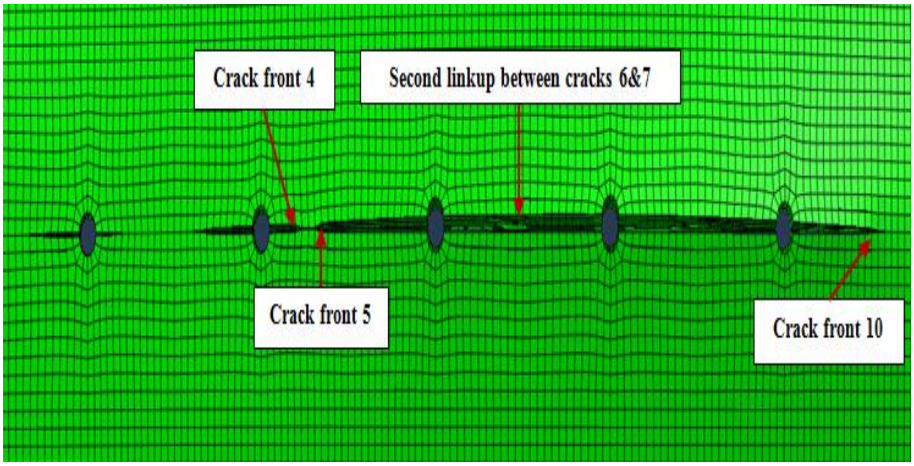

Figure 5-64 XFEM model of MSD after cracks opening (step 45), D=4 m

The third linkup occurred at step 46 between cracks 4 and 5 as shown in figure 5-65; the coalesced cracks produced one crack which had new crack fronts 3 and 10. Also, figure 5-65 shows the shape of the final accumulative crack with its fronts.

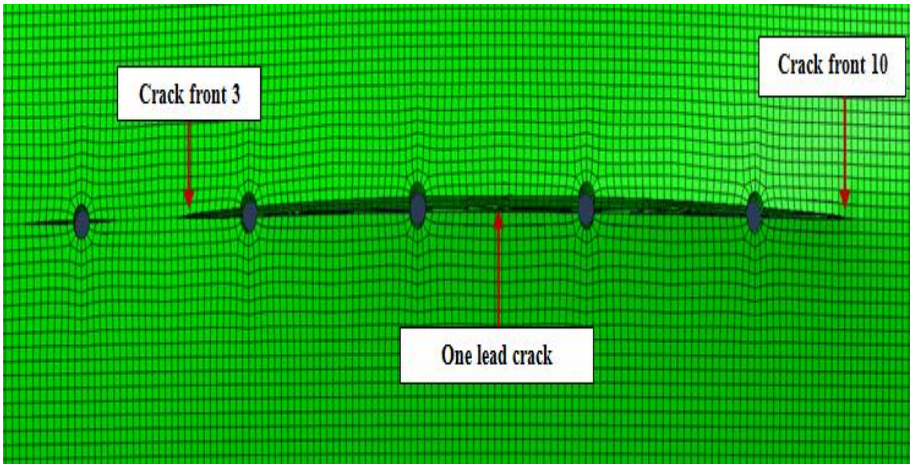

Figure 5-65 XFEM model of MSD after cracks opening (step 50), D=4 m

5.2.6 SIF evaluation of crack 6 at different fuselage diameters

The figure 5-66 describes crack 6 growing trend as D changed from 1.6 m to 4 m, it showed that as crack 6 extends as SIF increases and in the most cases a steep rise in SIFs values occurred especially at the last steps of the simulation; this indicates the tested panel has weakened and there is a possibility of linking up process between adjacent cracks. The longest crack 6 length recorded when D equal to 2.4 m (CL =12.0705 mm, K_I=13119.3 MPa $\sqrt{mm}$), followed by when D changed to 4 m (CL =11.1262 mm, K_I=13926.6 MPa $\sqrt{mm}$), and subsequently when D equal to 1.6 m (CL =7.9478 mm, K_I=15129.6 MPa $\sqrt{mm}$). Finally, the lowest crack 6 length recorded when D was equal to 3.2 m (CL = 5.17194 mm, K_I = 5168.06 MPa $\sqrt{mm}$).

Also, the documented results in the case of crack 6 showed that K_I is still the dominant responsible of the failure mechanism due to its higher values compared to the other existence failure mechanism K_{II} and K_{III} which had effective values in most simulation steps, as shown in appendix (C) section (2C-6), tables from 48 to 51.

The following are some selected images from the simulation steps, they show the growing stages of cracks 6 and 7 which are expected their tips interact with each other to form one new crack: Figure 5-67 represents step 5 of cracks 6 and 7 when D equal to 2.4m, at this step the recorded crack 6 length was equal to (1.92188 mm) while crack 7 length was equal to (1.3633mm).

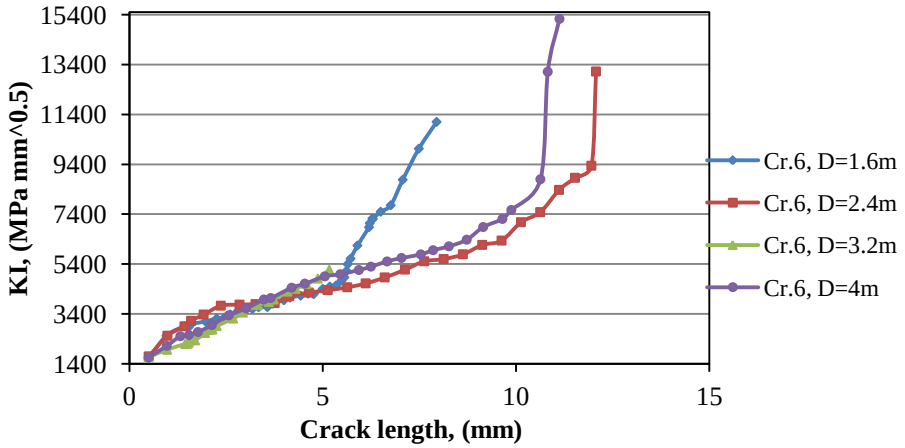

Figure 5-66 SIF histories of crack 6

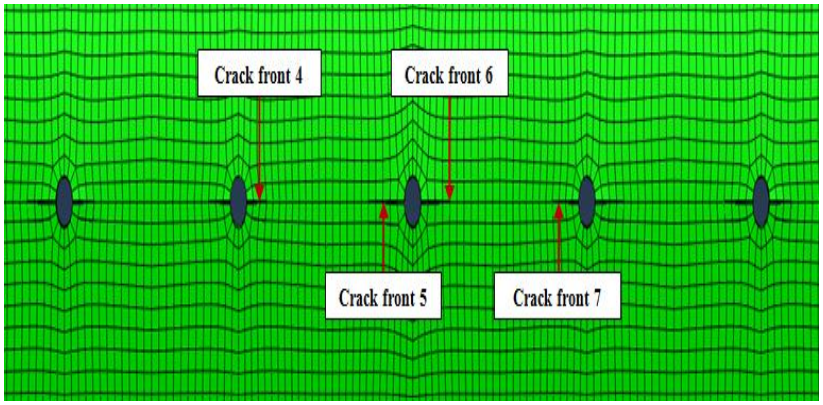

Figure 5-67 XFEM model of MSD after cracks opening (step 5), D=2.4 m

Also, figure 5-68 shows step 15 of the simulation, at this step crack 6 lengths was equal to (6.60566 mm), and crack 7 length was equal to (4.4085 mm).

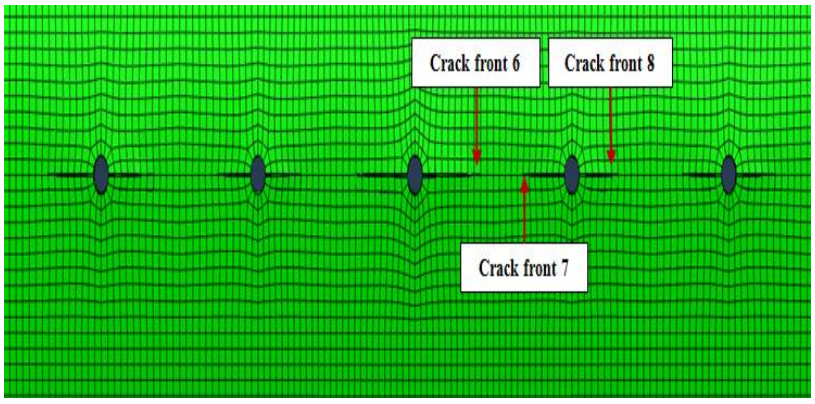

Figure 5-68 XFEM model of MSD after cracks opening (step 15), D=2.4 m

Step 25 was the step before cracks 6 and 7 linked up as illustrated in figure 5-69, at this step crack 6 lengths was (11.5281 mm) and crack 7 length was (7.5089 mm). Crack 6 was longer due to the stress concentration location was at the position of hole number 3.

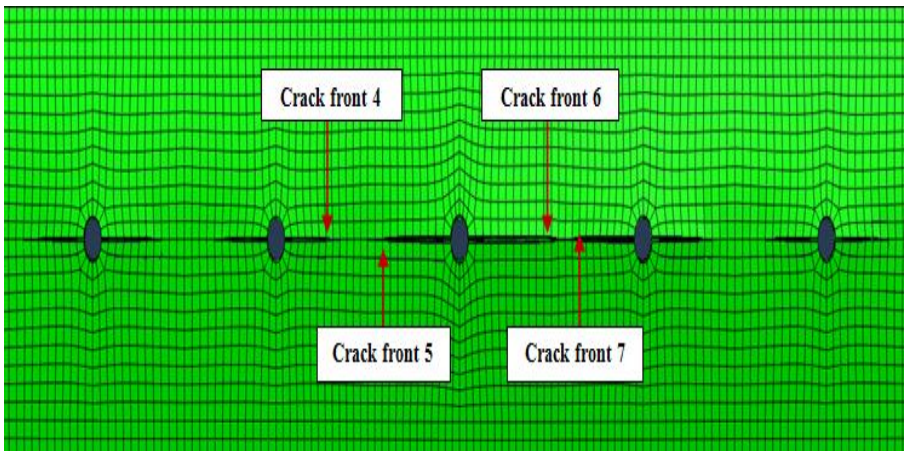

Figure 5-69 XFEM model of MSD after cracks opening (step 25), D=2.4 m

The linking up process occurred between cracks 6 and 7 at step 26, as shown in figure 5-70. They formed a new crack which had a two new crack fronts (crack front 5 and 8).

Returning back to the previous figures, such as figures 5-62, 5-63, 5-64 and 5-65 were representing the crack 6 and 7 propagation steps when D equal to 4 m. Figure 5-62 explains the simulation step of 24, at this step crack 6 recorded lengths was (9.6504 mm) and crack 7 was (8.209 mm). Due to the linking up process between cracks 8 and 9 as shown in figure

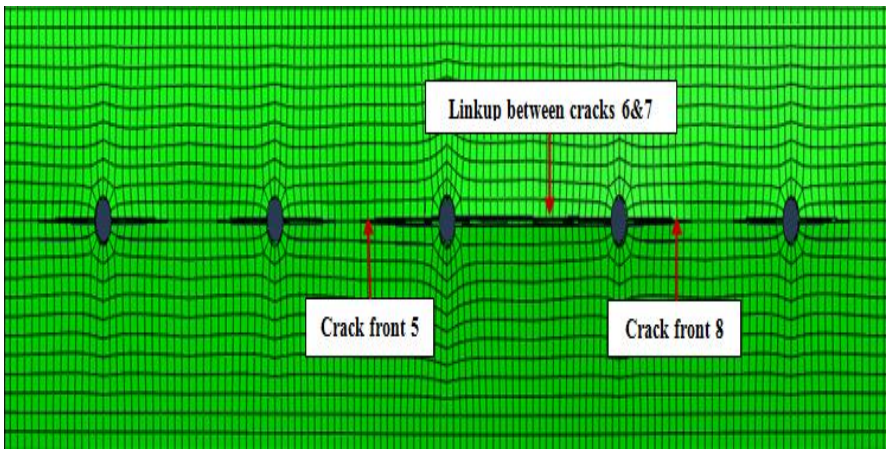

Figure 5-70 XFEM model of MSD after cracks opening (step 26), D=2.4

5-63, the cracks propagation rates should be accelerated due to the weakening of the panel at this location. At this step crack 6 lengths was (9.8816 mm) and crack 7 length was (8.5039 mm). The second linking up process between cracks 6 and 7 occurred at step 27 to form new crack which had a new crack fronts (crack front 5 and 10) as shown in figure 5-64.

5.2.7 SIF evaluation of crack 7 at different fuselage diameters

Figure 5-71 represents the effect of changing the fuselage diameters from1.6 m to 4 m on SIFs and cracks 7 propagation rates. It showed that as the crack grows as SIF rises and unstable crack growth occurred especially at the last simulation steps. The longest crack 7 length recorded when D equal to 1.6 m (CL = 12.1079 mm, K_I=11445.5 MPa $\sqrt{mm}$) while the second longest crack 7 length was when D equal to 4 m (CL =9.0727 mm, K_I=15529.5 MPa $\sqrt{mm}$). Crack 7 length was (8.4115 mm, K_I=13081.7 MPa $\sqrt{mm}$) when D equal to 2.4 m and lastly the shortest crack 7 length recorded when D equal 3.2 m (CL= 6.0192 mm, K_I=4885.62 MPa $\sqrt{mm}$). The tables 52, 53, 54 and 55 in appendix (C) section (2-C-7) show some selected achieved simulation results; it's a clear that K_I was the main dominate of the failure mechanism with the existence effect of K_{II} and K_{III} as shown in the first three tables. The results in table 55 showed that K_I had the principle effect of the failure mechnism due to K_{II} and K_{III} had a negative values at the most simulation steps.

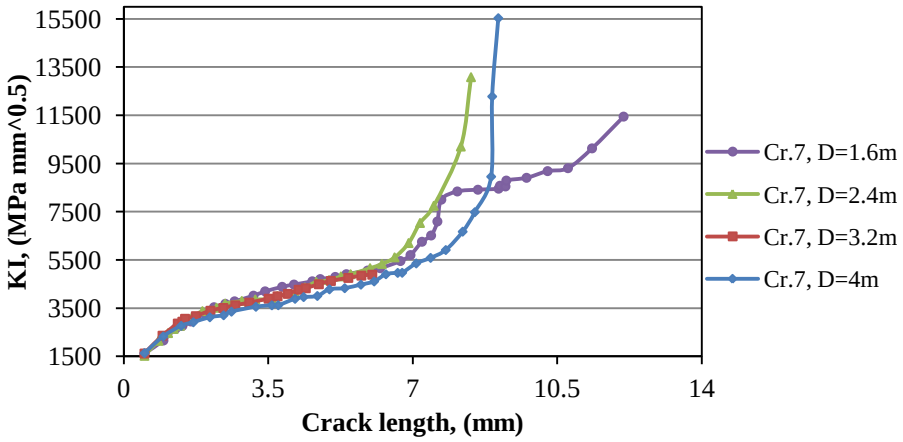

Figure 5-71 SIF histories of crack 7

The figures below describe some selected simulation steps images of crack 7 which expected to link up with crack 6:

Figure 5-72 shows the step 5 of cracks propagation, at this step crack 7 length was equal to (1.42 mm) and crack 6 was (1.6262 mm).

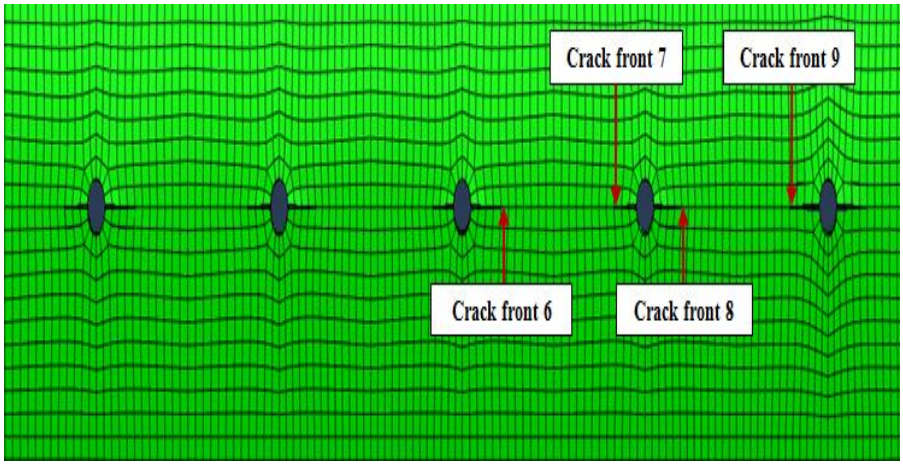

Figure 5-72 XFEM model of MSD after cracks opening (step 5), D=1.6 m

At step 24, the first linkup occurred at this simulation between cracks 8 and 9, crack 7 length was equal to (7.4444 mm) and crack 6 was (5.56347 mm). The cracks 7, 8,9 and 10 coalesced and formed one new crack which had a new crack fronts (crack front 7 and 10), as shown in figure in figure 5-73.

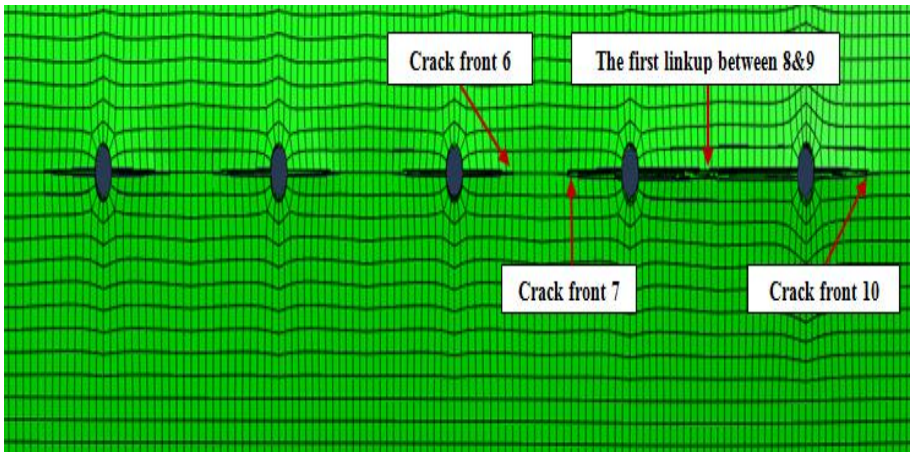

Figure 5-73 XFEM model of MSD after cracks opening (step 24), D=1.6 m

Step 36 considered as the step before linking up process between cracks 6 and 7, crack 7 length at this stage was equal to (11.3434 mm) and crack 6 was (7.48827 mm). Crack 7 had

a longer length than crack 6 due to the weakening of the panel at the location of the first link up process, see figure 5-74.

The second linkup process occurred between cracks 6 and 7 at step 37 as shown in figure 5-75, the formed crack which consists from cracks 5, 6, 7, 8, 9 and 10 had a new crack fronts (crack fronts5 and 10). After step 37, the other cracks such as cracks 4 and 5 propagated and linked up at step 50.

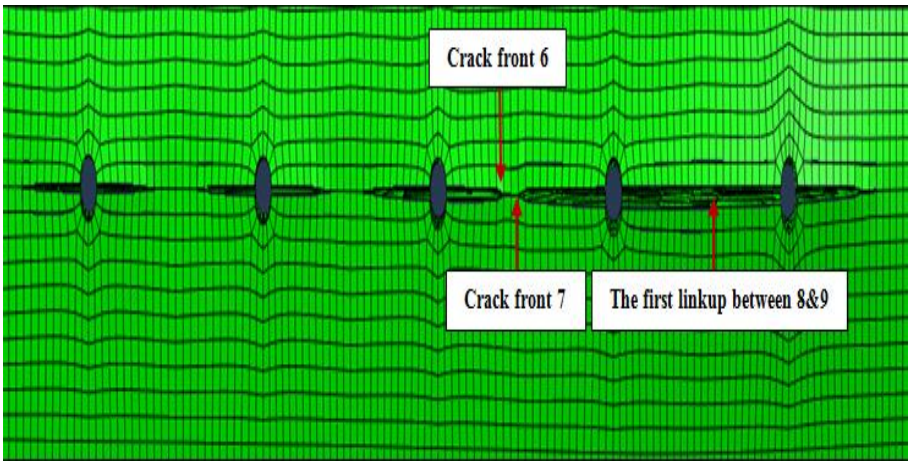

Figure 5-74 XFEM model of MSD after cracks opening (step 36), D=1.6 m

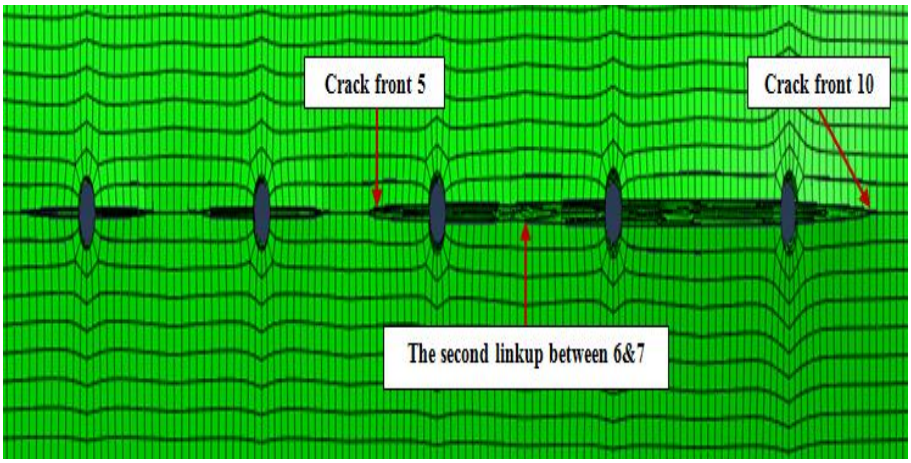

Figure 5-75 XFEM model of MSD after cracks opening (step 37), D=1.6 m

5.2.8 SIF evaluation of crack 8 at different fuselage diameters

Crack 8 SIFs histories represented in figure 5-76, it showed the effect the change of fuselage diameter on crack 8 extension and its SIFs. From this figure it's clear that as the crack grows as the values its SIF rises, but crack 8 also had different lengths as it can be seen in the figure; it's observed that the longest crack 8 length recorded when D equal to

2.4 m (12.5041mm, K_I=17479.4 MPa $\sqrt{mm}$), the second longest length was when D equal 4 m (11.192 mm, K_I=10974.8 MPa $\sqrt{mm}$). The third longest length recorded when D equal to 1.6 m (8.0083 mm, SIF = 9355.12 MPa$\sqrt{mm}$) and lastly when D equal to 3.2 m (6.0079 mm, K_I = 5598.77 MPa $\sqrt{mm}$).

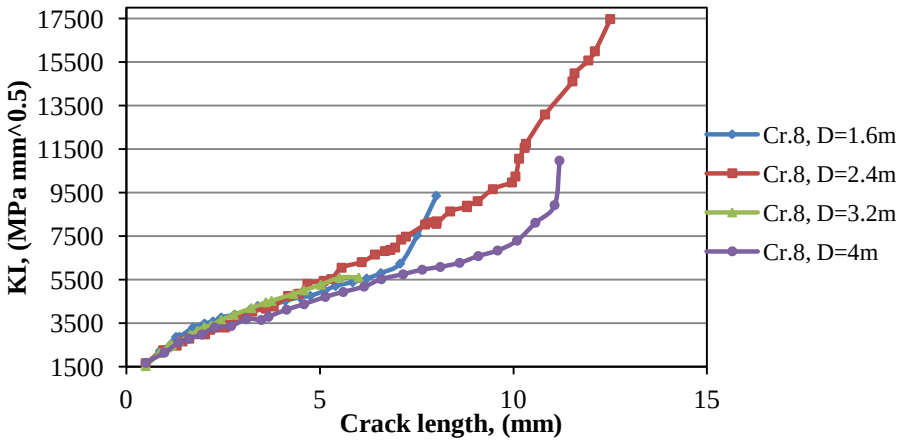

Figure 5-76 SIF histories of crack 8

Tables 56, 57, 58 and 59 in appendix (C) section (2-C-8) show some selected simulation results, they explain that K_I was the dominant of the failure mechanism with the existence effect of K_{II} and K_{III} in some simulation steps.

Recalling the figures from section 5.2.6 (fig. 5-67 till fig. 5-70) which describes the crack 8 propagation steps as following:

Figure 5-67 shows the step 5 of crack 8 propagation, at this step crack 8 length was equal to (1.6257 mm) and crack 9 length was (1.9489 mm) which expected to interact with crack 8. By step 15 crack 8 length reached (3.8093 mm) while crack 9 length was (4.3558 mm), see figure 5-68. Also figure 5-69 describes simulation step 25, at this step crack 8 length was (6.8215 mm) and crack 9 length was (5.8387 mm). It is noticeable on this step crack 8 was longer than crack 9 due to the panel has weakened at the location of hole 3 which is closer to crack 8 than crack 9.

Figure 5-77 illustrates simulation step 39, crack 8 length at this step was (9.965 mm) and crack 9 length was (6.9418 mm). At this step the coalesced crack was consists from crack 3, 4, 5, 6, 7 and 8 with two crack fronts 3 and 8. Crack 8 had faster crack propagation than

8, as shown in figure 5-78 which describes step 45 crack 8 recorded length was (11.5283 mm) and crack 9 length was (7.7201 mm).

The linking up process occurred between crack 8 and crack 9 at step 46 as shown in figure 5-79, the formed crack at this stage had two new crack fronts (crack front 3 and 10). This kind of multiple cracks interaction cause catastrophic damage to some aero structures such as air craft wing and the fuselage of the airplane.

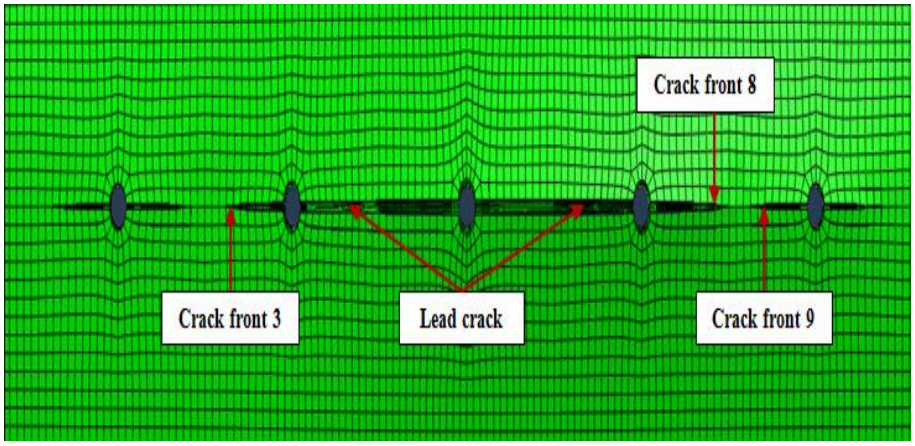

Figure 5-77 XFEM model of MSD after cracks opening (step 39), D=2.4 m

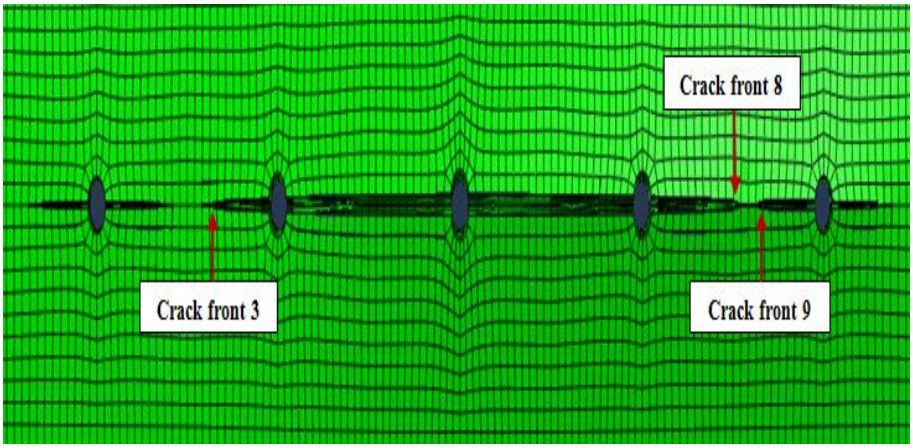

Figure 5-78 XFEM model of MSD after cracks opening (step 45), D=2.4 m

The second longest length to crack 8 was recorded when D equal to 4 m and return back to the figures which mentioned in section 5.2.5, figures from 5-59 till 5-65, they give idea about the propagation stages of cracks 8 and 9 in this case. Figure 5-59 describe step 10 of

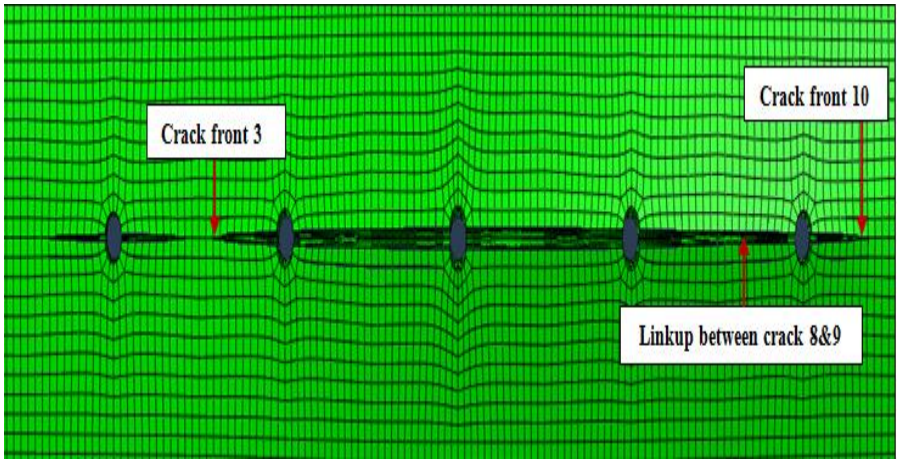

Figure 5-79 XFEM model of MSD after cracks opening (step 46), D=2.4

cracks propagation, crack 8 length was equal to (3.6757 mm) and crack 9 was (3.7223 mm). Figure 5-60 shows step 20, both cracks were extended in different lengths, and the recorded length of crack 8 was (8.6125 mm) and crack 9 was (6.7506 mm). At step 24 as illustrated in figure 5-61, crack 8 length was equal to (10.5682mm) and crack 9 was (8.4074 mm). The linking up process between both cracks occurred at step 25, see figure 5-62. Finally, figure 5-66 shows the final shape of the deformed panel at the location of the holes and the formed lead crack with two crack fronts 3 and 10.

5.2.9 SIF evaluation of crack 9 at different fuselage diameters

Figure 5-80 illustrates the growing trend of crack 9 with the change of the fuselage diameter, it showed the crack had an increase in its length compared to corresponded SIFs values except approximately the last steps which a steep rise in SIFs values occurred except one case (D=3.2 m). Also, the figure shows the longest crack 9 length recorded when D was equal to 1.6 m (CL = 11.9402 mm, K_I=11996 MPa $\sqrt{mm}$), the second long recorded length when D was equal to 4 m (CL = 9.173 mm, K_I= 10969.9 MPa $\sqrt{mm}$). The third length was (CL = 8.4484 mm, K_I=5550.14 MPa $\sqrt{mm}$) when D equal to 3.2 m and the shortest length was recorded when D was equal to 2.4 m (CL = 8.0215 mm, K_I=15736.8 MPa $\sqrt{mm}$). Tables 60, 61, 62, and 63 in appendix (C) section (2-C-9) represent some selected simulation results; they showed that K_{II} and K_{III} had effective values contribute in

the failure mechanism except the case of D equal to 3.2 m where K_{II} and K_{III} had a limited effect to the failure mechanism. Referring to figure 5-72, section 5.2.7, which shows the simulation step 5, at this step crack 9 lengths was equal to (2.3613 mm) and crack 8 was (1.3705 mm). At simulation step 23 crack 9 recorded lengths was equal to (11.0843 mm) and crack 8 was (7.5136 mm), as illustrated in figure 5-81. Also, referring to figure 5-73, section 5.2.7, which describes the linking up process at step 24 between cracks 9 and 8 and the formed crack, had crack fronts of 7 and 10. Figure 5-75 shows the final deformed shape of the panel at the location of the holes and the formed crack had a new crack fronts (crack front 5 and 10). Crack 9 propagation rates when D equal to 4 m was described in detail in the previous section (5.2.8).

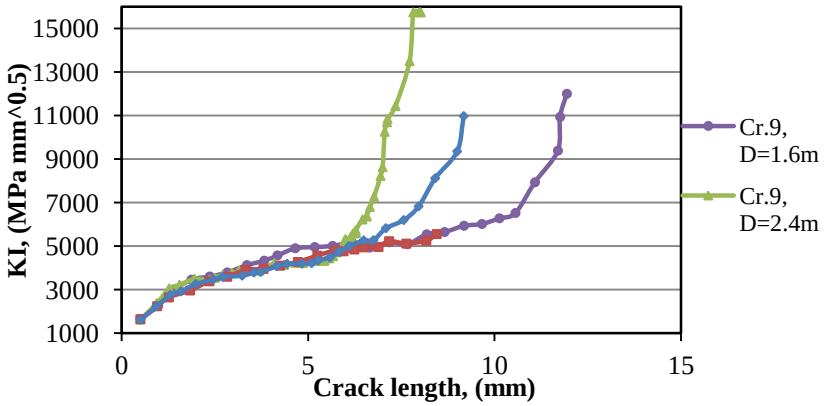

Figure 5-80 SIF histories of crack 9

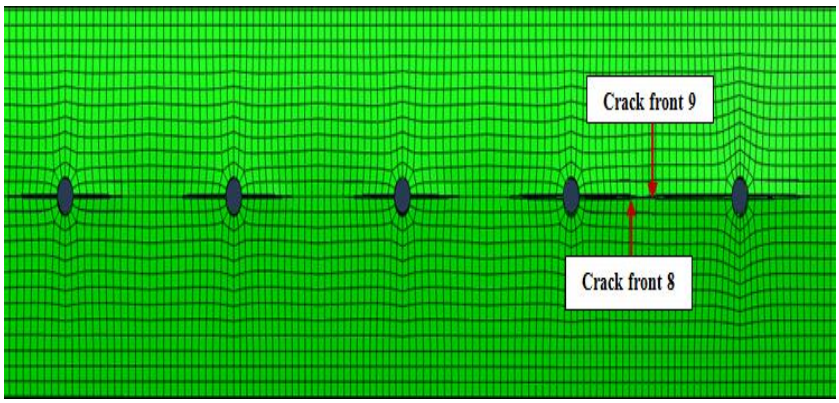

Figure 5-81 XFEM model of MSD after cracks opening (step 23), D=1.6 m

5.2.10 SIF evaluation of crack 10 at different fuselage diameters

Figure 5-82 and 5-83 illustrate the growing trend of crack 10 and the effect of changing fuselage diameter D from 1.6 to 4 m on SIF values and its lengths. The growing mechanism of crack 10 when D equal to 2.4 m separated due to the higher of its SIFs values and length than the other diameters. Figure 5-83 showed crack 10 had 3 growing stages: the first one crack 10 exhibits stable crack growing, the second unstable crack growing occurred and the last stage stable crack growing occurred. All three stages take about 146 simulation steps. Additionally, both figures showed that the longest crack 10 length recorded when D equal to 2.4 m (CL=29.0878 mm, K_I=11850.4 MPa $\sqrt{mm}$), the second recorded long length was when D equal to 4 m (CL=12.8237 mm, K_I=7338.27 MPa $\sqrt{mm}$), followed by when D equal to 1.6 m (CL=10.2041 mm, K_I= 8973.37 MPa $\sqrt{mm}$) and the shortest length was when D equal to 3.2 m (CL=7.8719 mm, KI=5823.81 MPa $\sqrt{mm}$).

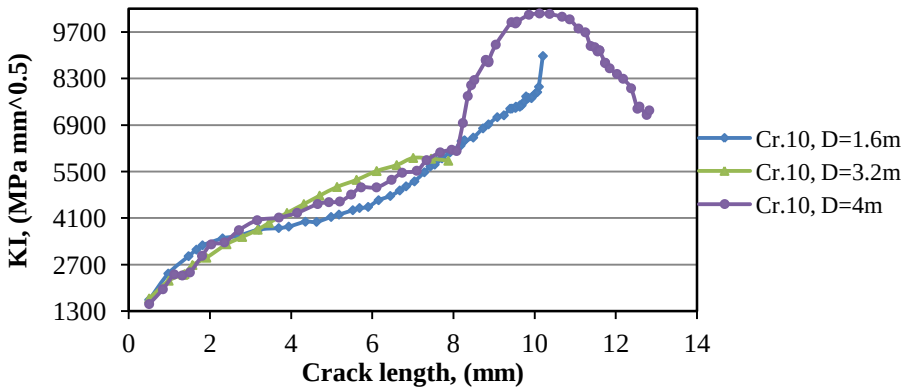

Figure 5-82 SIF histories of crack 10

In addition, tables 64, 65, 66 and 67 in appendix (C) section (2-C-10) show some selected simulation results; it showed K_I is the dominate principle to the failure mechanism with existence effect of K_{II} and K_{III} except the case of D equal to 1.6 m where the most values of K_{II} and K_{III} were negative.

Here below, some chosen simulation steps of crack 10:

Figure 5-84 shows step 26 of crack 10 propagation, at this step crack 10 length was (5.5649 mm). Crack 10 has a space to grow and it will not interact with the other cracks. The first linking up occurred between cracks 6&7and the formed crack had two crack fronts (5 and

8). When crack 10 reached step 38, the second linkup occurred between crack 4 and 5 and the new coalesced crack which now consisted from cracks 3, 4, 5, 6, 7 and 8 had two new crack fronts (3 and 8) as shown in figure 5-85. Crack 10 length at this step was (6.0071 mm). The third linkup in this case occurred at step 46 between cracks 8 and 9 and the formed crack for now which consisted from cracks 3, 4, 5, 6, 7, 8, 9, and 10 had new crack fronts (3 and 10). At this step crack 10 length was equal to (6.2804 mm), see figure 5-86. By simulation step 58 the fourth linkup occurred between cracks 2 and 3 and in this stage the formed crack had two crack fronts (1 and 10). Crack 10 length on this stage was equal to (7.1807 mm), see figure 5-87. Until step 58 crack 10 propagation rate was very slow due

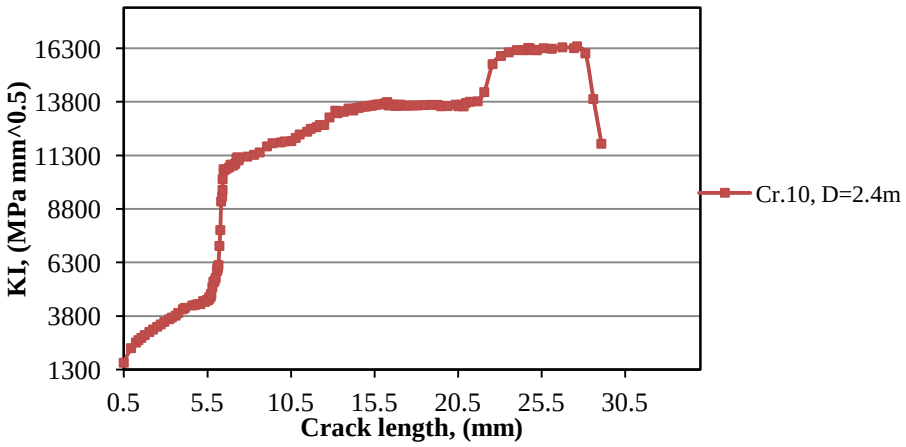

Figure 5-83 SIF histories of crack 10, D=2.4m

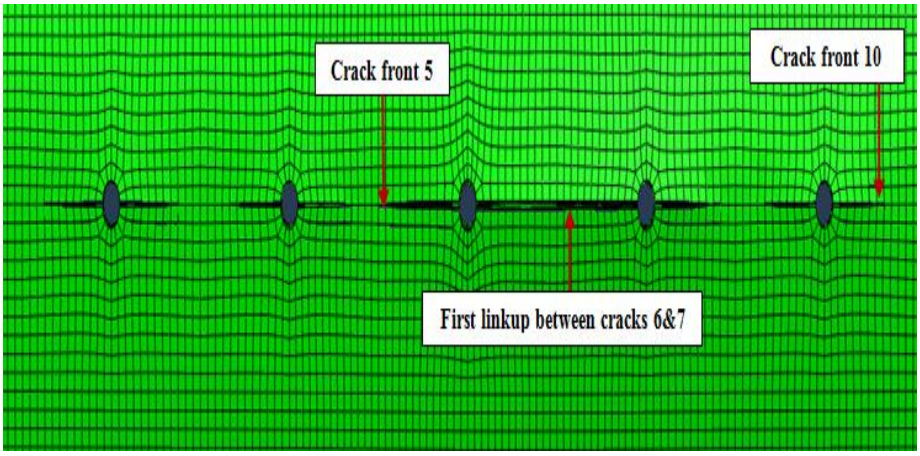

Figure 5-84 XFEM model of MSD after cracks opening (step 26), D=2.4 m

to the linkup process occurred between the internal cracks which were propagating with a faster rate.

After step 58 the internal cracks were connected and the stress started to concentrate on the positions of crack fronts 1 and 10. Figure 5-88 illustrates simulation step 100, in this step crack 10 recorded length was equal to (16.3481 mm) while crack 1 reached (24.6462 mm). Figure 5-89 shows the final step of the simulation, crack 10 length was equal to (29.0878 mm) and rack 1 was (42.5053 mm) at the same time.

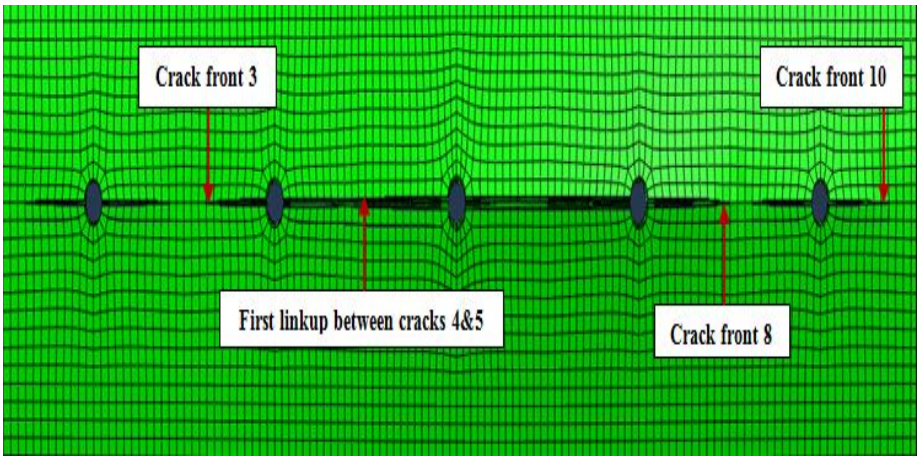

Figure 5-85 XFEM model of MSD after cracks opening (step 38), D=2.4 m

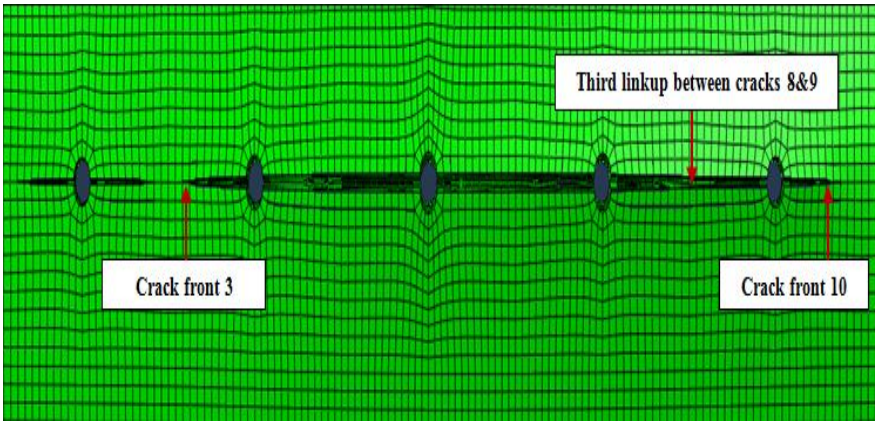

Figure 5-86 XFEM model of MSD after cracks opening (step 46), D=2.4 m

The second longer length of crack 10 was when D equal to 4 m and the following some selected propagation steps: figure 5-90 shows the simulation step 25, at this step crack 10 recorded length was (8.0754 mm) and the first linkup occurred between crack 8 and 9 to form new crack with two fronts (7 and 10). In this case the second linkup occurred between crack 6 and 7 at simulation step 27, crack 10 length was (8.3507 mm) and the formed crack had new crack fronts (5 and 10) as shown in figure 5-91.

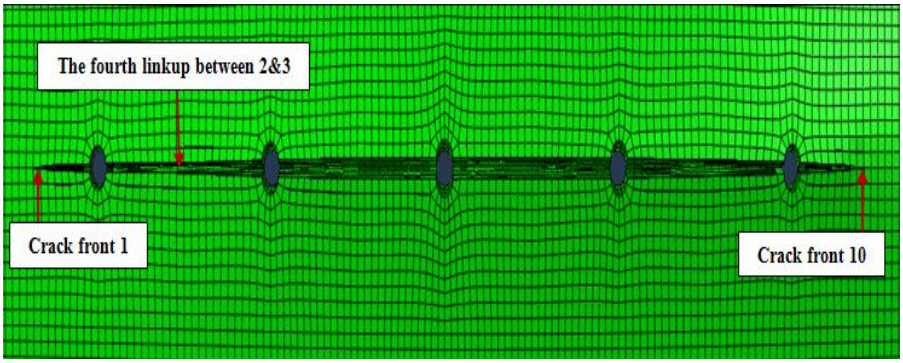

Figure 5-87 XFEM model of MSD after cracks opening (step 58), D=2.4 m

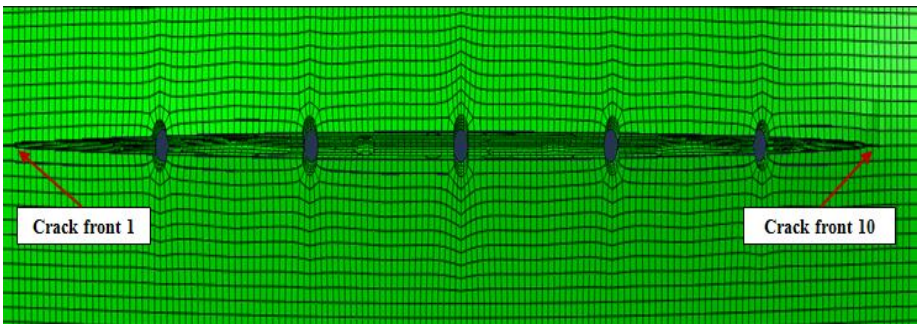

Figure 5-88 XFEM model of MSD after cracks opening (step 100), D=2.4 m

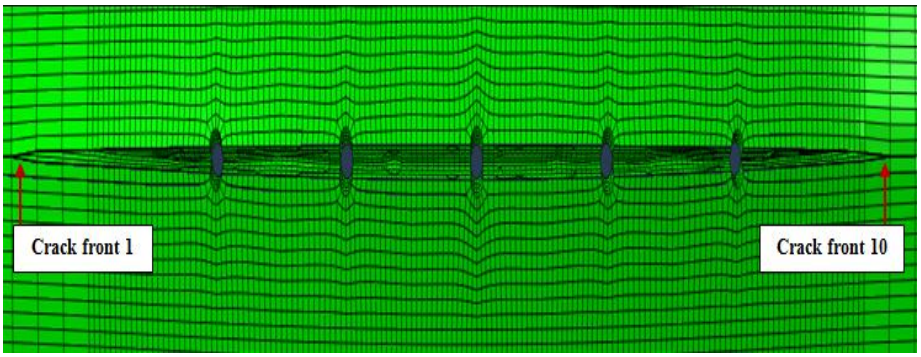

Figure 5-89 XFEM model of MSD after cracks opening (step 146), D=2.4 m

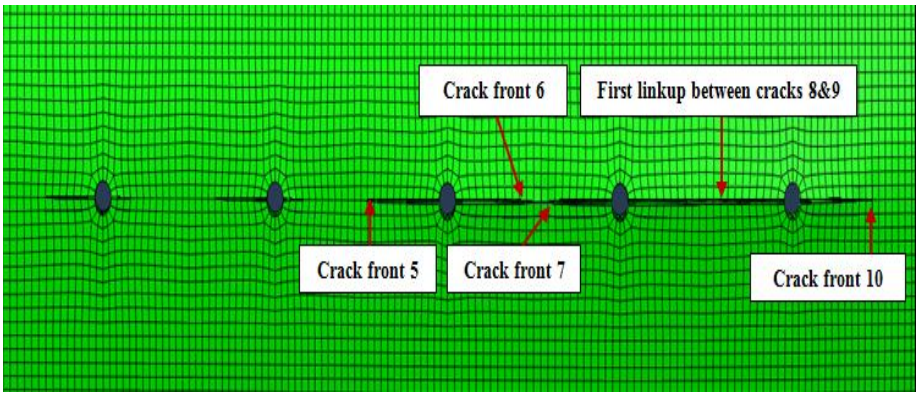

Figure 5-90 XFEM model of MSD after cracks opening (step 25), D=4 m

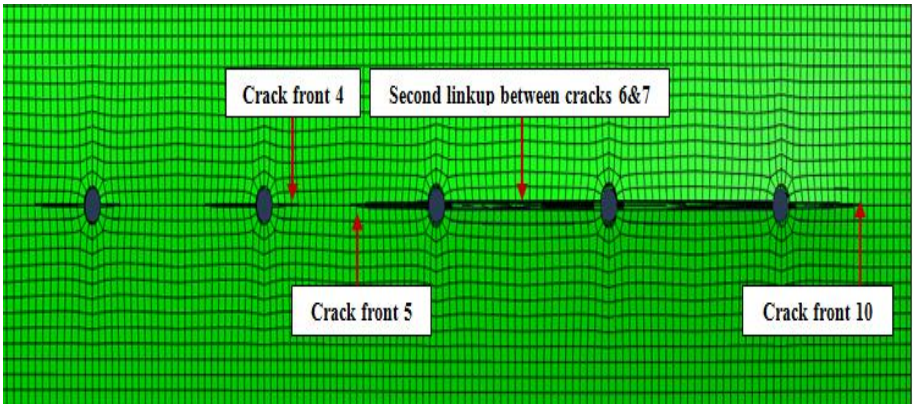

Figure 5-91XFEM model of MSD after cracks opening (step 27), D=4 m

Crack 10 recorded length was equal to (11.4794 mm) in the simulation step 46, as shown in figure 5-92. The third linkup occurred at this step and the new formed crack had new crack fronts (3 and 10). The total length of the formed crack was equal to (98.1293 mm) in this step. Figure 5-93 show the last step of the simulation (step 59), crack 10 length was equal to (12.8237 mm) and crack 3 reached (10.6367 mm) length, and the total length of the formed crack was (102.8604 mm).

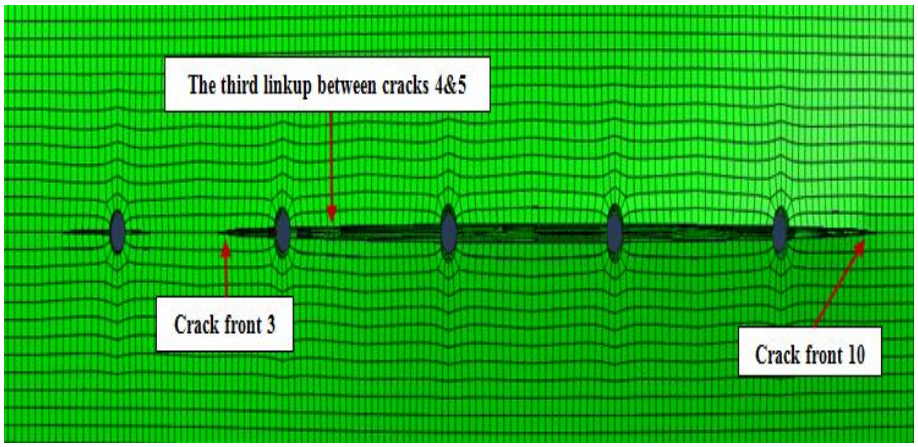

Figure 5-92 XFEM model of MSD after cracks opening (step 46), D=4 m

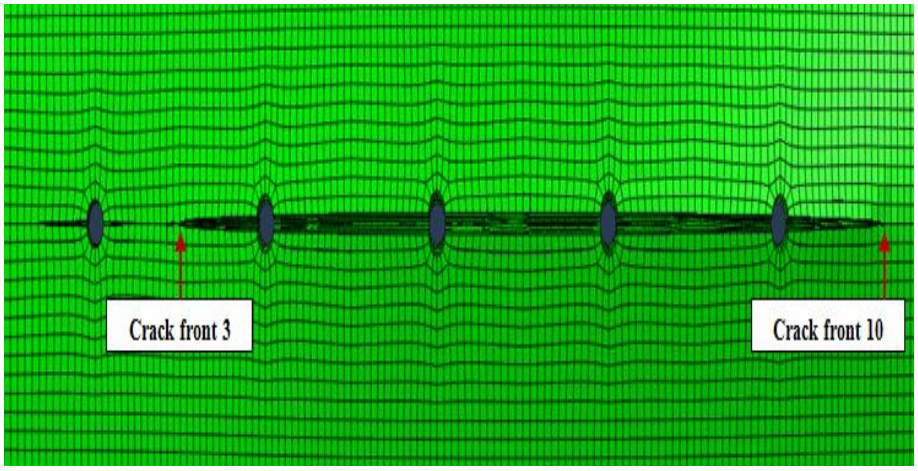

Figure 5-93 XFEM model of MSD after cracks opening (step 59), D=4 m

5-3 THIRD NUMERICAL EXAMPLE

In this simulation, the same panel material, dimentions and boundary conditions which mention in section 5.1 are used, except the number of the rivet holes in this case are increased to 7 holes. Figure 5-94 shows the cracks positioning and numbering. Also, a uniform pressure was applied at the internal face of the model Fig. 5-95. Figure 5-96 also shows a portion of the mesh around the holes, and as it can be seen mesh was refined around the cracks at the edges of each hole and a uniform template of elements around each crack front was used. The characteristics of the final mesh are summarized in table 5-3.

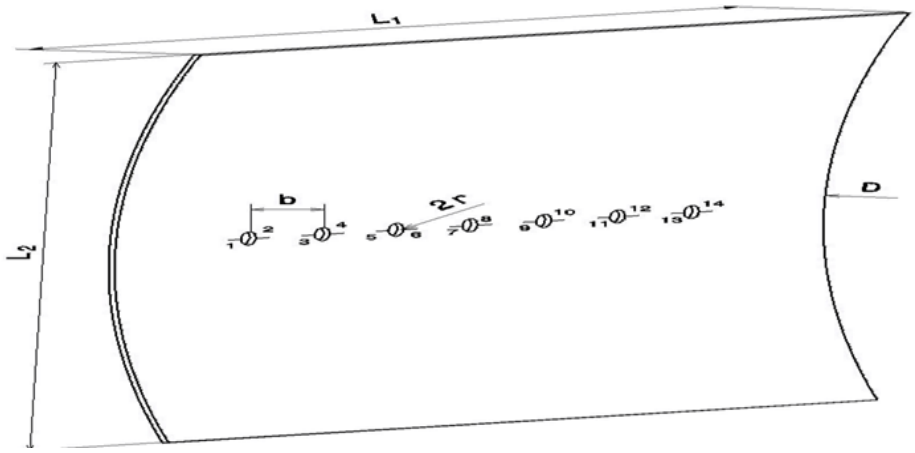

Figure 5-94 Analyzed configuration with multiple cracks (not to scale)

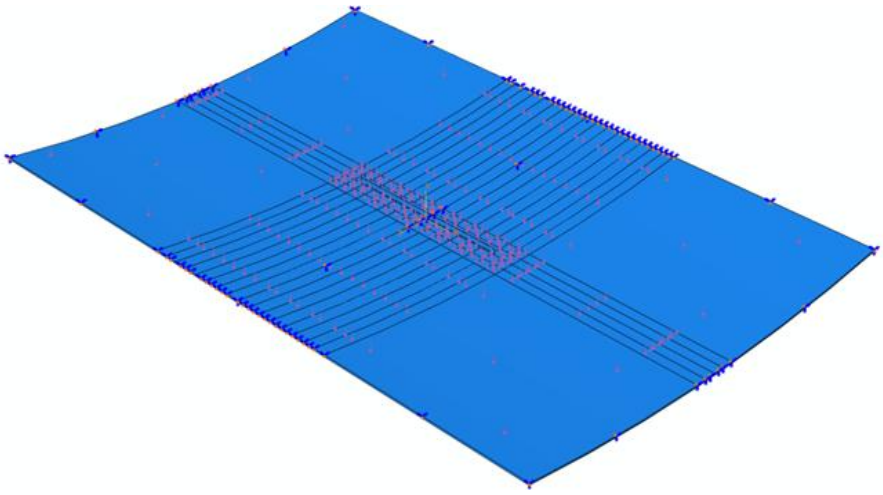

Figure 5-95 Panel with pressure load and boundary conditions

Results of this procedure can be seen in the following section. The initial crack length used was 0.5mm.

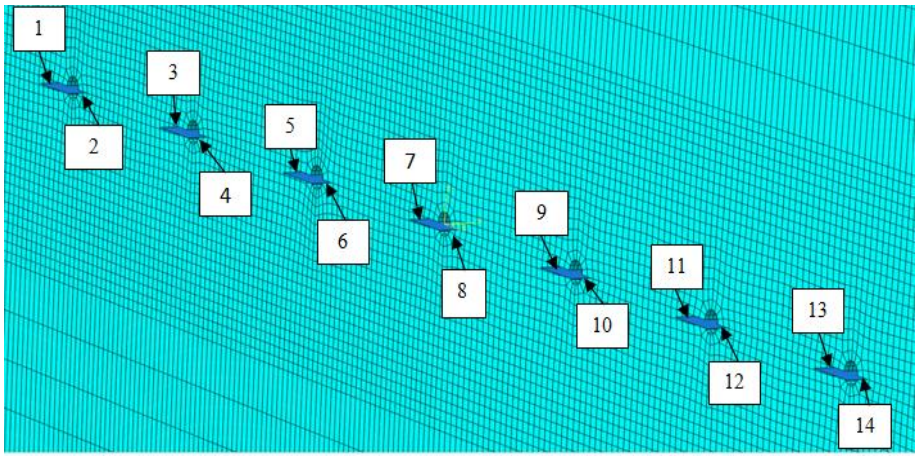

Figure 5-96 Cracks positions and numbering

Table 5-3 Characteristics of the panel final mesh

D (m)	No. of steps (max.)	No. of nodes	No. of elements	Type of element
1.6	32	219770	173824	C3D8R
2.4	143	155620	122752	C3D8R
3.2	18	156750	123648	C3D8R
4	34	156205	123216	C3D8R

5.3.1 SIF evaluation of crack 1 at different fuselage diameters

Figure 5-97 and 5-98 describe the effect of changing fuselage diameter (D) on crack 1 length during the simulation and its SIF values. Also, the figure showed that the rapid and unstable growth of the crack occurred at the last steps of the simulation and the longest crack 1 recorded when D was equal 2.4 m (48.276 mm, K_I=18168.5 MPa $\sqrt{mm}$), unstable crack growing in this case occurred after step 37 (CL=6.1455 mm). Crack 1 length was lower about 5 times when D equal to 3.2 m (5.4815 mm, K_I=3501.11 MPa$\sqrt{mm}$) compared to its length when D equal to 2.4 m, and it reaches (5.0199 mm, K_I=6267.59 MPa $\sqrt{mm}$) when D changed to 4 m. The shortest recorded crack 1 length was when D equal to 1.6 m (4.4802 mm, K_I=4196.87 MPa $\sqrt{mm}$).

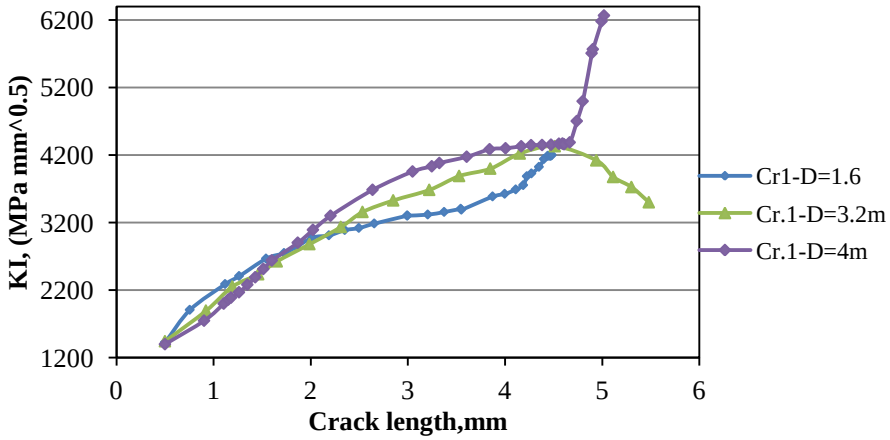

Figure 5-97 SIF histories of crack 1

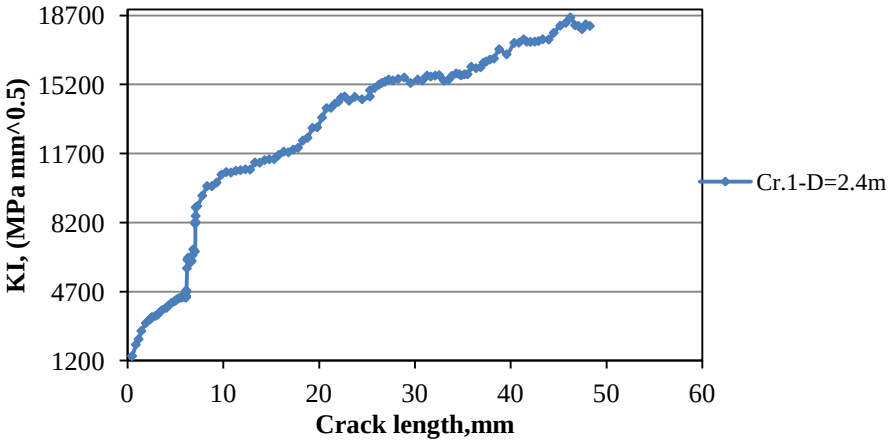

Figure 5-98 SIF histories of crack 1

Additionally, the documented simulation results showed that K_I was the principle domination of the failure mechanism with the presence effect of K_{II} and K_{III}. For more extensively description of the results, the following are some selection of simulation images:

Figure 5-99 represent the first step simulation when fuselage diameter was equal to 2.4 m, it showed the stress distribution around the rivet holes and crack 1 in this simulation will not interact with other cracks, meaning the crack has a space to grow more than the other cracks except crack 14.

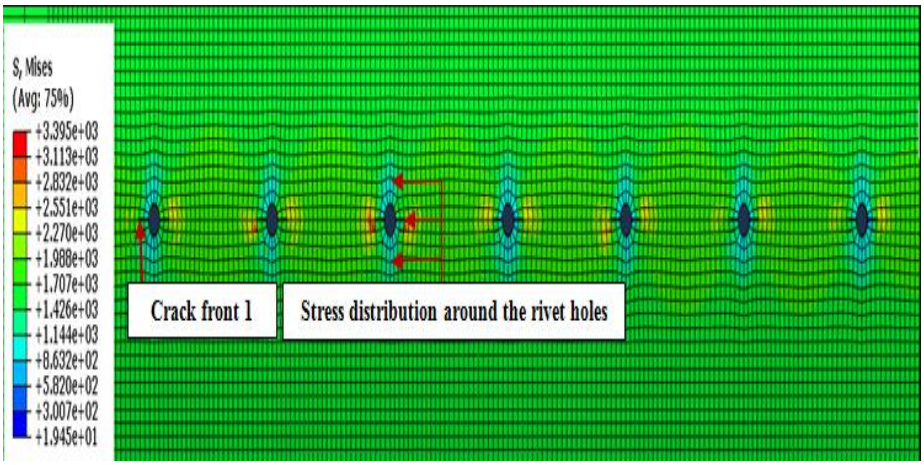

Figure 5-99 XFEM model of MSD panel after cracks opening (the first step of crack propagation)

Figure 5-100 describes the simulation step 28, it can be seen from the figure that the first linkup occurred between cracks 4 and 5 and the second was between cracks 6 and 7. At this step, crack 1 length was equal to (6.0675 mm) and the formed crack at this step had new crack fronts (3 and 8).

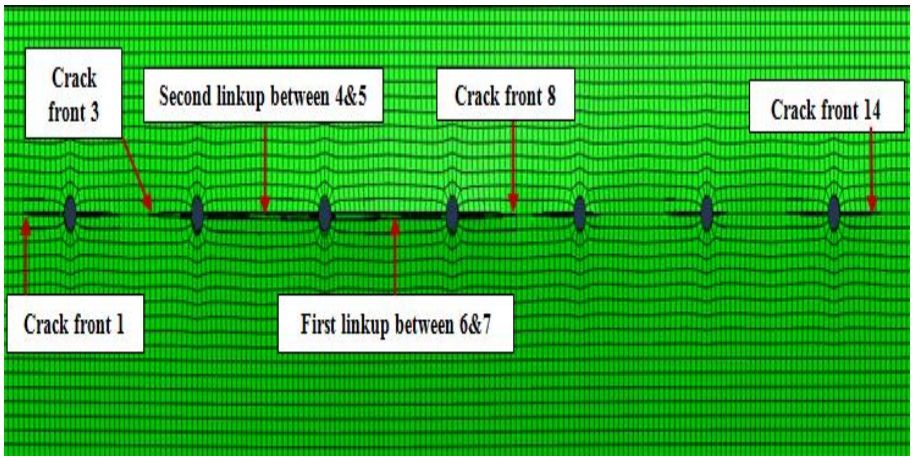

Figure 5-100 XFEM model of MSD panel after cracks opening (step 28 of crack propagation)

Crack 1 propagation rate was very slow from steps 28 till 54 due to the linking up process between cracks started in the holes 2, 3 and 4 which means the panel was weak at this location. Crack 1 reached (6.5172 mm) length as illustrated in figure 5-101, also, the third

linkup occurred between crack 8 and 9. Now the formed crack had new crack fronts (3 and 10).

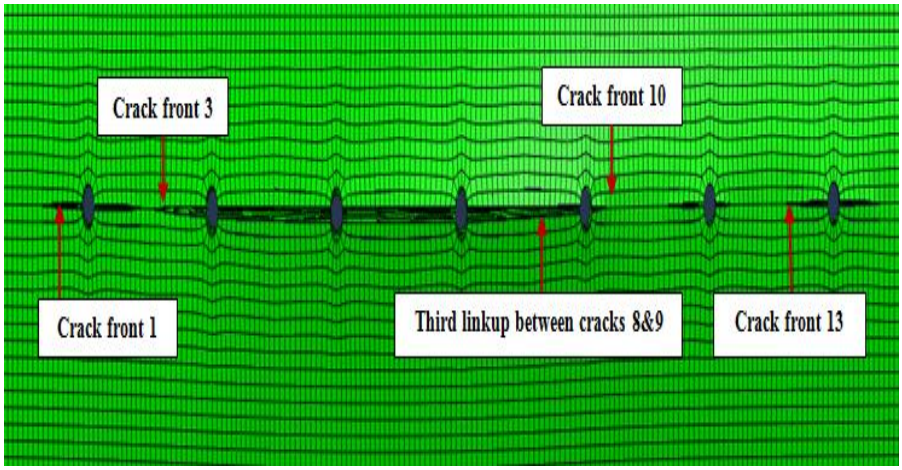

Figure 5-101 XFEM model of MSD panel after cracks opening (step 44 of crack propagation)

At step 54 crack 1 recorded length was equal to (7.1298 mm) and the fourth linkup process occurred between cracks 2 and 3. The formed crack fronts now are 1 and 10 as seen in figure 5-102.

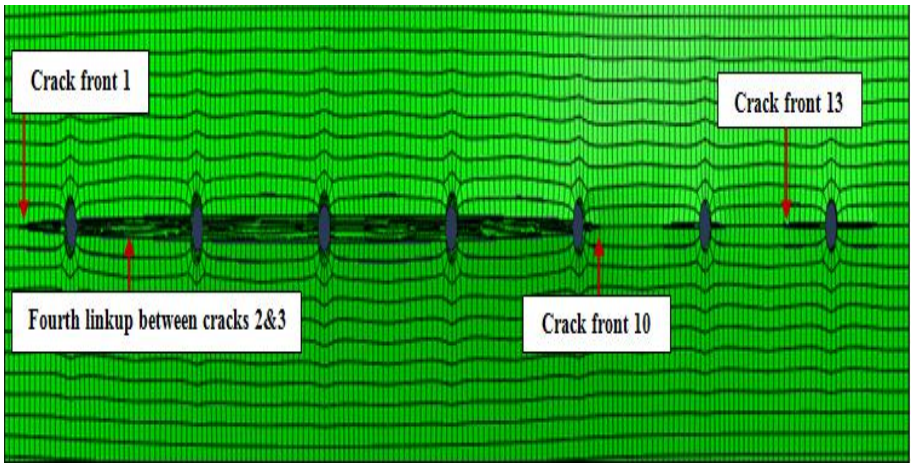

Figure 5-102 XFEM model of MSD panel after cracks opening (step 54 of crack propagation)

Figures 5-103 and 5-104 show the simulation step 100 and last step 143, it showed the formed crack was extended in the direction of crack front 1. At step 100 crack 1 recorded length was equal to (28.268 mm) and at step 143 it reached (48.276 mm).

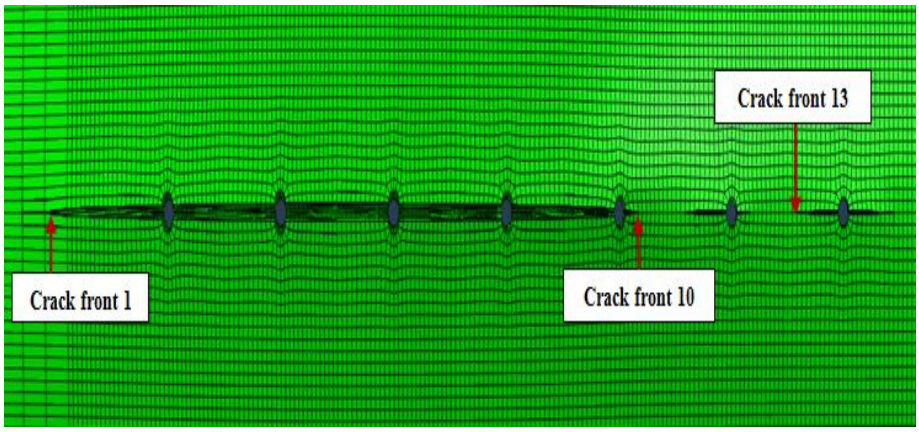

Figure 5-103 XFEM model of MSD panel after cracks opening (step 100 of crack propagation)

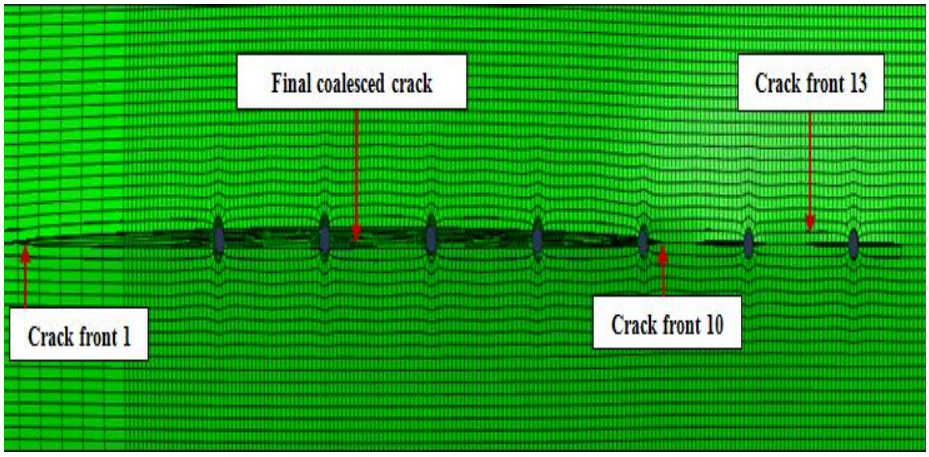

Figure 5-104 XFEM model of MSD panel after cracks opening (step 143 of crack propagation)

5.3.2 SIF evaluation of crack 2 at different fuselage diameters

Figure 5-105 shows the effect of changing fuselage diameters on crack 2 lengths and its SIF histories, it can be seen from this figure that the longest crack 2 length recorded when D was equal to 2.4 m (CL = 8.9568 mm, K_I=18400.5 MPa $\sqrt{mm}$). The second longest recorded length was when D equal to 4 m (CL =5.8144 mm, K_I=6551.37 MPa $\sqrt{mm}$) at the end of the simulation. When D equal to 3.2 m, the crack 2 length was (CL=5.2357 mm, K_I= 4011.57 MPa $\sqrt{mm}$), and Finally, the shortest crack 2 length recorded when D was equal to 1.6 m (CL=4.1132 mm, K_I=3992.61 MPa $\sqrt{mm}$).

Also, the documented results in this case showed the opening mode (Mode I) was the principle to the failure mode during the simulation, with the existence effect of the other failure modes (K_{II} and K_{III}) in some simulation steps: K_{III} had a limited effective values due to their negative value when was D equal to 2.4m and 3.2 m, K_{II} and K_{III} had a limited effect when D was equal to 1.6m due to the their negative values at the most simulation steps

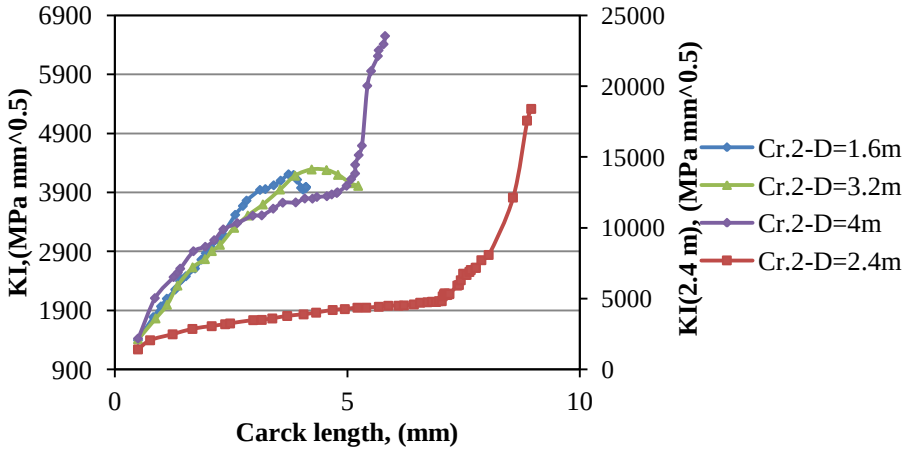

Figure 5-105 SIF histories of crack 2

Referring to the simulation images in the previous section (5.3.1) for more adequately description of the results, the figures from 5-100 to 5-101 show the propagation steps of crack 2:

Figure 5-100 shows the simulation step 28, at this step crack 2 length was equal to (7.033 mm) and crack 3 length which expected to linkup with crack 2 was equal to (6.8417 mm). At step 44 as shown in figure 5-101, the propagation rate of cracks 2 and 3 changed due to the effect of linking up between cracks from 3 till 9 and the panel weakened closer to the location of crack 3. Furthermore, at this step crack 2 length was equal to (7.6274 mm) and crack 3 length was (8.8911 mm).

Figure 5-106 shows the simulation step 49, at this step crack 2 length was equal to (8.0415 mm) and crack 3 length was (10.2293 mm). The linkup process between two adjacent

occurred from step 50 and they fully linked up at step 52 as shown in figure 5-107, at this coalesced crack length was equal to (113.0344 mm).

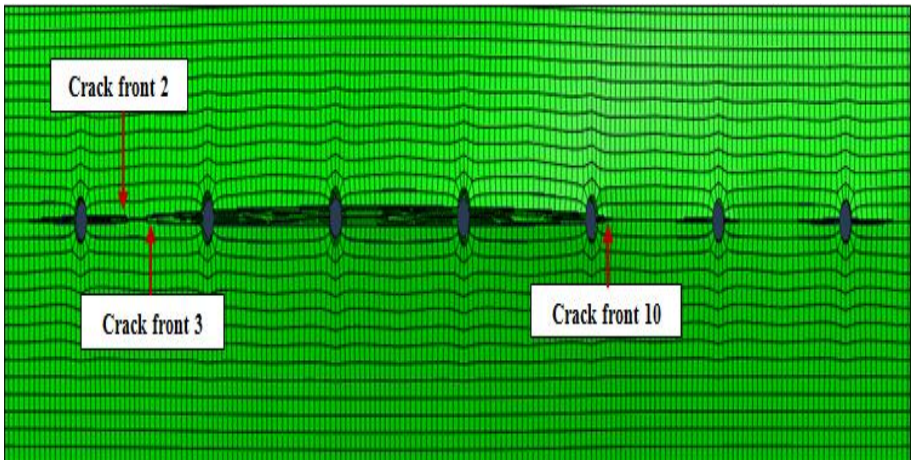

Figure 5-106 XFEM model of MSD panel after cracks opening (step 49 of crack propagation)

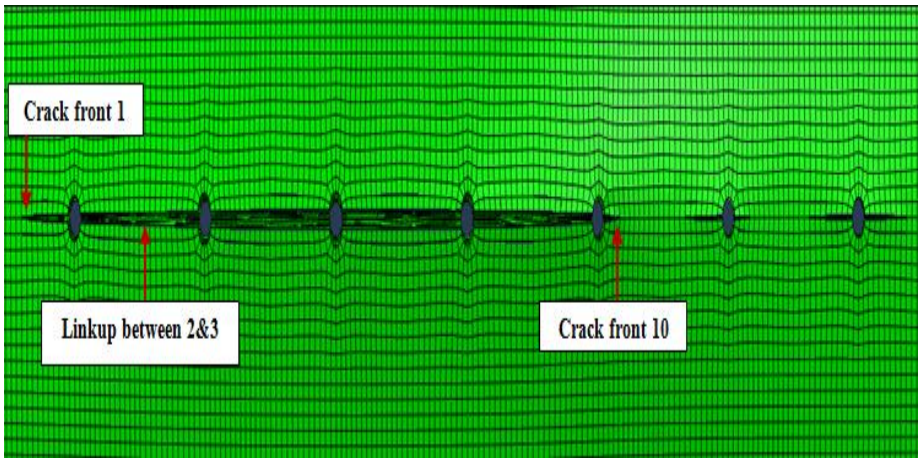

Figure 5-107 XFEM model of MSD panel after cracks opening (step 52 of crack propagation

5.3.3 SIF evaluation of crack 3 at different fuselage diameters

It is noticeable that Crack 3 growing trend was similar to crack 2, where it reached its longest length when D was equal to 2.4 m (CL =11.0718 mm, K_I=16289.8 MPa $\sqrt{mm}$). A steep rise in SIF values occurred to crack 3 at the last ten simulation steps when D was equal to 4 m and crack 3 length at this case was (CL =8.1842 mm, K_I=8564.15 MPa $\sqrt{mm}$) , while crack 3 reached (CL =6.3313 mm, K_I=4343.56 MPa $\sqrt{mm}$) when D was equal to

3.2 m. The shortest recorded length to crack 3 was when D equal to 1.6 m (CL =4.4991 mm, K_I=6040.34 MPa$\sqrt{mm}$), see Figure 5-108. Additionally, the results showed that the K_I was the major dominant of the failure mechanism (Mode I) with influential values to K_{II} and K_{III}.

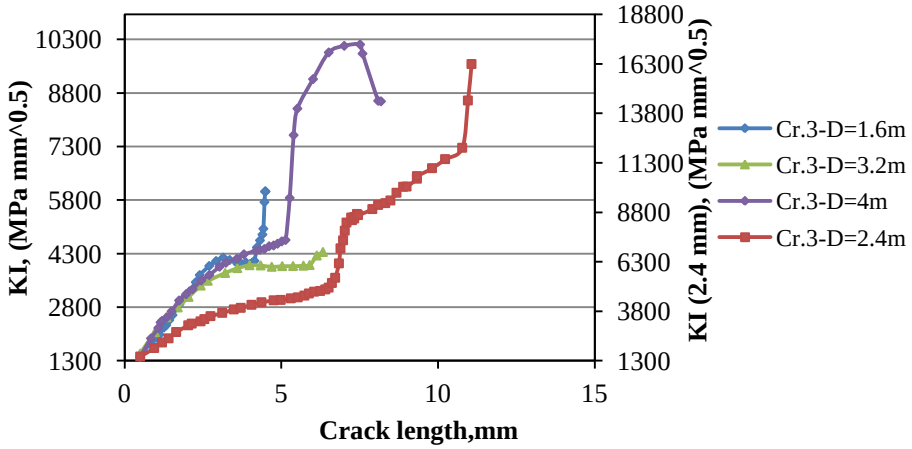

Figure 5-108 SIF histories of crack 3

The simulation images which describe the propagation stages of crack 3 were illustrated in section (5.3.1) and (5.3.2). Crack 3 length at the step before coalesced with crack 2 (step 49) reached (10.2293 mm) and crack 2 was (8.0415 mm), this length difference occurred due to the linking up process between cracks 4, 5, 6, 7, 8, 9 and 10 which led to the weakening of the panel at the location closer to crack 3 than crack 2, see figures 5-106 and 5-107. The following images show some simulation images to crack 3 when D equal to **4m** as a second long length recorded to crack 3 during the simulation:

figure 5-109 shows the simulation step 25, at this step crack 3 recorded length was equal to (5.2706 mm) and crack 2 was (5.1699 mm) and crack 4 and crack 5 linked up at this step to form new crack which had a new crack fronts (3 and 6). Also, figure 5-110 describe the simulation step 33, at this step crack 3 reached (8.0936 mm) and crack 2 (5.7821 mm).

The other fuselage diameters 1.6 m and 3.2 m no linkup process occurred between crack 3 and 2 as shown in figures 5-111 and 5-112: figure 5-111 which describes the last simulation step (step 32) when D equal to 1.6, at this step crack 3 length was equal to (4.4991 mm) and crack 2 was (4.1132 mm) and the linking up process occurred between cracks from 5 to 10.

When D equal to 3.2 m no link up occurred between all cracks and crack 3 reached (6.3313 mm) while crack 2 was (5.2357 mm), see figure 5-112.

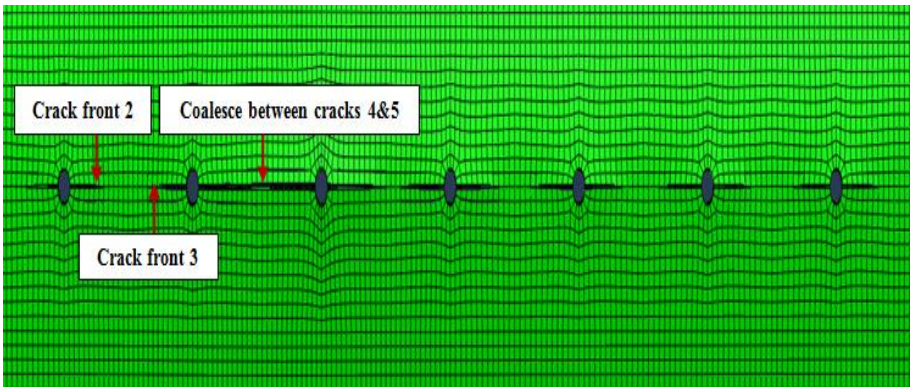

Figure 5-109 XFEM model of MSD panel after cracks opening (step 25 of crack propagation)

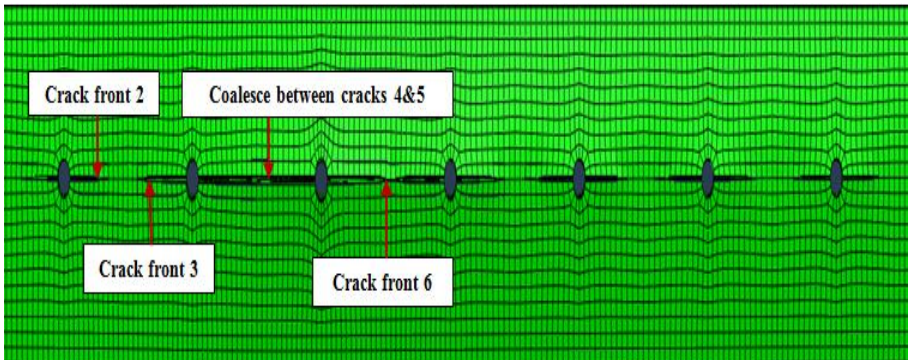

Figure 5-110 XFEM model of MSD panel after cracks opening (step 33 of crack propagation

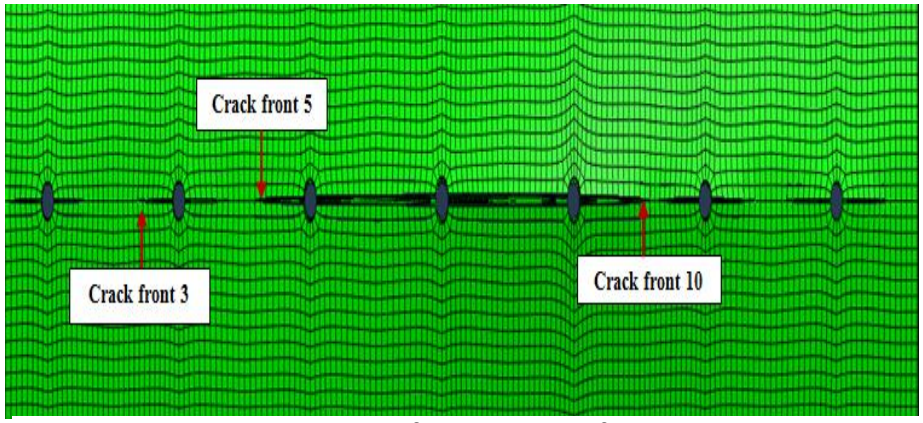

Figure 5-111 XFEM model of MSD panel after cracks opening (step 32 of crack propagation)

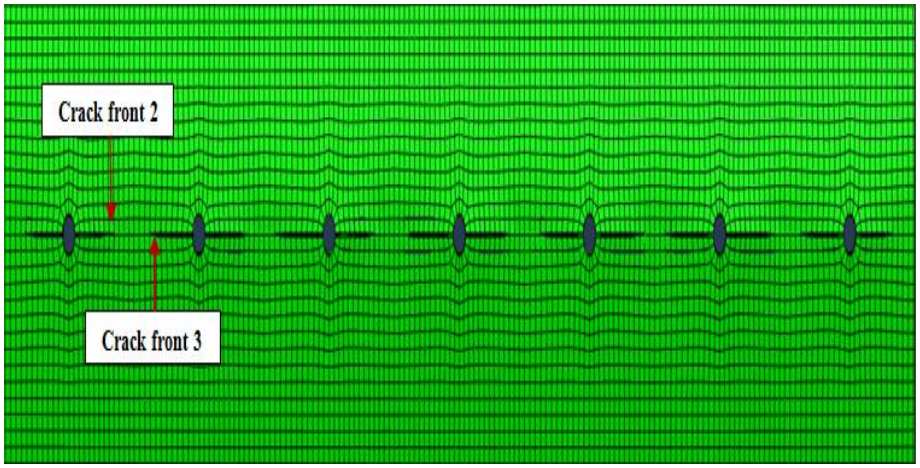

Figure 5-112 XFEM model of MSD panel after cracks opening (step 18 of crack propagation)

5.3.4 SIF evaluation of crack 4 at different fuselage diameters

It can be seen from 5-113 the figure that the longest recorded crack 4 length were when D equal to 2.4 m (CL =9.3509 mm, K_I=12115.85 MPa$\sqrt{mm}$), followed by its length when D was equal to 4 m (CL =8.1436 mm, K_I=13083.36 MPa$\sqrt{mm}$). Also, crack 4 length was equal to (CL =6.7985 mm, K_I=5680.22 MPa$\sqrt{mm}$) when D was equal to 3.2 m and the shortest reached length recorded when D was 1.6 m (CL=6.0822, K_I=4975.32 MPa$\sqrt{mm}$). In addition, the recorded simulation results showed that the most effective failure mode was mode I (opening mode) with presence effect of K_{II} and K_{III} (tearing and shearing modes) in some steps. Here below are some selected simulation images when D equal **2.4 m**:

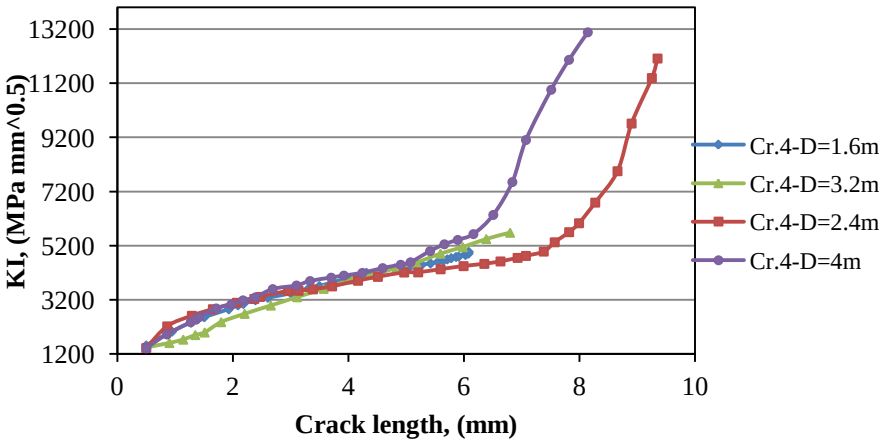

Figure 5-113 SIF histories of crack 4

Figure 5-114 shows the simulation step 10, at this step crack 4 recorded length was equal to (3.3858 mm) and crack 5 length which considered to linkup with crack 4 was equal to (3.5257 mm):

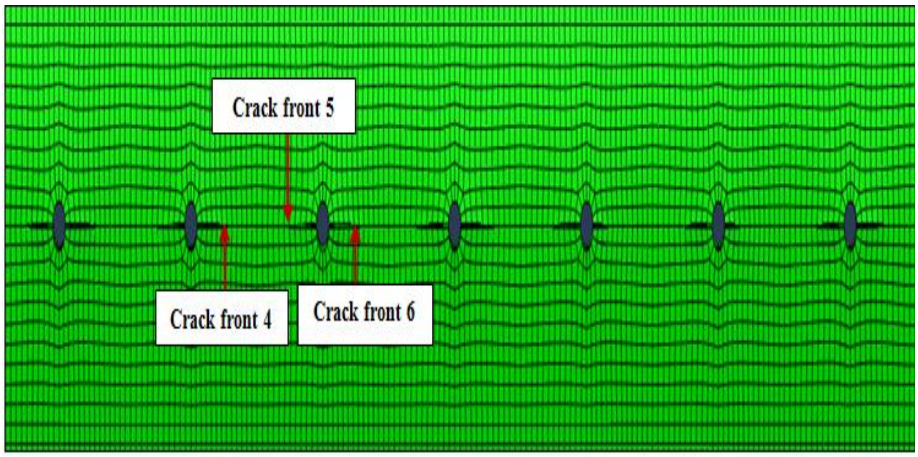

Figure 5-114 XFEM model of MSD panel after cracks opening (step 10 of crack propagation)

Figure 5-115 represent the simulation step 18, it showed that the recorded length of crack 4 was equal to (6.3532 mm) while crack 5 length was equal to (6.3251 mm). At step 27 as it can be seen in figure 5-116, the first linking up process occurred between cracks 6 and 7

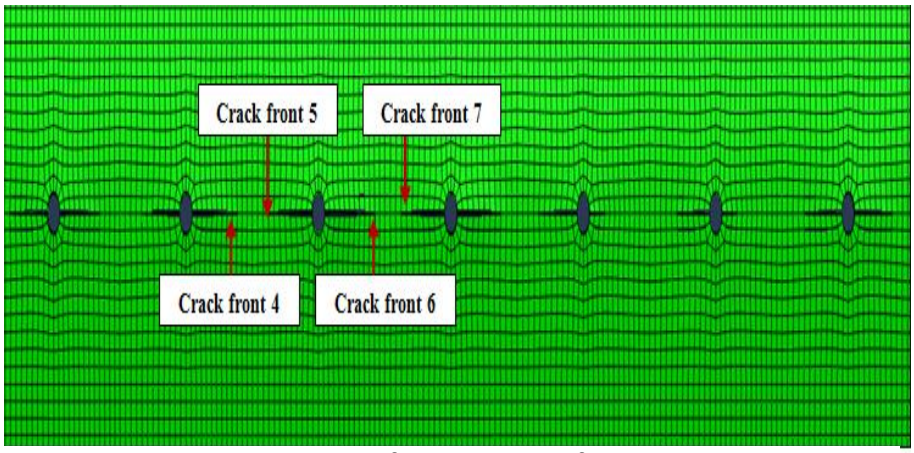

Figure 5-115 XFEM model of MSD panel after cracks opening (step 18 of crack propagation)

Which represent the weakest location on the panel was in this location. In this step, crack 4 length was (8.6578 mm) and crack 5 length was (10.6754 mm).

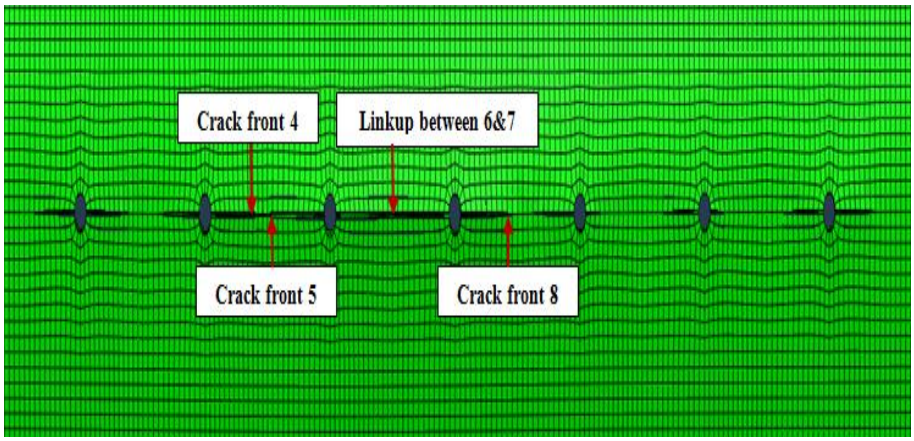

Figure 5-116 XFEM model of MSD panel after cracks opening (step 27 of crack propagation)

Figure 5-100 in section (5.3.1) describes the simulation step 28 which the linking up process between crack 4 and 5 occurred. Also figures from 5-101 till 5-104 explain the 143 simulation steps in case of D equal to 2.4 m for the whole cracks.

5.3.5 SIF evaluation of crack 5 at different fuselage diameters

Figure 5-117 explains the relation between SIFs values of crack 5 with its crack length at different fuselage diameters. It showed that there were a stable rise in SIFs values as crack propagate in the most simulation steps, while there were s steep rise in SIFs values at the last steps of the simulation (D= 1.6m, 2.4m, and 4 m). The longest crack 5 length was recorded when D was equal to 4 m (CL =12.0166 mm, K_I=11917.4 MPa $\sqrt{mm}$), followed by its length when D was equal to 2.4 m (CL =10.8491 mm, K_I=12915.9 MPa $\sqrt{mm}$) and then when D was equal to 1.6 m (CL =7.5788 mm, K_I=8102.75 MPa $\sqrt{mm}$). The shortest crack 5 length recorded when D was equal to 3.2 m (CL =6.8574 mm, K_I=5309.11 MPa$\sqrt{mm}$).

For more extensively explanation of crack 5 propagation behavior in this case (D=4 m), the following are some selected simulation images: Figure 5-118 represent simulation step 10, at this step crack 5 recorded length was (4.7055 mm) while crack 4 length was (2.6897 mm). At step 24, crack 5 length was equal to (11.6515 mm) and crack 4 length was equal to (6.8379 mm), see figure 5-119. Also, those steps showed that crack 5 had a faster crack

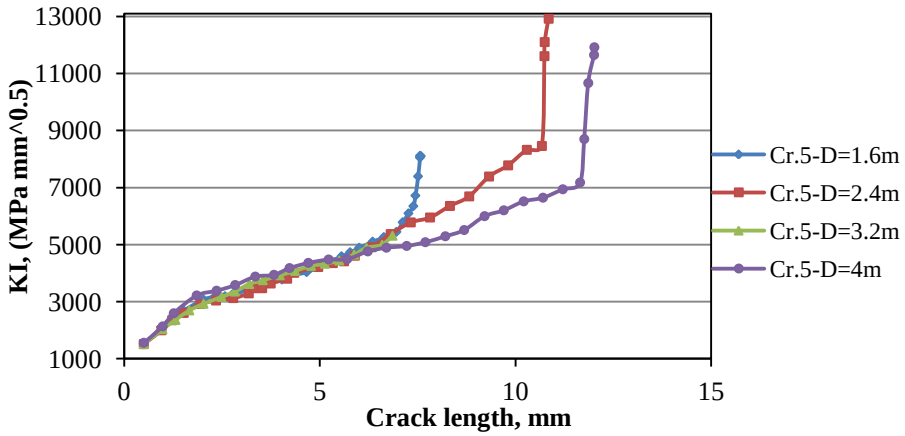

Figure 5-117 SIF histories of crack 5

growing which due to the weakened of the panel at this location of rivet hole 3.

The linking up process occurred between cracks 5 and 4 at step 25, as illustrated in figure 5-120. The coalesced crack which consisted from crack 3 till 6 had new crack fronts (3 and 6). In addition, crack 3 recorded length was (5.2706 mm) and crack 6 length was (9.0414 mm). Figure 5-121 shows the last step of the simulation when D equal to 4 m, the coalesced crack was growing from step 25 till step 33 and the crack 3 reached (8.0936 mm) while crack 6 reached (10.9401 mm) length.

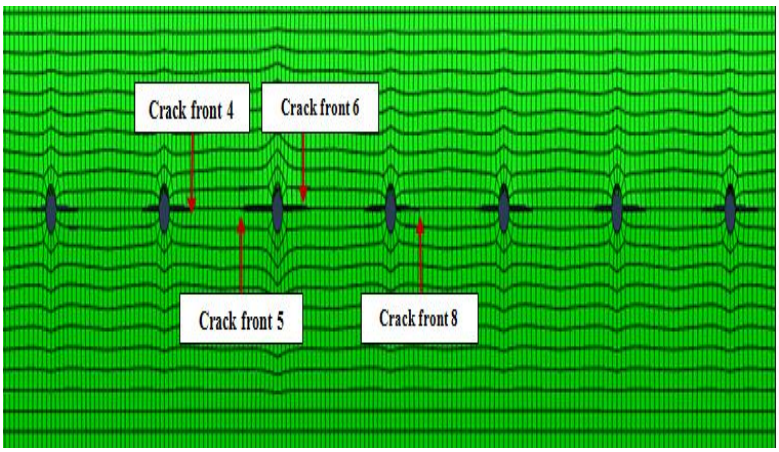

Figure 5-118 XFEM model of MSD panel after cracks opening (step 10 of crack propagation)

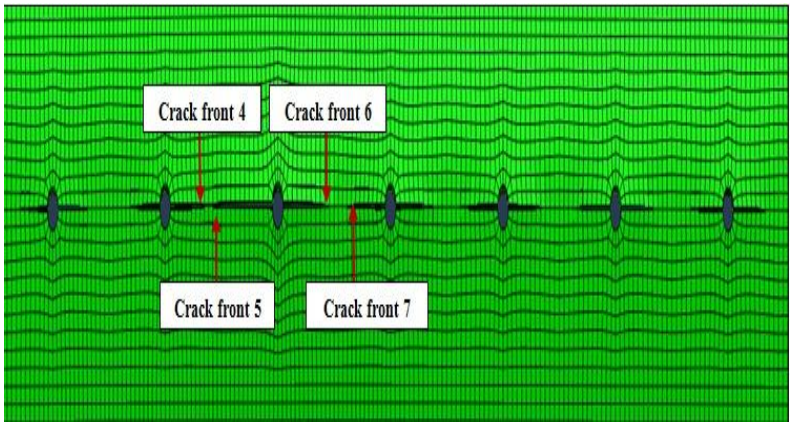

Figure 5-119 XFEM model of MSD panel after cracks opening (step 24 of crack propagation

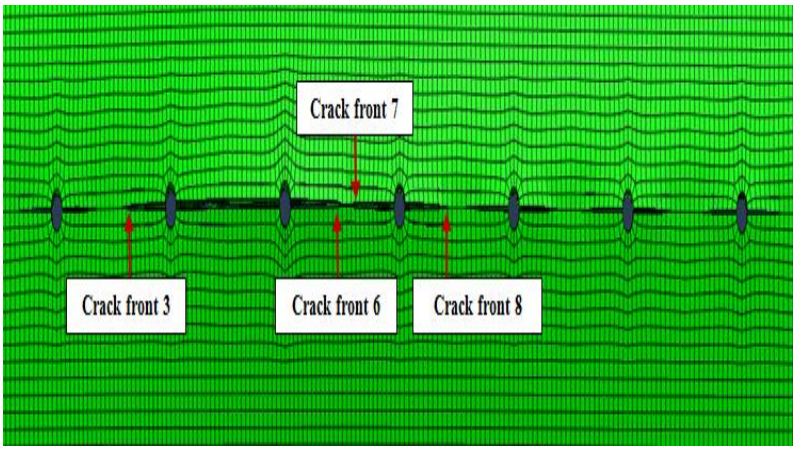

Figure 5-120 XFEM model of MSD panel after cracks opening (step 25 of crack propagation)

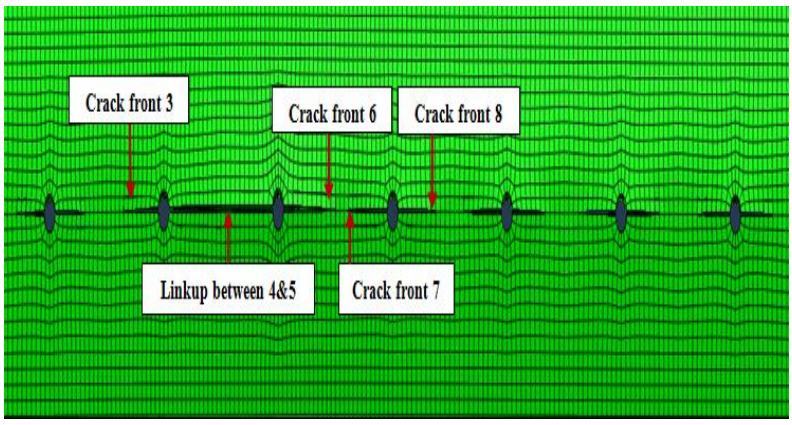

Figure 5-121 XFEM model of MSD panel after cracks opening (step 33 of crack propagation)

5.3.6 SIF evaluation of crack 6 at different fuselage diameters

Figure 5-122 shows the relation between SIF values of crack 6 and its crack length. It also showed the effect of changing fuselage diameters (D) on the growing trend of crack 6. The steep rise in SIFs values occurred in this case when D equal to 1.6 m, 2.4m and 3.2 m at almost the last steps (lower crack propagation with an increase in SIFs values). The longest crack 6 length in this case recorded when D equal to 4 m (CL =11.0046 mm, K_I=12171.3 MPa $\sqrt{mm}$), and it had almost the same length when D equal to 2.4 m (CL =11.0002 mm, K_I=15067.5 MPa $\sqrt{mm}$, average difference=0.04%).The third length was when D equal to 1.6 (CL =10.5727 mm, K_I=10050.1 MPa $\sqrt{mm}$) and the shortest length was when D equal to 3.2 m (CL = 5.7723 mm, K_I=5288.38 MPa $\sqrt{mm}$).

To describe the crack 6 propagation, some mentioned images in the previous section (5.3.5) will be used for this purpose as follows:

Figure 5-118 shows the simulation step 10 when **D** equal to **4 m**, at this step crack 6 length was equal to (4.0161 mm), while crack 7 length which supposed to interact with crack 6 was equal to (2.40402 mm). In figure 5-119 which describes propagation step 24, crack 6 length reached (8.7701 mm) and crack 7 recorded length was (6.31992 mm), a step further (simulation step 25) crack 6 length was (9.0414 mm) and crack 7 length was (6.52152 mm), see figure 5-119. Figure 5-121 shows the simulation step 33, at this step crack 6 length was equal to (10.9401 mm) and crack 7 recorded length was equal to (8.0479 mm). In this case, no linkup occurred between crack 6 and crack 7.

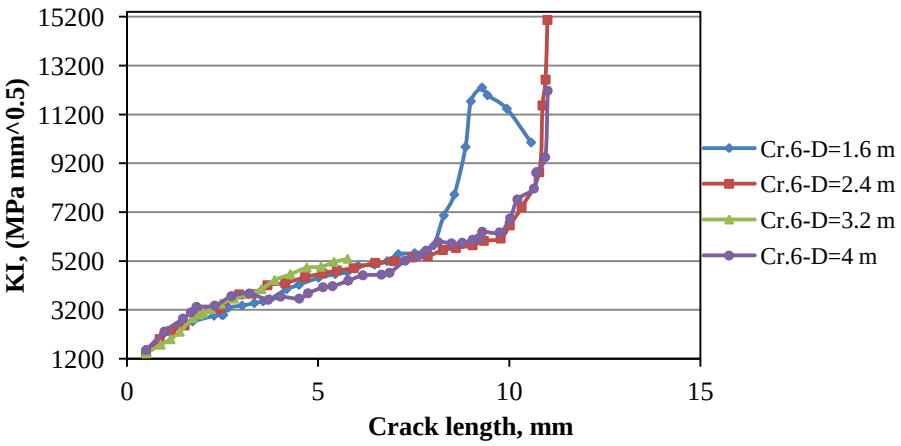

Figure 5-122 SIF histories of crack 6

Additionally, the second long length of crack 6 recorded when **D** equal to **2.4 m**, and some selected images to describe the growing steps of crack 6 and 7 are mentioned in section (5.3.4), figures from 5-114 till 5-116:

Figure 5-114 shows the simulation step 10, crack 6 recorded length was (3.6734 mm) and crack 7 was equal to (3.64773 mm). Figure 5-115 describes the simulation step 18, at this step crack 6 recorded length was equal to (7.4614 mm) and crack 7 was equal to (6.13151 mm). The following image (figure 5-123) represent the step before the linking up step between crack 6 and 7 (step 26), at this step crack 6 length was (10.324 mm) and crack 7 was (8.0569 mm).

The linking up process occurred between crack 6 and 7 at step 27, as illustrated in figure 5-116, and the formed crack consisted from cracks 5, 6, 7 and 8 with two crack fronts (5 and 8). The following images represent some selected simulation steps when **D** equal to **1.6 m**: Figure 5-124 shows the simulation step 20, at this step crack 6 length was equal to (6.81089 mm) and crack 7 was equal to (7.14845 mm).

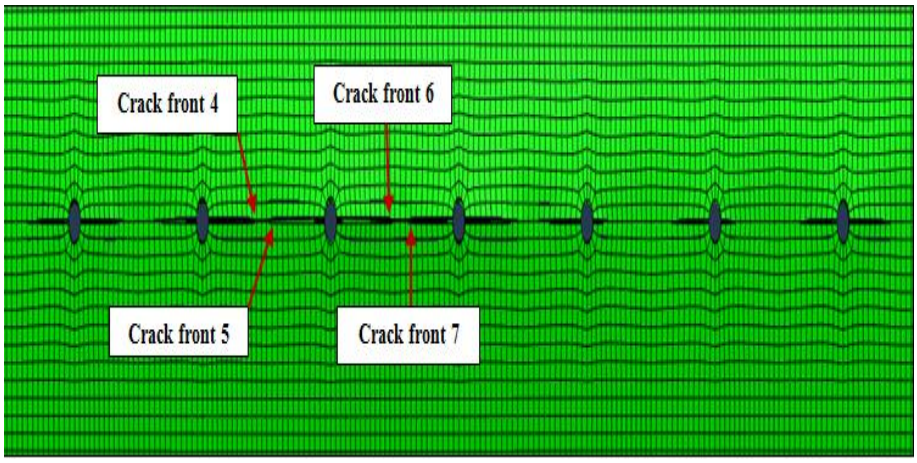

Figure 5-123 XFEM model of MSD panel after cracks opening (step 26 of crack propagation

After five steps, as shown in figure 5-125, crack 6 propagate and reached length of (8.2897 mm) and crack 7 length was equal to (9.397 mm). Crack 8 1nd 9 had a longer crack lengths due to the panel was weaker at the position of between holes 4 and 5(8.4293 mm and 10.1396 mm respectively) then the position between holes 3 and 4.

The first linking up occurred between crack 8 and 9, as illustrated in figure 5-126, at this

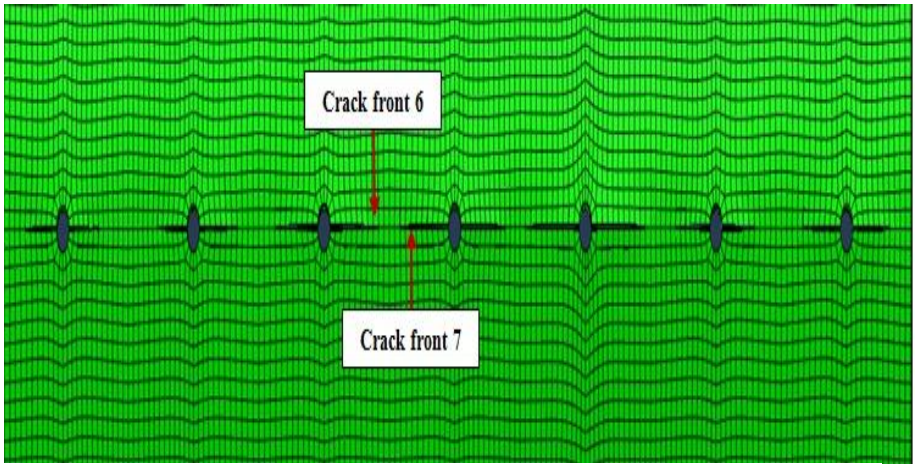

Figure 5-124 XFEM model of MSD panel after cracks opening (step 20 of crack propagation)

step crack 6 recorded length was equal to (8.8569 mm) and crack 7 was equal to (10.3279 mm); this explains why crack 7 had a faster crack growing rate due to crack 7 was closer to first linking location than crack 6. The new formed crack which consisted from cracks 7, 8, 9 and 10 at this step had two crack fronts (7 and 10). The second linkup occurred between cracks 6 and 7, as shown in figure 5-127, now; the coalesced crack which consisted from crack 5 till crack 10 had new crack fronts (5 and 10).

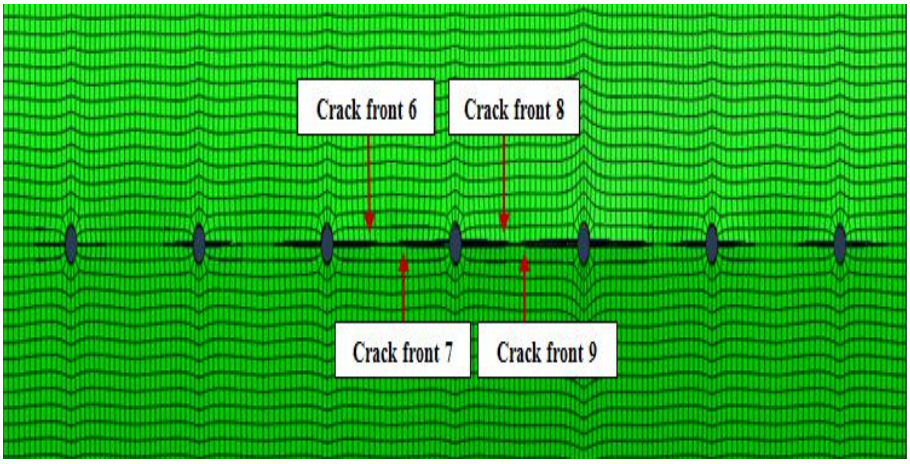

Figure 5-125 XFEM model of MSD panel after cracks opening (step 25 of crack propagation)

Figure 5-128 shows the last simulation step in this case, it showed the coalesced crack was consisted from crack 5, 6,7,8,9 and 10. The total recorded length for the formed crack was equal to (73.8937 mm).

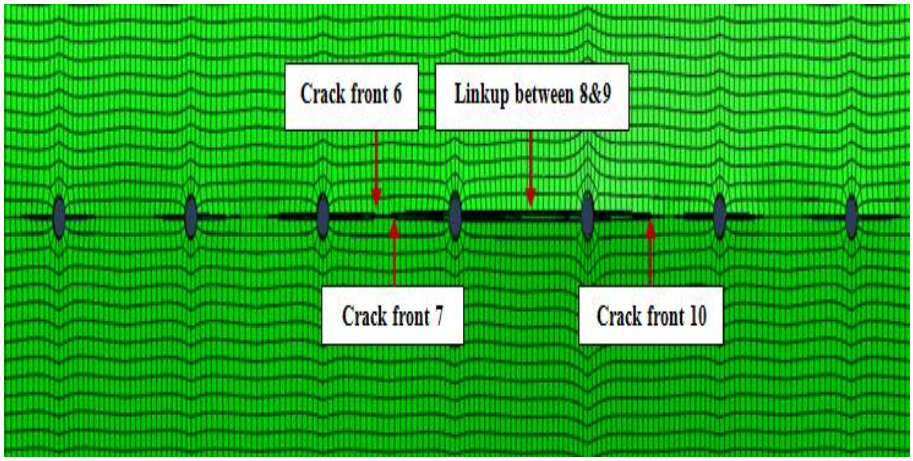

Figure 5-126 32 XFEM model of MSD panel after cracks opening (step 27 of crack propagation)

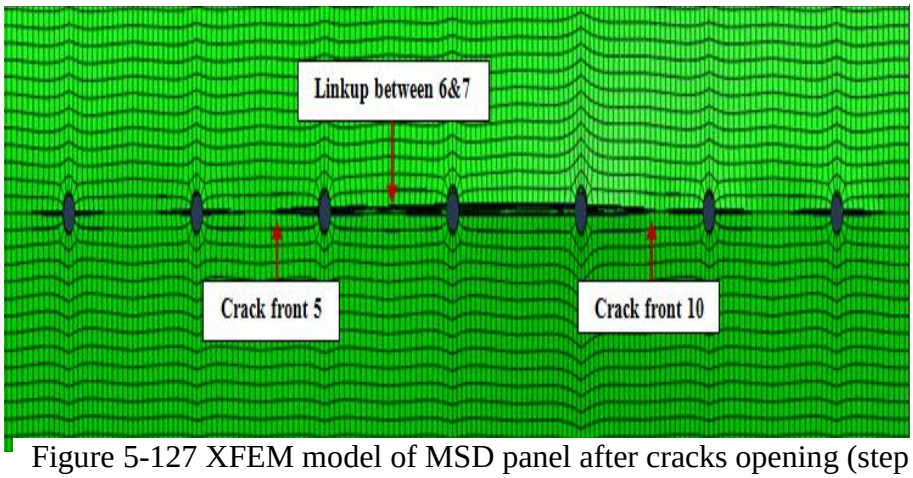

Figure 5-127 XFEM model of MSD panel after cracks opening (step 28 of crack propagation)

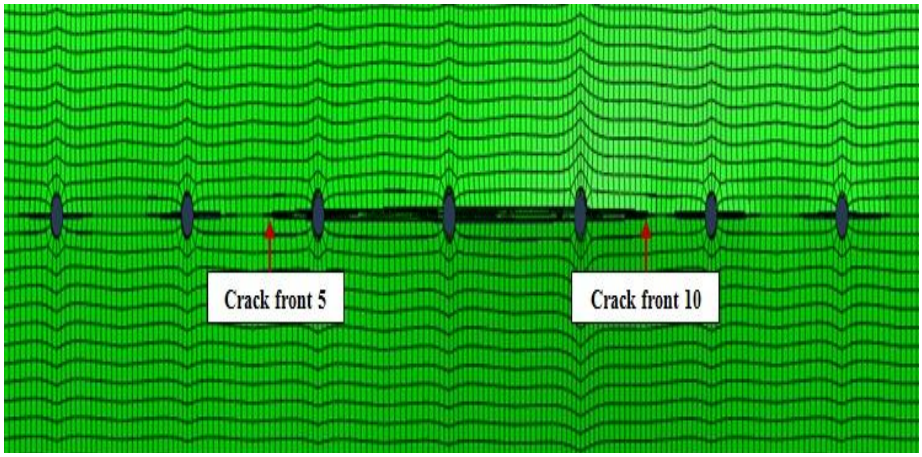

Figure 5-128 XFEM model of MSD panel after cracks opening (step 32 of crack propagation)

5.3.7 SIF evaluation of crack 7 at different fuselage diameters

Figure 5-129 shows the relationship between SIF histories of crack 7 as the crack grows; it showed that the steep rise in crack 7 SIFs values occurred at almost the ten last simulation steps except for the case of D equal to 3.2 m. Also, the figure illustrates the effect of changing the fuselage diameters to 1.6, 2.4, 3.2 and lastly to 4 m on crack growing trend. The longest crack 7 length recorded when D was equal to 1.6 m (11.178 mm, KI=15185.9 MPa$\sqrt{mm}$), followed by its length when D was equal to 2.4 m (9.279 mm, KI=16988.1 MPa$\sqrt{mm}$), then when D was equal to 4 m (8.04779 mm, KI=9776.01 MPa$\sqrt{mm}$). The shortest crack 7 length recorded when D was equal to 3.2 m (7.38939 mm, KI=5597.81 MPa$\sqrt{mm}$).

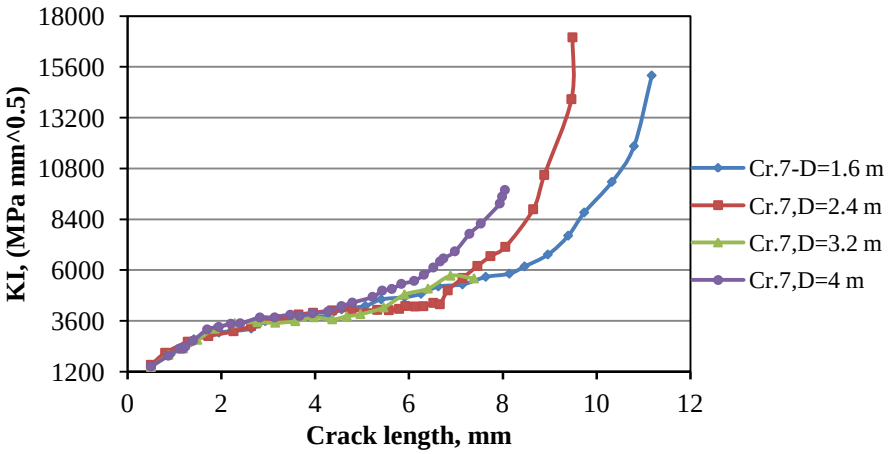

Figure 5-129 SIF histiries of crack 7

For more extensively explanation of crack 7 growing steps, here below some selected simulation steps when **D** equal to **1.6m**: Figure 5-130 shows the simulation step 20, at this step crack 7 reached length was (7.14245 mm) while crack 6 length was (6.8089 mm). Five steps further, as it can be seen in figure 5-131, crack 7 extended and reached length of (9.3976 mm) and crack 6 length was equal to (8.2897 mm). Also, at this step crack 8 length was equal to (8.4293 mm) and crack 9 was equal to (10.1396 mm).

Figure 5-132 shows the simulation step 27, at this step the first linking up process occurred between cracks 8 and 9 to form new crack which consisted from cracks 7, 8, 9 and 10; at this step crack 7 length was equal to (10.3279 mm) and crack 6 was (8.8569 mm).

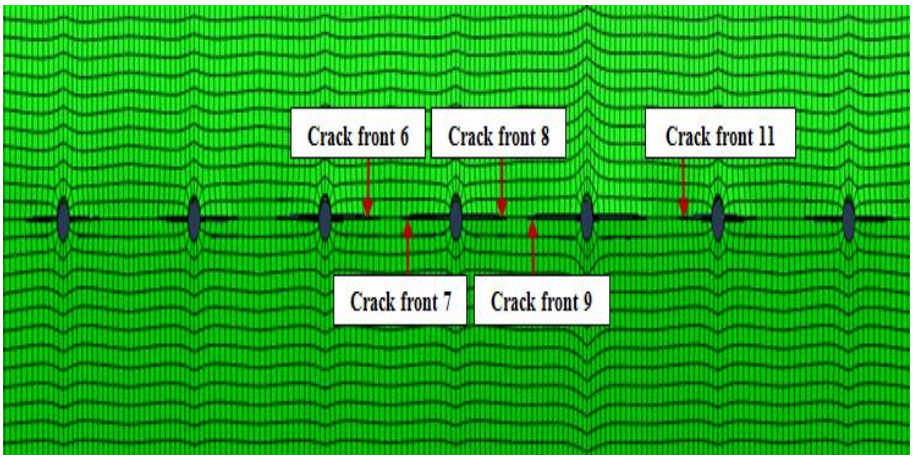

Figure 5-130 XFEM model of MSD panel after cracks opening (step 20 of crack propagation)

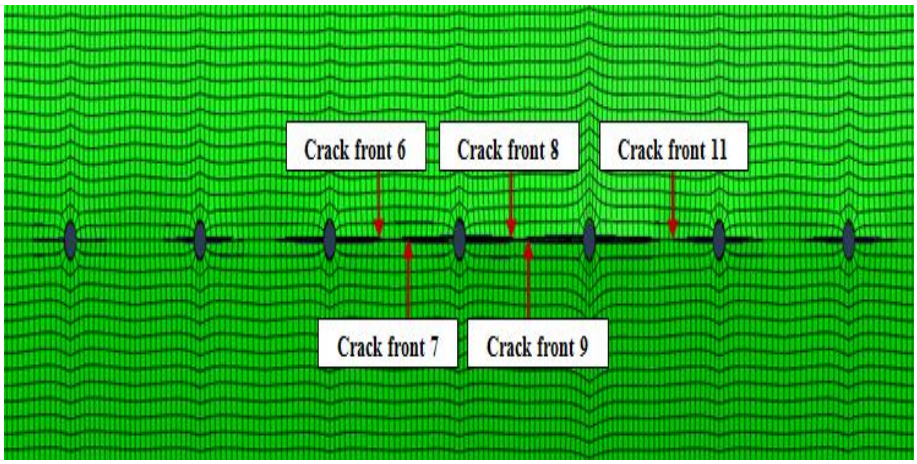

Figure 5-131 XFEM model of MSD panel after cracks opening (step 25 of crack propagation)

The second linkup process occurred at step 28 between crack 6 and 7, now the coalesced crack consisted from crack 5, 6, 7, 8, 9 and 10 and the total length for the new crack was (73.4477 mm), see figure 5-133.

Figure 5-134 shows the last step of the simulation; at this step, the coalesced crack length was equal to (73.8937 mm). Additionally, it worth to mention that the interaction between

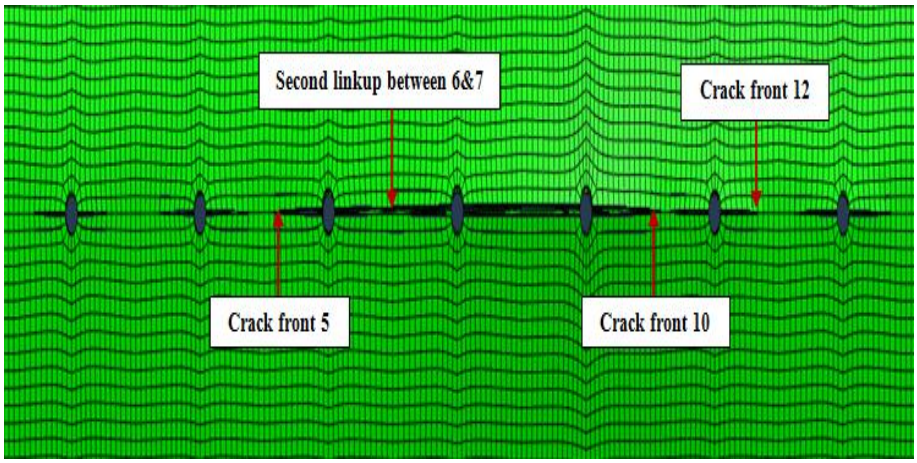

Figure 5-132 XFEM model of MSD panel after cracks opening (step 27 of crack propagation)

.

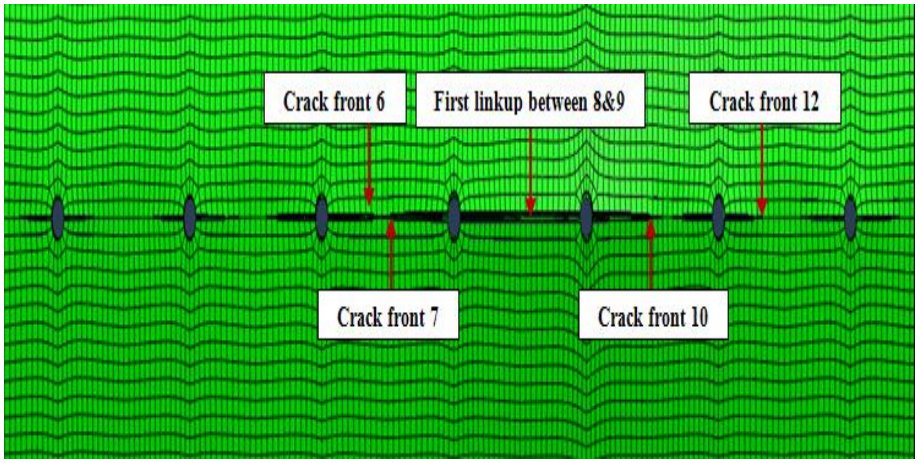

Figure 5-133 XFEM model of MSD panel after cracks opening (step 28 of crack propagation)

crack fronts occurred two times in this simulation (the interaction between crack fronts 6 and 7and the interaction between crack fronts 8 and 9).

Section (5.3.4) illustrates simulation steps of crack 7 growth rate also, where figure 5-114 shows the simulation step 10, at this step crack 7 length was (3.64773 mm) while crack 6 was (3.6734 mm). The whole cracks will continue to grow till the panel losses its strength and fail at the end of the simulation; figure 5-115 shows step 18 where crack 7 reached (6.13151 mm) length and crack 6 length was equal to (7.4614 mm). The first linkup

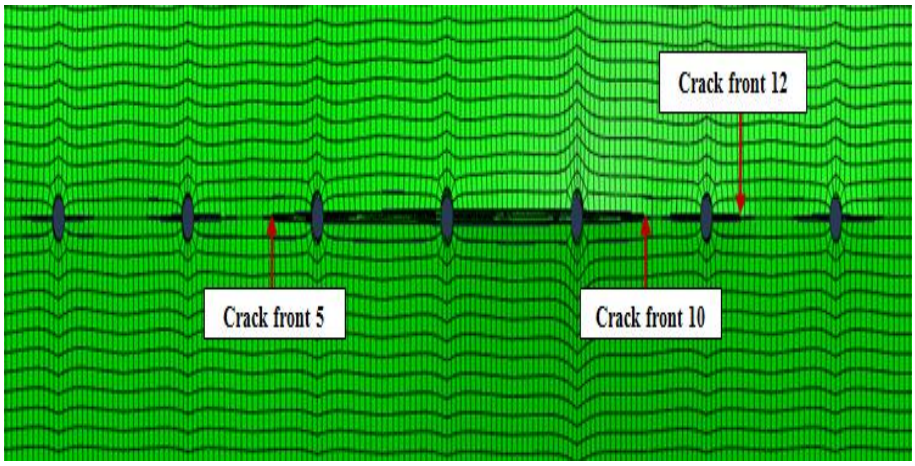

Figure 5-134 XFEM model of MSD panel after cracks opening (step 32 of crack propagation)

occurred in this simulation between cracks 7 and 6 at step 27, as illustrated in figure 5-116. The linkup resulted in a lead crack of total length of (49.3667 mm).

Figures from figures 5-118 until 5-121 in section (5.3.5) explain the growing steps of crack 6 and 7 when D was equal to 4 m; Figure 5-118 shows step 10 of cracks propagation where crack 7 length was equal to (4.0161 mm) while crack 6 was equal to (2.40402 mm). Figure 5-120 shows the first linkup occurred in this case between cracks 4 and 5, crack 7 length was equal to (6.52152 mm) and crack 6 was (9.0414 mm). The last simulation step illustrated in figure 5-121 where crack 7 length was equal to (8.0479 mm) and crack 6 was (10.9401 mm), crack 6 was longer than 7 because crack 6 was closer to linkup location (the weakest area).

The linking up process, in this case, occurred one time (between crack 3 and 4). Figure 5-1358 shows the last simulation step (step 18) when **D** was equal to **3.2 m**, in this case, no linkup between the cracks occurred and the final length of crack 7 was equal to (7.38939 mm) and crack 6 length was (5.7723 mm).

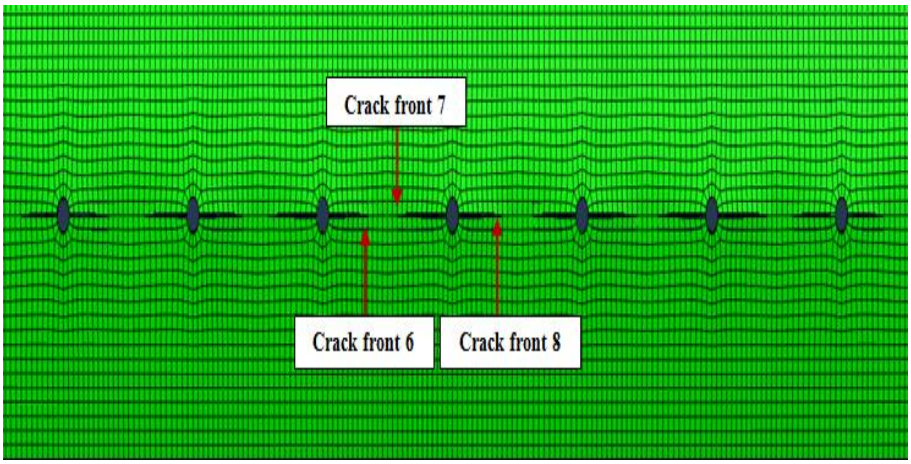

Figure 5-135 XFEM model of MSD panel after cracks opening (step 18 of crack propagation)

5.3.8 SIF evaluation of crack 8 at different fuselage diameters

Figure 5-136 shows the simulation results of crack 8 at different fuselage diameters, it showed the relationship between crack length and the corresponded SIF values for every crack propagation increment. Also, it can be seen in the figure the longest crack 8 length recorded when D was equal to 2.4 m (CL =12.1676 mm, K_I=16035.7 MPa$\sqrt{mm}$), followed by its length when D was equal to 1.6 m (CL =9.1887 mm, K_I=11830.9 MPa$\sqrt{mm}$).

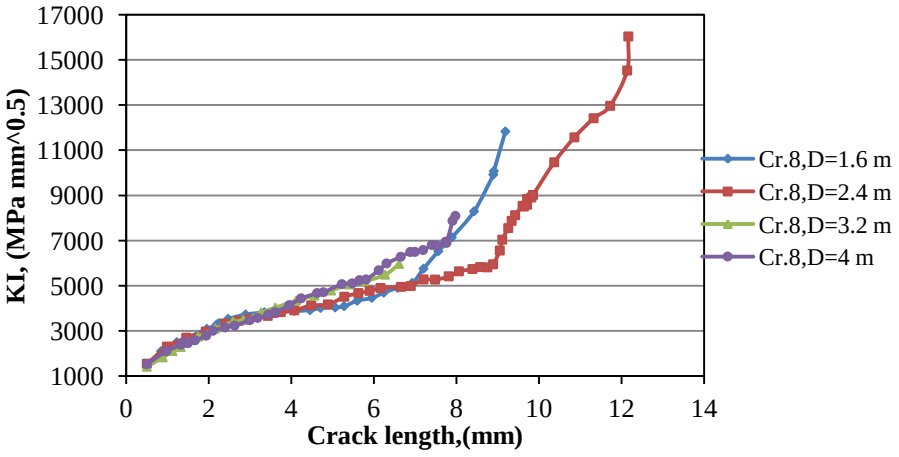

Figure 5-136 SIF histories of crack 8

Also, the documented simulation results showed that mode I was the dominant to the failure mode due to K_I had the highest values compared to the other SIFs values (K_{II} and

K_{II}). For more explanation of crack 8 growing steps when **D** equal to **2.4 m**, the following Images describe some selected simulation steps to crack 8 and crack 9 which are considered as adjacent crack: figure 5-137 illustrates step 20 of crack propagation, at this step crack 8 length was equal to (7.20563 mm), while the adjacent crack (crack 9) length was equal to (5.441 mm).

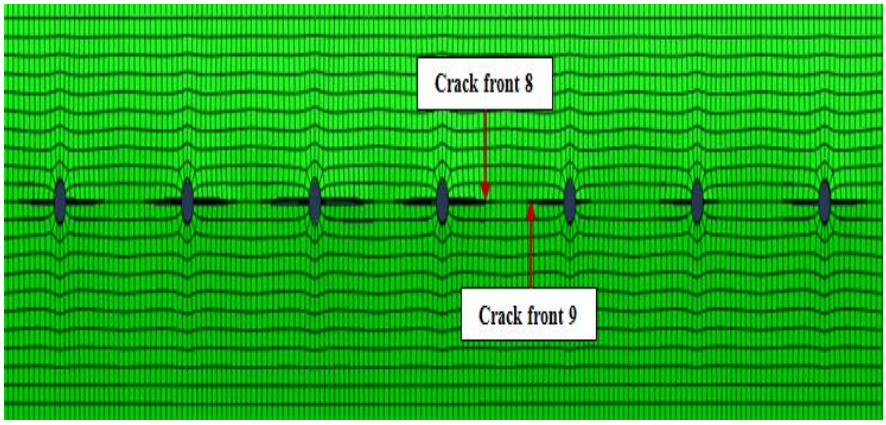

Figure 5-137 XFEM model of MSD panel after cracks opening (step 20 of crack propagation)

The first and the second linkup process between cracks 4, 5 and 6, 7 occurred at step 27 and 28 and 29 respectively, as shown in figure 5-138. At this step crack 8 length was (9.053 mm) and crack 9 length was (6.1732 mm). It's clear from the past figures that crack 8 had a faster crack growing because it was closer than crack 9 to the linking up location (the weakest location on the panel).

Figure 5-139 shows propagation step 42, at this step crack 8 reached length was (11.7283 mm) and crack 9 length was equal to (7.4276 mm).

Figure 5-101 in section (5.3.1) illustrates the simulation step 44; the linking up process occurred between cracks 8 and 9 at this step. The coalesced crack which consisted from cracks 3 till 10 had a total length of (89.5114 mm) at this step.

In the previous section (5.3.7), figures 5-130, 5-131 and 5-132 illustrate some selected simulation images also fro crack 8 and 9 when **D** equal to **1.6** m as following:

Figure 5-130 shows step cracks propagation 20, at this step crack 8 length was equal to (6.57664 mm) and crack 9 was equal to (8.0643 mm); five step further, as shown in figure

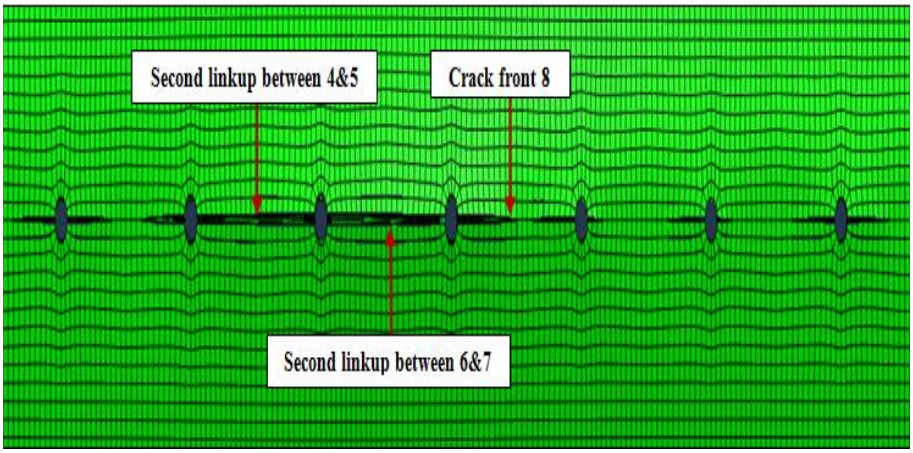

Figure 5-138 XFEM model of MSD panel after cracks opening (step 29 of crack propagation)

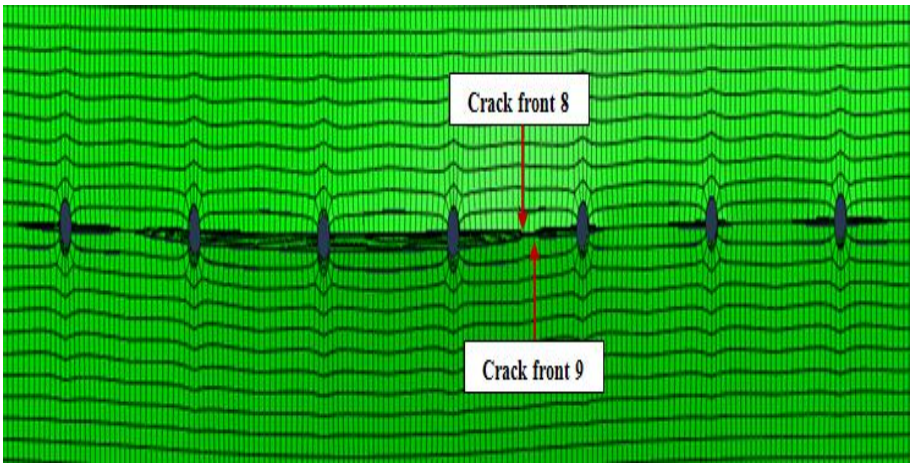

Figure 5-139 XFEM model of MSD panel after cracks opening (step 42 of crack propagation)

5-131 which illustrates the simulation step 25, crack 8 length was equal to (8.4293 mm) and crack 9 was equal to (10.1396 mm). The linking up process occurred between cracks 8 and 9 at step 44, as it can be seen in figure 5-132. The total length of the formed crack at this step was equal to (51.2356 mm).

In addition, the third longest length recorded to crack 8 when **D** was equal to **4** m, figures from 5-118 to 5-121(section 5.3.5) could be used also to describe the growing step of cracks 8 and 9. As it can be seen in figure 5-118 which shows the simulation step 10 crack length was equal to (2.62622 mm) and crack 9 was equal to (2.7213 mm), after some steps

as shown in figure 5-120 crack 8 had a longer length (6.65199 mm and crack 9 length = 6.414 mm) due to the linking up between cracks 4 and 5. Figure 5-121 describes the last step of the simulation (step 33), at this step crack 8 reached a length of (7.907 mm) and crack 9 was equal to (7.1558 mm).

The shortest crack 8 length was when D equal to 3.2m and figure 5-135 shows the last simulation step (step 33), at this step crack 8 length was (6.61181 mm) and crack 9 length was (6.3109 mm).

5.3.9 SIF evaluation of crack 9 at different fuselage diameters

The figure bellow shows the relationship between crack 9 length and the corresponding values of SIF, it showed that there was a steep rise in SIF values compared to the crack extension especially when D was equal to 2.4 m. Additionally, as it can be seen in the figure the longest crack 9 length recorded when D was equal to 1.6 m (CL =10.937 mm, K_I=12947.6 MPa$\sqrt{mm}$). The second longest length recorded in this simulation when D was equal to 2.4 m (CL =8.0461 mm, K_I=16135 MPa$\sqrt{mm}$). The shortest crack 9 length recorded when D was equal to 3.2 m (CL =6.3109 mm, K_I=4694.18 MPa$\sqrt{mm}$).

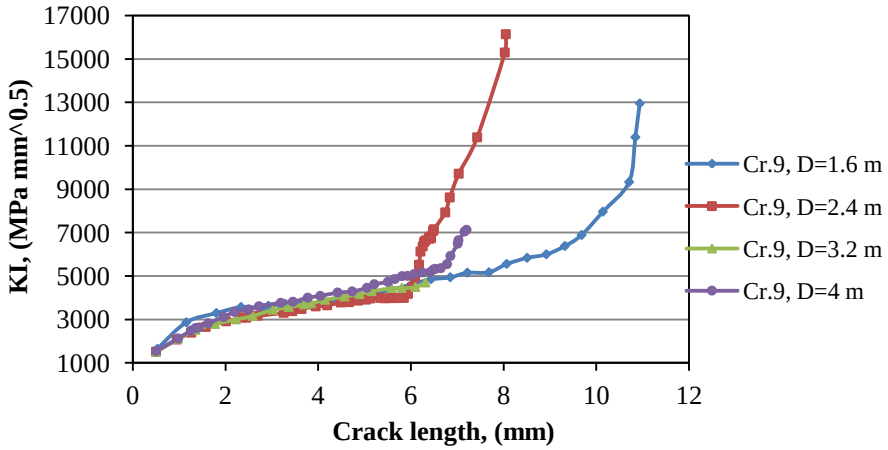

Figure 5-140 SIF histories of crack 9

To show more extensive illustration of crack 9 propagation steps, some selected simulation images in section (5.3.7) could be used also here to describe crack 9 growing behavior (**D=1.6 m**) as following: Figure 5-130 shows the simulation step 20, at this step crack 9

length was equal to (8.0643 mm) while crack 8 length was equal to (6.57664 mm). When the simulation continued and reach step 25 as shown in figure 5-131 crack 9 recorded length was (10.1396 mm) while crack 8 length was (8.4293 mm); the linking up process between both cracks occurred at step 27 the formed crack total length was equal to (51.2356 mm). The second crack 9 long length recorded when **D** equal to **2.4 m** and some selected images from the previous section could be used to illustrate the extension steps of crack 9 as following:

By step 20, crack 9 recorded length was (5.441 mm) and crack 8 was (7.20563 mm), see figure 5-137 section (5.3.8). After nine steps from the previous step as illustrated in figure 7.44, crack 8 had a faster growth rate than crack 9 as subsequent to the first and second linking up process; where crack 9 was equal to (6.2053 mm) and crack 8 length was (9.1129 mm).

Figure 5-139 also illustrates the simulation step 42, crack 9 length was equal to (7.4276 mm) in this step and crack 8 length was (11.7283 mm). Again, at this step, the linking up processes produced on lead crack consisted of cracks 3 to 8 and the total length was equal to (75.0137 mm). Figure 5-101 in section (5.3.1) shows the simulation step 44; the linking up process occurred between cracks 8 and 9 at this step. The coalesced crack which consisted from cracks 3 till 10 had a total length of (89.5114 mm) at this step. The simulation steps and images of crack 9 when fuselage diameters (D) equal to 3.2m and 4m illustrated previous section (5.3.8).

5.3.10 SIF evaluation of crack 10 at different fuselage diameters

Obviously, the longest crack 10 length recorded in this simulation was when D equal to 1.6 m (CL =11.5149 mm, K_I=10830 MPa$\sqrt{mm}$), and the shortest was when D equal to 2.4 m (CL = 1.1603 mm, K_I=2018.57 MPa$\sqrt{mm}$). The recorded crack 10 length when D equal to 3.2 was (CL = 6.92 mm, K_I=5520.88 MPa$\sqrt{mm}$), while the crack length was equal to (6.4447 mm, K_I=6313.57 MPa$\sqrt{mm}$) when D was equal to 4 m, see figure 5-141.

It is worth to mention that crack 10 when D equal to 2.4 m had two growing steps only, and the documented results showed, in this case, all failure modes (K_I, K_{II} and K_{III}) had minus signs. Also the rest results which related to D equal to 1.6 m, 3.2 m and 4 m K_I was the

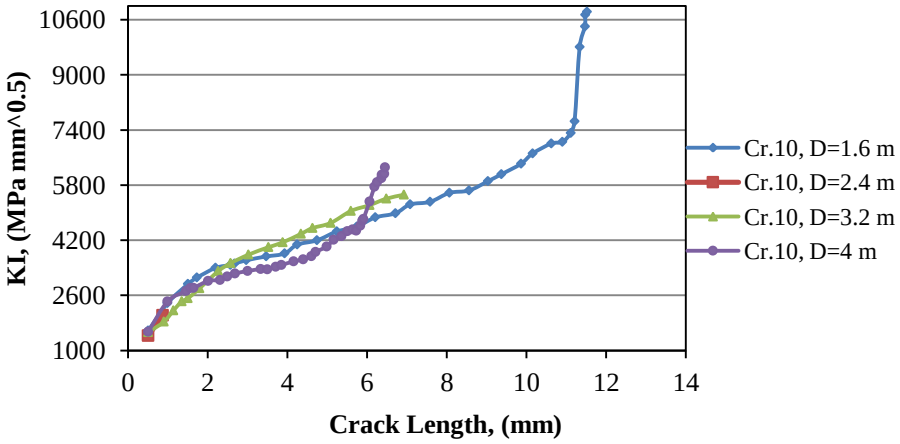

Figure 5-141 SIF histories of crack 10

dominant to the failure mode (mode I) with existence effect of K_{II} and K_{III} in some simulation steps. For more extensive description of crack growing step, here below some selected simulation images: Figure 5-142 shows the simulation step 28; crack 10 length was equal to (11.2055 mm) while crack 11 was equal to (5.7004 mm). Crack 10 had faster crack growing rate than crack 11 due to the linking up process which occurred in the previous step (step 27) between cracks 8 and Figure 5-143 illustrates the last simulation step (step 32) where crack 10 reached length of (11.5149 mm) and crack 11 length was equal to (5.8405 mm). The total length of the formed crack was equal to (73.8937 mm)

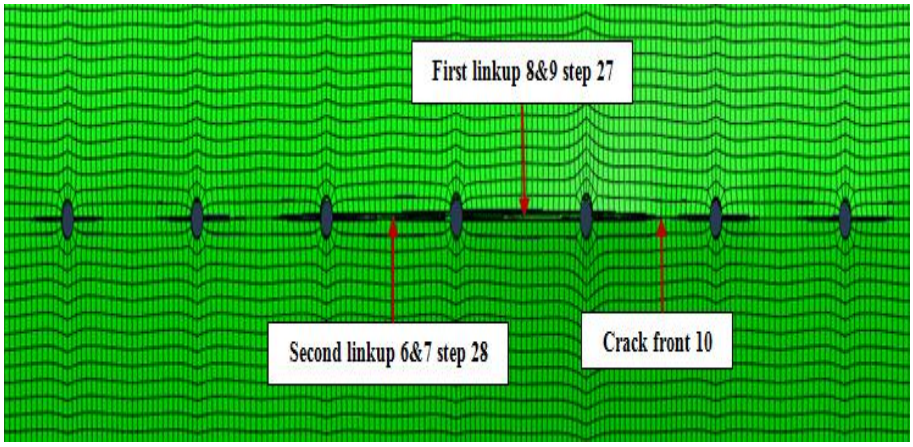

Figure 5-142 XFEM model of MSD panel after cracks opening (step 28 of crack propagation)

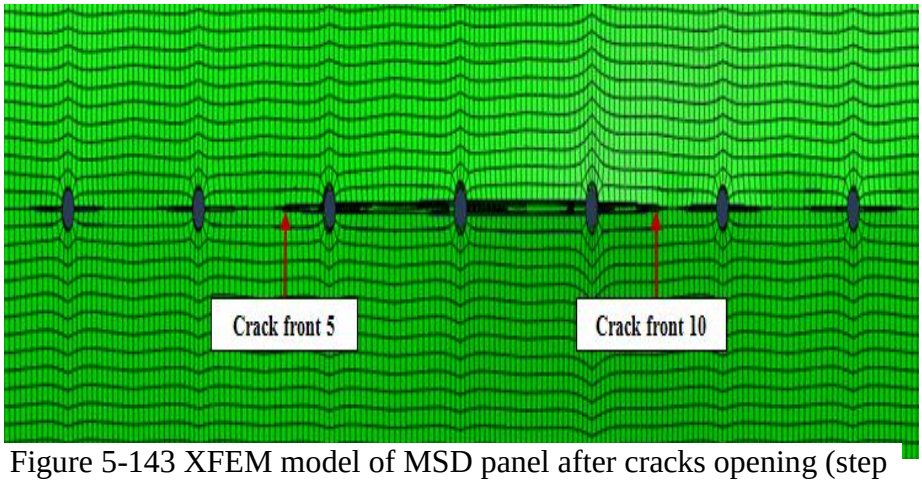

Figure 5-143 XFEM model of MSD panel after cracks opening (step 32 of crack propagation)

The second long recorded crack 10 length was when **D** equal to **3.2 m**, no linking up occurred in this case at it can observed in figure 5-144; Crack 10 recorded length was equal to (6.92 mm) while crack 11 was equal to (7.096 mm).

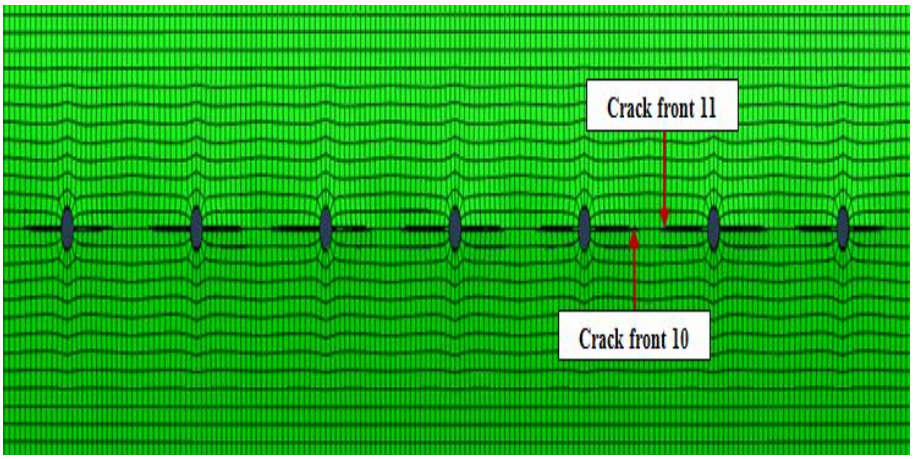

Figure 5-144 XFEM model of MSD panel after cracks opening (step 18 of crack propagation)

The following images describe the third case (**D=4 m**) of crack 10 length, there is no interaction or linking up occurred between cracks 10 and 11:

Figure 5-145 shows the simulation step 20 which crack 10 recorded length was equal to (5.1539 mm) and crack 11 length was (5.6283 mm).

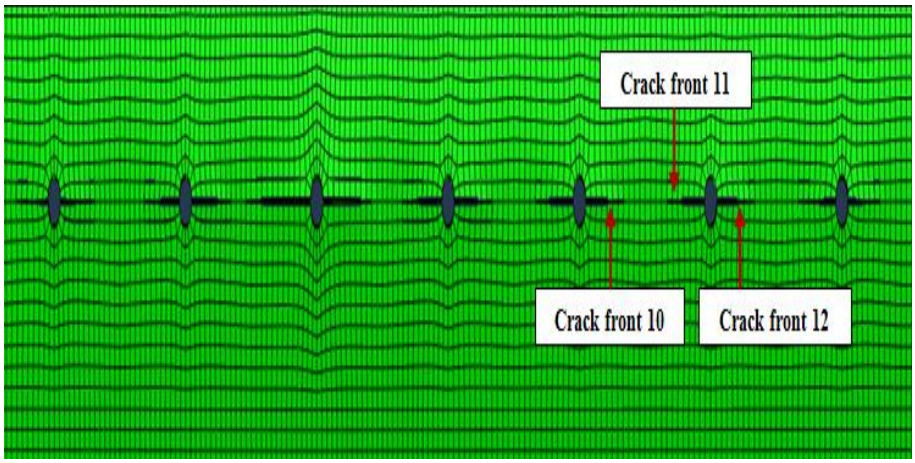

Figure 5-145 XFEM model of MSD panel after cracks opening (step 20 of crack propagation

At step 25, as illustrated in figure 5-146, crack 10 length was equal to (5.8244 mm) and crack 11 was equal to (6.5241 mm). Also, at this step, the linking up process occurred between cracks 4 and 5 to form crack consisted from cracks 3 till 6.

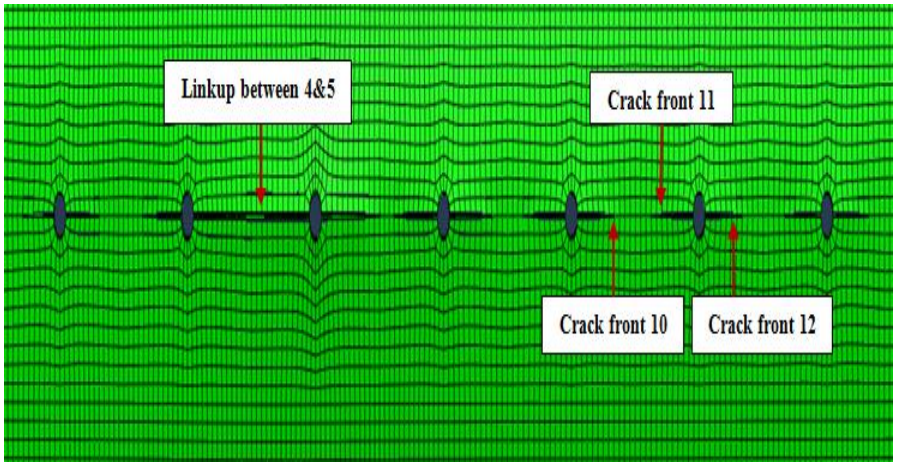

Figure 5-146 XFEM model of MSD panel after cracks opening (step 25 of crack propagation)

Crack 10 reached (6.4264 mm) at the end the simulation while crack 11 was equal to (6.9987 mm), see figure 5-147. The total length of the formed crack which had two crack fronts (3 and 6) was equal to (44.8718 mm).

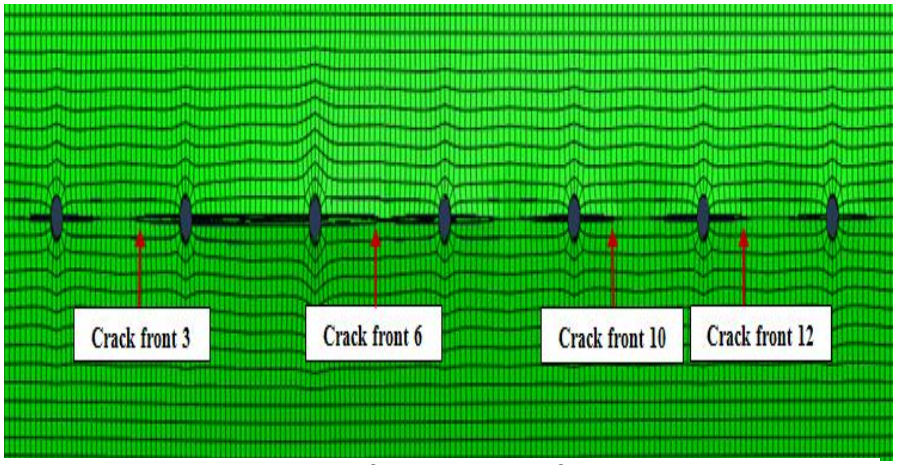

Figure 5-147 XFEM model of MSD panel after cracks opening (step 32 of crack propagation)

The figure below shows the last step of the simulation (step 142) when **D** was equal to **2.4 m**, the final length reached by crack 10 was equal to (1.1603 mm) and crack 11 was equal to (9.2839 mm), see figure 5-148.

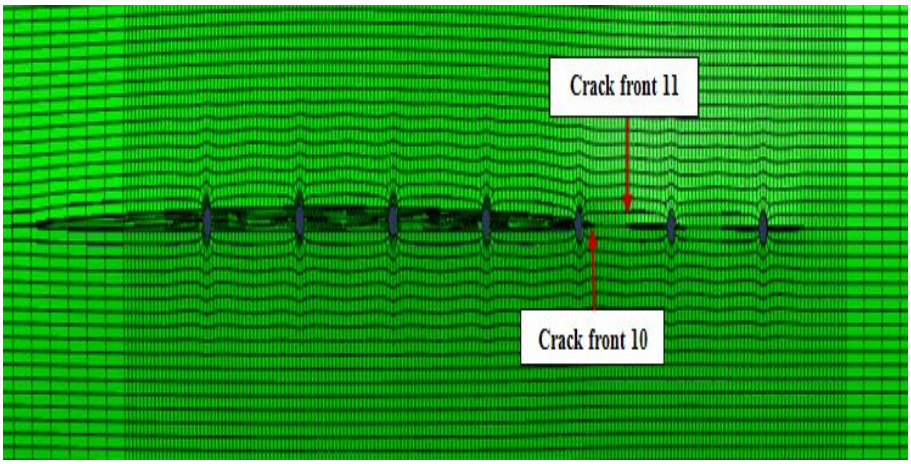

Figure 5-148 XFEM model of MSD panel after cracks opening (step 142 of crack propagation)

5.3.11 SIF evaluation of crack 11 at different fuselage diameters

It can be observed from figure 5-149 that the longest crack 11 recorded length was when D equal to 2.4 m (CL =9.329 mm, K_I=9467.41 MPa$\sqrt{mm}$), while the shortest length recorded

when D was equal to 1.6 m (CL =7.096 mm. K_I=7422.59 MPa$\sqrt{mm}$); crack 11 had almost the same length when D was equal to 4 m (CL =7.0187 mm, K_I=5393.55 MPa$\sqrt{mm}$), compared to its length when D was equal to 3.2 m (CL =7.096 mm, K_I=5393.35 MPa$\sqrt{mm}$).

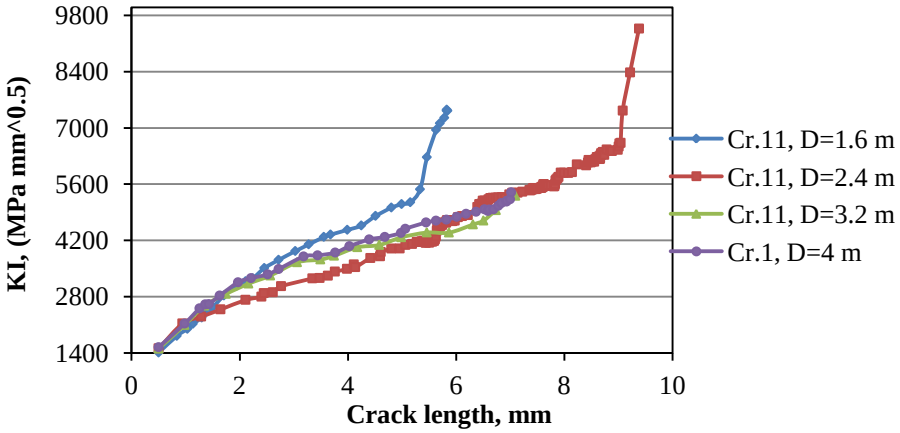

Figure 5-149 SIF histories of crack 11

Additionally, the documented results of the simulation showed that K_I was dominant to the failure mode (mode I) with the existence effect of K_{II} and K_{III} in the most simulation steps. To extensively explanation for crack 11 growing steps, the figures which mentioned in section (5.3.1) show the growing steps as following:

Figure 5-100 shows the simulation step 28 when D equal to 2.4 m, crack 11 recorded length at this step was equal to (5.437 mm), while crack 10 length was equal to (1.1603 mm). Also, in this step two linking up process occurred between cracks from 3 till 8 to form one new crack with crack fronts 3 and 8. Figure 5-101 illustrates the simulation step 44, at this step crack 8 and 9 linked up and the formed crack now had new crack fronts (3 and 9); crack 11 length reached (5.6439 mm) while crack 10 had the same previous length (not growing).

The fourth linking up process occurred at step 54 between cracks 2 and 3 as shown in Figure 5-102, now the lead crack had two new crack fronts 1 and 10. At this step crack 11 length was equal to (5.8324 mm) and crack 10 was equal to (1.1603 mm). After 46 steps (step 100), crack 11 recorded length was equal to (7.6692 mm) while crack 10 was not growing. It observed that crack 11 had a slow crack growing rate (2.2272 mm for 72 steps)

due to the weakest location in the panel located at the position of rivet holes from 1 till 4.
Figure 5-104 shows the last step in the simulation (step 143), crack 11 recorded length was (9.3829 mm) while crack 10 had the same crack length (1.1603 mm).
In the case of **D** equal to **3.2 m**, no linkup occurred between the whole cracks as shown in figure 5-150. At the last simulation step (step 18) crack 11 length was equal to (7.096 mm) and crack 10 length was equal to (6.92 mm)
The growing steps of crack 11 when **D** equal to **4 m** is illustrated in the figures from 5-145 until 5-147 in the previous section (5.3.10).
By considering the second longest crack 11 length was when D equal to **1.6 m**, section (5.3.7) also gives detailed description of crack 11 growing steps as following:
Crack 11 length changed from (4.2474 mm), (5.3332 mm) and to (5.6297 mm) at the simulation steps 20, 25, and 27. At step 27 the first linking up process occurred between cracks 8 and 9, see figures 5-130, 5-131 and 5-132. Crack 10 had a faster crack growing and it reached (11.1077 mm) at step 27 because it was closer to the weakest location in the panel than crack 11. Also, figure 5-133 describes the simulation step 27, the second linkup occurred at this step between cracks 6 and 7 and crack 11 length was equal to (5.7004 mm) while crack 10 length was equal to (11.2055 mm). Figure 5-134 illustrates the simulation step 32; crack 11 length was (5.8405 mm) while crack 10 was equal to (11.5149 mm). There is no linking up process between crack 11 and 10 occurred in this simulation and the formed crack length was equal to (73.8937 mm) with two crack fronts 5 and 10.
By considering the second longest crack 11 length was when D equal to **1.6 m**, section (5.3.7) also gives detailed description of crack 11 growing steps as following:
Crack 11 length changed from (4.2474 mm), (5.3332 mm) and to (5.6297 mm) at the simulation steps 20, 25, and 27. At step 27 the first linking up process occurred between cracks 8 and 9, see figures 5-130, 5-131 and 5-132. Crack 10 had a faster crack growing and it reached (11.1077 mm) at step 27 because it was closer to the weakest location in the panel than crack 11. Also, figure 5-133 describes the simulation step 27, the second linkup occurred at this step between cracks 6 and 7 and crack 11 length was equal to (5.7004 mm) while crack 10 length was equal to (11.2055 mm). Figure 5-134 illustrates the simulation step 32; crack 11 length was (5.8405 mm) while crack 10 was equal to (11.5149 mm).

There is no linking up process between crack 11 and 10 occurred in this simulation and the formed crack length was equal to (73.8937 mm) with two crack fronts 5 and 10.

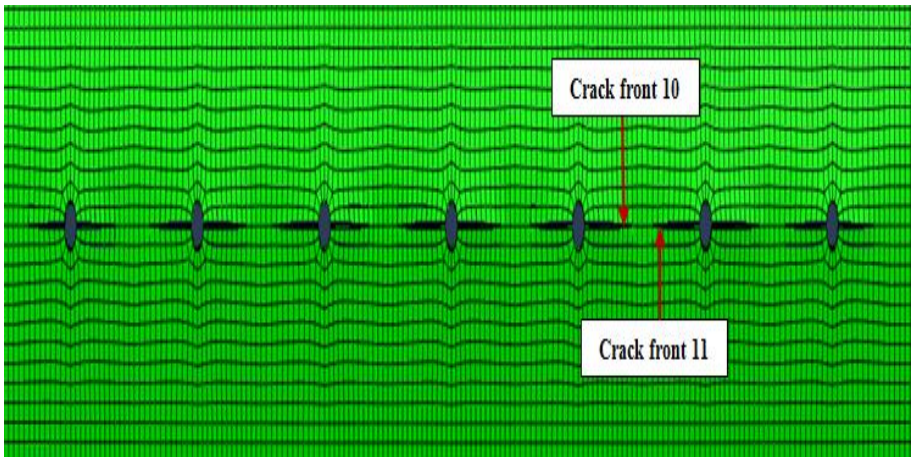

Figure 5-150 XFEM model of MSD panel after cracks opening (step 18 of crack propagation)

5.3.12 SIF evaluation of crack 12 at different fuselage diameters

Figure 5-151 shows SIF histories according to the change of fuselage diameters from 1.6, 2.4, 3.2, and 4 m, it observed that as the crack grows as SIFs values increases, especially in the case of D equal to 1.6 where the highest SIFs values recorded shorter crack length compared to when D equal to 3.2 m and 4 m. The shortest crack 12 length recorded when D was equal to 2.4 m (CL =0.8638 mm, K_I=2017.71 MPa$\sqrt{mm}$), while the longest was when D equal to 3.2 m (CL =7.8741 mm, K_I=5267.1 MPa$\sqrt{mm}$). At the end of the simulation the documented crack 12 length when D equal to 1.6 m was (5.9873 mm, KI=6435.89 MPa$\sqrt{mm}$), and it was equal to (6.2169 mm, K_I=4802.23 MPa$\sqrt{mm}$) when D was equal to 4 m.

In addition, the simulation results showed that mode I was still the dominant to the failure mechanism with existence effect to mode II and mode III in some simulation steps. For more explanation to the growing steps of the longest crack 12 length (D=**3.2**), here below some selected simulation images:

Figure 5-152 shows simulation step 6, at this step crack 12 recorded length was equal to (2.7372 mm) and crack 13 was equal to (2.9104 mm).

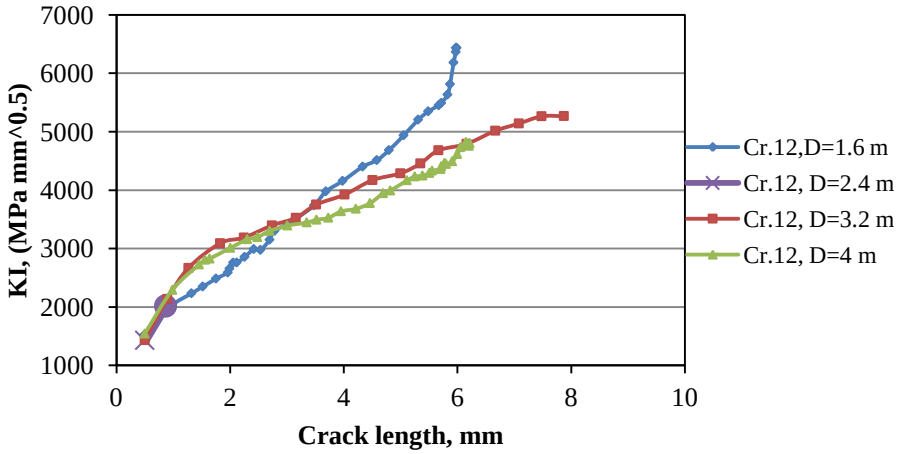

Figure 5-151 SIF histories of crack 12

After more six steps (step 12), crack 12 extended and reach length (5.3489 mm) while crack 13 length was equal to (4.7833 mm), see figure 5-153. Figure 7-154 shows the last step of the simulation (step 18), the final crack 12 length was equal to (7.8741 mm) and crack 13 was equal to (6.1187 mm). It is worth to mention that there is no linking between the adjacent cracks in this case.

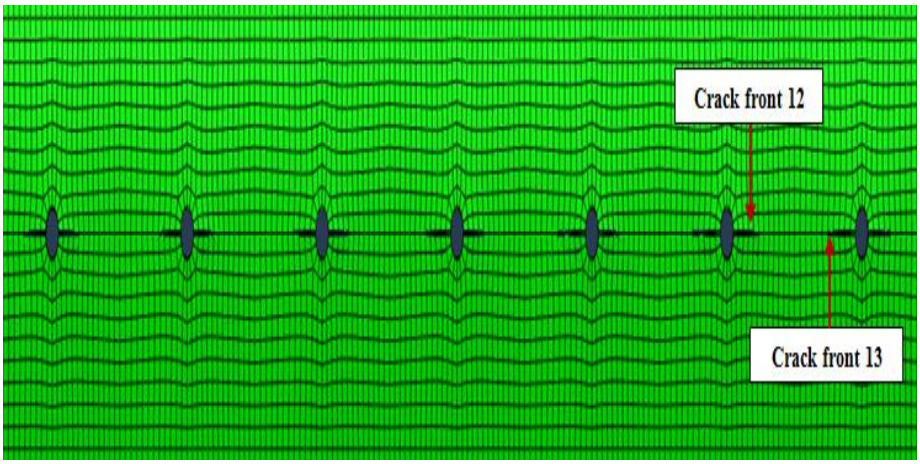

Figure 5-152 XFEM model of MSD panel after cracks opening (step 6 of crack propagation)

In the second case (**D=4m**), crack 12 simulation steps described also in section (5.3.10), figures from 5-145 till 5-147 as following:

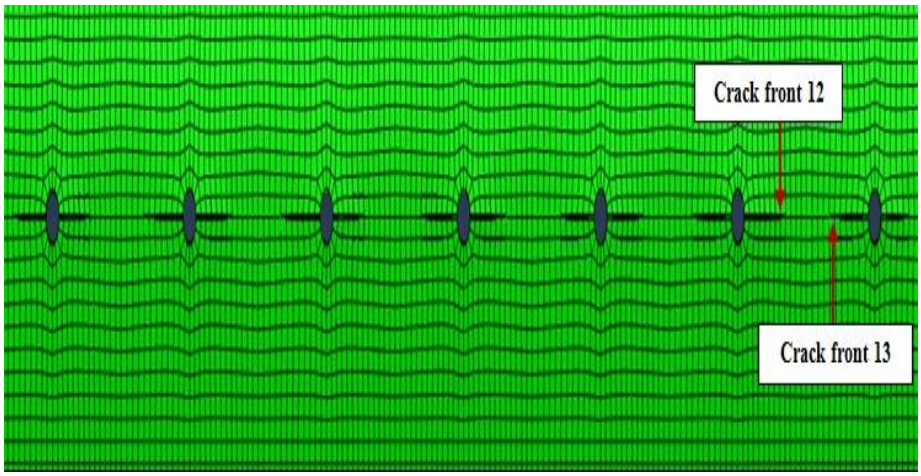

Figure 5-153 XFEM model of MSD panel after cracks opening (step 12 of crack propagation)

Figure 5-145 shows the simulation step 20 which crack 12 recorded length was equal to (5.2508 mm) and crack 13 length was (5.0121 mm). At step 25, as illustrated in figure 5-146, crack 12 length was equal to (5.7166 mm) and crack 11 was equal to (5.6868 mm). Also, at this step, the linking up process occurred between crack 4 and 5 to form crack consisted from cracks 3 till 6.

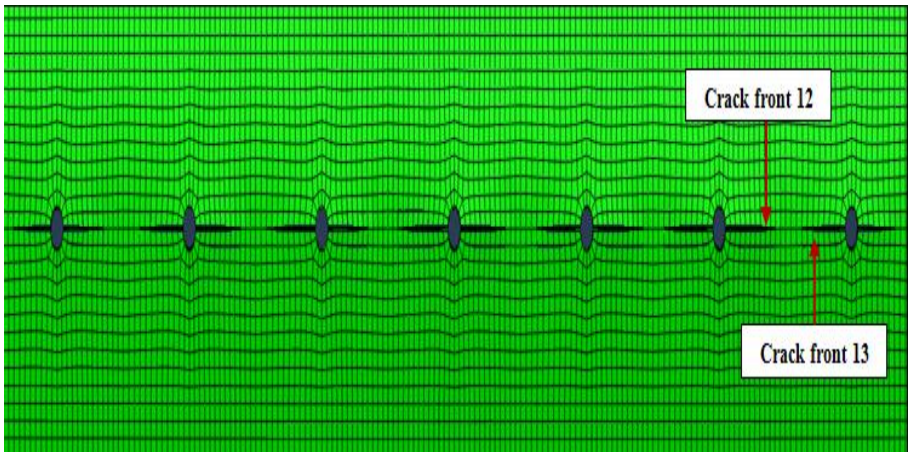

Figure 5-154 XFEM model of MSD panel after cracks opening (step 18 of crack propagation)

Crack 11 reached (6.1525 mm) at the end the simulation (step 32) while crack 13 was equal to (5.9463 mm), see figure 5-147. The total length of the formed crack which had two crack

fronts (3 and 6) was equal to (44.8718 mm).

Also, figures from 5-130 till 5-134 in section (5.3.7) can be used to illustrate the growing steps of crack 12 and crack 13 when **D** equal to **1.6 m** as following:

Figures 5-130 and 5-131 showed the simulation steps 20 and 25, both cracks propagated and the recorded crack 12 length was (5.6711 mm) and crack 13 length was (6.2142 mm) at step 25. After two steps further (step 27), the first linking up process occurred between crack 8 and crack 9, crack 12 length was equal to (5.8268 mm) and crack 13 was (6.3467 mm), see figure 5-132. The second linkup process occurred at step 28 between crack 6 and 7 as shown in figure 5-133, crack 12 reached the length of (5.871 mm) and crack 13 was (6.3694 mm). The last simulation step (step 32) illustrated in figure 5-134, crack 12 length was equal to (5.9873 mm) and crack 13 was (6.409 mm). The coalesced crack length which consisted from cracks 5 to 10 was equal to (73.8937 mm) and no linkup occurred between crack 12 and 13.

The shortest crack 12 length recorded when **D** was equal to **2.4 m**, the crack propagated in two step only and reached the length of (0.8638 mm) while crack 13 recorded length was equal to (8.0644 mm) at the last step of the simulation (step 143), see figure 5-155.

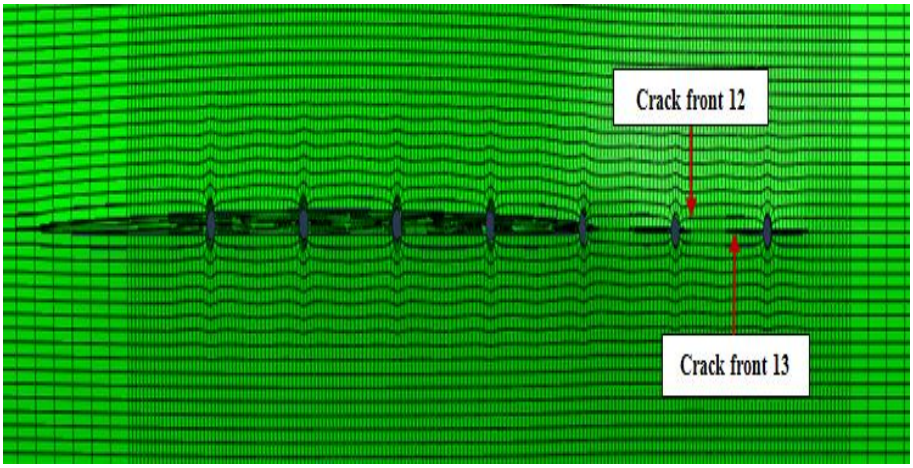

Figure 5-155 XFEM model of MSD panel after cracks opening (step 143 of crack propagation)

7.3.13 SIF evaluation of crack 13 at different fuselage diameters

Figure 5-156 shows the relationship between crack 13 length and the corresponding values of SIF, it showed that there was a steep rise in SIF values compared to the crack extension especially at the last steps o the simulation when D was equal to 2.4 m. Additionally, as it can be seen in the figure the longest crack 13 length recorded when D was equal to 2.4 m (CL =8.0644 mm, K_I=5509.07 MPa$\sqrt{mm}$). The second longest length recorded in this simulation when D was equal to 1.6 m (CL =6.409 mm, K_I=5016.13 MPa$\sqrt{mm}$). The shortest crack 13 length recorded when D was equal to 4 m (CL =5.9887 mm, K_I=4752.66 MPa$\sqrt{mm}$). The recorded crack 13 length when D was equal to 3.2 was (6.1187 mm, K_I=4358.08 MPa$\sqrt{mm}$).

The major dominant of the failure mode mechanism was mode I (opening mode) according to the documented results; with existence effect of the other failure modes (mode II and mode III) in the most simulation steps.

In addition, for more extensively explanation of crack 13 simulation steps when **D** equal to **2.4 m**, figures from 5-100 till 5-104 in section (5.3.1) could be used to illustrate the propagation steps as following:

Figure 5-100 describes the simulation step 28, at this step the linkup process occurred between cracks 4, 5 and cracks 6 and 7. The recorded crack 13 length was (6.0018 mm)

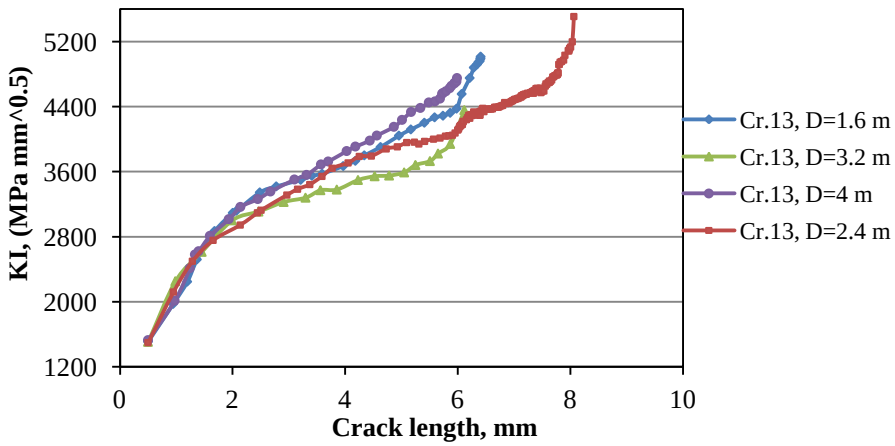

Figure 5-156 SIF histories of crack 13

and crack 12 was (0.8638 mm). Also, it is worth to mention that crack 12 propagated at two first steps only. Crack 13 propagation rate was slow rate due to the linking up process started between rivet holes 2, .3 and 4; it extended about (0.395 mm) from step 28 (6.0018 mm) to step 54 (6.3968 mm) as shown in figures 5-101 and 5-102. Figure 5-103 shows step propagation 100, at this step crack 13 recorded length was equal to (7.3928 mm) while crack 12 length was (0.8638 mm). The last simulation step illustrated in figure 5-104, crack 13 final length was equal to (8.0644 mm) and no interaction occurred between crack 13 and crack 12 in this case.

Also, in the case of **D** equal to **1.6 m**, no linkup process occurred between crack 13 and 12. The following are some selected simulation images to describe the growing steps of cracks 13 and 12: Figure 5-157 shows the simulation step 20, at this step crack 13 length was equal to (5.5908 mm) while crack 12 length was (4.5819 mm).

Five steps further as illustrated in figure 5-158 crack 13 length was equal to (6.2142 mm) and crack 12 was (5.6711 mm).

At step 26 and 28, the linking up process occurred between cracks 8, 9 and 6, 7 respectively to form one lead crack which had two crack fronts (5 and 10) as shown in figure 5-159. Crack 13 length was equal to (6.3694 mm) while crack 12 was (5.871 mm).

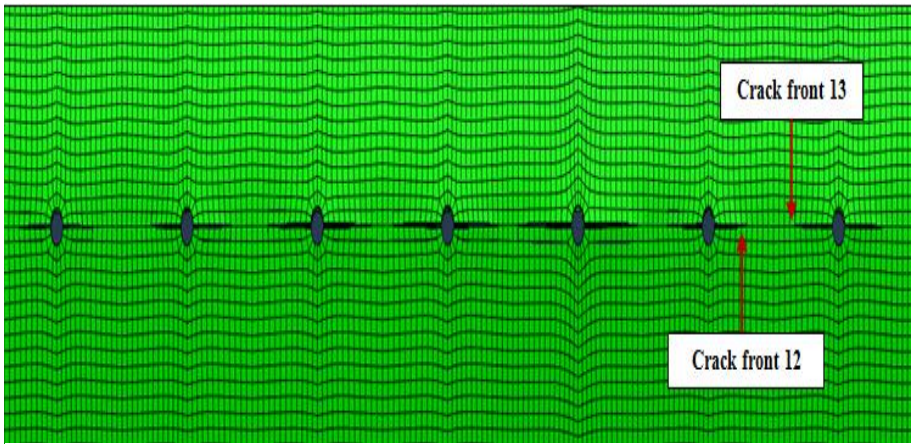

Figure 5-157 XFEM model of MSD panel after cracks opening (step 20 of crack propagation)

Nothing has changed at the end of the simulation (step 32), the total length of the lead crack was equal to (73.8937 mm), and also it is worth to mention that crack 13 had longer length than 12 but with lower extension rate.

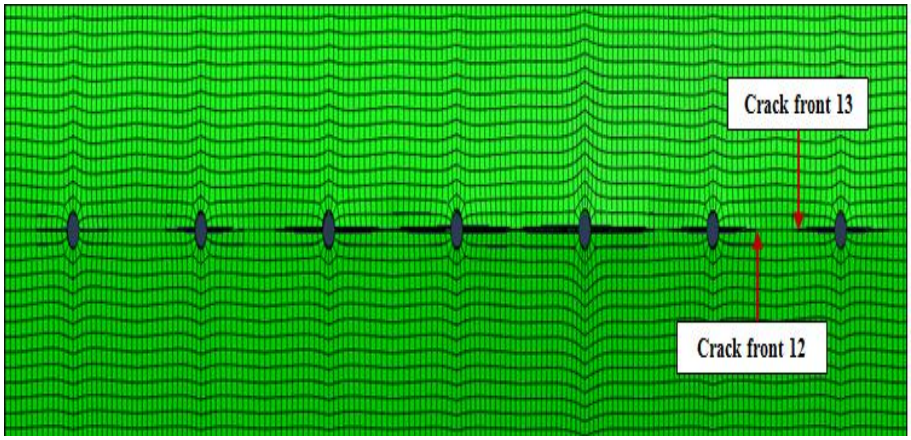

Figure 5-158 XFEM model of MSD panel after cracks opening (step 25 of crack propagation)

In the case of **D** equal to **3.2 m**, there is no linkup processes occurred between the whole cracks in the tested model as illustrated in the following figures:

Figure 5-160 shows the simulation step 12, at this step crack 13 reached the length of (4.7833 mm) and crack 12 length was (5.3489 mm).

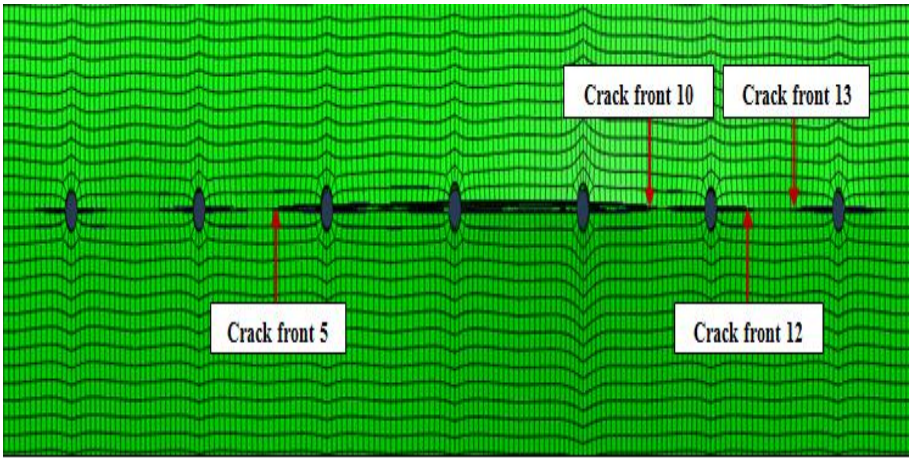

Figure 5-159 XFEM model of MSD panel after cracks opening (step 28 of crack propagation)

At the end of the simulation crack 13 final length was equal to (6.1187 mm) and crack 12 was equal to (7.8741 mm), see figure 5-161. The last simulation case (**D=4 m**), figures 5-144 to 5-146 in section (5.3.10) illustrate the growing steps of crack 13 as following:

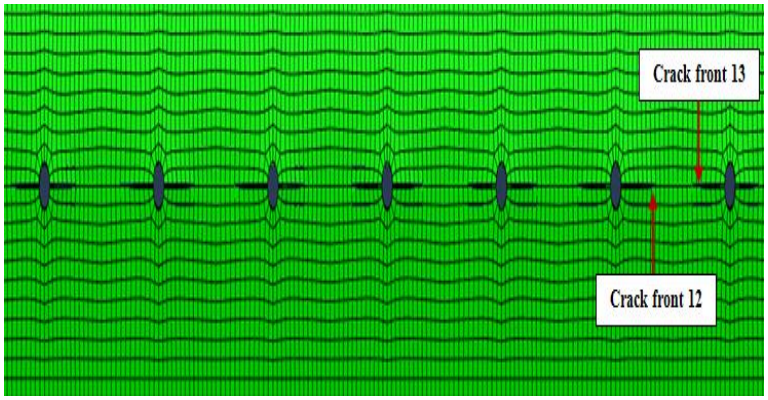

Figure 5-160 XFEM model of MSD panel after cracks opening (step 12 of crack propagation)

Figure 5-144 shows the simulation step 20 which crack 13 recorded length was equal to (55.0121 mm) and crack 12 length was (5.2508 mm). At step 25, as illustrated in figure 5-145, crack 13 length was equal to (5.6868 mm) and crack 12 was equal to (5.7166 mm). Also, at this step, the linking up process occurred between cracks 4 and 5 to form crack consisted from cracks 3 till 6. Crack 13 reached (5.9787 mm) at the end the simulation while crack 12 was equal to (6.2038 mm), see figure 5-146. The total length of the formed crack which had two crack fronts (3 and 6) was equal to (44.8718 mm). In addition, in this case no linkup occurred between crack 13 and crack 12.

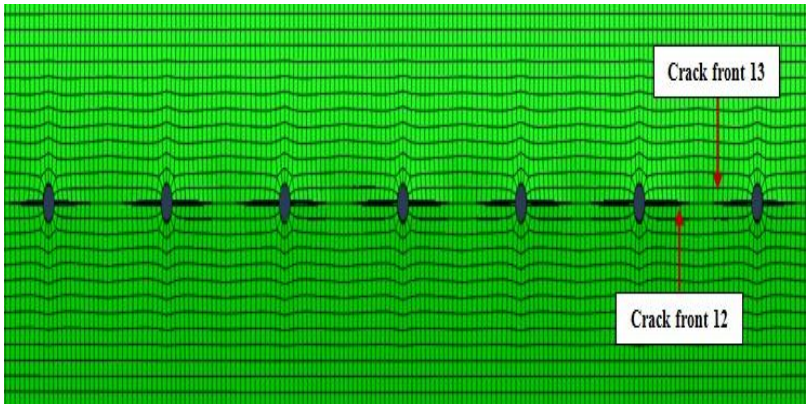

Figure 5-161 XFEM model of MSD panel after cracks opening (step 18 of crack propagation)

5.3.14 SIF evaluation of crack 14 at different fuselage diameters

The purpose of changing the fuselage diameter from 1.6 m to 4 m was to study this effect on fatigue crack growth rate for different models. Figure 5-162 shows the simulation results of crack 14, it showed that the longest recorded length of crack 14 was when D was equal to 2.4 m (CL=8.5362 mm, K_I=4512.53 MPa $\sqrt{mm}$) while the second long length recoded when D was equal to 1.6 m (CL=6.1223 mm, K_I=4545.16 MPa $\sqrt{mm}$). The recorded length when D changed to 4 m was (CL=5.4445 mm, K_I=4307.56 MPa $\sqrt{mm}$) and the shortest crack length recorded when D was equal to 3.2 m (CL=4.9235 mm, K_I=4471.83 MPa $\sqrt{mm}$).

Also, the documented results showed that K_I was the dominant to the failure mechanism (mode I, opening mode), with existence effect of K_{II} and K_{III} in the most simulation steps. For more extensively presentation of growing steps of crack 14, the figures from 5-100 to 5-104 in section (5.3.1) can be used to describes the growing steps when **D** equal to **2.4 m:** Figure 5-100 shows the simulation step 28, at this step crack 14 recorded length was (6.1451 mm) and two linking up process occurred between cracks 4, 5 and 6, 7. The third linkup occurred between cracks 8 and 9 at step 44 as described in figure 5-101 and crack 14 length was equal to (6.401 mm). A ten steps after (step 54), the forth linkup occurred between cracks 2 and 3 and crack 14 recorded length at this step was equal to (6.6 mm), see figure 5-102.

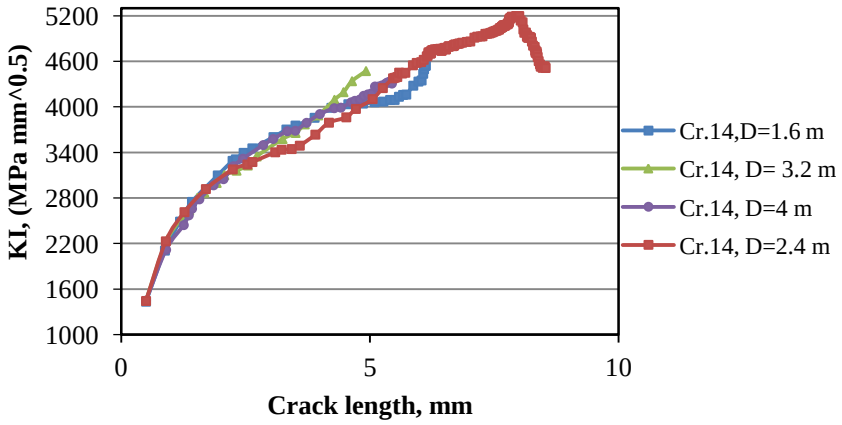

Figure 5-162 SIF histories of crack 14

crack 14 reaches its final length (8.5362 mm) at step 143 as it can be seen in figure 5-104. Crack 14 had a faster crack growing at the first 30 steps, after that the growing was with slow rate and at the last simulation step there was a drop in SIFs values with small crack extension values, as illustrated in figure 5-162. Figures from 5-130 to 5-134 in section (5.3.7) can be used to illustrate the second case (**D=1.6 m**) as the second long length of crack 14 as following: Figure 5-130 represent simulation step 20, crack 14 propagate and reached the length of (5.499 mm). After more five steps (step 25) crack 14 length was equal to (5.9779 mm), as illustrates in figure 5-131. The first linkup process occurred in this simulation occurred between crack 8 and 9 at step 27 as it can be seen in figure 5-102, crack 14 recorded length was (6.0734 mm), and the second linkup process occurred at step 28 between cracks 6 and 7 as sown in figure 5-133; crack 14 length was (6.0903 mm) in this step. Crack 14 reaches its final length at step 32 (6.1223 mm) as illustrated in figure 5-134; also the documented crack 14 was growing in slow rate after step 20. Figures from 5-145 to 5-147 in section (5.3.10) also can be used to illustrate the growing steps of crack 14 when **D** equal to **4 m** as following: Figure 5-145 shows the simulation step 20, the crack propagated and reached the length of (4.6993 mm); also the figure showed that the cracks which emanating from rivet hole 3 had a faster crack growth. The first linkup process occurred between crack 4 and occurred at step 25 an showed in figure 5-146, crack 14 recorded length at this step was (5.1036 mm). Figure 5-147 represent the last step of the simulation, no further linkup occurred between the cracks and the final crack 14 length was equal to (5.4354 mm). It worth to mention that the documented results showed in this case crack 14 had a slow crack growing after step 20 compared to the first 20 step. The shortest crack 14 length recorded when **D** was equal to **3.2** m, and to represent the growing steps of the crack, figures 5-160 and 5-161 section (5.3.13) can be used for this purpose; additionally, there no linkup process between the whole cracks in this case as shown in the figures below: Figure 5-160 shows the simulation step 12, crack 14 recorded length at this step was equal to (3.5075 mm). The last step represented in figure 5-161 (step 18), the final crack 14 length was equal to (4.9235 mm).

5.4 FOURTH NUMERICAL EXAMPLE

In this simulation, the same panel material, dimentions and boundary conditions which mention in section 5.1 are used, except the number of the rivet holes in this case are increased to 11 holes. Figure 5-163 shows the cracks positioning and numbering. Also, a uniform pressure was applied at the internal face of the model Fig. 5-164. Figure 5-165 also shows a portion of the mesh around the holes, and as it can be seen mesh was refined around the cracks at the edges of each hole and a uniform template of elements around each crack front was used. The characteristics of the final mesh are summarized in table 5-4.

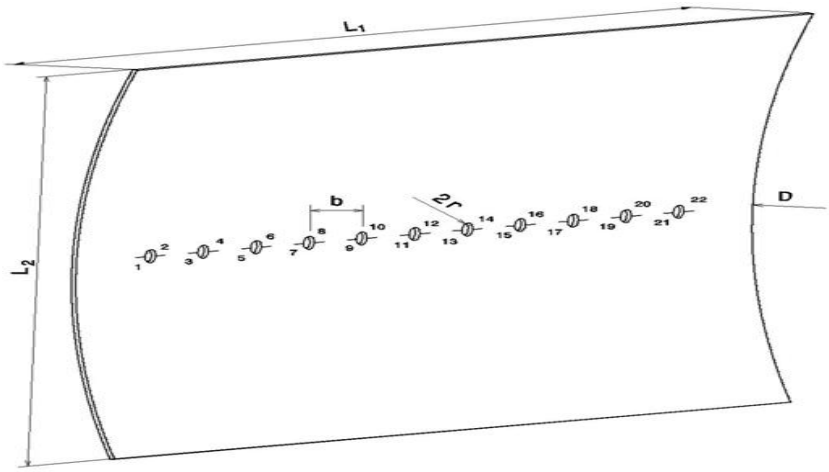

Figure 5-163 Analyzed configuration with multiple cracks (not to scale)

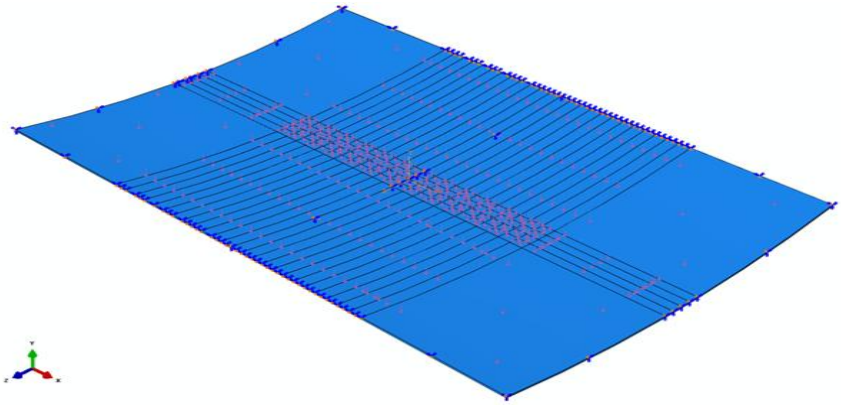

Figure 5-164 Panel with loads and boundary conditions (drawn to scale)

Table 5-4 Characteristics of the panel final mesh

D (m)	No. of steps (max.)	No. of nodes	No. of elements	Type of element	D (m)
1.6	52	188885	149004	C3D8R	1.6
2.4	86	172560	135936	C3D8R	2.4
3.2	20	205480	162176	C3D8R	3.2
4	17	204350	161280	C3D8R	4

Results of this procedure can be seen in the following section. The initial crack length used was 0.5mm.

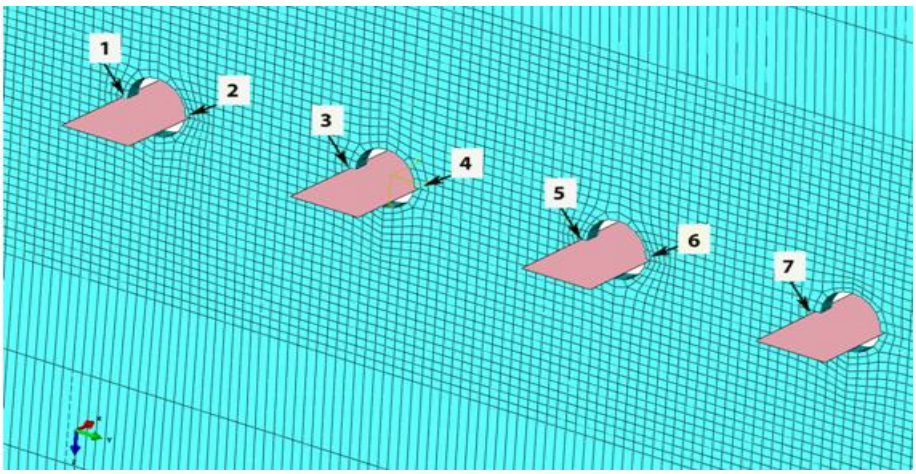

Figure 5-165 Cracks positions and numbering

It is worth to mention that in the case of the curved model with 11 rivet holes the longest cracks lengths recorded during the simulation when fuselage diameter was equal to 2.4 m and 1.6 m. The following sections describe the propagation behavior for 22 cracks in the case of multiple- site damage; all graphs are drawn as a relationship between crack lengths and the corresponding stress intensity factor values for each step of cracks propagation:

5.4.1 SIF evaluation of crack 1 at different fuselage diameters

Figure 5-166 shows the relationship between SIFs histories of crack 1 as a function of its extension, it showed that as the crack propagates as SIF values increases. In the case of fuselage diameter (D) of 1.6 m, the curve showed there was a steep rise in SIFs values compared to crack propagation at the end of the simulation steps. Also, the figure showed the longest recorded crack 1 length was when D equal to 2.4 m (CL = 6.299 mm, K_I=4067.7 MPa $\sqrt{mm}$), followed by its length when D was equal to 1.6 m (CL = 6.112

mm, K_I=6958.69 MPa $\sqrt{mm}$). The third longest recorded length was when D equal to 3.2 m (CL = 3.195 mm, K_I=3986.39 MPa $\sqrt{mm}$); and the shortest recorded length was when D equal to 4 m (C. = 3.122 mm, K_I=4277.06 MPa $\sqrt{mm}$).

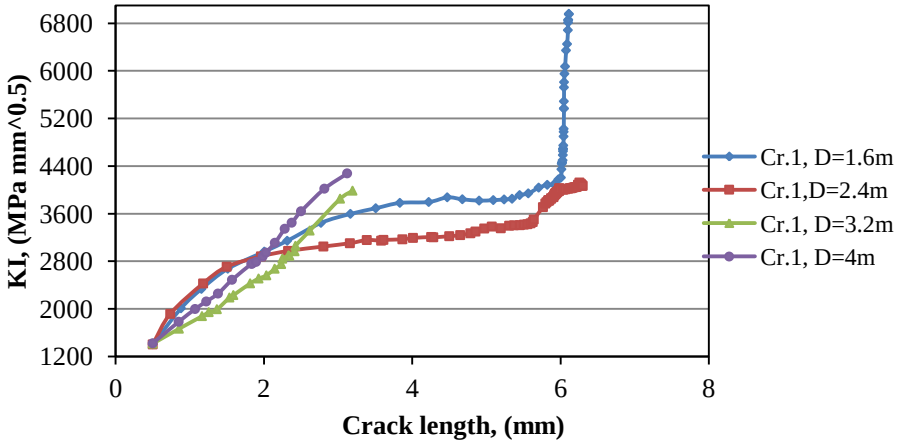

Figure 5-166 SIF histories of crack 1

The propagation behavior of crack 1 in the case of D equal to 3.2 m and 4 m were somewhat different from the other diameters, they had almost a linear relationship between crack extension and SIFs values, as shown in figure 5-166.

For more explanation of crack growing steps, the following figures are some selected propagation steps in the case of **D** equal to **2.4 m**:

Figure 5-167 represents the stress distribution around the rivet holes after the first step load; the figure explains that the holes are causing an inhomogeneous stress distribution. It is clear from the figure the stress concentration was at the root of the holes.

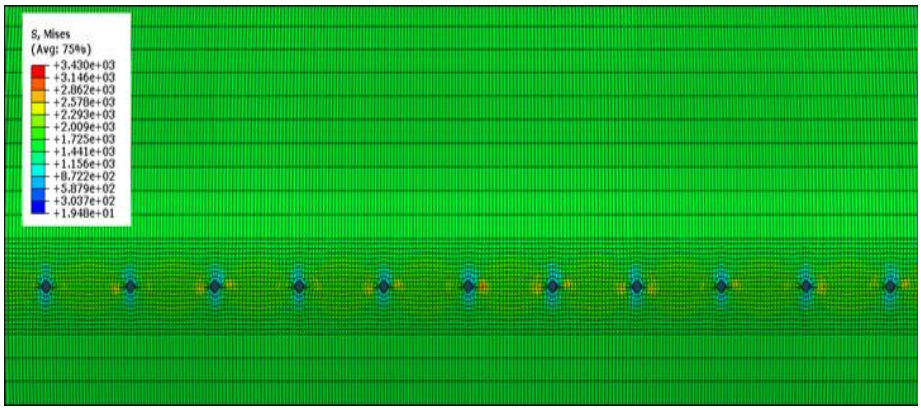

Figure 5-167 XFEM model of MSD panel after crack opening (first step load)

Figure 5-168 describes the simulation step 28; at this step, the first linkup process occurred between crack 12 and 13 to form temporary one new lead crack with new crack fronts 11 and 14. The recorded crack 1 length at this step was equal to (5.596 mm). The documented results showed before this step the crack 1 had a slow growth rate especially after step 24 due to the panel was weakened at the location of rivet holes 6 and 7.

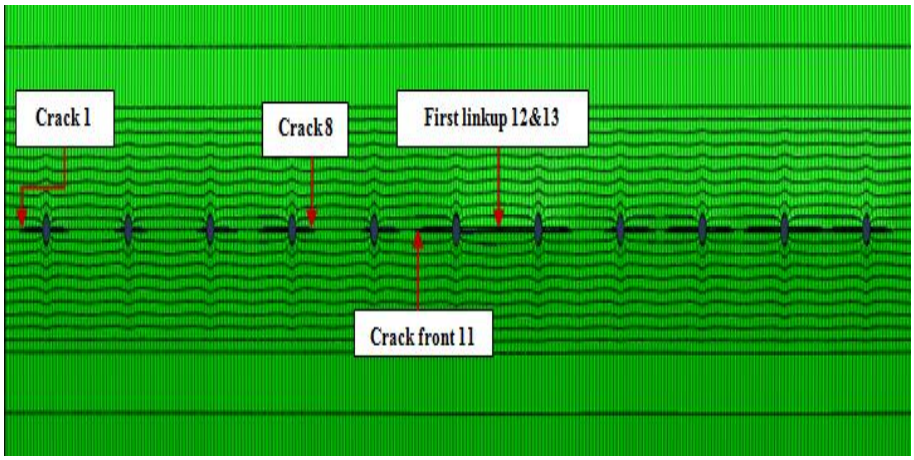

Figure 5-168 XFEM model of MSD panel after crack opening (step twenty eighth)

The second linkup process occurred between cracks 20 and 21 which were emanating from rivet holes 10 and 11 at step 31, the cracks were growing towards each other and they linked up as described in figure 5-169. The recorded crack 1 length at this step was equal to (5.763 mm) and the linkup resulted temporary lead crack with two crack fronts of 19 and 22 with total length equal to (45.3288 mm) at this step.

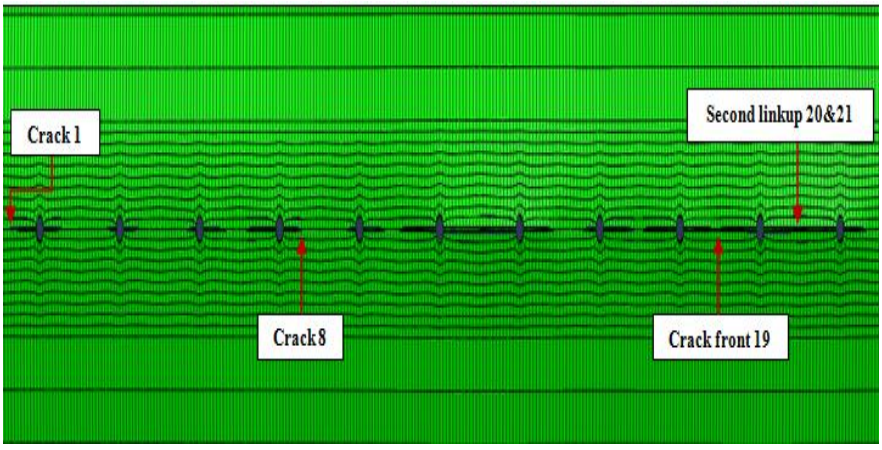

Figure 5-169 XFEM model of MSD panel after crack opening (step thirty one)

The crack 1 length was equal to (5.812 mm) at step 33, as illustrated in figure 5-170, also, at this step the third linkup process occurred between cracks 18 and 19. The formed crack now consisted from cracks 17, 18, 19, 20, 21 and 22 with total length (69.3474 mm). Additionally, the figure also shows there were two lead cracks formed until this step, the first had two crack fronts 11 and 14 and the other one with two crack fronts 17 and 22.

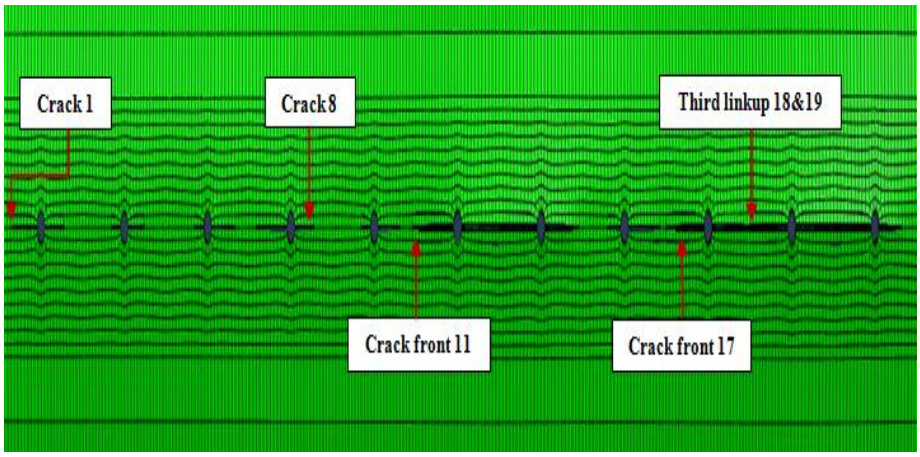

Figure 5-170 XFEM model of MSD panel after crack opening (step thirty three)

Figure 5-171 shows the simulation step 44, at this step crack 1 reached (5.912 mm) and the fourth linkup process occurred between crack 16 and 17. Now, the lead crack had new crack front (15) and the total length was equal to (93.9997 mm) at this step.

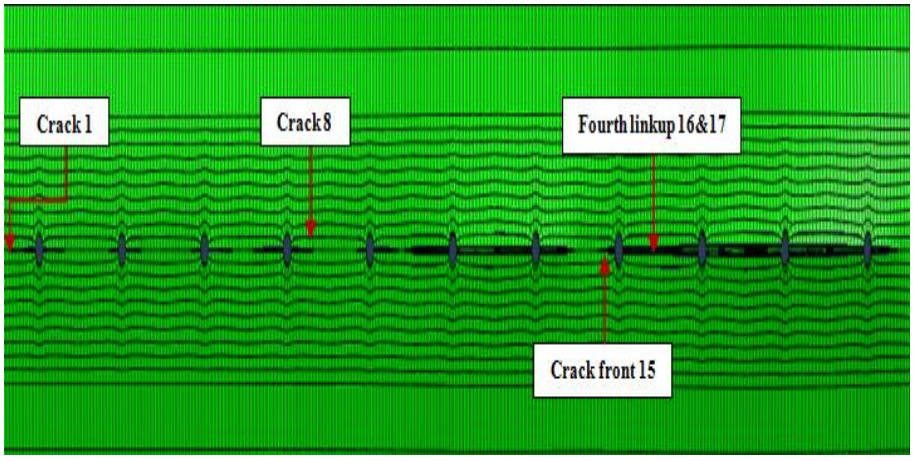

Figure 5-171 XFEM model of MSD panel after crack opening (step fourth four)

The fifth linkup process in this simulation occurred at step 56 between cracks 10 and 11 as illustrated in figure 5-172. Crack 1 length at this step reached (5.96 mm).

The last linkup (sixth linkup) occurred at step 62 as shown in figure 5-173, also, at this step the formed lead crack at this step consisted from cracks 9 until 22 with total length equal to (162.4114 mm). The recorded crack 1 length at this step was equal to (5.98 mm).

Figure 5-174 shows the last step of the simulation in the case of fuselage diameter 2.4 m, at this step crack 1 reached its final length (6.229 mm) and the formed lead crack propagated at the direction of crack front 22 (crack 22 length changed from 6.503 mm at step 62 to 13.578 mm at the last step. Crack 1 was growing with slow rate due to the fast growing rate at the location of rivet holes from 5 to eleven.

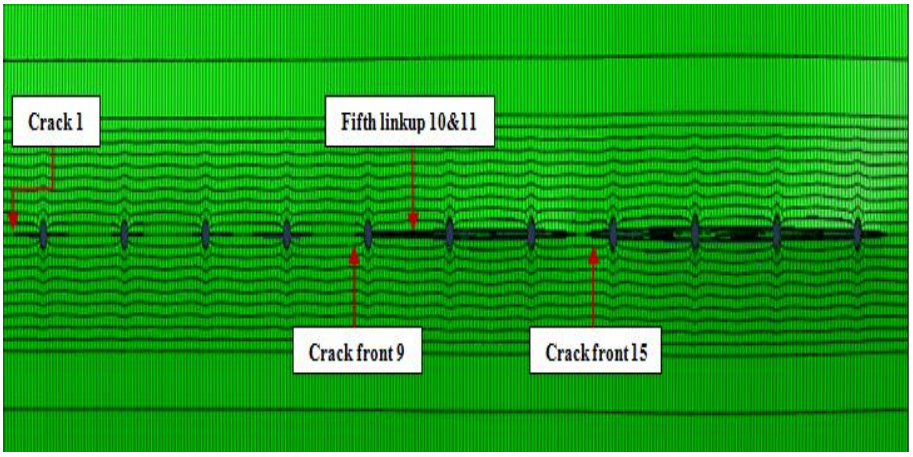

Figure 5-172 XFEM model of MSD panel after crack opening (step fifty six)

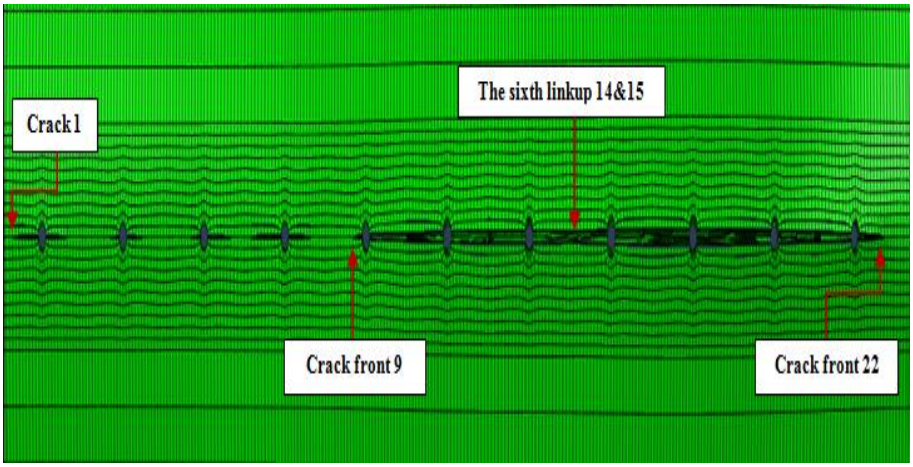

Figure 5-173 XFEM model of MSD panel after crack opening (step sixty two)

Figure 5-175 shows the last simulation step (step 52) in the case of D was equal to 1.6 m, at this step crack 1 final length was equal to (6.112 mm). Also, the figure shows that the

interaction between the adjacent cracks occurred between the cracks from 3 to 16.

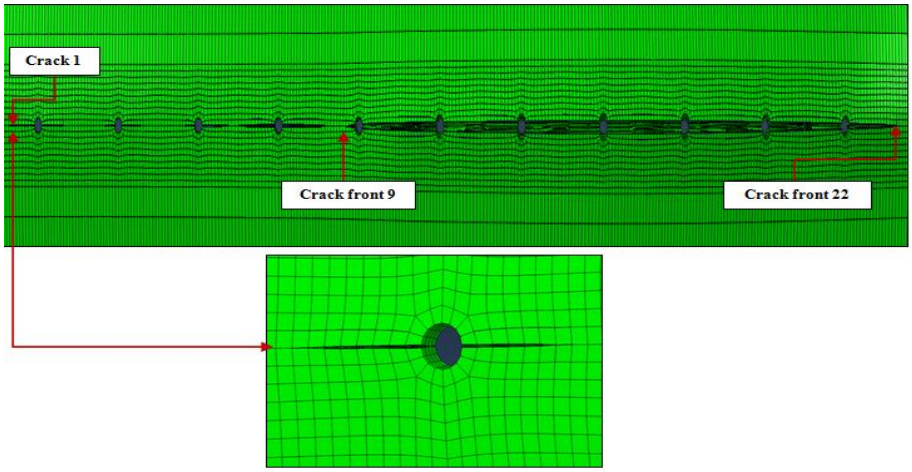

Figure 5-174 XFEM model of MSD panel after crack opening (step eighty seven)

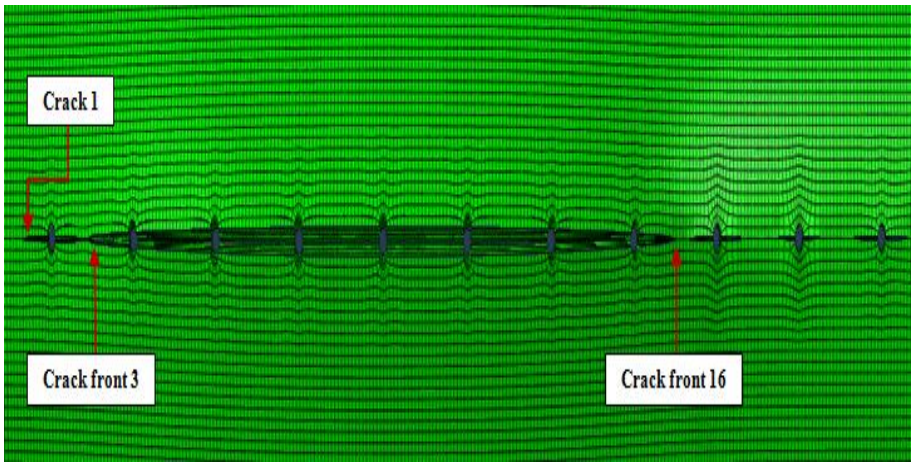

Figure 5-175 XFEM model of MSD panel after crack opening (step fifty two)

The interaction between the cracks in the model did not occur when **D** was equal to **3.2 m**, as illustrated in figure 5-176. The final crack 1 length in this simulation was equal to (3.195 mm).

Due to the longest lengths of cracks from 2 to 7 recorded at the simulation when D was equal to 1.6 m, the following sections summarize and describe the growing steps and cracks growing trend as following:

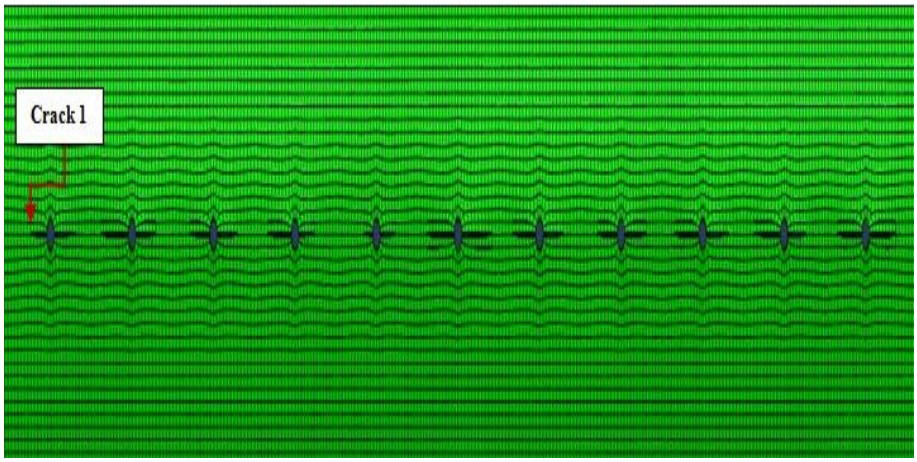

Figure 5-176 XFEM model of MSD panel after crack opening (step twenty)

5.4.2 SIF evaluation of cracks 2 and 3 at different fuselage diameters

Tables 5-5 and 5-6 illustrate the relationship between crack 2 and 3 lengths as a function in changing the fuselage diameter from 1.6 m to 4 m during the multiple cracks simulation. The tables showed that the longest crack 2 and crack 3 recorded when D was equal to 1.6 m

Table 5-5 Crack 2 length comparison as a function of changing fuselage diameter

S.N	D (m)	Crack final length (mm)	K_I (MPa $\sqrt{mm}$)
1	1.6	6.766	13515
2	2.4	5.179	4665.71
3	3.2	4.381	3597.42
4	4	3.818	3818

The growing trend of the mentioned cracks is described in the following figures:

Table 5-6 Crack 3 length comparison as a function of changing fuselage diameter

S.N	D (m)	Crack final length (mm)	K_I (MPa $\sqrt{mm}$)
1	1.6	11.741	16108
2	2.4	0.85	1743.03
3	3.2	6.412	4319.22
4	4	3.801	4045.29

Figure 5-177 shows the effect of crack 2 propagation on SIF values; a steep rise in crack 2 SIF values occurred in this case after step 30 of the simulation while the other curves showed almost a linear function. In the simulation the linking up process between crack 2 and 3 did not occur in the four studying cases. Crack 2 is adjacent to crack 3 and it

supposed to interact with each other as a result of multiple site damage phenomena, but in this simulation, the linking up did not occur due to the panel weakened at the location far from rivet holes 1 and 2. Figure 5-178 represents the relationship between crack 3 propagation and its SIF values, also, the longest crack 3 length also occurred when D was equal to 1.6 m and the steep rise also occurred in this simulation after step 25. Also, it's worth to mention that the shortest crack 3 length occurred when D was equal to 2.4 m.

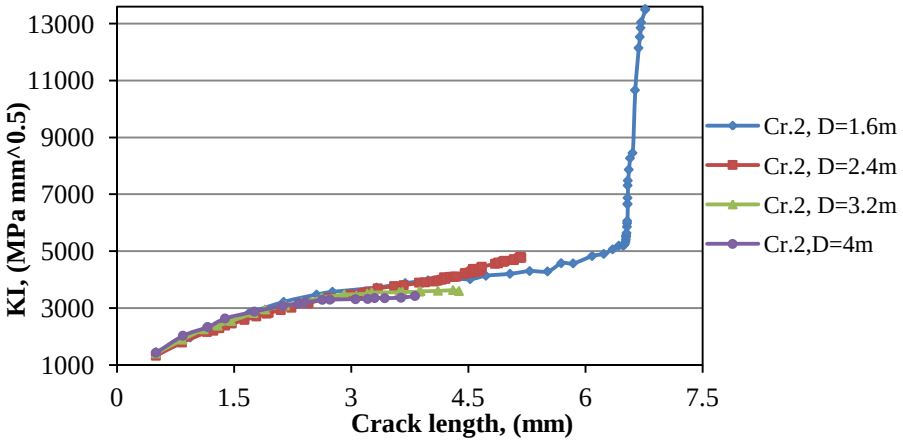

Figure 5-177 SIF histories of crack 2

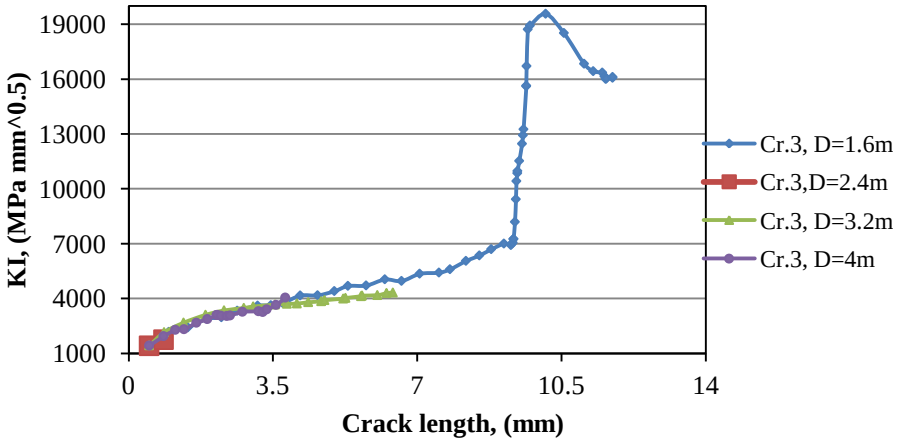

Figure 5-178 SIF histories of crack 3

For extensively explanation for the cracks propagation steps, the following are some selected simulation images which will be used to describe growing steps for the cracks 2 and 3, and also for the cracks from 3 to 7 because those cracks had its longest length during the simulation when **D** was equal to **1.6 m**: The documented results showed that the growth

rates of crack 2 and 3 were faster before the linking up processes start to occur from step 23. Figure 5-179 shows the simulation step 22, at this step crack 2 recorded length was (6.349 mm) and crack 3 was (8.797 mm). The growing steps which were described in the figures from 5-180 to figure 5-189 (last simulation step 52) showed after the linkup processes the growth rate for both cracks were slowed due to the panel weakened at the location of rivet holes from 2 to 8. In addition, it should be noted that during the simulation crack 3 had a longer crack length because it was closer than crack 2 to the weak area. Figure 5-189 shows the last step of the simulation (step 52), at this step the final crack 3 length was (11.741 mm) and crack 2 was (6.766 mm). The linking up process also did not occur during the simulation when D was equal to 3.2 m and 4m.

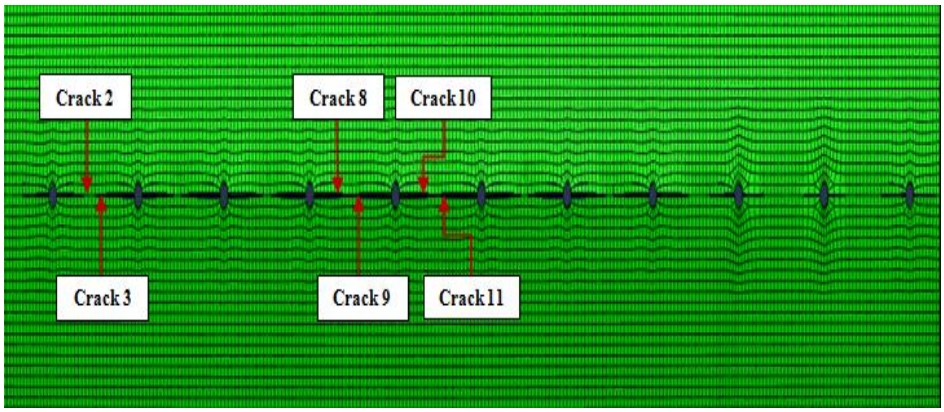

Figure 5-179 XFEM model of MSD panel after crack opening (step twenty two)

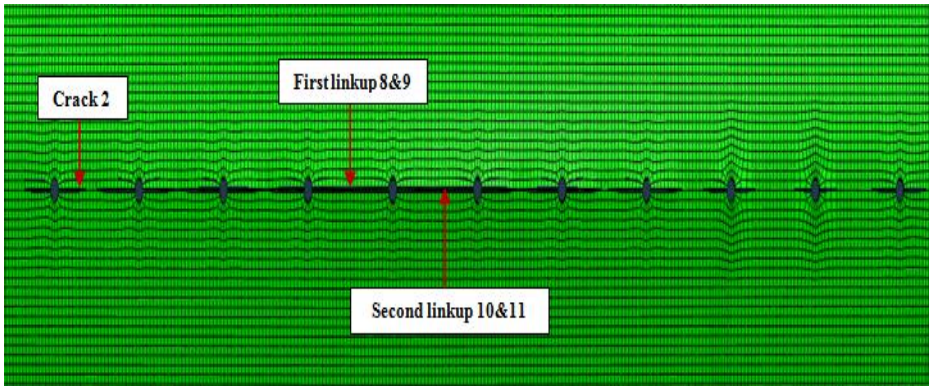

Figure 5-180 XFEM model of MSD panel after crack opening (step twenty three)

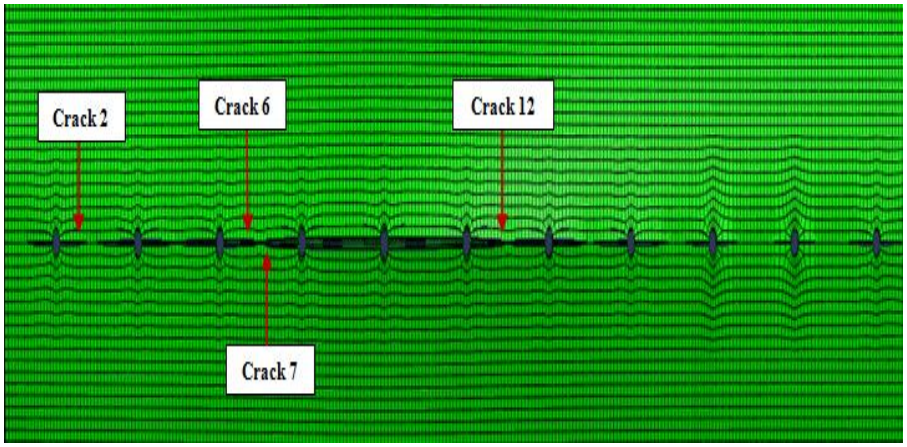

Figure 5-181 XFEM model of MSD panel after crack opening (step twenty eight)

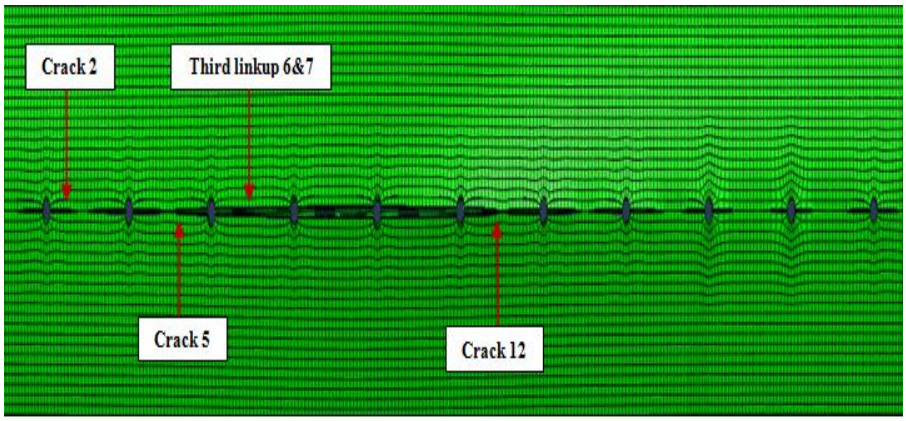

Figure 5-182 XFEM model of MSD panel after crack opening (step twenty nine)

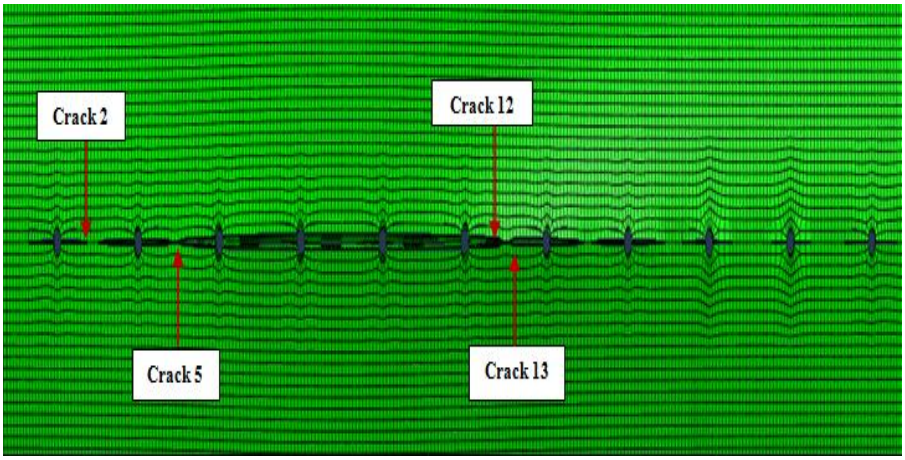

Figure 5-183 XFEM model of MSD panel after crack opening (step thirty three)

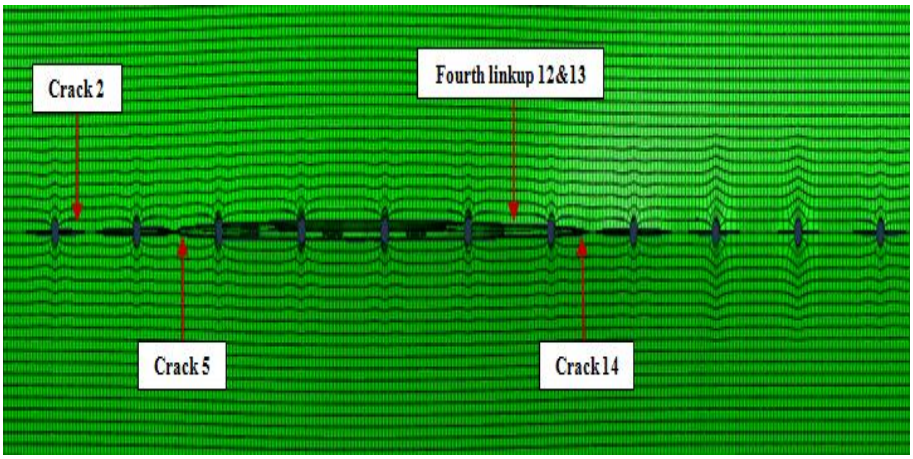

Figure 5-184 XFEM model of MSD panel after crack opening (step thirty four)

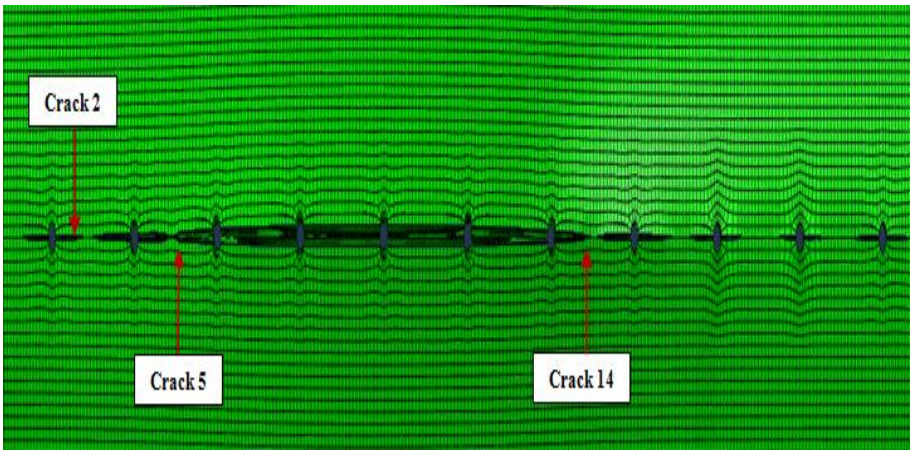

Figure 5-185 XFEM model of MSD panel after crack opening (step thirty six)

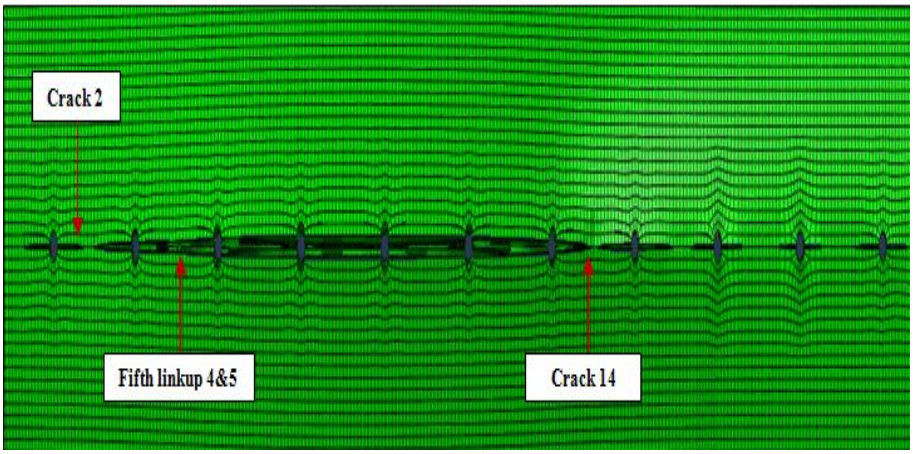

Figure 5-186 XFEM model of MSD panel after crack opening (step thirty seven)

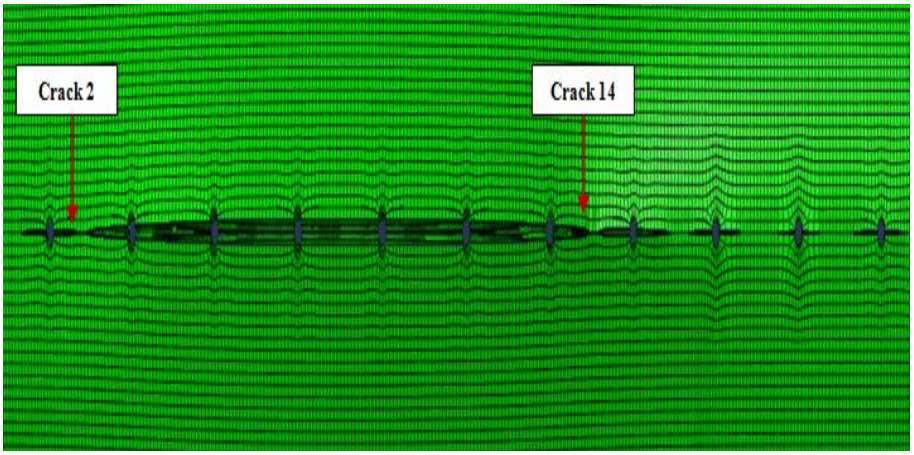

Figure 5-187 XFEM model of MSD panel after crack opening (step fourth five)

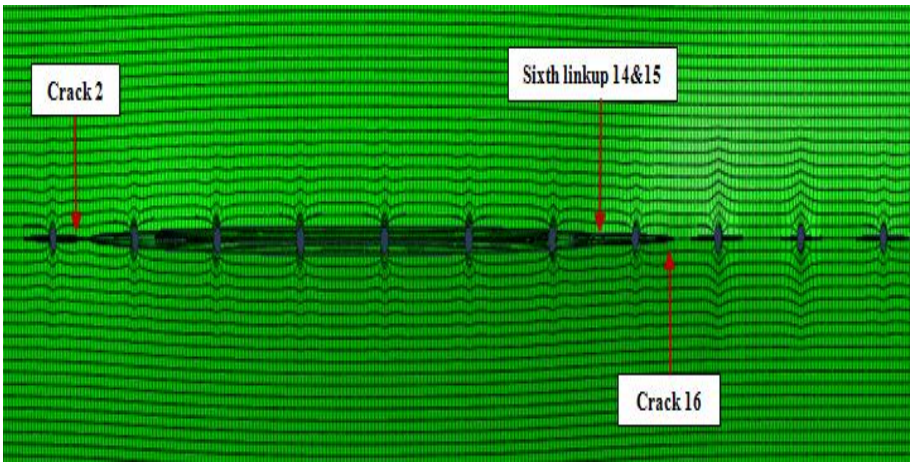

Figure 5-188 XFEM model of MSD panel after crack opening (step fourth six)

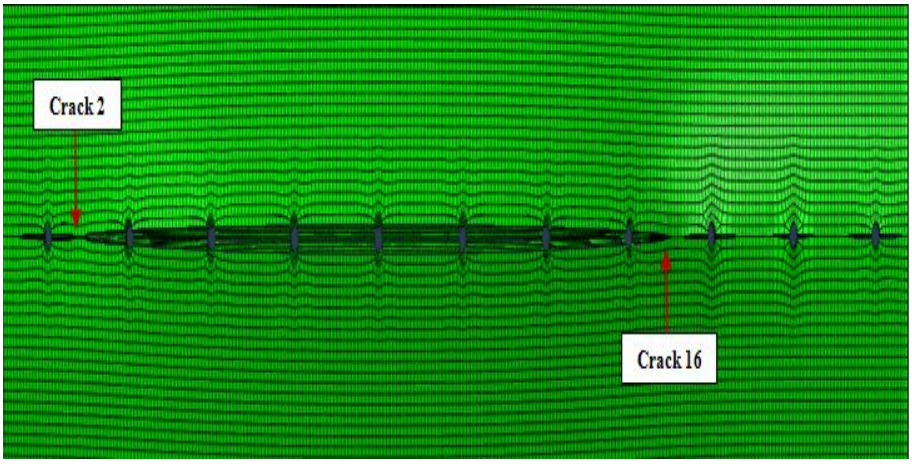

Figure 5-189 XFEM model of MSD panel after crack opening (step fifty two)

5.4.3 SIF evaluation of cracks 4 and 5 at different fuselage diameters

Tables 5-7 and 5-8 show the effect of changing the fuselage diameter from 1.6 m to 4 m on crack 4 and 5 lengths; it showed that the longest cracks length was recorded when D was equal to 1.6 m.

Table 5-7 Crack 4 length comparison as a function of changing fuselage diameter

S.N	D (m)	Crack final length (mm)	KI (MPa $\sqrt{mm}$)
1	1.6	9.1095	35494.5
2	2.4	3.6009	4190.3
3	3.2	4.2241	3984.62
4	4	2.6525	2900.53

Table 5-8 Crack 5 length comparison as a function of changing fuselage diameter

S.N	D (m)	Crack final length (mm)	KI (MPa $\sqrt{mm}$)
1	1.6	11.0905	35231.9
2	2.4	0.8611	1760.62
3	3.2	4.0365	4040.47
4	4	4.8454	3948.49

The following charts are achieved by plotting crack length versus corresponded SIF values for each simulation step:

Figure 5-190 showed there was a steep rise in SIF of crack 4 occurred when D was equal to 1.6 m after simulation step 23, before this step the relation step between crack 4 extension and the corresponded SIF was a linear, meaning as crack 4 propagate as SIFs rise.

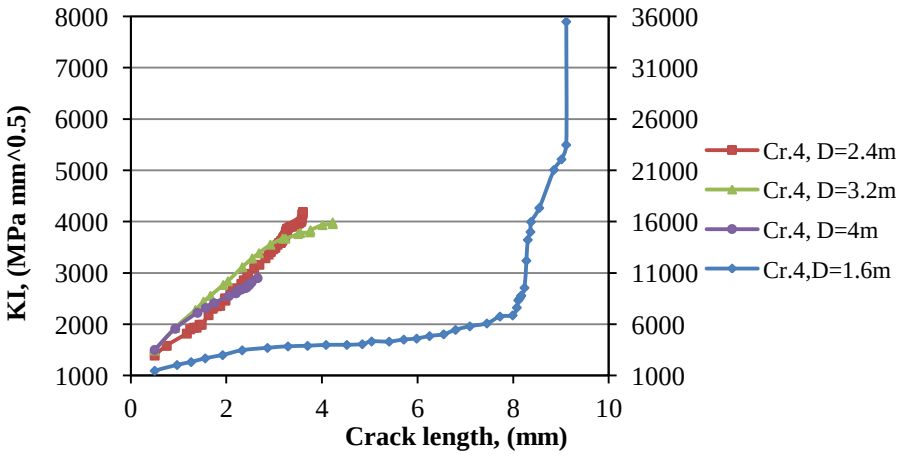

Figure 5-190 SIF histories of crack 4

The adjacent crack to crack 4 was crack 5, it exhibits almost the same propagation trend of crack 4, the steep rise in SIF s values for this crack occurred after simulation step 29. In this case the lowest crack 5 length recorded when D was equal to 2.4m, as it can be in figure 5-191.

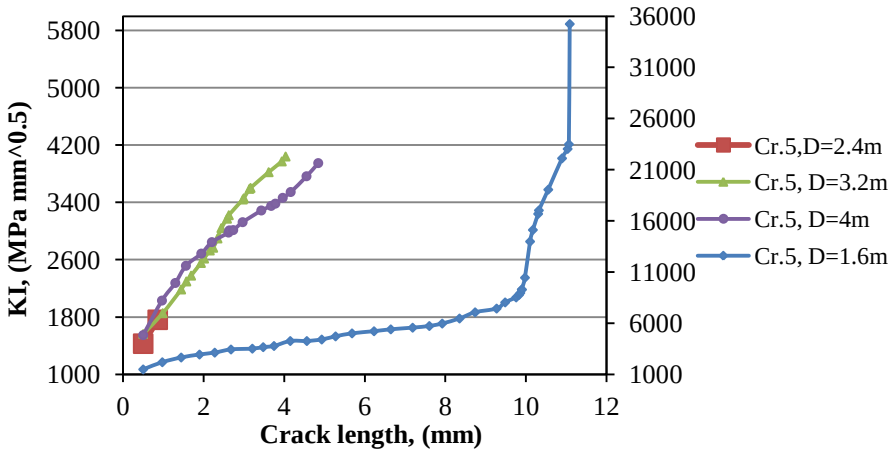

Figure 5-191 SIF histories of crack 5

For a more comprehensive explanation of cracks propagation behavior, in this case (D=1.6m), the mention previous image will be used for this purpose as follows:

The documented simulation results of cracks 4 and 5 showed that crack 5 had a longer length due to crack 5 was closer the deformed area. Figure 5-181 shows step 28, at this step crack 4 recorded length was equal to (7.723 mm) and crack 5 was equal to (9.2743 mm). Both cracks were propagate towards each other with different propagation rate as it can be seen in figures from 5-182 to 5-184; figure 5-185 shows the before the interaction process (step 36) between both cracks, at this step crack 4 length was equal to (9.011 mm) and crack 5 was (11.0371 mm).

Figure 5-186 represents the linking up step between cracks 4 and 5 (step 37), the lead crack length at this step was equal to (147.9148 mm).

Figure 5-189 shows the final shape of the deformed panel at the last step of the simulation. The following table shows the final lengths of cracks 4 and 5 by changing fuselage diameters, no interaction occurred between cracks 4 and 5:

Table 5-9 Crack 4 and 5 lengths comparison as a function of changing fuselage diameter

S.N	D (m)	Crack 4 final length, (mm)	Crack 5 final length, (mm)
1	2.4	3.6009	0.8611
2	3.2	4.2241	4.0365
3	4	2.6525	4.8454

5.4.4 SIF evaluation of cracks 6 and 7 at different fuselage diameters

Tables 5-10 and 5-11 show the final crack lengths of cracks 6 and 7 at different fuselage diameters, also, it is clear that the longest length for both cracks recorded when D was equal 1.6 m.

Table 5-10 crack 6 length comparison as a function of changing fuselage diameter

S.N	D (m)	Crack final length (mm)	K_I (MPa $\sqrt{mm}$)
1	1.6	10.15045	26887.5
2	2.4	6.8034	6825.9
3	3.2	4.7425	3571.74
4	4	3.6076	4190.86

Table 5-11 crack 7 length comparison as a function of changing fuselage diameter

S.N	D (m)	Crack final length (mm)	K_I (MPa $\sqrt{mm}$)
1	1.6	10.204	278726
2	2.4	9.1318	6882.55
3	3.2	5.449	3972.72
4	4	0.8539	2238.7

The results of the simulation for both cracks plotted as a relationship between crack length for each increment and the corresponded stress intensity factor values (SIF). The following charts show the mentioned information as following:

Figure 5-192 shows SIF histories of crack 6 during the multiple crack simulation, the crack exhibits a steep rise in SIF values when D was equal to 1.6 after step 23 (a step which cracks from 8 to 11 linked up) while the first steps showed almost a linear rise in SIF values. The other simulations (D = 3.2 m and 4 m) exhibit a nearly linear rise in SIF values as the crack grows.

Also, crack 7 showed the same propagation trend as it can be seen in figure 5-193, but it is worth to mention that crack 7 had the shortest length when D was equal to 4 m.

The following are some selected simulation images which describes the growing step for both cracks:

Figure 5-179 shows the simulation step 22; at this step crack 6 length was equal to (8.147 mm) while crack 7 was equal to (8.6735 mm). One step further as illustrates in figure 5-180, crack 6 recorded length was (8.4455 mm) and crack 7 was equal to (8.9743 mm). Additionally, at this step the linking up process occurred between cracks from 8 to 11, this explains why crack 7 had a longer length than crack 6.

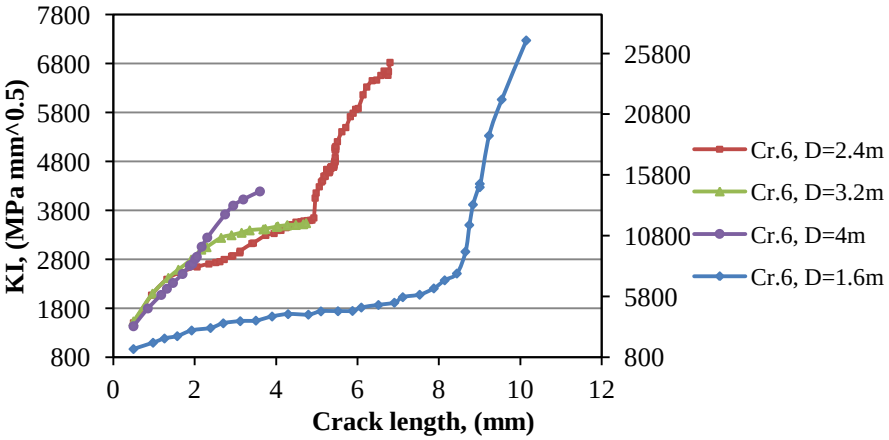

Figure 5-192 SIF histories of crack 6

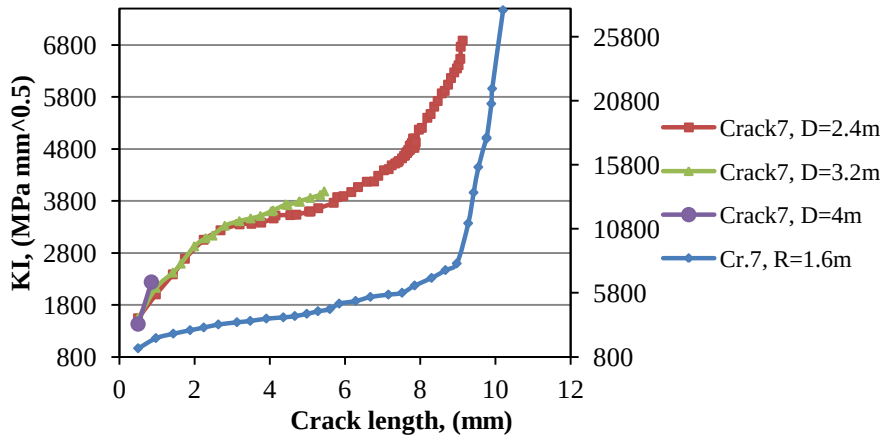

Figure 5-193 SIF histories of crack 7

Figure 5-181 shows step 28, crack 6 and 7 still growing towards each other and the recorded lengths were (9.0093 mm) for crack 6 and (9.7673 mm) for crack 7. The linking up step between both cracks occurred at step 29 as it can be seen in figure 5-182; the length

of the formed lead crack which consisted from crack 5, 6, 7, 8, 9, 10, 11 and 12 was equal to (101.1505 mm) at this step.

5.4.5 SIF evaluation of crack 8 at different fuselage diameters

The longest crack 8 length recorded during the simulation performing at different fuselage diameters was when **D** equal to **2.4**, as shown in figure 5-194. The following table shows the final crack 8 length according to documented simulation results:

Table 5-12 Crack 8 length comparison as a function of changing fuselage diameter

S.N	D (m)	Final crack 8 length, (mm)	K_I (MPa $\sqrt{mm}$)
1	1.6	9.3131	19042
2	2.4	11.3496	11131.4
3	3.2	2.57	3556.19
4	4	3.5326	3154.18

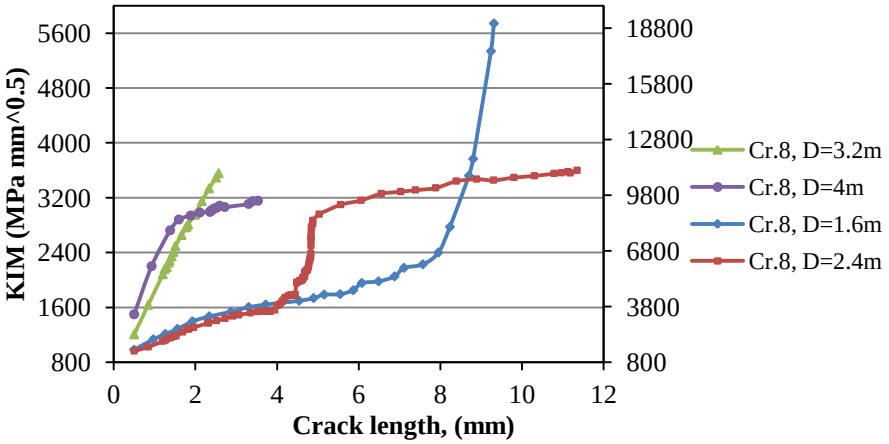

Figure 5-194 SIF histories of crack 8

Crack 8 was propagating with slow rate especially after step 25 while crack 9 in this case propagate in just two steps and it reached its final length during the simulation. Figures from 5-168 to 5-174 describe the growing steps for both cracks and show the recorded length for each propagation steps as following:

The recorded steps were 87 steps at the end of the simulation; figure 5-168 represents the simulation step 28, at this step crack 8 length was equal to (4.1274 mm) and crack 9 length was (0.8495 mm). Four steps further crack 8 length was (4.2762 mm) as shown in figure 5-169, while crack 9 length was (0.8495 mm).

The growing steps from step 33 until step 62 are shown in the figures from 5-170 to 5-173, the recorded crack 8 length in step 33 was equal to (4.3673 mm) and it was equal to (4.827) at step 62 while crack 9 was not propagated.

Crack 8 reached its final length at step 87; it was equal to (11.3496 mm) as shown in figure 8.12. Figure 5-195 shows the deformed panel at the location of linked cracks (from 9 to 22). The panel was bended at this location due to the effect of the linking up process between cracks from 9 to 22 and crack 9 might not growing due to this effect.

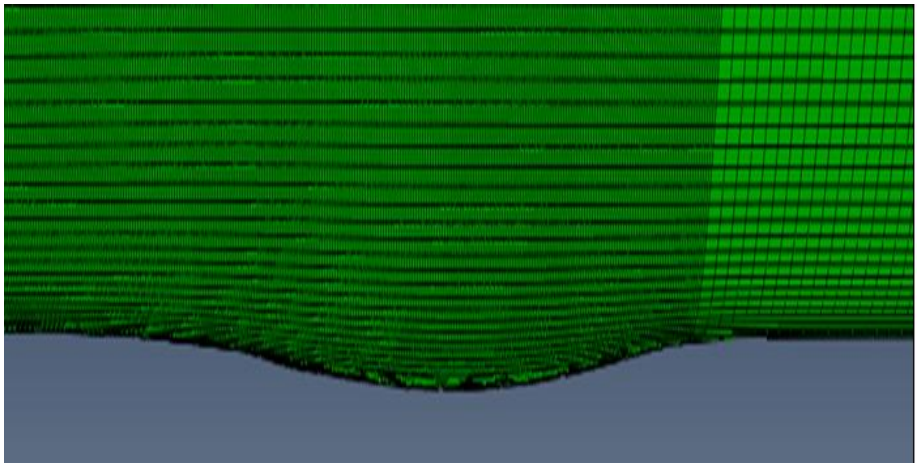

Figure 5-195 The deformed panel, (D = 2.4 m)

5.4.6 SIF evaluation of crack 9 at different fuselage diameters

Table 5-13 shows the final reached crack 9 length according to the changing of fuselage diameters; it is clear from the table that the longest recorded length was when D was equal to 1.6 m.

Table 5-13 Crack 9 length comparison as a function of changing fuselage diameter

S.N	D (m)	Final crack 9 length, (mm)	K_I (MPa $\sqrt{mm}$)
1	1.6	11.011	16242
2	2.4	0.8495	1745.95
3	3.2	0.84825	1747..8
4	4	4.7692	4090.91

Also, figure 5-196 shows SIFs histories versus crack 9 length, it is observed that when D equal to 1.6 m the crack exhibits a linear rise in SIFs values until step 21, after this step a steep rise in SIFs values occurred. At the simulation when D equal to 4 m, crack 9 exhibits

a linear rise in SIF values until the end of the simulation, while at the other fuselage diameters (2.4m and 3.2m) crack 9 extended in two steps only.

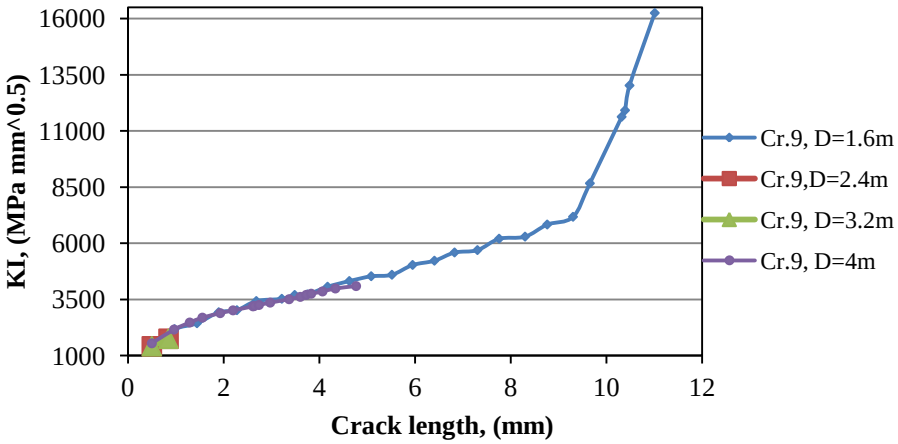

Figure 5-196 SIF histories of crack 9

The figures which are mentioned in the previous section (5.4.2) will be used to describe the propagation trend for both cracks as following:

Figure 5-179 shows the simulation step 22, at this step crack 9 length was equal to (9.655 mm) and crack was (8.2363 mm). It is observed in this figure the panel weakened at the location of the rivet holes 4, 5 and 6; and figure 5-180 is a proof the previous information where the linking up process occurred between cracks 8, 9 and between 10, 11 at simulation step 23. No interaction between crack 8 and 9 occurred during the simulation D equal to 2.4 m, 3.2m and 4 m.

5.4.7 SIF evaluation of crack 10 at different fuselage diameters

Table 5-14 shows the final crack 10 length at the end of the simulation according to the change of fuselage diameters from 1.6 m to 4 m. At D equal to 1.6 m the longest crack 10 recorded.

Table 5-14 Crack 10 length comparison as a function of changing fuselage diameter

S.N	D (m)	Final crack 10 length, (mm)	K_I (MPa $\sqrt{mm}$)
1	1.6	9.1071	14868.3
2	2.4	7.1228	15079.6
3	3.2	2.8668	3902.14
4	4	3.6909	3815.4

Figure 5-197 represents the relationship between crack 10 length and the corresponded SIF values for each increment of crack extension, it showed there was almost linear relationship between both factors until step 22 when D was equal to 1.6 and until step 49 when D was equal 2.4 m, after that a steep rise occurred in SIFs values. Other simulation the crack 10 exhibit a linear rise in SIFs values due to no interaction occurred between the whole cracks when D was equal to 3.2 and 4 m.

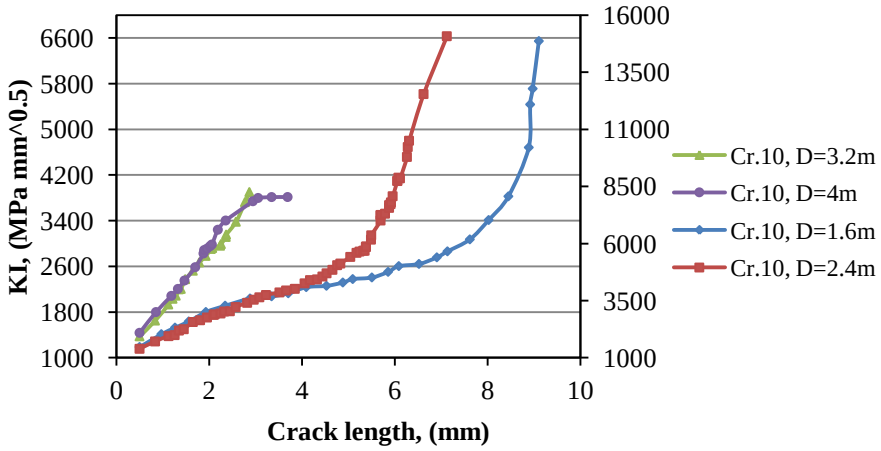

Figure 5-197 SIF histories of crack 10

Figures from 5-179 to 5-189 can be used to describe the propagation steps of crack 10 as following: Figure 5-179 shows the simulation step 22, at this step crack 10 length was equal to (8.4508) while crack 11 length was (9.8805 mm). One step further (step 23) the linking up process occurred between crack 10 and 11 and between crack 8 and 9, as shown in figure 5-180. Figure 5-189 shows the last step of the simulation and the final shape of the deformed panel.

Furthermore, Figure from 5-168 till 5-172 also can b used to describe the growing steps of crack 10 in the case of **D** equal to **2.4 m** as following:

Figure 5-168 shows the simulation step 28, at this step crack 10 length was equal to (4.6575 mm) and crack 11 was equal to (9.1065 mm). Crack 10 had a longer length due to it was closer the linking up area (linking up between cracks 12 and 13 occurred at this step). Figure 5-169 represents the simulation step 31, the second linking up occurred at this step between cracks 20 and 21, and crack 10 length was equal to (5.0421 mm) and crack 11

Length was (9.8043 mm) at this step.

Figures 5-170 and 5-171 represent the growing steps 33 and 44 respectively, at those steps the linking up process occurred two times, between crack 18 and 19 at step 33, and between crack 16 and 17 at step 44. At step 44, crack 10 length was (5.7907 mm) and crack 11 was (11.5593 mm). The fifth linking up process occurred between cracks 10 and 11 at step 56, as shown in figure 5-172. Figure 5-174 shows the final shape of the deformed panel. No interaction between crack 10 and 11 occurred during the simulation D equal to 3.2m and 4m.

5.4.8 SIF evaluation of crack 11 at different fuselage diameters

Table 8.12 shows the simulation results of crack11, apparently the longest crack 11 length recorded when D was equal to 2.4 m.

Table 5-15 Crack 11 length comparison as a function of changing fuselage diameter

S.N	D (m)	Final crack 11 length, (mm)	K_I (MPa $\sqrt{mm}$)
1	1.6	11.1006	13504.7
2	2.4	13.1172	14619.9
3	3.2	6.41263	4388.07
4	4	5.15964	4208.39

SIFs histories of crack 11 are shown in figure 5-198, The steep rise in SIFs values of the crack 11 occurred at the last steps of simulation when D was equal to 2.4 m and 1.6 m due to the interaction effect between crack 11 and crack 10, the other simulations using D equal to 3.2 and 4 m did not show interaction effect, meaning no interaction occurred between the whole crack in the panel during the simulation.

The growing steps of crack 11 when **D** was equal to **2.4** m explained in section (5.4.5), but it is worth to mention that crack 11 had a longer crack length (11.5593 mm) than crack 10 (5.7907 mm) at step 44 as shown in figure 5-171. The linking up between crack 11 and 10 occurred at step 56 as illustrated in figure 5-172. Also, the second case when **D** equal to **1.6 m**, the growing steps illustrated in the previous section (5.4.2); figure 5-179 shows the growing step 22 at this step crack 11 length was equal to (9.8805 mm) and crack 10 length was (8.4508 mm). Figure 5.180 shows the linking up step between cracks 11 and 10.

The simulations when **D** equal to **3.2** m and **4 m** did not showed any interaction between both cracks as shown in figures 5-176 and 5-198.

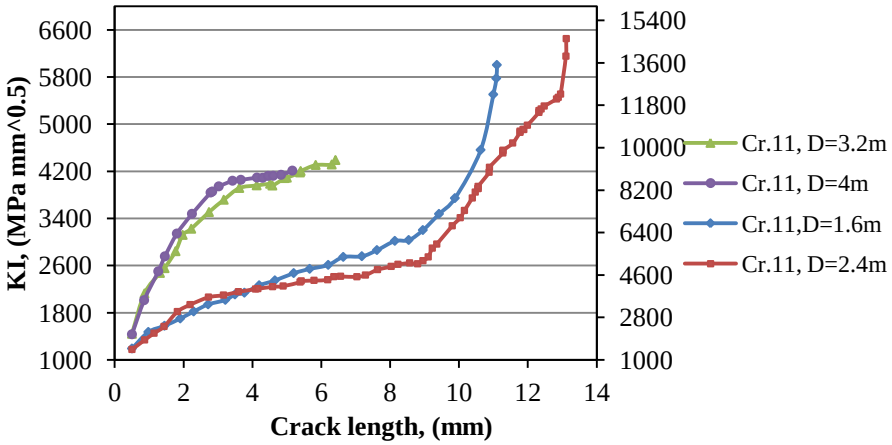

Figure 5-198 SIF histories of crack 11

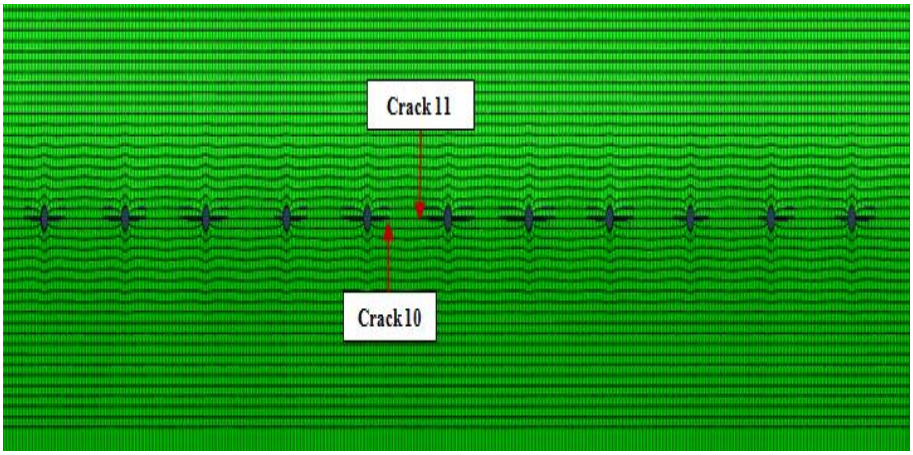

Figure 5-199 The deformed panel at last step 17, (D = 4 m)

5.4.9 SIF evaluation of crack 12 at different fuselage diameters

Table 5-16 shows the simulation results according to the change of fuselage diameters from 1.6 to 4 m, it is clear the longest recorded length was when D was equal to 2.4 m.

Also, figure 5-200 shows SIFs histories of crack 12 according to crack propagation increment, a clear steep rise occurred when D was equal to 1.6 m after step 23 of the simulation. Other simulations (D=3.2 m and 4m) showed almost a linear rise in SIFs values until the end of the simulation and there is no linking up process occurred between the whole crack in the panel. To illustrate the growing process of crack 12, the figures below

will describe the growing steps as following: Figure 5-201 shows propagation step 27, at this step crack 12 recorded length was equal to (10.4342 mm), while crack 13 length was equal to (8.5915 mm). The followed step (step 28) cracks 12 and 13 linked up as shown in figure 5-168 in shown in figure (5.4.1).

Table 5-16 crack 12 length comparison as a function of changing fuselage diameter

S.N	D (m)	Final crack 12 length, (mm)	K_I (MPa $\sqrt{mm}$)
1	1.6	10.26	30931.52
2	2.4	11.04	10680.19
3	3.2	6.83262	4700.63
4	4	5.77504	4492.44

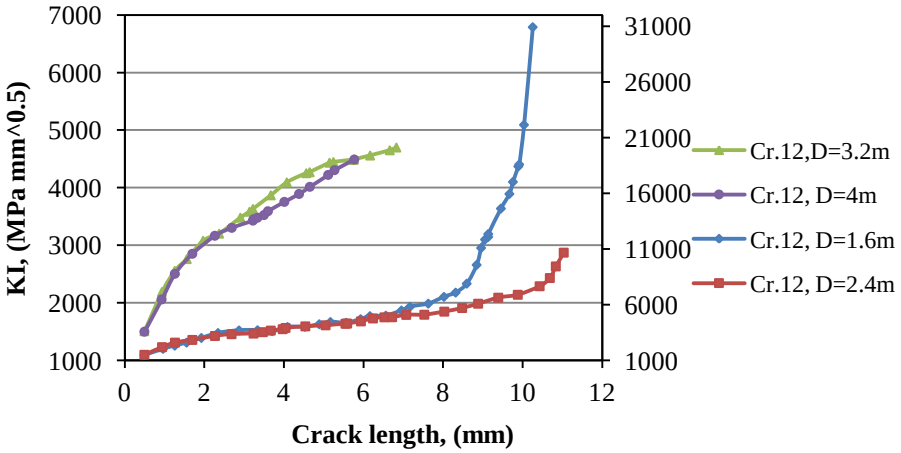

Figure 5-200 SIF histories of crack 12

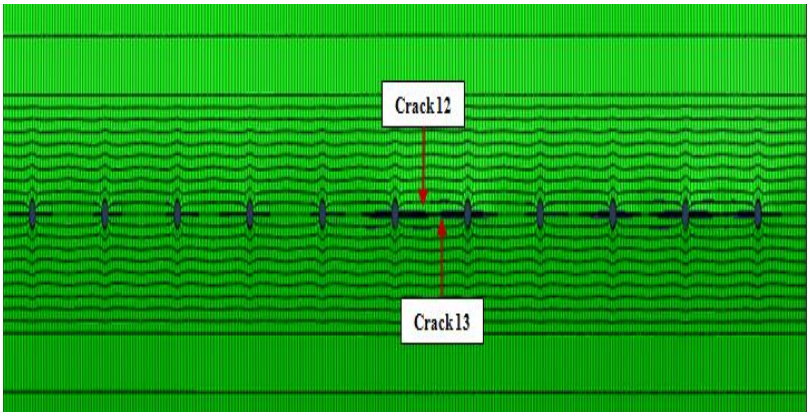

Figure 5-201 XFEM model of MSD panel after crack opening, D=2.4
(Step twenty seven)

5.4.10 SIF evaluation of crack 13 at different fuselage diameters

The final documented simulation results are represented in table 5-17; it showed the effect of changing fuselage diameters on crack 13 length. It is clear from the table the longest recorded length was when D was equal to 1.6 m.

Table 5-17 Crack 13 length comparison as a function of changing fuselage diameter

S.N	D (m)	Final crack 13 length, (mm)	K_I (MPa $\sqrt{mm}$)
1	1.6	10.3887	31433.3
2	2.4	9.2008	10489.14
3	3.2	5.1448	4519.98
4	4	5.7931	4008.47

In addition, figure 5-202 represents crack 13 SIFs histories during the simulation with different fuselage diameters; crack13 had a clear linear rise in SIFs values at the beginnings of the simulation steps, while the crack showed a steep rise in SIFs values at the last the steps when D was equal to 2.4m and 1.6 m.

The other simulations when D equal to 3.2 m and 4 m showed almost a linear rise in SIFs values until the end of the simulation and, additionally, no link up occurred between the whole cracks.

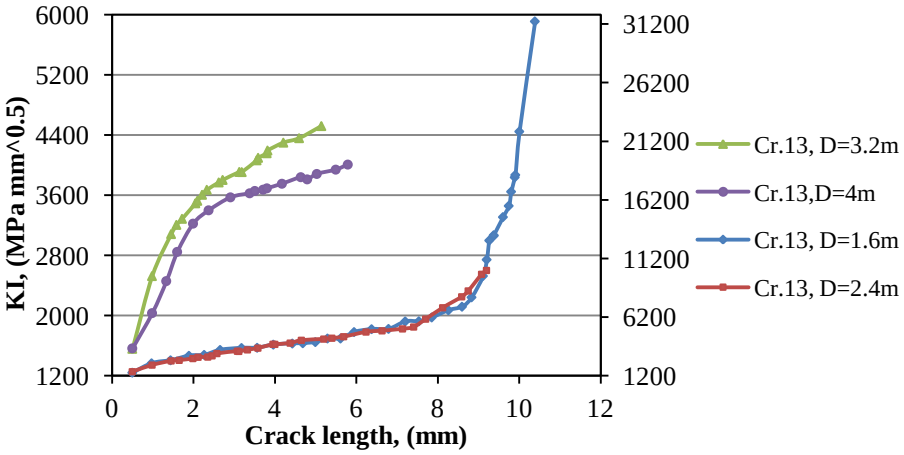

Figure 5-202 SIF histories of crack 13

For more explanation to growing trend of crack 13 during the simulation, some selected figures from section (5.4.2) will be used to describe the growing steps as following: Figure

5-179 shows the growing step 22, at this step crack13 recorded length was equal to (8.5988 mm) and crack 12 was equal to (8.3226 mm). The following growing steps as described in figures from 5-180 to figure 5-183 and the related crack 13 and 12 lengths are recorded in table 5-18

Table 5-18 Crack lengths and growing steps of cracks 13 and 12

S.N	Fig. No.	Step No.	Crack 13 length, (mm)	Crack 12 length, (mm)
1	5-180	23	8.8333	8.6017
2	5-181	28	9.93778	9.1426
3	5-182	29	9.6044	9.4607
4	5-183	33	9.9086	9.9206

The linking up process between cracks 13 and 12 occurred at step 34 as shown in figure 5-184. The other simulations using D equal to 3.2 and 4 m did not show linkup process between the whole cracks in the panel as, as mention in the previous sections.

5.4.11 SIF evaluation of crack 14 at different fuselage diameters

The table below shows the summary of the simulation results of crack 14 length according to the change of fuselage diameters; the longest recorded length was when D was equal to 2.4 m:

Table 5-19 Crack 14 length comparison as a function of changing fuselage diameter

S.N	D (m)	Final crack 14 length, (mm)	K_I (MPa $\sqrt{mm}$)
1	1.6	11.1004	38798.1
2	2.4	12.04	45798.1
3	3.2	4.5986	3740.97
4	4	4.9119	3909.13

On the other hand, figure 5-203 represent SIFs histories of crack 14, the steep rise in SIF values occurred in the simulation cases of D equal to 1.6 and 2.4 m, but the other simulations (D=3.2m and 4 m) showed a rise in SIFs values (D=3.2m) and decline in SIFs values (D=4m) at the last steps of the simulation.

Figures in section (5.4.1) also can be used to describe the propagation steps of crack 14 and 15 as following: Crack 14 recorded length was equal to (7.4917 mm) while crack 15 recorded length was (3.4819 mm), as shown in figure 5-168 in section (5.4.1). The

following table represents the growing steps and the corresponded crack length for each step:

Table 5-20 Crack length and growing steps of cracks 14 and 15, (D=2.4m)

S.N	Fig. No.	Step No.	Crack 14 length, (mm)
1	5-169	31	7.8541
2	5-170	33	8.1195
3	5-171	44	8.8875
4	5-172	56	10.0261

It is observed that during the simulation and the documented results crack 14 had a faster crack growing rate than crack 15 until the linking up process between both cracks which occurred at step 62, see figure 5-173.

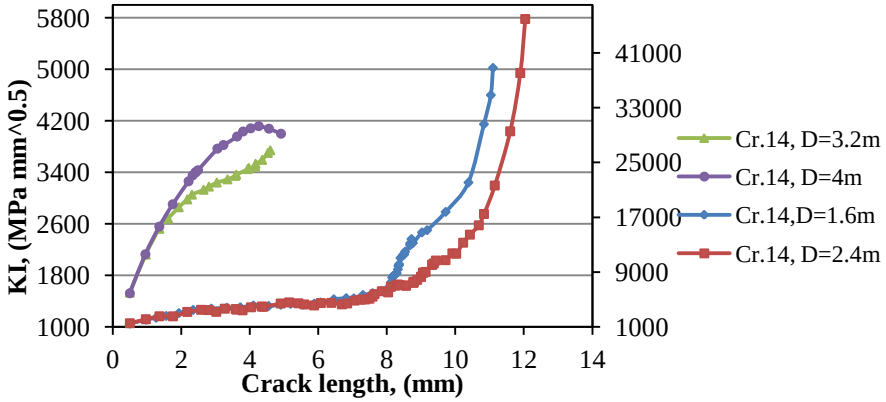

Figure 5-203 SIF histories of crack 14

The second recorded length was when D was equal to 1.6 m and table 5-21 shows the growing steps for both cracks and the corresponded length for each growing steps.

Both cracks are linked up at step 46 as shown in figure 5-188, the total length of the formed lead crack was equal to (175.2993 mm) with two crack fronts (3 and 16).

The other simulations (D=3.2 m and 4 m) did not show linking up process between the whole cracks in the panel as mentioned before.

Table 5-21 Crack length and growing steps of cracks 14 and 15, (D=1.6m)

S.N	Fig. No.	Step No.	Crack 14 length, (mm)	Crack 15 length, (mm)
1	5-179	22	7.8509	7.7859
2	5.180	23	8.04	8.0198
3	5.181	28	8.2219	8.202
4	5.182	29	8.2894	8.2371
5	5.183	33	8.3598	8.2703
6	5.184	34	8.3987	8.2845
7	5.185	36	8.5097	8.3136
8	5.186	37	8.5348	8.3183
9	5.187	45	9.7181	8.6107

5.4.12 SIF evaluation of crack 15 at different fuselage diameters

The final simulation results according to the change of fuselage diameters are represented in table 5-22; it is clear that the longest crack 15 length was when D equal to 1.6 m.

Table 5-22 crack 15 length comparison as a function of changing fuselage diameter

S.N	D (m)	Final crack 15 length, (mm)	K_I (MPa $\sqrt{mm}$)
1	1.6	9.101	46625.4
2	2.4	8.1608	46430.3
3	3.2	4.3891	4878.6
4	4	3.7857	4329.95

Also, figure 5-204 shows SIF histories of crack 15, it is clear while the both cracks growing towards each other the linear rise in SIF values occurred and the steep rise occurred at the last steps of the simulation which give indication the panel is weakened at the location between rivet holes 9 and 10 due to the rise of the value of stress concentration.

Additionally, the crack showed a linear rise in SIFs values during the simulation when D was equal to 3.2 m and 4 m and there no link up process occurred between the whole cracks in the panel. The growing steps of cracks 15 and 14 when D equal to 1.6 m and 2.4 m are illustrated in the previous section (5.4.9).

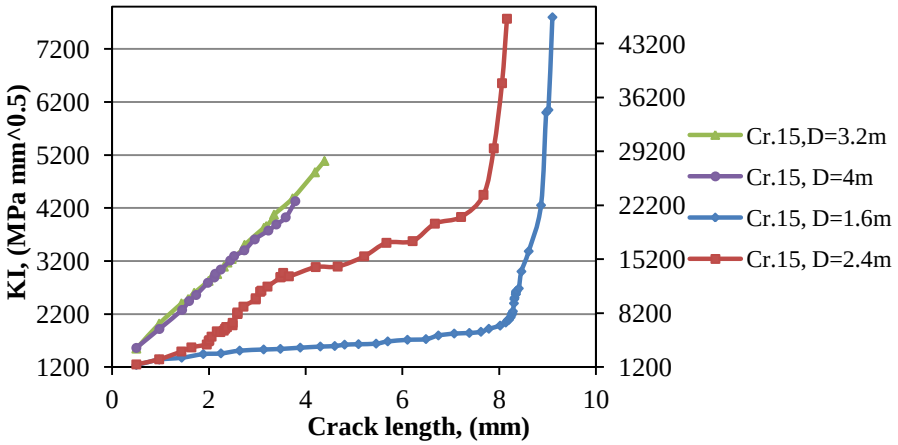

Figure 5-204 SIF histories of crack 15

5.4.13 SIF evaluation of cracks 16 and 17 at different fuselage diameters

Tables 5-23 and 5-24 show the final crack lengths of cracks 16 and 17 at different fuselage diameters, also, it is clear that the longest length for both cracks recorded when D was equal 2.4 m.

Table 5-23 Crack 16 length comparison as a function of changing fuselage diameter

S.N	D (m)	Final crack 16 length, (mm)	K_I (MPa $\sqrt{mm}$)
1	1.6	8.7583	20626.4
2	2.4	9.2781	16832.7
3	3.2	4.8782	3660.13
4	4	4.5888	3909.66

Table 5-24 Crack 17 length comparison as a function of changing fuselage diameter

S.N	D (m)	Final crack 17 length, (mm)	K_I (MPa $\sqrt{mm}$)
1	1.6	5.5076	4555.98
2	2.4	11.1243	16867.11
3	3.2	5.8174	4362.79
4	4	2.7296	3290.76

The documented simulation results for both cracks were summarized and plotted as a relationship between crack extension and corresponded SIF values for each crack increment, as following: Figure 5-205 shows SIF histories of crack 16, in this chart a steep

rise in SIF values occurred at the last steps of the simulation in the case of D equal to 1.6 m and 2.4 m, which gave an indication that both cracks might linkup at any time. Other simulation when D was equal to 3.2 and 4 m did not show any linkup process between the whole cracks in the tested panel; In addition, the cracks showed almost a linear rise in SIF values until the end of the simulation.

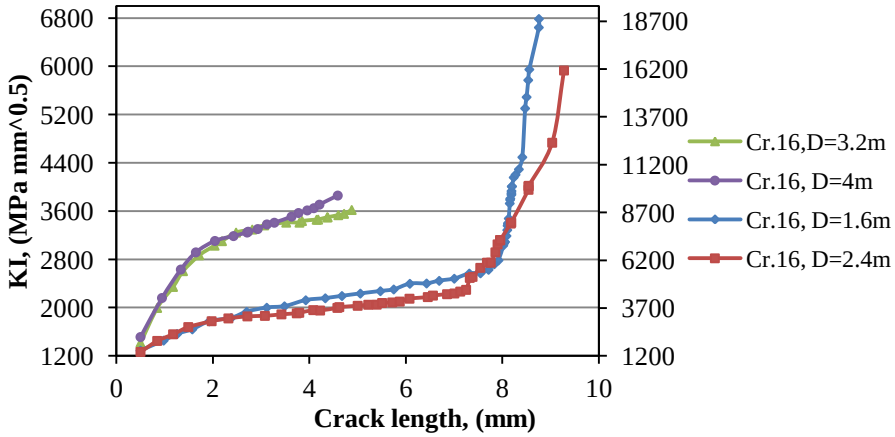

Figure 5-205 SIF histories of crack 16

Also, figure 5-206 shows SIF histories of crack 17, the crack had the same propagation trend of crack 16 with a little different in the case of D equal to 1.6 m, the crack was shorter in length and had a less simulation steps.

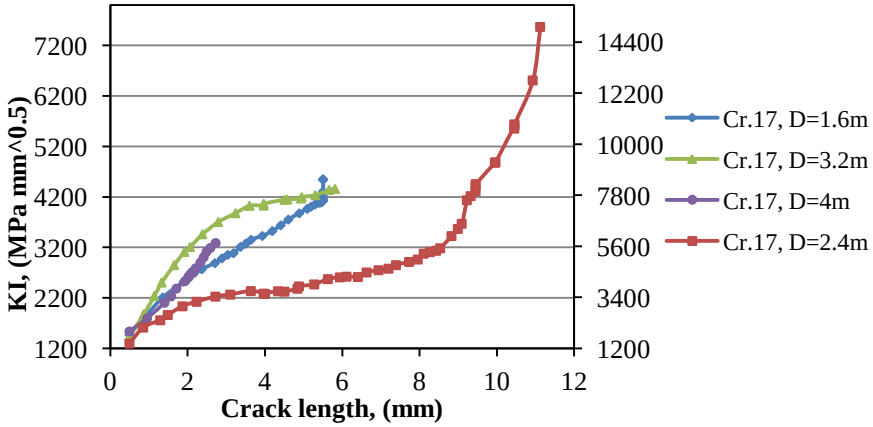

Figure 5-206 SIF histories of crack 17

Furthermore, some selected figures which are mentioned in section (5.4.1) could be used to describe the propagation steps of both cracks 16 and 17 in the case of the longest recorded

length occurred in the case of D equal to 2.4 m: The table 5-25 describes some details of selected simulation steps, its showed that crack 17 had a faster crack growing rate than

Table 5-25 Crack length and growing steps of cracks 16 and 17, (D=2.4 m)

S.N	Fig. No.	Step No.	Crack 16 length, (mm)	Crack 17 length, (mm)
1	5-168	28	7.2488	8.2735
2	5-169	31	7.5429	8.8296
3	5-170	33	7.7602	9.0944

crack 16 due to Crack 17 was closer to interacted cracks (cracks from 18 to 22) than crack 16. Also, figure 5-171 showed the linkup step between both cracks while figure 5-174 shows the last step of the simulation and the final shape of the formed lead crack and the deformed panel.

The second longest recorded crack 16 length recorded when D was equal to 1.6 m; the documented results showed that crack 16 had a longer crack length and no linkup occurred between both crack in this case, and the growing steps for both could be described using the figures which mentioned in section (5.4.2); table 5-26 shows some selected propagation steps of both crack.

The second longest crack 17 length recorded when D was equal to 3.2 m, also, in this case no linkup occurred between both cracks and the final recorded crack 17 length was (5.8174 mm) while crack 16 was equal to (4.8782 mm).

Table 5-26 Crack length and growing steps of cracks 16 and 17, (D=1.6m)

S.N	Fig. No.	Step No.	Crack 16 length, (mm)	Crack 17 length, (mm)
1	5-179	22	7.7143	5.4128
2	5.180	23	7.8338	5.4505
3	5.181	28	8.0517	8.4826
4	5.182	29	8.0855	5.4873
5	5.183	33	8.1181	5.4909
6	5.184	34	8.1325	5.4921
7	5.185	36	8.1612	5.4942
8	5.186	37	8.1654	5.4952
9	5.187	45	8.3425	5.5008
10	5.182	46	8.4148	5.5032
11	5.183	52	8.7583	5.5076

5.4.14 SIF evaluation of cracks 18 and 19 at different fuselage diameters

Tables 5-27 and 5-28 showed the final reached length of crack 18 and 19 at the end of the simulation using different fuselage diameters, it is clear that the longest length for both was when D was equal to 2.4 m.

Table 5-27 Crack 18 length comparison as a function of changing fuselage diameter

S.N	D (m)	Final crack 18 length, (mm)	K_I (MPa $\sqrt{mm}$)
1	1.6	4.1836	9903.01
2	2.4	9.1016	13886.6
3	3.2	4.7209	4073.25
4	4	2.9768	3217.55

Table 5-28 Crack 19 length comparison as a function of changing fuselage diameter

S.N	D (m)	Final crack 19 length, (mm)	K_I (MPa $\sqrt{mm}$)
1	1.6	2.9516	3469.69
2	2.4	11.1001	14010.2
3	3.2	5.6737	4089.66
4	4	0.855	2300.41

Also, figure 5-207 shows SIF histories of crack 18, it is a clear from the figure that the steep rise in SIF values occurred in the case of D equal to 1.6 m and 2.4 m at the last step of the simulation while the other diameters showed almost a linear rise in SIF values until the end of the simulation.

The shortest length of crack 19 recoded when D was equal to 4 m as it can be seen in figure 5-208, the steep rise in SIF values occurred at the last simulation steps when D was equal to 2.4 m.

To have more extensively explanation, some selected figures which mentioned in section (5.4.1) will be used for this purpose as following (D=2.4 m):

Figure 5-168 shows the simulation step (28), crack 18 recorded length was (7.0859 mm) at this step, while crack 19 length was (9.5801 mm). The linking up process occurred between crack 20 and 21 occurred at step 31 as shown in figure 5-169; crack 18 length at this step was (7.756 mm) while crack 19 length was equal to (10.2598 mm). Crack 19 had a longer crack length than crack 18 due to the mentioned linkup and it was closer to crack 19. Figure

5-170 shows the linking up step (step 33) between both cracks in the case of D equal to 2.4 m, and figure 5-174 shows the final simulation step.

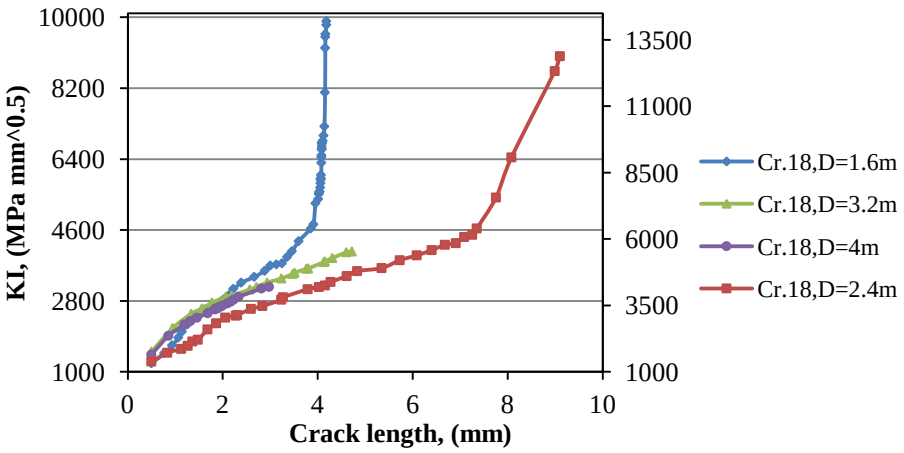

Figure 5-207 SIF histories of crack 18

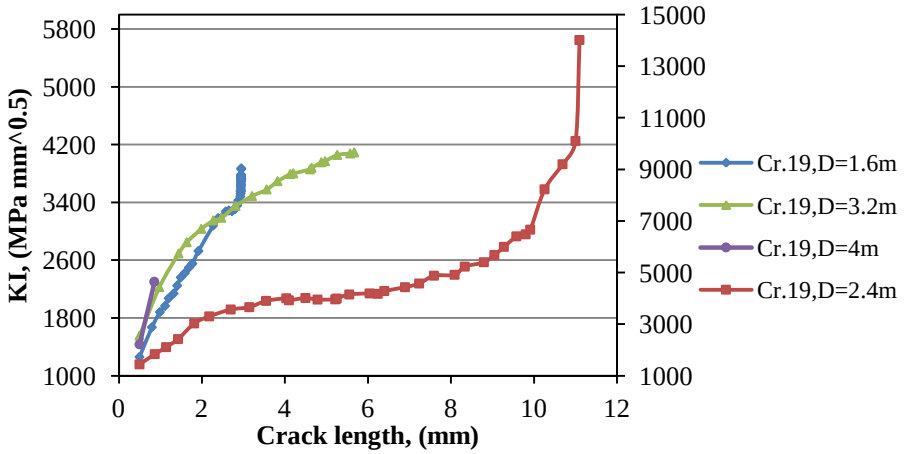

Figure 5-208 SIF histories of crack 19

Regarding to the second longest recorded length for both crack it occurred when D was equal to 3.2 m and final recorded crack 18 length was equal to (4.7209 mm), while crack 19 length was equal to (2.9516 mm). The other simulations did not show linkup process during the simulation for the whole cracks in the panel.

5.4.15 SIF evaluation of cracks 20 and 21 at different fuselage diameters

Tables 5-29 and 5.30 represent the crack lengths at the end of the simulation according to the change of fuselage diameters; it is clear that the longest recorded lengths were when D equals to 2.4 m for both crack 20 and 21.

Table 5-29 Crack 20 length comparison as a function of changing fuselage diameter

S.N	D (m)	Final crack 20 length, (mm)	K_I (MPa $\sqrt{mm}$)
1	1.6	2.946	4267.91
2	2.4	10.108	10510.79
3	3.2	3.507	4070.98
4	4	4.397	3710.3

Table 5-30 Crack 21 length comparison as a function of changing fuselage diameter

S.N	D (m)	Final crack 21 length, (mm)	K_I (MPa $\sqrt{mm}$)
1	1.6	5.553	4116.29
2	2.4	10.104	10268.01
3	3.2	6.051	4303.68
4	4	2.7251	3227.45

Figure 5.209 shows SIF histories of crack 20 during the simulation with different fuselage diameters, it is clear from the figure that the longest crack 20 recorded when D was equal to 2.4 m and the steep rise occurred in this case at the last simulation steps which give indication that the stress is concentrated and the material is yielded at the location of linking up with crack 21.

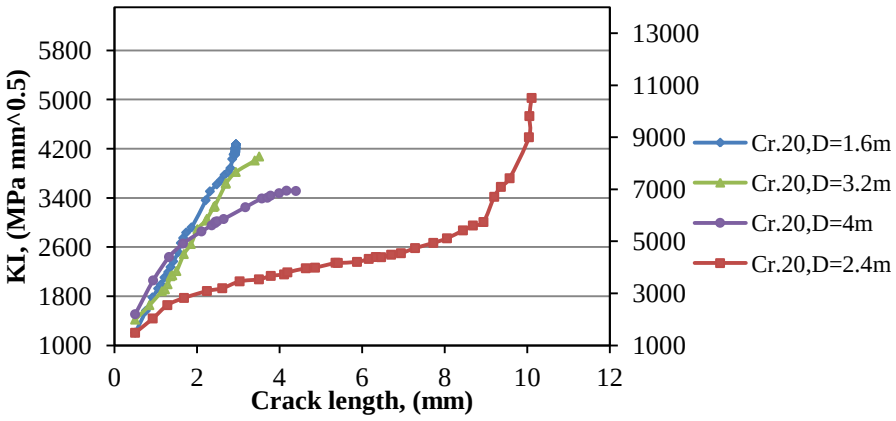

Figure 5-209 SIF histories of crack 20

Also figure 5-210 shows the relationship between SIF values for each increment of crack 21 extension, the steep rise in SIF vales occurred in the case of D equals 2.4 m at the end of the simulation while the other simulation cases (D=1.6 m, 3.2 m) showed a rise in SIF values.

Some selected figures from section (5.4.1) will be used to describe propagation steps for both cracks (20 and 21) as following:

The documented of simulation results of crack 20 showed that the crack had a faster crack growing than crack 21, figure 5-168 showed the simulation step 28, at this step crack 20 was equal to (9.202 mm) while crack 21 length was equal to (8.788 mm). Figure 5-169 shows the linking up step between cracks 20 and 21, while figure 5-174 shows the last step of the simulation (step 87) in the case of D equal to 2.4 m, the formed lead crack in this figure consisted from crack 9 to crack 22. The other simulations (D=1.6 m, 32.m, and 4 m) did not show linkup between cracks 20 and 21.

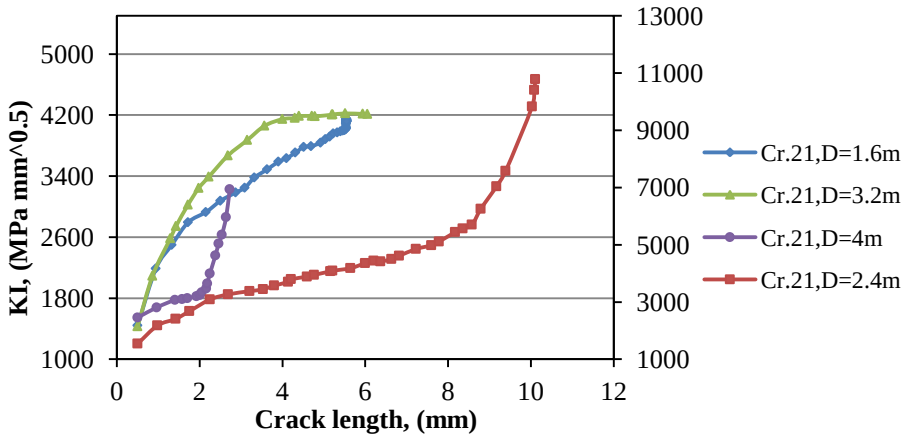

Figure 5-210 SIF histories of crack 21

5.4.16 SIF evaluation of crack 22 at different fuselage diameters

Table 5-31 represents the final reached crack 22 length at the end of the simulation according to different fuselage diameters.

The longest length recorded when D was equal to 2.4 m, as it can be seen in table below:

Table 5-31 crack 22 length comparison as a function of changing fuselage diameter

S.N	D (m)	Final crack 22 length, (mm)	K_I (MPa $\sqrt{mm}$)
1	1.6	4.843	5089.76
2	2.4	13.578	13155.4
3	3.2	6.171	4691.91
4	4	4.552	3806.38

Additionally, figure 5-211 shows SIF histories of crack 22 during the simulation, due to the is not interact with adjacent cracks, the growing trend almost linear, meaning as the crack grows as the corresponded SIF values increases. In the case of D equal to 1.6 m, the crack exhibits a steep rise in SIF values at the end of the simulation.

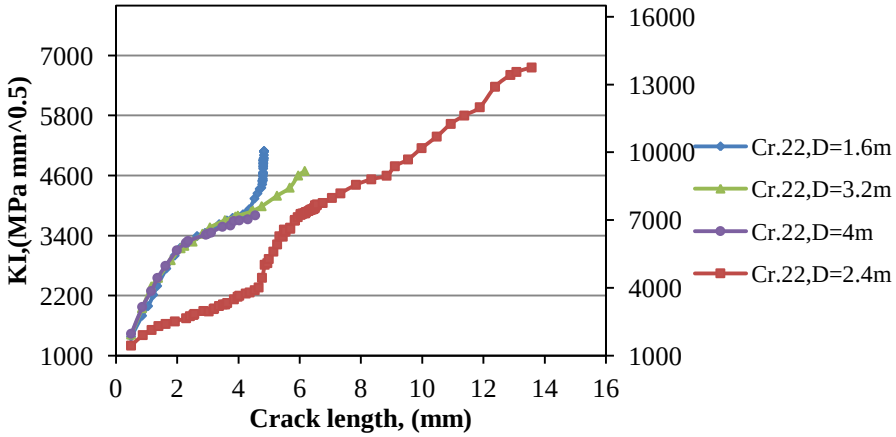

Figure 5-211 SIF histories of crack 22

Also, all selected figures which are used to describe the propagation steps of the previous cracks might be used to describe the growing trend of crack 22, but due to the crack did not interact with any crack, the figures showed only length different, as mentioned in table 5-31.

Chapter 6 Study of Panel Radius Effect on Stress Intensity Factors Values

6.1 EFFECT OF FUSELAGE DIAMETER ON K_I VALUES:

During the study of the effect of rivet holes number in the tested panel and fuselage diameters on stress intensity factors values of the cracks which emanated from each rivet hole; the recorded results showed that the values of K_I are increased as the number of the rivet holes increased in the tested panel, and the longest crack lengths recorded during the simulation when D was equal to 2.4 m.

The following sections describe the comparisons between the flat model (first numerical model) with three applied stresses (50, 100 and 200 MPa) and the curved panel which had the same dimensions with D equal to 2.4 m with applied differential stress equal to (0.054 MPa):

6.1.1 Results comparison in the case of applies stress 50 MPa and D equal to 2.4 m

As mentioned before, SIFs were calculated for each crack front and different crack sizes. Maximum values of SIFs calculated along the crack fronts were used as a reference. The SIF results shown in following figures which represent the solutions for cracks 1, 2, 11, 12, 21 and 22 only. These six cracks were selected because of their unique positions. That is, at these positions the influences of adjacent cracks interaction are either minimal (at the first and the eleventh hole; cracks 1, 2, 21 and 22 respectively) or maximal (the sixth hole; cracks 11 and 12).

The figure 6-1 shows the SIFs histories of crack 1 during the simulation using the flat and curved panel; it showed that crack 1 in the case of the curved panel was a longer length about (17.12%) than its value in the flat panel simulation case. Also, SIFs values in the curved panel were higher about (40) times at the end of the simulation. Additionally, crack 2 in the curved plate was longer about (24%) than its value in the flat plate; SIF value of crack 2 was higher about (30) times than its value in flat plate at the end of the simulation.

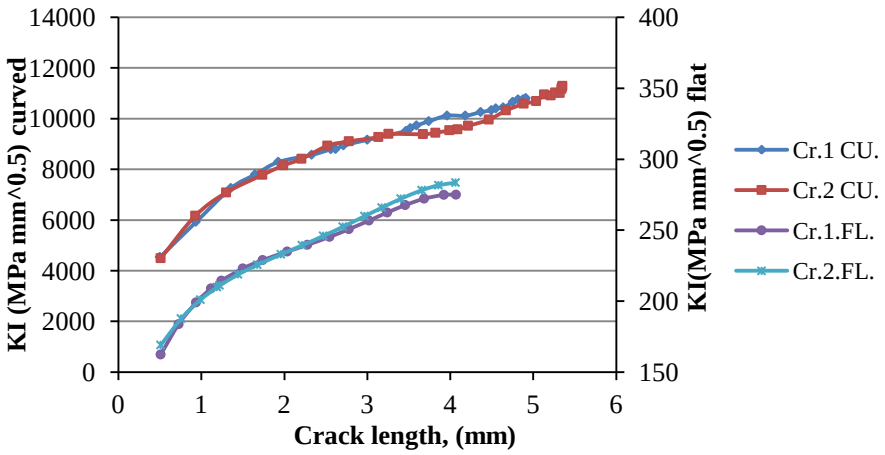

Figure 6-1 Cracks 1 and 2 K_I histories comparison for flat and curved panel

Figure 6-2 represents the comparison SIFs histories and crack 11 and 12 lengths for the curved and flat panel, it showed that crack 11 in the curved panel was longer about (58.2%) than its length in the flat panel, while crack 12 was longer about (53.2%). In addition, crack 11 SIF value in the curved panel was higher about (90) times compared to the SIF value in the flat panel, and (100.3) times higher in the case of crack 12.

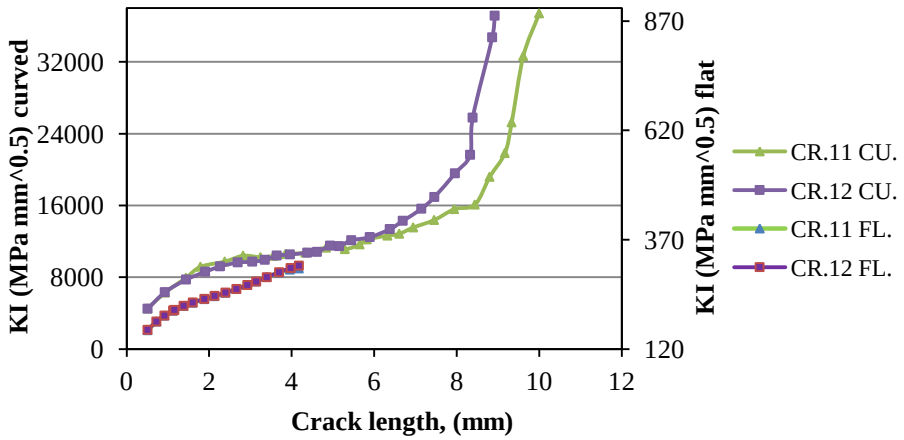

Figure 6-2 cracks 11 and 12 K_I Comparison between flat and curved panels

Figure 6-3 illustrates the simulation results comparison of cracks 21 and 22 in the case of curved and flat panel; it showed that crack 21 in the curved panel was longer about (28.81%) than its value in the case of the flat panel, while it was higher about (33.54%) in

the case of crack 22. Also, SIFs comparisons showed that crack 21 SIF value was higher about (42.46) times than its value in the case of the flat panel, meanwhile, it was higher about (47.6) times in the case of crack 22.

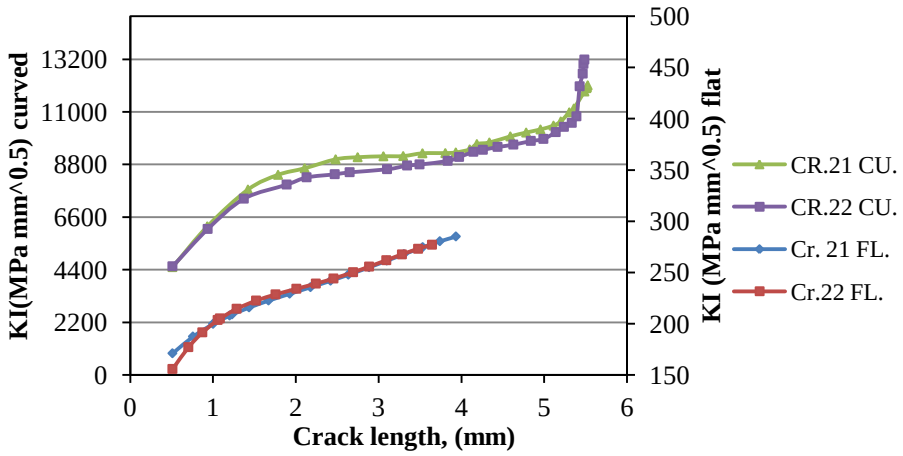

Figure 6-3 Cracks 21 and 22 K_I Comparison between and curved panels

6.1.2 Results comparison in the case of applies stress 100 MPa and D equal to 2.4 m

Increasing the applied stress to 100 MPa to the flat panel caused an increase in crack lengths, where crack 1 length increased by (26.33%) compared to the previous case, while crack 2 increased by (30.93%). It is clear in figure 6-4 that crack 1 length in the flat panel was lower about (12.5%) than its value in the case of curved panel, while crack 2 length in the case of curved panel was lower about (10%) than its length in the case of flat panel. Also, SIF' s comparisons showed that the value of crack 1 SIF was higher about (16.8) times than its value in the case of the flat panel, while it was higher about (14.3) times than its value in the case of the flat panel. Also, it's noticeable that the SIF values in the case of flat panel has increased as the applied stress is doubled compared to the first case (50 MPa), where it increased about (58.55%) for crack 1 and about (62.46%) for crack 2.

Figure 6-5 represents the second selected cracks , 11 and 12, it showed that the recorded length in the case of curved panel at the end of the simulation was longer about (25.85%) than its length in the case of the flat panel, while crack 12 length was longer about (16.91%) than its value in the case of flat panel. Also, crack SIF value in the case of curved

panel was higher about (25.1) than its value in the case of flat panel, while crack 12 SIF it was higher about (28.63) than its value in the case of flat panel at the end of the simulation.

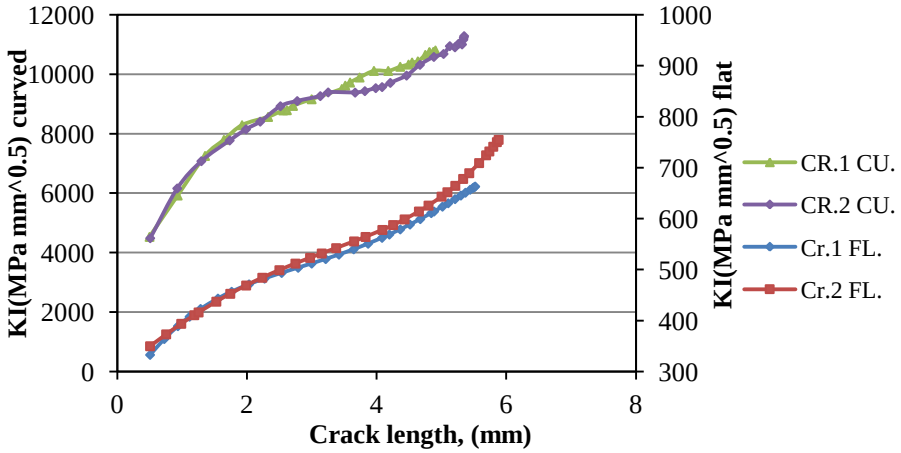

Figure 6-4 crack 1 and 2 K_I Comparison between flat and curved panels

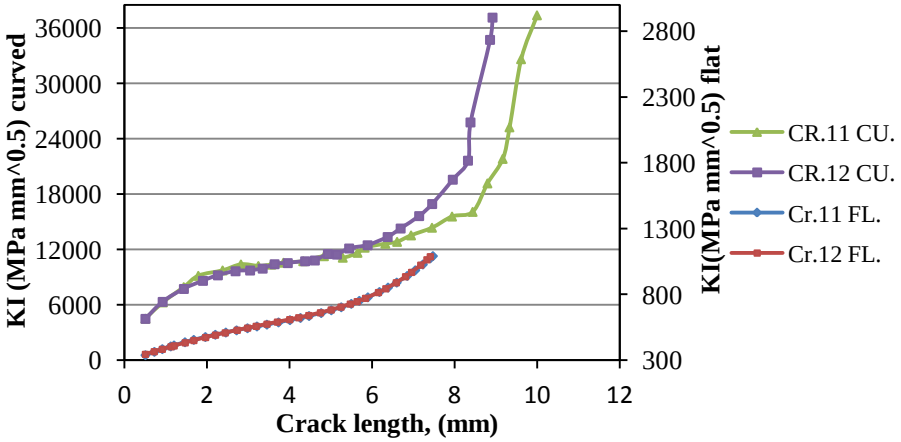

Figure 6-5 Crack 11 and 12 K_I Comparison between flat and curved panels

Figure 6-6 shows the results of SIFs histories of cracks 21 and 22 in the case of flat and curved panel's simulations, the results showed that crack 21 length in the case of flat panel was longer about (6.4%) than its length in the case of the curved panel, while crack 22 length in the case of curved panel was longer about (5.91%) than its length in the case of flat panel. Also, crack 21 SIF value in the case curved panel was higher about (14.42) times than its value in the case of the flat panel, while it was higher about (18.13) times in the

case of crack 22. Additionally, in the case of the flat panel, the rose in applies stress value showed an increase of crack 21 and 22 lengths, crack 21 length increased about (33.37%) and crack 22 length increased about (39.37%) compared to their lengths in the case of applied stress 50 MPa.

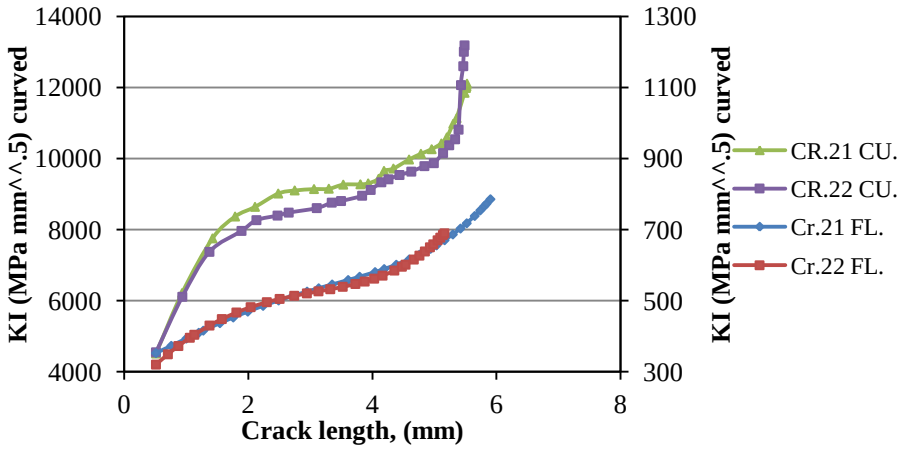

Figure 6-6 Cracks 21 and 22 KI Comparison between flat and curved panels

6.1.3 Results comparison in the case of applies stress 200 MPa and D equal to 2.4 m

The documented results in the case of applies stress 200 MPa showed an increase in crack lengths in the whole model, for example, crack 11 length increased about (44%) when the applied stress changed from 50 MPa to 100 MPa, and about (49.5%) when applied stress changed from 100 MPa to 200 MPa.

Also, the SIFs histories result from the comparison in the case of the curved panel (D=2.4 m) and the flat panel (applied stress 200 MPa) is described in the some selected figures as follows:

Figure 6-7 shows SIFs histories of crack 1 and 2 in the both cases, crack 1 in the case of flat panel was longer about (11.54%) form its length in the case of curved panel, while crack 2 was longer about (10.64%) form its length in the case of curved panel. Also, in the case of flat panel both cracks showed a sheep rise in SIFs values at the end of the simulation. In addition, SIF value of crack 1 was higher about (6) times than its value in the case of flat panel, almost higher about (4%) in the case of crack 2.

Figure 6-8 shows the second selected comparison case between cracks 11 and 12 in both cases, it showed that crack 11 length in the case of the curved panel was longer about (17.3%) than its length in the case of flat panel, while crack 12 length was longer about (8%) in the case of flat panel than its length in the case of curved panel. SIFs values in the case of curved panel was higher about (crack 11, 9.6%) and (crack 12, 7.6%) than its values in the case of flat panel.

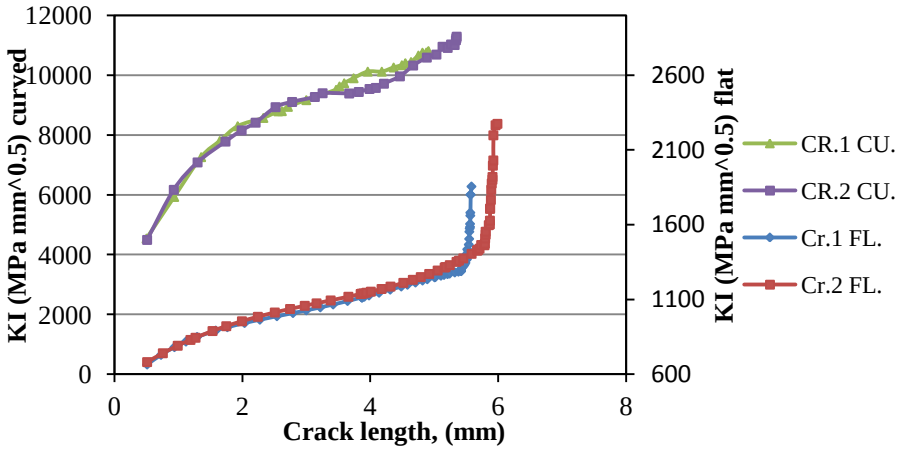

Figure 6-7 Cracks 1 and 2 K_I Comparison between flat and curved panels

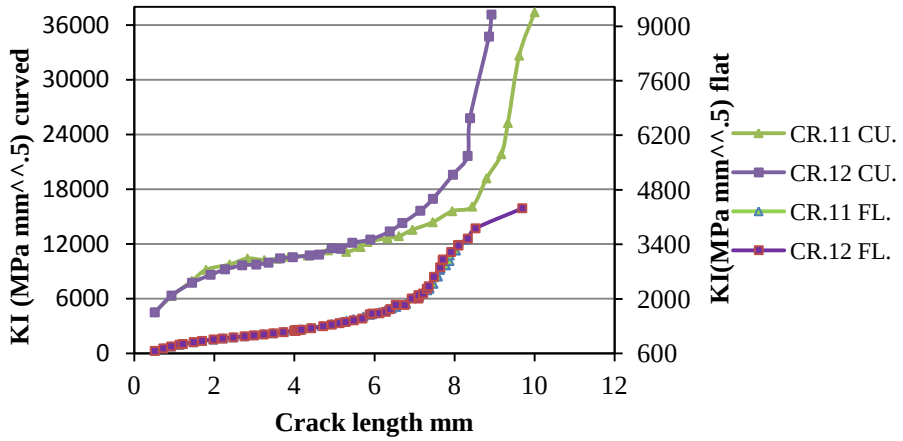

Figure 6-8 Cracks 11 and 12 K_I Comparison between flat and curved panels

Figure 6-9 shows the last comparison case which is done between cracks 21 and 22 in the case of flat and curved panel, it showed that crack 21 length in the case of flat panel was longer about (2.8%) than its length in the case of curved panel, while crack 22 length was longer about (8%) in the case of curved panel than its value in the case of flat panel. Also,

SIFs values of crack 21 and 22 in the case of curved panel was higher about (7.2%) and (9%) compared to its value in the case of flat panel.

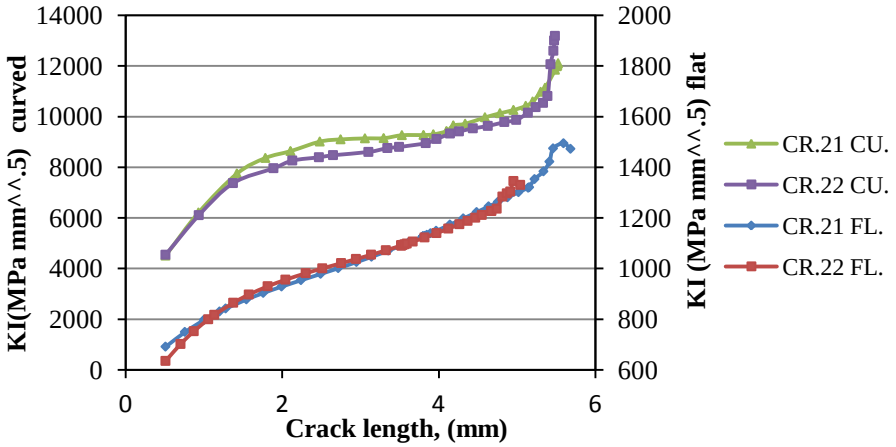

Figure 6-9 Cracks 21 and 22 KI Comparison between flat and curved panels

6.2 COMPARISON ANALYSIS AND DISCUSSION

The documented results of the curved panel showed that this kind of panel the loading method produces an effective value of failure modes (mode II and mode III), but mode I still dominant failure mode.

Figure 6-10 shows first step loading, it showed the stress distribution values around the loaded rivet holes, it can be seen from the figure the maximum stresses were concentrated at the space between the holes, the place of crack extension area.

The tables in appendix (D) section (1-D) show simulation results of crack 11 and 12.
As mentioned above, this type of loading produces high-stress distribution and as a result of that it will cause three failure modes (mixed mode failure) and the tested panel will have a short life (low number of cycles to failure), (see tables in section (1-D) appendix (D) tables 68 and 69).

.

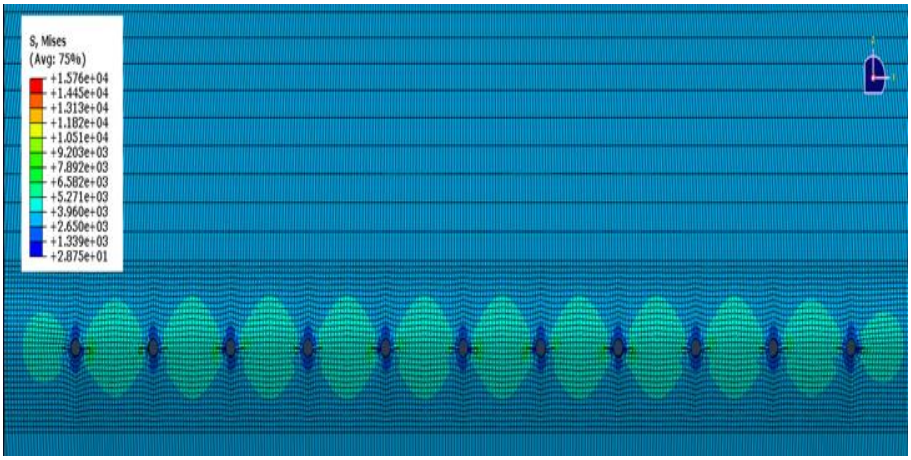

Figure 6-10 step simulation 1 of XFEM model of curved panel (D=2.4 m)

Figure 6-11 represent the simulation step10, and table 6-1 below shows some crack length at this step:

Table 6-1 Some selected crack lengths during the simulation step 10

Step no.	Crack 1 length (mm)	Crack 10 length (mm)	Crack 11 length (mm)	Crack 12 length (mm)	Crack 13 length (mm)
10	3	4.1651	4.33422	3.96123	4.2839

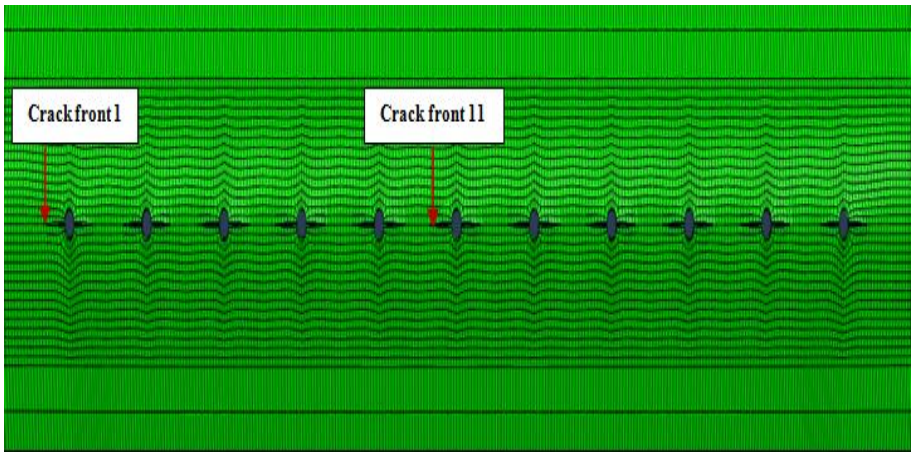

Figure 6-11 step simulation 10 of XFEM model of curved panel (D=2.4 m)

In addition, Figure 6-12 shows the stress distribution around the rivet holes 5, 6 and at step 10, those holes selected due to the stress are concentrated around those middle holes and the color legend describes the values of the stress.

The adjacent cracks as shown in figure 6-13 are growing towards each other every step of simulation, also, it can be seen from this figure the middle cracks (10, 11, 12, and 13) are growing faster than the other crack due to the stress concentration at their location and the table below shows their lengths at this step:

Table 6-2 some selected crack lengths during the simulation step 22

Step no.	Crack 1 length (mm)	Crack 10 length (mm)	Crack 11 length (mm)	Crack 12 length (mm)	Crack 13 length (mm)
22	4.817	8.084	9.1698	8.3283	9.034

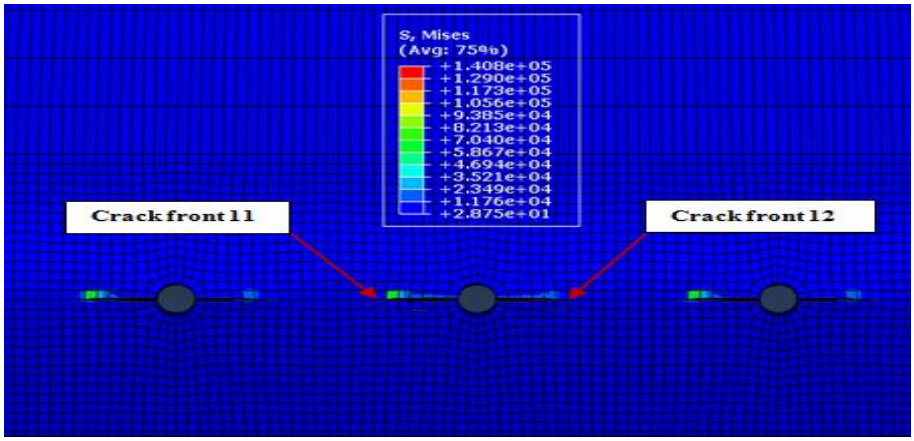

Figure 6-12 stress distribution (Von Mises) around rivet holes 5, 6 and 7, step 10

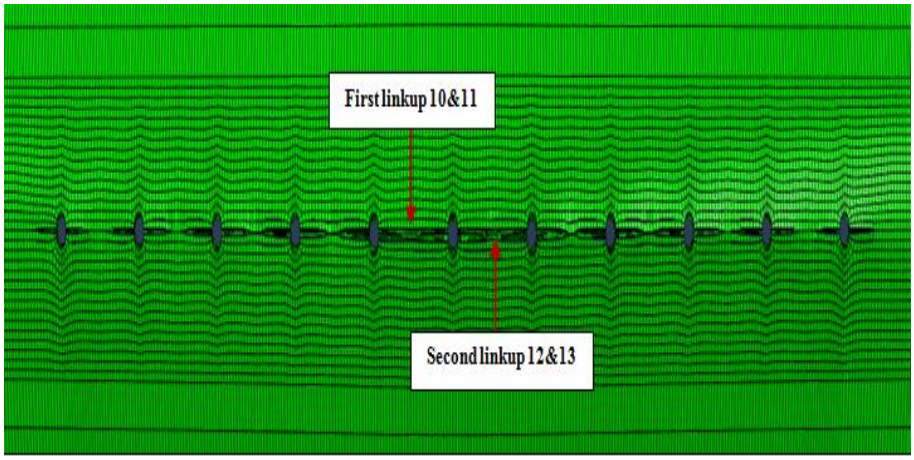

Figure 6-13 Step simulation 22 of XFEM model of curved panel (D=2.4 m)

Additionally, figure 6-14 represents the stress distribution around the middle holes; it's clear comparing to the previous selected step the value of the stress increased.

A step further, (step 23), the adjacent crack 10 and 11 linked up and the second linkup occurred between cracks 12 and 13, those cracks at this step formed one lead crack with two crack fronts (9 and 14). Also, figure 6-15 shows the stress distribution around the holes and the cracks and it can be seen from this figure the values of the stresses are increased compared to the previous selected step. It is clear that due to the high values of stress concentration at the location of rivet holes 5, 6 and 7 the first and the second linkup occurred, see figure 6-16.

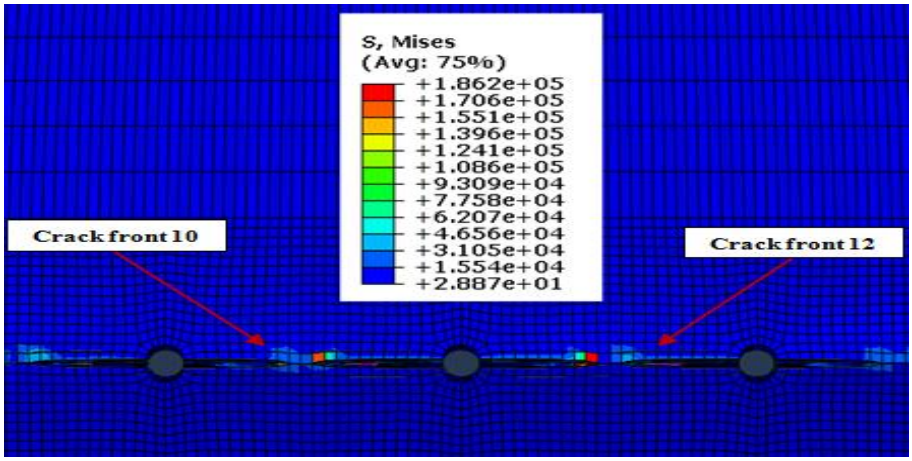

Figure 6-14 Stress distribution (Von Mises) around rivet, holes 5, 6 and 7, step 22

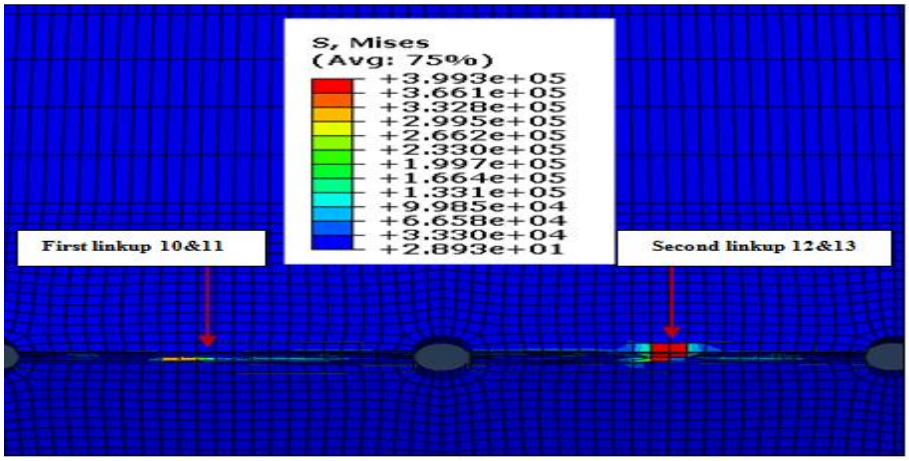

Figure 6-15 stress distribution (Von Mises) around rivet holes 5, 6 and 7, step 23

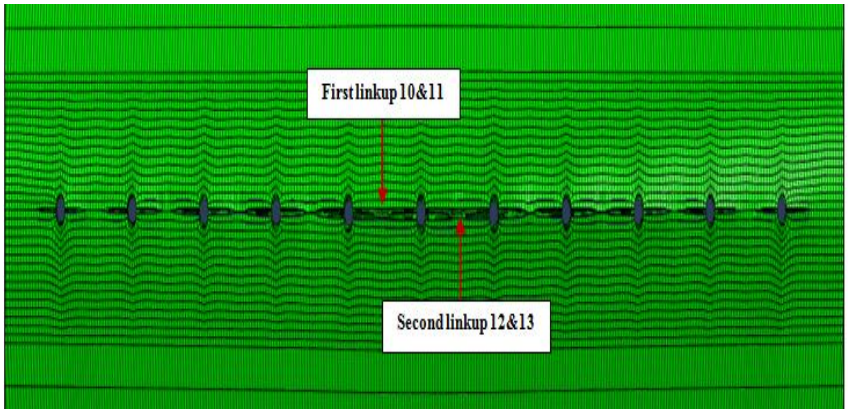

Figure 6-16 step simulation 23 of XFEM model of curved panel (D=2.4 m)

The third linkup occurred between crack 14 and 15 at simulation step 25, at this step the formed lead crack length was equal to (104.0964 mm) with two crack fronts (9 and 16), see figure 6-17. Figure 6-18 illustrates the stress distribution at the location of crack 14 and 15 was very high and this let both crack to interact with each other.

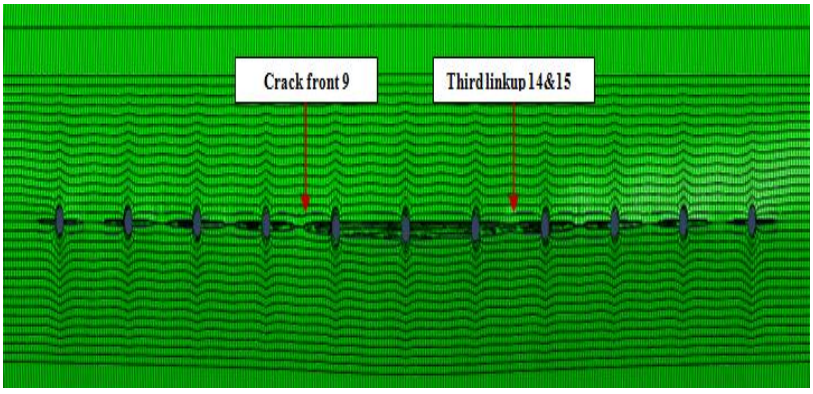

Figure 6-17 step simulation 25 of XFEM model of curved panel (D=2.4 m)

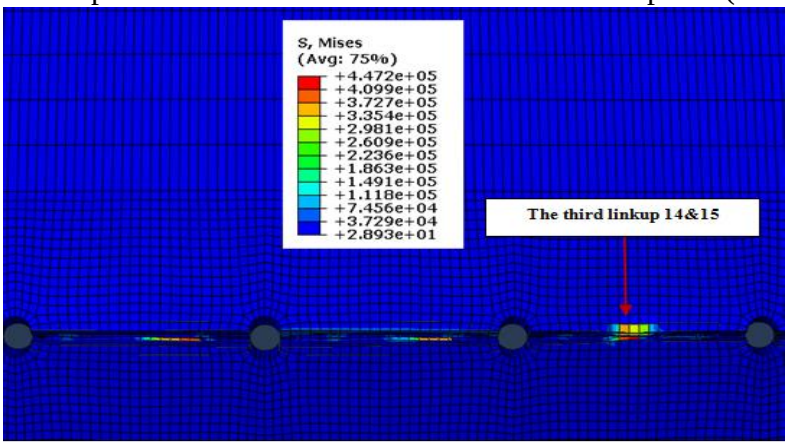

Figure 6-18 stress distribution (Von Mises) around rivet holes 5, 6 and 7, step 25

The last simulation step was step number 26 is shown in figure 6-19, no more interaction between cracks occurred and the panel failed at this step, and the final reached length of interacted cracks (lead crack) is (104.4011 mm). Figure 6-20 shows the stress distribution at the last simulation step.

Figure 6-21 shows last simulation step in the case of flat panel (applied stress=200MPa), in this case, more cracks linked up to form a lead crack. It can be seen from figures 6-20 and

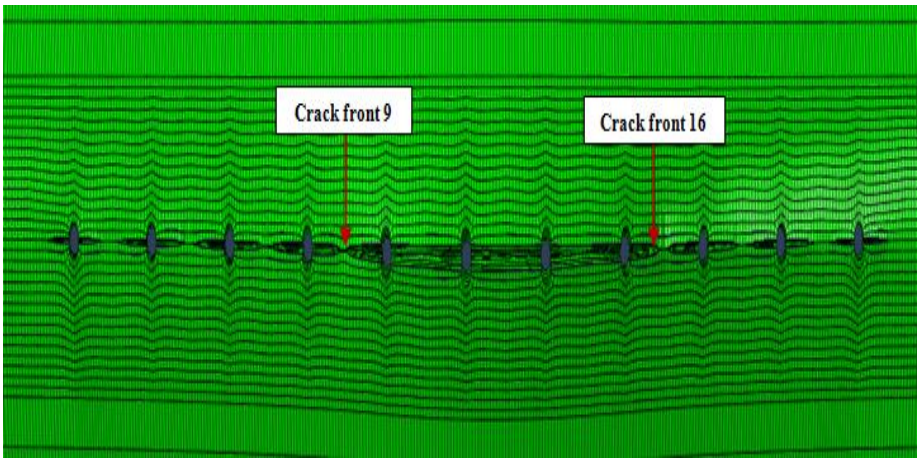

Figure 6-19 step simulation 26 of XFEM model of curved panel (D=2.4 m)

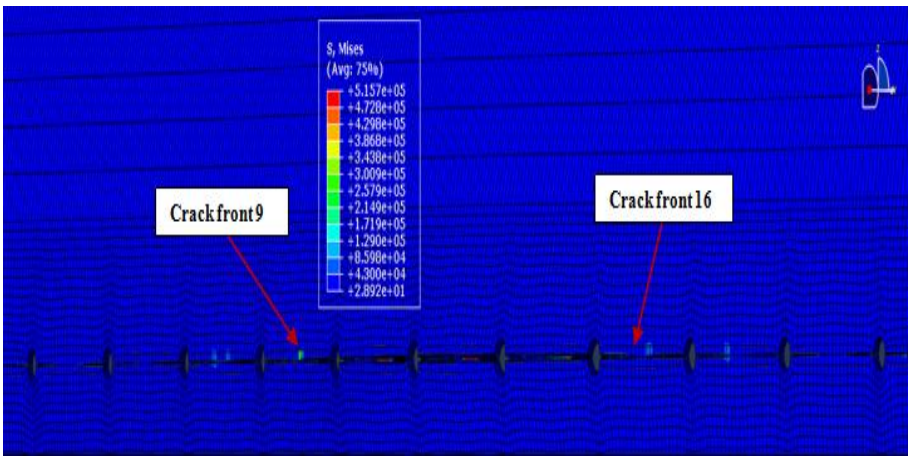

Figure 6-20 stress distribution (Von Mises) around rivet holes 5, 6 and 7, step 26

6-21 that the stress contours showed that the maximum stress (Von mises) measured in the case of curved panel was higher about 48 times than the maximum measured stress in the

case of flat panel. According to recorded results which presented in the Tables 68 and 69 in appendix (D) section (1-D) for the curved panel and tables 70 and 71 at the same section for the flat panel, the recorded values of K_I very was high in the case of curved panel compared to K_I in the case of flat panel might be due to the effective existence of K_{II} and K_{III}, (see table 68 and 69).

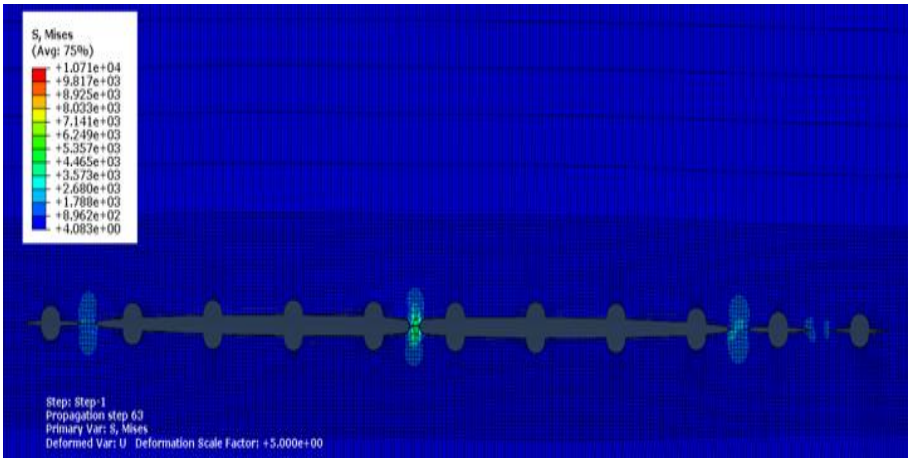

Figure 6-21 Flat panel Von Mises stress distribution for the last step of the simulation

6-3 EFFECT OF PANEL REINFORCEMENT BY USING FRAMES ON K_I VALUES

The basic functions of an aircraft's structure are to transmit and resist the applied loads and to provide an aerodynamic shape and to protect passengers, payload, systems, and the like from the environmental conditions encountered in flight. These requirements, in most aircraft, result in thin-shell structures where the outer surface or skin of the shell is usually supported by longitudinal stiffening members and transverse frames to enable it to resist bending, compressive, and torsional loads without buckling, [99].

The previous numerical curved panels were studied without any kind of panel support or truss, like adding fuselage frames or stingers which represent the real fuselage structure, and the model below represent the fifth numerical model with 11 holes (22 cracks) supported by two frames as shown in figure 6-22. The simulation results showed that this

truss showed a reduction in SIFs values (K_I, K_{II} and K_{III}) and the following are some results comparison between the fifth model and the same model but with frames: Tables 72 and 73 in appendix (D) section (2-D) show the simulation results of crack 1 in the case of with and without frames; it showed a reduction in SIF value almost 16 times (for the highest SIF values in two cases) by using the frames as truss component. Cracks 11 and 12 which emanating from the sixth hole showed the same previous tendency, where the frames reduce SIFs values for crack 11 almost 56 times and 54 times for crack 12, see tables 74,75 and 76,77 in section (2-D) appendix (D). Tables 78, 79, 80 and 81 in section (2-D) appendix (D) show the results comparison for cracks 21 and 22 (cracks emanating from rivet hole 11); it showed the same value or reduction in SIFs of cracks 1 and 2(almost 16 times). The function of ribs, frames, and stringers is that they support the skin. Without them, the skin of the fuselage, wings, or tails would buckle even at moderate loads. This is not their only purpose though. Stringers are usually busy resisting tensile and compressive loads resulting from bending in the fuselage and wing. Frames also transmit forces into the structure whether they are air loads on the wing or fuselage or point loads such as bombs. Rib is the name given to a frame in a wing. Properly designed, this type of construction is efficient for the job it has to do, [100]. Figure 6-23 represents the last simulation step for the panel with frames, it showed that the frames subjected to the maximum values of stress while the fuselage skin subjected to the minimum stresses, this explains the function of the frames (preventing skin buckling or deforming).

The results which obtained from the case study in chapter 6, the panel was a fuselage skin without any kind of truss and K_I values were very high compared to K_I results of the trussed panel. Also, the panel with frames showed no linkup process occurred during the simulation while the linking up process occurred between cracks from crack 9 to crack 16 for un-trussed panel, (see figure 6-20).

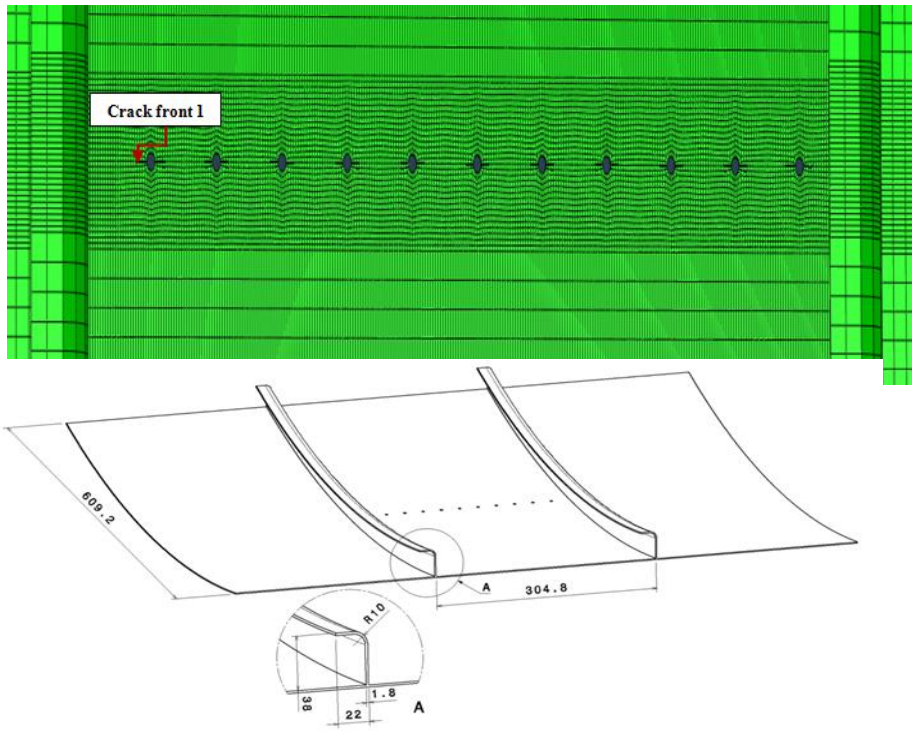

Figure 6-22 Frames details and cracks positioning

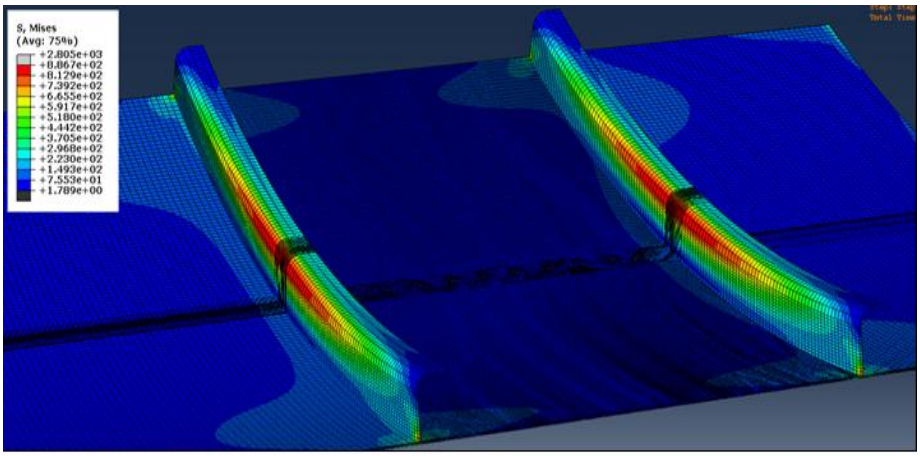

Figure 6-23 Von Mises stress distribution at the last simulation step

Chapter 7 Stress Intensity Factors Calculation Using Standard Models

In this chapter, the stress intensity factor evaluated using NASGRO software and the empirical equation which mentioned in the stress analysis of cracks handbook [58], (cracks in a shell section). All boundary conditions which related to empirical equations were applied especially configuration correction factors for SIF (f (ς)) and the ratio of two systems of applied shell parameter (ς). The following information has been used in section (7-1) calculations:

Table 7-1 Fuselage dimensions and the applied stresses

D(mm)	R(mean radius, mm)	P(MPa)	σ(MPa)	t(mm)
1600	799.2	0.054	26.973	1.6
2400	1199.2	0.054	40.473	1.6
3200	1599.2	0.054	53.973	1.6
4000	1999.2	0.054	67.473	1.6

7.1 CYLINDER MODEL WITH LONGITUDINAL THROUGH CRACK

Figure 7-1 shows the shell sample which used to calculate stress intensity factor using two mentioned methods, taking in consideration the following equation and conditions:

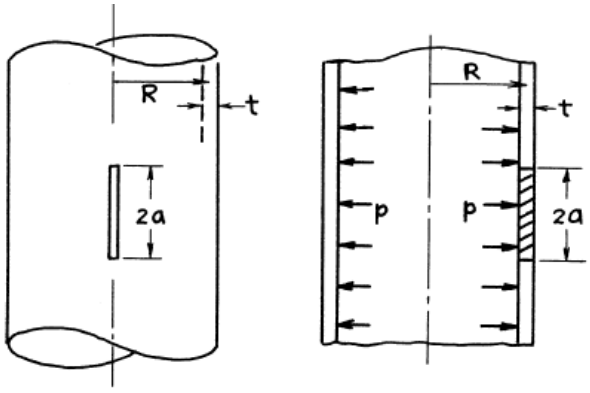

Figure 7-1Through crack in cylinder (longitudinal)

-The applied stress$(\sigma) = p * \frac{R}{t}$ (7.1), R: the mean radius $= \frac{(D-t)}{2}$, (7.2)

D: shell diameter

t: shell thickness

p: internal pressure in the shell

-The ratio of two systems of applied shell parameter $\varsigma = \frac{a}{\sqrt{R*t}}$, (7.3)

-Configuration correction factor for SIF $F(\varsigma) = (1 + 1.25 * \varsigma^2)^{0.5}$ if $0 < \varsigma \leq 1$, (7.4)

Or $F(\varsigma) + 0.6 + 0.9 * \varsigma$ if $1 \leq \varsigma \leq 5$, (7.5)

-Stress intensity factor $K_I = \sigma * \sqrt{\pi * a} * F(\varsigma)$, (7.6)

The obtained results are described and classified in figures as following:

7.1.1 SIF results at D equal to 1.6 m and the initial crack length 2.9 mm

Figure 7-2 shows the results comparisons using both methods; in this case, the maximum differential value between two calculating methods was (9.625%) and the lowest was (1.096%).

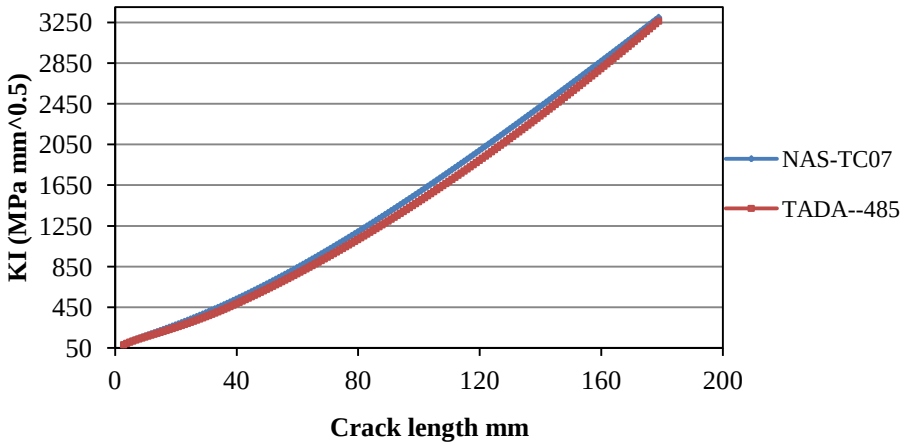

Figure 7-2 SIF results, D=1.6 m

7.1.2 SIF results at D equal to 2.4 m and the initial crack length 2.9 mm

Figure 7-3 shows the results comparisons using both methods; in this case, the maximum differential value between two calculating methods was (9.633%) and the lowest was (1.123%). The results showed that the increase of fuselage diameter from 1.6 m to 4 m caused difference up to 59.63% and 68.07% for the initial and last step of calculation in the case of using NASGROW software, 59.92% and 68.05% for the initial and last step of calculation in the case of using the empirical equations.

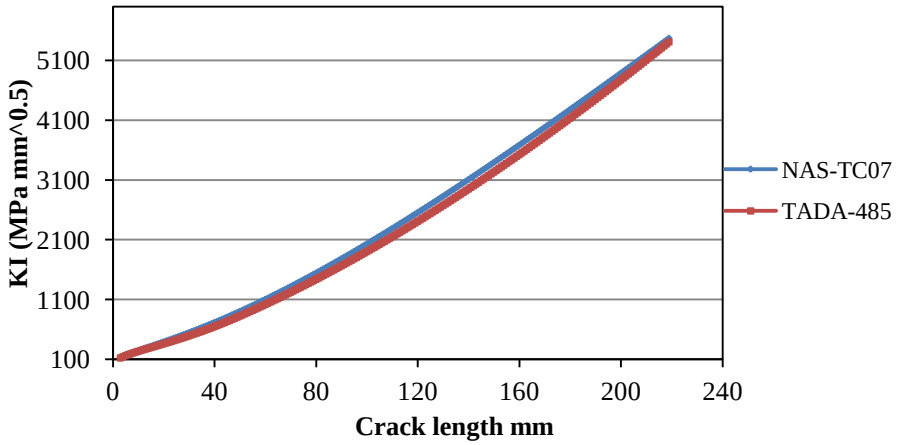

Figure 7-3 SIF results, D=2.4 m

7.1.3 SIF results at D equal to 3.2 m and the initial crack length 2.9 mm

Figure 7-4 shows the results comparisons using both methods; in this case, the maximum differential value between two calculating methods was (9.636%) and the lowest was (1.123%).

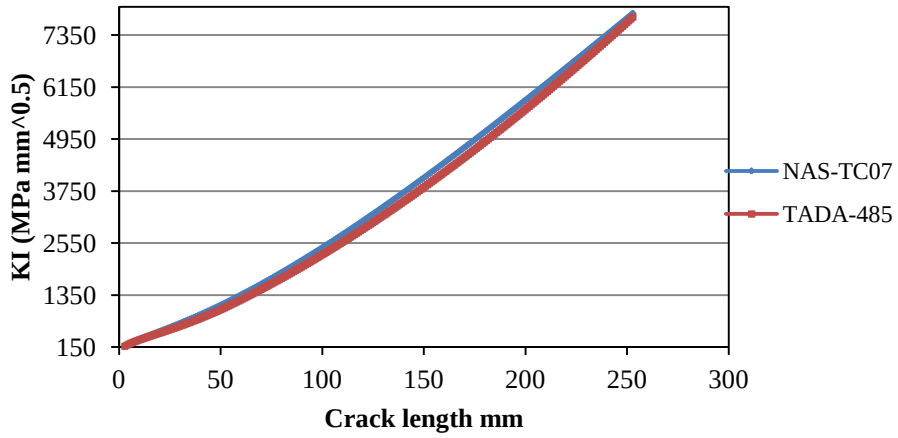

Figure 7-4 SIF results, D=3.2 m

7.1.4 SIF results at D equal to 4 m and the initial crack length 2.9 mm

Figure 7-5 shows the results comparisons using both methods; in this case, the maximum differential value between two calculating methods was (9.638%) and the lowest was (1.170%).

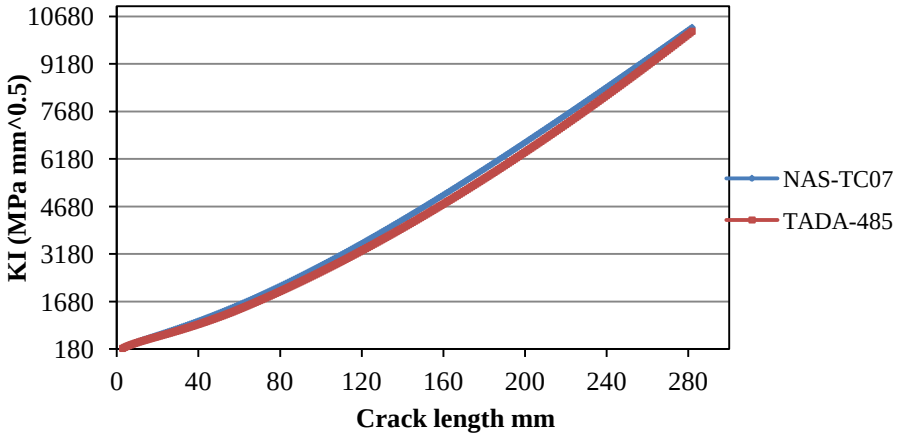

Figure 7-5 SIF results, D=4m

The results shows the same propagation trend for different fuselage diameters from 1.6 m to 4 m, the highest differential value was (9.638%) and the lowest was (1.096%).

7.2 CYLINDER MODEL WITH CIRCUMFERENTIAL THROUGH CRACK

The second standard model which used to calculate SIFs is circumferential through crack in cylinder, see figure 7-6.

The calculations based on the empirical equations and its boundary conditions, which are mentioned in the stress analysis of cracks handbook, [58], and using NASGROW software.

Table 7-2 shows some information which used in SIFs calculations.

Figure 7-6 shows the second selected model and the equations and conditions which related to stress intensity factor calculation for this model are described below.

Table 7-2 Fuselage dimensions and the applied stresses and forces

D(mm)	R(mean radius, mm)	P(MPa)	$F_o(N)\times10^{-6}$	σ_1(MPa)	t(mm)
1600	799.2	0.054	6.72	13.4865	1.6
2400	1199.2	0.054	4.48	20.2365	1.6
3200	1599.2	0.054	3.36	26.9865	1.6
4000	1999.2	0.054	2.68	33.7365	1.6

:

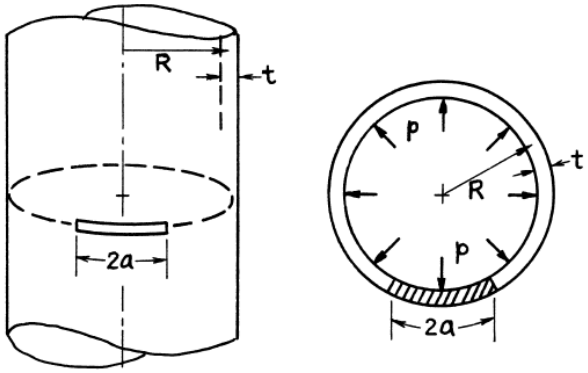

Figure 7-6 Circumferential crack in cylinder

-The applied stress$(\sigma) = p * \frac{R}{2t}$, (7.7) *R*: the mean radius $= \frac{(D-t)}{2}$, (7.8)

D: shell diameter

t: shell thickness

p: internal pressure in the shell

-The ratio of two systems of applied shell parameter $\varsigma = \frac{a}{\sqrt{R*t}}$, (7.9)

-Configuration correction factor for SIF $F(\varsigma) = (1 + 0.3225 * \varsigma^2)^{0.5}$ if $0 < \varsigma \leq 1$, (7.10)

Or $F(\varsigma) = 0.9 + 0.25 * \varsigma$ if $1 \leq \varsigma \leq 5$, (7.11)

-Stress intensity factor $K_I = \sigma * \sqrt{\pi * a} * F(\varsigma)$, (7-12)

The obtained results are represented in charts as a relation between crack length and corresponded stress intensity factor as following:

7.2.1 SIF results at D equal to 1.6 m and the initial crack length 2.9 mm

Figure 7-7 shows SIF histories at fuselage diameter 1.6 m using two mentioned methods, it showed that as the crack grows as SIF values increases.

SIF value using the empirical method was higher about (3.16%) than its value using NASGROW software, while the lowest recorded differential value was at the seventh step (0.0%).

7.2.2 SIF results at D equal to 2.4 m and the initial crack length 2.9 mm

Figure 7-8 shows SIF histories at fuselage diameter 2.4 m using two mentioned methods; it showed the same growing trend of the previous figure. Also, SIF value using the empirical

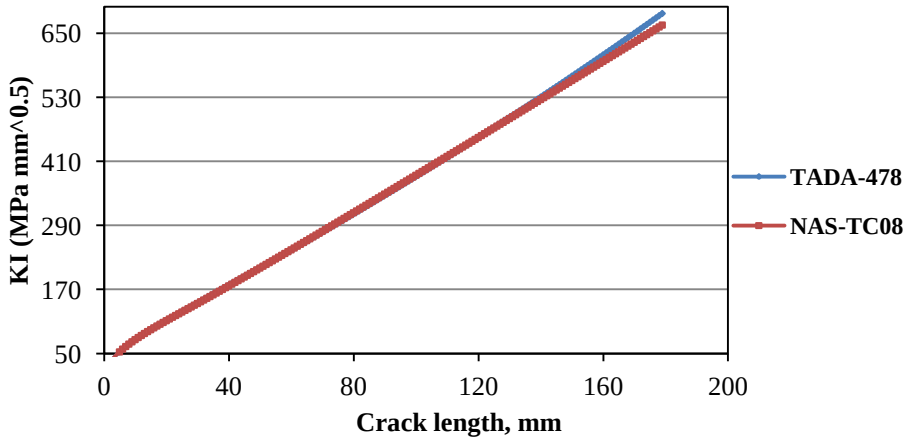

Figure 7-7 SIF results, D=1.6 m

method was higher about (3.18%) than its value using NASGROW software, while the lowest recorded differential value was at the seventh and tenth step (0.0%).

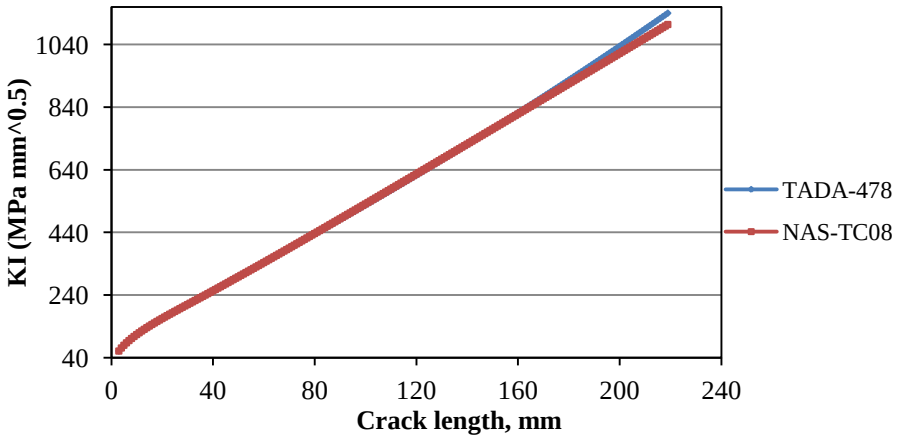

Figure 7-8 SIF results, D=2.4 m

7.2.3 SIF results at D equal to 3.2 m and the initial crack length 2.9 mm

Figure 7-9 shows the growing trend of SIF values when D equal to 3.2 m using the two mentioned method. Also, SIF value using the empirical method was higher about (3.20%)

than its value using NASGROW software, while the lowest recorded differential value was at the eleventh step (0.0%).

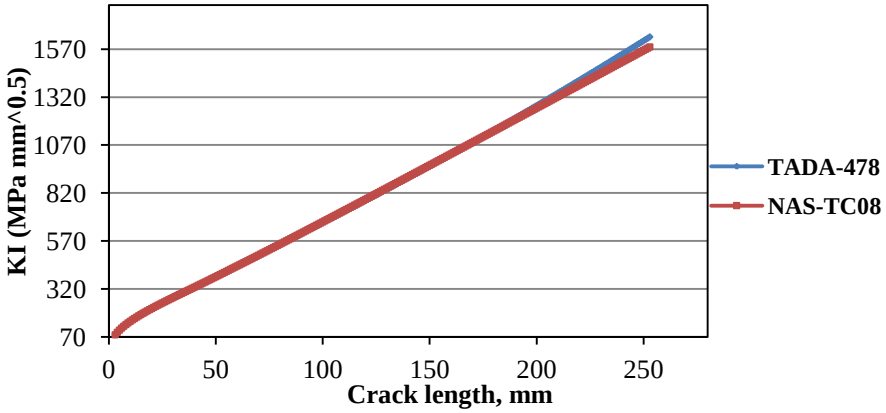

Figure 7-9 SIF results, D=3.2 m

7.2.4 SIF results at D equal to 4 m and the initial crack length 2.9 mm

Figure 7-10 shows the last calculation case (D=4 m), Also, SIFs value using the empirical method was higher about (2.42%) than its value using NASGROW software at the last step, while the lowest recorded differential value was at step 215 (0.0%).

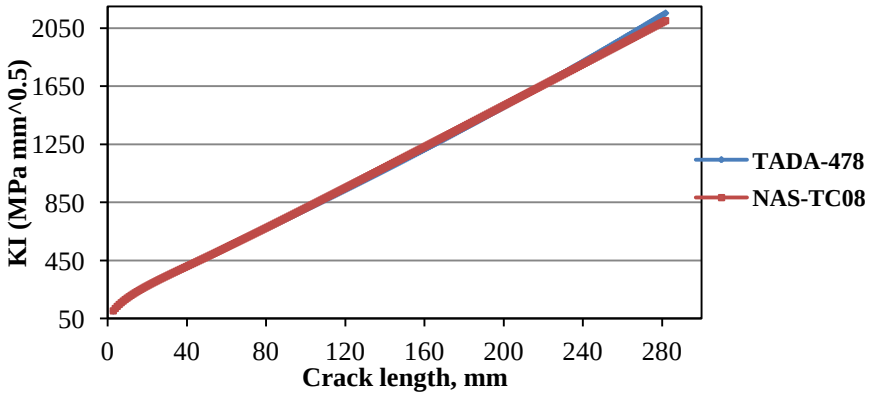

Figure 7-10 SIF results, D=4 m

The results showed that the increase of fuselage diameter from 1.6 m to 4 m caused difference up to 60.31% and 68.33% for the initial and last step of calculation in the case of using NASGROW software, 60% and 68.08% for the initial and last step of calculation in the case of using the empirical equations.

Chapter 8 Conclusions and Recommendations

The prediction of crack growth rate and residual strength of cracked structure demands accurate calculation of stress intensity factors. There are continuous researches that deal with the problem of SIFs determination. Some solutions are available, but only for simple geometry configurations with few cracks. As technology and computer sciences develop and become more available, the researchers are trying to introduce and apply new computational methods and techniques in order to find solutions for complex geometries with multiple cracks. This study represents an effort in that direction. Here, the SIFs calculations based on implementation of XFEM in Abaqus, are conducted for a typical aero structural configuration with MSD.

First, the analyzed model was a unique 3D configuration with 22 cracks that propagate at the same time, whereas stress intensity factors are computed along the crack fronts for all 22 cracks. As it can be seen in Figures which are mentioned in sections 4.1.1.1, 4.1.2.1 and 4.1.3.1 (description to cracks propagation steps for each applied stress) the cracks spread all the time through unchanged mesh and can reach long lengths. With XFEM the need for new mesh creation after each step is eliminated.

In order to check the significance of obtained values, SIFs were also obtained by means of FRANC2D/L software, and by superposition based approximate method. The analysis of the results has shown that the values obtained by means of XFEM can be used for the evaluation of fatigue life of analyzed configuration with acceptable accuracy. The results comparisons, as described in sections (4-4-1, 4-4-2 and 4-4-3) by using the relationship between geometry factor and crack length, showed the following:-

- At applied stress 50 MPa the maximum difference recorded between XFEM and F2D/L was recorded at the initial simulation step 11.71373% (crack 22), while the lowest was recorded at the last step of the simulation 0.44997% (crack 2). The maximum and minimum difference between XFEM and approximation method were recorded to crack 22, 17.35899% and 0.00807% respectively.

- At applied stress 100 MPa the maximum difference recorded between XFEM and F2D/L was recorded at the initial simulation step 14.14178% (crack 21), while the lowest was recorded at the fifth step of the simulation 0.48864% (crack11). The maximum and difference between XFEM and approximation method was recorded at initial step to crack 22, 14.354976%, while the lowest was 0.02612% at the fifth simulation step of crack 12.
- At applied stress 200 MPa the maximum difference recorded between XFEM and F2D/L was recorded at the initial simulation step 12.54913% (crack 21) , while the lowest was recorded at the eighth step of the simulation 0.03276% (crack11). The maximum and difference between XFEM and approximation method was recorded at initial step to crack 22, 15.2%, while the lowest was 0.07% at the seventh simulation step of crack 12.

It is interesting to note that – when compared with FRANC2D/L values – there is a trend of increasing differences between obtained SIFs as cracks grow, which may be related to the differences in methods for simulating crack interaction. Also, FRANC2D/L analysis was carried out on the two-dimensional structure. This kind of analysis doesn't take into account the effect of three-dimensional stress state in unstiffened panel which is actual 3D structure.

Although, XFEM is time consuming and requires substantial computer resources (especially when multiple cracks are involved), this study showed that with a well-defined mesh, and well-set boundary conditions 3D simulations of multiple cracks' growth gives good results. It also showed that for three-dimensional cracked structures, this kind of analysis can be fully acknowledged. This is of great importance for fatigue life estimation of aircraft structures, such as fuselage or wing with riveted joints, which are very often exposed to multiple site damage.

Also, the analyses using XFEM were conducted on the curved cracked panels, as well. Based on the results from those analyses following conclusions can be made:

-First numerical example:

1- The longest recorded crack lengths occurred when the diameter of the fuselage was equal to 2.4 m (crack 2, 17.81802 mm) followed by crack number 1 when D equal to 2.4 m

(17.1846 mm), while the shortest crack length recorded for crack number 6 (0.7047 mm) when D was equal to 1.6 m.

2- The MSD crack linkup in the panel occurred between cracks 2 and 3 when D equal to 1.6 m and 2.4 m, while the MSD linking up occurred between cracks 2 and 3 and between crack 4 and 5 when D was equal to 4 m. the resulted long lead crack for each linkup was 20.2 mm.

3- The applied pressure in this simulation (see figure 5.2) is considered too high due to the fact that panel was not supported with any kind of truss such as stringers or frames and this is the reason of the higher obtained K_I values and the existence effect of the failure modes II and mode III.

-Second numerical example:

1- At this numerical example, cracks 2, 3, 4, 6, 8, and 10 had their longest length when D was equal to 2.4 m (the longest recorded length was to crack 10, CL= 29.0878 mm, but the longest recorded length in this case was recorded for crack 1 (42.6233 mm) when D was equal to 4 m. Cracks 3, 5, 6, 7, 8, and 10 had their shortest length when D was equal to 3.2 m (crack 6, 5.17194 mm), while the shortest length in this simulation recorded to crack 2 (2.3956 mm) when D was equal to 4 m

2- The linking up process between the multiple cracks which represents MSD phenomena occurred between all cracks in the case when D was equal to 2.4 m, between cracks from 3 to 10 in the case when D was equal to 3.2 m and 4 m.

3- The applied pressure in this simulation (figure 5-32) which produced a high applied stress, is considered too high due to the fact that panel was not supported with any kind of truss such as stringers of frames and that is also the reason of the higher obtained SIFs values and the existence effect of the failure modes II and mode III.

-Third numerical example:

1- The longest crack lengths occurred when the diameter of the fuselage was equal to 2.4 m (crack 1, CL=48.28 mm) while the shortest occurred also when D was equal to 3.2 m crack 12, CL=0.8638).

2- The linking up process between the multiple cracks which represents MSD phenomena occurred between the cracks in the most cases.

3- The applied pressure in this simulation (figure 5-95) which produced a high applied stress, is considered too high due to the fact that panel was not supported with any kind of truss such as stringers or frames and this is also the reason of the higher obtained SIFs values and the existence effect of the failure modes II and mode II

4- During the simulation, the interaction between crack fronts occurred between cracks from 1 to 10 when D was equal to 2.4 m while the interaction occurred between cracks from 5 to 10 when D was equal to 1.6 m. The interaction between crack fronts from 3 to 6 occurred when D was equal to 4 m; however, no interaction occurred between the whole cracks when D was equal to 3.2 m.

-Fourth numerical example:

1- The longest crack lengths occurred when the diameter of the fuselage was equal to 2.4 m (crack 9, CL=13.578 mm) followed by its lengths when D was equal to 1.6 m (crack 3, CL=11.741 mm), also, during this simulation, in the most cases the longest recorded length was recorded when D was equal to 1.6 m and 2.4 m.

2- The minimum recorded lengths at this simulation were when D was equal to 3.2 m (crack 9. CL=0.8482 mm), but in the most cases the shortest recorded lengths were recorded when D was equal to 4 m (crack 19, CL=0.8539 mm).

3- The linking up process between the multiple cracks which represents MSD phenomena occurred between cracks from crack 9 to crack 22 in the case when D was equal to 2.4 m, and between cracks from 3 to crack 16 in the case when D was equal to 1.6 m; While the other simulations when D was equal to 3.2 m and 4 m did not show any interaction between the crack in the whole panel.

4- The applied pressure in this simulation (figure 5-164) which produced a high applied stress, is considered too high due to the fact that the panel was not supported with any kind of truss such as stringers or frames and this is, again, the reason of the higher obtained SIFs values and the existence effect of the failure modes II and mode II.

Chapter six showed the results comparisons between flat panel (first numerical example, applied stress 200 MPa) and the curved panel (D=2.4m); the results showed that as the applied stress increased from 50 to 200 MPa, the cracks length were increased too. The last

comparison case (applied stress 200 MPa, flat panel) showed that the lengths of selected cracks were longer than the similar cracks lengths in the case of curved panel ; but the difference was that the recorded SIFs in the case of curved panel was higher due to the fact that applied pressure produced the effect of the failure modes K_{II} and K_{III}. Also, this chapter showed the effect of curved panel truss by using frames. It is established that this kind of truss reduces the values of K_I, K_{II} and K_{III} for crack 11 to almost 56 times and 54 times for crack 12.

The future study includes:

- Deduction of the geometry factor (β) equations, with special attention on the relation of geometry factor on cracks propagation for the curved panels.

- Analysis of the effects of certain parameters on SIFs value for the flat panels such as: effect of panel's thickness and different panel material like modern alloys AA7075, AA2017 and AA7085.

References

[1] *Schmidt, H. J. and Brandecker, B.*, On widespread fatigue damage, durability of metal aircraft structures, Proceedings of the International Workshop on Structural Integrity of Aging Airplanes, 31 March 2 April, Atlanta, Springer-Verlag, 1992, pp. 279-295.

[2] *Schmidt, H. J.*, Current and future airworthiness regulations regarding damage tolerance and fatigue evaluation of structure, Technology Seminar Advanced Fuselage design with respect of fatigue and Damage Tolerance, EADS Airbus GmbH, January 2001

[3] *Nesterenko, G. I.*, Multiple site fatigue damages of aircraft structures and Widespread fatigue damage in military aircraft, 80th Meeting of the AGARD (Advisory Group for Aerospace Research and Development) Structures and Materials Panel Conference Proceedings, Rotterdam, The Netherlands, ISBN 92-836-1021-0, May 1995.

[4] *Dawicke, D. S., Phillips, E. P., Swenson, D. V. and Gondhalekar. S.*, Crack growth from loaded countersunk rivet holes, durability of metal aircraft structures, Proceedings of the International Workshop on Structural lntegrity of Aging Airplanes, 31 March-2 April, Atlanta, Springer-Verlag, 1992, pp. 75-90.

[5] *Broek, D.*, Analysis concerning the inspection threshold for multi-site damage, DOT/FAA/CT-93/7

[6]*Sampath, S. and Broek, D.*, Estimation of requirements of inspection intervals for panels susceptible to multiple site damage, Structural lntegrity of Aging Airplanes, Springer-Verlag, 1991

[7] *Broek, D.*, Elementary Engineering Fracture Mechanics, Njihoff, 1985.

[8] *Tong, P., Greif. R. and Chen, L.*, Computational Mechanics, 1994, 13, p. 285-294.

[9] *Tan. P. W., Bigelow, C. A., O'Donoghue, P. E. and Atluri, S, N.*, Stress-intensity factor solutions for cracks at countersunk rivet holes under uniaxial tension, Atlantic City International Airport. NJ 08405, February 1994.

[10] *Swift, T.*, Repairs to damage tolerant aircraft, Structural Integrity of Aging Airplanes, Spirnger-Verlag, pp 433-483,1991.

[11] *Berens, A. P., Burns, J. G. and Rudd, J. L.*, Risk analysis for aging aircraft fleets, Structural Integrity of Aging Airplanes,. Springer-Verlag, 1991, p. 38-51.

[12] *Samavedam, G., Hoadley, D. and Davin, J.*, Test facility for evaluation of structural integrity of stiffened and jointed aircraft curved panels, Structural Integrity of Aging Airplanes, Springer-Verlag, 1991, p. 321-337.

[13] *Broek, D.*, The civil damage tolerance requirements in theory and practice, Structural Integrity of Aging Airplanes Springer-Verlag, 1991, p. 73-86.

[14] J. Schijve, Fatigue of Structures and Materials, 2ed edition, Springer (2008)

[15] Irwin, G.R., Analysis of stresses and strains near the end of a crack traversing a plate. Trans. ASME, J. Appl. Mech., Vol. 24 (1957), pp. 361–364.

[16] Paris, P.C. and Erdogan, F., A critical analysis of crack propagation laws. Trans. ASME, Series D, Vol. 85 (1963), pp. 528–535

[17] Forman, R.G., Kearney, V.E. and Engle, R.M., Numerical analysis of crack propagation in cyclic-loaded structures. J. Basic Engrg., Trans. ASME, Vol. D89 (1967), pp. 459–464.

[18] Priddle, E.K., High cycle fatigue crack propagation under random and constant amplitude loadings. Int. J. Pressure Vessels & Piping, Vol. 4 (1976), p. 89.

[19] Klesnil, M. and Lukáš, P., Influence of strength and stress history on growth and stabilization of fatigue cracks. Engrg. Fracture Mech., Vol. 4 (1972), pp. 77–92.

[20] Elber, W., The significance of fatigue crack closure. Damage tolerance in aircraft structures. ASTM STP 486 (1971), pp. 230–242.

[21]Rice, J.R., The mechanics of crack tip deformation and extension by fatigue. Fatigue crack propagation. ASTM STP 415 (1967), pp. 247–309

[22] J. Schijve, Some formulas for the crack opening stress level. Engrg. Fracture mechanics, Vol. 14 (1981), pp. 461-465.

[23] Van der Linden, H.H., NLR test results as a database to be used in a check of crack propagation prediction models. A Garteur activity. Nat. Aerospace Lab. NLR, TR 79121U, Amsterdam (1979).

[24] "Aircraft Accident Report – Aloha Airlines, Flight 243, Boeing 737 – 200, N73711, near Maui, Hawaii, April 1988", NTSB/AAR-89/03, National Transportation Safety Board, Washington, D.C. 20594, June 1989.

[25]Andrzej. S. Malgorzata. S,"Riveted Lap Joints in Aircraft Fuselage",Solid Mechanics and its Applications, Vol.189, 2012.

[26] G. Kastratovic, A. Grbovic, N. Vidanovic and B. Rasuo, "A Finite Element Calculation of Stress Intensity Factors in Structures with Multi-Site Damage (MSD)", International Conference on Damage Mechanics, Belgrade, Serbia,25-27 June 2012.

[27] E. Rakipovski, A. Grbovic, G. Kastratovic and N. Vidanovic, "Application of Extended Finite Element Method for Fatigue Life Predictions of Multiple Site Damage in Aircraft Structure", Structural Integrity and Life, Vol. 15, pp. 3-6.

[28] G. Kastratovic, A. Grbovic and Nenad Vidanovic, "Approximate Method for Stress Intensity Factors Determination in case of Multiple site damage",Applied Mathematical Modelling, 39 (2015) 6050-6059.

[29] G. Kastratovic, A. Grbovic and N. Vidanovic, "Approximate determination of stress intensity factors for Penny Shaped cracks in Three Dimensional Elastic Solids",5th International Congress of Serbian Society of Mechanics, Serbia, June 15-17, 2015.

[30] G. Kastratovic, "Assessment of the Interaction between Multiple Crack tips Effect on Stress Intensity Factor", First Serbian (26th YU) Congress on Theoretical and Applied Mechanics, Kopanik, Serbia , April 10-13,2007.

[31] H. Rajiyah and S. N. Atluri, "Evaluation of K-Factors and Weight Functions for 2-D Mixed-Mode Multiple Cracks by the Boundary Element Alternating Method ", Engineering Fracture Mechanics, Vol.32,No. 6, pp. 911-922, 1989.

[32] Bert L. Smith, Perry A. Saville, Adil Mouak and Roy Y. Myose, "Strength of 2024-T3 Aluminum Panels with Multiple Site Damage", Journal of Aircraft, Vol.37, No.2, March-April 2000.

[33] J. H. Kuang and C. K. Chen, "Use of Strip Yield Approach for Multiple Site Damage Failure Scenarios", Journal of Aircraft. Vol.37, No. 5, September-October 2000.

[34] Dawicke, D. S. and Newman, Jr. J. C., "Analysis and prediction of multiple-site damage (MSD) fatigue crack growth", NASA Technical paper 3231, 1992.

[35] O. Partl and J. Schijve, "Multi Site Damage in 2024-T3 Alloy Sheet", Report LR-660, January 1992.

[36] G. Labeas, J. Diamantakos and Th. Kermanidis, "Crack Link-up for Multiple Site Damage using an Energy Density Approach", Theoretical and Applied Fracture Mechanics, 43 (2005) 233-243.

[37] C. Proppe, "Probabilistic Analysis of Multi-Site Damage in Aircraft Fuselages", Computational Mechanics, 30 (2003) 323-329.

[38] R. Elangovan, B. Dattaguru, T.S. Ramamurthy and V. Selladurai, "Development of Design Charts for Stress Intensity Factors at Tips of Multi-Site Cracks in Un-stiffened Curved Panels", Engineering Fracture Mechanics, 119 (2014) 116-123.

[39] M. F. J. Koolloos, F. P. Grooteman and H. J. T. Hoeve,"Analysis of Residual Strength of Flat and Curved Panels, with and without Stiffeners, with Multiple Site Damage", National Aerospace Laboratory NRL, Report No.: DOT/FAA/AR-06.37, December 2006.

[40] A. Ng, C. Bil and G. Clark, "Suitability of Different Crack Growth Models for Analysing Multi-Site Damage in Different Aircraft Structural Configuration", Thirteenth Australian International Aerospace Congress, 10-12 March, 2016.

[41] A. R. Ingraffea, "Crack Interaction and Multi-Site Damage", DTD Handbook,

[42] lsida, M., Bulletin of the JSME, 1970, 13(59).

[43]Jones, R., Hammond, S. and Williams, J. F., Computers and Structures, 1995, p.178-183.

[44] lsida, M. and lgawa, H., International Journal of fracture. 1992., 55, p.249-260.

[45]Rajiyah, H. and Atluri, S. N., Engineering Fracture Mechanics, 1989, 32(6), p. 911-922.

[46]Binienda, W. K., Arnold, S. M., Tan. H. Q. and Xu. M. H. Computational Mechanics, 1993, 12, p.297-314.

[47]Beuth, J. L. and Hutchinson, J. W., Computational Mechanics, 1994, 13, p.315-331.

[48]Dawicke, D. S. and Newman, Jr. J. C., Analysis and prediction of multiple-site damage (MSD) fatigue crack growth, NASA Technical paper 3231, 1992.

[49]Bowie, O. L., Rectangular tensile sheet with symmetric edge cracks, J. Appl. Mech. 31, (1964)

[50] Benthem, J. P., Koiter, W. T., Mechanics of fracture, Vol. I, Ch. 3, 1973.

[51]Brown, W. F., Strawley, J. E., STP 410, ASTM 1966.

[52]Willmore, Q. J., Mech. Appl. Math., 2, 53, 1949.

[53]Tranter, C. J., Mech. Appl. Math., 14, 283, 1961.

[54]Savin, G. N., Stress distribution around holes, NASA TT F-607, Ch. VII, 1970.

[55]Sih, G. C., Handbook of Stress Intensity Factors, Institute of Fracture and Solid Mechanics, Lehigh University, 1973.

[56]Timoshenko, S. P., and Goodier, J. N., Theory of Elasticity, Third ed. McGraw-Hill Book Co., Inc., 1970.

[57]Westergaard, H. M., Bearing Pressures and cracks, J. Appl. Mech. Vol. 6, p. A49-A53 June 1939.

[58]Tada, H., and Paris, P.C., Irwin, G.R., The Stress Analysis of Cracks Handbook, Del Research Corp., 1973., 1986.

[59]Rice, J. R., A path independent integral and the approximate analysis of strain concentration by notches and cracks. J. appl. Mech. 35, 379, 1968.

[60]Cartwright, D. J. and Rooke, D. P. Approximate stress intensity factors compounded from known solutions, Engineering Fracture Mech. 6, 1974.

[61]Rooke, D. P., and Cartwright, D. J., Compendium of Stress Intensity Factors, London, HMSO, 1976.

[62]Pu, S. O., and Hussain, M. A., Stress intensity factors for a circular ring with uniform array of radial cracks using cubic isoparametric singular elements, Fracture Mechanics, ASTM STP 677, 1979.

[63]Rooke, D. P., Stress intensity factors for cracked holes in the presence of other boundaries, Fracture Mechanics in Engineering Practice, Applied Science, London 1977.

[64]Kastratović, G., i Krivošić, I., Uticaj interakcije izmedu granica na vrednost faktora intenziteta napona, Tehnika – Mašinstvo, 3, str. M1-M6, 2005.

[65]Kastratović, G., Uticaj oblika nosece vazduhoplovne strukture na vrednost faktora intenziteta napon, Magistarski rad, Mašinski fakultet Univerziteta u Beogradu, jul 2003.

[66] Singh, Krishna Lok, Kamal Keswani, and Mallikarjun Vaggar. "Crack growth simulation of stiffened fuselage panels using XFEM techniques." (2014).

[67]Ahmed, Awais. "Extended finite element method (XFEM)-modeling arbitrary discontinuities and failure analysis." *Research degree thesis* (2009).

[68] Datta, Dibakar. "Introduction to eXtended Finite Element (XFEM) Method." *arXiv preprint arXiv:1308.5208* (2013).

[69] Zhang, Chao, et al. "Using Finite Element Software to Simulation Fracture Behavior of Three-point Bending Beam with Initial Crack." *JSW* 8.5 (2013): 1145-1150.

[70] Kumar, Vineet, Indra Vir Singh, and Bhanu Mishra. "XFEM, Crack Growth Examination Of Cryo-Rolled (CR) 6082 Al Alloys." *Int. J. Emerg. Technol. Adv. Eng* 4.1 (2014): 264-271.

[71] Du, Zhen-zhong. "eXtended Finite Element Method (XFEM) in Abaqus." *Retrieved February* 9 (2009): 2013.

[72] Belytschko, Ted, Robert Gracie, and Giulio Ventura. "A review of extended/generalized finite element methods for material modeling." *Modelling and Simulation in Materials Science and Engineering* 17.4 (2009): 043001.

[73] Giner, E., et al. "An Abaqus implementation of the extended finite element method." *Engineering fracture mechanics* 76.3 (2009): 347-368.

[74] Sepehri, Jay. *Application of extended finite element method (XFEM) to simulate hydraulic fracture propagation from oriented perforations*. Diss. 2014.

[75] Melenk, Jens M., and Ivo Babuška. "The partition of unity finite element method: basic theory and applications." *Computer methods in applied mechanics and engineering* 139.1-4 (1996): 289-314.

[76] Osher, Stanley, and James A. Sethian. "Fronts propagating with curvature-dependent speed: algorithms based on Hamilton-Jacobi formulations." *Journal of computational physics* 79.1 (1988): 12-49.

[77] Dolbow, John, Nicolas Moës, and Ted Belytschko. "Discontinuous enrichment in finite elements with a partition of unity method." *Finite elements in analysis and design* 36.3 (2000): 235-260.

[78] Fleming, M., et al. "Enriched element-free Galerkin methods for crack tip fields." *International journal for numerical methods in engineering* 40.8 (1997): 1483-1504.

[79] Stazi, F. L., et al. "An extended finite element method with higher-order elements for curved cracks." *Computational Mechanics* 31.1 (2003): 38-48.

[80] Fries, Thomas-Peter. "A corrected XFEM approximation without problems in blending elements." *International Journal for Numerical Methods in Engineering* 75.5 (2008): 503-532.

[81] Dessault systems, Abaqus Manual, 2012

[82] Hansbo, Anita, and Peter Hansbo. "A finite element method for the simulation of strong and weak discontinuities in solid mechanics." *Computer methods in applied mechanics and engineering* 193.33 (2004): 3523-3540.

[83]Ren, X. D., et al. "Comparison of the simulation and experimental fatigue crack behaviors in the nanoseconds laser shocked aluminum alloy." *Materials & Design* 32.3 (2011): 1138-1143.

[84]Baumgart, Bruce G. "A polyhedron representation for computer vision." *Proceedings of the May 19-22, 1975, national computer conference and exposition*. ACM, 1975.

[85]Weiler, Kevin. "Edge-based data structures for solid modeling in curved-surface environments." *IEEE Computer graphics and applications* 5.1 (1985): 21-40.

[86]Henshell, R. D., and K. G. Shaw. "Crack tip finite elements are unnecessary." *International journal for numerical methods in engineering* 9.3 (1975): 495-507.

[87] Shaw, R. D., and R. G. Pitchen. "Modification to the Suhara-Fukuda method of network generation." *International Journal for Numerical Methods in Engineering* 12.1 (1978): 93-99.

[88] Erdogan, Fazil, and G. C. Sih. "On the crack extension in plates under plane loading and transverse shear." *Journal of basic engineering* 85.4 (1963): 519-527.

[89] Hussain, M. A., S. L. Pu, and J. Underwood. "Strain energy release rate for a crack under combined mode I and mode II." *Fracture Analysis: Proceedings of the 1973 National Symposium on Fracture Mechanics, Part II*. ASTM International, 1974.

[90]Sih, George C. "Strain-energy-density factor applied to mixed mode crack problems." *International Journal of fracture* 10.3 (1974): 305-321.

[91] J.J. Luzar, Pre-corroded Fastener Hole Multiple Site Damage Testing, Final Report, EA 96-135OTH-041, Boeing ISDS Post-Production/Derivative Aircraft Division, December 1997.

[92] E. Rakipovski, A. Grbovic , G. Kastratovic, N. Vidanovic, Application of XFEM for fatigue life predictions of MSD in aircraft structure, Structural integrity and life, 15 (2015) 3-6.

[93] U. Zerbst, M. Heinimann, C.D. Donne, D. Steglich, Fracture and damage mechanics modeling of the walled structures-an overview, Engineering Fracture Mechanics, 76 (2009) 5–43.

[94] R. Elangovan, B. Dattaguru, T.S Ramamurthy, V. Selladurai, Development of design charts for stress intensity factors at tips of multisite cracks in unstiffened curved panels, Engineering fracture mechanics, 119 (2004) 116-123.

[95] Wang, X., M. Modarres, and P. Hoffman. "Analysis of crack interactions at adjacent holes and onset of multi-site fatigue damage in aging airframes." *International journal of fracture* 156.2 (2009): 155-163.

[96] A. R. Khoei, Extended finite element method: theory and applications, John Wiley & Sons, Ltd., 2015

[97] G. Kastratović, Determination of stress intensity factor of supporting aero structures with multiple site damage, PhD Thesis, (in Serbian), Faculty of Mechanical Engineering, University of Belgrade, Serbia, (2006).

[98] J. L. Beuth and J. W. Hutchinson, 1994), Fracture analysis of multi-site cracking in fuselage lap joints, Computational Mechanics, 13 (1994) 315-331.

[99] Megson, Thomas Henry Gordon. Introduction to aircraft structural analysis. Butterworth-Heinemann, 2013.

[100] J.E. Gordon. Structures or Why Things Don’t Fall Down. Da Capo Press, Inc. 1978.